UNCLASSIFIED

AD NUMBER

AD894688

NEW LIMITATION CHANGE

TO

Approved for public release, distribution unlimited

FROM

Distribution authorized to U.S. Gov't. agencies only; Test and Evaluation; 05 JUN 1972. Other requests shall be referred to Army Advanced Ballistic Missile Defense Agency, ATTN: RDMH-M, PO Box 1500, Huntsville, AL 35807.

AUTHORITY

BMDSC D/A ltr dtd 19 Feb 1975

THIS PAGE IS UNCLASSIFIED

AD894688

FILE COPY

VOLUME II: APPENDIXES

RADIATION-TOLERANT LASER GYRO SUBSYSTEM DEVELOPMENT

Final Report

Prepared for

U.S. Army Advanced Ballistic
Missile Defense Agency
Huntsville, Alabama

Contract No. DAHC60-71-C-0041

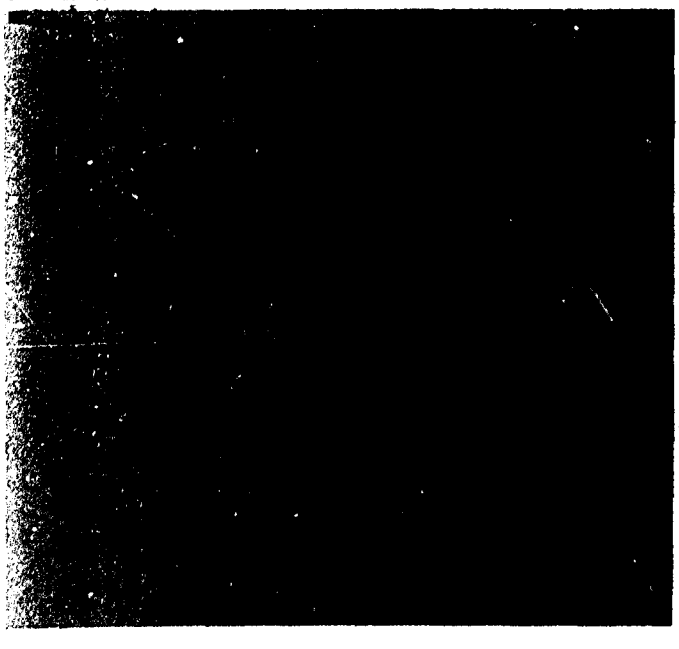

Honeywell

GOVERNMENT AND AERONAUTICAL PRODUCTS DIVISION

Z9080-3010

30 May 1972

For Mr. Riviere
8/742-3802

Distribution limited to U.S. Gov't. agencies only; Test and Evaluation; 5 JUN 1972. Other requests for this document must be referred to

U.S. Army Advanced Ballistic Missile Defense Agency
attn: RDMH-M
P.O. Box 1500
Huntsville, Ala. 35807

R. Newsom
6-5-72

ACCESSION for
CFSTI WHITE SECTION ☐
DDC Buff SECTION ☑
UNANNOUNCED ☐
JUSTIFICATION .....
.....
BY .....
DISTRIBUTION/AVAILABILITY CODES
DIST. | AVAIL. and or SPECIAL
A

Honeywell

(11) 30 May 72

(12) 487 p.

(6) RADIATION-TOLERANT LASER GYRO SUBSYSTEM DEVELOPMENT.

[redacted]

Volume II. Appendixes.

Prepared for

(9) Final rept.,

U.S. Army Advanced Ballistic
Missile Defense Agency
Huntsville, Alabama 35807
attn: RDMH-M

Contract No. DAHC60-71-C-0041

(15)

Distribution limited to U.S. Gov't. agencies only; Test and Evaluation; for this document 5 JUN 1972. Other requests for this document must be referred to

Prepared by:

(10) R. R. Johnson
Sr. Development Engineer

Approved by:

M. F. Demos
Project Engineer

T. A. Thompson
Contract Administrator

Government and Aeronautical Products Division
2600 RIDGWAY PARKWAY, MINNEAPOLIS, MINNESOTA 55413

Z9080-3010 Printed in U.S.A.

AD-A141 505

FOREWORD

The development of a radiation-tolerant LARS subsystem involves five main phases:

- Circuit design
- Computer modeling of circuits
- Transient radiation testing to verify the computer models
- Neutron radiation testing to verify the computer models
- Computer-aided analysis to determine the radiation tolerance levels

Because of the bulk of testing and test data generated, the report has been divided into two sections with the circuit design approaches (classified), the circuit analyses (classified), and the summary of the results (classified) presented in Volume I (classified). This volume contains the following five appendices:

CONTENTS:

Appendix A - Vulnerability Analysis and Nuclear Hardening of Laser Gyro Circuit Assemblies;

Appendix B - Superflash X-Ray Test;

Appendix C - Hardened Laser Angular Rate Sensor;

Appendix D - Paper "The Laser Gyro" by ~~J. E. Killpatrick~~ Gmt

Appendix E - Predicted Effects of X-Radiation Upon the Glow Discharge and Output Signal of a Helium-Neon Laser, ~~T. J. Podgorski~~

APPENDIX A

VULNERABILITY ANALYSIS AND NUCLEAR HARDENING OF LASER GYRO CIRCUIT ASSEMBLIES -- FINAL REPORT (U)

VOLUME I

VULNERABILITY ANALYSIS AND NUCLEAR HARDENING OF LASER GYRO CIRCUIT ASSEMBLIES - FINAL REPORT (U)

Honeywell, Inc., P.O. No. DY 690401

March 1972

OR 11,843

Prepared by: J. M. Tanke
Principal Investigator

Approved by: J. E. Krips
Manager, Electronics,
Advanced Air Defense

Approved by: W. P. Wesley
Manager
Advanced Air Defense

Martin Marietta Corporation
Orlando, Florida

FOREWORD

This final report was prepared in accordance with Honeywell Incorporated P.O. DY690401, which is a subcontract under the Advanced Ballistic Missile Defense Agency (ABMDA) prime contract DAHC60-71-C-0041. The report covers vulnerability analysis and nuclear hardening of laser gyro circuit assemblies.

Program objectives were as follows:

1. Develop analytic models and perform analyses to predict circuit response to a nuclear environment.

2. Analyze the electronic circuit assemblies of the laser gyro to the neutron and gamma environment specified for advanced interceptor systems.

3. Assist Honeywell Incorporated in conducting laboratory radiation tests on breadboard and prototype circuits.

4. Use the SECURE computer code to determine the vulnerability of the system to a SPRINT weapon profile and a SPRINT underground test profile.

Accomplishment of the program objectives is presented in two volumes. Volume I (Unclassified) contains various component and computer modeling data. Volume II (Secret Restricted Data) contains the system vulnerability analysis.

The program accomplishments were made possible only through the close cooperation of the Honeywell and Martin Marietta staff. Specific Martin Marietta personnel who assisted during the course of the contract are as follows:

Program Coordination

W. W. Mras

Analytic Support

Dr. E. H. Lowe

W. J. Dillon

S. J. Monte

CONTENTS

1. Introduction 1-1

2. Component Selection 2-1

3. Semiconductor Model Parameters 3-1

4. Readout Amplifier 4-1

5. Trigger Circuit 5-1

6. Direction Logic Circuit 6-1

7. Divide-by-16 Counter Circuit 7-1

8. Pulse Stretcher and Line Driver Circuits 8-1

9. Start/Restart Circuit 9-1

10. +5 Volt Switching Regulator 10-1

11. +10 Volt Switching Regulator 11-1

12. DC-to-DC Converter and High Voltage Power Supply 12-1

Appendixes

A. Nuclear Radiation Hardness Assurance for Electronics . . A-1

B. Fairchild Radiation Test Data for 2N5107 and 2N5244 . . . B-1

C. SPRINT II Nuclear Test Plan Fast Burst Reactor/WSMR - February 7, 1972 . . . . . C-1

References R-1

ILLUSTRATIONS

1-1. Laser Angular Rate Sensor System Block Diagram 1-2

2-1. Motorola MCE5400 Chip 2-4
2-2. MCE5400 Two-Input NAND Gate 2-5
2-3. Computer Simulation of TI and Motorola 54H00 Gates 2-6
2-4. Summary of 5400d 10, 20, 30, and 04 Gate Characteristics . . . 2-8
2-5. Summary of 54H00, 10, 20, 30, and 04 Gate Characteristics . . . 2-10
2-6. Gamma Dot Response of TTL 54H00 Digital Integrated Circuits . . 2-11

3-1. TRAC NPN Transistor Model 3-4
3-2. TRAC PNP Transistor Model 3-5
3-3. TRAC Diode Model 3-6

4-1. Readout Amplifier 4-2
4-2. Readout Amplifier with Output Stage 4-3
4-3. Predicted Response of Readout Amplifier without Output Stage . 4-4
4-4. Modified Readout Amplifier 4-5
4-5. Readout Amplifier Trigger Circuit 4-6
4-6. Readout Amplifier 4-7
4-7. New Readout Amplifier Trigger Circuit 4-9
4-8. Readout Amplifier and Trigger Circuit Response to FBR Environment 4-10
4-9. Computer Simulation of Readout Amplifier and Trigger Circuit to FBR Environment 4-12
4-10. Computer Simulation of Readout Amplifier and Trigger Circuit to FBR Environment 4-13
4-11. Computer Simulation of Readout Amplifier and Trigger Circuit to FBR Environment 4-14

5-1. Readout Amplifier Trigger Circuit 5-2
5-2. Predicted Response - Readout Amplifier and Trigger Circuit at FBR 5-3
5-3. Readout Amplifier Trigger Circuit 5-4

5-4. Redesigned Trigger Circuit Response to Beta Degradation 5-5

5-5. Direction Circuit and Normal UP-Count Timing Diagram 5-6

5-6. Timing Diagram for a Less Than 24 Percent Duty Cycle 5-7

5-7. Timing Diagram for a More Than 75 Percent Duty Cycle 5-8

5-8. Trigger Circuit Duty Cycle Sensitivity Due to Input Voltage and Reduced Transistor Gains 5-9

5-9. Transistor Q3 Turnoff Circuit 5-10

5-10. Trigger Circuit 5-11

6-1. UP-Count Direction Logic 6-2

6-2. 5401 One-Shot Ionization 6-3

7-1. 54H103 J-K Flip-Flop 7-2

8-1. UP-Count Line Driver 8-2

8-2. Timing Circuit 8-3

8-3. Predicted Radiation Response of Line Driver 8-4

9-1. Laser Gyro Start/Restart Circuit 9-2

9-2. Start/Restart Circuit Output 9-3

10-1. +5 Volt Switching Regulator 10-2

10-2. Computer Simulation of +5 Volt Regulator Output in SFXR Environment 10-3

10-3. +5 Volt Regulator Response to a Dose Rate of Approximately $1x10^9$ rads(Si)/s 10-4

10-4. +5 Volt Regulator Response to a Dose Rate of Approximately $5x10^{11}$ rads(Si)/s 10-5

10-5. Transistor Current Gain - Bursts 2 and 3 10-7

10-6. Transistor Current Gain - Burst 7 10-8

10-7. Predicted Response of +5 Volt Regulator at FBR (15 Volt Input) 10-9

10-8. Predicted Response of +5 Volt Regulator for FBR Environment . . 10-11

10-9. +5 Volt Regulator No. 2 Response to FBR Burst 9 10-12

10-10. Computer Simulation of +5 Volt Regulator with Ionization Input Only (17.5 Volt Input) 10-12

10-11. Modified +5 Volt Switching Regulator 10-13

10-12. Power Stage 10-15

10-13. Photocurrent Alternate Path 10-16
10-14. Photocurrent Distribution - Q2 OFF 10-17
10-15. Photocurrent Distribution - Q1 OFF 10-17
10-16. +5 Volt Regulator Response to Long Ionization Pulse Using Martin Marietta Photocurrent Compensation Technique 10-18

11-1. +10 Volt Switching Regulator 11-2
11-2. Predicted Response of +10 Volt Regulator for FBR Environment . 11-3
11-3. +10 Volt Regulator No. 1 Response to FBR Bursts 5 through 8 . . 11-5
11-4. +15 Volt Regulator No. 2 Response to FBR Bursts 9 through 12 . 11-6
11-5. Predicted Response of +10 Volt Regulator for an SFXR Dose Rate of $1x10^9$ rads(Si)/s 11-8
11-6. +10 Volt Regulator Response for a Dose Rate of 1.0 to $1.5x10^9$ rads(Si)/s 11-9
11-7. Predicted Response of +10 Volt Regulator for an SFXR Rate of $5x10^{11}$ rads(Si)/s 11-10
11-8. +10 Volt Regulator Response for a Dose Rate of 2.0 to $4.1x10^{11}$ rads(Si)/s 11-11
11-9. +15 Volt Regulator Response for a Dose Rate of 4.0 to $6.6x10^{11}$ rads(Si)/s 11-12

12-1. Laser Gyro High Voltage Supply 12-2
12-2. Converter Response - Collector Voltage versus Time 12-3
12-3. Converter Response - Transistor Power versus Time 12-4
12-4. Converter Response - Start Voltage versus Time 12-5
12-5. Converter Response - 1000 Volt Supply versus Time 12-6
12-6. General Form of Nuclear Response at the Output Terminals . . . 12-8

1. INTRODUCTION

The laser gyro hardening program was conducted to develop and evaluate a laser angular rate sensor (LARS) system for use in high performance missile applications in a nuclear environment. A block diagram of the LARS system is presented in Figure 1-1. Volume I (Unclassified) contains component test data, individual circuit descriptions, computer modeling data, and individual circuit test data taken at various radiation facilities. Volume II (Secret-Restricted Data) contains system nuclear design goals, system nuclear analysis, and the results of the system vulnerability determination. Conclusions and recommendations are also included in Volume II.

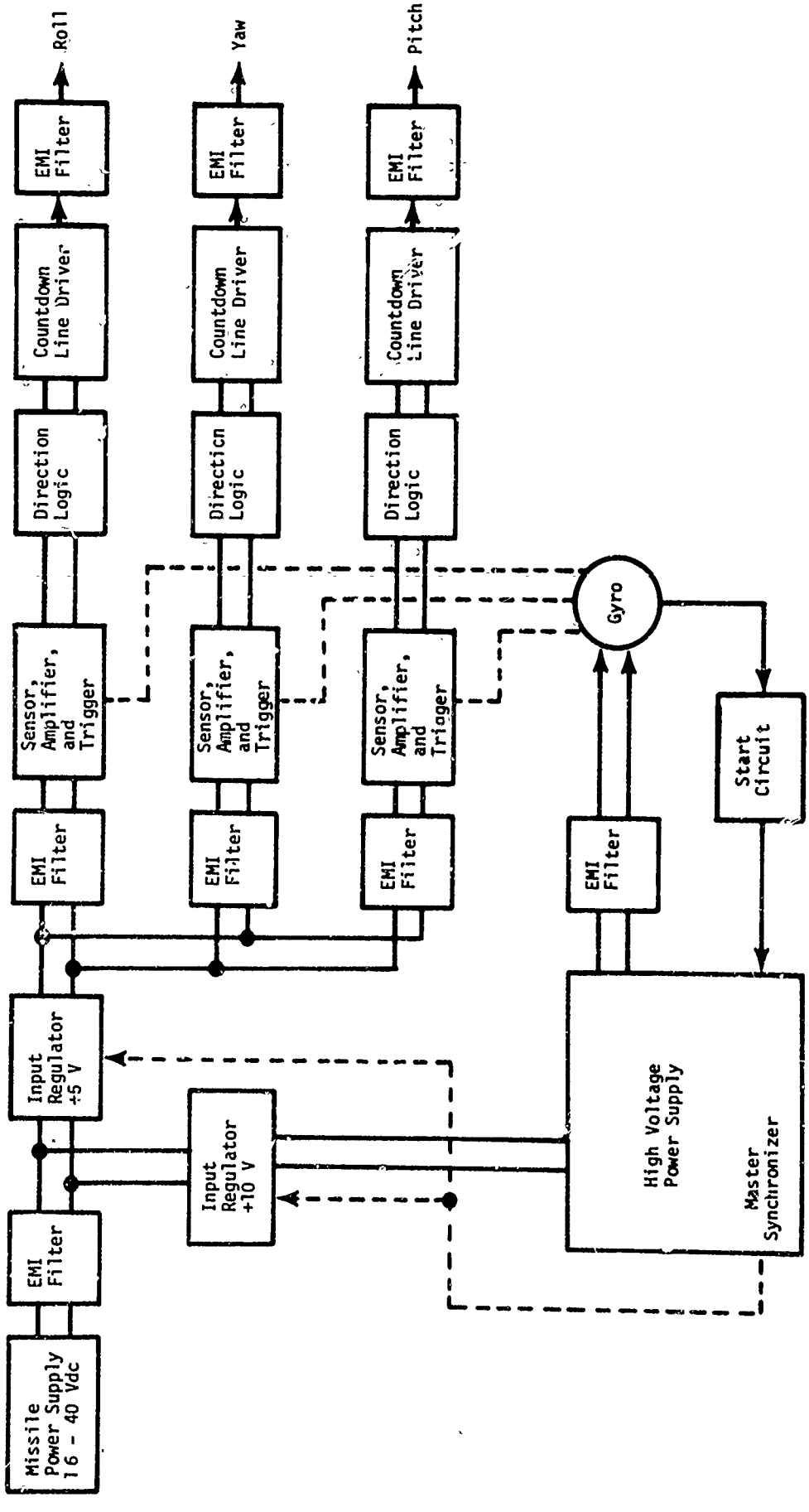

Figure 1-1. Laser Angular Rate Sensor System Block Diagram

2. COMPONENT SELECTION

Hardening of the laser gyro electronic circuits required a complete redesign to include the radiation hardened devices. These devices, normally selected by test and analysis, were choosen from available radiation resistant components listed in the literature. This method of selection was used because of time and fund limitations of the program.

Several circuits in the laser gyro use differential amplifiers that consist of a matched pair of NPN transistors in a single package. For this application, the Union Carbide 2N4878 (2N4040) was selected, due to its high gain. The 2N4878 is a monolithic silicon planar dual transistor with dielectric isolation, incorporating many features that are desirable for differential amplifier application. Although this device is not called out as a radiation hardened device (f_T = 200 MHz), the initial high h_{FE} of 225 minimum (350 nominal) and the neutron test data called out in Reference 1 indicated that there would be sufficient gain at the specified levels.

Other discrete devices originally considered were the 2N2222A and 2N2907, but these were gradually replaced by the commercially available radiation resistant Fairchild 2N5244 and 2N5107 transistors. The only available power transistors were the Solitron BR100 and the higher power BR200. The BR100 was found to be adequate in all applications and therefore was selected for use. The 2N3302 and 2N4035 were used as diodes to provide low cost photocurrent compensation for the 2N5107 and 2N5244 transistors.

The digital logic originally selected was the Texas Instrument (TI) or Motorola dielectrically isolated radiation resistant 5400 series. However, manufacturers' delivery time prohibited using the 5400 series. For that reason, the 54H series TTL logic was selected. A comparison of the switching times and dissipation per gate is listed below:

Digital Logic Series	Dissipation/Gate	Switching Speed
54 standard	10 mW	10 ns
54 H	20 mW	6 ns
54 L	1 mW	30 ns

Table 2-I summarizes the transistors used in the laser gyro hardening program.

TABLE 2-I

Laser Gyro Transistor Selection

Device	Type and Application	Manufacturer
2N4878	NPN dual monolithic silicon planar differential amplifier	Union Carbide
2N5107	NPN radiation resistant general purpose amplifier and switch	Fairchild
2N5244	PNP radiation resistant general purpose amplifier and switch	Fairchild
2N3302	Low cost photocurrent compensator for 2N5107	Fairchild
2N4035	Low cost photocurrent compensator for 2N5244	Fairchild
2N3251	PNP high speed switch and RF amplifier	Fairchild
BR100	NPN radiation resistant high power transistor	Solitron Devices

Because the selection of devices was made from a radiation tolerance point of view, it is convenient to present the data that were obtained and used in the computer analysis.

The neutron degradation information was provided by References 1, 2, and 3. The damage constant was calculated using the Messenger damage equation:

$$\frac{1}{h_{FE}(\Phi)} - \frac{1}{h_{FE}(o)} = K_D \Phi$$

where:

$h_{FE}(\Phi)$ = transistor gain after neutron exposure

$h_{FE}(o)$ = transistor gain before exposure

K_D = damage constant

Φ = fluence level in neutrons/cm^2

The damage constants for the devices used in the computer analysis are presented in Table 2-II. These constants were calculated using 1×10^{14} n/cm^2 as a reference level as called out in Reference 1.

TABLE 2-II

Damage Constants

Device	$h_{FE}(o)$	$h_{FE}(\phi)$	K_D
2N4878	340	60	1.3×10^{-16}
2N2907	184	29	2.93×10^{-16}
2N2222A	240	25	3.6×10^{-16}
2N5107	200	50	1.5×10^{-16}
2N5244	200	50	1.5×10^{-16}
2N3251	200	30	2.83×10^{-16}
BR100F	80	15 (Min)	5.5×10^{-16}

The digital logic design was completed early in the program; therefore, it was the first to be analyzed. To determine the ionization hardness of the digital circuits, since there was no test data available, it was necessary to estimate the photocurrent of the transistors used in the computer model. A Motorola MCE5400 chip, shown in Figure 2-1, was examined for circuit topology verification (see Figure 2-2) and collector-base junction area measurement. Using the equation,

$$I_{ppc} = \text{S.F. (amperes/cm}^2\text{/rad(Si)/s)} \times \text{Area (cm}^2\text{)} \times \dot{\gamma} \text{ (rads(Si)/s)},$$

the photocurrent of the various transistors in the digital logic model were determined. In previous efforts, it has been found that a scale factor (SF) of 1×10^{-8} amperes/cm^2/rad(Si)/s provides good data correlation. The performance difference between the two logic lines is the increase in speed and power of the 54H series. The increase in speed is due to an additional gain stage in the output pull-up circuit and a decrease in the circuit resistance values. The TI and Motorola 54H00 gates are shown in Figure 2-3. A slight increase in ionizing radiation hardness is achieved by the reduction of resistance of R4 from 1000 to 470 ohms. This can be explained briefly by using the circuit shown in the following sketch.

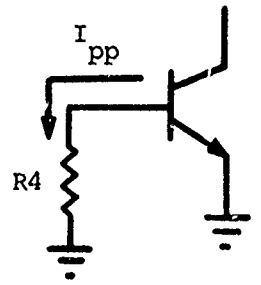

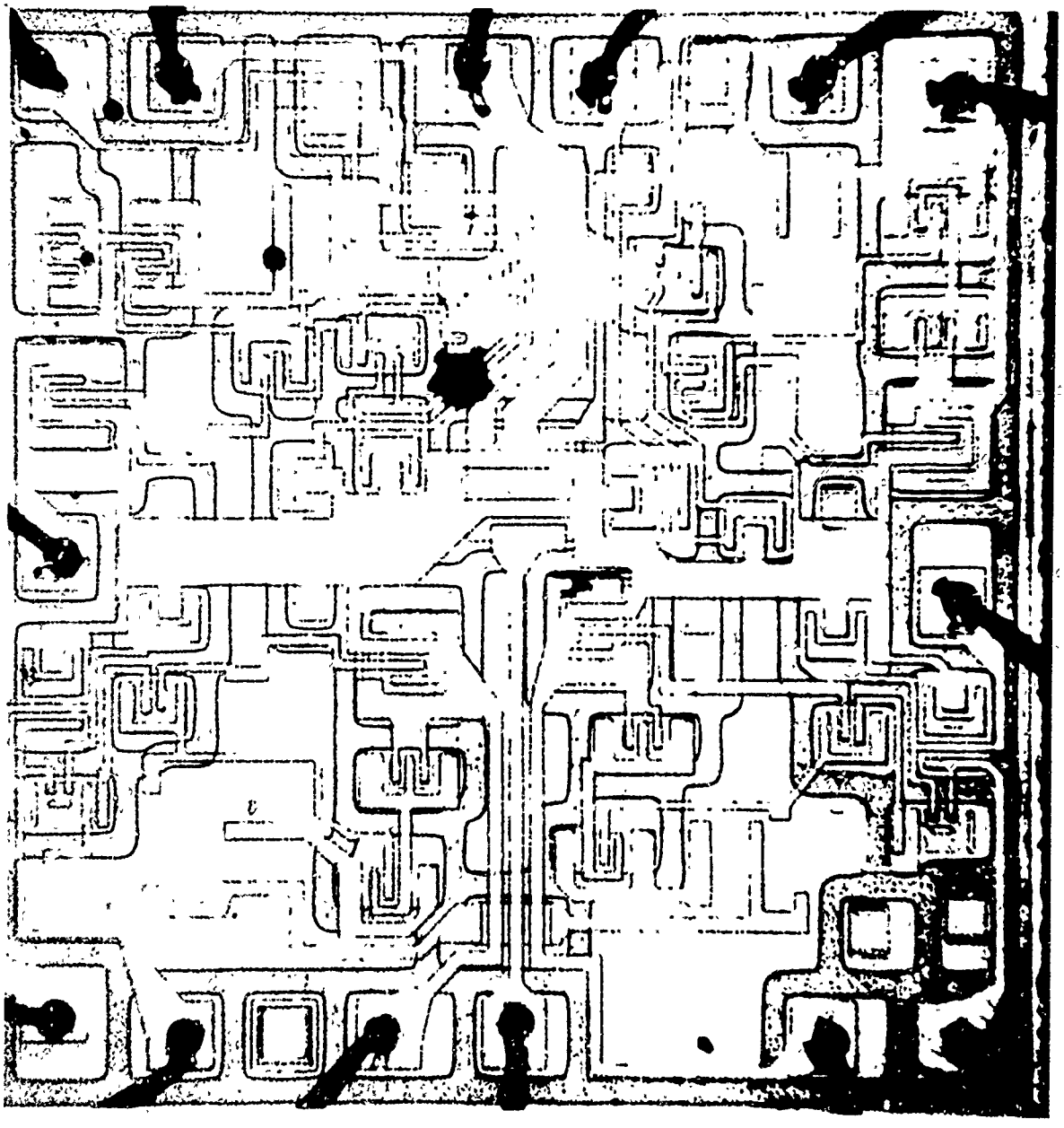

Figure 2-1. Motorola MCE5400 Chip

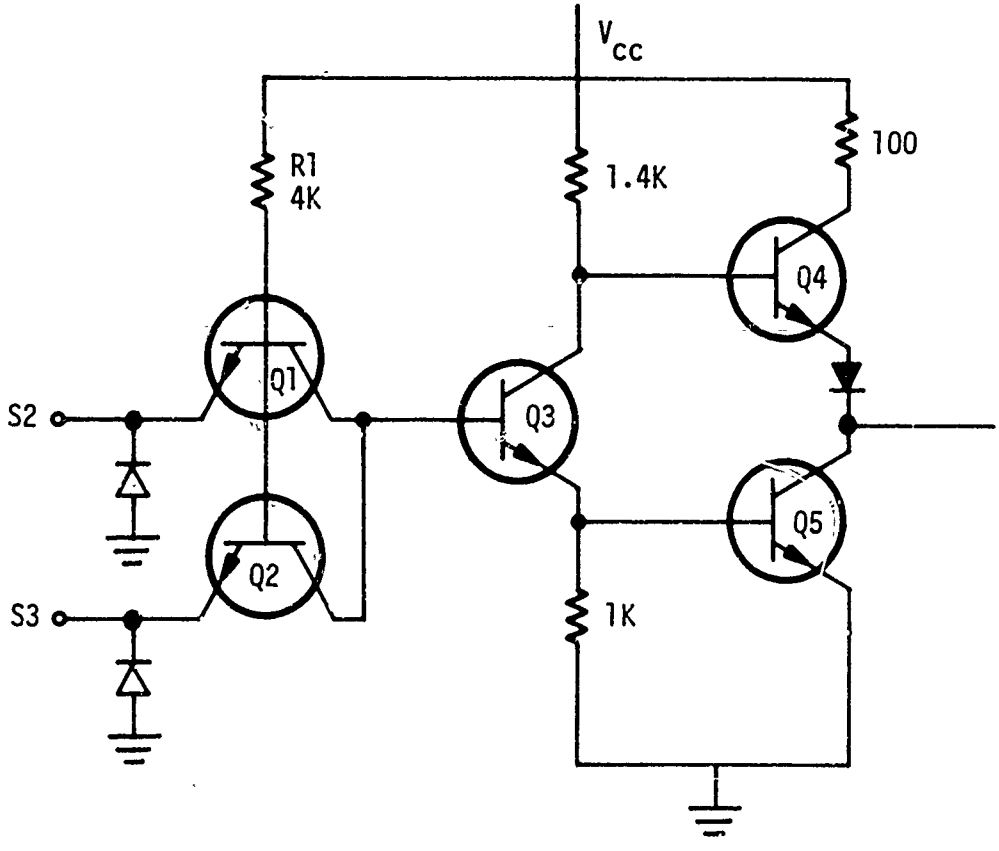

Figure 2-2. MCE5400 Two-Input NAND Gate

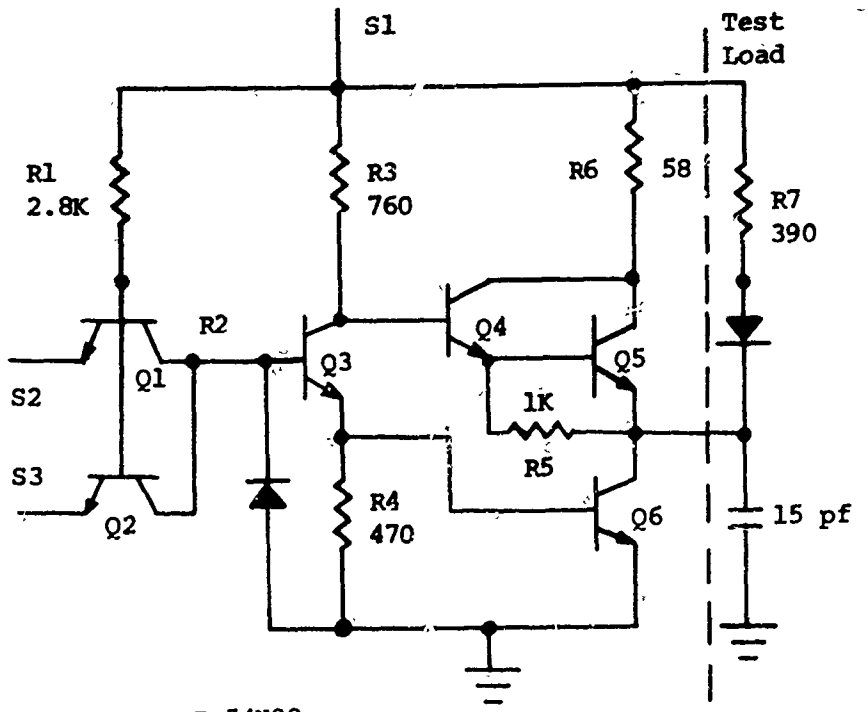

TI 54H00

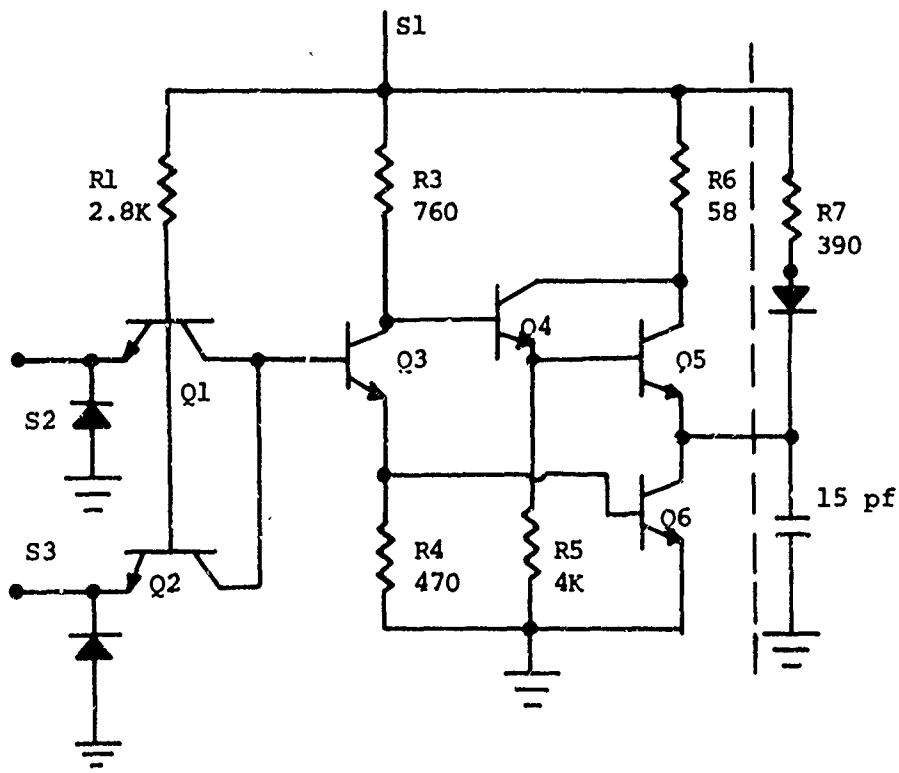

MCE 54H00F

Figure 2-3. Computer Simulation of TI and Motorola 54H00 Gates

To turn on the pull-down transistor with photocurrent for the 54H00 gate,

$$I_{pp} = \frac{V_{BE(SAT)}}{0.47k} + I_b$$

$$\approx \frac{0.5v}{0.47k} + 0.25 \text{ mA}$$

$$= 1.25 \text{ mA (worst case)}$$

$$= 2.5 \text{ mA (best case)}$$

where the typical minimum $V_{BE}(SAT)$ of 0.5 volt represents the worst case. A base-emitter voltage of 1.0 volt represents a best case situation, since it requires an I_{pp} of 2.5 mA to put the transistor into saturation.

The ionization dose rate, $\dot{\gamma}$, can be determined from the following expression:

$$I_{pp} = K\dot{\gamma}$$

where:

$$K = 5 \times 10^{-6} \text{ A}/10^{7} \text{ rads(Si)/s.}$$

For $I_{pp} = 1.25 \times 10^{-3}$A

$$\dot{\gamma} = 2.5 \times 10^{9} \text{ rads(Si)/s (worst case)}$$

and for $I_{pp} = 2.5 \times 10^{-3}$A

$$\dot{\gamma} = 5 \times 10^{9} \text{ rads(Si)/s.}$$

For the 5400 gate

$$I_{pp} = \frac{0.5V}{1k} + 0.25 \text{ mA}$$

$$= 0.75 \text{ mA (worst case)}$$

$$= 1.25 \text{ mA (best case).}$$

The dose rate $\dot{\gamma}$ was calculated to be 1.5×10^{9} rads(Si)/s (worst case) and 2.5×10^{9} rads(Si)/s (best case). The results of the analysis of a computer simulation for the 5400 series gates are shown in Figure 2-4. Nominal operating conditions are shown in Figure 2-4a. Figure 2-4b shows the gate to be hard (no change in state) at 1×10^{9} rads(Si)/s and to have changed state at 5×10^{9} rads(Si)/s. Figure 2-4c shows the predicted response to the SFXR pulse at a dose rate of 1×10^{12} rads(Si)/s.

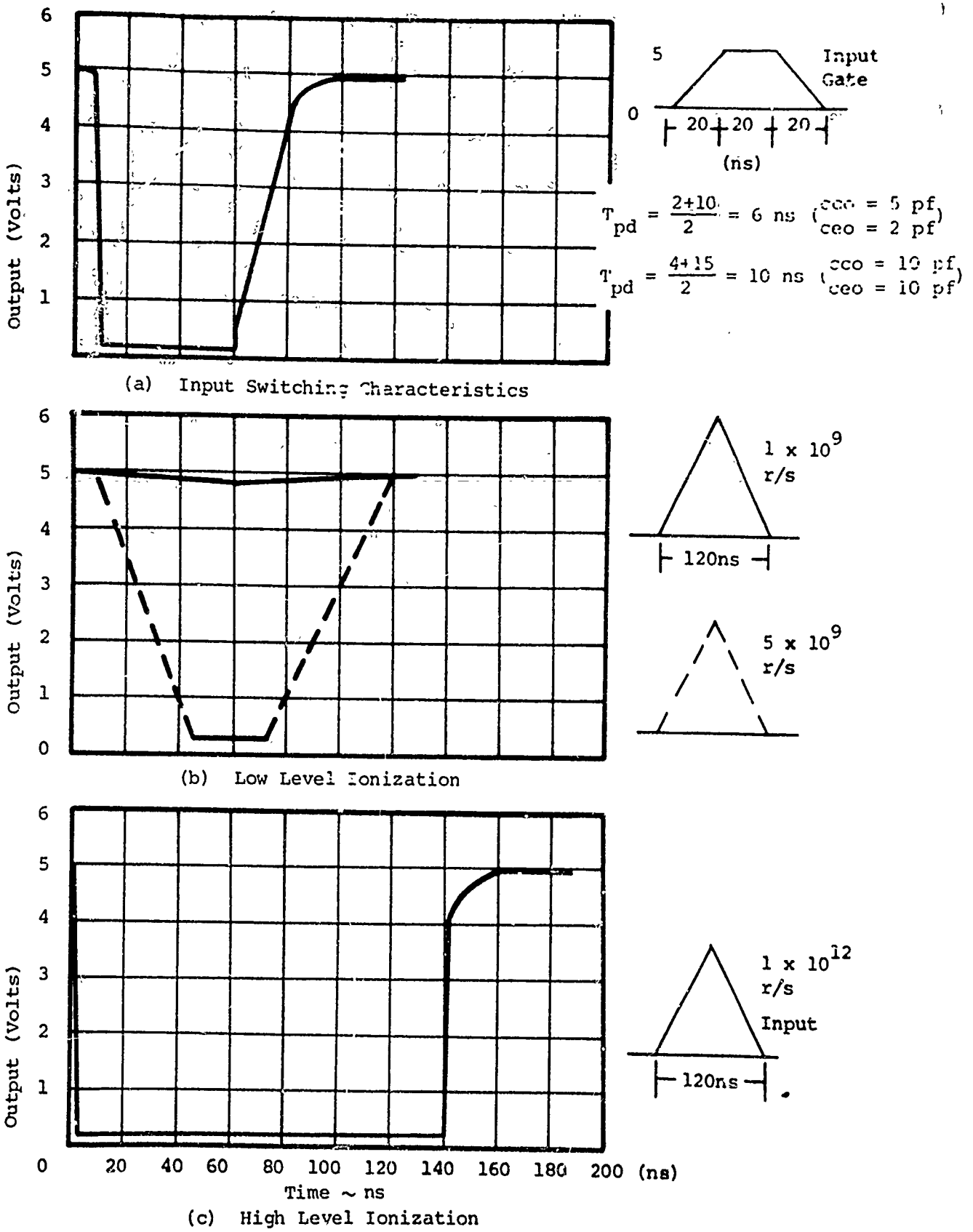

Figure 2-4. Summary of 5400d 10, 20, 30, and 04 Gate Characteristics

Figure 2-5a shows the nominal response of a 54H gate to the signal shown at the input gate. The response of the 54H gate to the SFXR characteristic wave shape with a peak dose rate of 5×10^9 and 1×10^{11} rads(Si)/s is shown in Figures 2-5b and 2-5c, respectively. Both 54H00 configurations were analyzed to determine if any possible fan out degradation resulted from the reduction of the transistor gains. The transistor gains (h_{FE}) were reduced to 5 and the gate performed satisfactorily, indicating normal fan out criteria are acceptable under the present nuclear specification. The performance was verified at the scheduled FBR tests.

The response of six Motorola MCE 54H00 gates recently tested indicates very close agreement between the predicted gamma rate hardness and the test data. Figure 2-6 shows the output drop versus gamma dose rate for these devices. For a normal gate voltage high of 4.5 volts, allowing approximately a 1.5 volt drop yields a gate hardness of 4×10^9 rads(Si)/s.

Photocurrent information from radiation test data for the 2N5107 and 2N5244 was provided by the manufacturer (see Appendix B). Included with the data were collector-base junction area measurements (i.e., 131.2 $mils^2$ for the 2N5107 and 21.1 $mils^2$ for the 2N5244). Using these data, a scale factor of approximately 7.5×10^{-9} amperes/cm^2/rads(Si)/s was obtained, which is in good agreement with the 10×10^{-9} scale factor used for photocurrent estimates for the digital logic elements. The photocurrent data for the 2N2907 and 2N2222A were available at Martin Marietta from previous radiation testing. The final photocurrent data used in the computer simulation for the above devices are listed in Table 2-III.

TABLE 2-III

Photocurrent Data

Device	I_{ppc} at 10^7 rads(Si)/s	Source of Data
2N4044	65.0×10^{-6}	Reference 1
2N2907	250.0×10^{-6}	Martin Marietta Test Data
2N2222A	250.0×10^{-6}	Martin Marietta Test Data
2N5107	65.0×10^{-6}	Vendor Data and Junction Area
2N5244	10.0×10^{-6}	Vendor Data and Junction Area
2N3251	120.0×10^{-6}	Reference 1
BR100F	4.0×10^{-3}	Appendix A

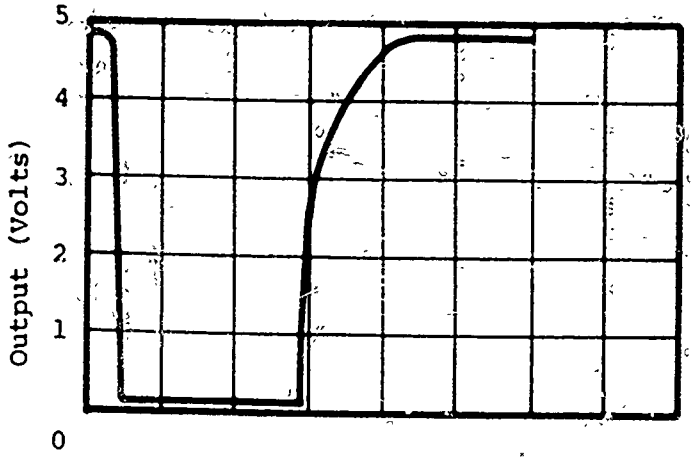

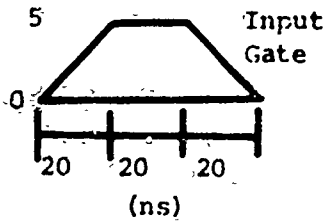

$T_{pd} = \frac{2+8}{2} = 5$ ns (C_{eo} = 10 pf, C_{eo} = 10 pf)

(a) Input Switching Characteristics

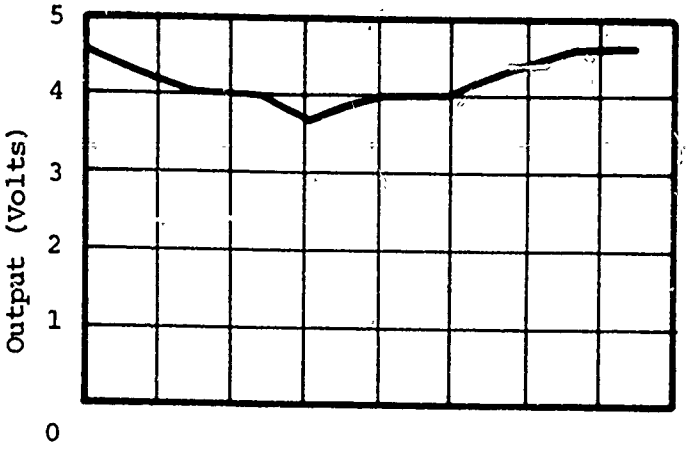

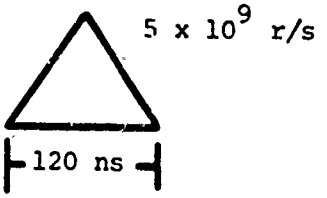

(b) Low Level Ionization

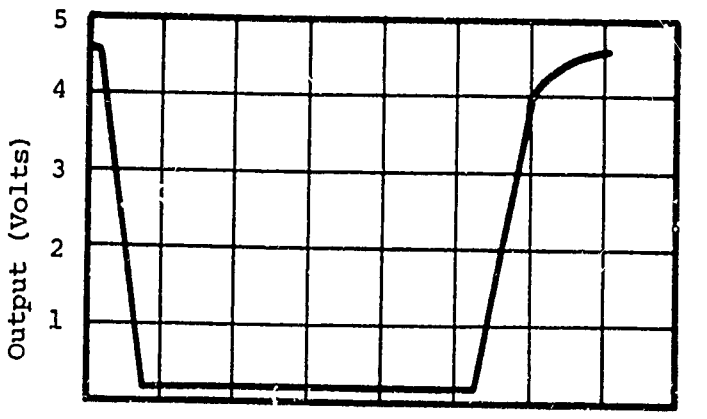

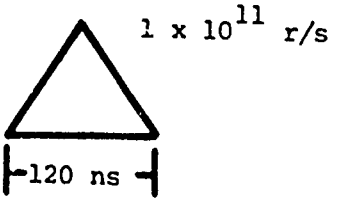

(c) High Level Ionization

Figure 2-5. Summary of 54H00, 10, 20, 30, and 04 Gate Characteristics

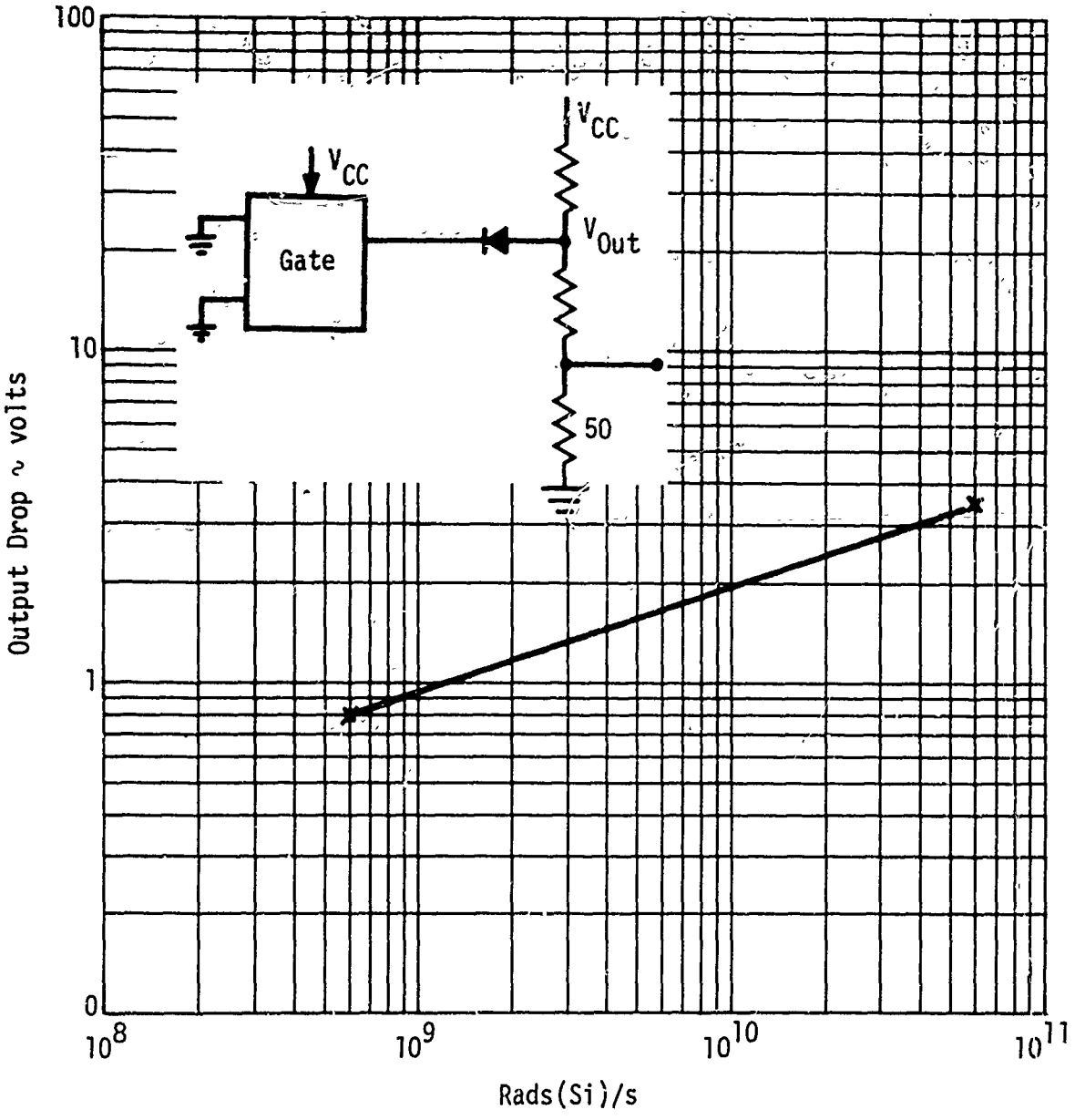

Figure 2-6. Gamma Dot Response of ¡4H00 Digital Integrated Circuits

3. SEMICONDUCTOR MODEL PARAMETERS

The assessment of nuclear vulnerability of circuit or system operation requires the extensive use of computer codes. These codes are used for the prediction and analysis of the equipment in the simulator environments and to evaluate the effects of a probable threat environment. The code that was used for circuit analysis throughout this program was the TRAC computer code (Reference 4). Approximately midway into the vulnerability assessment, the SECURE computer program (Reference 5) was made available to Martin Marietta Corporation for the system evaluation of the laser gyro electronics. The semiconductor model for the SECURE code is an expanded TRAC model and all discussions concerning the TRAC model are directly applicable to the SECURE model. A brief description of the TRAC model parameters is included in the following paragraphs.

A list of the semiconductor model parameters necessary for the TRAC computer code is presented in Table 3-I. Normally, a comprehensive component selection and parameter determination program is incorporated in parallel with the design and analysis effort; however, it was not possible to incorporate a study of this type because of the limitations of the program.

TABLE 3-I

Definition of Symbols

Transistor Model

HFEN	Forward current gain
HFEI	Inverted current gain
TN	Emitter diode junction time constant
TI	Collector diode junction time constant
ICS	Collector diode saturation current
MC	Collector diode proportionality constant
CCO	Collector diode junction capacitance at zero volts bias
VCBI	Collector diode intrinsic voltage
RCL	Collector leakage resistance

TABLE 3-I (Continued)

Transistor Model

IES	Emitter diode saturation current
ME	Emitter diode proportionality constant
CEO	Emitter diode junction capacitance at zero volts bias
VEBI	Emitter diode intrinsic voltage
REL	Emitter leakage resistance
I_{ppc}	Collector junction diode primary photocurrent
I_{ppe}	Emitter junction diode primary photocurrent

Diode Model

IS	Diode reverse saturation current
MD	Diode proportionality constant
RDL	Diode leakage resistance
CDO	Diode junction capacitance at $V_D = 0$
VDBL	Diode intrinsic built-in voltage
TD	Diode time constant
I_{pp}	Diode junction primary photocurrent

From the list of parameters in Table 3-I the most significant values for the transistor models to be used in this study are:

1. H_{FEN} - Forward current gain
2. T_N - Emitter diode junction time constant
3. T_I - Collector diode junction time constant
4. CCO - Collector diode junction capacitance at zero volts bias
5. CEO - Emitter diode junction capacitance at zero volts bias
6. I_{pp_c} - Collector junction diode primary photocurrent

Items 1 and 2 can be generally obtained from the manufacturer's specification sheet. Item 3, the collector diode junction time constant was estimated to be 10 to 50 times the emitter time constant or

$$T_{I_{max}} = 50\ T_N \approx 50 \times \frac{1}{6.28 \times f_T} ,$$

where f_T is the current gain-bandwidth product. Items 4 and 5 can be obtained using data from the specification sheet and the following equations:

$$C_{CB} = \frac{CCO}{[1 - V_{BC}(t)/V_{CBI}]^{1/2}}$$

$$C_{BE} = \frac{CEO}{[1 - V_{BE}(t)/V_{EBI}]^{1/2}}$$

Item 6, the collector junction diode primary photocurrent can be estimated using various methods but, normally, test data are the best source of information. The photocurrent information, as well as past neutron data, was obtained from manufacturer's tests data, junction area measurements, and various references that are available (Reference 1) that characterize the radiation parameters.

The TRAC semiconductor models for the diode, NPN transistor, and PNP transistor are shown in Figures 3-1, 3-2, and 3-3. Units for the TRAC semiconductor model are presented in Table 3-II. The bipolar transistor is represented as two diodes, plus two current generators. The diode model in the transistor is identical to the diode model except for a slight change in notation necessary to differentiate between the base-collector diode and the base-emitter diode.

TABLE 3-II

TRAC Semiconductor Model Units

Parameter	Unit
Resistance	Ohms
Capacitance	Farads
Voltage	Volts
Time	Seconds

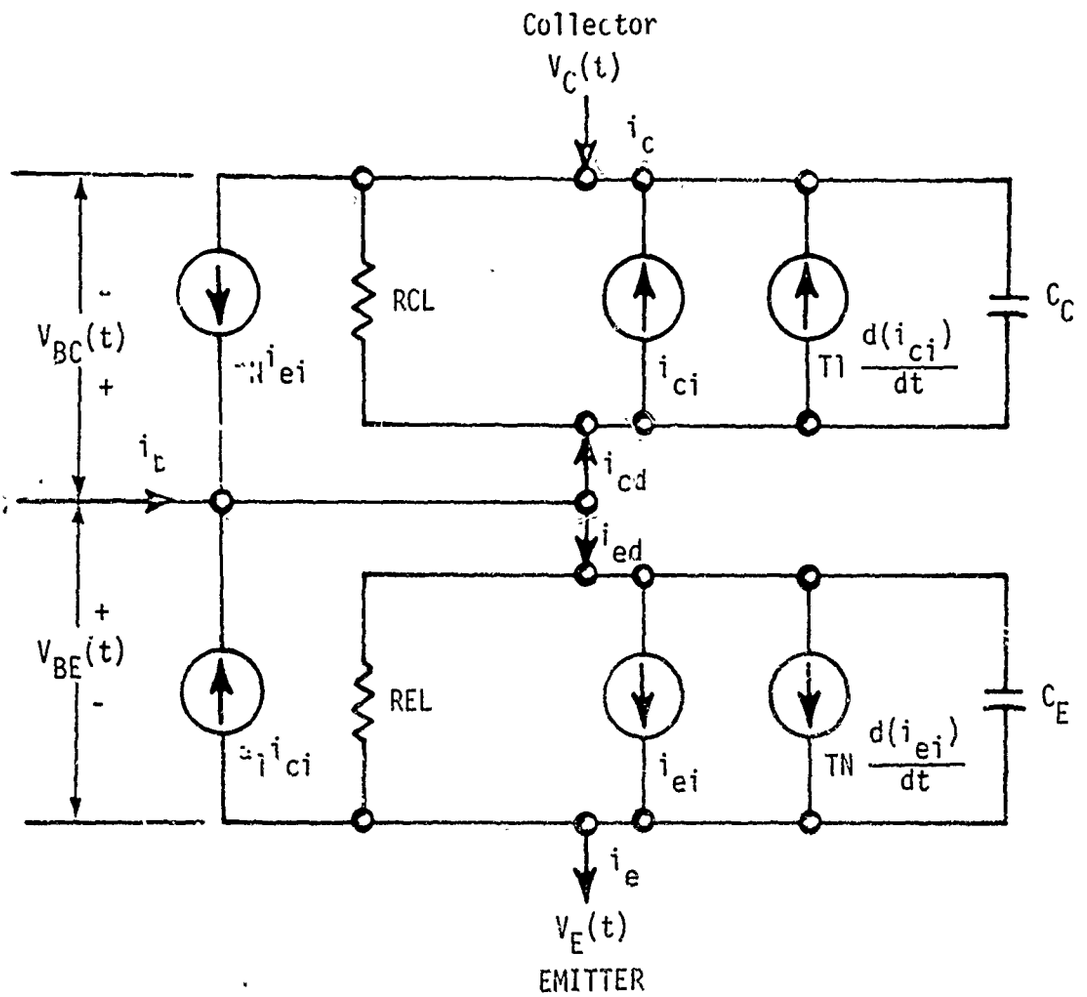

Figure 3-1. TRAC NPN Transistor Model

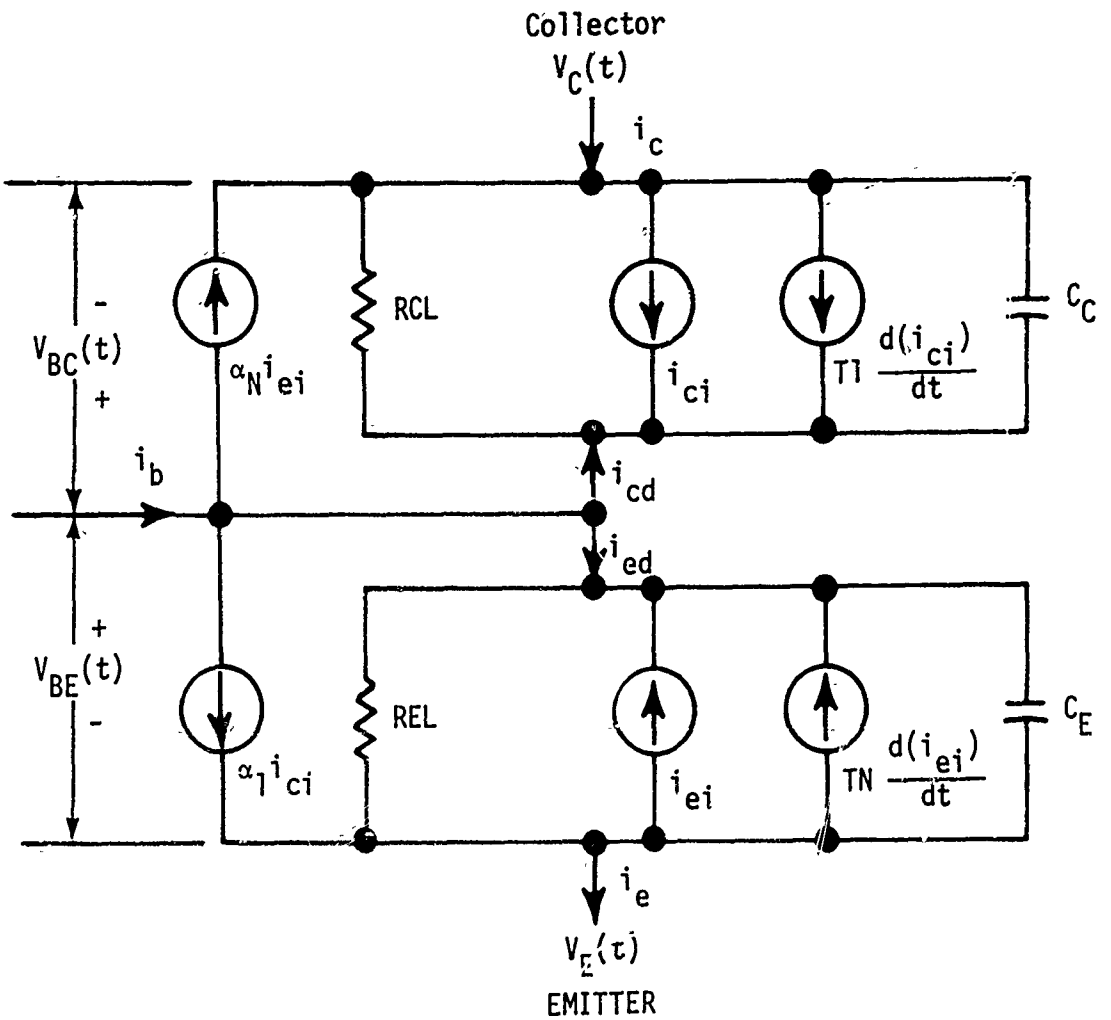

$$C_C = \frac{CCO}{\sqrt{1 - V_{BC}(t)/VCBI}} \qquad C_E = \frac{CEO}{\sqrt{1 - V_{BE}(t)/VEBI}}$$

$$i_{ci} = ICS\ [\ \exp\ (V_{BC}(t)/(MC * KT/q)) - 1]$$

$$i_{ei} = IES\ [\ \exp\ (V_{BE}(t)/(ME * KT/q)) - 1]$$

$$\alpha_N = \frac{HFEN}{HFEN + 1} \qquad \alpha_I = \frac{HFEI}{HFEI + 1}$$

Figure 3-2. TRAC PNP Transistor Model

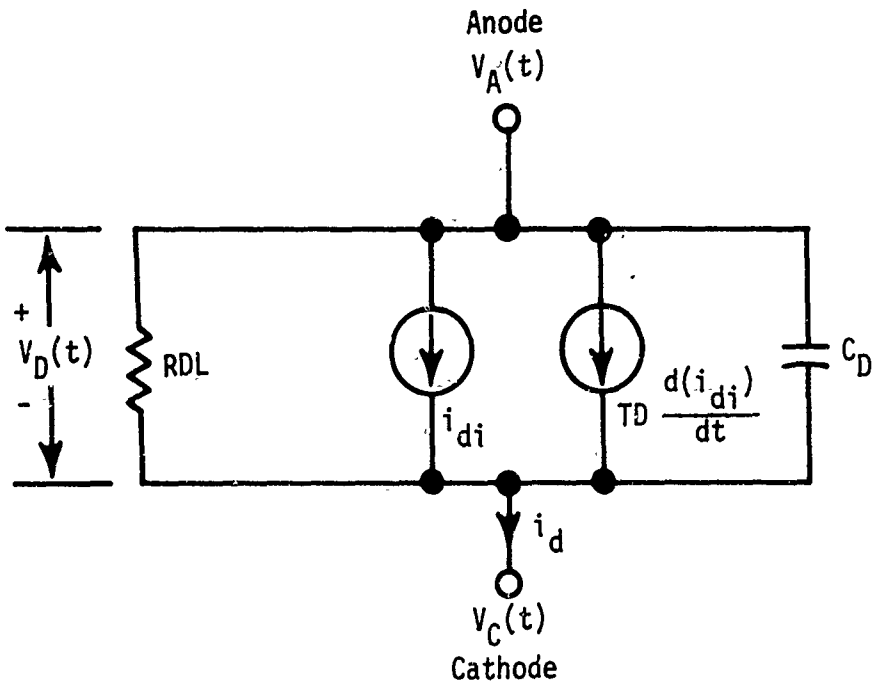

$$i_{di} = IS\ [\ \exp(V_D(t)/(MD * KT/q)) - 1]$$

$$C_D = \frac{CDO}{\sqrt{1 - V_D(t)/VDBL}}$$

Figure 3-3. TRAC Diode Model

The relationship between the current and voltage in an ideal PN junction diode can be shown to be exponential in character. Assuming voltages less than the breakdown voltage of the junction and ignoring diode series resistance, the relationship can be written as follows:

$$I = Is\ (e^{qV/KT} - 1),$$

in which:

Is = Saturation current

V = Applied junction voltage

q = Charge of an electron

k = Boltzmann's constant

T = Temperature in degrees Kelvin.

The exponential dependence is slightly modified in the TRAC program to compensate for diodes that deviate from the "ideal" case shown below. That is, the exponent is given more exactly by

$$I = Is\ (e^{qV/M_DKT} - 1),$$

where M_D = constant having a value near 1.0.

The value of q/K is a constant and is not required for semiconductor input data. Values of M_D and T are required as TRAC data. The diode and transistor models are large-signal nonlinear models. That is, the model is good in both the conducting and nonconducting state. The model does not, however, take into account voltage breakdown caused by the Zener effect, or the avalanche effect.

The TRAC program mechanizes a form of the Ebers and Moll equations in the transistor model. These equations use the same exponential dependence of current to voltage as the diode but in addition include the effect of the transistor common-base current gains.

The effect of junction capacitance has been accounted for in the TRAC program. This inclusion was made by mechanizing a charge control model that takes into account the dependence of junction capacitances on the applied junction voltage and the relationship of this capacitance to the transient times involved in switching the PN junction from an OFF state to an ON state, or vice versa.

The definition of the required input parameters for the diode and transistor models are given in Reference 1.

The data used in this study for the semiconductor parameters are listed in Table 3-III.

TABLE 3-III

Semiconductor Parameters for TRAC Computer Code

	2N2907	2N2222	2N4044	2N3251
HFEN	216	136	340	200
HFEI	4.2	2.3	1.0	0.68
TN	4.97E-10	3.97E-10	6.0E-10	2.38E-10
TI	3.55E-10	8.36E-08	2.0E-09	4.8E-08
ICS	1.48E-13	1.19E-13	5.0E-10	1.19E-13
MC	1.43	1.018	1.30	1.075
CCO	2.6E-11	1.37E-11	1.2-12	6.85E-12
VCBI	1.0	0.9	0.75	0.75
RCL	5.0E+08	5.0E+08	5.0E+08	5.0E+08
IES	2.21E-14	3.02E-14	2.0E-10	4.02E-15
ME	0.9675	0.967	1.3	0.9675
CEO	2.1E-11	2.32E-11	9.0E-13	5.06E-12
VEBI	1.0	0.9	0.75	0.75
REL	5.0E+07	5.0E+07	5.0E+07	5.0E+07
I_{ppc}	250.E-06	250.E-06	65.0E-06	120.E-06
I_{ppe}	0	0	0	0

Notes: I_{pp} values are taken at 1×10^{7} rad(Si)/s.

TABLE 3-III (Cont)

Semiconductor Parameters for TRAC Computer Code

	2N5107	2N5244	BR100F	Digital Logic Transistors
HFEN	200	200	80	50
HFEI	1.09	1.09	1.09	0.8
TN	6.0E-10	3.0E-10	1.0E-09	2.0E-11
TI	1.0E-09	1.5E-09	2.0E-08	2.0E-10
ICS	7.14E-15	7.14E-15	3.06E-10	5.0E-10
MC	1.0	1.0	1.39	1.70
CCO	6.0E-12	2.0E-12	6.8E-10	1.0E-11
VCBI	0.75	0.75	0.75	0.75
RCL	5.0E+08	5.0E+08	3.88E+09	5.0E+08
IES	5.94E-15	5.94E-15	5.55E-10	2.0E-10
ME	1.0	1.0	1.44	1.70
CEO	1.2E-11	4.0E-12	3.97E-09	1.0E-11
VEBI	0.75	0.75	0.75	0.75
REL	5.0E+07	5.0E+07	9.2E+07	5.0E+07
I_{ppc}	65.E-06	10.0E-06	4.0E-03	5.0E-06
I_{ppe}	0	0	0	0

Notes: All I_{pp} values are taken at 1×10^{7} rads(Si)/s.

TABLE 3-III (Cont)

Semiconductor Parameters for TRAC Computer Code

	Digital Logic Diodes	Photo Sensor Diode	Zener Diode Back Biased	Zener Diode Forward Biased
IS	5.0-10	1.9E-09	1.9E-09	1.9E-09
MD	1.50	1.58	1.58	1.58
RDL	5.0E+8	5.0E+08	5.0E+08	5.0E+08
CDO	10.0E-12	2.5E-12	10.0E-12	200.E-12
VDBL	0.75	0.75	0.75	0.75
TD	2.0E-10	1.0E-10	8.0E-09	1.0E-09
I_{pp}	5.0E-06	1.5E-03	0.4E-03	0

Note: I_{pp} values are taken at 1×10^{7} rad(Si)/s.

4. READOUT AMPLIFIER

The readout amplifier receives the input signal from the germanium photosensor and amplifies the signal to a reasonable working level. The photosensor's output at 1 MHz is 4.2 μA peak-to-peak. Because of its noise suppression characteristics, a high gain differential amplifier circuit was chosen to amplify this low level signal. The attempts at designing a dc amplifier were abandoned in favor of a conventional differential ac amplifier scheme. Figure 4-1 shows the readout amplifier and trigger circuit as of 1 April 1971. Assuming an input current of 4.2 μA pp at 1 MHz, the output is as shown in Figure 4-2b. The low input impedance of the output transistors, when the transistors go into saturation, causes the driver transistor to saturate. This forces non-linear operation of the input stage as shown in Figure 4-2d. To get better noise rejection and high frequency characteristics, the trigger circuit was redesigned. The redesigned circuit is discussed in more detail in section 5.

A preliminary analysis of the linear stages of the readout amplifier, using the SFXR radiation profile, was conducted to determine the approximate recovery time. Figure 4-3 shows the response of the three amplifier stages to the 120 ns ionization pulse. Because of the large voltage excursions during and shortly after the burst, the ac signal cannot be seen at the output of the first and second stages. The sine wave output of the driver stage (Figure 4-3b) recovers approximately 1 μs after the radiation burst. There is a 250 mV change at the output of the first stage due to the discharge of the coupling capacitors. The capacitors will charge up over a much longer period but, because of the common mode rejection of the differential stages, the output (driver stage) is not affected.

The readout amplifier was modified, as was the trigger circuit, to achieve better gain and bandwidth characteristics. These modifications are shown in Figures 4-4 and 4-5. The readout amplifier had to be further modified because the photo sensors used to detect the laser interference pattern are no longer being manufactured. This created a shortage of parts that resulted in the readout amplifier input having only two diodes instead of four. Figure 4-6 shows the readout amplifiers used in the first FBR test. The FBR analytic predictions (OR 11,148-3) on the readout amplifier and trigger circuit of Figures 4-4 and 4-5 showed an undesirable high frequency oscillation in the trigger circuit. This high frequency oscillation was also present in normal operation: hence, the trigger circuit was again redesigned. Any designation of the readout amplifier invariably requires discussion of the trigger circuit because in any test situation only the output of the trigger circuit is monitored. The output of the trigger circuit has a low output impedance which makes it possible to drive the cables necessary for signal monitoring.

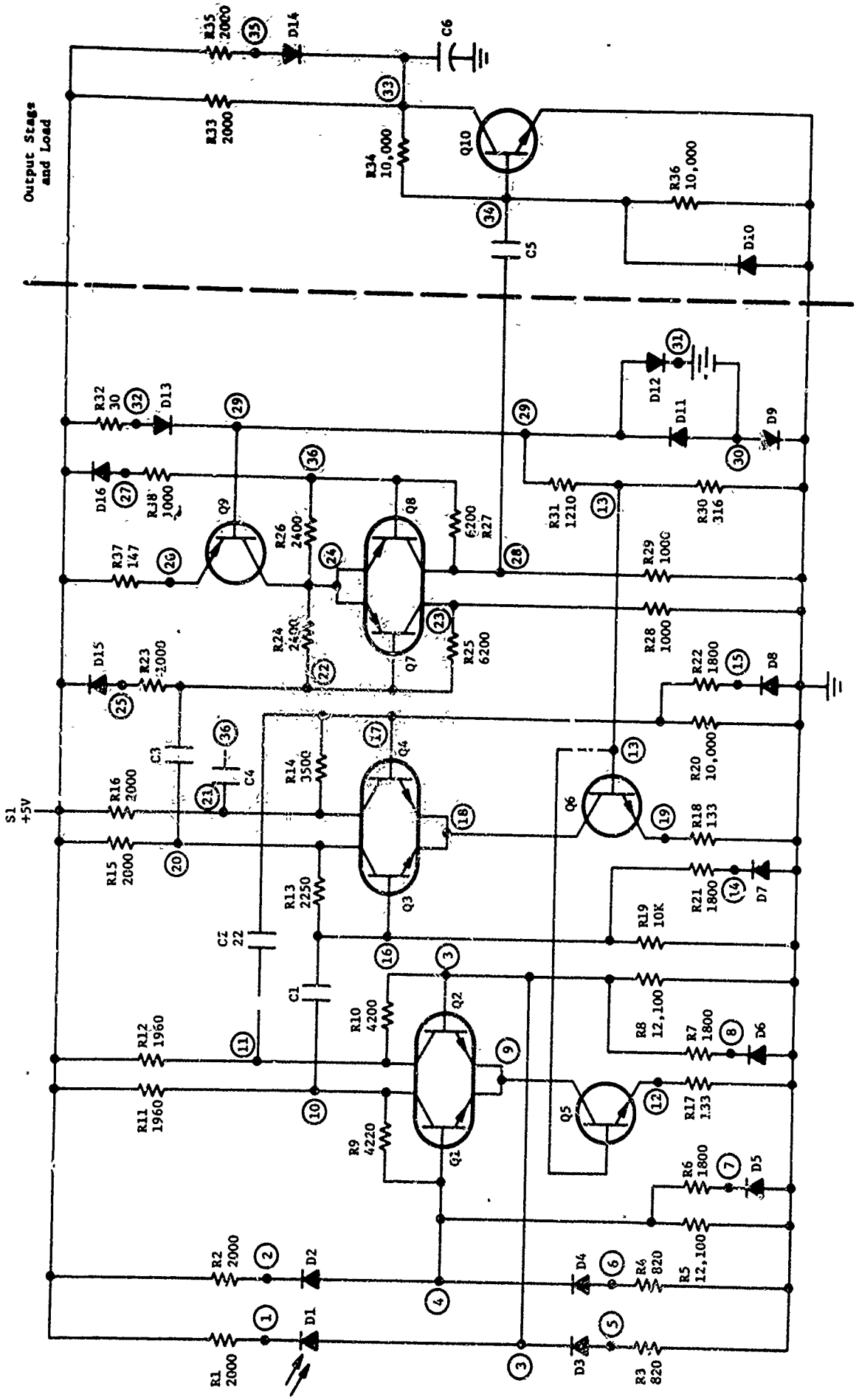

Figure 4-1. Readout Amplifier

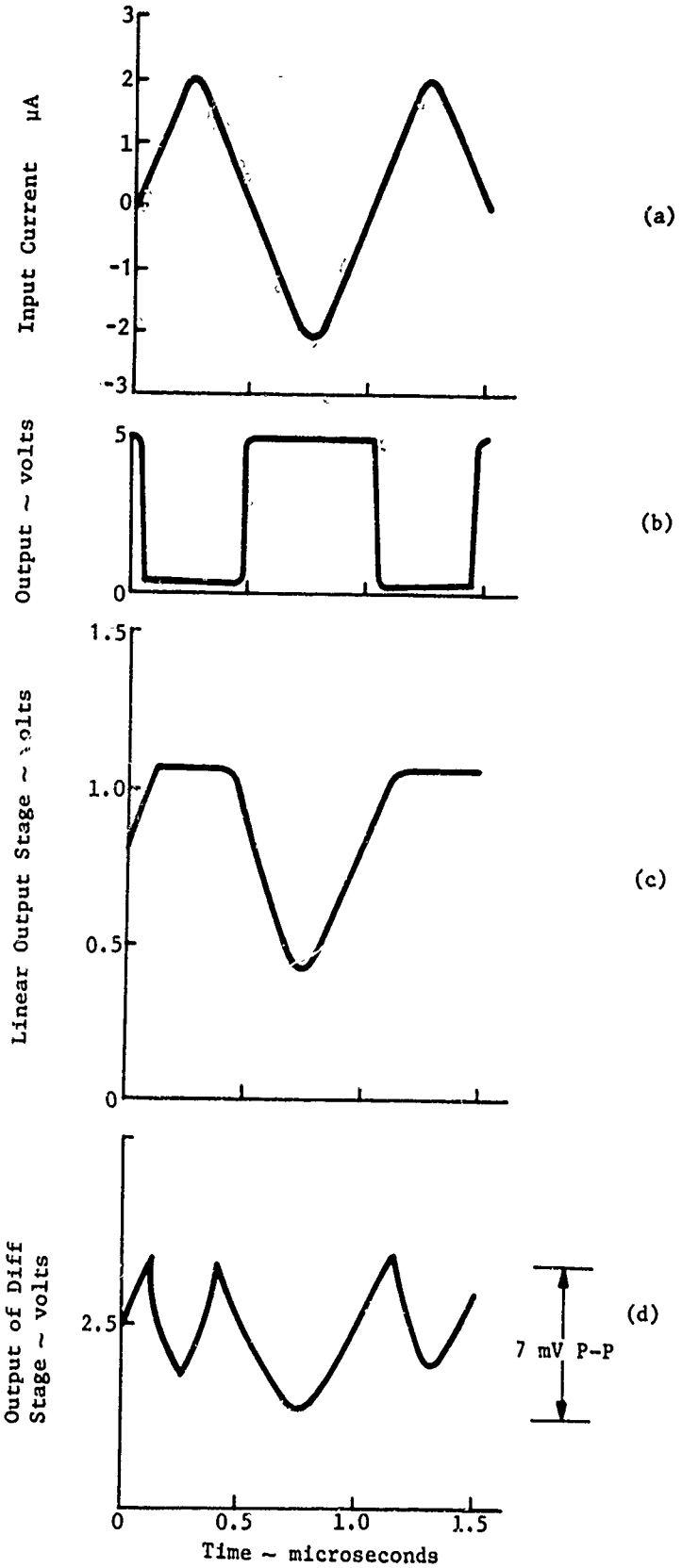

Figure 4-2. Readout Amplifier with Output Stage

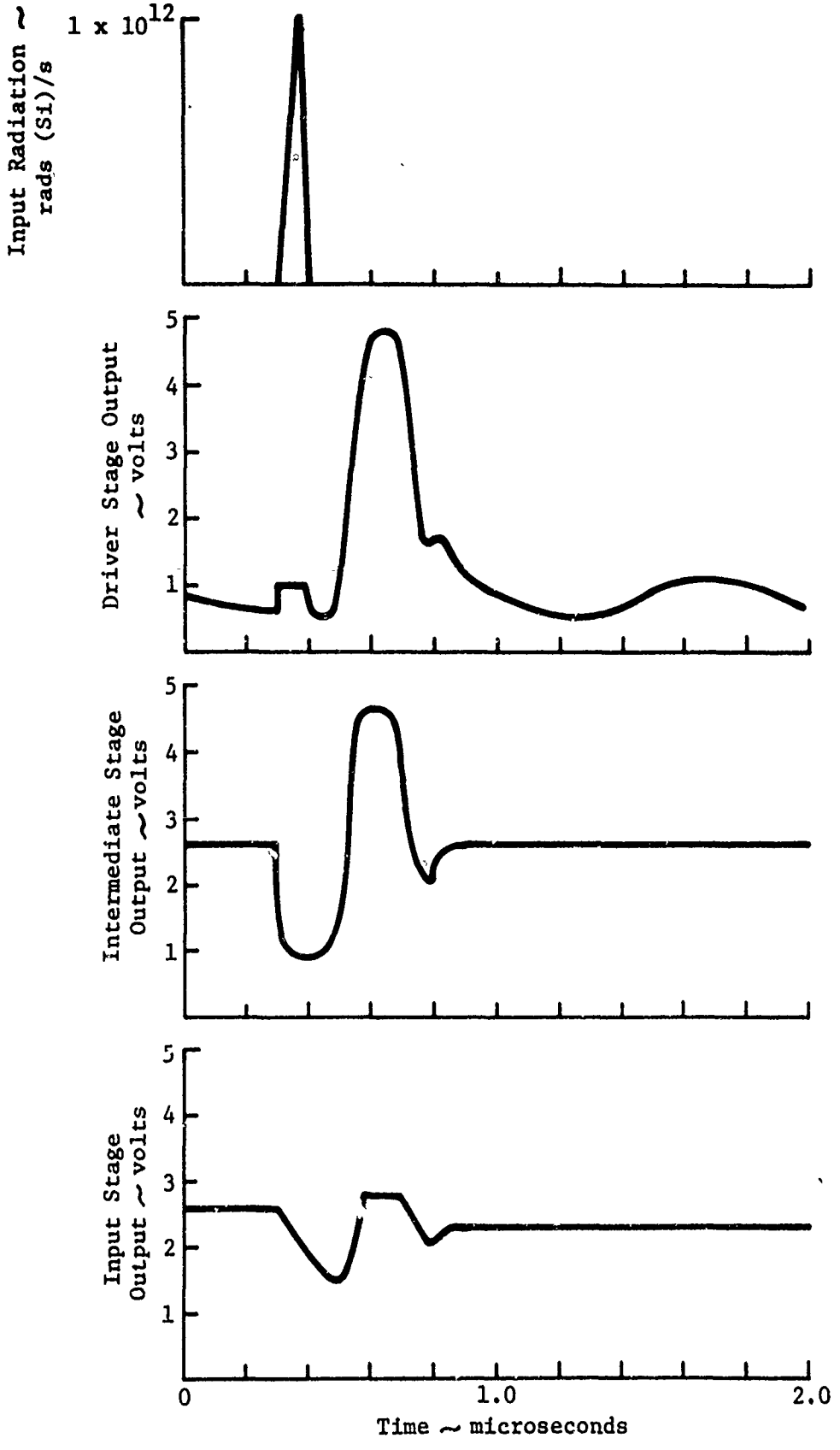

Figure 4-3. Predicted Response of Readout Amplifier without Output Stage

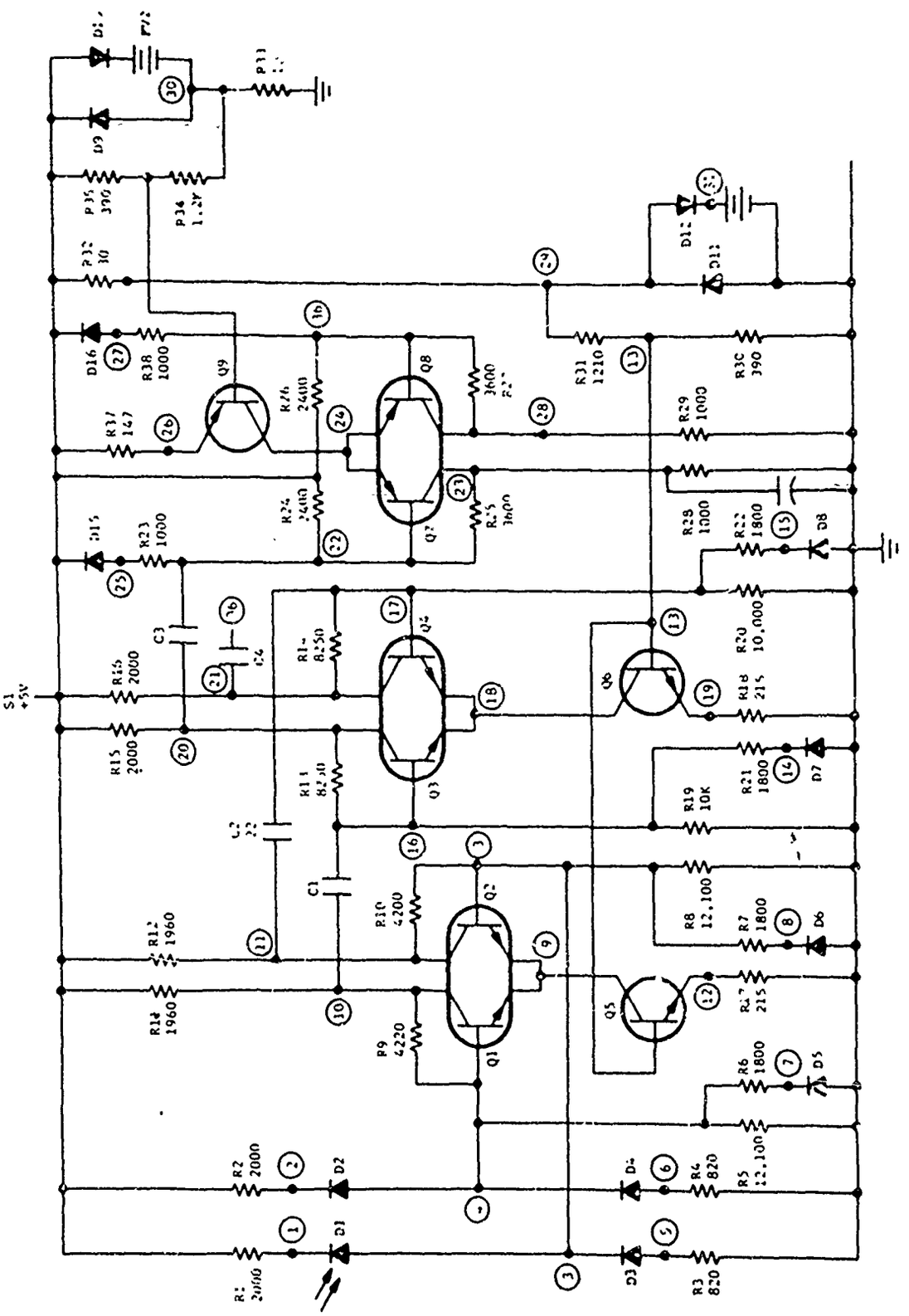

Figure 4-4. Modified Readout Amplifier

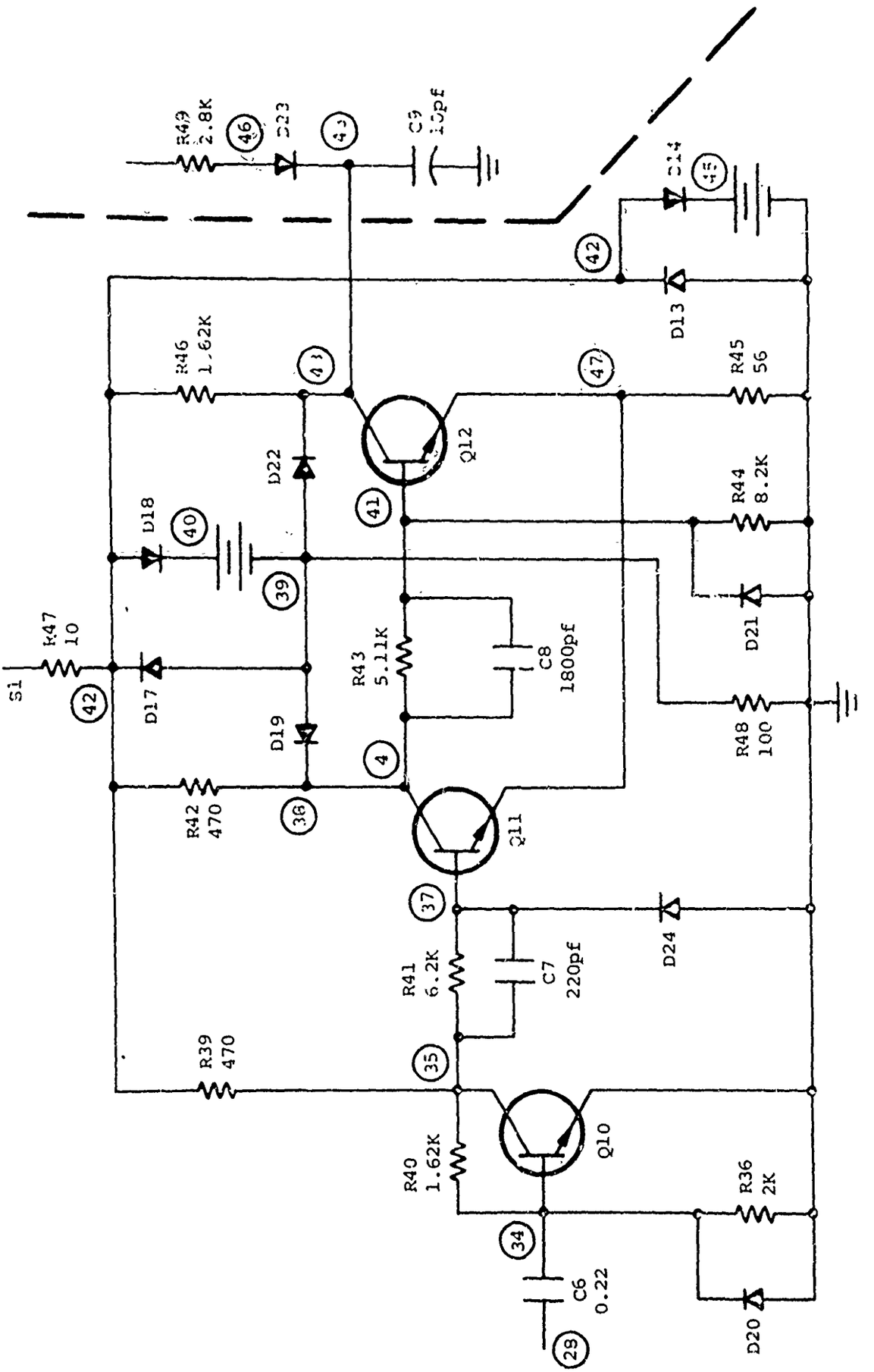

Figure 4-5. Readout Amplifier Trigger Circuit

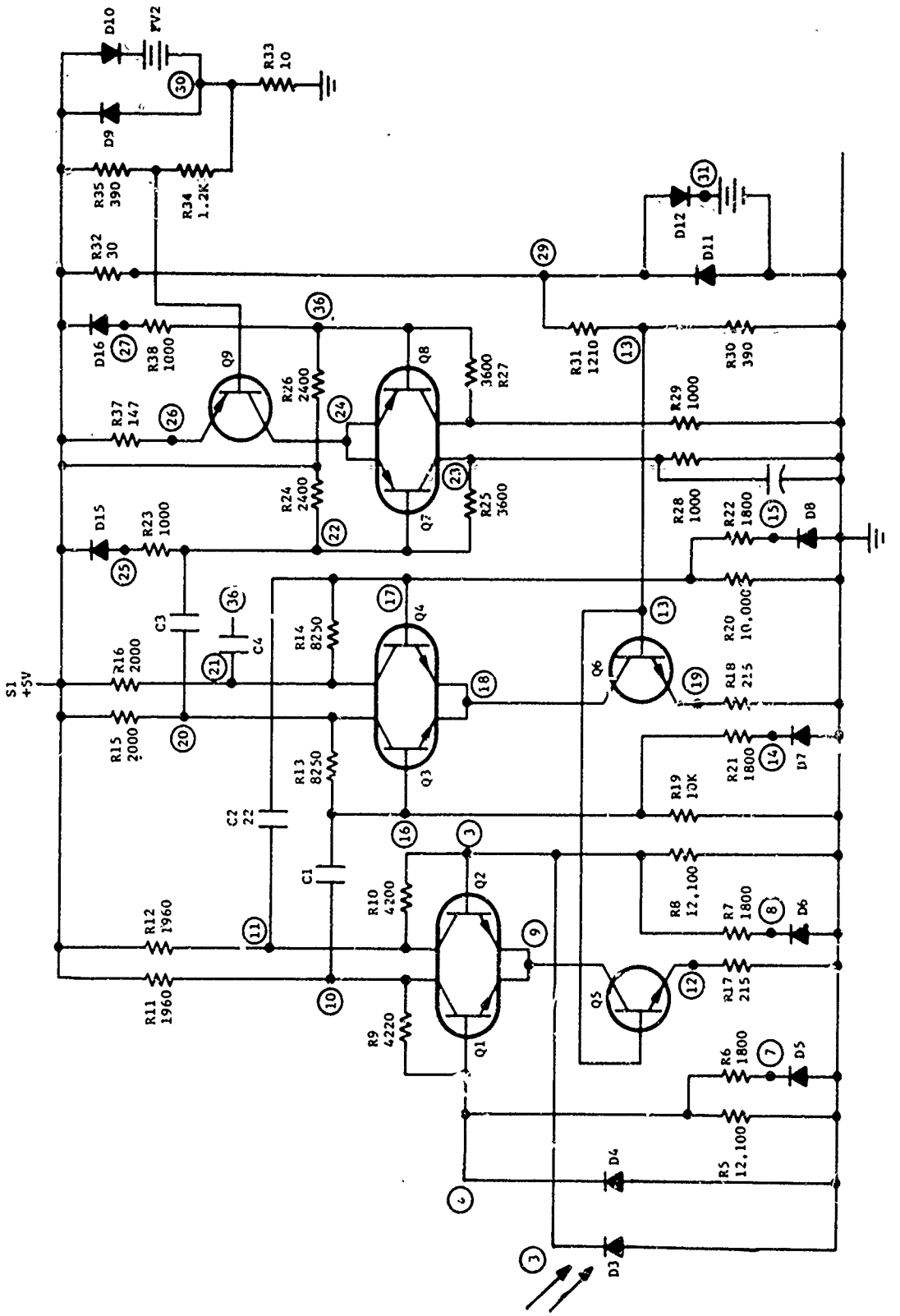

Figure 4-6. Readout Amplifier

The new trigger circuit shown in Figure 4-7 and its associated readout amplifier (Figure 4-6) were included in the first FBR test along with the readout amplifier and trigger circuit of Figures 4-6 and 4-5, respectively. The response of the readout amplifier and the two different trigger circuits to an FBR environment is shown in Figure 4-8. The readout amplifier and trigger circuit of Figures 4-5 and 4-6 recovered approximately 500 μs after the burst. The readout amplifier and trigger circuit of Figures 4-6 and 4-7 recovered within 200 μs after the burst. Because of the superior performance of this combination of readout amplifier and trigger circuit at the FBR, all other designs were abandoned.

The system modeling of the readout amplifier and trigger circuit on the SECURE computer code was being undertaken at this time. The best radiation test data was that taken at the FBR: hence, the computer model would have to be matched against this data (Figure 4-8b). The transistor photocurrent values and damage constants used in the computer simulation are shown in Table 4-I.

TABLE 4-I

Transistor Forward Current Gains (h_{FE})

Device	$h_{FE}(o)$	$h_{FE}(\phi)$ ($\phi = 1x10^{14} n/cm^2$)	K_D	I_{pp} at 10^7 rads(Si)/s (amperes)
2N4044	340	60	$1.3x10^{-16}$	$65.0x10^{-6}$
2N2907	184	30	$2.9x10^{-16}$	$250.0x10^{-6}$
2N2222A	240	25	$2.6x10^{-16}$	$250.0x10^{-6}$
2N5107	200	50	$1.5x10^{-16}$	$65.0x10^{-6}$
2N5244	200	50	$1.5x10^{-16}$	$10.0x10^{-6}$
2N3261	200	30	$2.8x10^{-16}$	$120.0x10^{-6}$
BR100	80	15 (min)	$5.5x10^{-16}$	$4.0x10^{-3}$

The maximum single burst at the FBR is expected to produce approximately 5 to 6 x 10^{13} n/cm^2. Using the damage equation, the transistor gains would be reduced for the following devices as shown in Table 4-II.

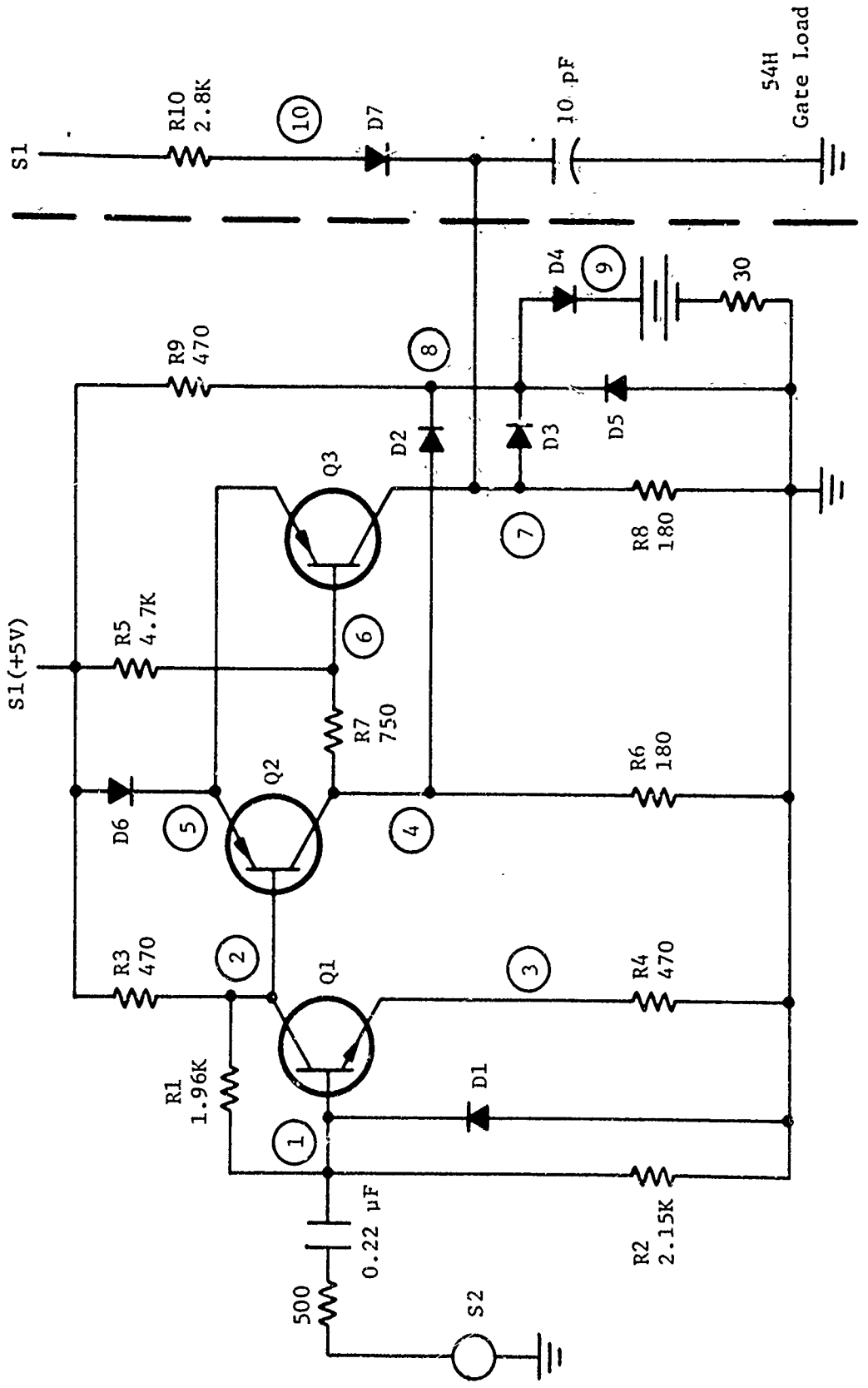

Figure 4-7. New Readout Amplifier Trigger Circuit

(a)

Upper Trace - 50 μs/cm

Lower Trace - 500 μs/cm

Readout Amplifier - Figure 4-6

Trigger Circuit - Figure 4-5

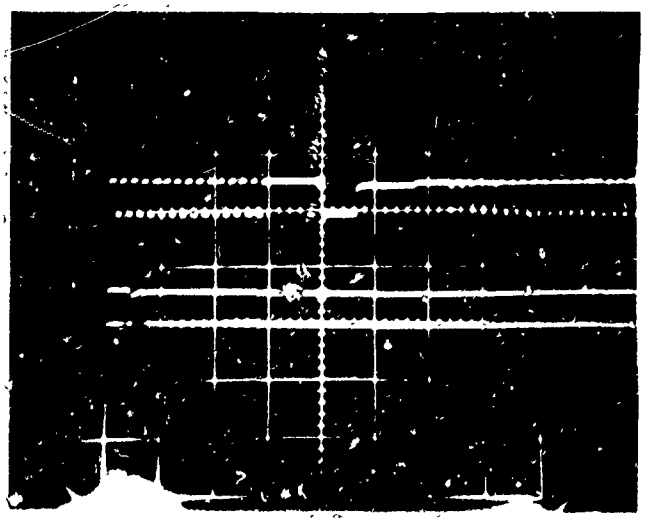

(b)

Upper Trace - 50 μs/cm

Lower Trace - 500 μs/cm

Readout Amplifier - Figure 4-6

Trigger Circuit - Figure 4-7

Figure 4-8. Readout Amplifier and Trigger Circuit Response to FBR Environment

TABLE 4-II

Transistor Gain Reduction

Device	$h_{FE}(o)$	$h_{FE}(\phi)$ ($\phi = 5x10^{13}$ n/cm^2)	$h_{FE}(\phi)/2$	$h_{FE}(\phi)$ ($\phi = 1x10^{14}$ n/cm^2)
2N4044	340	100	50	60
2N2907	200	50	25	30
2N5244	200	80	40	50
2N5107	200	80	40	50
2N3251	200	50	25	30
BR100	80	25	12.5	15 (min)

An accepted approximation to the minimum transistor gain immediately after neutron exposure is 50 percent of the final annealed value. This would reduce the transistor gains calculated by means of the damage equation by a factor of two. Since these values are very similar to the neutron data taken at $1x10^{14}$ n/cm^2 (Table 4-II) and since much data are referenced at this level, it will be assumed that the maximum single burst neutron fluence at the FBR facility will degrade the transistors at the $1x10^{14}$ n/cm^2 level. The actual transistor gain during the burst is a nebulous quantity because measurement techniques are not possible during this time.

A simulation of the readout amplifier and trigger circuit using a linear degradation profile and an ionization profile with a peak dose rate of $1x10^8$ rads(Si)/s corresponding to the FBR environment is shown in Figure 4-9. The output of the trigger circuit drops immediately from the high state to the low state, which does not correlate very well to the test data of Figure 4-8b. Estimates of transistor gains during the interaction between the neutrons and the silicon material range from a factor of ten times lower than post test data to almost zero. A transistor gain degradation profile was constructed to reduce the gains to five during the burst simulation. The result of the simulation using the ionization and transistor gain degradation profiles is shown in Figure 4-10. A comparison between the data of Figure 4-8b and Figure 4-10 show that the simulation is much better, except that at the peak ionization rates the trigger output did not go to the low state as in the test data. It was then reasoned that the reduction of transistor gains to five would occur at the time of maximum neutron interaction, which is approximately at the time of the peak ionization rate. The simulation was repeated, delaying the transistor gain degradation to a time coincident with the peak dose rate. The results of the simulation, along with the ionization and transistor gain degradation profiles, is shown in Figure 4-11. The correlation between the test data of Figure 4-8 and computer simulation results of Figure 4-11 is excellent. The points of agreement are:

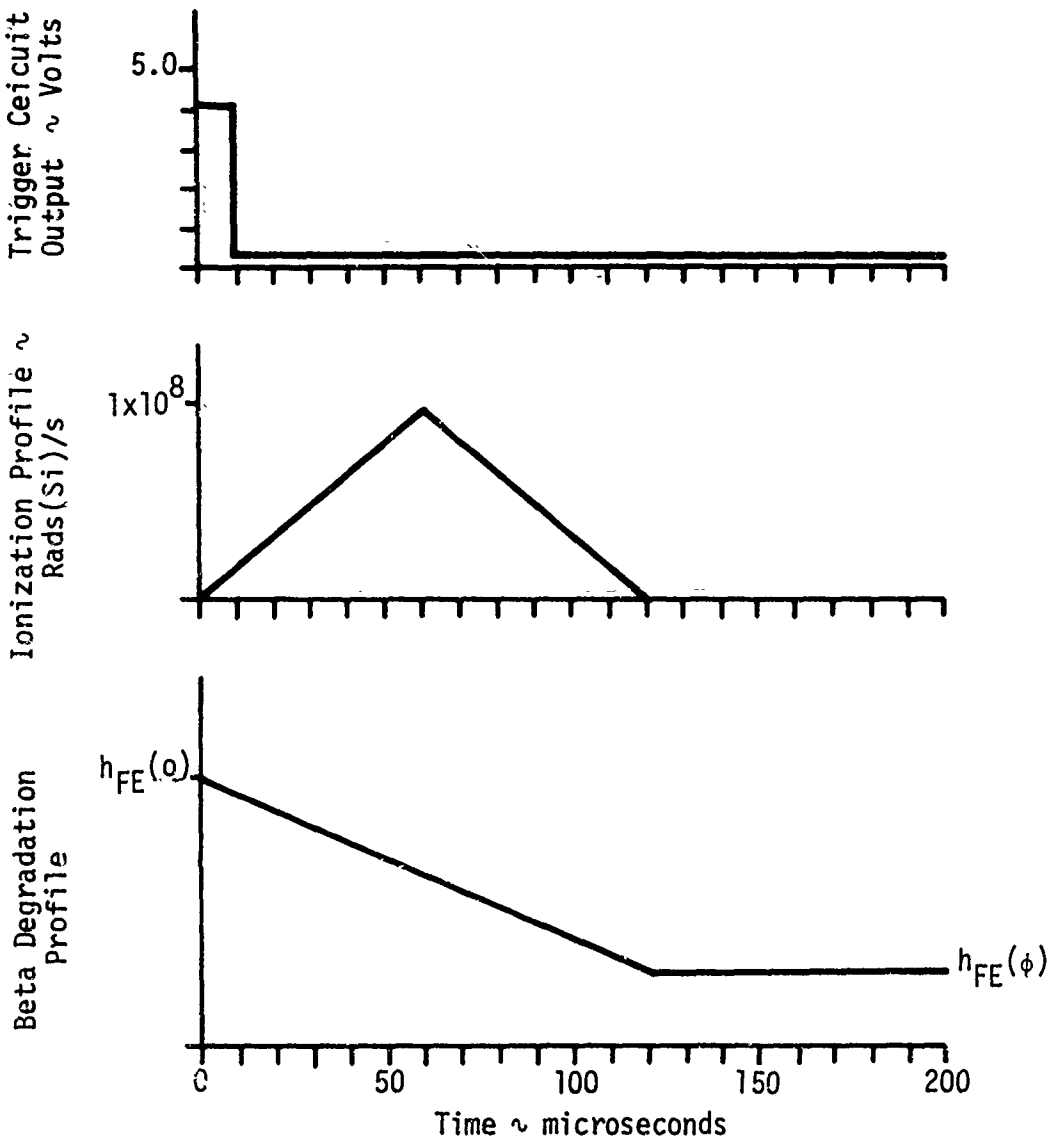

Figure 4-9. Computer Simulation of Readout Amplifier and Trigger Circuit to FBR Environment

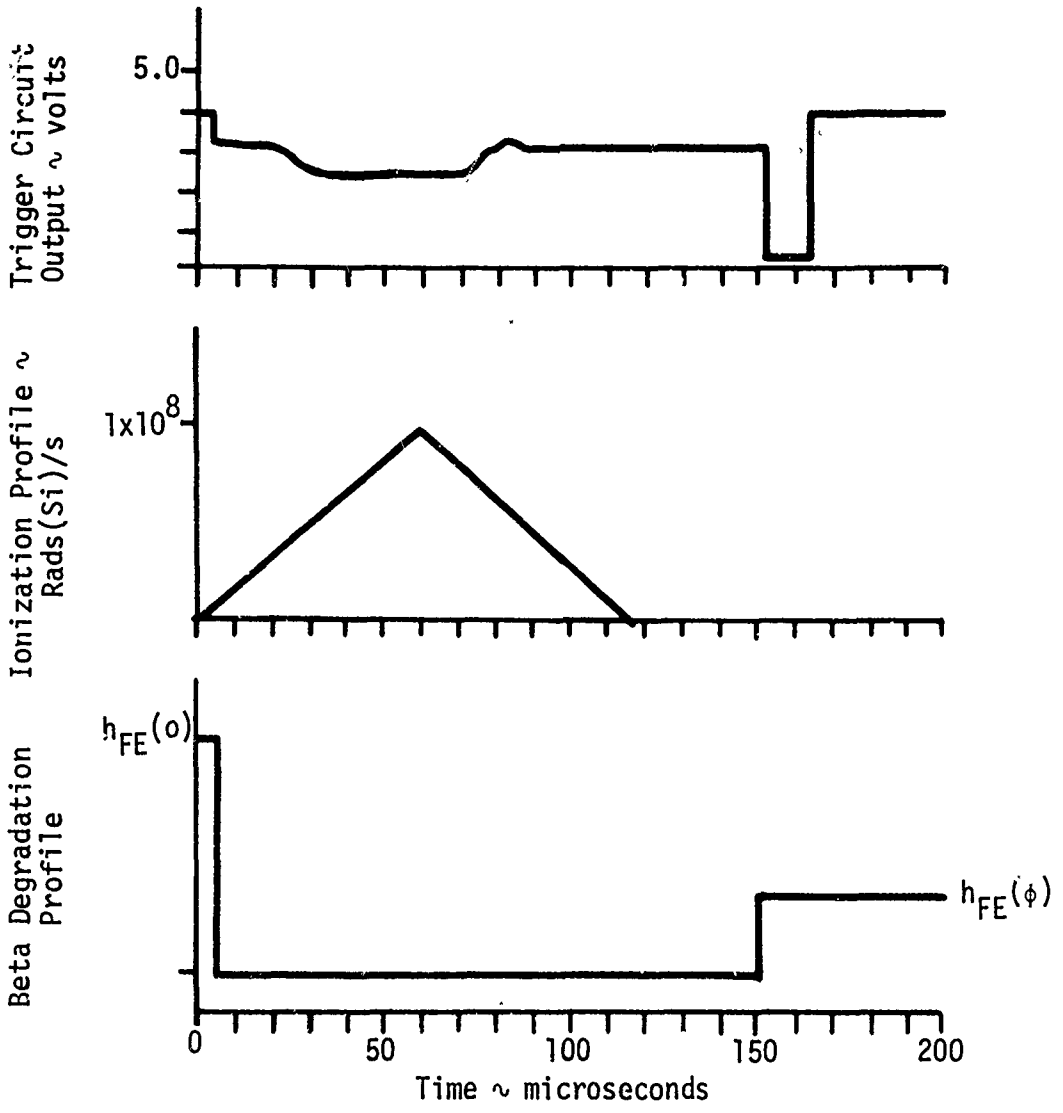

Figure 4-10. Computer Simulation of Readout Amplifier and Trigger Circuit to FBR Environment

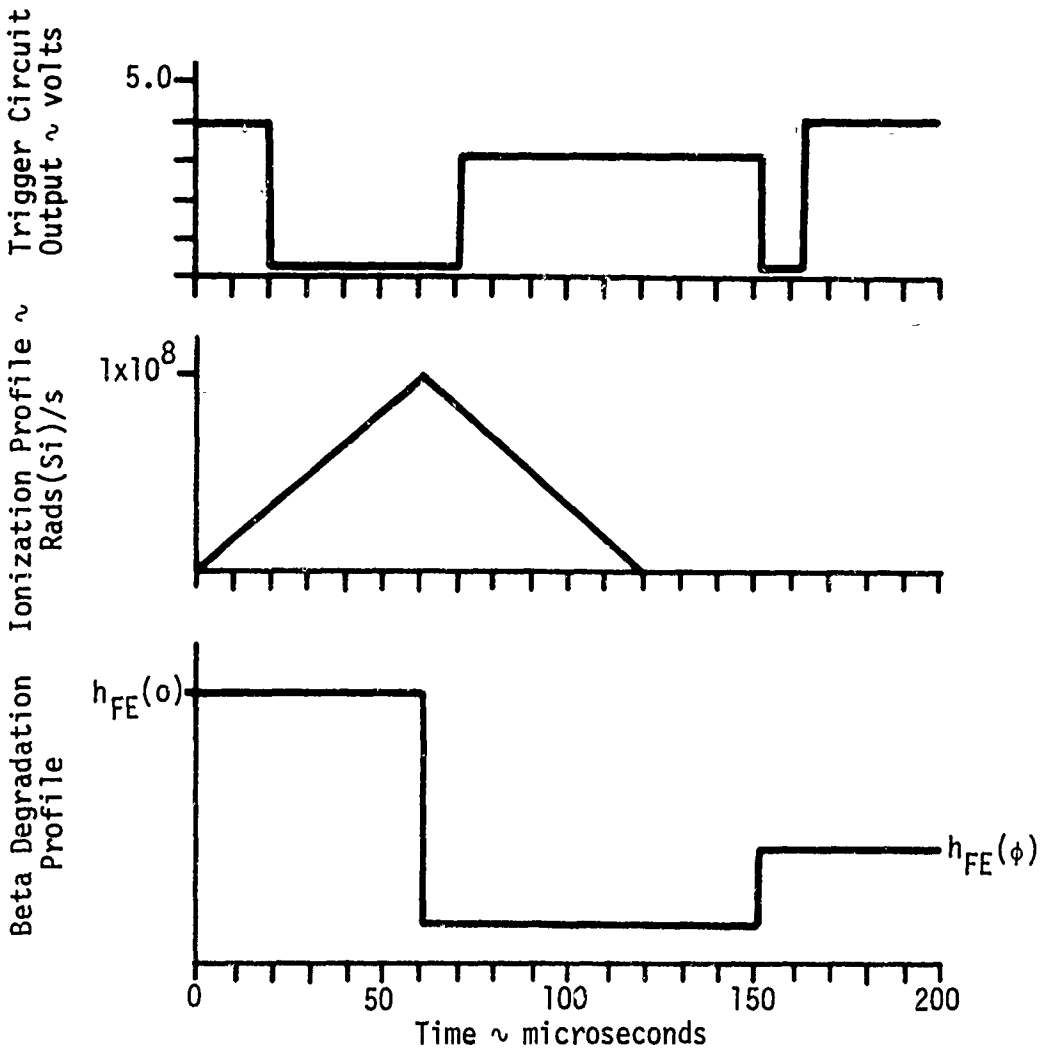

Figure 4-11. Computer Simulation of Readout Amplifier and Trigger Circuit to FBR Environment

1 Ceasing of normal operation at the start of the burst

2 The holding of the output at the high level (50 μs test data - 20 μs simulation)

3 The drop to the low state during peak dose rates (30 μs test data - 50 μs simulation)

4 The recovery to a level less than the original high state (60 μs test data - 80 μs simulation)

The time dependence between items 2 and 3 is directly attributed to exact measurements of photo current and ionization rate levels. The combination of the two times, 50 μs + 30 μs for the test, and 20 μs + 50 μs for the simulation is a measure of the correlation between the test and simulation.

The computer simulation restored the transistor gains to their post test levels immediately after 150 μs and the amplifier began to operate normally. In the test data, it is evident that transistor annealling is taking place as the magnitude of the signal increases for approximately 75 μs after normal switching begins. Because of the good correlation between the test data and the SECURE computer model, a high degree of confidence can be placed on the system simulation using these circuits.

5. TRIGGER CIRCUIT

The trigger circuit receives the amplifier laser gyro sinusoidal signal and generates a square wave signal for driving the digital logic circuitry. There are two signal channels that differ in phase by 90 degrees. This phase relationship makes it possible to determine the direction of rotation about that particular axis. Because the output drives digital logic elements, the maximum and minimum output requirements are the same as those defined for the digital logic.

One of the original trigger circuits to be analyzed is shown is Figure 5-1. This circuit was included in a single computer simulation with its associated readout amplifier. The predicted response to a maximum single burst at the FBR is shown in Figure 5-2. The amplifier and trigger circuit simulation was in a normal mode of operation (Figure 5-2a) at 5000 Hz until 220 µs. The ionization waveform corresponding to 2×10^8 rads(Si)/s and its time relationship with the output is shown in Figure 5-2b. The neutron degradation profile using the data discussed in section 2 is shown in Figure 5-2c. The normal output of the amplifier is disrupted from a minimum of 100 µs to a maximum of 200 µs after the burst. This recovery time is determined to the coupling capacitor between the readout amplifier and the trigger circuit as it returns to its initial conditions after being distributed by the semiconductor transients. The oscillation near 400 µs occurs in the computer simulation when the output of the readout amplifier is not driving the trigger circuit. The oscillation is the result of coupling via R47 from Q11 to the input transistor Q10, which is biased in an ambiguous state. This oscillation was observed during the FBR test, along with a 600 µs recovery time.

To incorporate better frequency and noise characteristics and faster radiation recovery times, the trigger circuit was redesigned. This circuit was modeled on the computer as shown in Figure 5-3. The circuit simulation was subjected to reduced transistor gains of 50. The response is illustrated in Figure 5-4. The duty cycle of the high (4.2V) state of the computer simulation changed from 33 to 70 percent. In normal operation, when being driven by the readout amplifier, the duty cycle of the trigger circuit is 50 percent. The system operates with two of these circuits (readout amplifier and trigger circuits). If the duty cycle of both units exceeds a 25 to 75 percent duty cycle, the inputs to the direction logic circuits will be incorrect and erroneous data will be generated. The 25 to 75 percent duty cycle requirement of the high state is best explained by use of the direction logic and timing diagrams of Figures 5-5, 5-6, and 5-7. Figure 5-5 shows the direction logic and the normal timing diagram

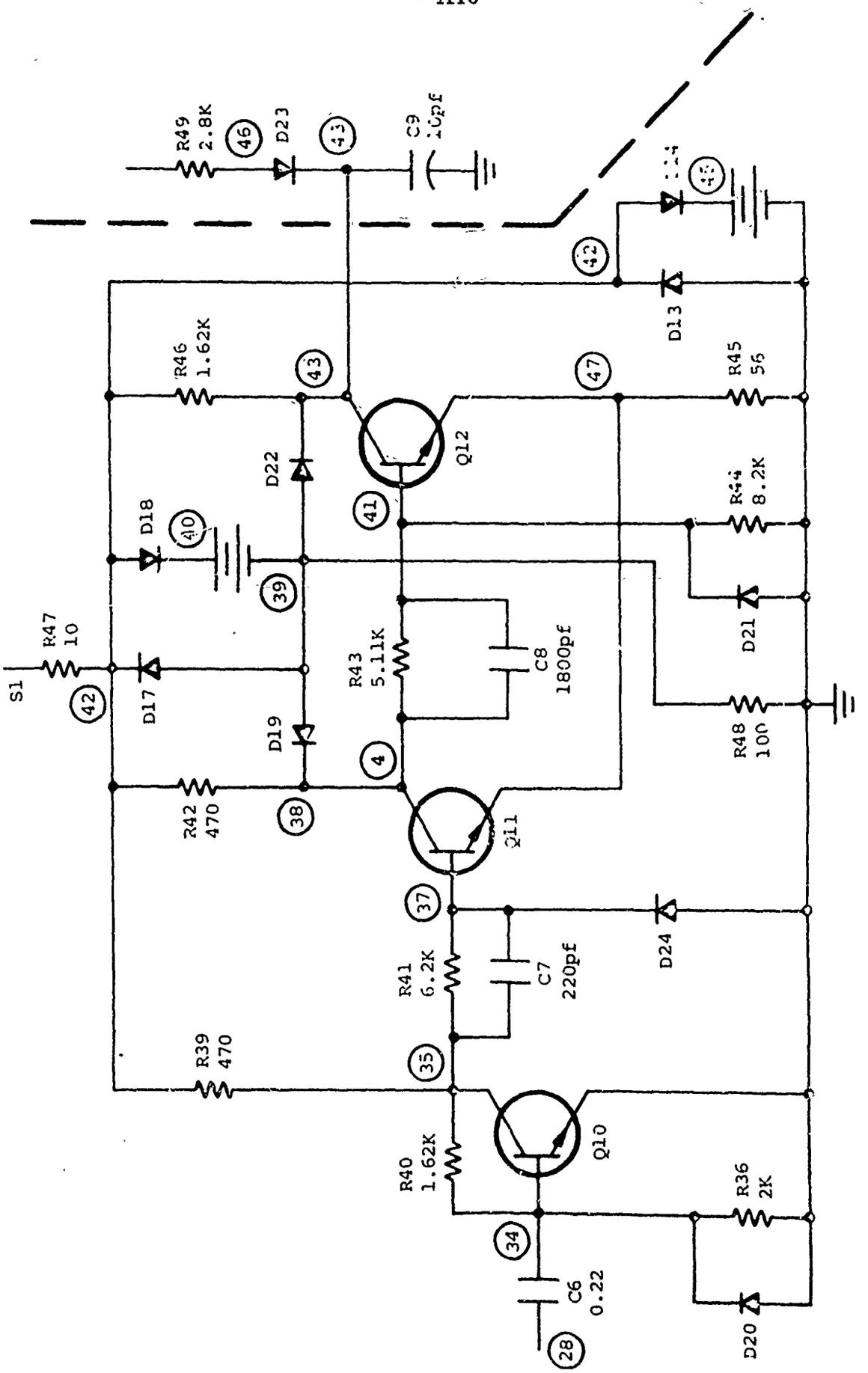

Figure 5-1. Readout Amplifier Trigger Circuit

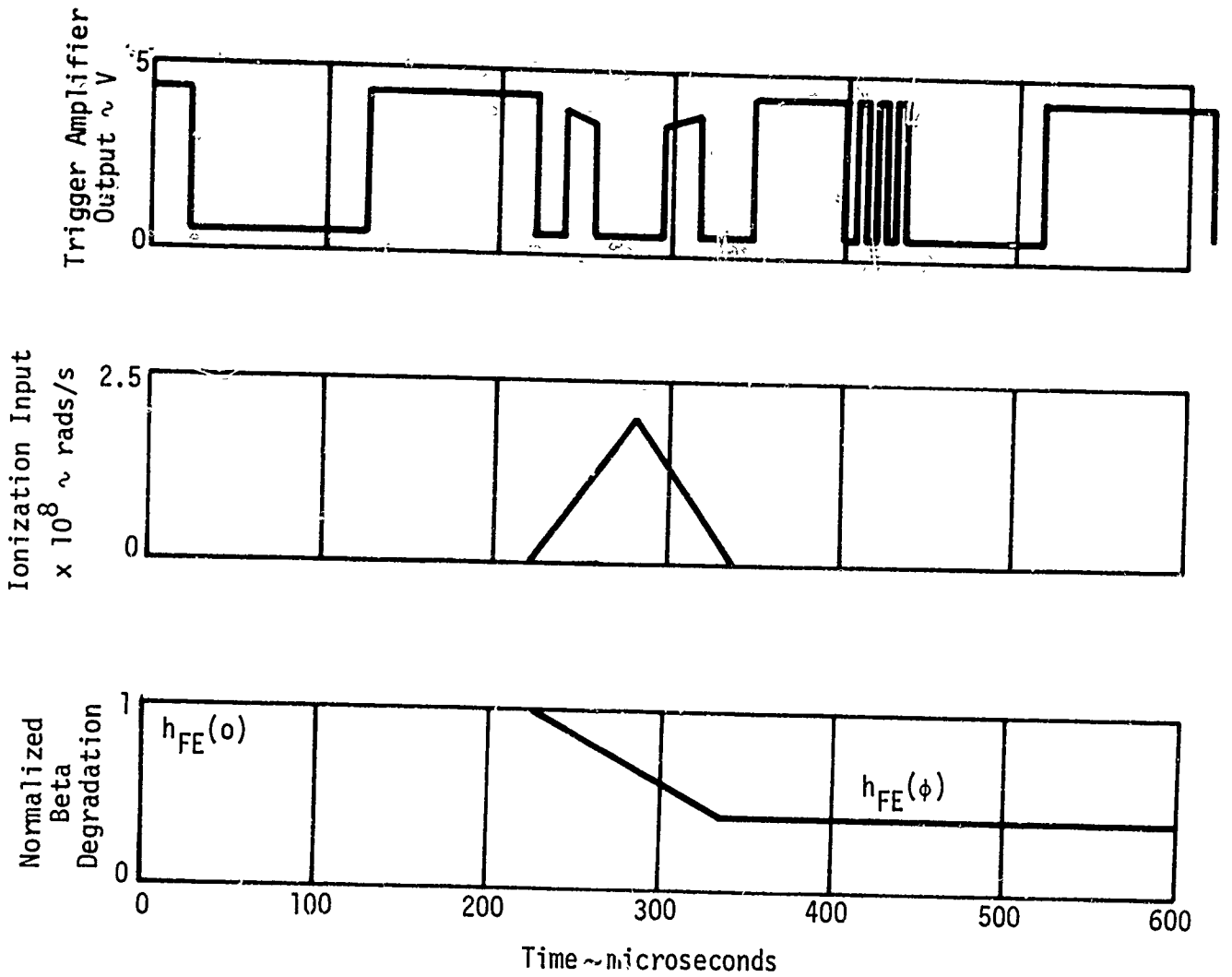

Figure 5-2. Predicted Response - Readout Amplifier and Trigger Circuit at FBR

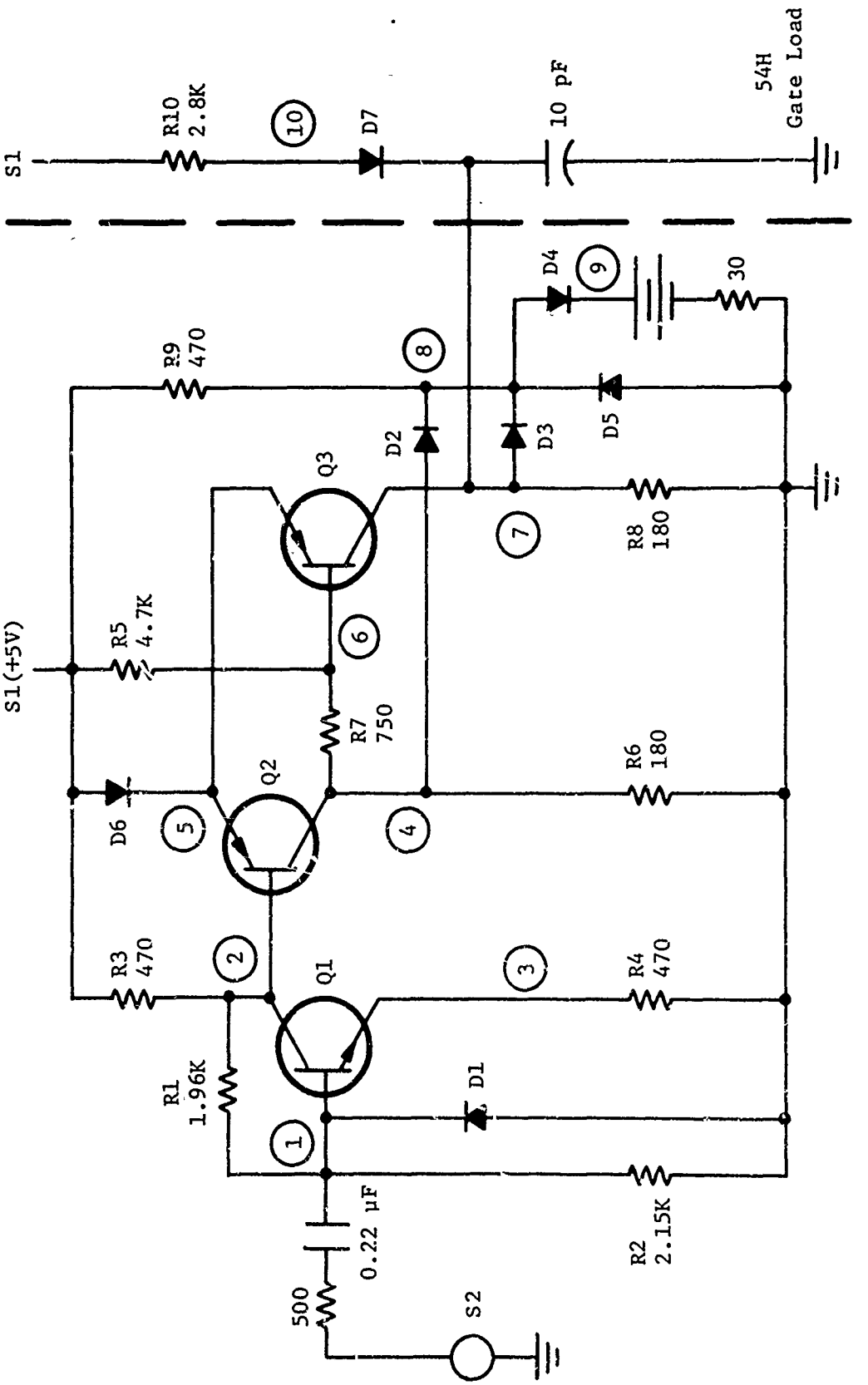

Figure 5-3. Readout Amplifier Trigger Circuit

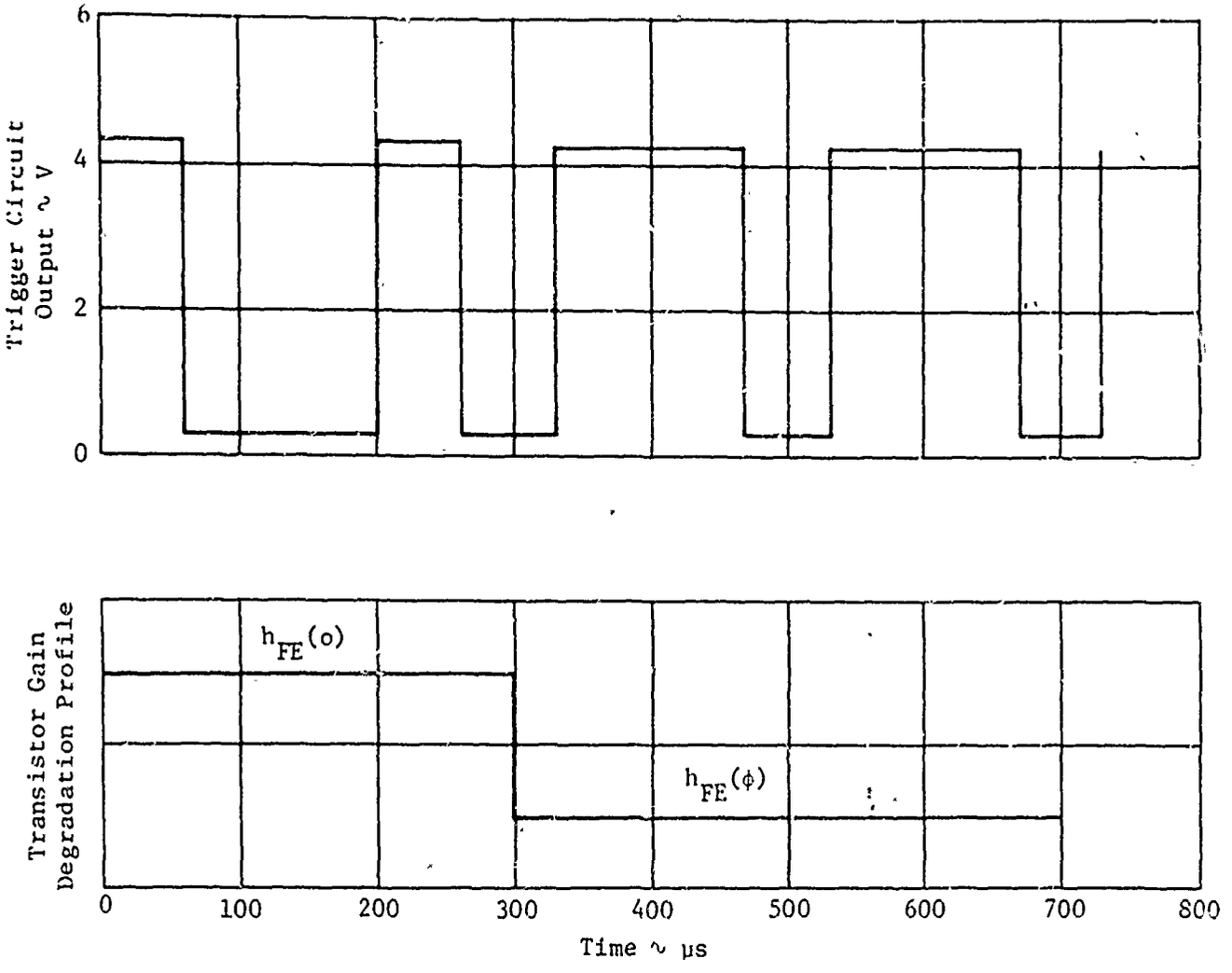

Figure 5-4. Redesigned Trigger Circuit Response to Beta Degradation

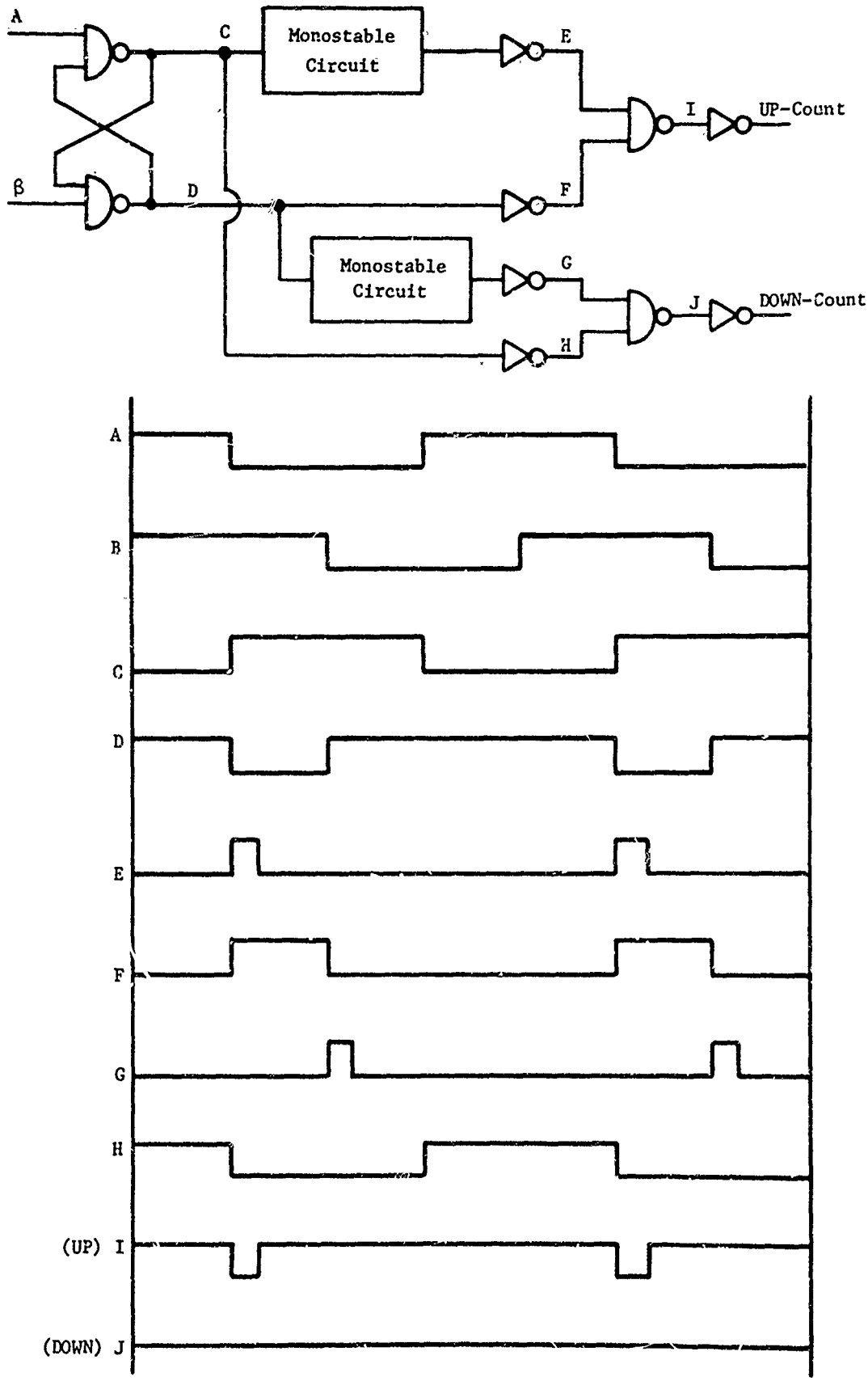

Figure 5-5. Direction Circuit and Normal UP-Count Timing Diagram

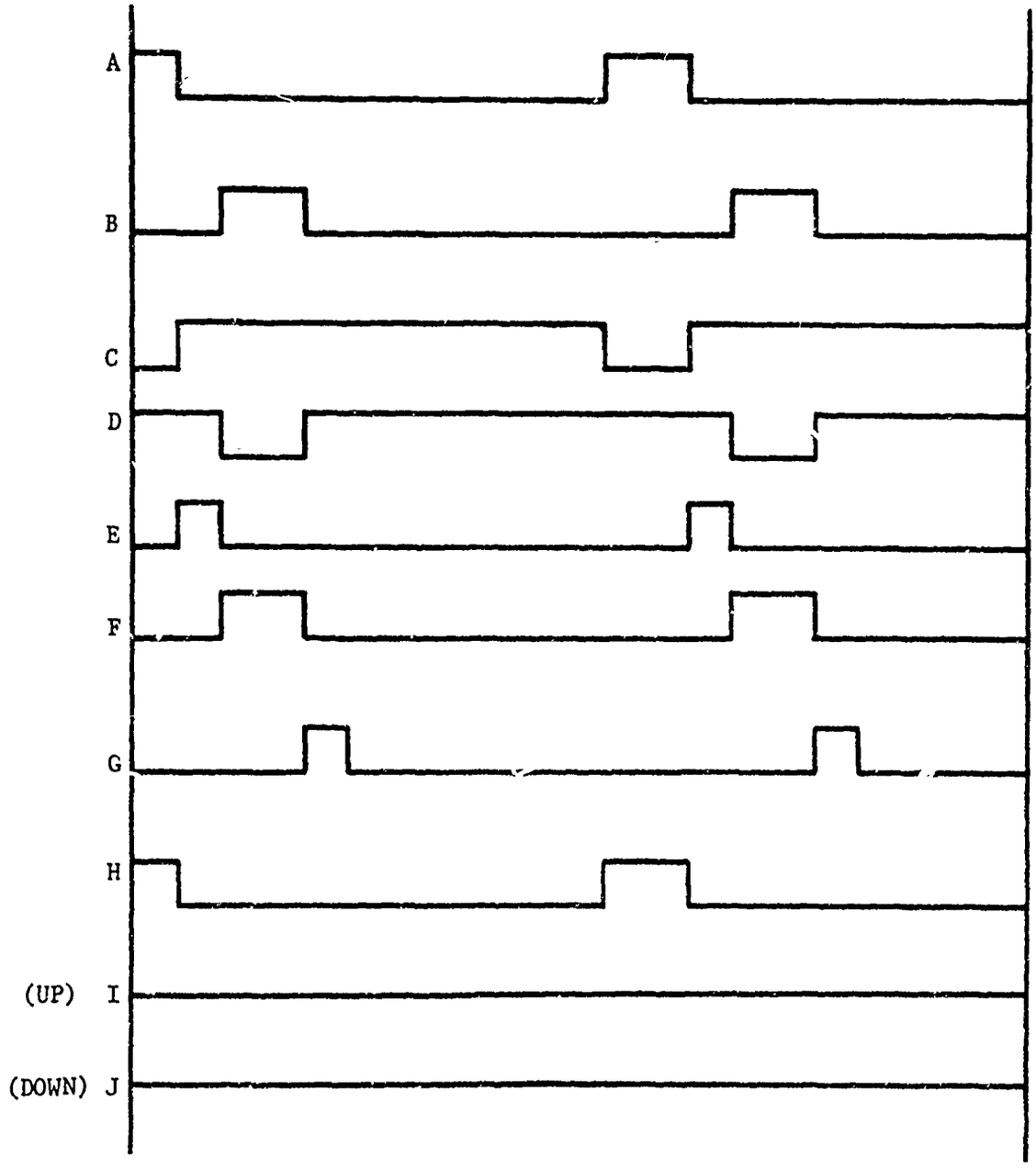

Figure 5-6. Timing Diagram for a Less Than 25 Percent Duty Cycle

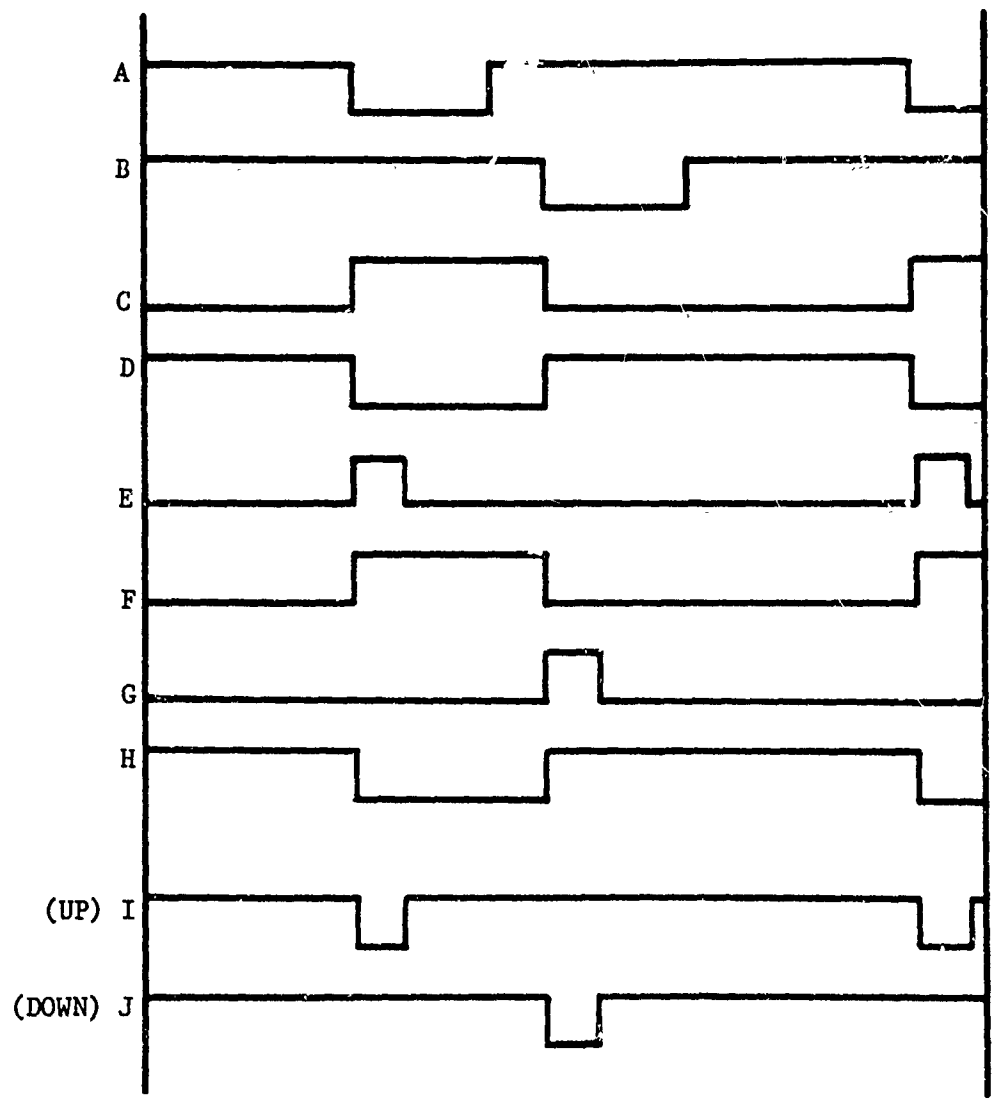

Figure 5-7. Timing Diagram for a More Than 75 Percent Duty Cycle

for the generation of an UP-count; i.e., input A leads B by 90 degrees. Figure 5-6 shows the timing diagram if the duty cycle is less than 25 percent. For this case, there will be no counts generated because the coincidence between signals E and F no longer exists. Figure 5-7 shows the timing diagram if the duty cycle is greater than 75 percent. For this case there will be both an UP- and DOWN-count generated.

The sensitivity due to input voltage and reduced transistor gains for the trigger circuit is shown in Figure 5-8. As the transistor gains decrease, the duty cycle of the high state increases, hence the high percentage duty cycle condition is the only one of interest. An analysis of the readout amplifier shows that the output voltage (input voltage to the trigger circuit) decreases from 1100 mV to approximately 900 mV. This magnitude assumes the lowest sensor input current of 4.2 μA peak-to-peak. Using 800 mV as a minimum voltage input of the trigger circuit, the minimum transistor gain (using all 2N5107's) has to be 35 to keep the duty cycle less than 75 percent. The circuit for turning off transistor Q3 is shown in Figure 5-9.

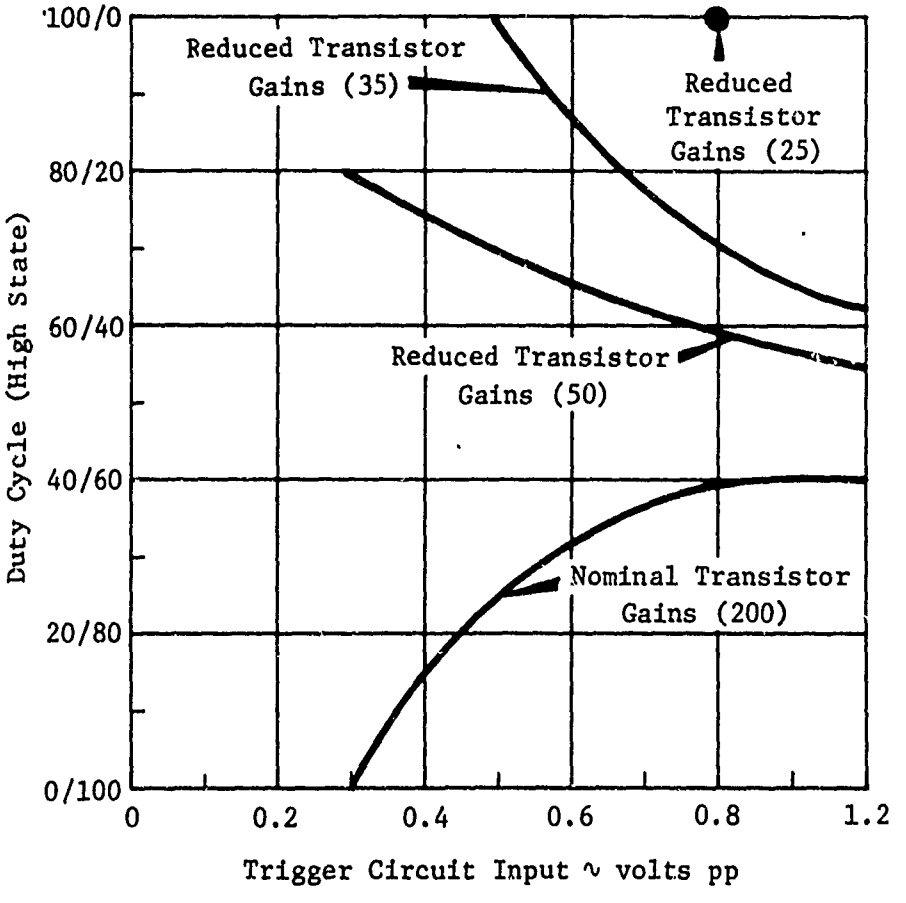

Figure 5-8. Trigger Circuit Duty Cycle Sensitivity Due to Input Voltage and Reduced Transistor Gains

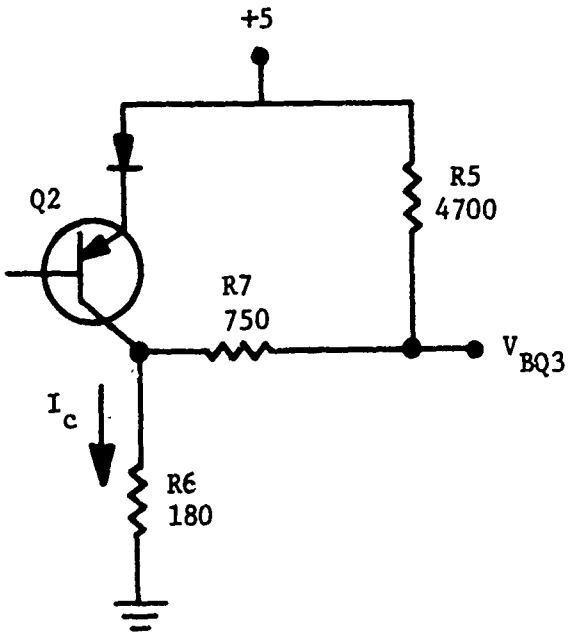

Figure 5-9. Transistor Q3 Turnoff Circuit

The voltage at the base of Q3 is:

$$V_{BQ3} = \frac{(180+750)}{4700+180+750} \times 5 + I_c \times 180 \times \frac{4700}{4700+750}$$

$$= 0.83 + I_c \times 180 \times 0.86.$$

For Q3 to be off, $V_{BQ3} = 3.6$, therefore,

$$I_c = \frac{3.6-0.83}{180 \times 0.86}$$

$$= 18 \text{ mA}.$$

Because of the input impedance of Q2, the peak base current of Q2 is 0.5 mA. With this base current, a minimum transistor gain of 36 is necessary to turn off Q3.

Although this calculation appears redundant in view of the computer analysis, it can be seen that by increasing resistor R6 (180 ohms) to a higher value, the required transistor gain decreases. Using a resistor value of 390 ohms, the change in duty cycle with reduced transistor gains increased only 10 percent. The trigger circuit was then modified as shown in Figure 5-10. This modified circuit was not analyzed separately but is covered in the system analysis.

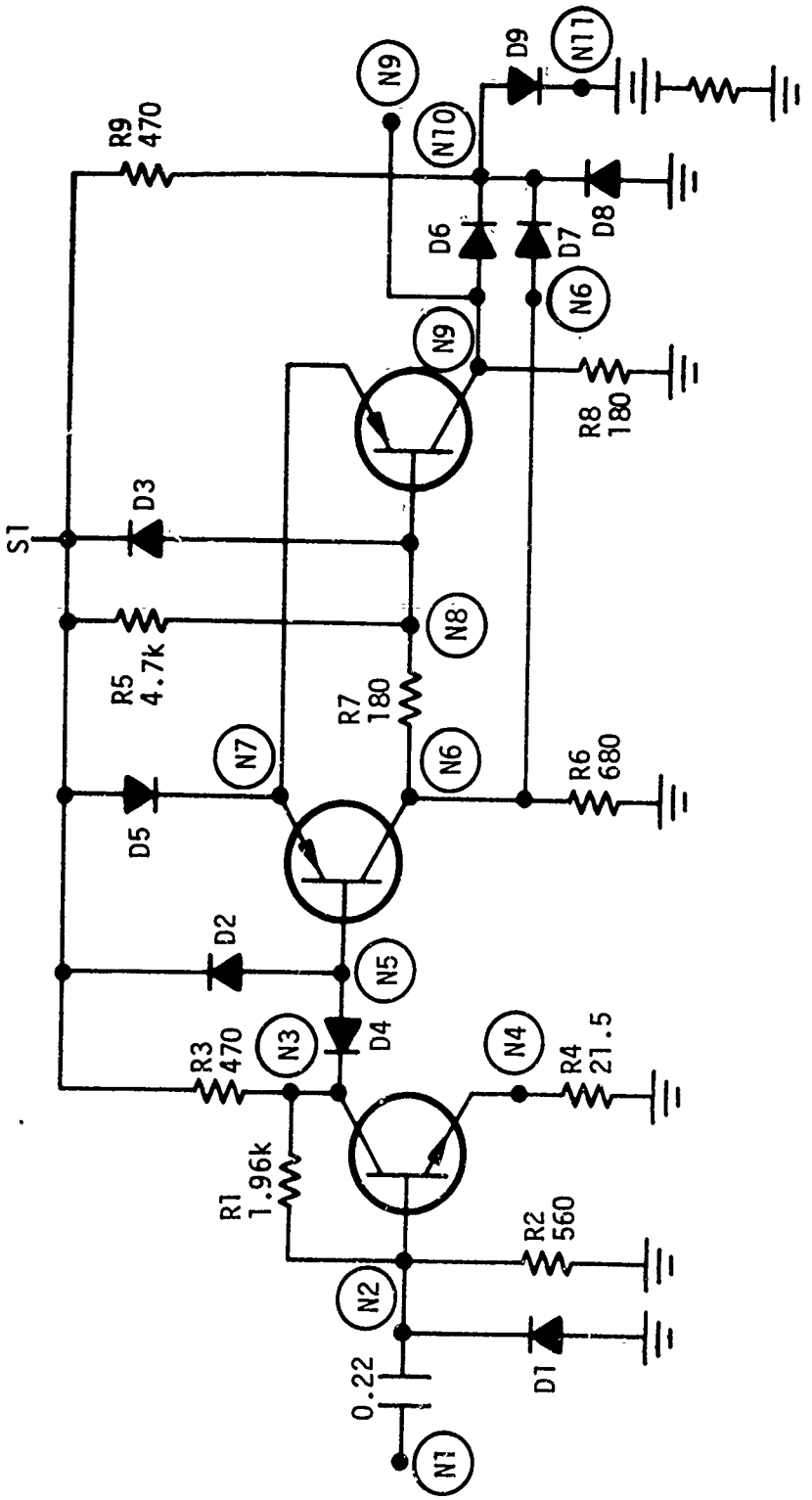

Figure 5-10. Trigger Circuit

6. DIRECTION LOGIC CIRCUIT

The computer simulation for the UP-count direction logic using the 54H series logic circuitry is shown in Figure 6-1. This simulation includes the input flip-flop and the one-shot (monostable) mechanism. Any discussions concerning the UP-count logic are directly applicable to the DOWN-count logic since the circuits are identical.

The monostable portion of this circuit was first analyzed in a pretest report to determine its response in the SFXR environment. The original analysis was for implementation using the 5400 series logic. The results of the computer analysis of that monostable at two different dose rate levels anticipated at the SFXR are shown in Figure 6-2. Figure 6-2a shows the normal operating condition at the output when switching at a 2 MHz rate. Figure 6-2b shows the transient response to ionizing radiation when the output is in the high state. The radiation transient appears as an additional output pulse whose width is a function of the radiation duration. Figure 6-2c shows the response to radiation when the output is in the low state. The transient delays the normal switching signal for approximately the duration of the radiation pulse because the gate remains in the low state during the radiation pulse, inhibiting the R-C action of the monostable. After the radiation pulse, the monostable action is again initiated. Figure 6-2d shows the negligible response to a lower radiation dose rate.

The UP-count direction logic as shown in Figure 6-1 uses the 54H series logic circuit. In normal operation, the one-shot circuit is activated by a positive gate at node 7. This gate comes from the input flip-flop, which is driven from the readout amplifier circuit. The input flip-flop can have four conditions at its input (inputs A and B). Assuming a normal UP-count sequence, the following comments can be made concerning the predicted response with a peak dose rate of 1×10^{12} rads(Si)/s. With A and B in the positive state, the input flip-flop changed state. Since all of the gates drop to a low state during ionization, the output gate, which is normally in the low state, gives no false indications. Immediately after the radiation, the one-shot sequence takes place to generate a 35 ns pulse. Since the logic gates perform normally after the radiation burst, the pulse from the one-shot appears at the output as an UP-count. When input A goes to a low state in normal operation, the flip-flop will not change state again because it is in the correct state for this set of inputs; hence, no UP-count is generated. This is of no consequence because the UP-count pulse was initialed by the radiation burst. The flip-flop with any other set of inputs returns to its preradiation state and the UP-count direction logic operates normally without any false triggering.

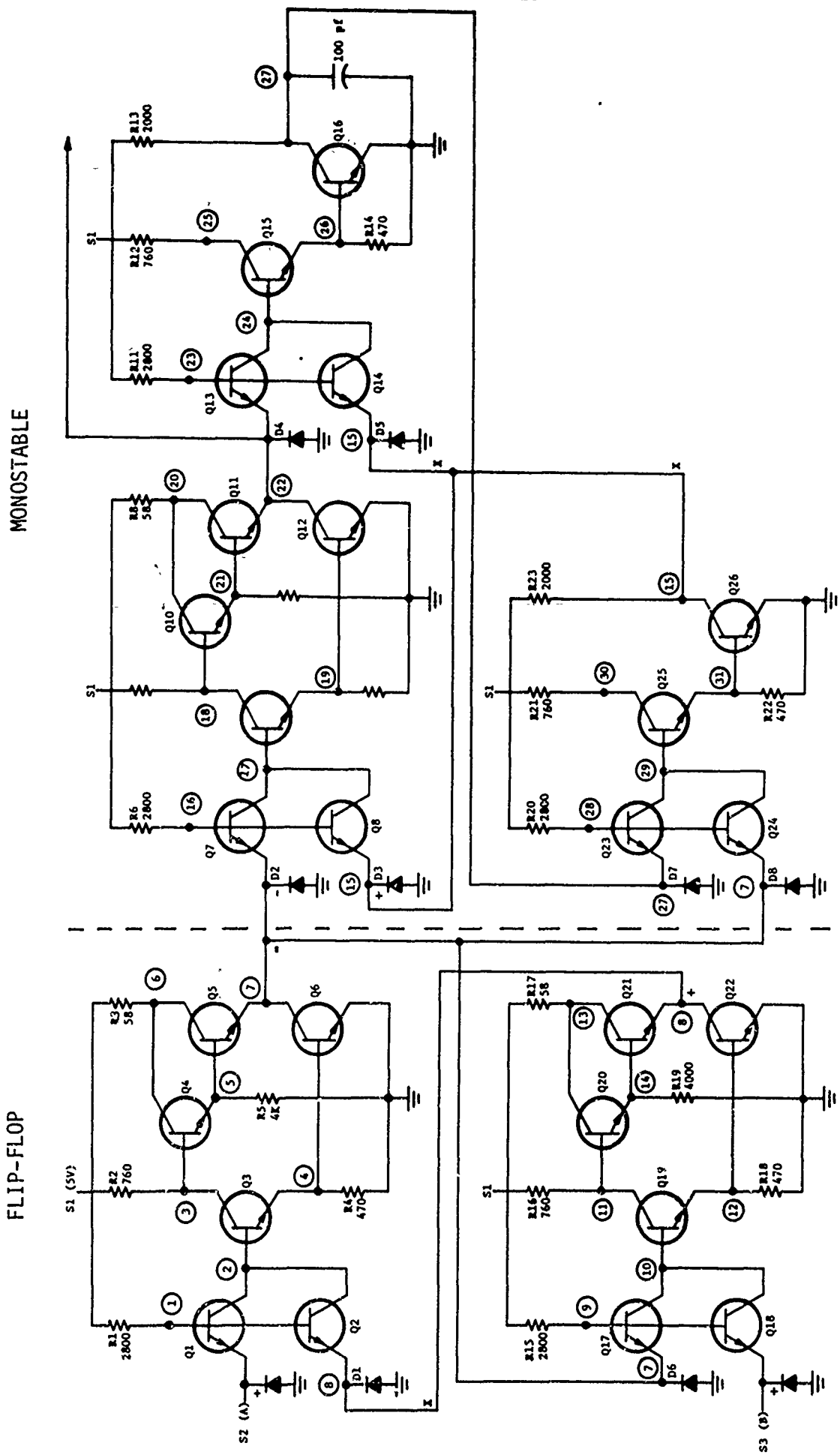

Figure 6-1. UP-Count Direction Logic

(a) Switching Characteristics at 2 MHz

(b) Ionization Response of One Shot for 1×10^{12} rads/s

(c) Ionization Response of One Shot for 1×10^{12} rads/s

(d) Ionization Response of One Shot for 1×10^{9} rads/s

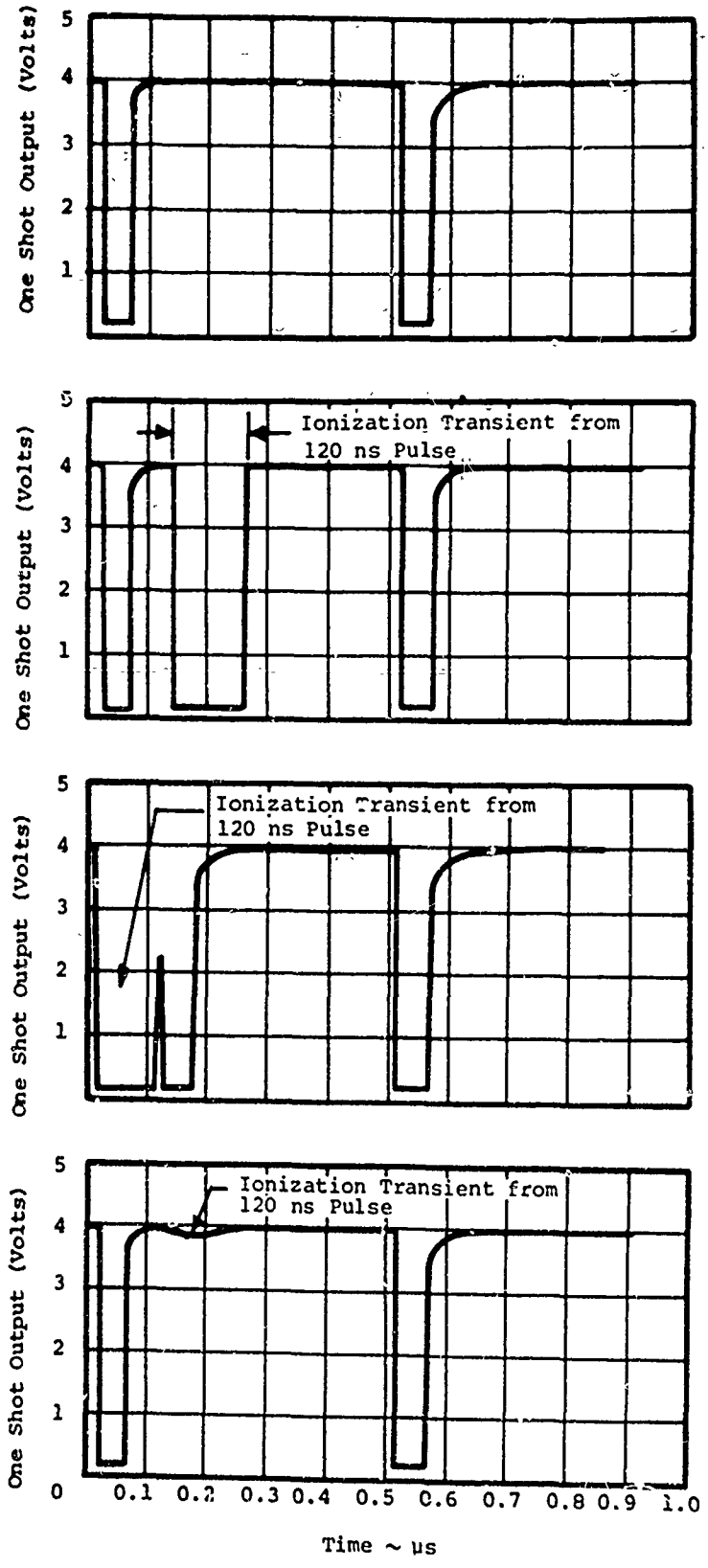

Figure 6-2. 5401 One-Shot Ionization SFXR Prediction

Test data taken at the SFXR (shot No. 9 with $\dot{\gamma}$ maximum approximately 2 to 4 x 10^{11} rads(Si)/s) shows normal direction logic operation resumes 1 to 2 microseconds after the burst at the above mentioned levels. Because of the large EMI signals, data during and shortly after the pulse (less than 2 μs) is not measurable. Data (Honeywell FBR Test Data) taken at the FBR showed there were no observable effects to the direction logic from a peak $\dot{\gamma}$ rate of 1 to 2 x 10^{8} rads(Si)/s. These test results support the pretest analysis and indicate that the simulation model is adequate.

7. DIVIDE-BY-16 COUNTER CIRCUIT

The divide-by-16 counter is made up of four flip-flops with their associated input gates. The original design called for an MCE 54H73 unit, but because these parts were not readily available, Motorola recommended the 54H103, which was used and analyzed. The schematic diagram of the 54H103 is shown in Figure 7-1. The response of the circuit simulation using the SFXR simulator radiation profile showed that the flip-flop does not return to the preradiated state but to a state determined by noise or by a parameter such as beta mismatch. This could result in a pulse being gained or lost. The flip-flop simulation remained in the preradiation state for ionizing radiation dose rates of up to 1×10^9 rads (si)/s.

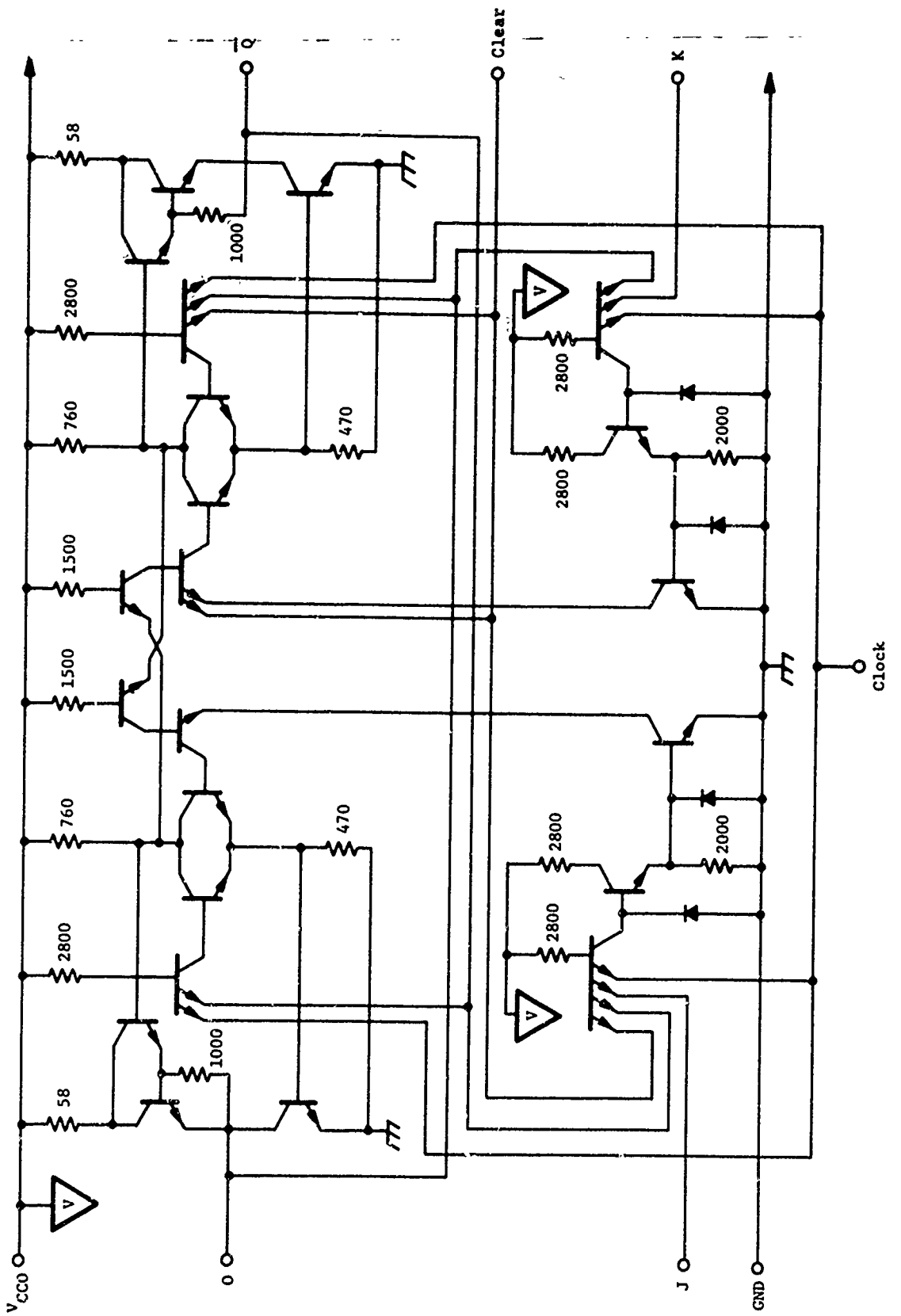

Figure 7-1. 54H103 J-K Flip-Flop

8. PULSE STRETCHER AND LINE DRIVER CIRCUITS

The pulse stretcher and line driver circuits receive a 35 ns pulse from the counter and increase the pulse width to 5 μs. The output line drivers are used to drive low impedance lines for monitoring and/or system interconnects. The pulse stretcher circuit is made up of an input flip-flop and the timing gates. The incoming 35 ns pulse from the counter changes the state of the flip-flop and initiates the timing mechanism. After the timing circuit has "timed out," the input flip-flop is returned to its normal state.

The UP-count line driver was modeled as shown in Figure 8-1. The computer simulation showed that the 5 μs monostable is dependent on transistor characteristics and not solely on external components. The timing circuit can be isolated as shown in Figure 8-2. An approximate equivalent resistance for determining the time constant during a charging cycle is:

$$\frac{1}{R_{eq}} = \frac{1}{6k} + \frac{1}{2.8k} + \frac{1}{\beta \times 470}$$

$$R_{eq} \approx 1.75k \text{ and } RC = 17.5\ \mu s.$$

Using V_{BE} of 0.7 volt nominal (0.6 minimum to 0.9 maximum), the time can be determined using the equation

$$V_C(t) = V(Q18)_{CE} + V(Q19)_{BE} + V(Q20)_{BE} - V_C(o)$$

where

$$V_C(t) = 5[1 - e^{-t/RC}].$$

For these calculations, $V(Q18)_{CE} \approx 0$.

Solving for the nominal case, $V_C(0) = 0$; $V(Q19)_{BE} = V(Q20)_{BE} = 0.7$ volt

$$5[1 - e^{-t/RC}] = 1.4$$

$$e^{-t/RC} = \frac{5 - 1.4}{5}$$

$$t = 5.8\ \mu s.$$

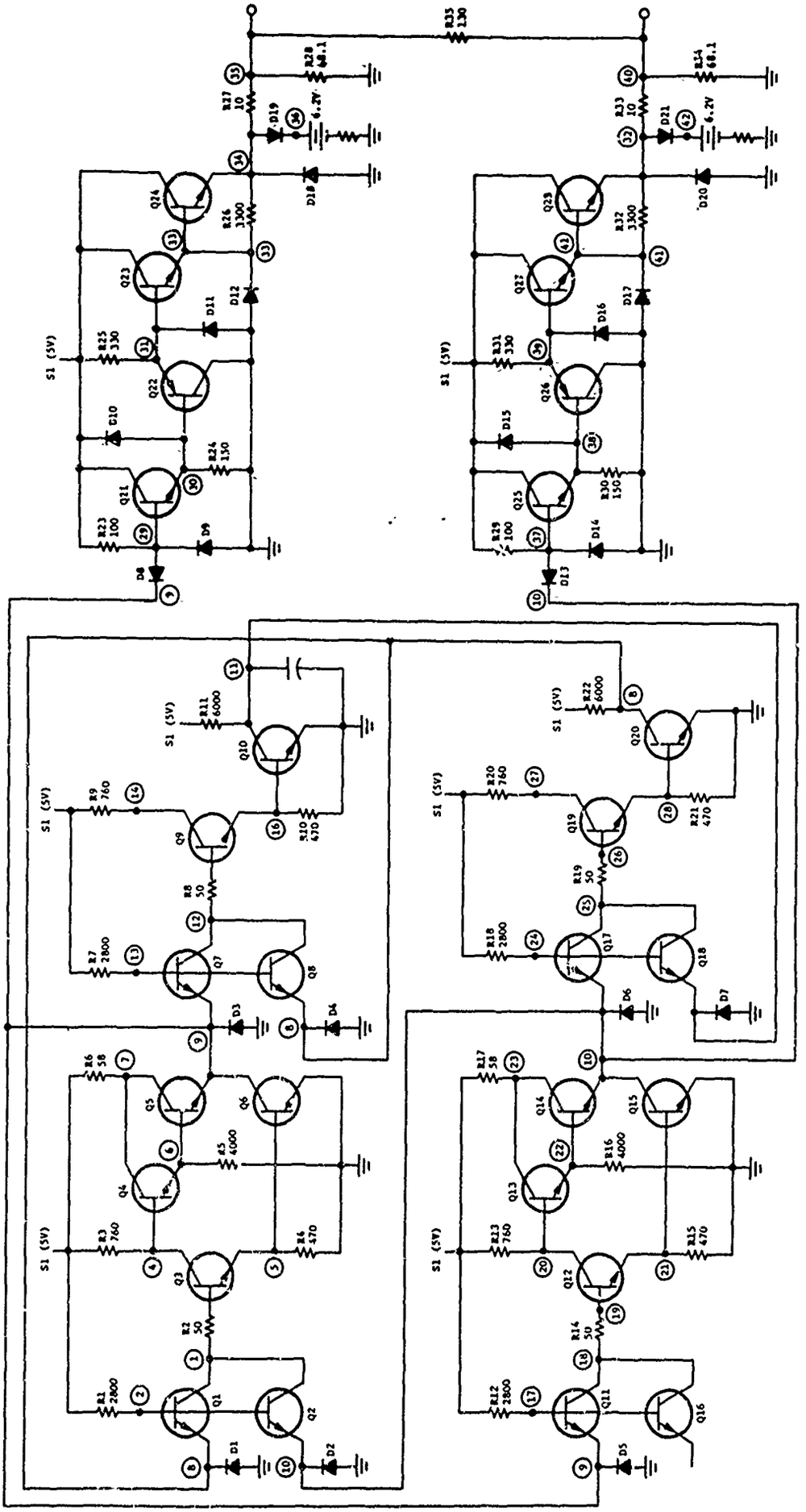

Figure 8-1. UP-Count Line Driver

Worst case (low) $V(Q19)_{BE} = V(Q20)_{BE} = 0.6$; $V_C(0) = 0.4$

$$5[1 - e^{-t/RC}] = 1.2 - 0.4$$

$$e^{-t/RC} = 5 - 0.8$$

$$t = 3.1\ \mu s.$$

Worst case (high) $V(Q19)_{BE} = V(Q20)_{BE} = 0.9$; $V_C(0) = 0$

$$t = 7.8\ \mu s.$$

A breadboard line driver (two monostables) at Honeywell, using standard parts, showed a pulse duration of 4.8 μs and 5.3 μs.

The radiation response of the line driver is shown in Figure 8-3. If the output is taken differentially, the predicted output will be zero for approximately 200 ns with total recovery at 300 ns; the reason for zero output during the radiation burst is due to the identical output stages which respond to the radiation in the same way. The 54H gates recover to the preradiation states when the ionization goes below the threshold level but because of the transistor and zener characteristics used in this simulation, total recovery is not achieved until 300 ns. The data for the transistors is accurate, but because of lack of information on the zener diode, typical model parameters were used corresponding to similar diodes used in the SPRINT program. The characteristics of these zener diodes were high photocurrents, approximately 40 ma at 10^9 rads(Si)/s and long storage times. The storage time using the same short duration ionization pulse was approximately 100 ns. This delayed recovery does not present any system impact. It should be noted that the monostable circuit

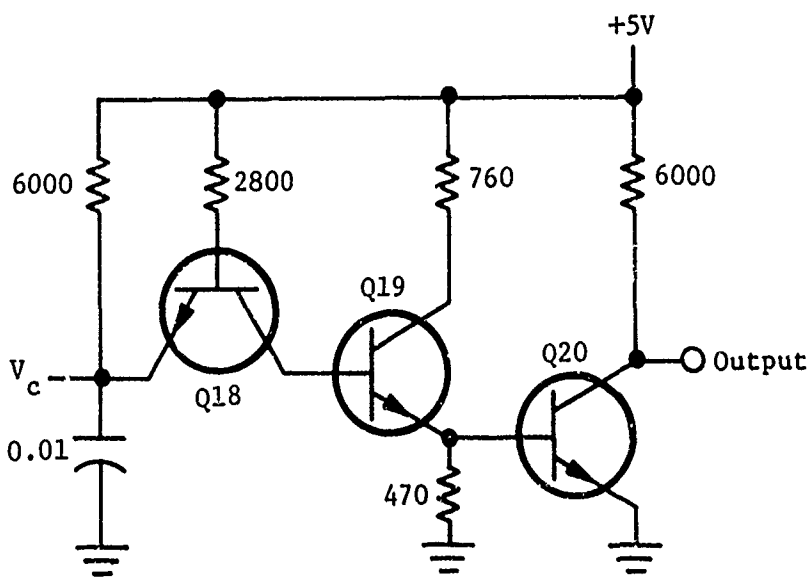

Figure 8-2. Timing Circuit

did not trigger in the computer simulation because the latching circuit recovered to its preradiation state. The SFXR test data at levels of 1 and 2 x 10^{11} rads(Si)/s (shot numbers 8 and 9) indicate the flip-flop recovered not to the preradiated state but to the triggered state generating a false 5 μs pulse. Because there is no preferred state, it is not unreasonable to expect the flip-flop to recover to this state although at levels of 5 x 10^{9} to 1 x 10^{10} rads(Si)/s (SFXR test data shots 6 and 7) and lower, these same units recovered to the preradiation state without generation of a false count. The generation of a false count during a high level gamma rate would not affect system operation because the circumvention circuits of the missile computer would be activated.

The UP-count line driver circuit was subjected, in the computer simulation, to the environment expected at the FBR facility and was found to have no appreciable response. The change in the output during the burst was only 250 mV. This magnitude will be difficult to observe because the normal output voltages are approximately ±3 volts. The decrease in transistor gains reduced the output voltage swing at node 35 from 2.950 volts to 2.900 volts, which is insignificant. The FBR tests showed no false triggering or performance degradation, as noted in the pretest analysis.

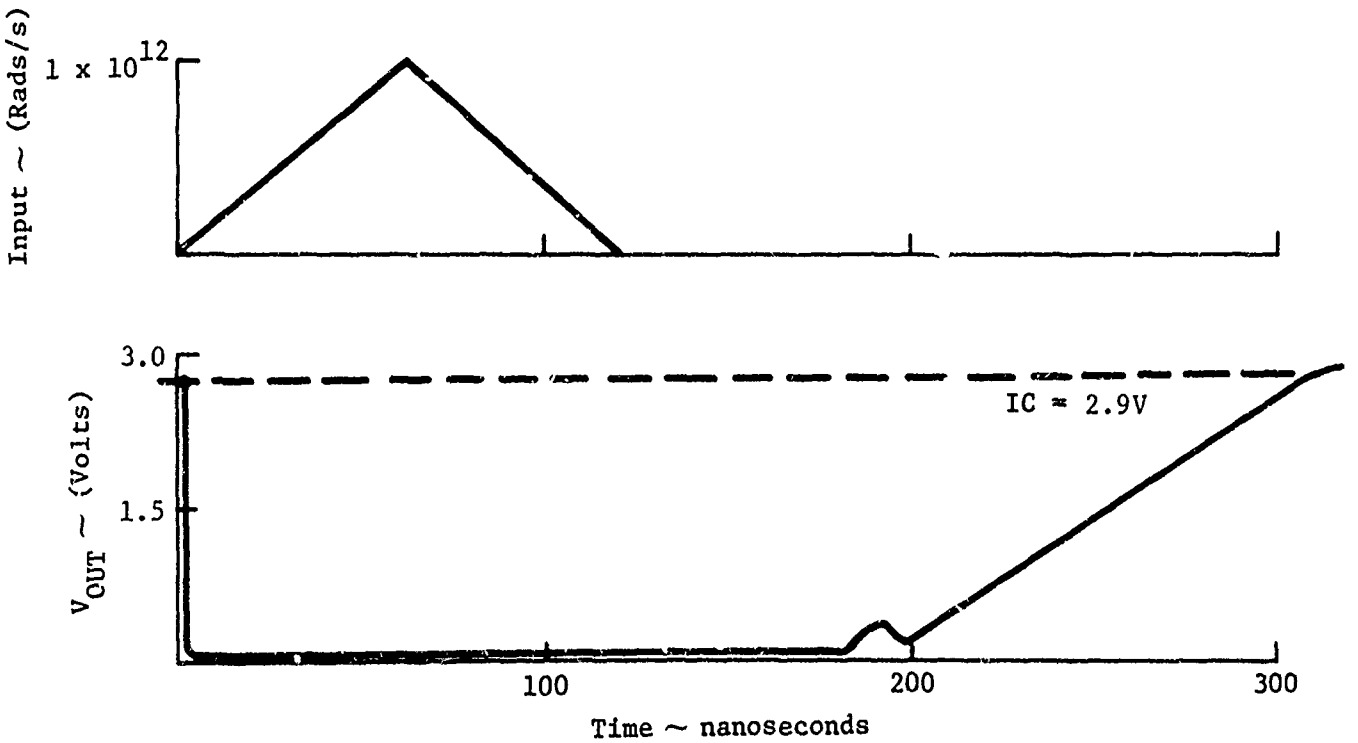

Figure 8-3. Predicted Radiation Response of Line Driver

9. START/RESTART CIRCUIT

The laser gyro start/restart circuit is shown in Figure 9-1. If the gyro lasing current decreases in any one of the six legs of the gyro, the 54H30 gate goes to a high level, turning on the transistors that ground the center tap of the high voltage transformer. Resistor R5 represents the transformer load that generates the voltage needed to start the lasing action.

The start/restart circuit was found to give a restart signal during the SFXR test even though the lasing action showed no signs of extinguishing. The output of the logic gate is normally in the low state; therefore, any ionizing radiation will only enhance the logic state. The discrete elements were modeled on the computer to determine a possible cause of the false triggering. The schematic is shown in Figure 9-2. Diodes D1, D2, and D3 are the collector-base junction of the same type (2N5107) of transistor used as Q1, Q2, and Q3. These diodes provide photocurrent theoretically of the same magnitude as that generated in the collector-base junction of the transistor. If the photocurrents are identically matched, there will be no current available to cause secondary photocurrent. Secondary photocurrent is the current that flows in the collector of the transistor that was generated by primary photocurrent flowing into the base. Generally, the photocurrent values are assumed to be independant of bias voltage, but this is not entirely true. Tests conducted by Martin Marietta on a single transistor using a reverse bias of 5 and 25 volts showed an increase in photocurrent of 30 percent at the higher bias level. The reverse bias on diode D3 and Q3 is approximately 0.5 and 5.0 volts, respectively. Postulating that this same photocurrent difference exists because of the voltage ratios, then the photocurrent of D3 would be 115 µA at 10^7 rads (Si)/s, instead of 150 µA.

For Q3 to be ON completely, its collector current would be 340 mA. With a transistor gain of 200, only 1.7 mA of base current is necessary to support the 340 mA of collector current. With a differential of 35 µA at 10^7 rads(Si)/s, transistor Q3 will be ON at 5×10^8 rads(Si)/s. The only way to ensure keeping Q3 OFF at levels up to 1×10^9 rads(Si)/s would be to use a diode with much more photocurrent than the transistor.

Testing at the FBR facility indicated that the restart circuit was triggering at the lower rate, not due to the output circuit but due to the levels created at the input to the gate. It was found that ionization of transistor Q5 (Figure 9-1) caused the transistor photocurrent to flow through the 19.6k resistors giving a false start signal. To prevent the

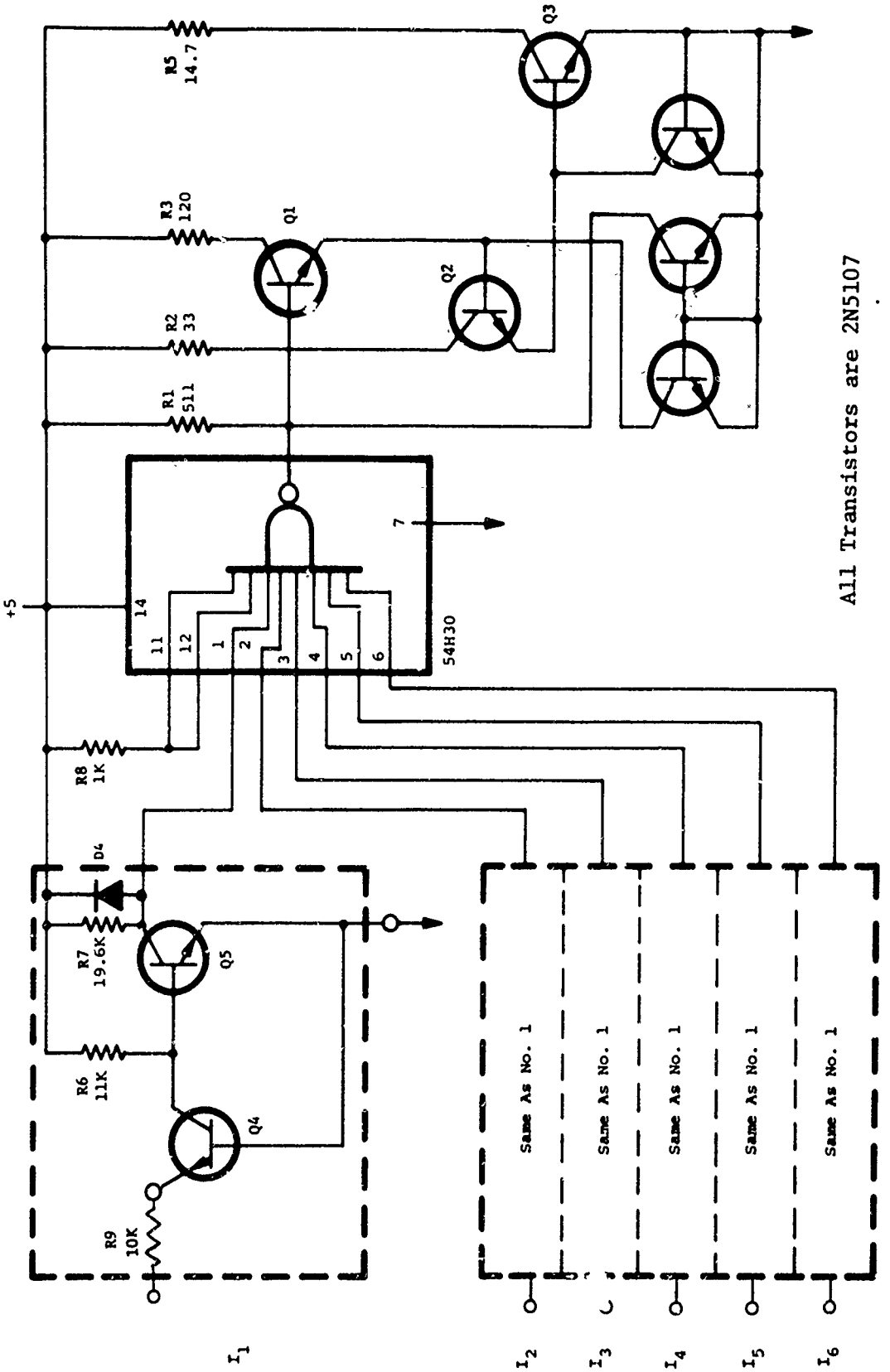

Figure 9-1. Laser Gyro Start/Restart Circuit

photocurrent from flowing through the 19.6k resistor, diode D4 was added to provide an alternate path for the photocurrent. This modification should prevent any false triggering of the start circuit at low ionization rates, although false triggering does not appear to hinder normal operation.

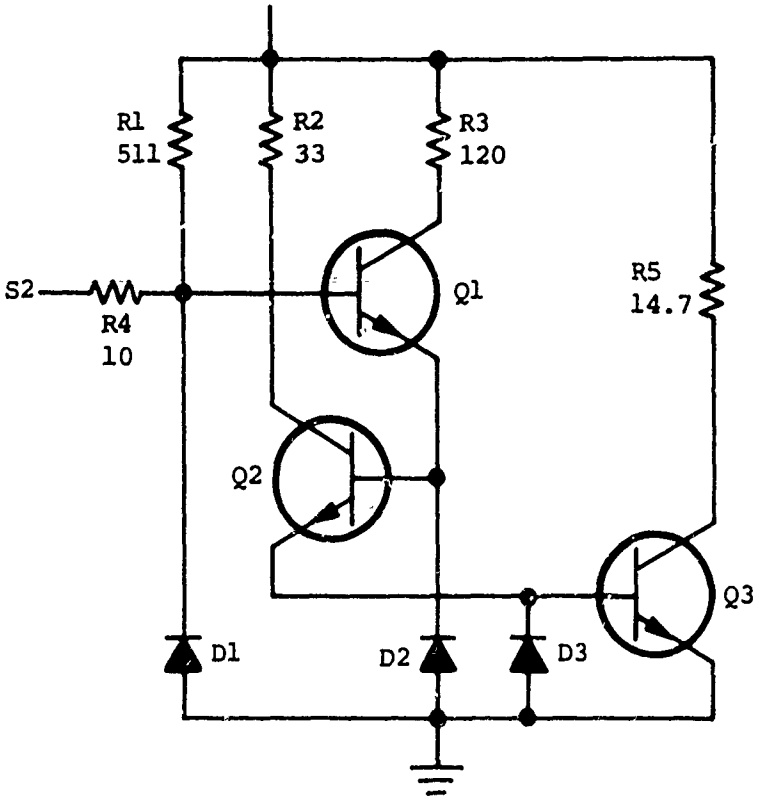

Figure 9-2. Start/Restart Circuit Output

10. +5 VOLT SWITCHING REGULATOR

The +5 volt switching regulator (Figure 10-1) provides the supply voltage for the readout amplifiers, the trigger circuits, and for all the digital electronics. It provides approximately 2.5 amperes of current at the regulated voltage.

The regulator design was not formulated in time to permit incorporation of the computer simulation results in the pretest report for the SFXR test. The post test computer simulation response of the +5 volt regulator in an SFXR environment with a peak dose rate of $1x10^9$ rads(Si)/s and a pulse width of 120 ns is shown in Figure 10-2a. The computed response to a peak dose rate of $5x10^{11}$ rads(Si)/s with the same pulse width is shown in Figure 10-2b. Figures 10-3 and 10-4 are oscilloscope presentations of the +5 volt regulator test data at approximately the same dose rate levels indicated previously. There is very good agreement between the computer simulation and the test data in both the overall long term response (0 to 200 μs) and the short duration response (0 to 2 μs). The mechanism that controls the response of the regulator is the discharge of capacitor C4 (Figure 10-1). The regulator recovery time is dictated by the time required to recharge this capacitor. Both the SFXR test data and computer simulations show that the regulator recovers completely within 200 μs.

The +5 volt switching regulator simulation was completed in time to be used for the pretest FBR analysis. The neutron and photocurrent information of Table 10-I was used in the simulation.

TABLE 10-I

Transistor Forward Current Gains (h_{FE})

Device	$h_{FE}(o)$	$h_{FE}(\phi)$ ($\phi = 1x10^{14} n/cm^2$)	K_D	I_{pp} at 10^7 rads(Si)/s (amperes)
2N4044	340	60	$1.3x10^{-16}$	$65.0x10^{-6}$
2N2907	184	30	$2.9x10^{-16}$	$250.0x10^{-6}$
2N2222A	240	25	$2.6x10^{-16}$	$250.0x10^{-6}$
2N5107	200	50	$1.5x10^{-16}$	$65.0x10^{-6}$
2N5244	200	50	$1.5x10^{-16}$	$10.0x10^{-6}$
2N3251	200	30	$2.8x10^{-16}$	$120.0x10^{-6}$
BR100F	80	15 (min)	$5.5x10^{-16}$	$4.0x10^{-3}$

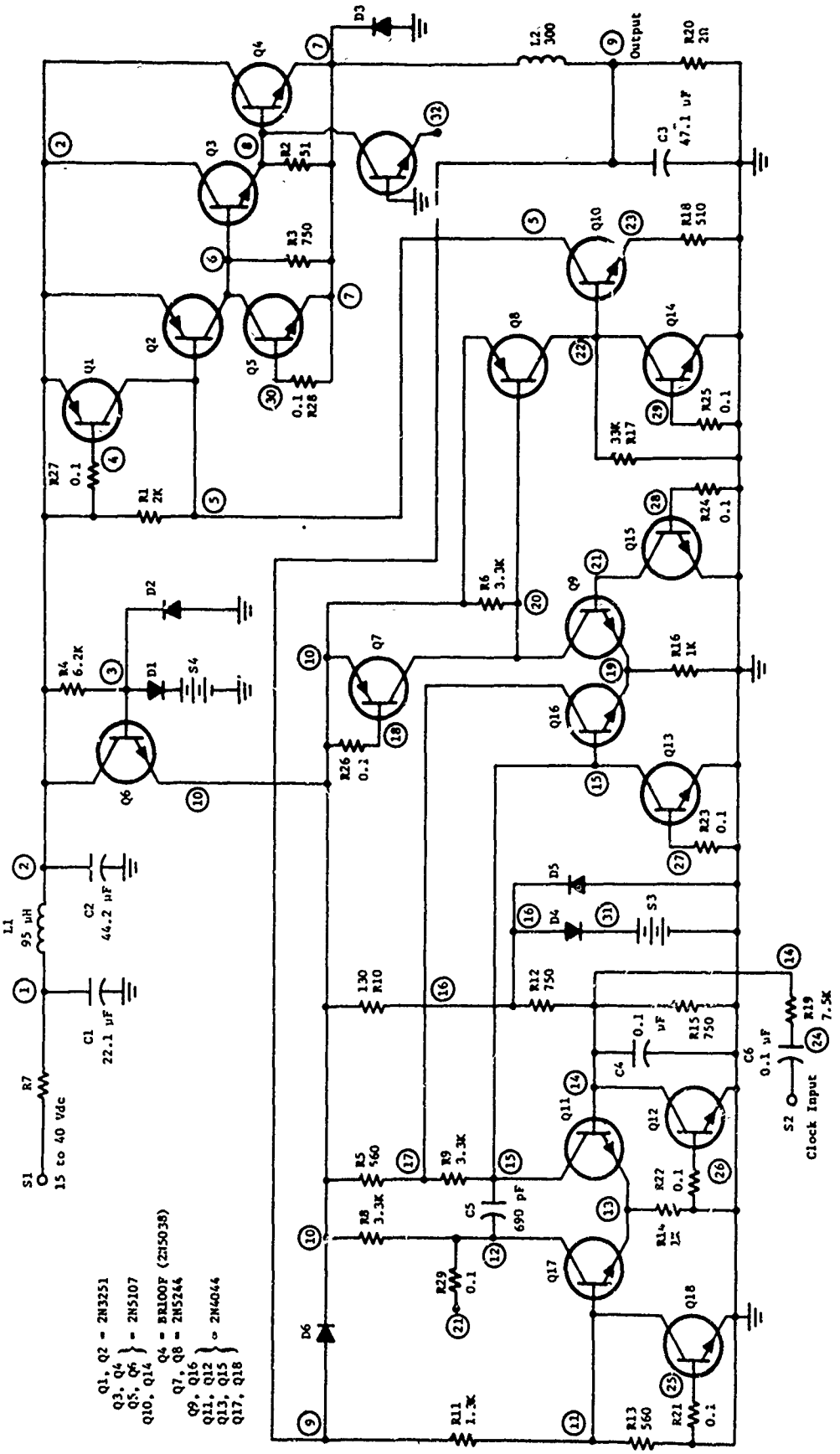

Figure 10-1. +5 Volt Switching Regulator

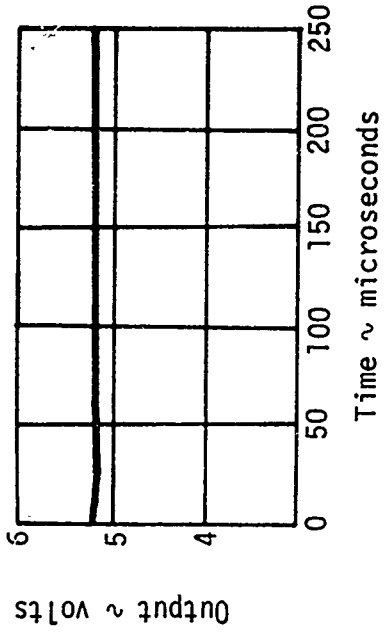

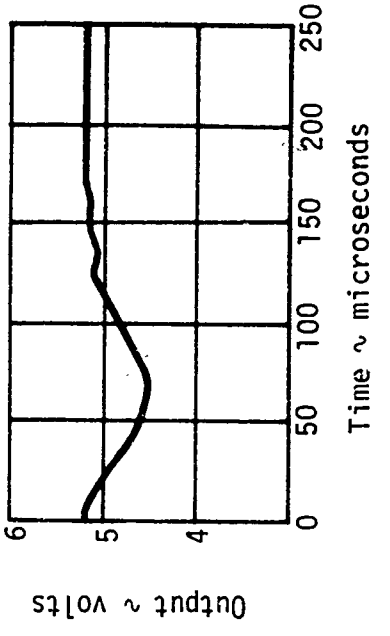

a) $\dot{\gamma} = 1 \times 10^{9}$ Rads(Si)/s

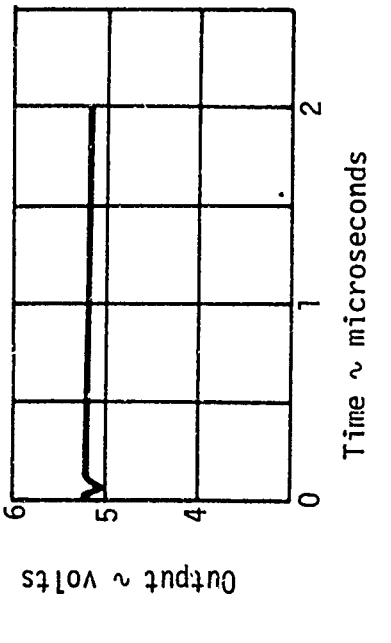

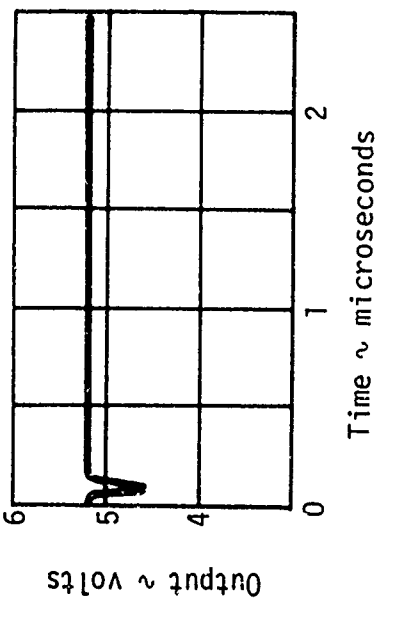

b) $\dot{\gamma} = 5 \times 10^{11}$ Rads(Si)/s

Figure 10-2. Computer Simulation of +5 Volt Regulator Output in SFXR Environment

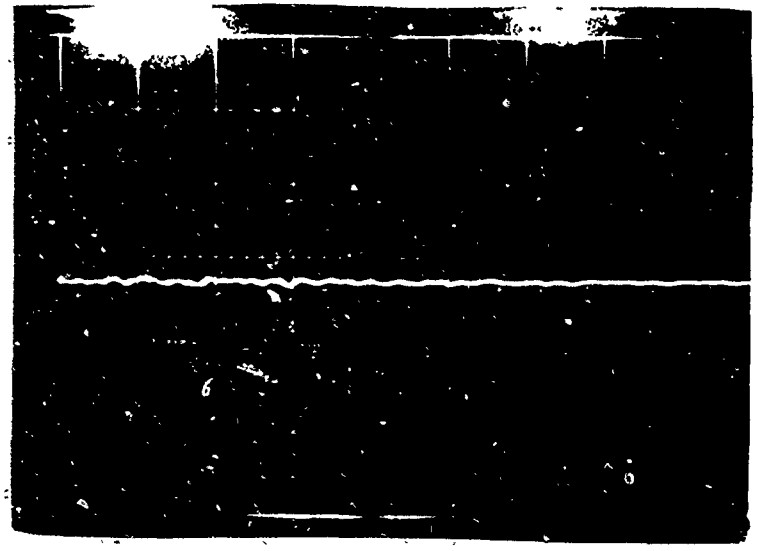

VOLTS/CM 2 SWEEP/CM 0.5 usec

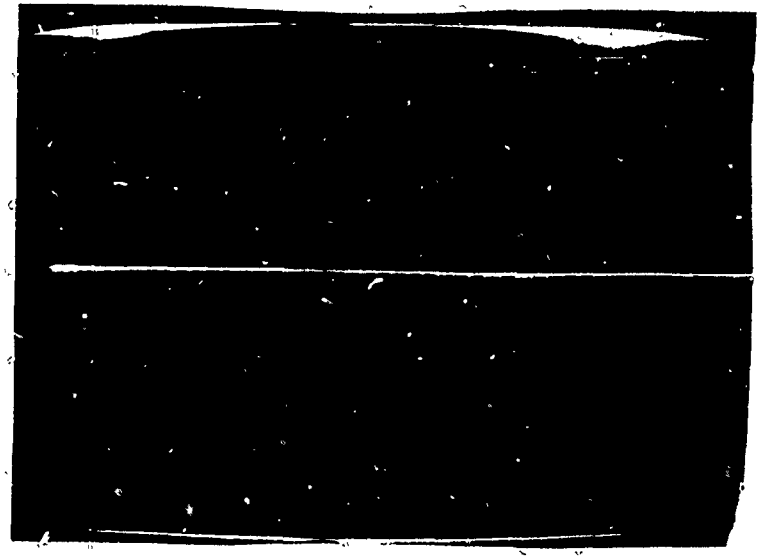

VOLTS/CM 2 SWEEP/CM 5 usec

TEST NO. 21 - 1, 2, 3: CIRCUITS TEST - 5 VOLT MONITOR

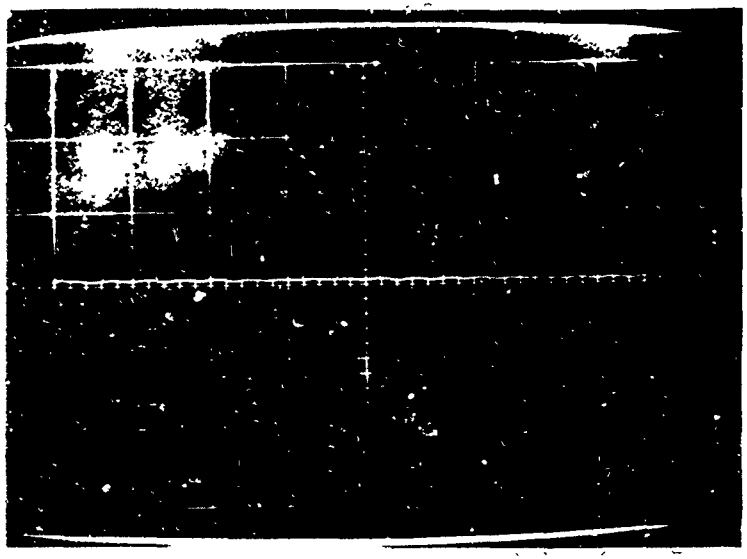

VOLTS/CM 2 SWEEP/CM 50 usec

VOLTS/CM _____ SWEEP/CM _____

Figure 10-3. +5-Volt Regulator Response to a Dose Rate of Approximately 1×10^9 rad (Si)/

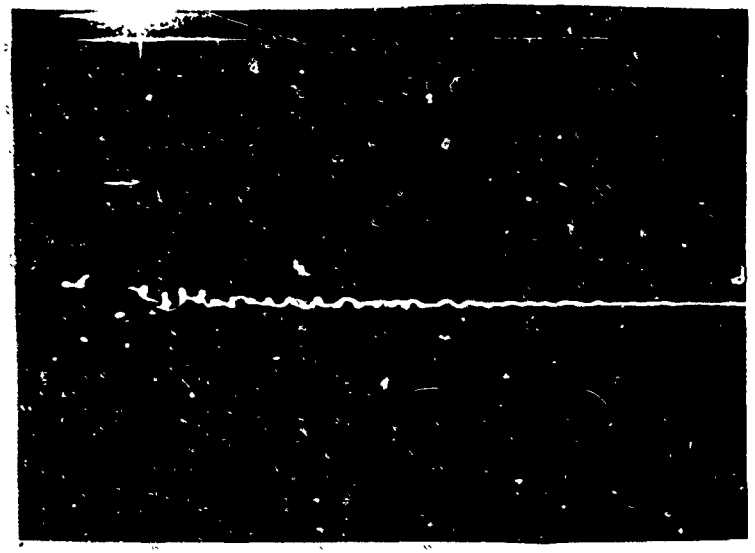

VOLTS/CM 2 SWEEP/CM 0.5 usec

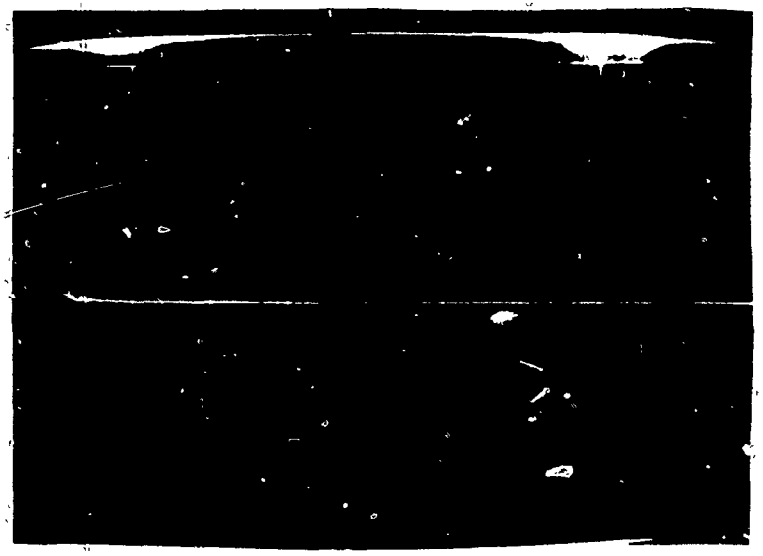

VOLTS/CM 2 SWEEP/CM 5 usec

TEST NO. 27 - 1, 2, 3: SUPPORT ELECTRONICS TEST - 5 VOLT MONITOR

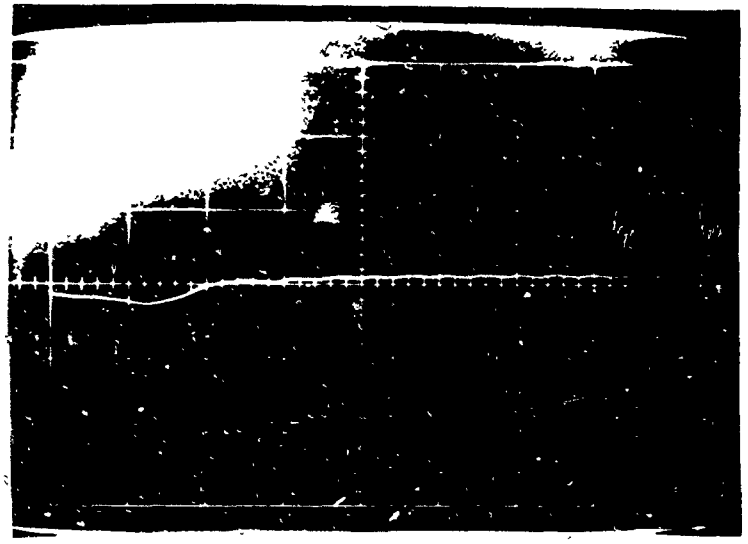

VOLTS/CM 2 SWEEP/CM 5 usec

VOLTS/CM _____ SWEEP/CM _____

Figure 10-4. +5-Volt Regulator Response to a Dose Rate of Approximately 5 x 10^{11} rad (Si)/s

The maximum single burst at the FBR is expected to produce approximately 5 to 6×10^{13} n/cm^2. Using the damage equation, the transistor gains would be reduced for the following devices as shown in Table 10-II.

TABLE 10-II

Transistor Gain Reduction

Device	$h_{FE}(o)$	$h_{FE}(\phi)$ ($\phi = 5 \times 10^{13}$ n/cm^2)	$h_{FE}(\phi)/2$	$h_{FE}(\phi)$ ($\phi = 1 \times 10^{14}$ n/cm^2)
2N4044	340	100	50	60
2N2907	200	50	25	30
2N5244	200	80	40	50
2N5107	200	80	40	50
2N3251	200	50	25	30
BR100F	80	25	12.5	15 (min)

One consideration not taken into account is the transistor anneal characteristics. Fast burst reactor tests on a G657046 device (very similar to a 2N2907) show that the anneal properties are significant in determining transient response in the time regime of the circuits in question. Figures 10-5 and 10-6 show the transistor current gain as a function of time. The time t = 0 is approximately 50 µs after the burst. Data earlier than this time are difficult to obtain due to the ionization of the devices. In view of this information it is evident that the damage equation is not sufficient in predicting post burst transistor gains.

An accepted approximation to the minimum transistor gain immediately after neutron exposure is 50 percent of the final annealed value. This would reduce the transistor gains calculated by means of the damage equation by a factor of two. Since these values are very similar to the neutron data taken at 1×10^{14} n/cm^2 (Table 10-II) and since much data are referenced at this level, it will be assumed that the maximum single burst neutron fluence at the FBR facility will degrade the transistors at the 1×10^{14} n/cm^2 level.

The response of the regulator to a simulated FBR environment is shown in Figure 10-7. This design had no photocurrent compensation for the output transistor.

The concern over the output voltage of the +5 volt regulator rising to +7.4 volts with a minimum input voltage of 15 volts is that both Motorola and Texas Instruments have 7.0 volt absolute maximum specifications for the digital logic supply voltage. Although the ionization of circuits connected to the +5 volt supply will tend to reduce the output rise, it is not possible to remain below the 7.0 volt level over the entire input voltage range of 15 to 40 volts with the present design.

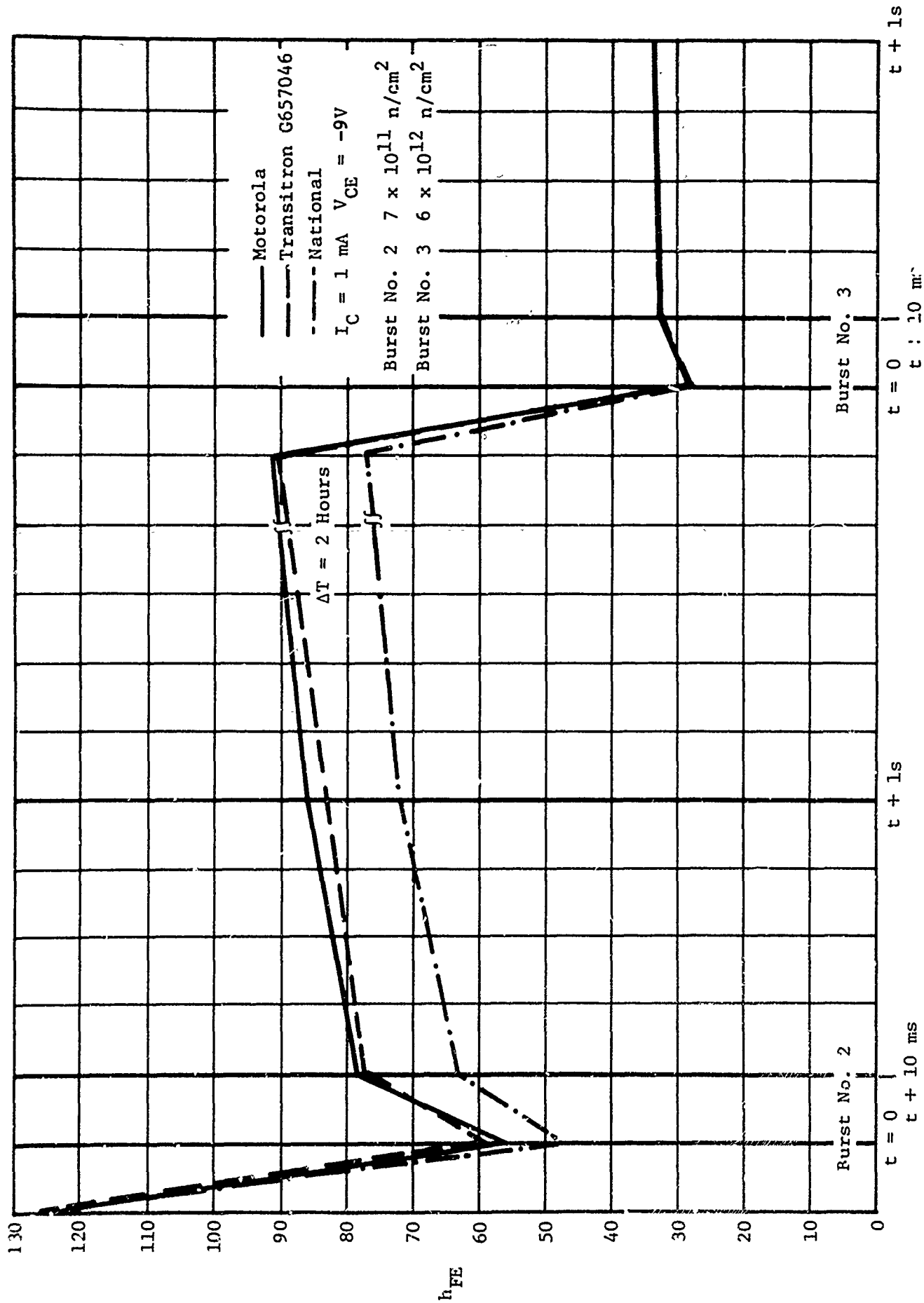

Figure 10-5. Transistor Current Gain - Bursts 2 and 3

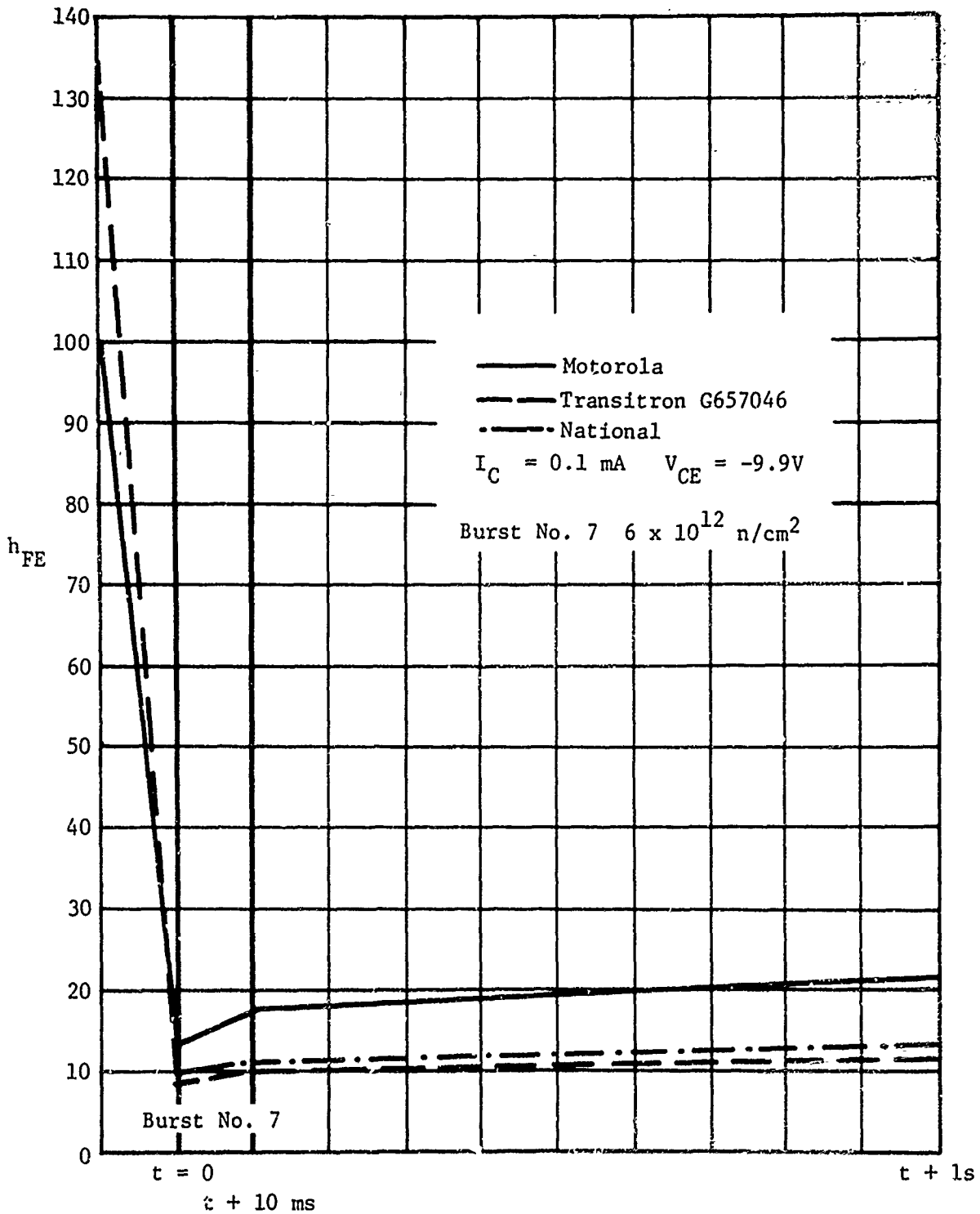

Figure 10-6. Transistor Current Gain - Burst 7

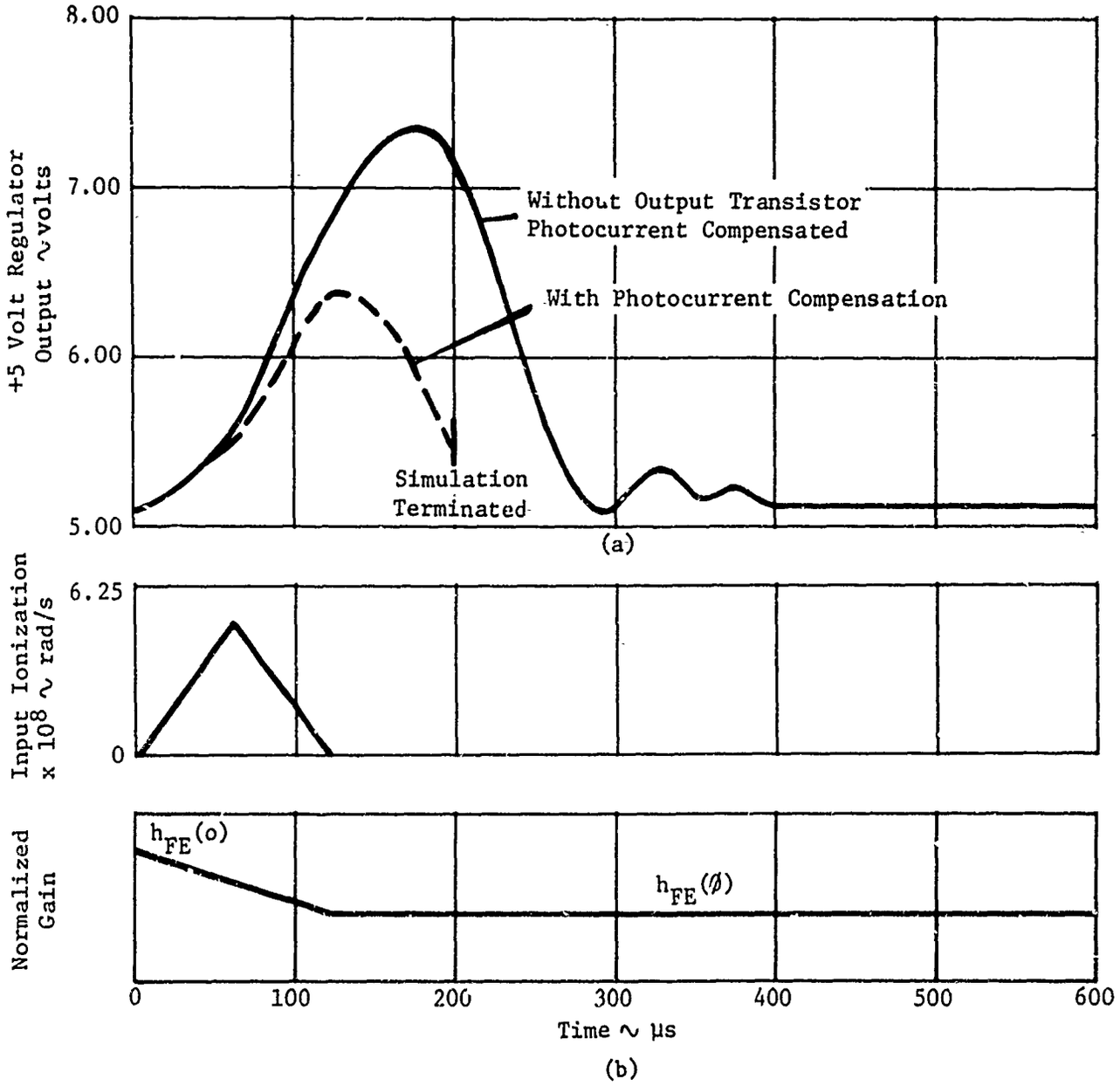

Figure 10-7. Predicted Response of +5 Volt Regulator at FBR (15 Volt Input)

The output stage was photocurrent compensated and the simulation was repeated. The response is illustrated in Figure 10-7. The output rise to 6.4 volts with a minimum input voltage of 15 volts leaves approximately 0.5 volt safety margin. The predicted response of the +5 volt regulator in an FBR environment, with several different supply voltages, is shown in Figure 10-8. The simulated ionization waveform and neutron degradation profile are also shown in the figure for reference. The ionization of the output transistor Q4 (Figure 10-1) during the radiation burst causes the load to be connected directly to the source voltage, hence the wider the ionization pulse, the higher the output voltage. Also, with higher supply voltages and a fixed ionization pulse width, the higher the output voltage rise. With a 17.5 volt supply, the predicted peak output was 7.5 volts and with a 40 volt supply, the output peak increased to 15.5 volts.

The test data of +5 volt regulator No. 2 for burst No. 9 is shown in Figure 10-9. The peak output amplitude is approximately 8 volts with a 300 microsecond duration. This agrees very well with the predicted 7.5 volt, 300 microsecond response of Figure 10-8. Because the peak transient is primarily determined by ionization, the +5 volt regulator No. 2 responded similarly for bursts 9 through 12. The initial voltage before burst 9 was 4.6 volts, and, with a total neutron accumulation of the four bursts, the output increased to 5.4 volts.

The rise of the +5 volt regulator in the FBR test to values greater than 7.0 volts produced the possibility that the digital electronics elements could be damaged. Although the regulator had peak value responses of 8 to 9 volts with no logic element failures, an extensive analysis effort was initiated to eliminate the problem.

The +5 volt regulator was again analyzed considering only ionization effects. The input ionization waveform used was a triangular pulse of 120 μs duration with a peak dose rate of 5×10^8 rads(Si)/s. The response of the original design to this waveform with a 17.5 volt input is shown in Figure 10-10. Also shown in Figure 10-10 is the response of the regulator with no photocurrent compensation whatsoever. From the figure, it can be seen that the peak response without compensation is 8.25 volts and is 7.5 volts with full compensation. Photocurrent compensation transistors Q18, Q12, Q13, Q15, Q14, and Q7 were then removed and the simulation was repeated. The output peak was still approximately 7.5 volts, which is still unacceptable. The removal of these photocurrent compensating transistors (see Figure 10-11 for the schematic of this configuration) resulted in the same response. This indicates that the response is primarily controlled by the output stages.

At the output, transistor Q11 provides compensation for Q3, transistor Q12 provides compensation for Q2 and Q1, and transistor Q13 provides photocurrent compensation for Q1. Transistor Q13 also provides a path for photocurrent for transistor Q7 so that this current does not flow

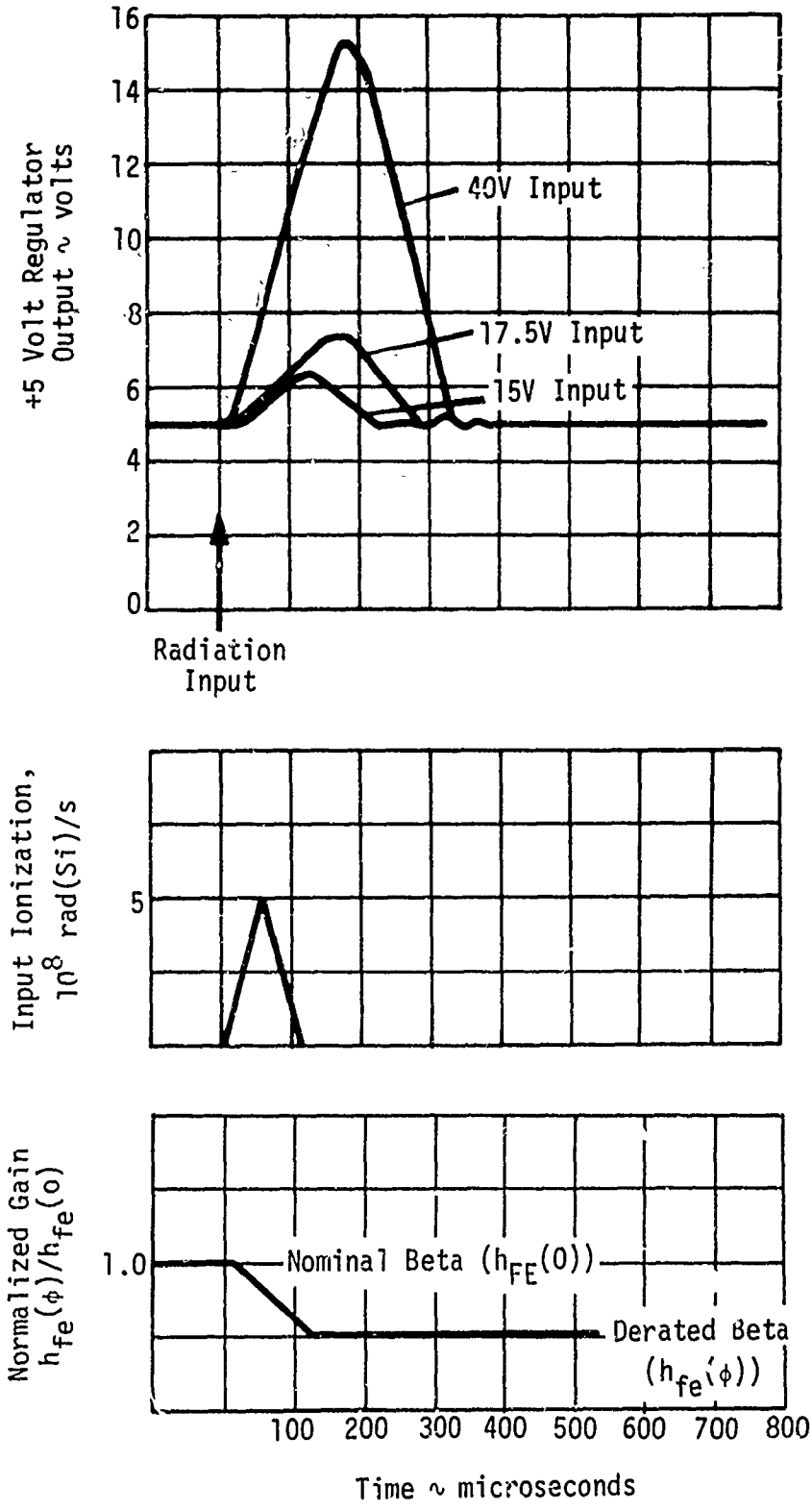

Figure 10-8. Predicted Response of +5 Volt Regulator for FBR Environment

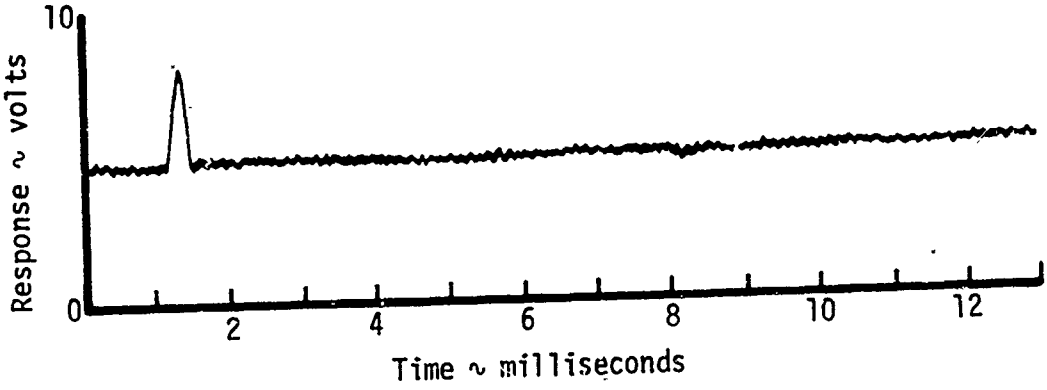

Figure 10-9. +5 Volt Regulator No. 2 Response to FBR Burst 9

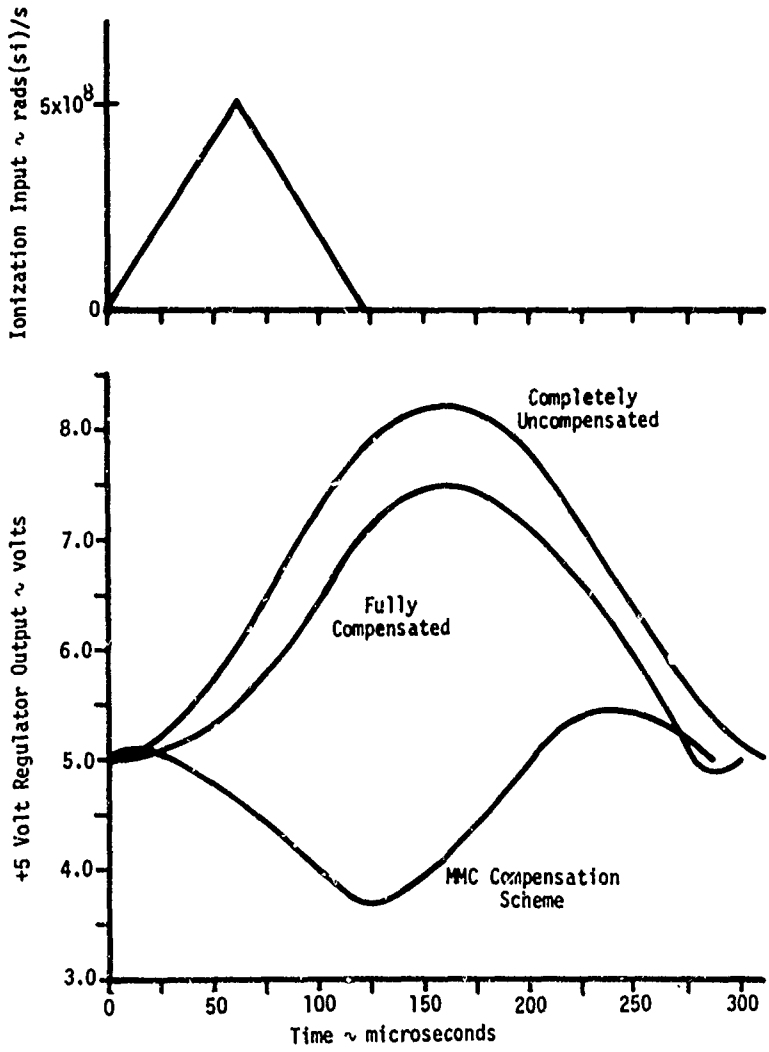

Figure 10 10. Computer Simulation of +5 Volt Regulator with Ionization Input Only (17.5 Volt Input)

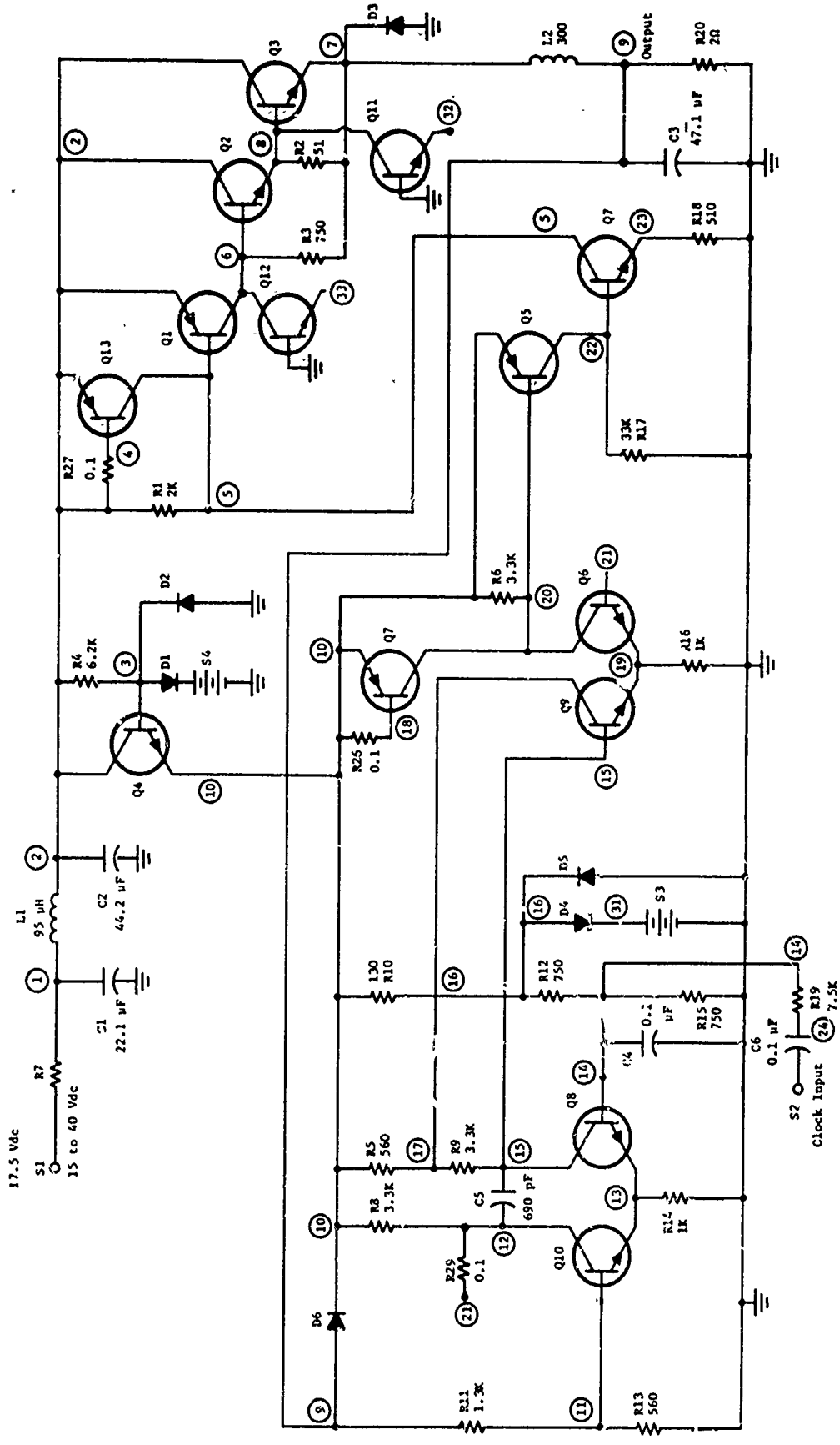

Figure 10-11. Modified +5 Volt Switching Regulator

through resistor R1. The by-passing of the 2k resistor (R1) by providing enough photocurrent from Q1 is most important in keeping the driver stage from turning ON. Using the photocurrent values shown in Table 10-III and using the same ionization waveform, the response of the regulator remained OFF during the radiation with a turn-ON peak rise to 5.5 volts as shown in Figure 10-10.

TABLE 10-III

Photocurrent Values Used for Simulation of Figure 10-11.

Transistor	I_{ppc} at 10^7 rads(Si)/s
Q1	120 μA
Q2	65 μA
Q3	4 mA
Compensators	
Q11	6 mA
Q12	0.5 mA
Q13	1.0 mA

Transistor models were used in the computer simulation for convenience but appropriate diodes can be used for the actual circuit compensation.

An explanation for the photocurrent compensation technique proposed by Martin Marietta and based upon the computer simulation results can best be explained using Figure 10-12. Figure 10-12 represents the power stage (taken from Figure 10-11) that acts as an on-off switch on command from the control portion of the regulator. To keep transistor Q3 from turning ON during radiation, assuming the previous stage remains OFF, an alternate path for the junction photocurrent is necessary. Without an alternate path, the junction photocurrent will flow through R2 (51 ohms) forward biasing the transistor. This photocurrent will also flow into the base and generate a collector current proportional to the base current (i.e., $I_C = h_{FE} \times I_B$). The photocurrent necessary to turn ON Q3 and support a collector current of 2.5 amperes is:

$$I_{ppc} = \frac{0.7}{R_1} + \frac{2.5}{h_{FE3}}$$

$$\approx 65 \text{ mA.}$$

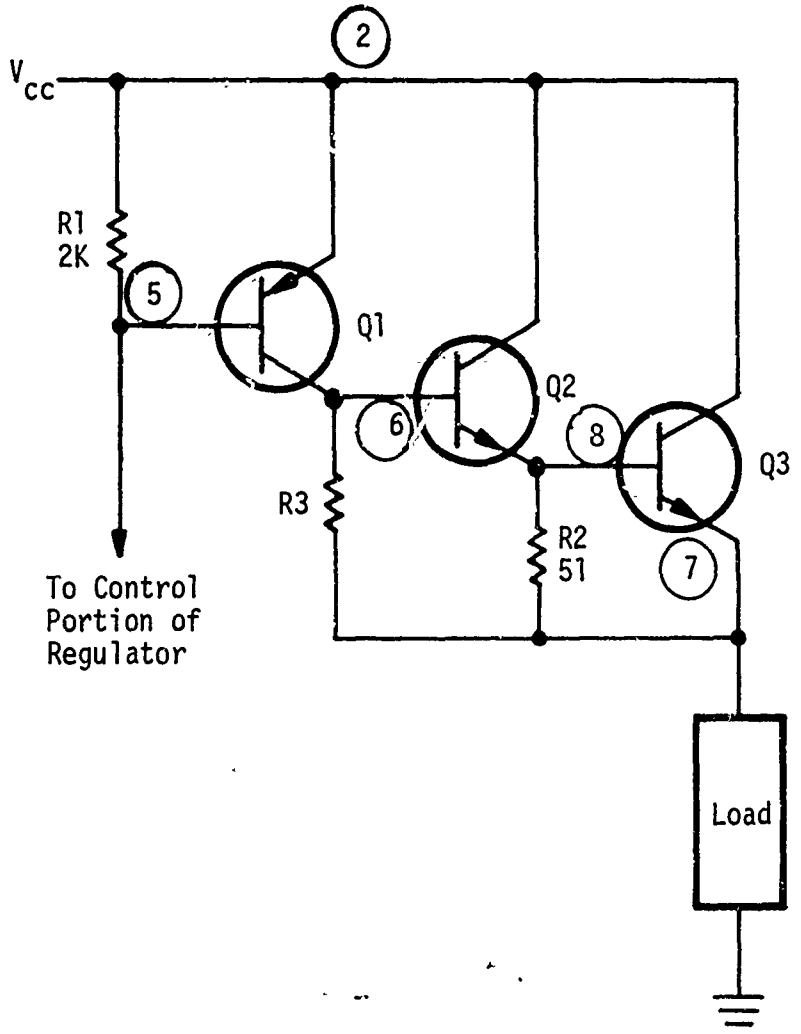

Figure 10-12. Power Stage

The minimum photocurrent generated by a gamma rate of 5×10^8 rads(Si)/s for the BR100F is 200 mA. An alternate path for the photocurrent is provided by including a diode (or transistor) from node 8 to ground with enough photocurrent capability (i.e., 6 mA at 10^7 rads(Si)/s versus 4.0 mA for the output transistor) to keep Q3 OFF. Assuming the previous stage is OFF and the output is compensated, it can be seen (Figure 10-13) from the computer simulation that there is not enough current for the generation of sufficient V_{BE} to turn the transistor ON, much less provide enough base current to support a large collector current.

The same analogy can be used for the previous stage (transistor Q2) except that there are photocurrents from both Q1 and Q2 to consider. The photocurrent necessary to turn ON Q2 is approximately:

$$I = \frac{0.7}{R_3} + \frac{0.065}{h_{FE2}}$$

$$\approx 2 \text{ mA.}$$

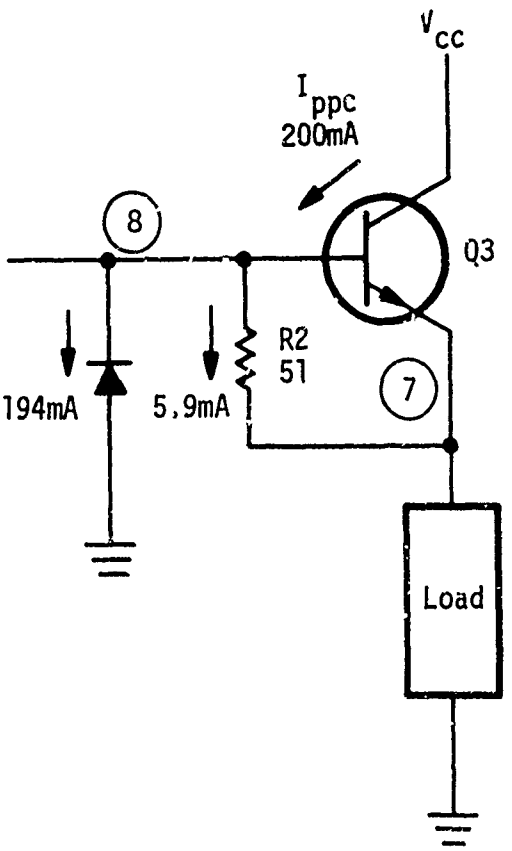

Figure 10-13. Photocurrent Alternate Path

Using a diode from node 6 to ground and providing enough photocurrent compensation capability for both transistor Q2 and Q1, transistor Q2 can be held OFF during the ionization time. Figure 10-14 shows the current distributions from the computer simulation.

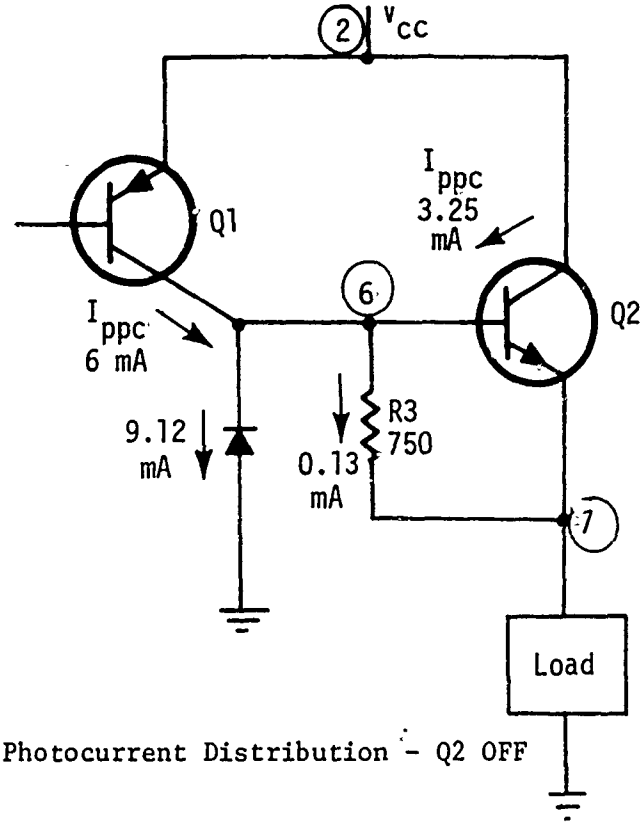

Figure 10-14. Photocurrent Distribution - Q2 OFF

Using the same reasoning for transistor Q1, taking into account that it is also necessary to provide photocurrent compensation to override any ON command from the control portion of the regulator (i.e., transistor Q7 of Figure 10-11), a diode was included from node 2 to node 5.

The current distribution in the circuit from the computer simulation is shown in Figure 10-15.

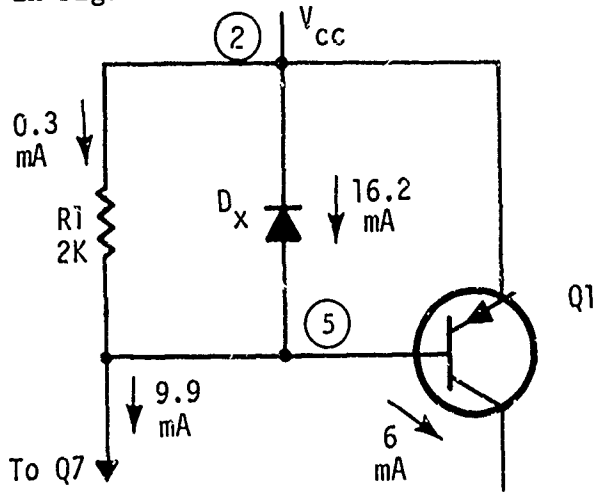

Figure 10-15. Photocurrent Distribution - Q1 OFF

Using the photocurrent compensation technique thus described, the +5 volt regulator computer simulation gave the results shown in Figure 10-16. The peak voltage remained well below the 7 volt maximum. This superior performance is the direct result of keeping the power stage OFF during the ionization pulse. Because the stage is OFF during the ionization pulse, the radiation response should be fairly independent of input voltage.

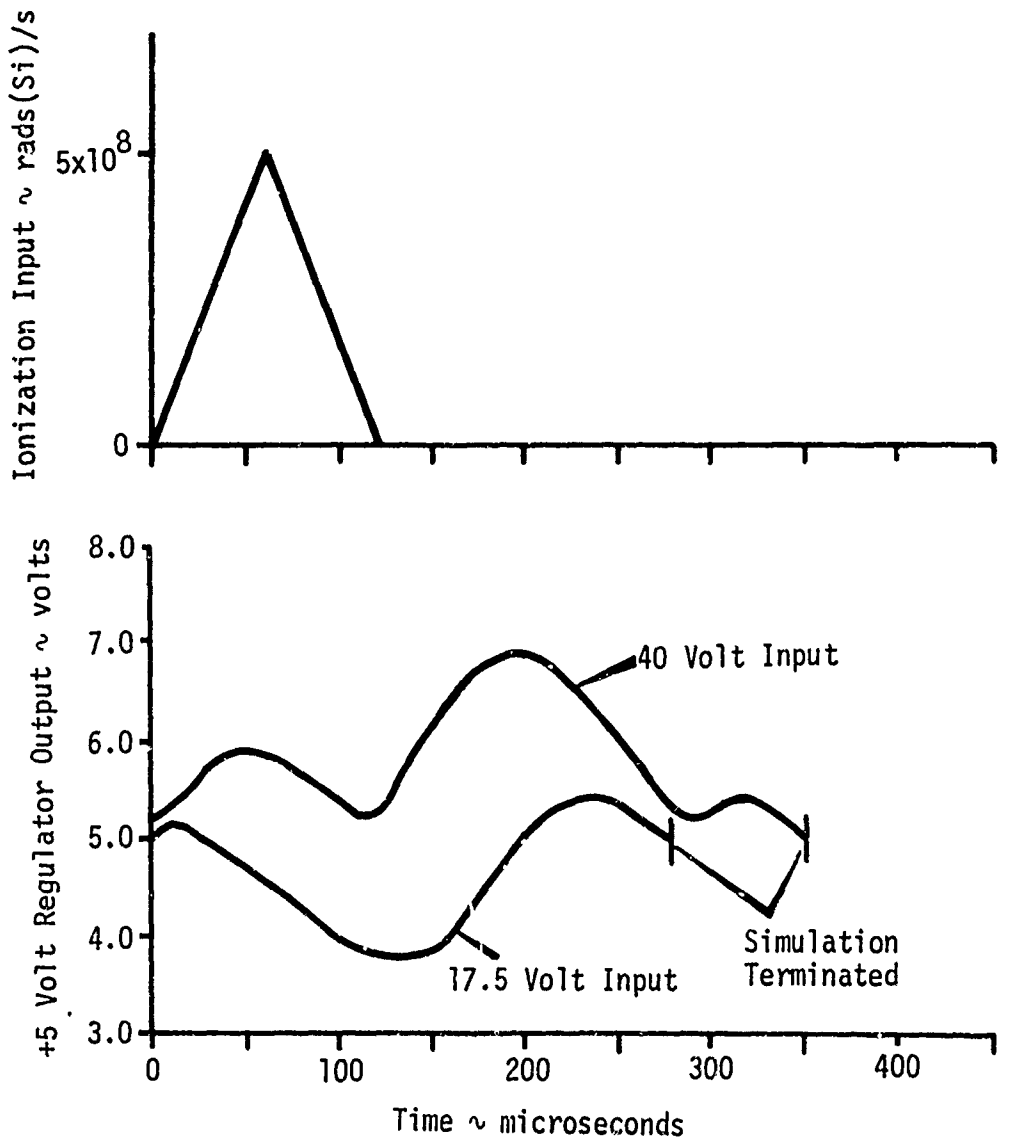

Figure 10-16. +5 Volt Regulator Response to Long Ionization Pulse using Martin Marietta Photocurrent Compensation Technique

The maximum input of 40V was then considered. To determine the maximum peak response, the initial conditions had the power stage in the ON condition at the start of the ionization pulse. This is a worst case condition because the photocurrent compensation had to drive the power stage OFF from an ON condition instead of just keeping the stage OFF. The results of this simulation is shown in Figure 10-16 along with the response from a 17.5 volt input. Since the mechanism is understood, it should be just a matter of selecting the appropriate compensating diodes; however, further tests should be made to verify the technique.

A word of caution in the use of photocurrent compensation is necessary at this time. The statement made concerning "adequate" compensation does not mean to imply "indiscriminant overcompensation." This is to say that with a low background ionization level and the use of "overcompensation" in any of the above mentioned stages, it might be possible to override a normal regulation command resulting in complete regulator shutdown.

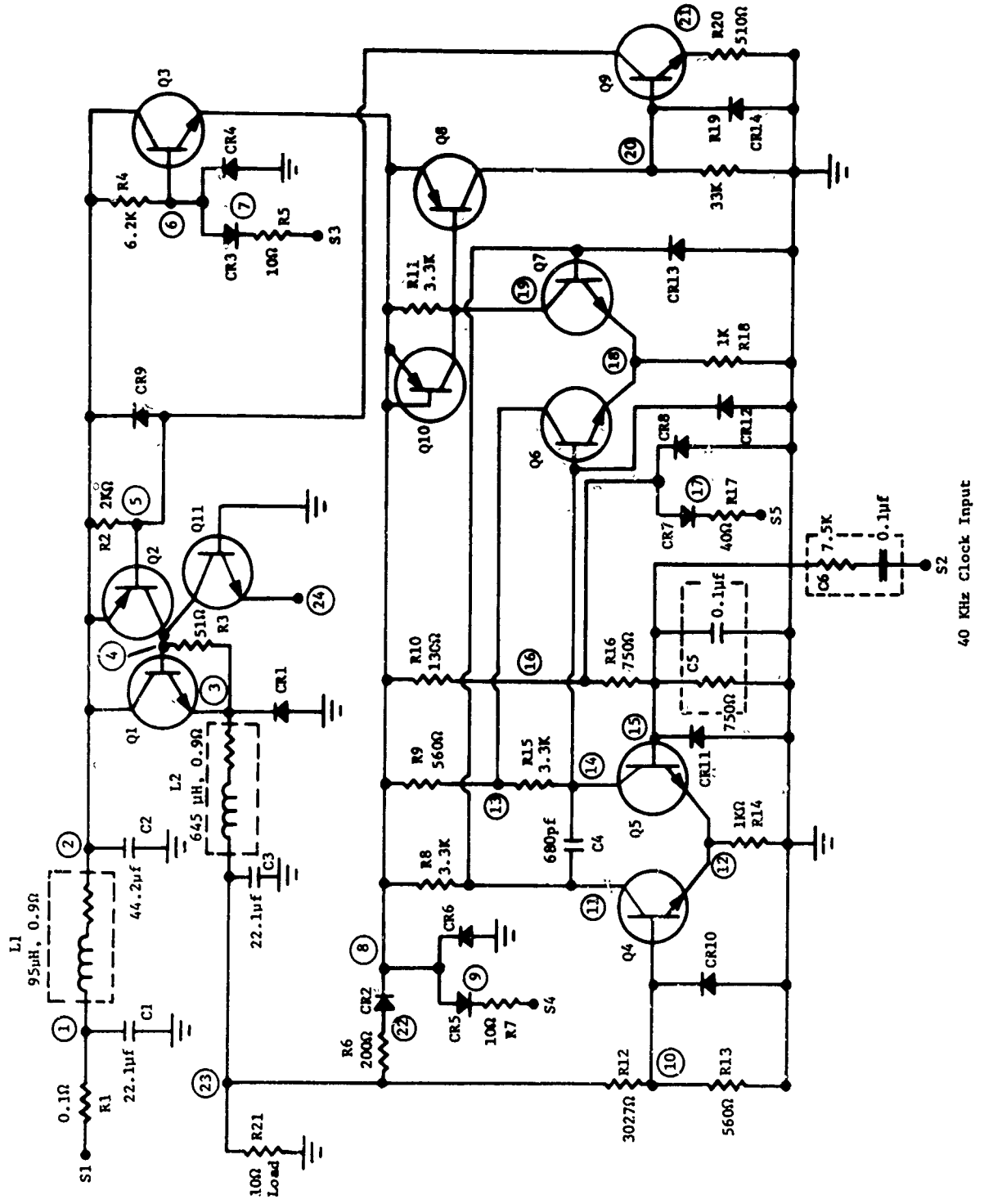

Figure 11-1. +10 Volt Switching Regulator

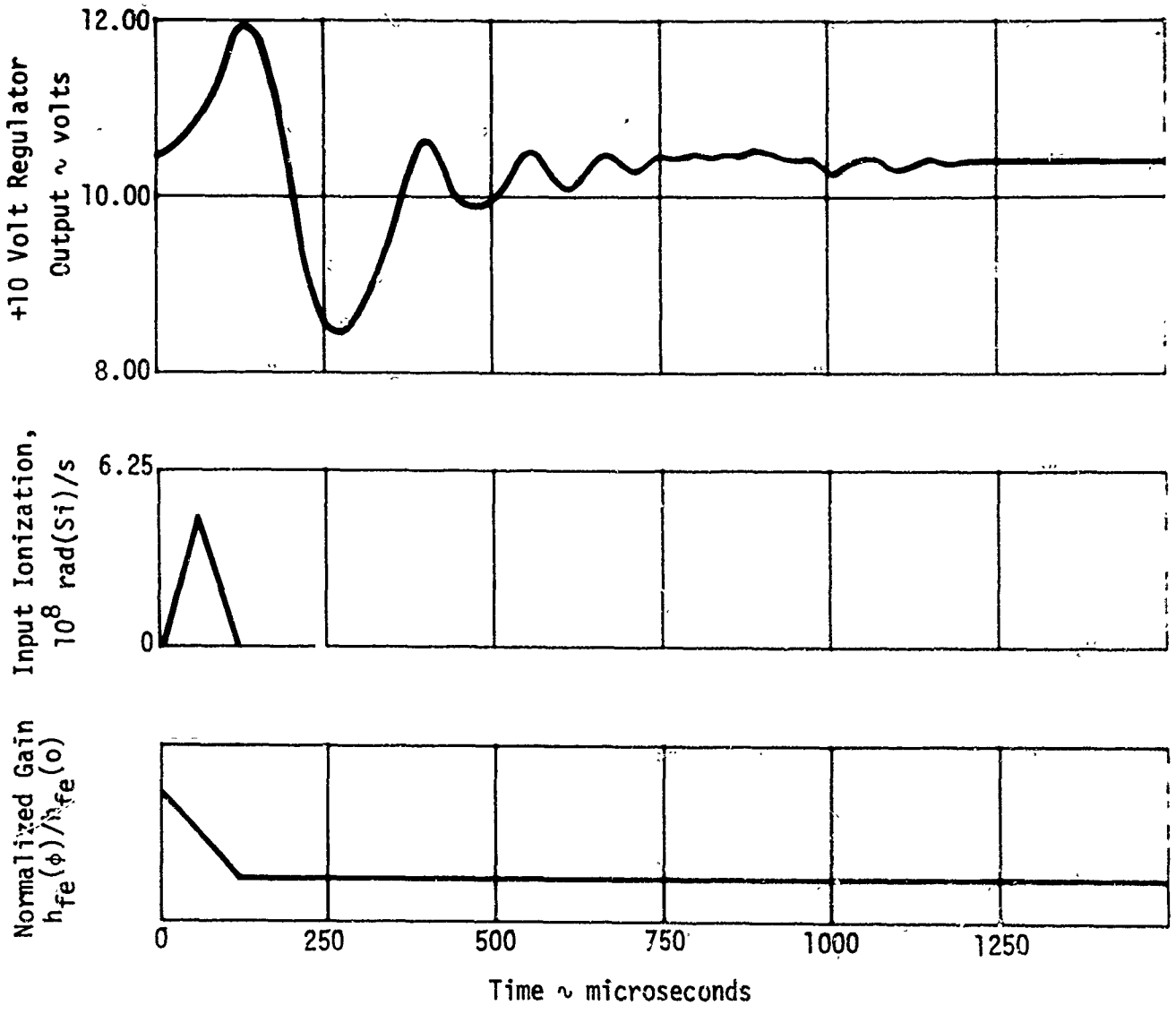

Figure 11-2. Predicted Response of +10 Volt Regulator for FBR Environment

The test data of +10 volt regulator No. 1 for bursts 5 through 8 are shown in Figure 11-3. Each of these responses agrees very well with the predicted response of Figure 11-2, as to peak output, minimum output, and recovery time. Table 11-II summarizes the data presented in Figure 11-3.

The test data of +10 volt regulator No. 2 for bursts 9 through 12 are shown in Figure 11-4. A power failure at the tape recorder prevented the burst 11 data from being recorded. Transient responses for this regulator agree fairly well with the predicted response. Table 11-III summarizes the data presented in Figure 11-4.

TABLE 11-II

+10 Volt Regulator No. FBR Results

Burst	Initial Voltage	Peak Voltage	Minimum Voltage	Final Voltage	Recovery Time (μs)
5	9.0	11.1	7.5	8.2	300
6	8.2	10.4	6.3	7.2	550
7	8.8	12.0	7.8	8.8	500
8	8.6	12.4	7.8	8.6	500

TABLE 11-III

+10 Volt Regulator No. 2 FBR Results

Burst	Initial Voltage	Peak Voltage	Minimum Voltage	Final Voltage	Recovery Time (μs)
9	8.6	9.3	7.8	8.6	400
10	8.5	10.2	7.5	8.5	400
11	-	-	-	-	-
12	9.8	11.3	8.4	9.8	500

Table 11-II shows that there was a significant shift in the output voltage (final value versus initial value) in bursts 5 and 6 and between bursts 6 and 7. In Table 11-III, similar changes occurred in burst 11. This shift can only have been caused by a change in the absolute value of the voltage at node 15 (Figure 11-1) or by a shift in the voltage difference between nodes 15 and 10. Assuming all resistors remained unchanged, a change in the voltage at node 15 can be attributed only to a shift in the V-I curve of the 3.3 volt Zener diode. A change in the voltage of node 15 is reflected as a change in the output voltage of three times this magnitude. A shift in the voltage of node 15 relative to node 10

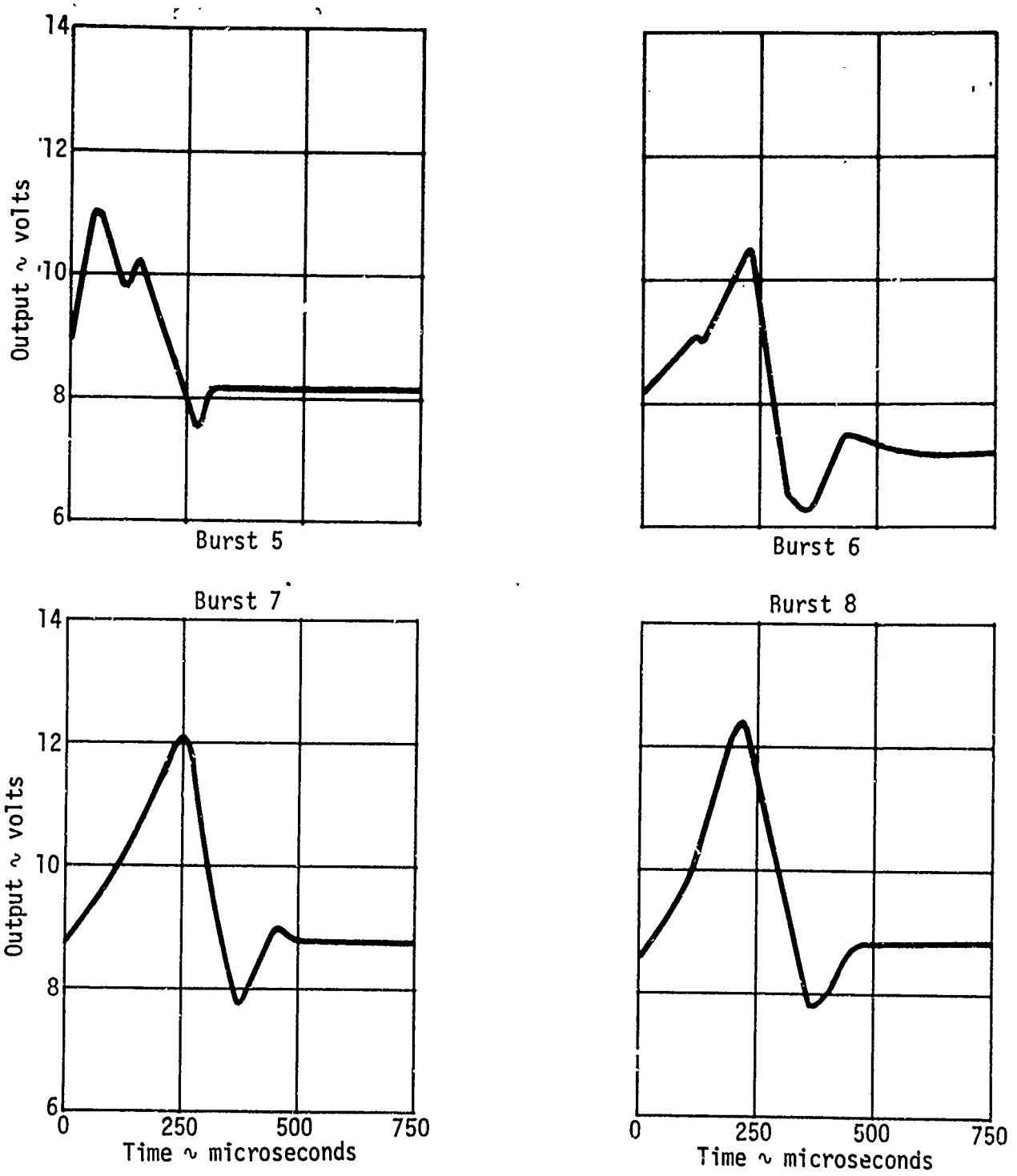

Figure 11-3. +10 Volt Regulator No. 1 Response to FBR Bursts 5 through 8

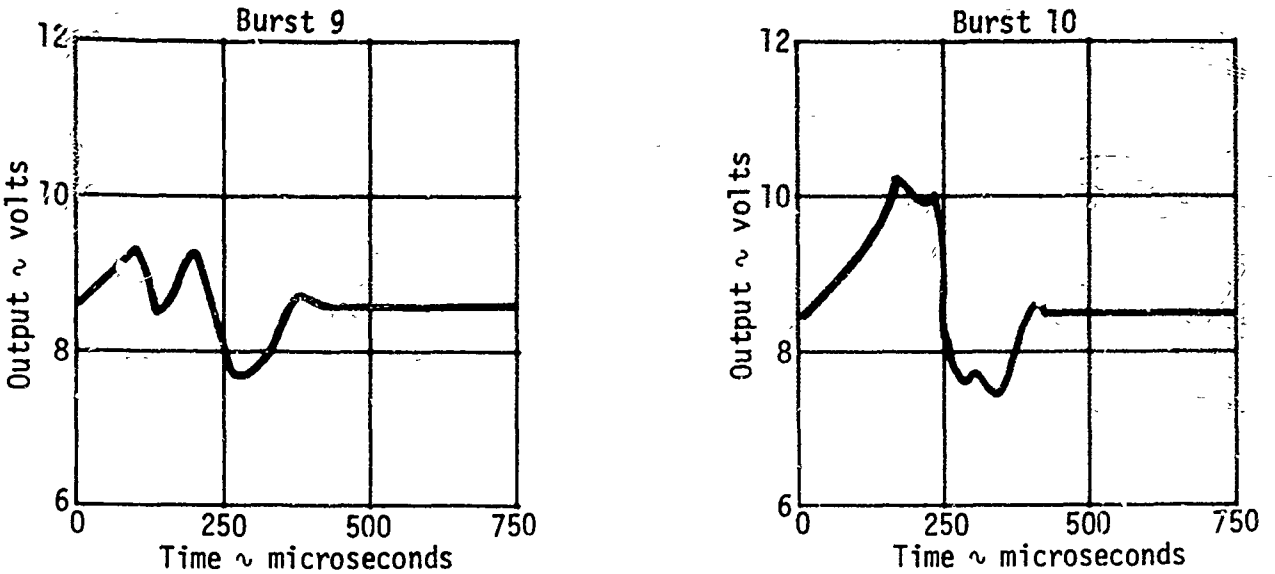

Note: The response from Burst 11 was not recorded because of a recorder power failure.

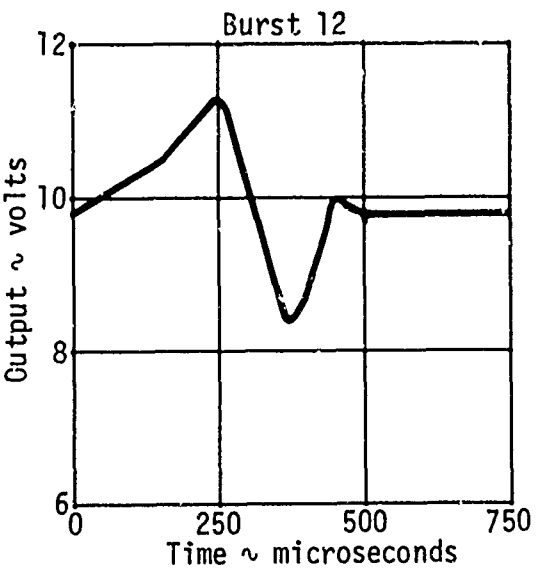

Figure 11-4. +15 Volt Regulator No. 2 Response to FBR Bursts 9 through 12

can only be caused by a V_{BE} change in Q4 or Q5. Since these transistors are two halves of a monolithic device, a significant change in one, unmatched by the other, is not likely. Nevertheless, a change here is reflected as a change in the output voltage of six times the amplitude.

The output of +10 volt regulator No. 2 following burst 10 shows very erratic behavior. Since the data from burst 11 was not recorded, and since the regulator performed properly both before and after burst 12, this behavior must remain unexplained.

The computer simulation of the +10 volt regulator in an SFXR environment with a peak dose rate of $1x10^9$ rads(Si)/s and a pulse width of 120 ns is shown in Figure 11-5. Test data for approximately this same dose rate is shown in Figure 11-6. The measured dose rate over the area occupied by the regulator varied from 1.0 to $1.5x10^9$ rads(Si)/s. There is excellent agreement between the computer simulation and the test results.

The predicted response for a peak dose rate of $5x10^{11}$ rads(Si)/s is shown in Figure 11-7. The tantalum capacitors C1, C2, and C3 were discharge 30 percent, corresponding to 1 percent per 1000 rads(Si), in the simulation. This caused the instantaneous voltage decrease. Recovery time is governed by the time required to recharge C5 and C6.

Test 24 data are shown in Figure 11-8. The simulation matches both the initial voltage drop and the recovery transient very well. The peak dose rate varied from 2.0 to $4.1x10^{11}$ rads(Si)/s over the regulator area. Test 27 data are shown in Figure 11-9. Recovery time is similar to the simulation, but the initial voltage decrease is greater than predicted. The peak dose rate varied from 4.0 to $6.6x10^{11}$ rads(Si)/s over the regulator area.

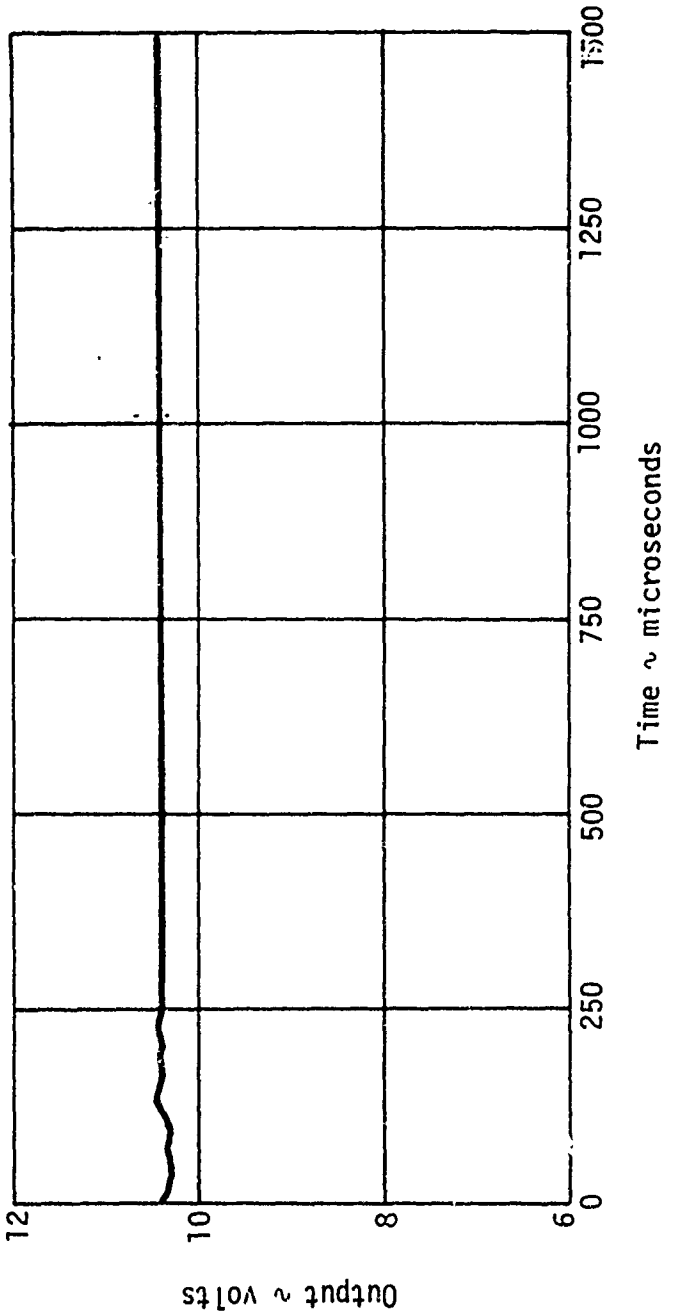

Figure 11-5. Predicted Response of +10 Volt Regulator for an SFXR Dose Rate of 1×10^9 rads(Si)/s

VOLTS/CM 5 SWEEP/CM .5 usec

VOLTS/CM 5 SWEEP/CM 5usec

TEST NO. 21 - 4, 5, 6: CIRCUITS TEST - 10 VOLT MONITOR

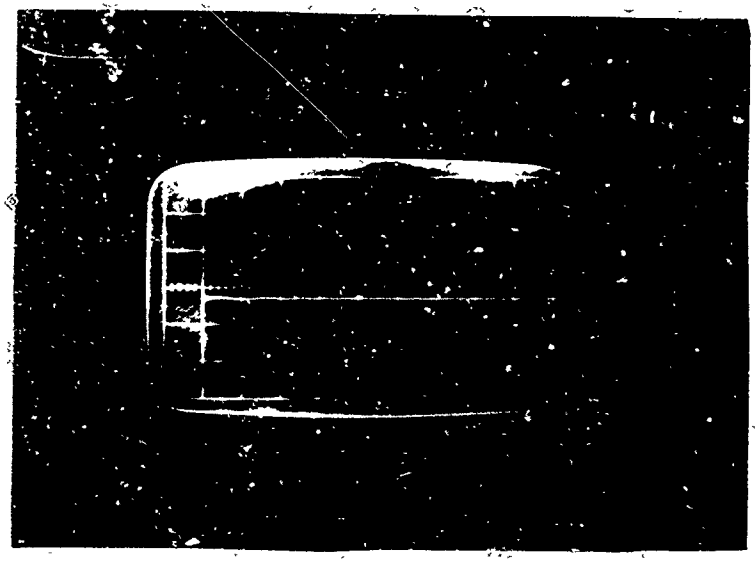

VOLTS/CM 5 SWEEP/CM 5 usec

VOLTS/CM _____ SWEEP/CM _____

Figure 11-6. +10-Volt Regulator Response for a Dose Rate of 1.0 to 1.5 x 10^9 rad (Si)/s

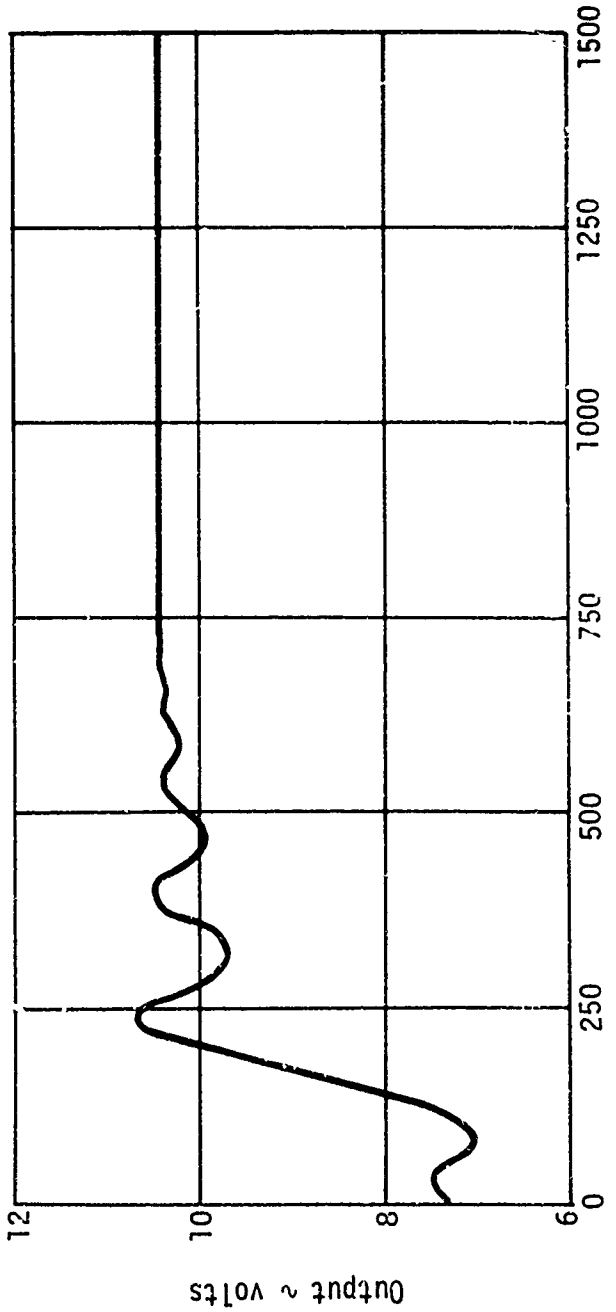

Figure 11-7. Predicted Response of +10 Volt Regulator for an SFXR Dose Rate of 5×10^{11} rads(Si)/s

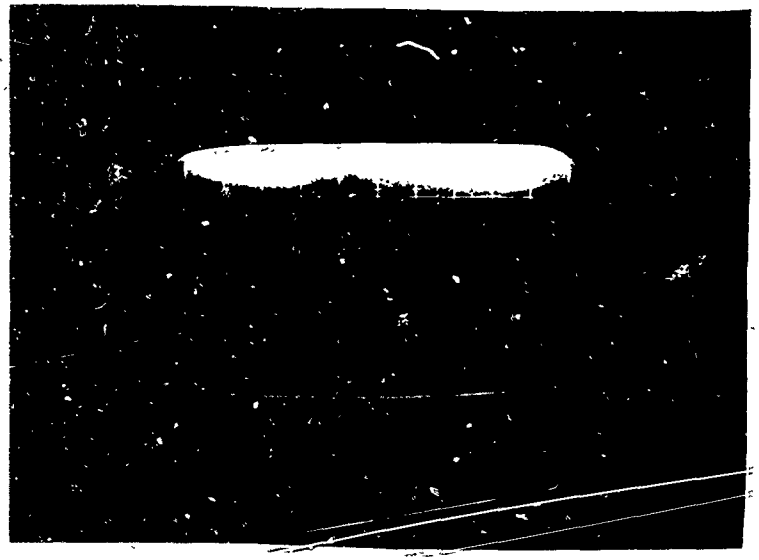

VOLTS/CM 5 SWEEP/CM .5 usec

VOLTS/CM 5 SWEEP/CM 5 usec

TEST NO. 24 - 4, 5, 6: CIRCUITS TEST - 10 VOLT MONITOR

VOLTS/CM 5 SWEEP/CM 50 usec

VOLTS/CM _____ SWEEP/CM _____

Figure 11-8. +10-Volt Regulator Response for a Dose Rate of 2.0 to 4.1 x 10^{11} rad (Si)/s

VOLTS/CM 5 SWEEP/CM .5 usec

VOLTS/CM 5 SWEEP/CM 5 usec

TEST NO. 27 - 4, 5, 6: SUPPORT ELECTRONICS TEST - 10 VOLT MONITOR

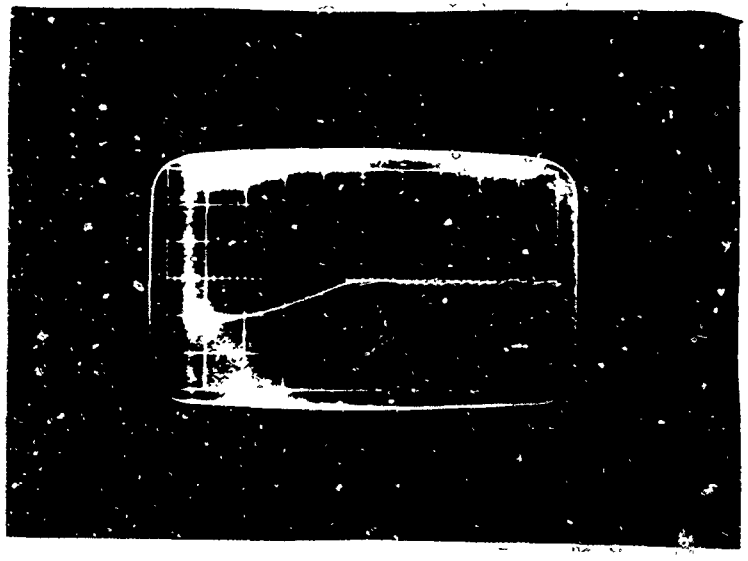

VOLTS/CM 5 SWEEP/CM 50 usec

VOLTS/CM _____ SWEEP/CM _____

Figure 11-9. +10-Volt Regulator Response for a Dose Rate of 4.0 to 6.6 x 10^{11} rad (Si)/s

12. DC-TO-DC CONVERTER AND HIGH VOLTAGE POWER SUPPLY

The dc-to-dc converter provides the +2000 volts necessary to start the lasing action and also furnishes the -1000 sustaining voltage. The input to the dc-to-dc converter is the +10 volts from the +10 volt regulator.

The circuit shown in Figure 12-1 was analyzed under the following conditions of operation:

1. Without radiation environment. The start switch was closed 20 microseconds after T_o, and was opened after an additional 120 microseconds at T = 140 microseconds.

2. In a radiation environment. The action of the start switch, described above, was synchronized with the beginning and ending of the radiation pulse (see Figures 12-2 through 12-5). Test data have shown that the start circuit would be energized by the radiation pulse.

Results of the computer analysis are shown in Figures 12-2 through 12-5. The radiation profile and start switch action are shown in each figure for convenient reference.

Figure 12-2 shows that, during normal operations, initiation of the start circuit causes the collector of Q2 to stay at +10 volts for approximately 80 microseconds (T = 20 to T = 100) or about 3 cycles of operation. Although not shown, the same behavior was observed at the collector of Q1. Loading of transformer T1 during the start period deprives the transistors of the induced 10 volt primary voltage which normally adds to the supply voltage. Since both collectors go to +10 volts, the base drive through transformer T2 drops to 0 and turns off both transistors.

For the radiation response, the collector of Q2 rises to +20 volts during the start interval. Although not shown, the Q1 collector fell to 0.2 volt during the same interval. The turning-on of Q1 accounts for the 10 volt boost added to Q2 collector voltage and provides an induced voltage at the base of Q2 which keeps it in the active region for a short period of time. This yields a peak collector current of 6 amperes in Q2 and is reflected in the 120 watts of peak power shown in Figure 12-3. The HFE of transistor Q1 was made higher than that of Q2 in the computer run, thus making it respond to radiation induced photocurrents before Q2.

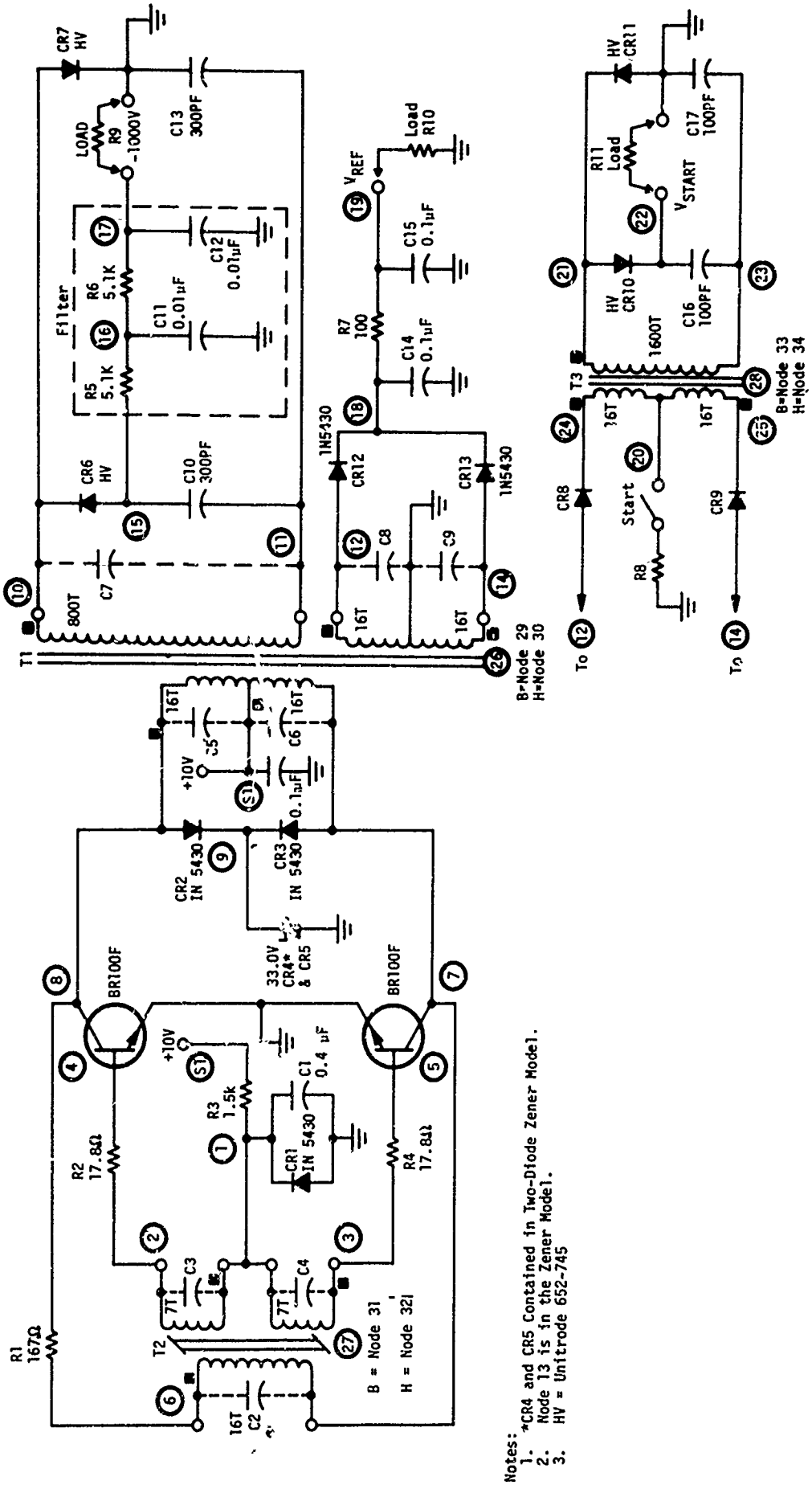

Figure 12-1. Laser Gyro High Voltage Supply

Notes:
1. *CR4 and CR5 Contained in Two-Diode Zener Model.
2. Node 13 is in the Zener Model.
3. HV = Unitrode 652-745

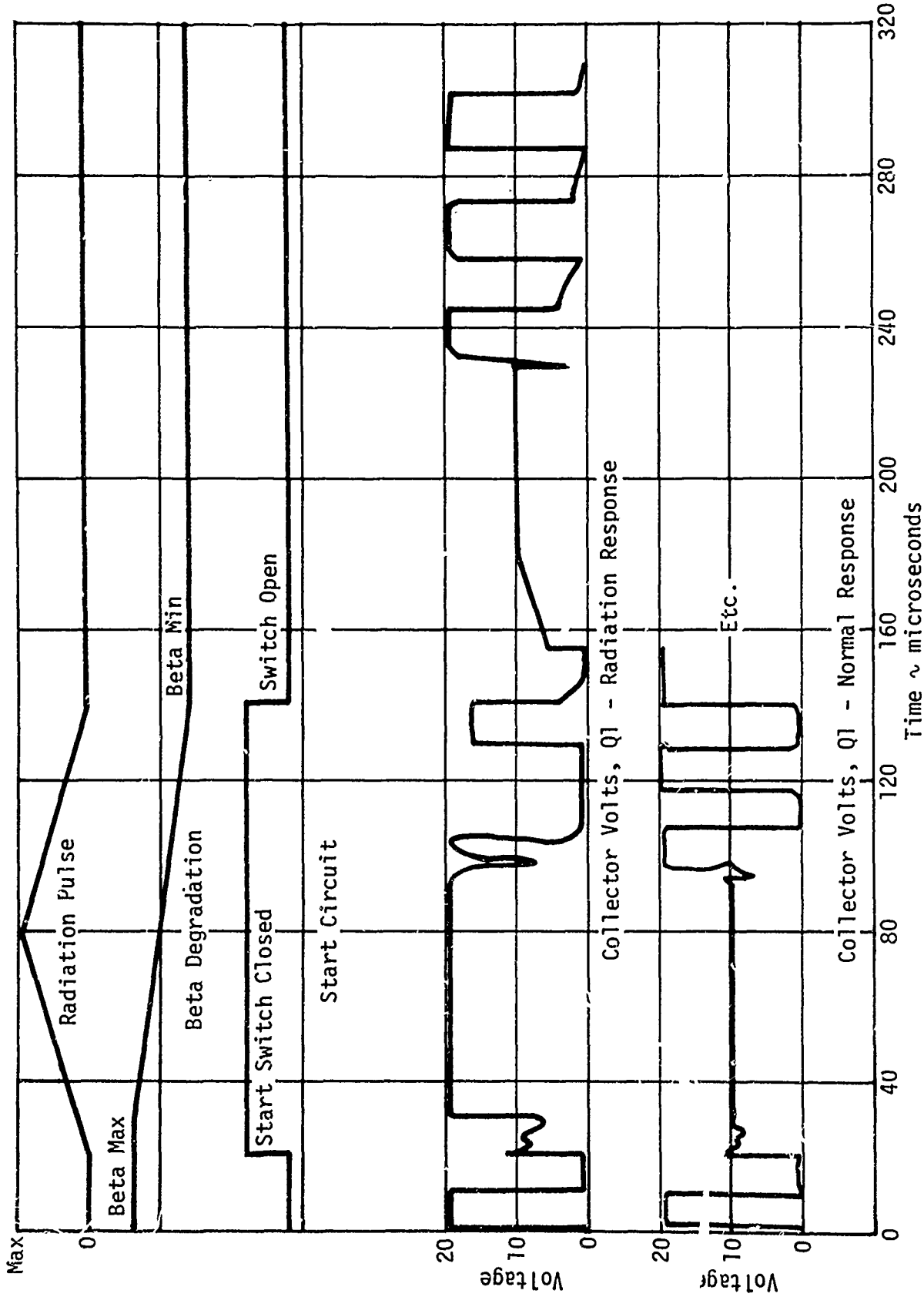

Figure 12-2. Converter Response - Collector Voltage versus Time

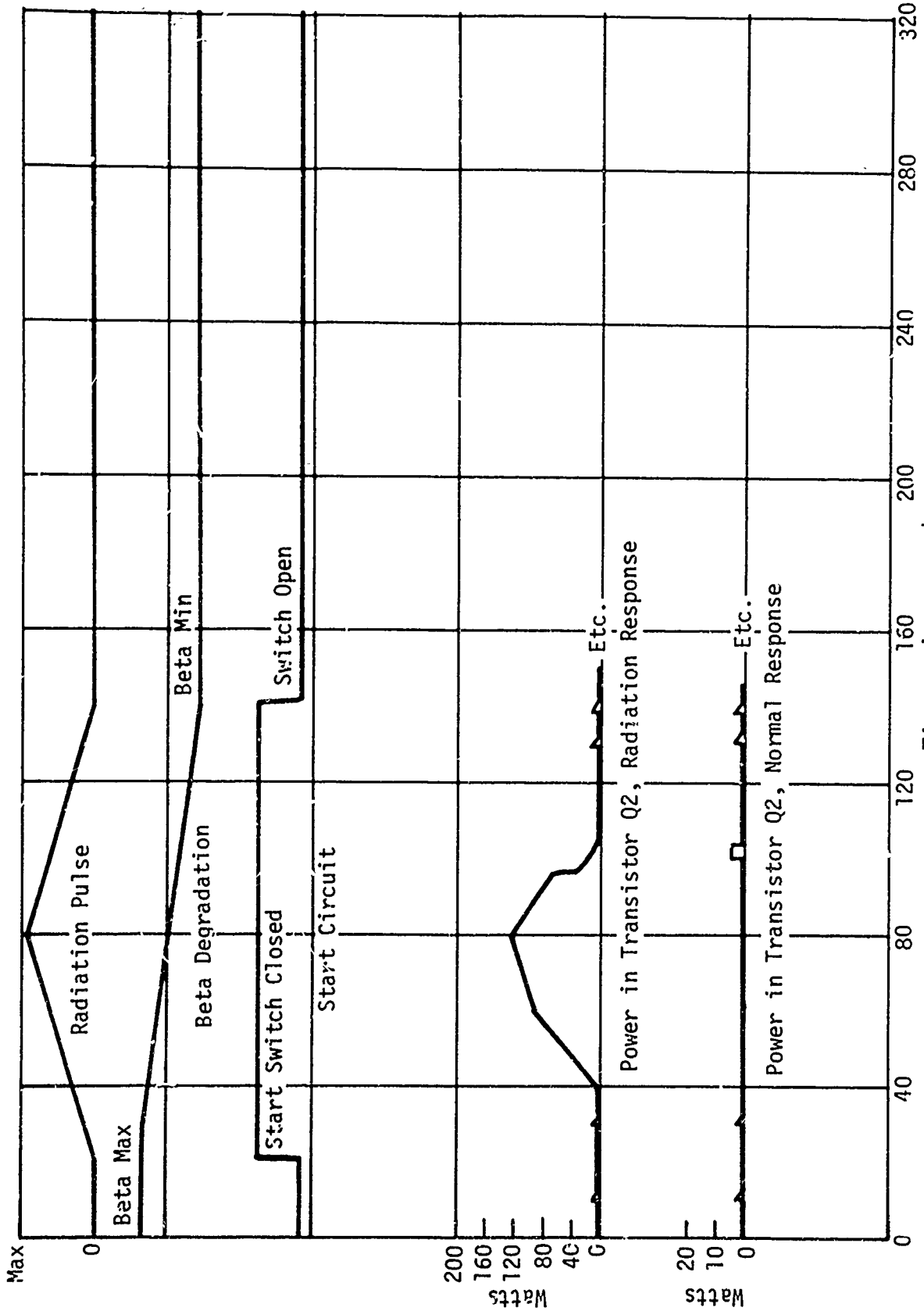

Figure 12-3. Converter Response - Transistor Power versus Time

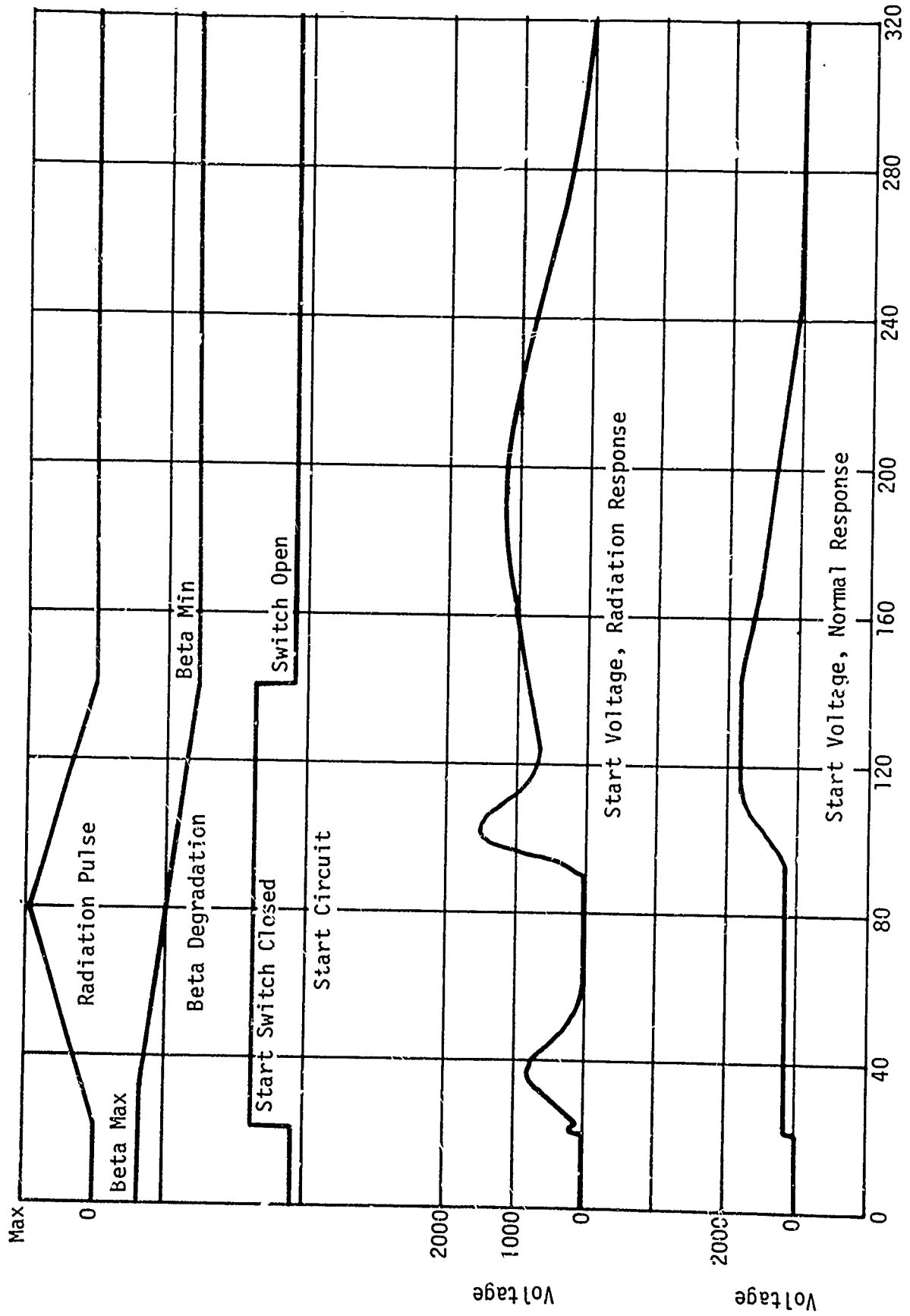

Figure 12-4. Converter Response - Start Voltage versus Time

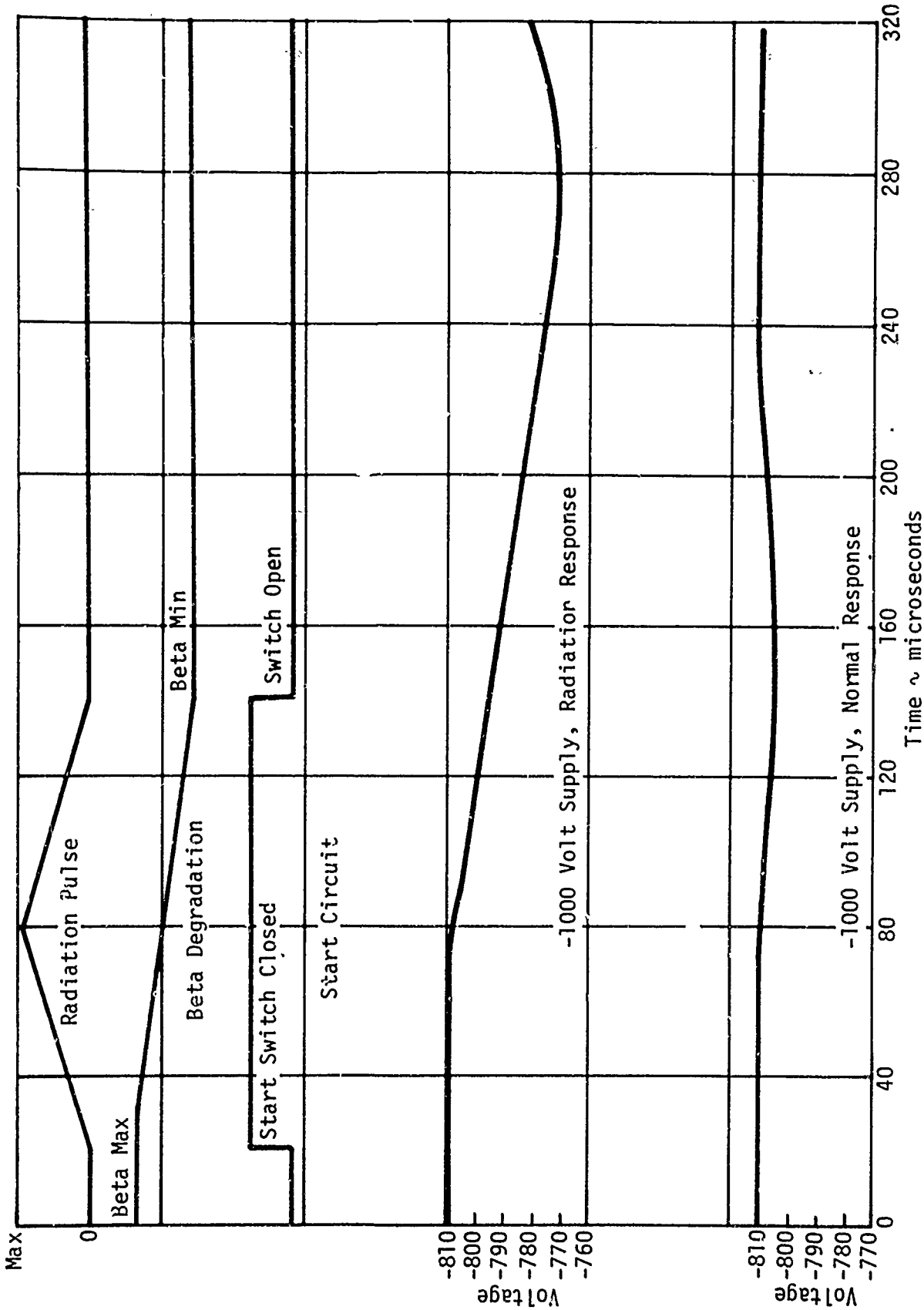

Figure 12-5. Converter Response -- -1000 Volt Supply versus Time

Figure 12-2 shows that the normal circuit response recovers completely after 100 microseconds. The radiation response recovery is complete after approximately 240 microseconds.

Figure 12-4 shows that the radiation transient at the start voltage terminal (node 17 in Figure 12-1) is a double-humped waveform with peaks at 36 microseconds (800 volts) and 100 microseconds (1500 volts). The normal circuit response is about 1800 volts after a 70 microsecond delay. This voltage decays slowly to 0 after opening of the start switch.

Figure 12-5 shows that under normal circumstances the -1000 volt supply is affected only slightly by operation of the start switch. During radiation, however, the voltage drops to approximately 95 percent of its peak value over a period of 300 microseconds. Since the converter is functioning normally at this time (approximately 240 microseconds), the recovery time to the steady state condition is dictated only by the RC time constant of the filter.

The high voltage supply decreased after every exposure at the FBR test facility. Because the dc-to-dc converter and high voltage supplies are an open loop system, any decrease in performance in the loop is reflected by a decrease in output voltage. To provide better circuit performance and better high voltage regulation, the dc-to-dc converter and high voltage power supply were redesigned. The output of the supply was monitored and fed back to the +10 volt regulator. In this way, any change in the output of the converter would be compensated by a change in the input voltage.

The revised dc-to-dc converter circuit was tested during the FBR test of 7 February 1972 at White Sands Missile Range. Results of this test are shown in Appendix C. Figure C-1 of the appendix shows the circuit schematic and associated monitoring points. Response at the output terminals generally consisted of a transient excursion, achieving a maximum value at the end of the nuclear burst, followed by a transient recovery period and then by a long term recovery period (Figure 12-6). The converter response at the -1000V terminal and the reference voltage terminal is summarized in Table 12-I. Both the transient excursion and the post burst voltages are expressed as percent deviation from the initial terminal voltages (measured previous to exposure).

The revised circuit (Figure C-1, Appendix C) was simulated in the TRAC program and produced the current and voltage waveforms which were expected under normal operating conditions. When subjected to a radiation pulse in the TRAC program, the model produced transient excursions at the outputs as shown in Table 12-II. Since these disturbances were so much smaller than those experienced during the hardware test, no attempt was made to determine long term recovery values.

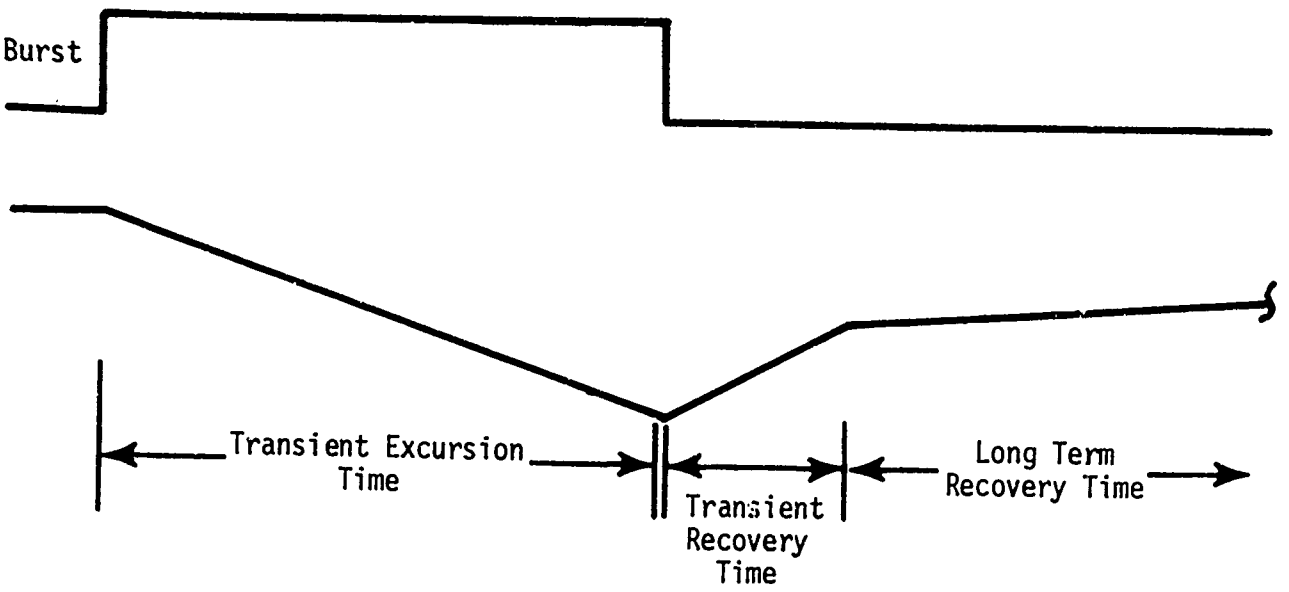

Figure 12-6. General Form of Nuclear Response at the Output Terminals

TABLE 12-I

DC-to-DC High Voltage Converter Radiation Test (7 February 1972) Results

Output Terminal	Pre-Radiation (Volts)	Transient (Percent)	Post Burst (Percent)
		Burst 1	
-1000V	-1090	-74.0	-8.2
V_{REF}	12.6	-13.3	-3.2
		Burst 2	
-1000V	-1001	-80.6	-3.2
V_{REF}	12.2	-12.3	-1.47
		Burst 3	
-1000V	-969	-66.7	
V_{REF}	12.02	-7.0	

TABLE 12-II

DC-to-DC High Voltage Converter TRAC Simulation Results

Output Terminal	Pre-Radiation Output	Transient (Percent)
-1000V	-900	2.3
V_{REF}	-10.0	5.2

The computer simulation of the dc-to-dc converter and high voltage power supply under normal operating conditions performed satisfactorily. The computer simulation of the radiation response was not as successful. The large decrease in output voltage was not evident nor was the wave form distortion of the switching transistors. A large portion of the discrepancies can be attributed to insufficient modeling data in the following areas:

1 Output transformer - Reasonably good data were available for the core material in the output transformer, but the model itself is somewhat inadequate in that it contains no direct means of simulating an air gap. To adjust the response for the expected remote saturation characteristic, the core length of the model was made much longer than that of the hardware. This adjustment was somewhat arbitrary but could be corrected by laboratory measurement of the actual current required to saturate the core.

2 Transistors - While the transistors are well characterized in most respects, there are no data available on saturation resistance during radiation. Data must be obtained at the particular operating point of the device, since R_{SAT} is a strong function of junction temperature.

3 High voltage diode and capacitor models - No radiation data were available on the performance of the Unitrode 652-745 diode or the high voltage capacitors used in the doubler circuits. The lack of data on high voltage supplies in a radiation environment points at an area for future work.

APPENDIX A

NUCLEAR RADIATION HARDNESS ASSURANCE FOR ELECTRONICS

This Appendix is Section 4 of the Final Report published 30 May 1970 by the Navigation and Control Division, Bendix Corporation, under contract F04701-69-C-0170, Part B, for Space and Missile Systems Organization, Norton AFB, San Bernardino, California.

APPENDIX A

4.0 LONG PULSE IONIZING RADIATION HARDNESS ASSURANCE

4.1 GENERAL

The objective of this task was to investigate screening techniques for the radiation response of hardened power transistors to long pulse transient ionizing radiation. The 25 MeV Linear Electron Accelerator (LINAC) at the White Sands Missile Range was used to irradiate 25 transistors with 5 microsecond pulses of electrons. The test devices consisted of 5 each from wafers with two different junction area geometries and two different epitaxial thicknesses. The remaining 5 transistors were taken from the first neutron test to evaluate the response of transistors with short collector region lifetimes. Each group of 5 transistors was exposed to four dose rates between 10^7 and 10^9 R/s. The transistor photocurrent responses from the pulse transient ionizing radiation were compared with gross predicted responses based on the electrical and physical measurement data. The predictions showed correlation with collector volume and diffusion volume within the limitations of measurement resolution and radiation dosimetry (about 30 percent). On production lines where processing variables are controlled to less than 30 percent variation, long pulse screening measurements for each transistor are unnecessary once gross predictions have been made and verified on a small test sample.

4.2 THEORY

The prediction technique employed in this investigation was derived from the steady state primary photocurrent equation: $I_{pp} = \dot{\gamma}\ G\ V_{eff}$. I_{pp} is the primary photocurrent in μa which flows across the collector-base junction. $\dot{\gamma}$ is the rate of ionizing radiation in R/s. G is the bulk current generation rate which is silicon is 6.4 μA/(cm^3 - R/s). V_{eff} is the effective volume in cm^3 from which generated carriers flow to the junction. If the collector diffusion length (L) is less than the epitaxial layer thickness we use the equation

$$I_{pp} = \dot{\gamma}\ G\ A_{CB}\ [(r_j/2) + (\varepsilon A_{CB}/C_{CBO}) + L] \qquad (4\text{-}1)$$

Where A_{CB} is area of the collector-base junction in cm^2, r_j is the radius of the collector-base junction edge or approximately the base diffusion depth (cm). The function $\varepsilon A_{CB}/C_{CBO}$ equals the collector-base junction depletion width. ε is a dielectric constant in farads per centimeter. C_{CBO} is the capacitance of the collector-base junction. Since the collector width is dependent on the epitaxial layer thickness in an epitaxial transistor, the equation for the case where the epitaxial thickness is small compared to the diffusion length is

$$I_{pp} = \dot{\gamma}\, G\, A_{CB}\, (T_{epi} - r_j/2) \qquad (4\text{-}2)$$

T_{epi} is the thickness of the epitaxial layer. The relationship at 10^8 R/s between epitaxial thickness, collector area, and primary photocurrent is shown in Figure 4-1. Plotted on the same figure are the area lines for both types of test transistors (BR200 and BR100). The graph also shows the physical parameter data for each of the four groups (wafers A and B for the BR200, and E and D for the BR100) of transistors not previously subjected to neutrons.

4.3 EXPERIMENTAL INVESTIGATIONS

The test fixtures and instrumentation for the long pulse transient ionizing radiation studies were designed to keep noise pick-up from the LINAC to a minimum. A double shield was provided for the test transistors and read-out circuitry. Two current probes were used to sense the photocurrent at the collector and base of each transistor. The emitter was left open. The test circuit is shown in Figure 4-2. The probe pairs were placed adjacent to each other to keep their noise pickup as near the same as possible. They were connected to provide photocurrent outputs of opposite polarity. When the two probes are monitored with the differential preamplifier in an oscilloscope the noise is subtracted and photocurrent is added. The resulting waveform displays twice the actual photocurrent with very little superimposed noise.

Each group of 5 transistors was mounted in the fixture on a 5 centimeter radius circle. A photodiode was used to align the center of the circle with the electron beam axis. The distances from the beam port were located with the use of the quick readout type of chip thermoluminescent dosimeter (TLD). Calibration dosimetry data were taken for each fixture position at the beginning and end of the series of tests. This was done by mounting five lithium fluoride TLD's at the transistor locations and exposing them to a series of pulses. The accuracy of the TLD's is generally considered to be ± 20 percent.

Figure 4-3 shows typical waveforms as observed on the oscilloscope during the test. These waveforms are of the photocurrents taken at approximately 0.8×10^8 R/s. The photocurrent response closely duplicated the radiation source pulse waveshape.

A total of 25 transistors were tested. These were divided into 5 groups of 5 transistors each. Two groups consisted of BR100 type of transistors; one with 0.9 mils and the other with 1.1 mils epitaxial layer thickness. Another two groups consisted of BR100 transistors with the same epitaxial thickness as the BR200's. The BR200's have an area 1.85 times that of the BR100's as noted on Figure 4-2. The fifth group was composed of five BR100 transistors that were irradiated in the first neutron test. Two of these devices had diffusion lengths of 5.8 μm while the other three had 10.6 μm.

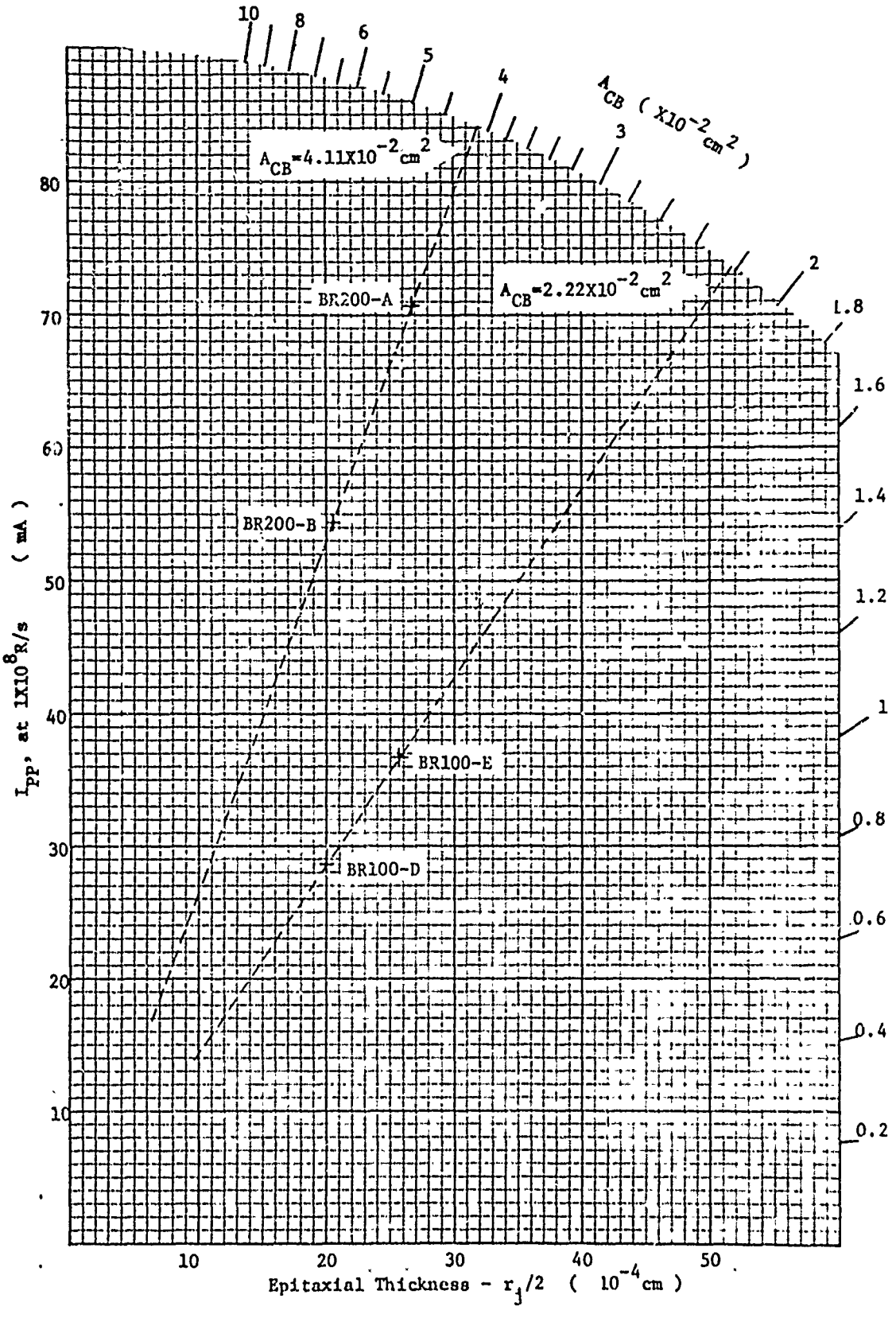

Figure 4-1. Photocurrent as a Function of Epitaxial Thickness and Collector Area

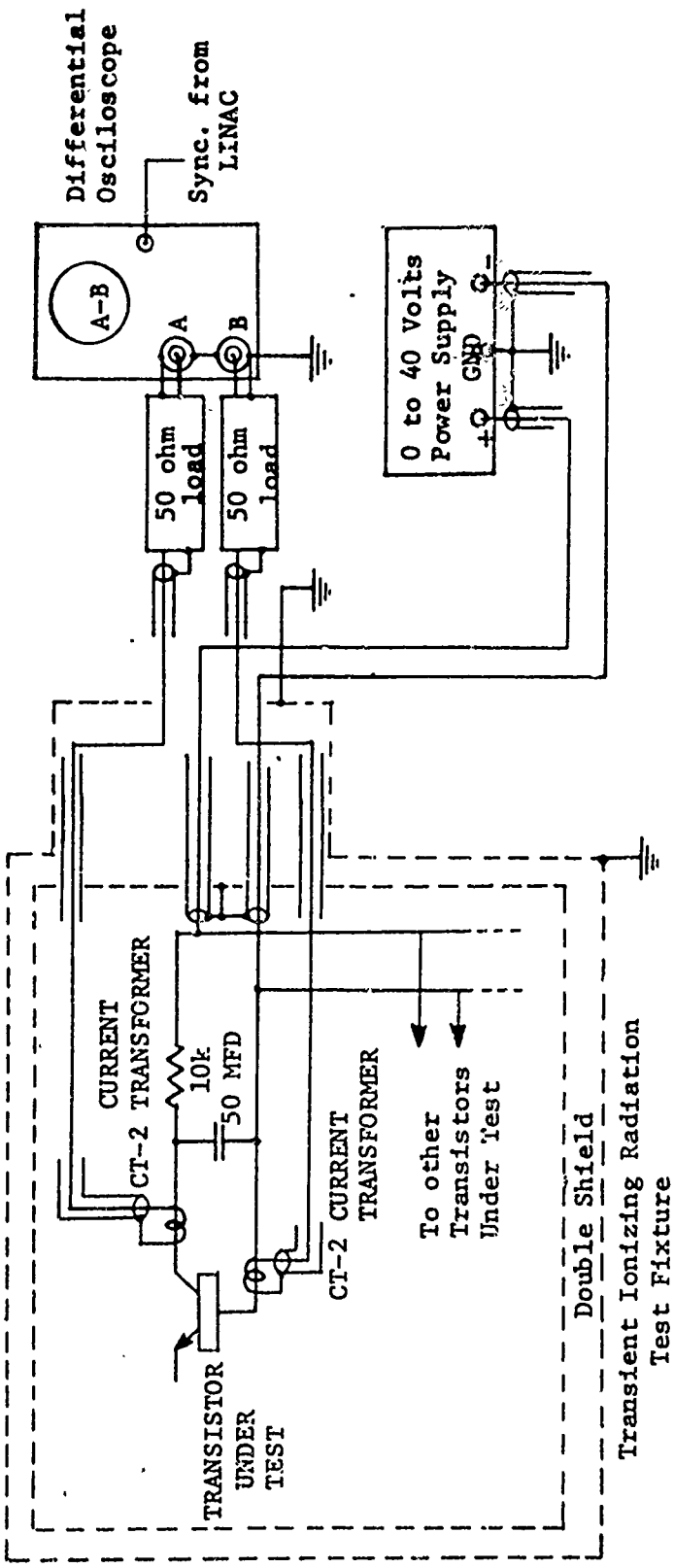

Figure 4-2. Test Circuit to Measure Transistor Photocurrent Response to Long Pulse Transient Ionizing Radiation

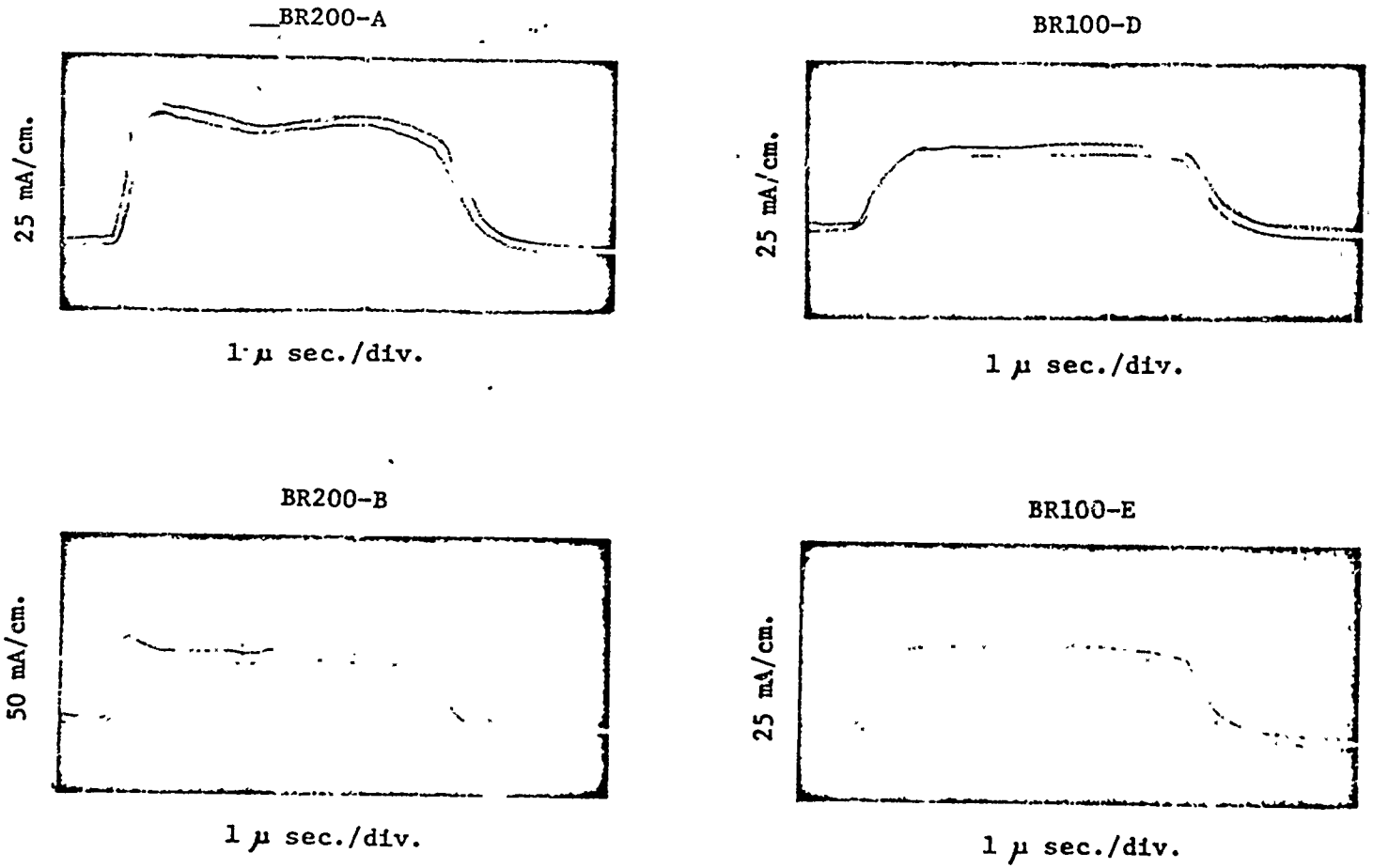

Figure 4-3. Typical Photocurrent Response Waveforms of the Transistors Tested

This combination of devices was selected to demonstrate the validity of the relationship stated in equations 4-1 and 4-2 for power transistors subjected to long pulse radiation.

A summary of the test device parameters of importance follows.

Group	Area (cm^2)	Epitaxial Thickness (μm)	Diffusion Length (μm)
BR100 Wafer D	2.22×10^{-2}	21.8	> 100
BR100 Wafer E	2.22×10^{-2}	27.7	> 100
BR200 Wafer A	4.11×10^{-2}	28.4	> 100
BR200 Wafer B	4.11×10^{-2}	22.2	> 100
BR100 Wafer E	2.22×10^{-2}	27.7	10.6
BR100 Wafer E	2.22×10^{-2}	27.7	5.8

The predicted and actual photocurrent responses of these devices as a function of dose rate are shown in Figures 4-4 to 4-8. Photocurrent measurements were made at V_{CB} = 20 volts except where noted. I_{pp} is linear with dose rate until about 10^8 R/s depending on the particular device) then secondary photocurrent generation takes place as indicated by the rapid nonlinear change shown dashed in the figures. Secondary photocurrent appears even with the emitter terminal open because of base-emitter junction breakdown. These photocurrents are voltage dependent as shown on the figure; they can be eliminated by reducing the supply voltage to avoid base-emitter junction breakdown. These results agree with the model presented by Habing and Wirth.[14]

As noted by the response curves, the predicted I_{pp}'s are in good agreement with the actual I_{pp}'s. The highest photocurrent measured at 10^8 R/s was approximately 90 mA for the BR200 with 28.4 μm epitaxial thickness. This is 27 percent above the predicted I_{pp} of 71 mA. Most of this difference is attributed to secondary photocurrent which starts to flow just before 10^8 R/s. An additional source of photocurrent could be one diffusion length into the high doped collector region, which was neglected in the prediction.

The ratio of the photocurrent response of the BR200 to BR100 transistors where the devices had the same collector widths was 1.36. This compares with an area ratio of 1.35. This is 27 percent lower than would be expected when prediction is based on effective collector volume. Among the transistors tested with the same areas but nominal collector widths having a ratio of 1.28, there was no detectable difference in photocurrents of the large collector area devices. The smaller collector area transistors, however, indicated a photocurrent response with a ratio of 1.12 which is hardly detectable in the data spread that was as high as ±30 percent. Of 20 devices which had collector widths much less than

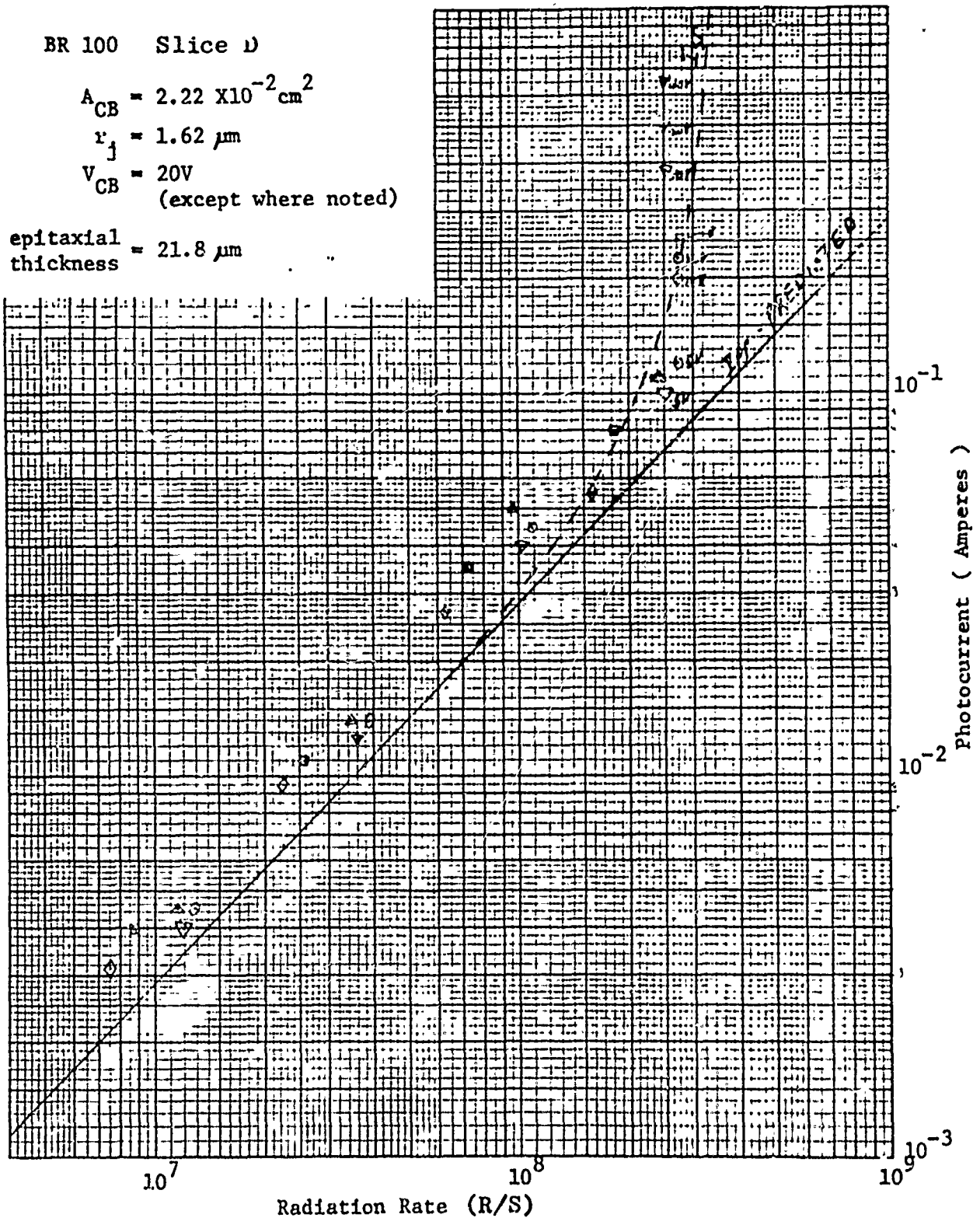

Figure 4-4. Photocurrent Response of Transistors BR100, Slice D
5 μs Pulse - White Sands

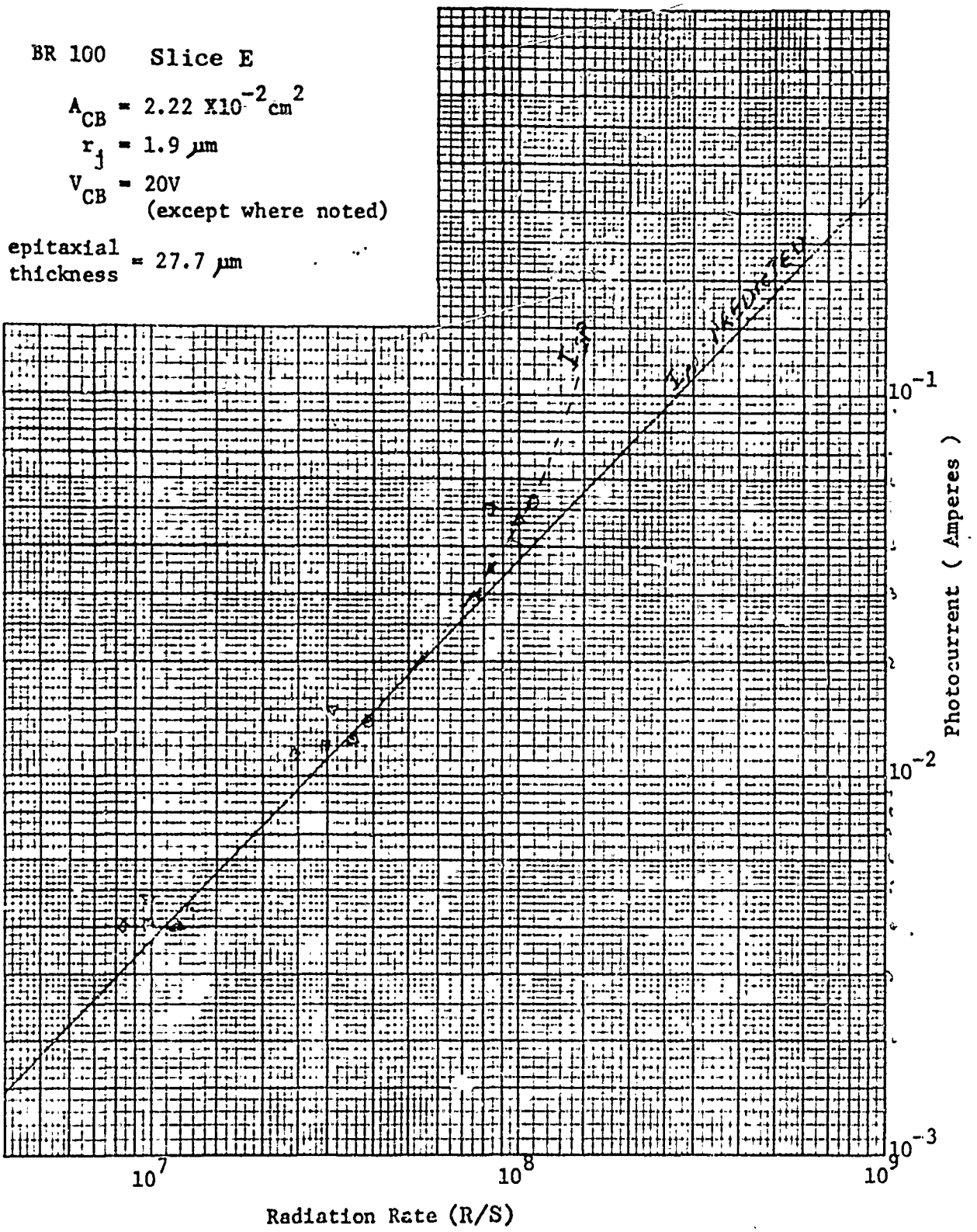

Figure 4-5. Photocurrent Response of Transistors BR100, Slice E
5 μs Pulse - White Sands

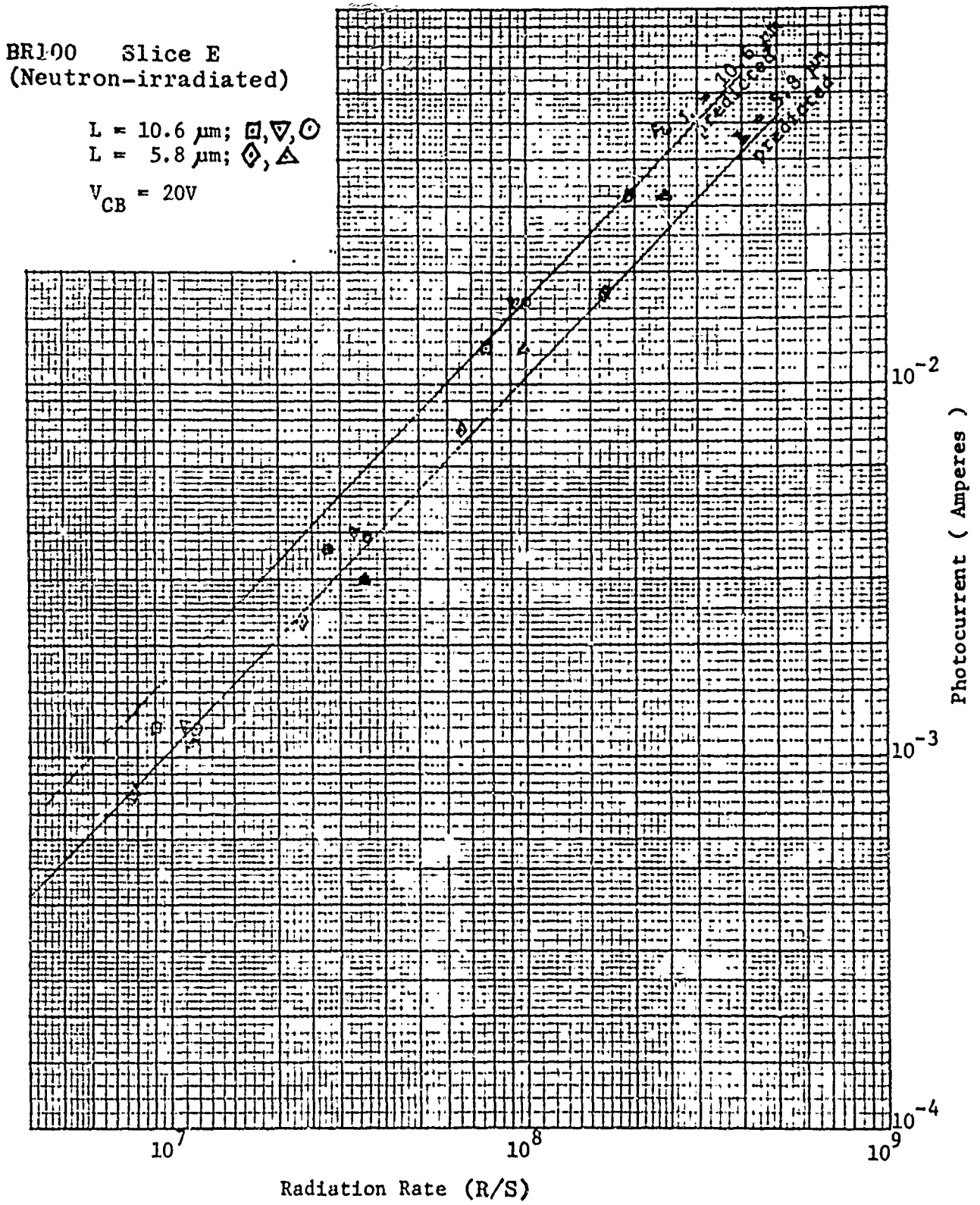

Figure 4-6. Photocurrent Response of Neutron-Irradiated Transistors

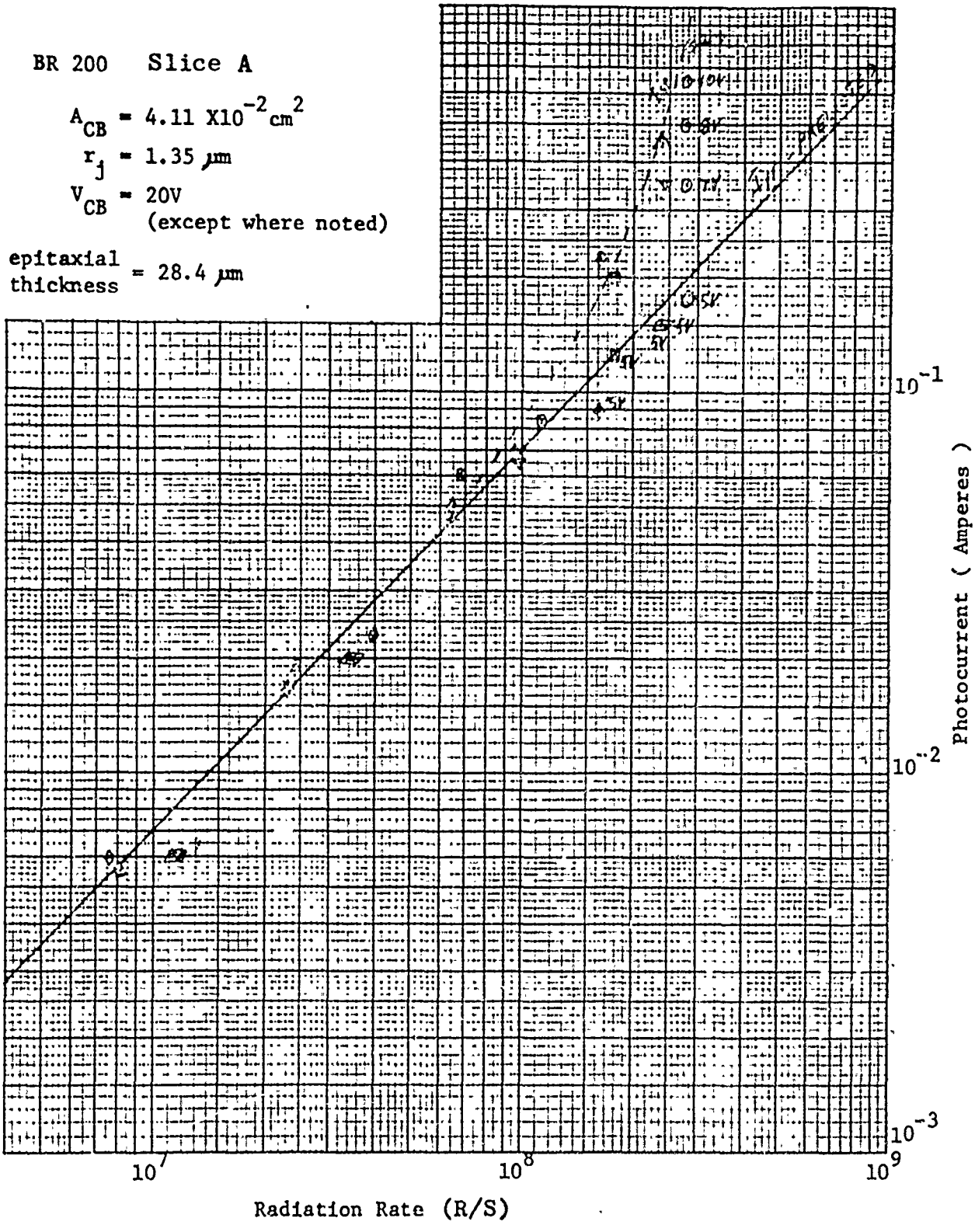

Figure 4-7. Photocurrent Response of Transistors BR200, Slice A

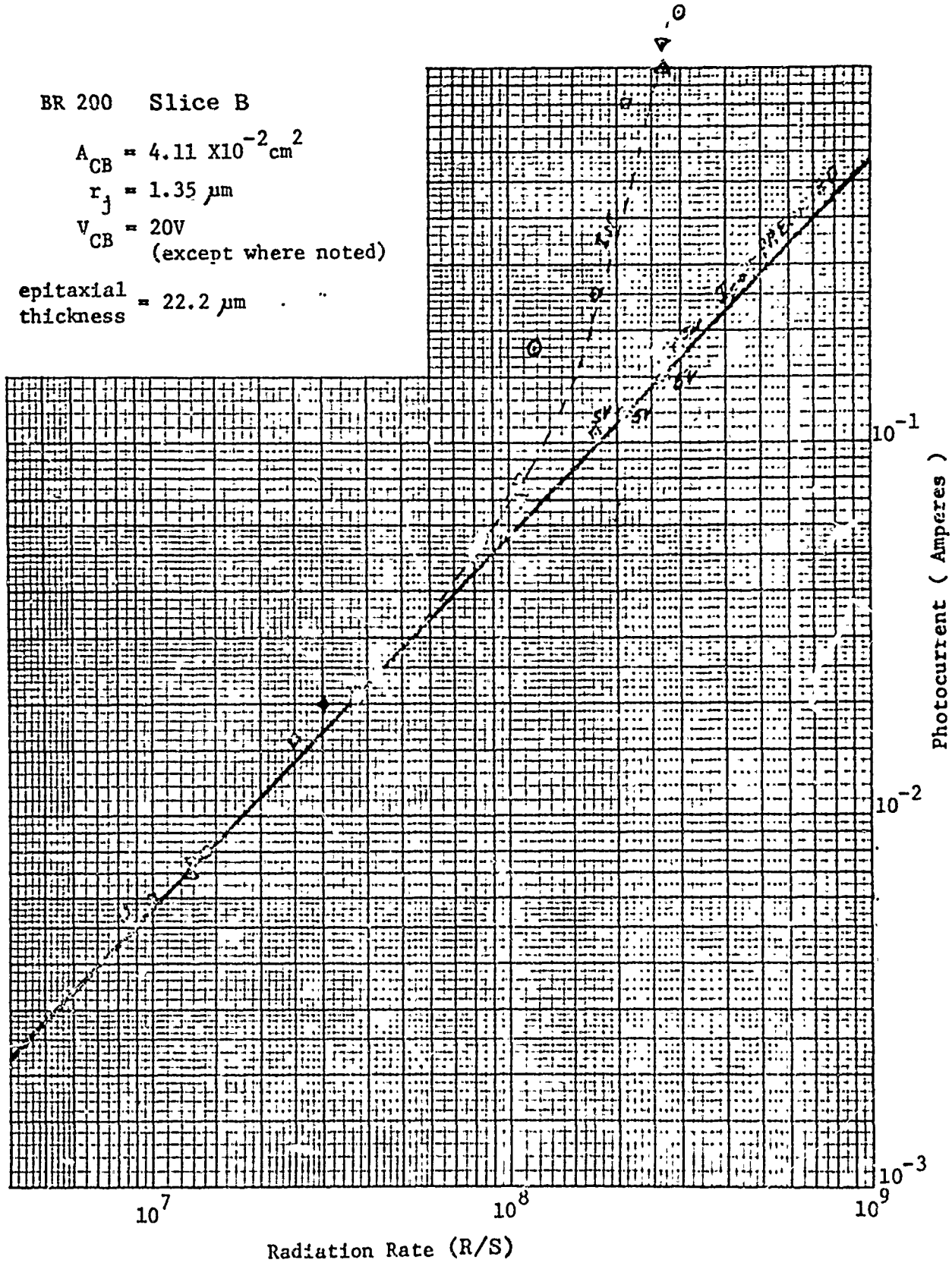

Figure 4-8. Photocurrent Response to Transistors BR200, Slice B

their collector diffusion length no significant change in primary photocurrent could be detected due to power supply voltage change. The lack of voltage dependency in primary photocurrents supports the theory that an epitaxial layer thickness limited collector volume does not vary with a change in the width of depletion region of the collector-base junction.

For the five devices with diffusion lengths less than the epitaxial thickness, predictions of primary photocurrents based on a measurement of lifetime in the collector were extremely good. These devices displayed a slight voltage dependence as expected. Three units having diffusion lengths of approximately 10.6 microns displayed a photocurrent increase of 10 percent with the junction voltage change from 20 to 40 volts. The remaining two units having a diffusion length of 5.8 microns displayed an increase of photocurrent of approximately 13 percent with the same voltage change.

APPENDIX B

FAIRCHILD RADIATION TEST DATA
FOR
2N5107 AND 2N5244

This Appendix is a letter from Fairchild Research and Development Corporation, in response to a request for data by Mr. Steve Callaghar of Honeywell, Inc.

FAIRCHILD
RESEARCH & DEVELOPMENT
DIVISION OF FAIRCHILD CAMERA AND INSTRUMENT CORPORATION

4001 MIRANDA AVENUE, PALO ALTO, CALIFORNIA 94304 · (415) · 321-7250
TWX: 910-379-6435

May 25, 1971

Mr. Steve Callaghan, MS A-1391
Honeywell - GAP
2600 Ridgeway Parkway
Minneapolis, Minnesota 55413

Dear Steve,

Per our conversation, I am enclosing a copy of the $3 \times 10^{14} n/cm^2$ data on 2N2219's which are similar to the 2N5107.

You requested information concerning the equilibrium photocurrents for the 2N5244 and 2N5107.

i_{pp} (mA) at

	A_{CB} mils^2	10^8	10^9	10^{10}
		RADS (Si)/sec		
2N5107	131.2	0.65	6.5	60.5
2N5244	21.1	0.094	0.94	9.4

The differences reflected above are better understood when you note the differences in the collector-base area, A_{CB}.

If you have any additional questions, please call me.

Sincerely,

David K. Myers
Radiation Effects Consultant

DKM/pe

Encl

2N 2219 (Ph II Predicting Ph III)

This is Type B Prediction of Beta at 3.03×10^{14}

Variable	Regression-Coefficient
1	-.747
2	.021
3	.241
4	-.024
5	3.367
6	-5.700
7	.013
8	-.500
9	.364
10	.343
11	.029

β-Actual	β-Calculated	Difference	Percent Different
13.30	12.28	1.02	7.690
9.80	8.83	.97	9.850
14.00	13.25	.75	5.329
10.40	9.84	.56	5.410
13.30	12.67	.63	4.766
11.10	11.26	-.16	-1.436
7.10	6.47	.63	8.821
10.00	8.77	1.23	12.335
9.50	8.31	1.19	12.514
11.50	10.69	.81	7.025
12.40	12.76	-.36	-2.927
10.00	7.39	2.61	26.068
13.20	12.30	.90	6.791
10.00	9.61	.39	3.908
11.50	9.75	1.75	15.234
11.50	11.24	.26	2.265
11.30	10.60	.70	6.205
11.20	11.10	.10	.931
10.60	10.32	.28	2.685
12.20	12.91	-.71	-5.802
11.90	12.01	-.11	-.896
11.80	11.28	.52	4.411
12.50	11.00	1.50	12.039
15.50	14.66	.84	5.411

β-Actual	β-Calculated	Difference	Percent Different
11.70	11.75	-.05	-.437
10.10	9.78	.32	3.216
9.50	9.26	.24	2.532
14.20	12.55	1.65	11.598
13.00	12.01	.99	7.612
10.20	9.62	.58	5.639
11.20	10.97	.23	2.028
10.70	11.33	-.65	-5.848
10.00	9.33	.67	6.715
10.30	9.81	.49	4.776
9.40	9.07	.33	3.518
10.20	9.30	.90	8.825
13.50	11.79	1.71	12.652
9.80	9.21	.59	6.049
10.00	9.39	.61	6.096
10.00	10.37	-.37	-3.726
10.00	9.28	.72	7.247
10.60	8.75	1.85	17.433
11.90	12.06	-.16	-1.318
15.10	15.77	-.67	-4.469
12.80	11.84	.96	7.509
8.80	8.52	.28	3.235
16.90	14.70	2.20	12.996
10.10	10.21	-.11	-1.049
14.90	14.29	.61	4.070
12.50	11.83	.67	5.399
8.70	9.24	-.54	-6.201
10.00	9.12	.83	8.803
10.50	9.93	.57	5.418
10.60	10.66	-.06	-.533
10.40	10.31	.09	.818
10.30	10.76	-.46	-4.460
11.70	12.47	-.77	-6.548
15.00	13.02	1.98	13.232
10.60	10.68	-.08	-.773
15.70	14.71	.99	6.304
11.30	11.50	-.20	-1.780
12.60	12.39	.21	1.650
10.00	9.94	.06	.648
12.00	12.13	-.13	-1.103
13.20	12.31	.89	6.776
12.20	13.30	-1.10	-9.052
7.90	7.99	-.09	-1.146
10.00	9.47	.53	5.331
10.90	10.87	.03	.311
14.00	13.62	.38	2.725
10.00	10.87	-.87	-8.748
10.50	10.04	.46	4.415
12.10	12.01	.09	.710

β-Actual	β-Calculated	Difference	Percent Different
12.60	12.40	.20	1.554
10.30	10.13	.17	1.548
12.40	12.43	-.03	-.248
12.40	12.59	-.19	-1.540
15.30	14.38	.92	5.989
10.10	9.18	.92	9.120
12.30	13.21	-.91	-7.437
10.00	10.48	-.48	-4.846
12.00	8.70	3.30	27.480
12.10	12.12	-.02	-.171
11.60	12.47	-.87	-7.517
12.70	11.86	.84	6.652
12.20	12.30	-.10	-.793
11.10	12.06	-.96	-8.663
10.00	11.33	-1.33	-13.267
10.20	9.84	.36	5.559
10.50	11.17	-.67	-6.398
11.60	12.47	-.87	-7.505
10.00	8.30	1.70	17.036
10.00	10.06	-.06	-.639
11.20	11.96	-.76	-6.743
10.30	9.69	.61	5.959
11.60	12.20	-.60	-5.171
14.60	9.69	4.91	33.618
11.10	10.14	.96	8.625
12.70	11.27	1.43	11.253
12.80	12.07	.73	5.669
13.00	13.19	-.19	-1.479
13.90	12.07	1.83	13.166
10.00	10.09	-.09	-.896
9.60	8.86	.74	7.677
12.10	11.49	.61	5.026
10.00	8.48	1.52	15.228
9.60	8.90	.70	7.313
11.20	10.02	1.18	10.530
10.60	9.61	.99	9.376
11.50	11.05	.45	3.878
10.40	10.36	.04	.337
11.00	10.31	.69	6.241
10.00	10.23	-.23	-2.315
11.90	11.83	.07	.549
12.10	9.58	2.52	20.834
12.70	11.20	1.50	11.814
11.80	11.35	.45	3.816
10.10	9.33	.77	7.582
8.10	7.46	.64	7.920
10.50	10.30	.20	1.927
10.50	10.75	-.25	-2.368
12.00	10.49	1.51	12.549

β-Actual	β-Calculated	Difference	Percent Different
12.00	9.74	2.26	18.844
8.70	9.17	-.47	-5.399
14.20	14.75	-.55	-3.889
12.80	14.46	-1.66	-12.953
11.00	10.41	.59	5.362
12.60	11.45	1.15	9.091
10.10	9.67	.43	4.261
13.30	11.93	1.37	10.306
13.00	13.54	-.54	-4.135
13.40	12.70	.70	5.188
10.30	9.19	1.11	10.802
8.80	9.21	-.41	-4.623
13.20	13.50	-.30	-2.235
9.70	8.29	1.41	14.515
8.60	8.58	.02	.185
12.20	10.72	1.48	12.170
8.80	9.32	-.52	-5.899
12.90	13.74	-.84	-6.524
11.40	10.64	.76	6.655
11.10	11.75	-.65	-5.894
9.50	9.41	.09	.974
11.90	12.15	-.25	-2.073
11.50	11.08	.42	3.647
16.10	14.81	1.29	8.015
11.60	11.13	.47	4.026
13.20	12.91	.29	2.225
10.00	8.34	1.66	16.607
9.20	9.39	-.19	-2.099
10.60	10.73	-.13	-1.182
12.30	12.07	.23	1.868
8.60	8.15	-.55	-6.411
11.80	11.93	-.13	-1.126
11.70	12.53	-.83	-7.115
9.00	9.32	-.32	-3.515
13.80	13.69	.11	.801
12.70	13.49	-.79	-6.198
12.50	12.61	-.11	-.875
10.20	9.89	.31	3.064
10.70	12.29	-1.59	-14.900
11.80	12.33	-.53	-4.506
10.50	9.85	.65	6.150
13.00	11.69	1.31	10.040
12.60	12.63	-.03	-.267
10.00	9.64	.36	3.552
8.50	7.88	.62	7.321
8.90	8.97	-.07	-.777
14.00	13.03	.97	6.910
10.30	9.34	.96	9.334
12.70	12.22	.48	3.788

β-Actual	β-Calculated	Difference	Percent Different
10.70	11.11	-.41	-3.839
12.40	12.09	.31	2.485
10.70	10.97	-.27	-2.521
11.10	11.24	-.14	-1.300
13.70	15.03	-1.33	-9.699
10.50	10.82	-.32	-3.042
13.50	13.40	.10	.764
11.90	12.44	-.54	-4.556
12.60	12.26	.34	2.685
12.00	12.40	0.40	-3.299
13.20	13.13	.07	.539
13.20	13.52	-.32	-2.408
12.10	12.54	-.44	-3.609
14.00	14.11	-.11	-.798
11.60	12.00	-.40	-3.488
12.30	13.26	-.96	-7.826
13.50	13.37	.13	.945
10.50	10.42	.08	.717
11.80	12.13	-.33	-2.834
11.00	11.45	-.45	-4.081

Average Absolute Percent Difference - 5.9240215

APPENDIX C

SPRINT II NUCLEAR TEST PLAN
FAST BURST REACTOR/WSMR - FEBRUARY 7, 1972

INTRODUCTION

The radiation characteristics required for radiation hardness evaluation of the Laser Gyro circuits are as follows:

1 Laser Gyro High Voltage power supply

2 Laser Gyro Photocurrent Experiment.

The radiation characteristics required for evaluation of these circuits are the transient and permanent changes in output voltages as a function of the nuclear environment. The circuits will be exposed to the nuclear environment of the fast burst reactor at WSMR. Permanent changes will be determined by comparison of steady state voltages taken before and after exposure. Magnetic tape recordings and oscilloscope photographs will be used to record output voltages during exposure.

TEST PLAN

I. LASER GYRO HIGH VOLTAGE POWER SUPPLY (Figures C-1 and C-2).

The Laser Gyro High Voltage Power Supply consists of a high voltage dc-to-dc converter, Figure C-1, and a +10 Vdc regulator, Figure C-2. The +10 Vdc regulator accepts +24 Vdc from an external source and supplies +10 Vdc to the dc-to-dc converter. Regulation of the high voltage output is accomplished through feedback from the high voltage secondary to the +10 Vdc regulator.

Outputs to be recorded during the burst are:

Coax Number	Test Point	Termination at Scope	Output Voltage
11	-1090V	51	-0.135 Vdc
12	Feedback (12.6)	51	+0.30 Vdc
13	+2100V	None	+0.30 Vdc
14	Converter (40 kHz)	51	0.9 Vac pp
15	10V Monitor (10.7V)	51	+0.60 Vdc

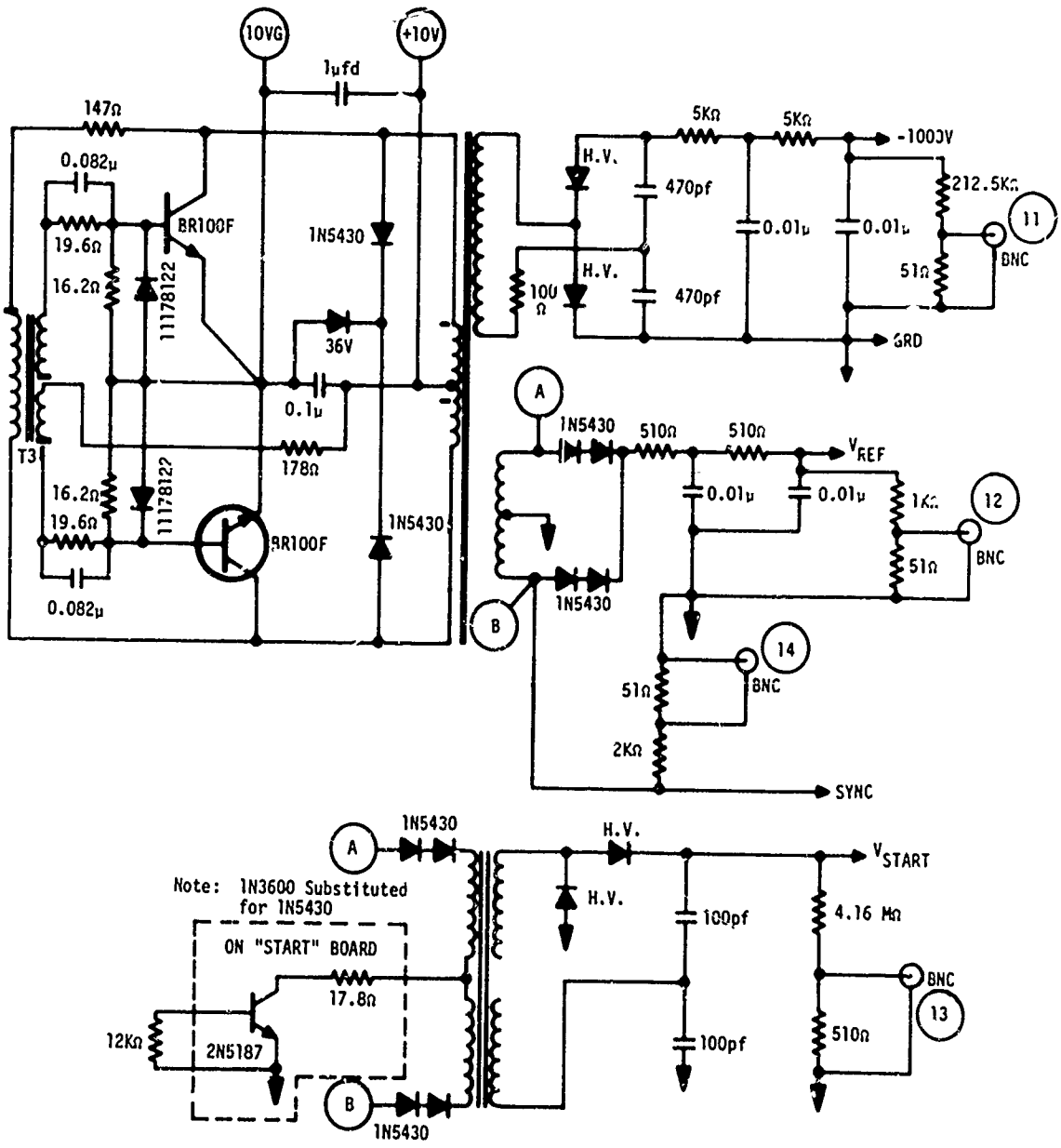

Figure C-1. High-Voltage dc-to-dc Converter

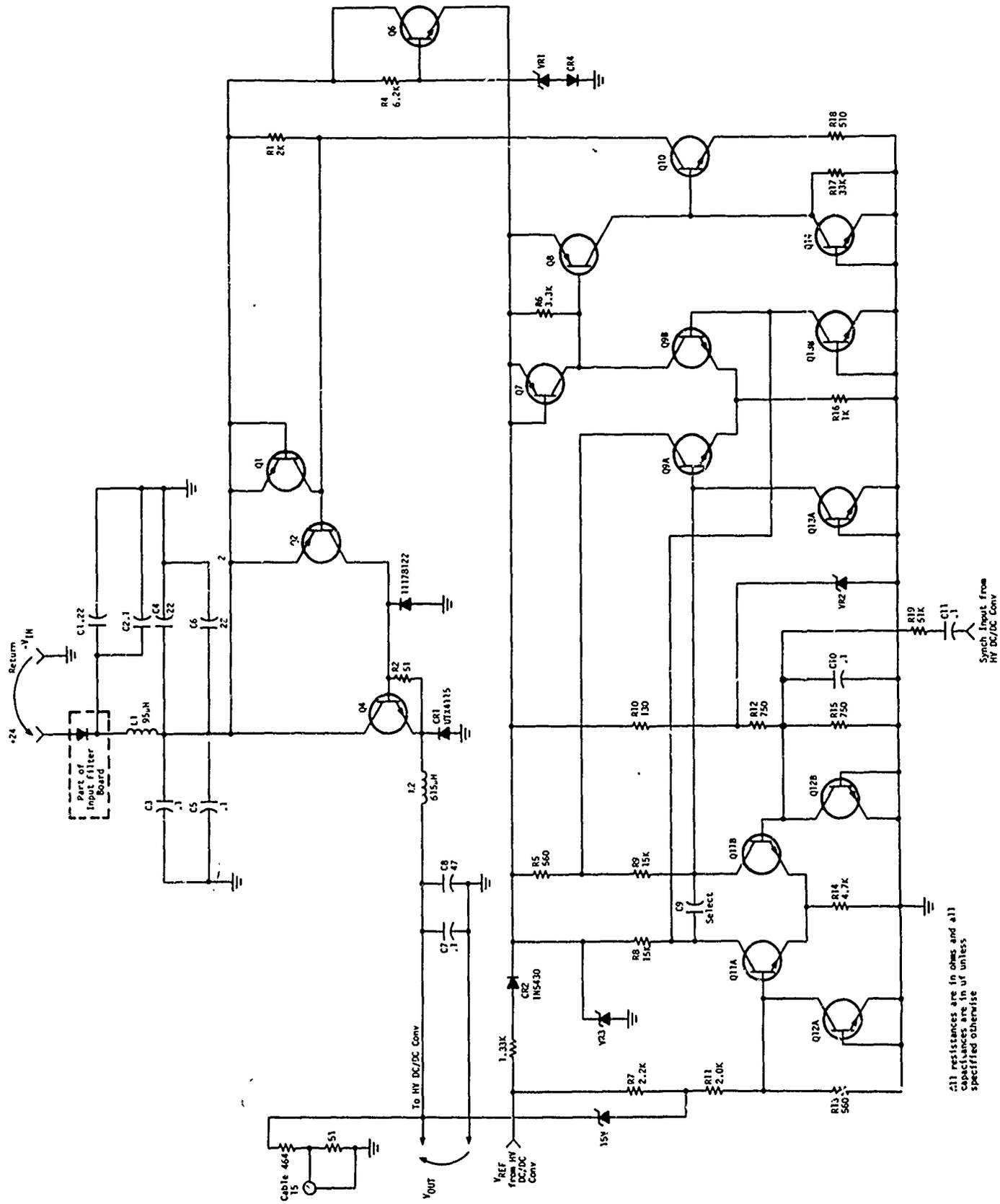

Figure C-2. +10 Volt Regulator

For permanent damage data, each dc output will be measured with a digital voltmeter before each burst and as soon as possible after the burst. The converter output will be measured with a frequency counter before and after the burst.

II. LASER GYRO PHOTOCURRENT EXPERIMENT

The purpose of this experiment is to measure diode photocurrent while the diodes are being exposed to nuclear radiation. The circuit shown in Figure C-3 was placed close to the reactor shield for one burst. Figure C-4 shows the cable connections for this experiment.

DOSIMETRY

Dosimeters will be located on each test item so that the average dose and dose rate can be calculated. Each dosimeter will be numbered and its location on the test item will be recorded. Three sulfur and 3 TLD dosimeters will be used for each test item. However, the reactor performance data that is provided by the test facility for each burst can be used, along with the location of the test item, to give a reasonable approximation of neutron dose and gamma dose rate.

TEST DATA

Table C-I presents test data and Tables C-II and C-III present equipment settings. Oscilloscope records of the test are presented in Figures C-5 through C-27.

TABLE C-I

Test Data

First Burst

High Voltage: $\Delta T = 196°C$

Second Burst

High Voltage: $\Delta T = 190°C$

High Voltage Power Supply

	BNC	Pre-Burst 1	Post Burst 1	Pre-Burst 2	Post Burst 2
Scaled	11	-0.135	-0.125	-0.125	-0.120
Actual		1090	1001	1001	969
Scaled	12	0.2998	0.290	0.290	0.286
Actual		12.6	12.2	12.2	12.02
	13				
	14				
Scaled	15	0.5355	0.5598	0.559	0.576
Actual		9.6	10.0	10.0	10.3

TABLE C-II

Laser Gyro High Voltage Power Supply

Coax Number	65 Ft Cable Number	Record Track Number and Cal Level	Oscilloscope Number and Settings	
			Vertical (V/cm)	Horizontal (ms/cm)
BNC 11 −1090V	1	Track 1 ±0.3V	Scope No. 1 Upper: 0.1 Lower: 0.1	 0.1 0.5
BNC 12 Feedback	2	Track 2 ±0.5V	Scope No. 2 Upper: 0.2 Lower: 0.2	 0.1 0.5
BNC 13 +2100V	3	Track 3 ±0.5V	Scope No. 3 Upper: 0.2 Lower: 0.2	 0.1 0.5
BNC 14 Converter	4	Track 4 ±1.5V Direct Record	Scope No. 4 Upper: 0.5 Lower: 0.5	 0.1 0.5
BNC 15 10V Monitor	5	Track 5	Scope No. 5 Upper: 0.5 Lower: 0.5	 0.1 0.5

TABLE C-III

Laser Photo Current Experiment

Coax Number	65 Ft Cable Number	Record Track Number and Cal Level	Oscilloscope Number and Settings	
			Vertical (V/cm)	Horizontal (μs/cm)
1 Detector Circuit Battery	1	Track 1 ±10V	Scope No. 1 Upper: 5.0 Lower: ac-1.0	 -5 -5
2 Diode No. 1 Output	2	Track 2 ±6V	Scope No. 2 Upper: 2.0 Lower: 0.5	 5 5
3 Diode No. 2 Output	3	Track 3 ±6V	Scope No. 3 Upper: 2.0 Lower: 0.5	 5 5
4 Compensator Circuit Battery	4	Track 4 ±6V	Scope No. 4 Upper: 5.0 Lower: ac-1.0	 5 5
5 Diode No. 4 Output	5	Track 5 ±6V	Scope No. 5 Upper: 2.0 Lower: 0.5	 5 5
6 Diode No. 5 Output	6	Track 6 ±6V	Scope No. 6 Upper: 2.0 Lower: 0.5	 5 5

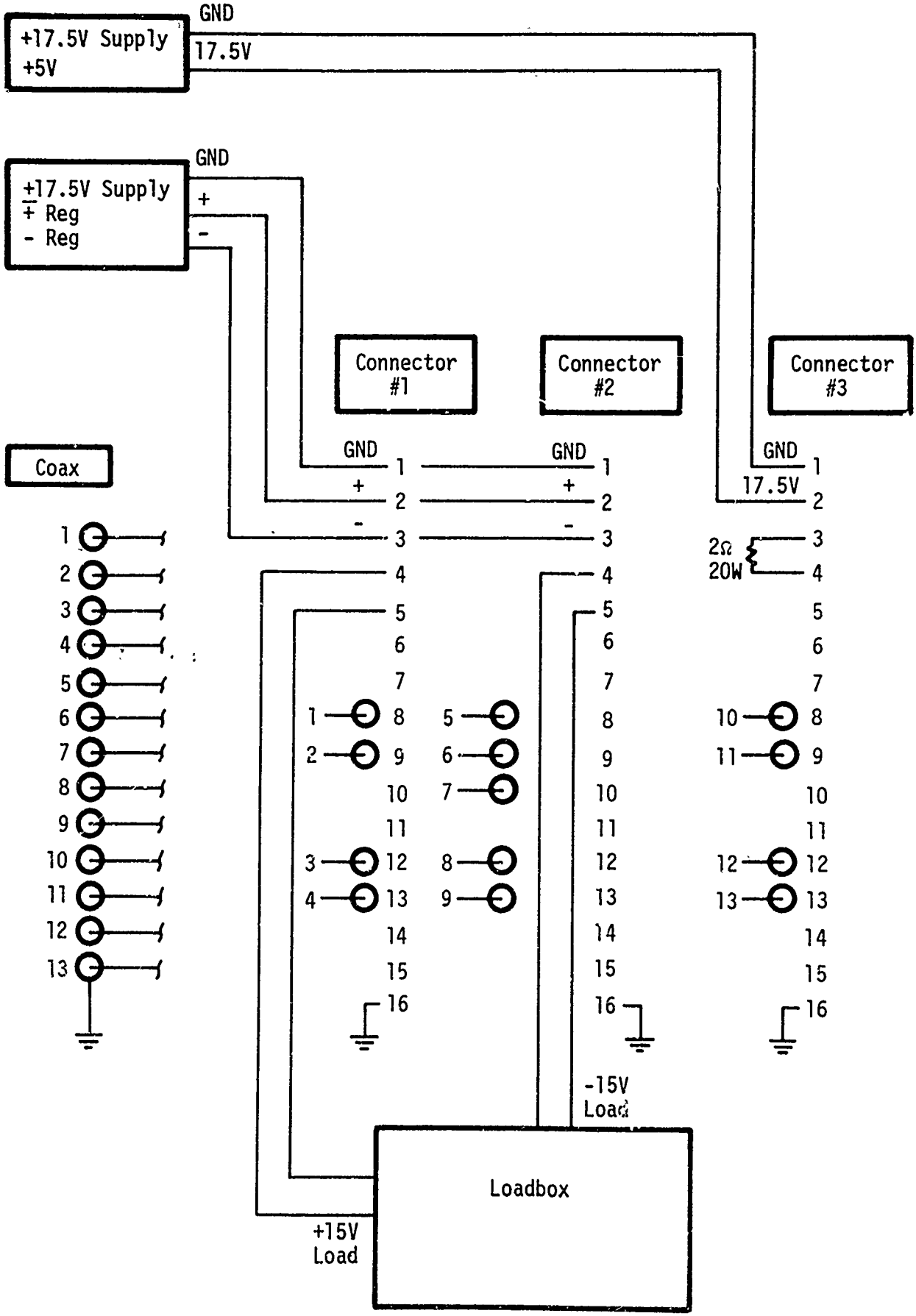

Figure C-3. Photocurrent Experiment

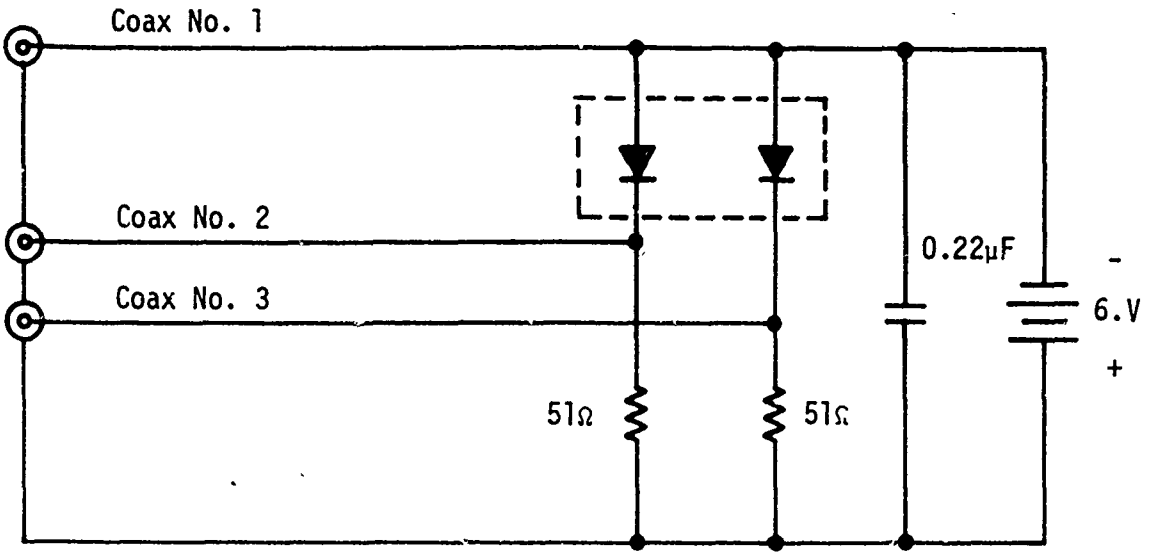

Germanium Dual Detector Circuit

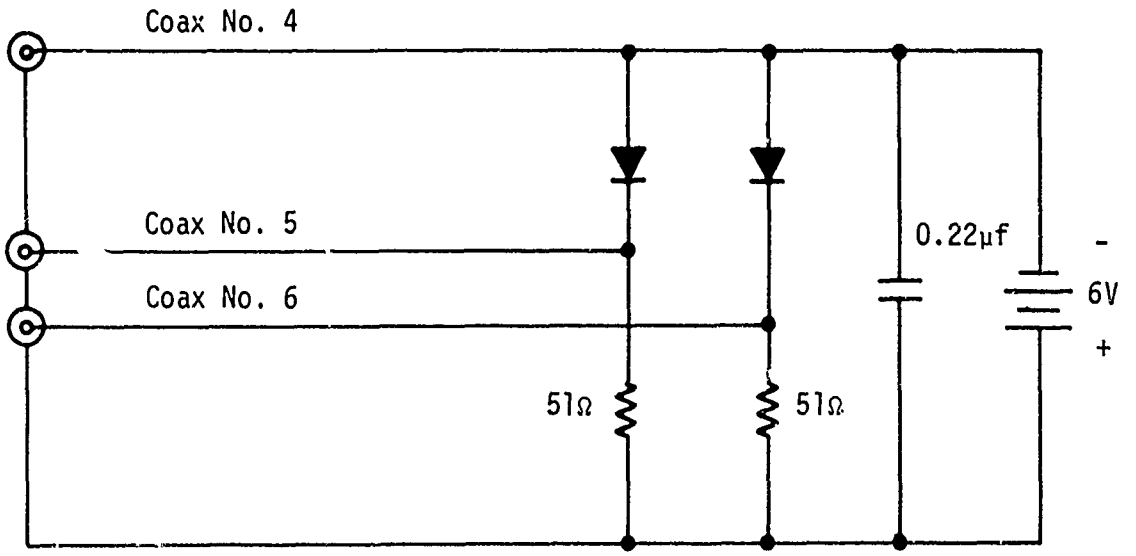

Compensator Circuit

Figure C-4. Photocurrent Experiment

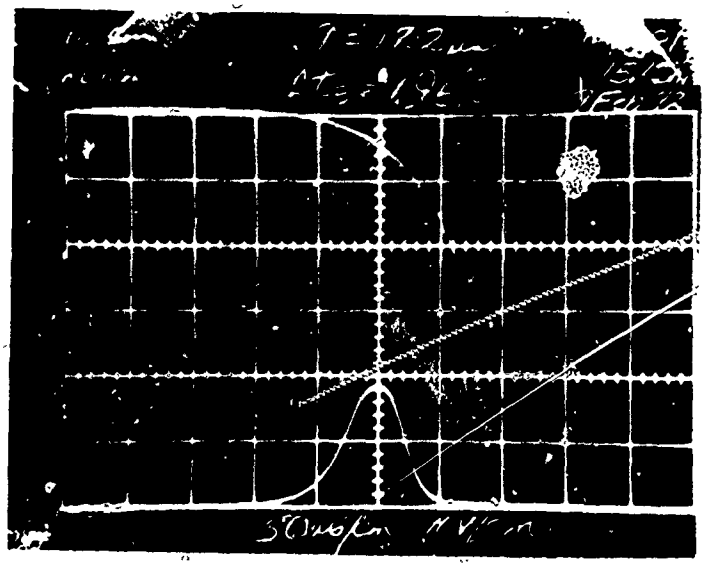

Upper Trace:
Vertical - 20 mV/cm
Horizontal - 20 μs/cm

Lower Trace:
Vertical - 10 V/cm
Horizontal - 50 μs/cm

Figure C-5. Reactor Gamma Profile - Burst 1

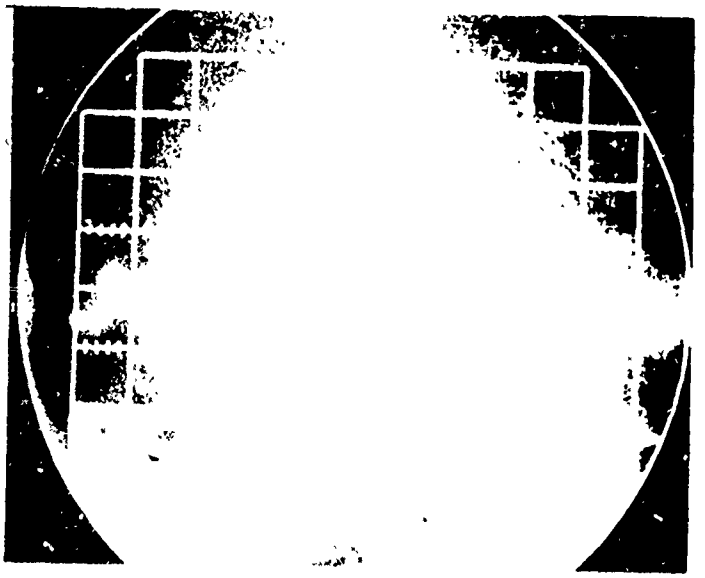

Upper Trace:
Vertical - 0.1V/cm
Horizontal - 500 μs/cm

Lower Trace:
Vertical - 0.1 V/cm
Horizontal - 2 μs/cm

Figure C-6. Laser Gyro BNC-11 -1090V - Burst 1

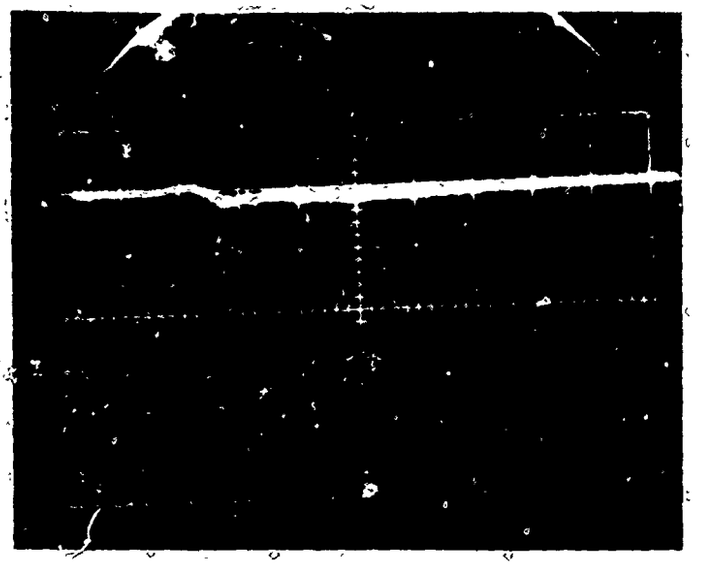

Vertical - 0.2 V/cm
Horizontal - 100 μs/cm

Figure C-7. Laser Gyro High Voltage Power Supply BNC-12 Feedback - Burst 1

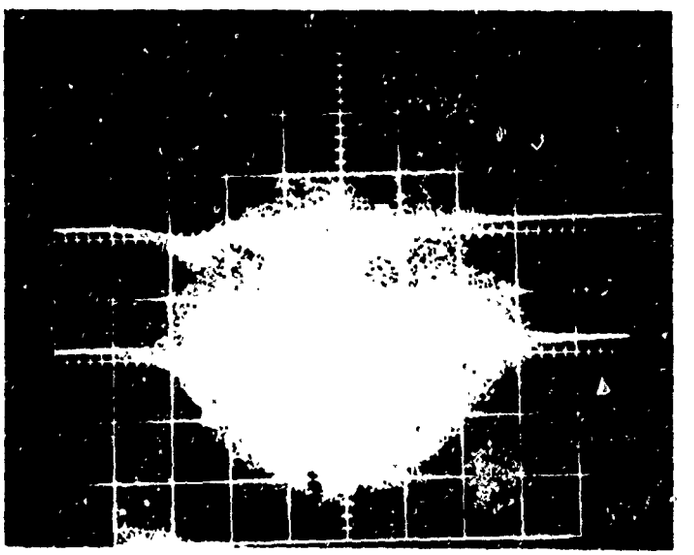

Upper:
Vertical - 0.2 V/cm
Horizontal - 100 μs/cm

Lower:
Vertical - 0.2 V/cm
Horizontal - 100 μs/cm

Figure C-8. Laser Gyro High Voltage Power Supply BNC-13 +2100V - Burst 1

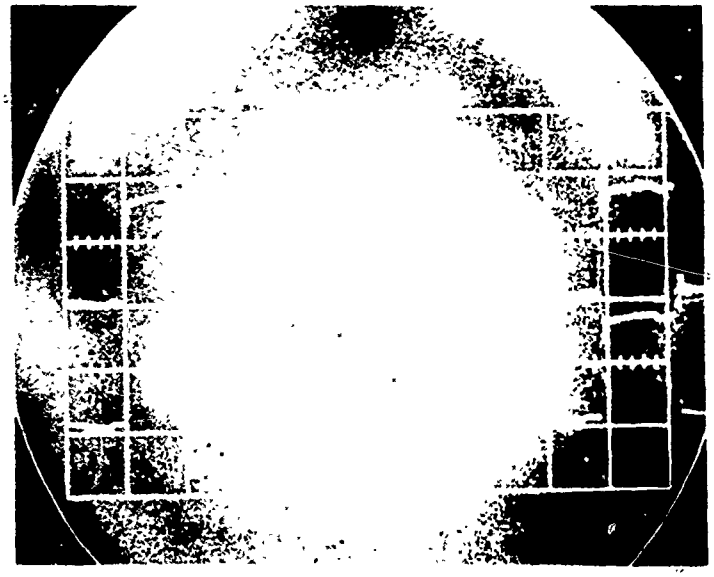

Upper Trace:
Vertical - 0.5 V/cm
Horizontal - 10 μs/cm

Lower Trace:
Vertical - 0.5 V/cm
Horizontal - 10 μs/cm

Figure C-9. Laser Gyro High Voltage Power Supply BNC-14 Converter - Burst 1

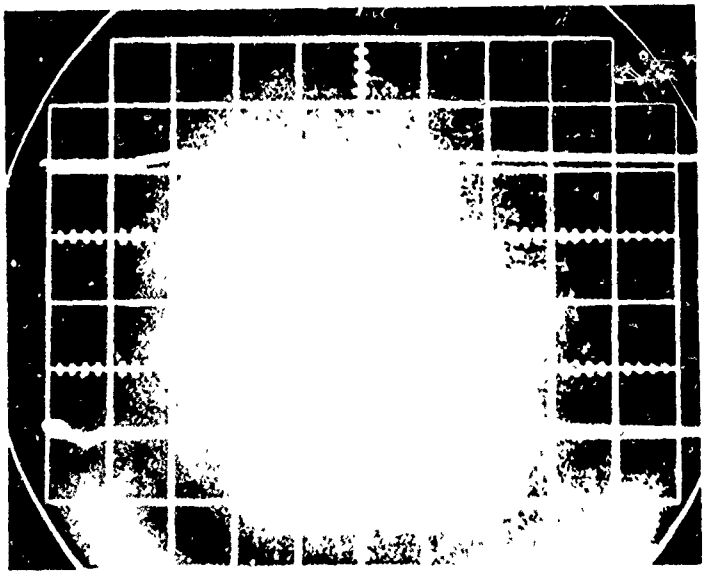

Upper Trace:
Vertical - 0.5 V/cm
Horizontal - 100 μs/cm

Lower Trace:
Vertical - 0.5 V/cm
Horizontal - 500 μs/cm

Figure C-10. Laser Gyro High Voltage Power Supply BNC-15 10V Monitor - Burst 1

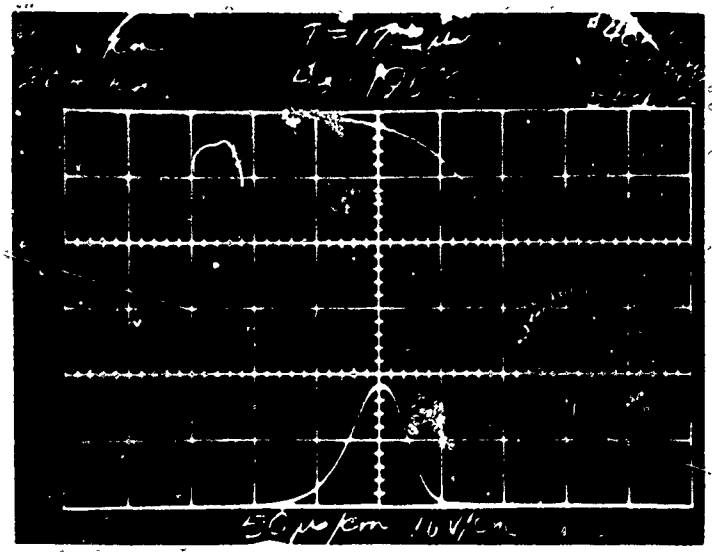

Upper Trace:
Vertical - 20 mV/cm
Horizontal - 20 μs/cm

Lower Trace:
Vertical - 10 V/cm
Horizontal - 50 μs/cm

Figure C-11. Reactor Gamma Profile - Burst 2

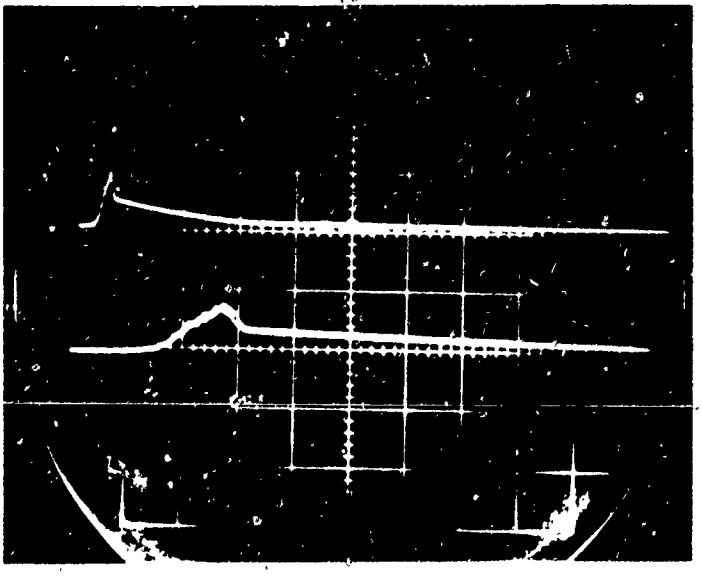

Upper Trace:
Vertical - -1 V/cm
Horizontal - 500 μs/cm

Lower Trace:
Vertical - 0.1 V/cm
Horizontal - 100 μs/cm

Figure C-12. Laser Gyro High Voltage Power Supply BNC-11 -1090V - Burst 2

Vertical - 0.2V/cm
Horizontal - 100 μs/cm

Figure C-13. Laser Gyro High Voltage Power Supply BNC-12 Feedback - Burst 2

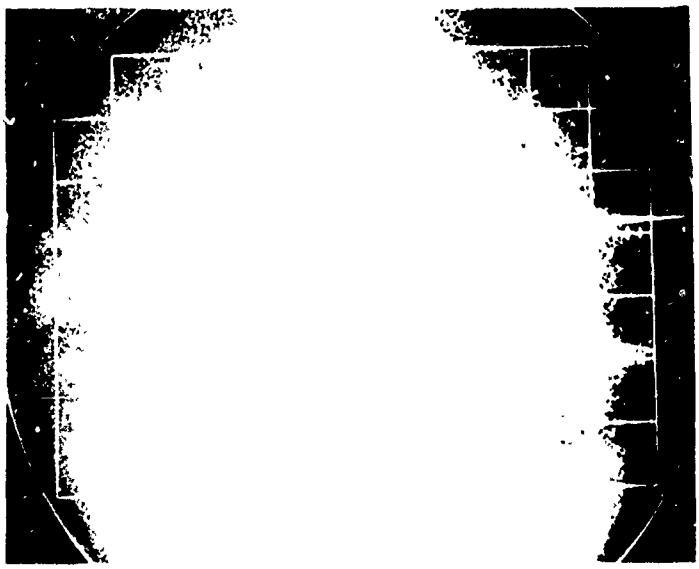

Upper Trace:
Vertical - 0.2V/cm
Horizontal - 100 μs/cm

Lower Trace:
Vertical - 0.2V/cm
Horizontal - 100 μs/cm

Figure C-14. Laser Gyro High Voltage Power Supply BNC-13 +2100V - Burst 2

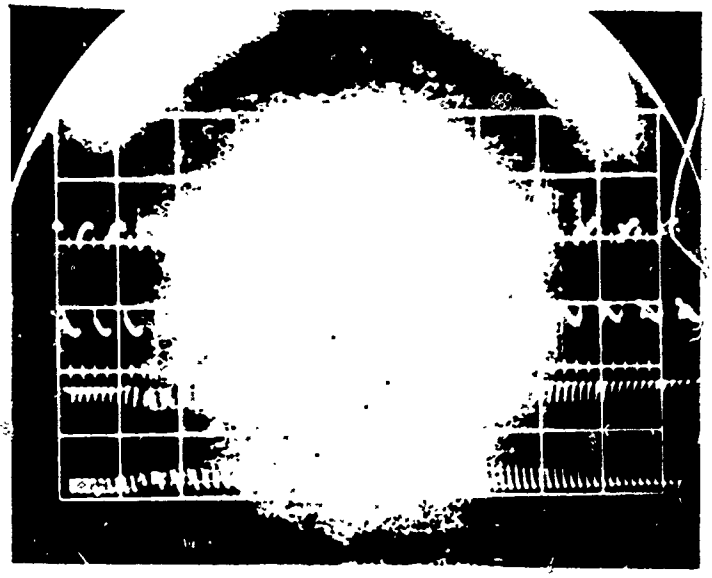

Upper Trace:
Vertical - 0.5V/cm
Horizontal - 50 µs/cm

Lower Trace:
Vertical - 0.5V/cm
Horizontal - 200 µs/cm

Figure C-15. Laser Gyro High Voltage Power Supply BNC-14 Converter - Burst 2

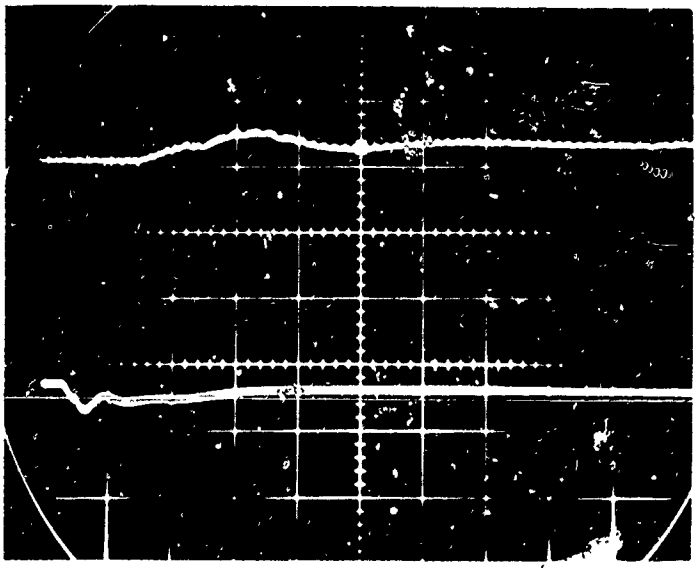

Upper Trace:
Vertical - 0.2V/cm
Horizontal - 100 µs/cm

Lower Trace (Inverted):
Vertical - 0.2 V/cm
Horizontal - 500 µs/cm

Figure C-16 Laser Gyro High Voltage Power Supply BNC-15 10V Mon - Burst 2

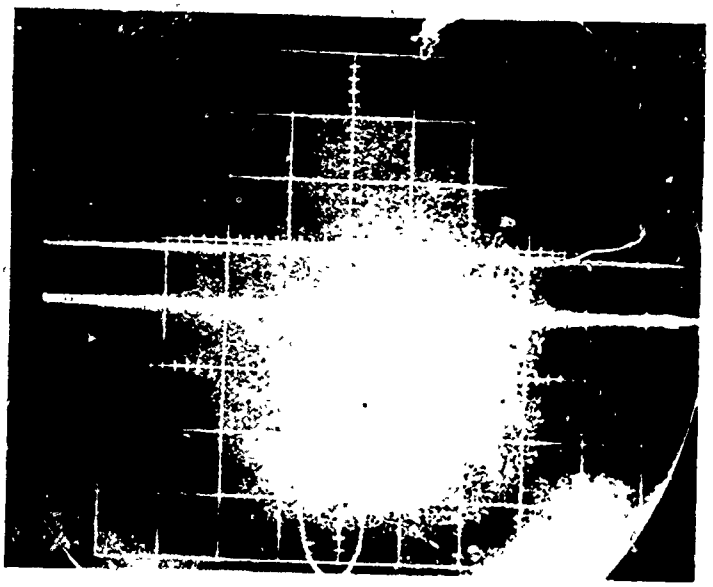

Upper Trace - Coax 1
Detector Circuit Battery:
Vertical - 1V/cm
Horizontal - 50 μs/cm

Lower Trace - Coax 2
Diode #1 Output:
Vertical - 0.2V/cm
Horizontal - 50 μs/cm

Figure C-17. Laser Photocurrent Experiment - Burst 2

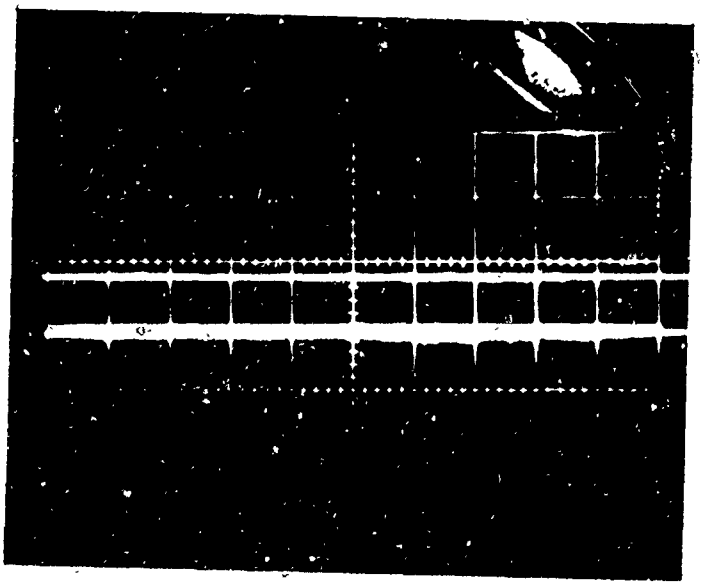

Upper Trace - Coax 3

Lower Trace - Boax 4

Battery for Photocurrent
Compensator Diodes

Figure C-18. Laser Photocurrent Experiment - Burst 2

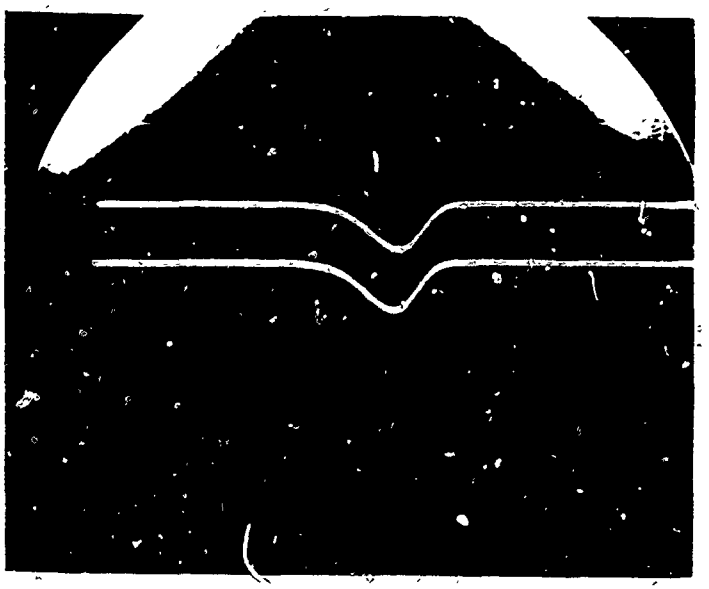

Upper Trace - Coax 4
Diode #3 Output
Vertical - 2V/cm
Horizontal - 50 μs/cm

Lower Trace - Coax 6
Diode #4 Output
Vertical - 0.2V/cm
Horizontal - 50 μs/cm

Figure C-19. Laser Photocurrent Experiment - Burst 2

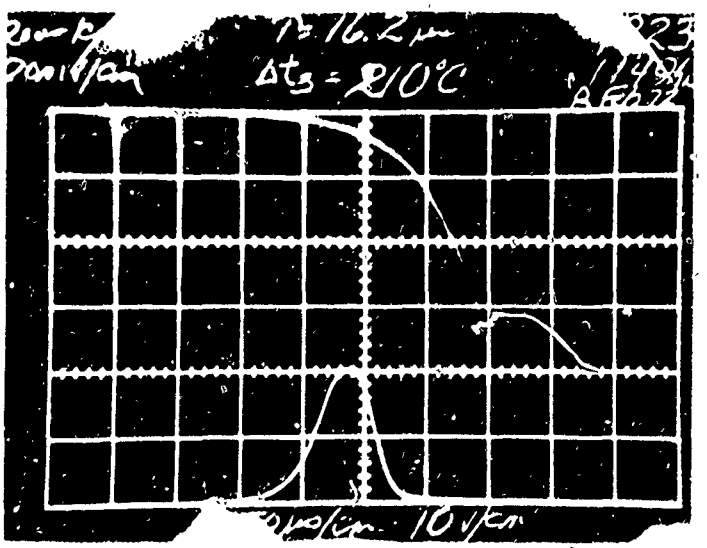

Upper Trace:
Vertical - 20 mV/cm
Horizontal - 20 μs/cm

Lower Trace:
Vertical - 20 V/cm
Horizontal - 50 μs/cm

Figure C-20. Reactor Gamma Profile - Burst 3

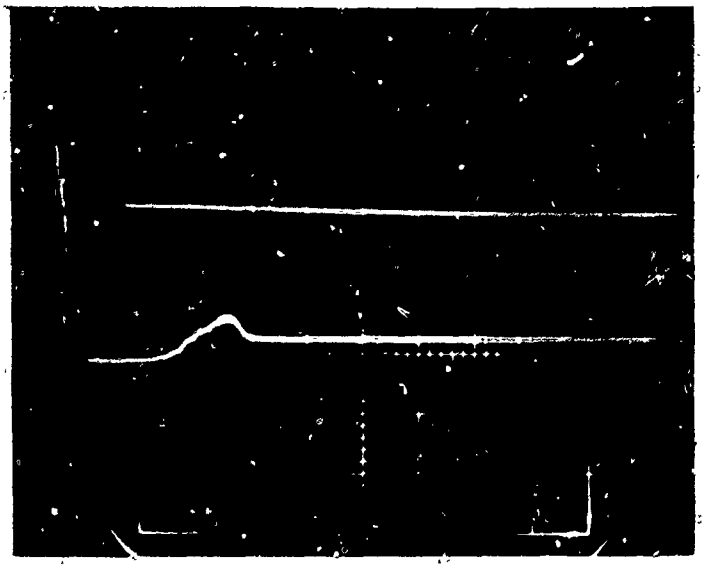

Upper Trace:
Vertical - 0.1V/cm
Horizontal - 500 μs/cm

Lower Trace:
Vertical - 0.1V/cm
Horizontal - 100 μs/cm

Figure C-21. Laser Gyro High Voltage Power Supply BNC-11 -1090V - Burst 3

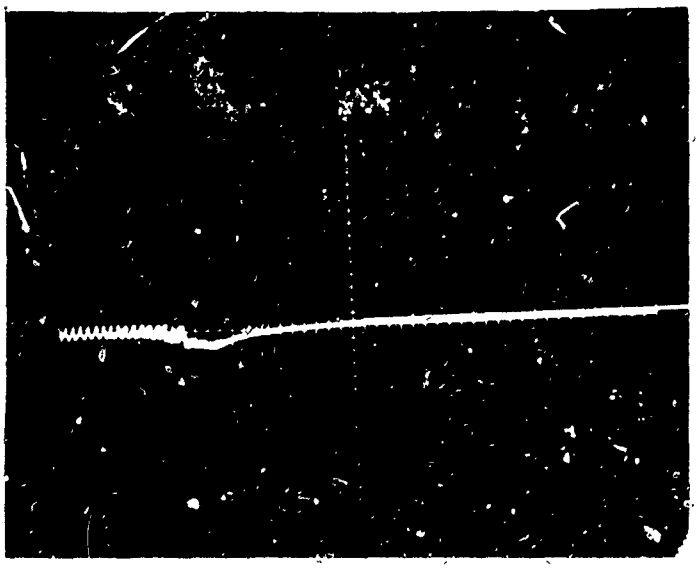

Vertical - 0.1V/cm
Horizontal - 100 μs/cm

Figure C-22. Laser Gyro High Voltage Power Supply BNC-12 Feedback - Burst 3

Upper Trace:
Vertical - 0.1V/cm
Horizontal - 100 μs/cm

Lower Trace:
Vertical - 0.1 V/cm
Horizontal - 100 μs/cm

Figure C-23. Laser Gyro High Voltage Power Supply BNC-12 +2100V - Burst 3

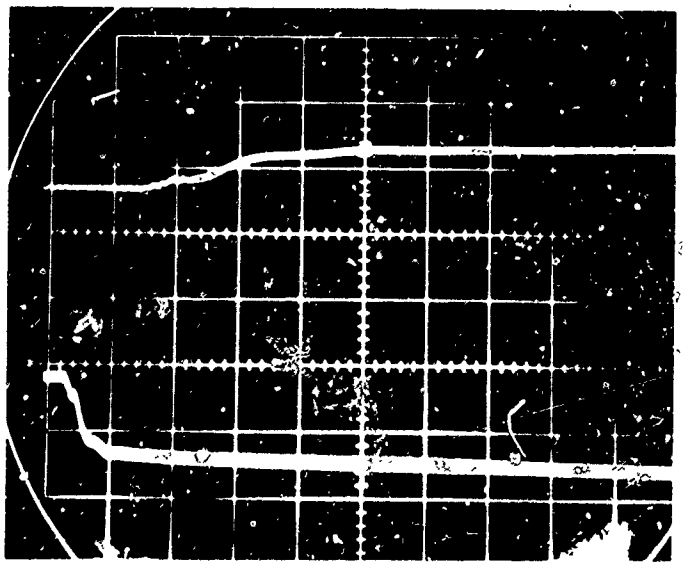

Upper Trace:
Vertical - 0.5V/cm
Horizontal - 100 μs/cm

Lower Trace:
Vertical - 0.1V/cm
Horizontal - 500 μs/cm

Figure C-24. Laser Gyro High Voltage Power Supply BNC-13 10V Monitor - Burst 3

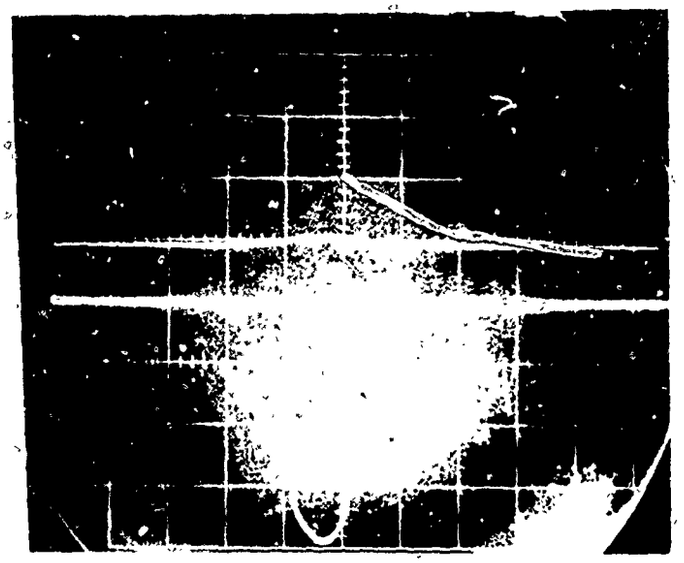

Upper Trace
Detector Circuit Battery:
Vertical - 1 V/cm
Horizontal - 50 μs/cm

Lower Trace
Diode #1 Output:
Vertical - 0.2 V/cm
Horizontal - 50 μs/cm

Figure C-25. Laser Photocurrent Experiment - Burst 3

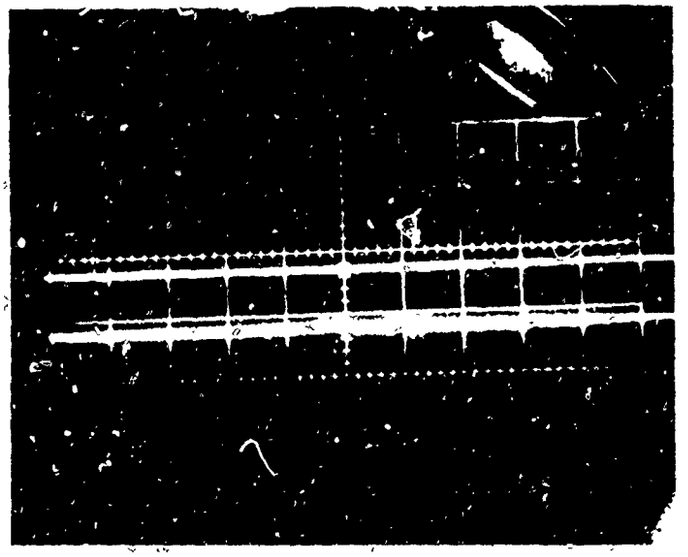

Figure C-26. Laser Photocurrent Experiment - Burst 3

Upper Trace
Diode #4 Output:
Vertical - 0.2 V/cm
Horizontal - 50 μs/cm

Lower Trace
Diode #5 Output:
Vertical - 0.2 V/cm
Horizontal - 50 μs/cm

Figure C-27. Laser Photocurrent Experiment - Burst 3

REFERENCES

1. "Transistor Radiation Effects Compilation (TREC), (U)," Technical Report No. AFSWC-TR-69-7, Volumes 1 and 2.

2. Fairchild Semiconductor and Diode Catalog, 1970.

3. Solitron/Bendix Engineering Data Sheet BR100 A-F, June 1967.

4. "Transient Radiation Analysis by Computer Program (TRAC) (U)," Autonetics Division of North American Rockwell Corp., AD-836684, June 1968.

5. "System Evaluation Code Under Radiation Environment (SECURE) (U)," DASA 2602, Final Report, 30 July 1971.

APPENDIX B
SUPER FLASH X-RAY (SFXR) TEST

APPENDIX B
SUPER FLASH X-RAY (SFXR) TEST

The SFXR test consisted of five separate test setups: 1) laser gyro, 2) digital boards, 3) individual circuits, 4) support electronics, and 5) the system. Schedule restraints prevented the fabrication of a complete set of duplicate electronics circuits (except for the digital boards) so some of the breadboards were used in three of the setups. The 5-volt regulator, 10-volt regulator, high-voltage d-c/d-c converter and start/restart circuits were all exposed during the individual circuits, support electronics, and system tests. In all setups the tested circuitry was enclosed in a double-shielded aluminum case and signals in and out were carried on conductors encased in double zip-tubing which was electrically connected to the double shield and the tie point made in the control room through a 10-ohm resistor.

Laser Gyro Test Setup

The gyro test setup (Page B6) consisted of a three-axis laser gyro with a single-axis readout provided from a close-coupled battery pack that included discharge current monitors and a battery-biased fringe pattern detector with signal monitors. The battery pack that supplied the discharge power used two 500-volt photoflash (Eveready EV497) batteries within the double-shielded enclosure with two sampling resistors that monitored the current in three discharge legs each. The fringe pattern monitor was biased from a 4.5-volt (Eveready No. 333) battery with a 68-ohm signal sampling resistor in each detector. The detector was a dual-element germanium photosensor manufactured by Philco-Ford. Appendix E presents "The Expected Effect on the Glow Discharge and Laser Output During Exposure to X-radiation." The appendix analyzes a He-Ne gas discharge table with approximately the same

gas fill, but with different physical dimensions and external circuitry. The tube resistance can be calculated from Equations (B1) and (B2):

$$V_S - i_o R_B - V_C = V_T = 657 \text{ volts} \tag{B1}$$

V_S = 900 v = source voltage

R_B = 142.2k = ballast resistance

i_o = 0.65 ma = discharge current

V_C = 150 v = cathode volt drop

$$R_T = \frac{V_T}{i_o} = \frac{657}{0.65 \times 10^{-3}} = 1 \times 10^6 \text{ ohms} \tag{B2}$$

Appendix E shows a three-times increase in conductivity at 2×10^4 rads of x-radiation. This reduces the tube resistance to 333 k ohms. Since the battery voltage is constant through the radiation, Equation (B3) will give the current flow at 2×10^4 rads (Si).

$$\frac{V_S - V_C}{R_T + R_B} = \frac{750 \text{ volts}}{475 \text{ k ohms}} = 1.58 \text{ ma} \tag{B3}$$

The maximum radiation during the test series was 1.3×10^4 rads (Si), which produces a two-times increase in conductivity, reducing the tube resistance to 500 k ohms. Equation (4) should then predict the current level at 1.3×10^4 rads (Si):

$$\frac{V_S - V_C}{R_T + R_B} = \frac{750 \text{ volts}}{642 \text{ ohms}} = 1.17 \text{ ma} \tag{B4}$$

Digital Boards Test Setup

The digital boards test setup consists of the direction logic, countdown, and line driver functions assembled on a single board with a simulated gyro input and with a 68-ohm line as a load. Power is supplied by a twisted-pair cable from a power supply located in the junction box. This test is similar to the following series called "Individual Circuits Test Setup", but was run separately because of x-ray beam cross-sectional area limitations.

Individual Circuits Test

The individual circuits consisted of five circuits: 1) +5-volt regulator, 2) +10-volt regulator, 3) high-voltage d-c to d-c converter, 4) start/restart circuit and 5) readout amplifier, all separately excited and separately loaded to evaluate their performance individually. The excitations required came from instrumentation mounted in the junction box in the exposure room. The radiation level in the junction box was monitored and found to be 2.24×10^7 rads (Si)/s. Lead shielding reduced the level to 0.90×10^7 rads (Si)/s during the individual circuits test. The circuits were exposed to six levels, 7.02×10^8, 5.06×10^7, 1.22×10^9, 6.87×10^9, 1.51×10^{11}, and 2.53×10^{11} rads (Si)/s. In all cases, there was no detectable permanent damage effect on the performance of the circuits. Volume I includes an appendix (I) commenting in detail about each photo. Table I-1 lists the various circuits in the various test setups and gives the maximum dose rate, rads (Si)/s, at which the circuits would function in the Honeywell system without error. There is a great disparity in numbers credited to the EMI generated in the double zip-tubing shielded cables which in most cases, supplied power input, excitation input, and performance monitor outputs.

Support Electronics Test Setup

The support electronics test consisted of the 5-volt regulator, 10-volt regulator, high-voltage converter, start circuit, and a readout amplifer. In this test, the circuits were interconnected and operated from an external +17.5-volt supply. The test photos (pages B131 through B174) reveal that the maximum radiation levels for normal operation as ascertained by this setup differ from those obtained from the individual circuit testing. EMI has more effect on the interconnected circuits as is evidenced by shot No. 30, which was run with the circuit power off. Table I-1 (see Volume I) shows the maximum gamma radiation level at which these circuit elements will operate normally.

System Test

The system test consisted of the laser gyro, +5-volt regulator, +10-volt regulator, high-voltage converter, start circuit, and two readout/trigger assemblies interconnected and run off +17.5 volts as a system. In this configuration the interconnecting leadwires are short, twisted pairs providing a more EMI-resistant setup. On completion of this test, the system components had received total dose as listed in Table I-2.

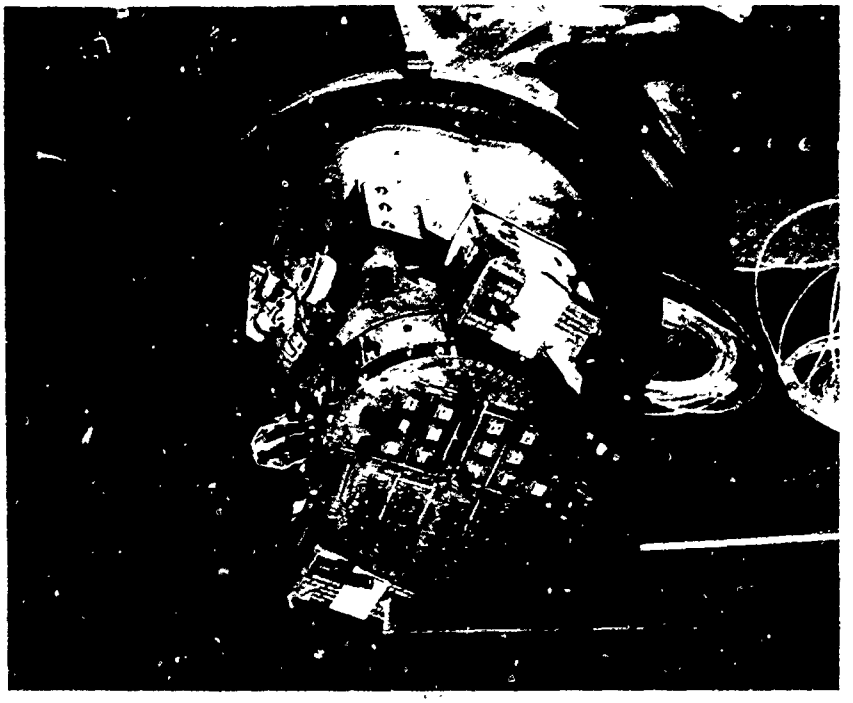

Gyro Test Cassette

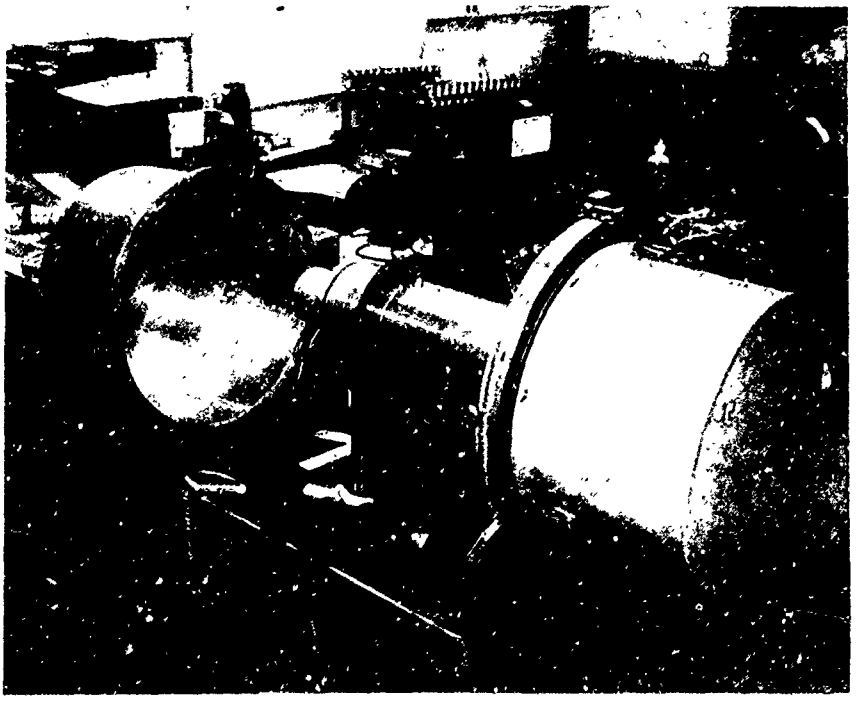

Gyro Test Setup

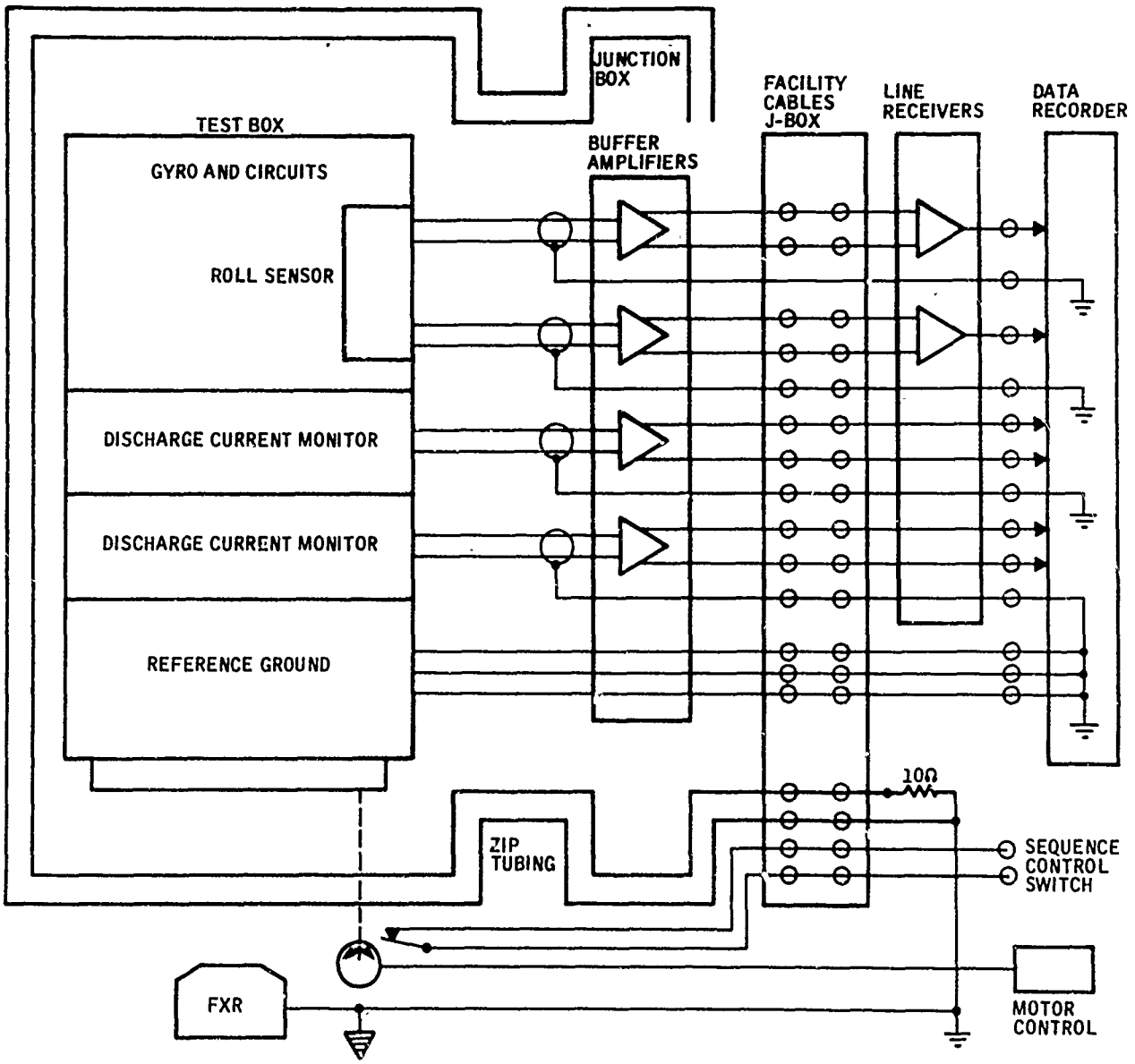
JUNCTION BOX
TEST BOX
GYRO AND CIRCUITS
ROLL SENSOR
DISCHARGE CURRENT MONITOR
DISCHARGE CURRENT MONITOR
REFERENCE GROUND
BUFFER AMPLIFIERS
FACILITY CABLES J-BOX
LINE RECEIVERS
DATA RECORDER
10Ω
ZIP TUBING
SEQUENCE CONTROL SWITCH
FXR
MOTOR CONTROL

Gyro Test

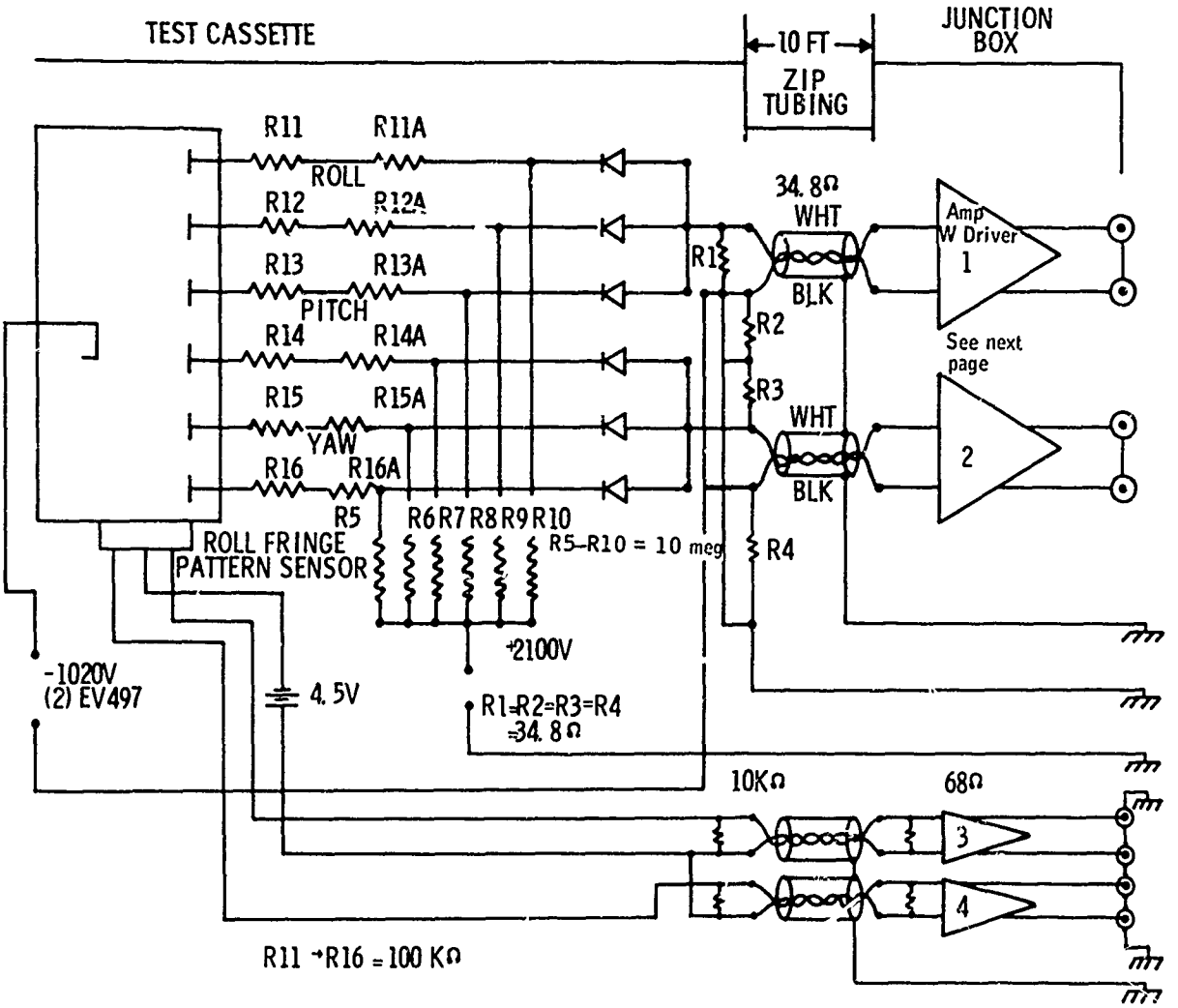
TEST CASSETTE
10 FT
ZIP TUBING
JUNCTION BOX
R11
R11A
ROLL
R12
R12A
R13
R13A
PITCH
R14
R14A
R15
R15A
YAW
R16
R16A
R5
R6 R7 R8 R9 R10
R5–R10 = 10 meg
ROLL FRINGE PATTERN SENSOR
+2100V
-1020V
(2) EV497
4.5V
R1=R2=R3=R4 =34.8Ω
R1
R2
R3
R4
34.8Ω
WHT
BLK
WHT
BLK
Amp W Driver
1
2
3
4
See next page
10KΩ
68Ω
R11 - R16 = 100 KΩ

Gyro Hookup

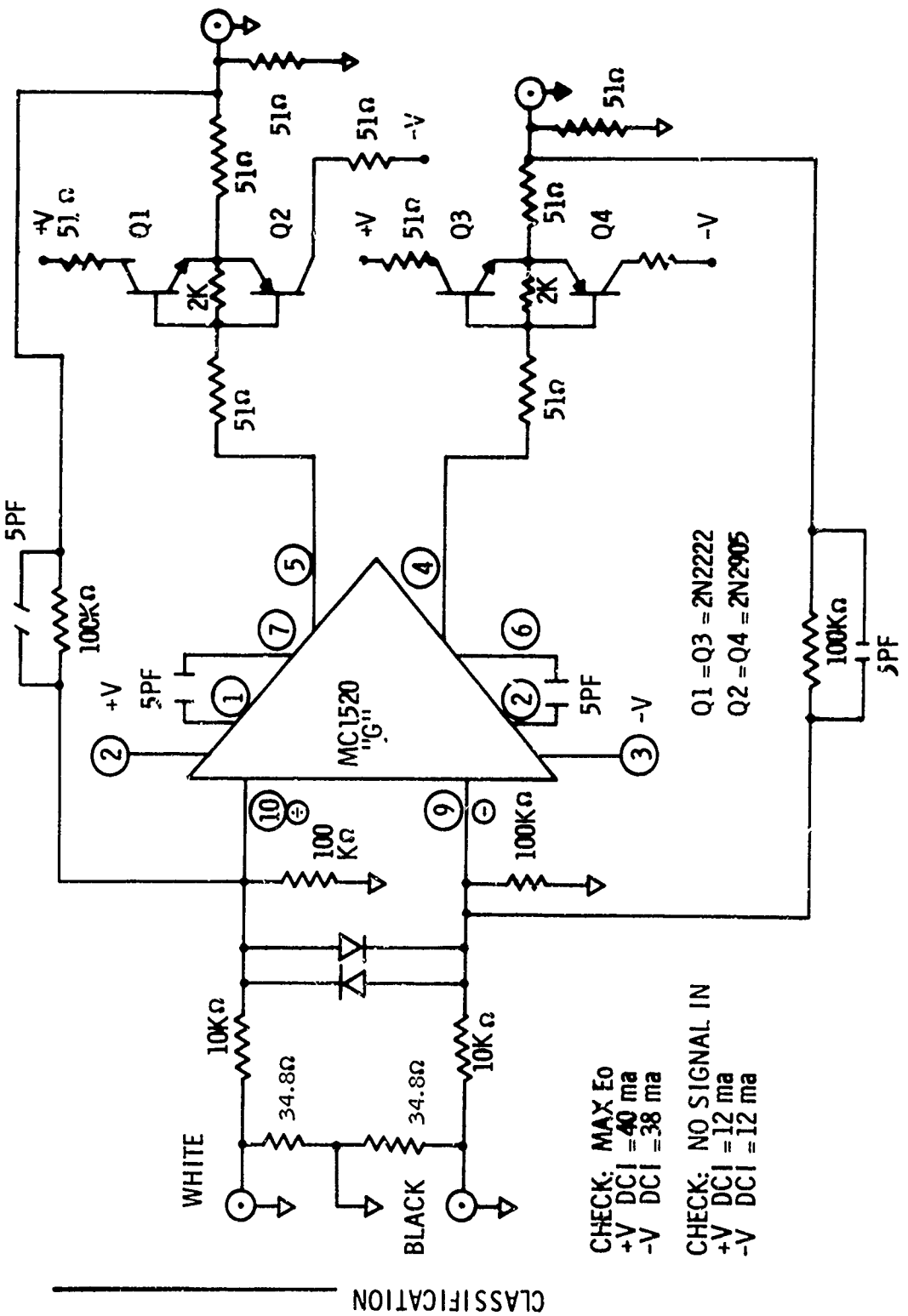

AMP with Driver

CLASSIFICATION

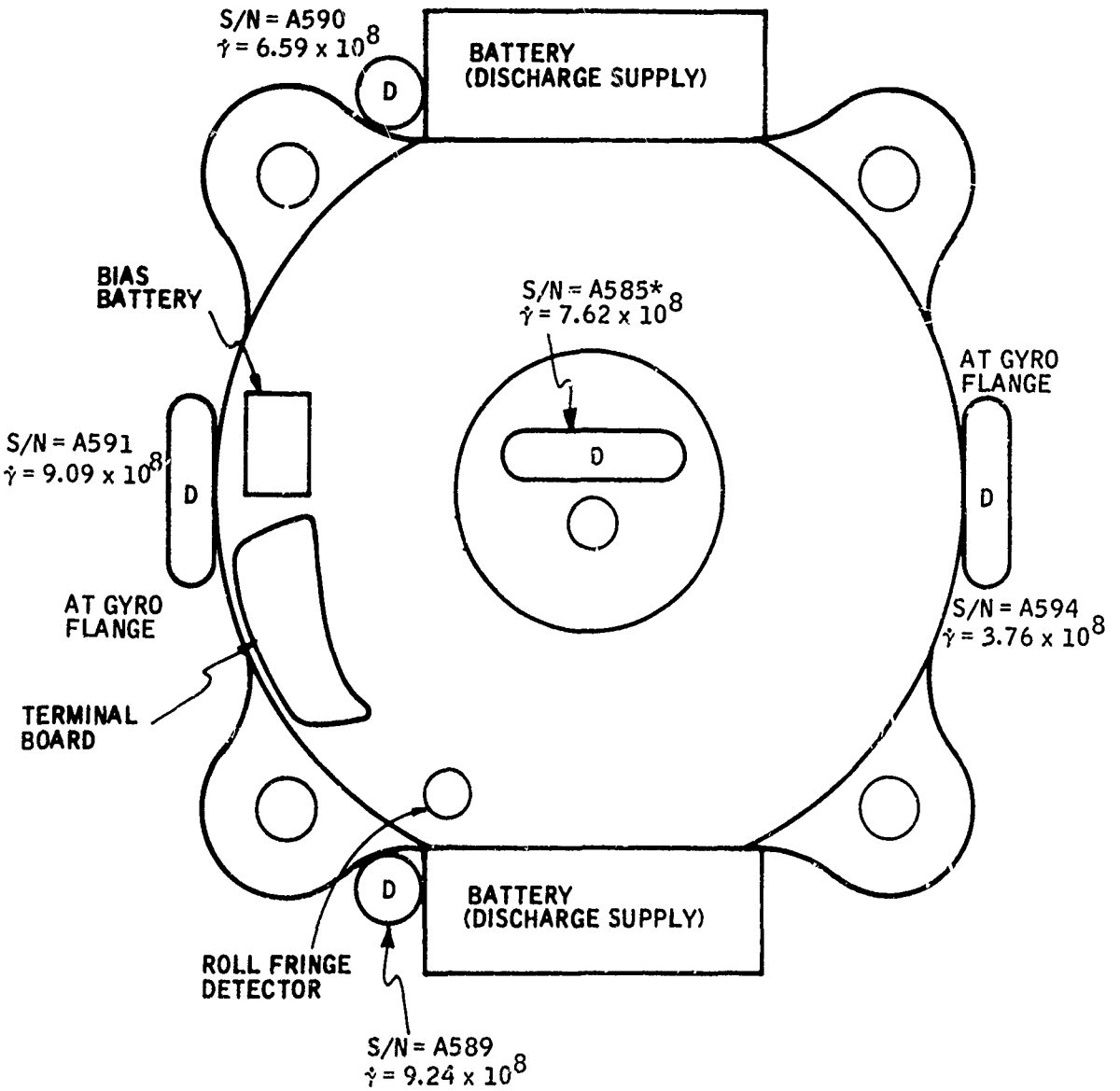

Gyro Test Shot No. 1 Dosimetry Data

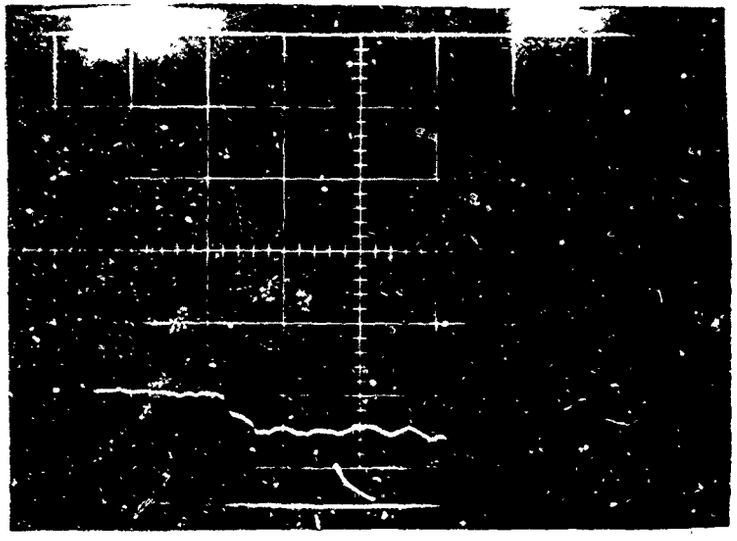

VOLTS/CM 1.0 SWEEP/CM .1 usec

VOLTS/CM 1 SWEEP/CM 1.0 usec

TEST NO. 1 - 1, 2, 3, 4: GYRO TEST - DISCHARGE CURRENT

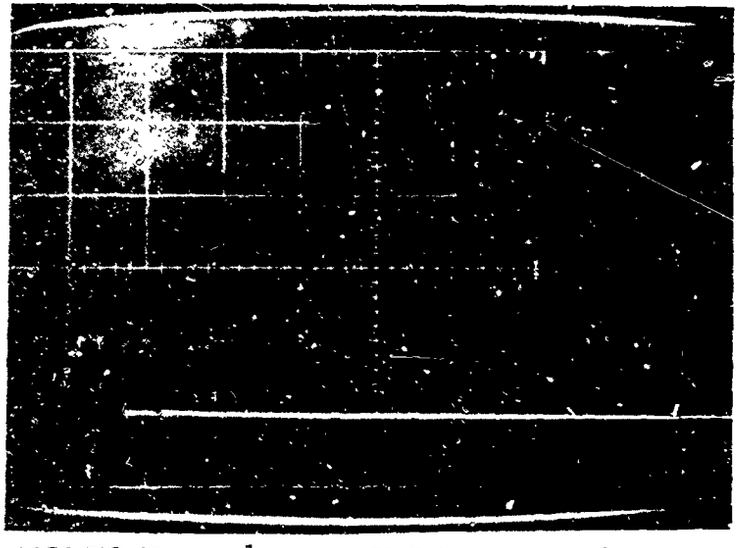

VOLTS/CM 1 SWEEP/CM .1 msec

VOLTS/CM 5 SWEEP/CM 10 usec

VOLTS/CM 1.0 SWEEP/CM .1 usec

VOLTS/CM 1 SWEEP/CM 1 usec

TEST NO. 1 - 5, 6, 7, 8: GYRO TEST - DISCHARGE CURRENTS

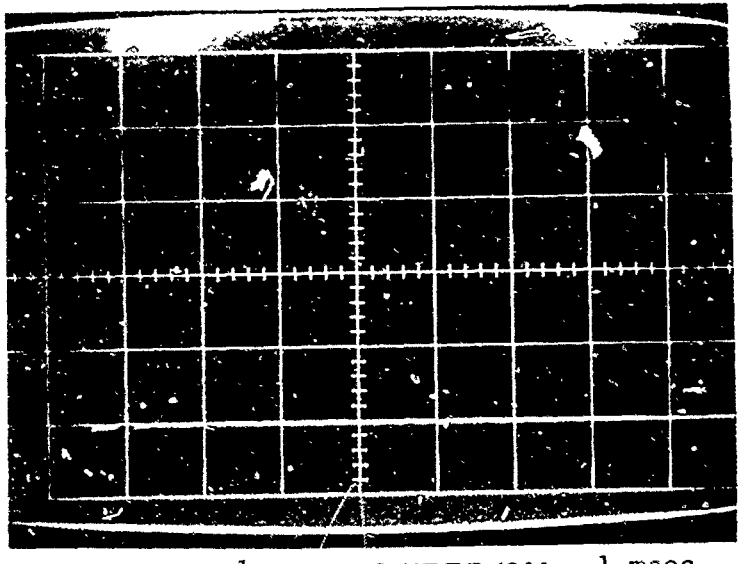

VOLTS/CM 1 SWEEP/CM .1 msec

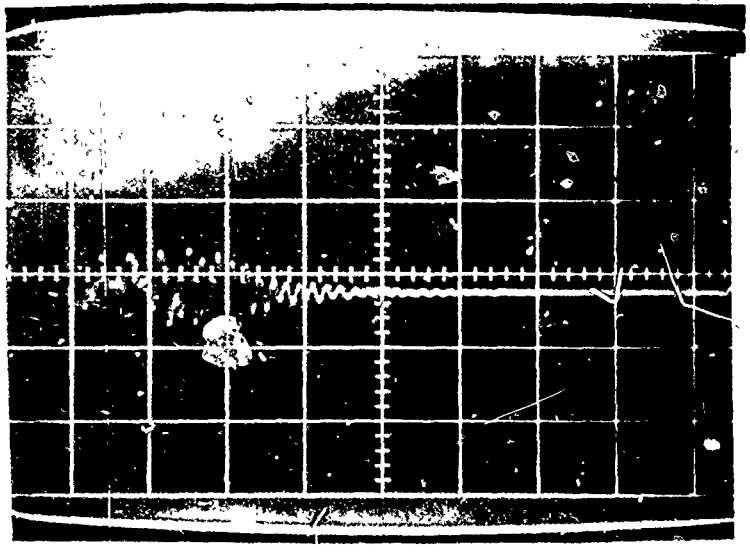

VOLTS/CM 5 SWEEP/CM 10 usec

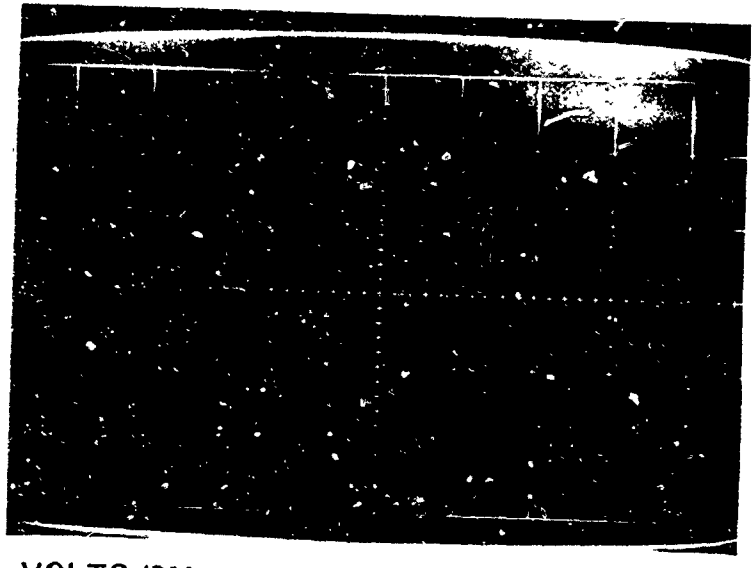

VOLTS/CM .1 SWEEP/CM .1 usec

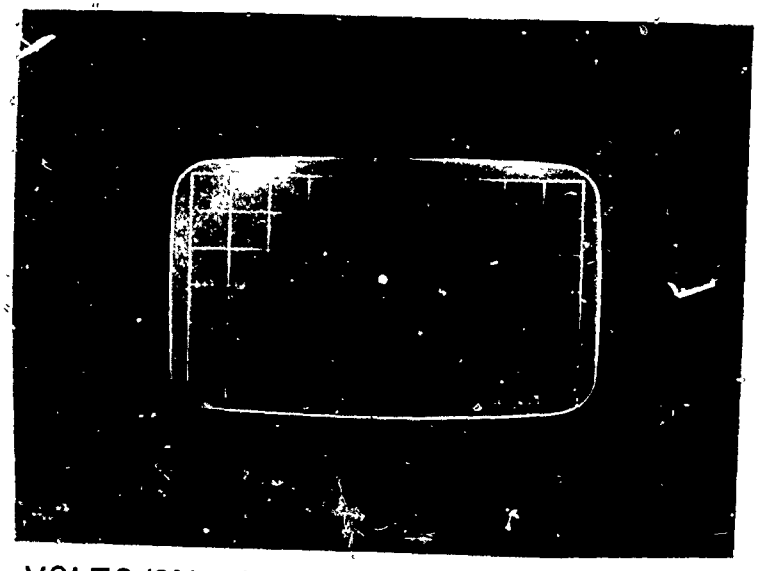

VOLTS/CM .1 SWEEP/CM 1 usec

TEST NO. 1 - 9, 10, 11, 12: GYRO TEST SENSOR OUTPUT

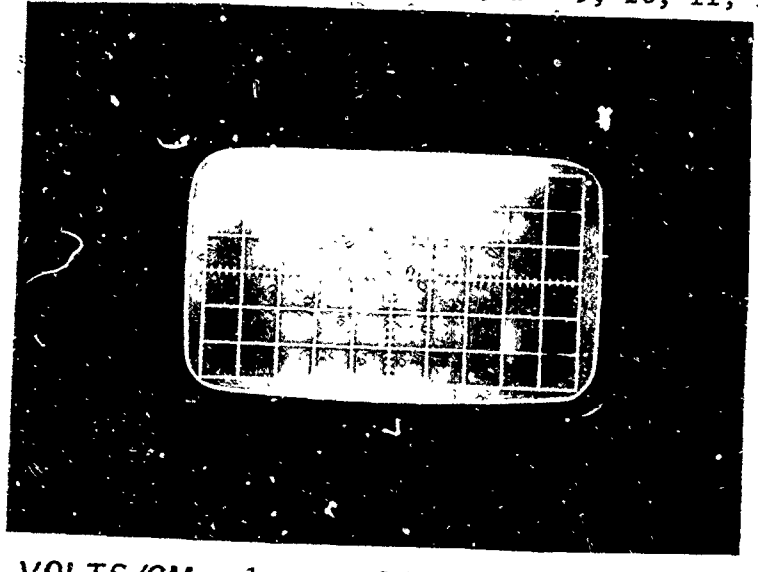

VOLTS/CM .1 SWEEP/CM .1 msec

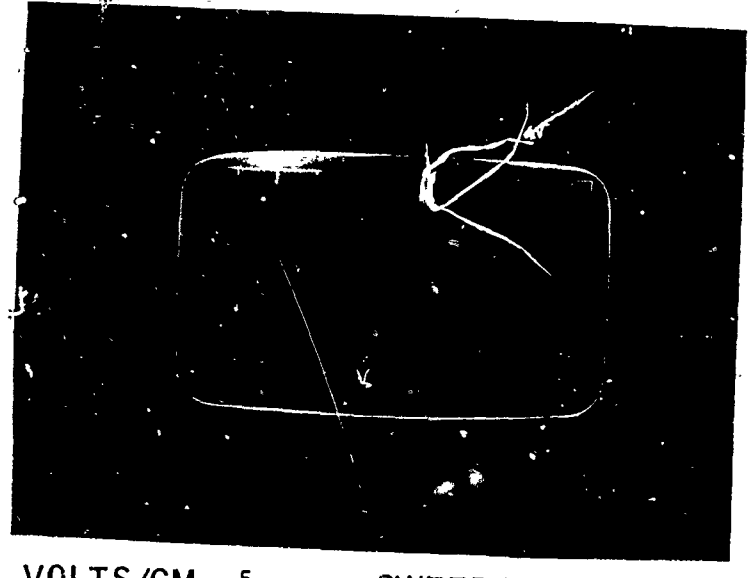

VOLTS/CM 5 SWEEP/CM 10 usec

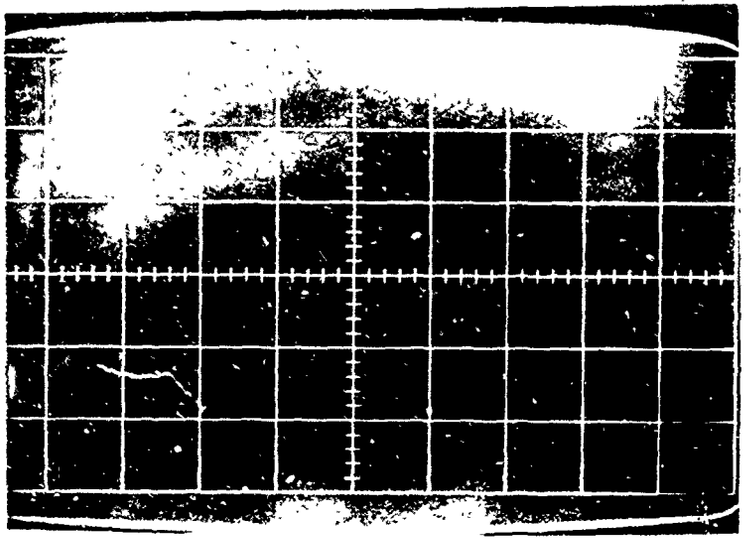

VOLTS/CM .1 SWEEP/CM .1 usec

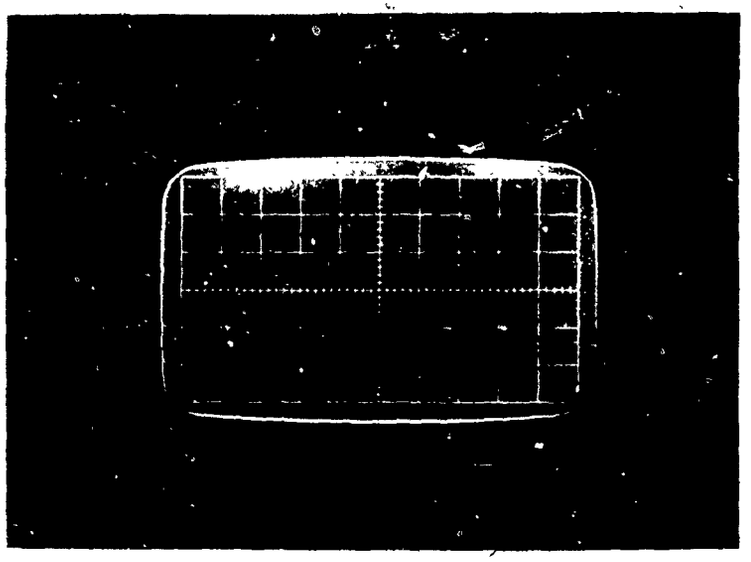

VOLTS/CM .1 SWEEP/CM 1 usec

TEST NO. 1 - 13, 14, 15, 16: GYRO TEST - SENSOR OUTPUT

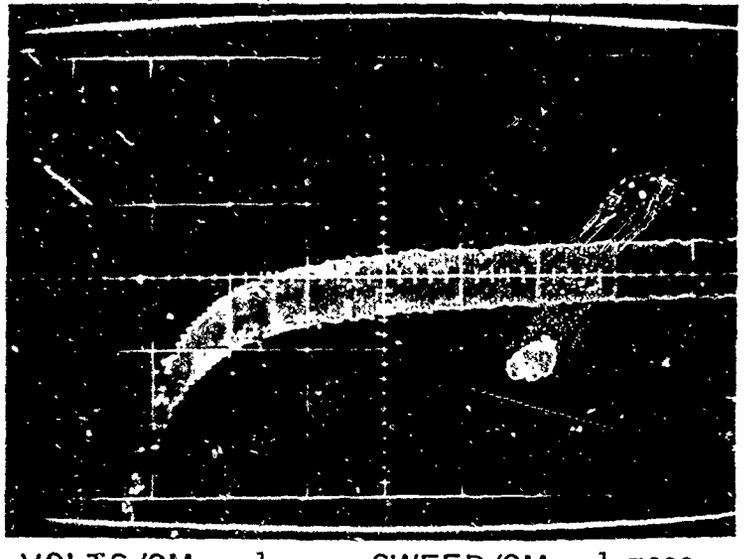

VOLTS/CM .1 SWEEP/CM .1 msec

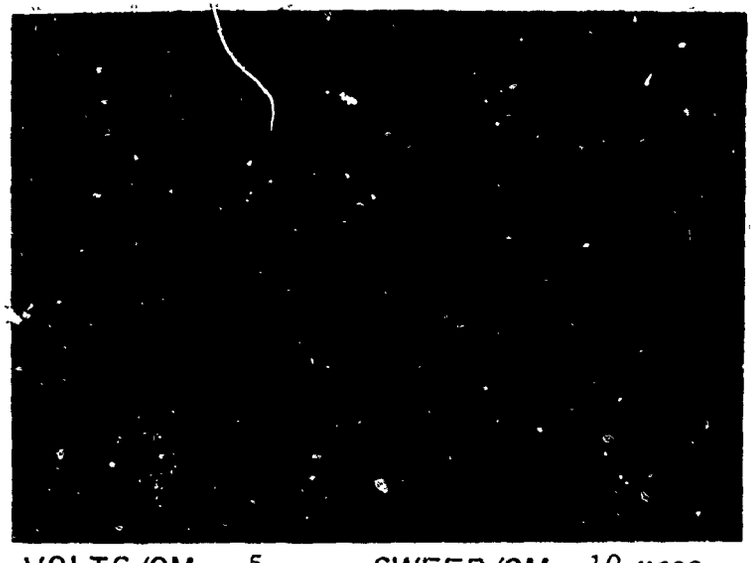

VOLTS/CM 5 SWEEP/CM 10 usec

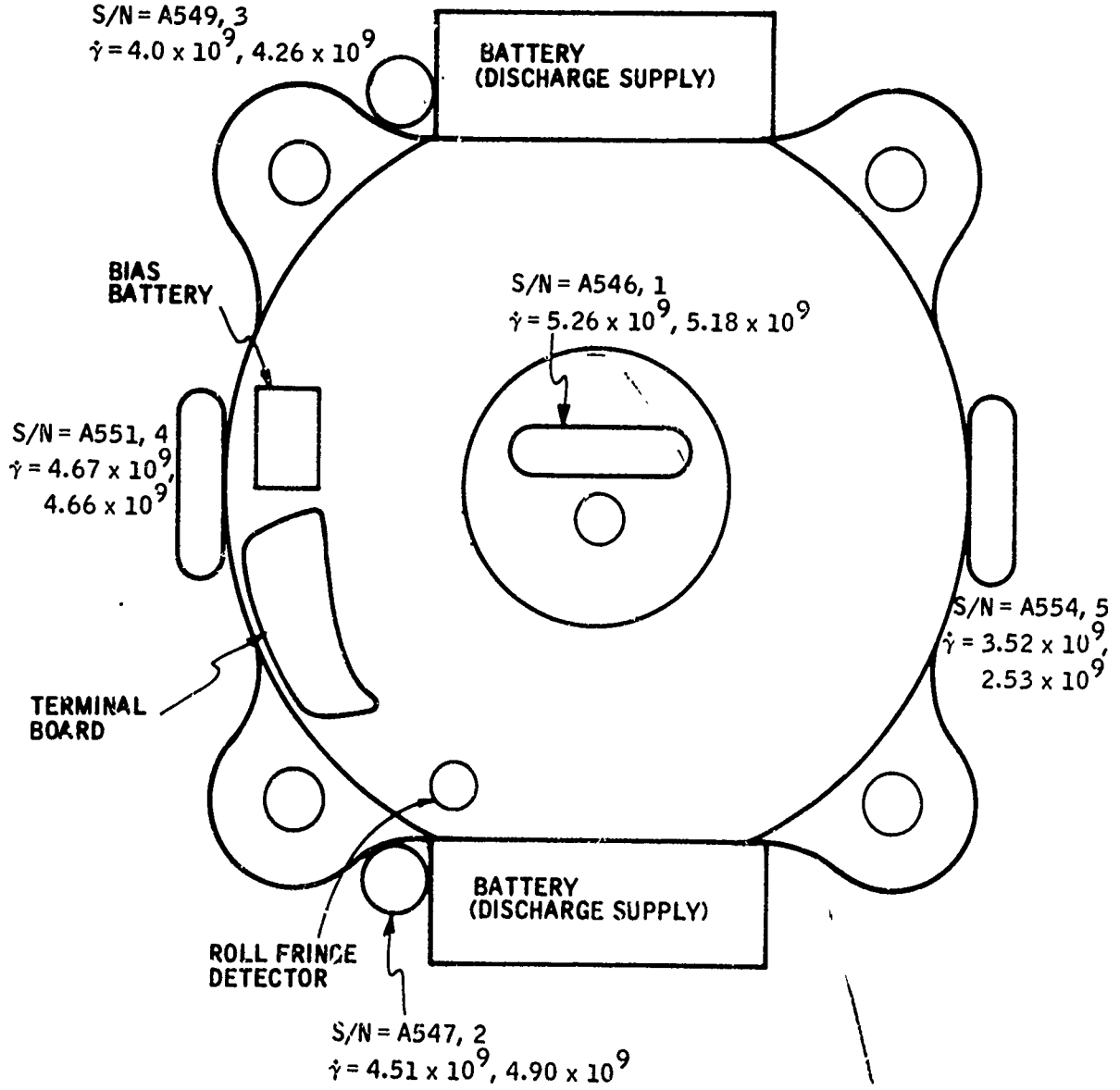

Gyro Test Shot No. 2 Dosimetry Data

VOLTS/CM 1 SWEEP/CM 0.1 usec

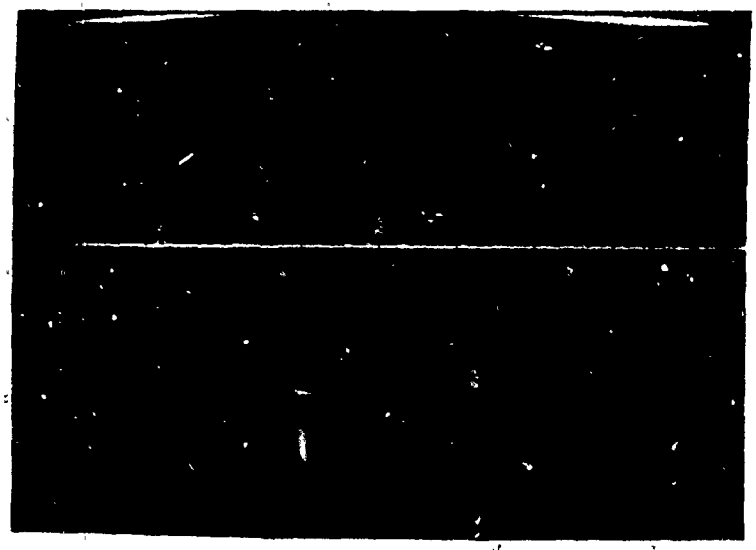

VOLTS/CM 1 SWEEP/CM 1 usec

TEST NO. 2 - 1, 2, 3, 4: GYRO TEST - DISCHARGE CURRENTS

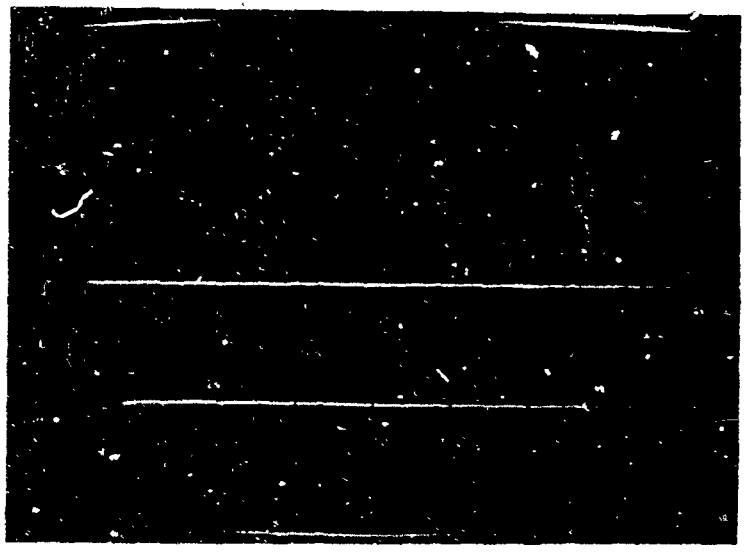

VOLTS/CM 1 SWEEP/CM 100 usec

VOLTS/CM 5 SWEEP/CM 10 usec

VOLTS/CM 1 SWEEP/CM 0.1 usec

VOLTS/CM 1 SWEEP/CM 1 usec

TEST NO. 2 - 5, 6, 7, 8: GYRO TEST - DISCHARGE CURRENTS

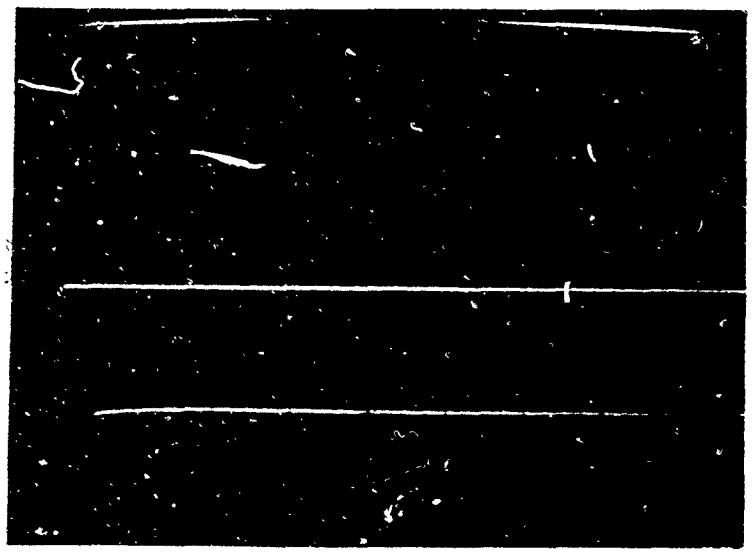

VOLTS/CM 1 SWEEP/CM 100 usec

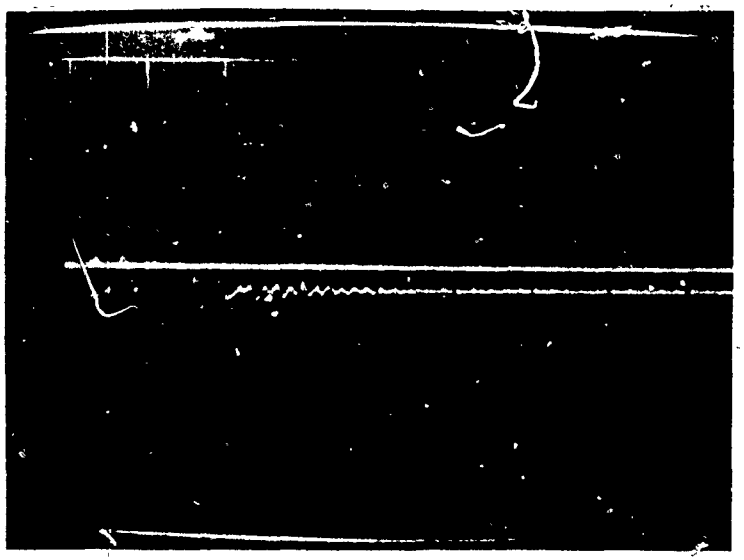

VOLTS/CM 5 SWEEP/CM 10 usec

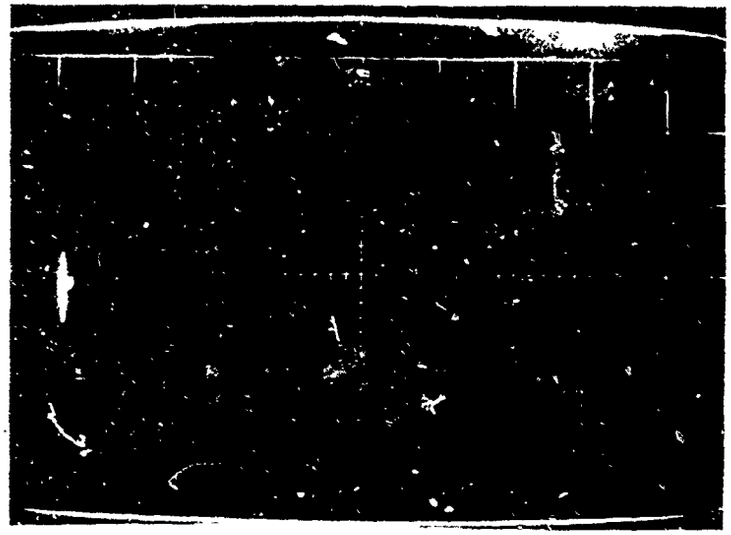

VOLTS/CM 0.1 SWEEP/CM 0.1 usec

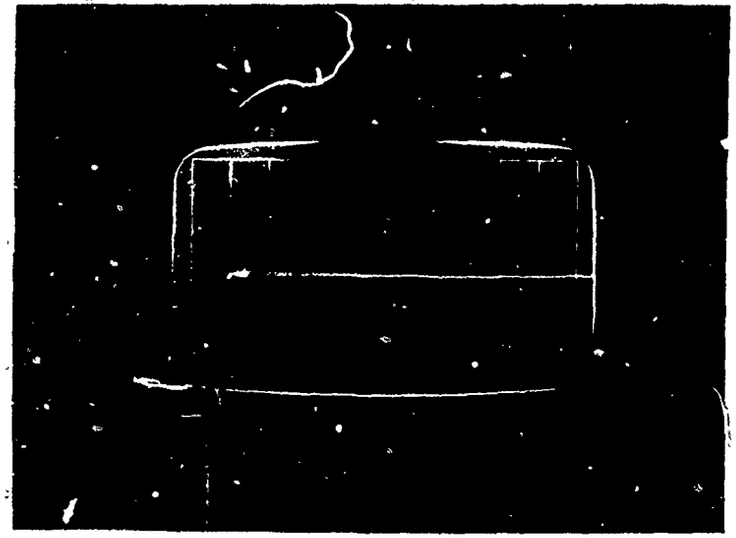

VOLTS/CM 0.1 SWEEP/CM 1 usec

TEST NO. 2 - 9, 10, 11, 12: GYRO TEST - SENSOR OUTPUT

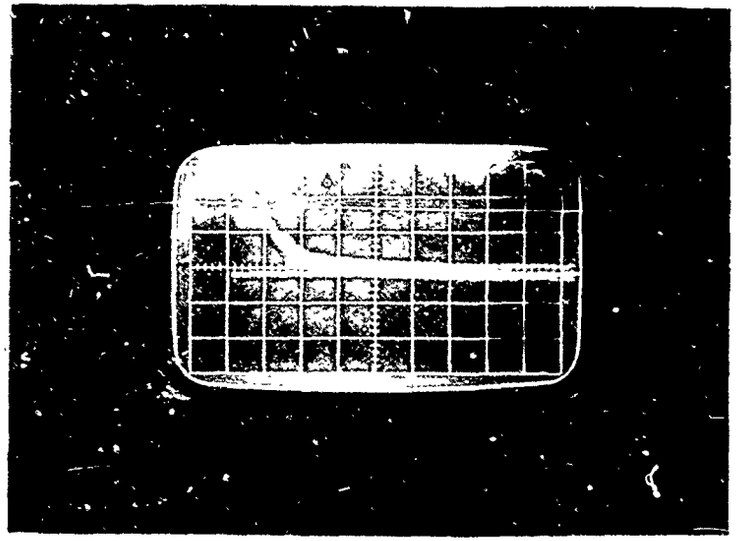

VOLTS/CM 0.1 SWEEP/CM 100 usec

VOLTS/CM 5 SWEEP/CM 10 usec

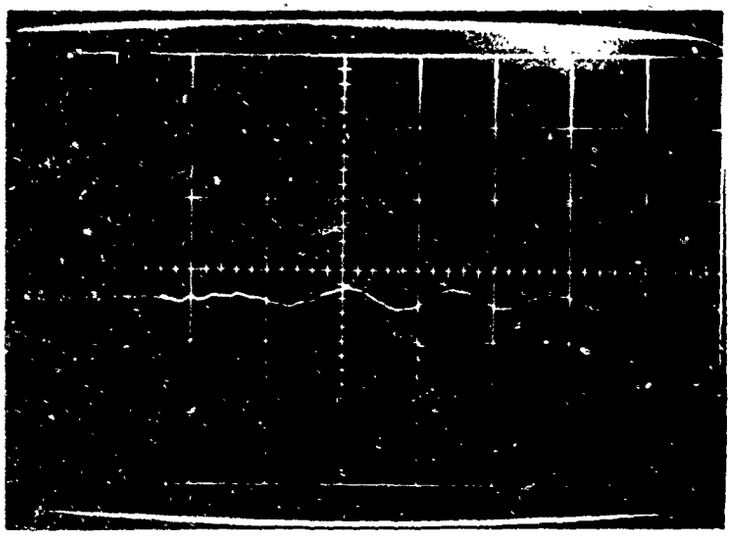

VOLTS/CM 0.1 SWEEP/CM 0.1 usec

VOLTS/CM 0.1 SWEEP/CM 0.1 usec

TEST NO. 2 - 13, 14, 15, 16: GYRO TEST - SENSOR OUTPUT

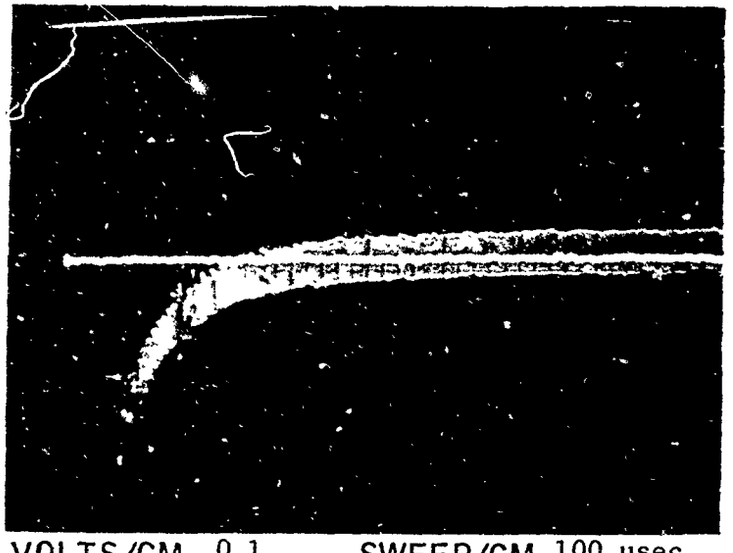

VOLTS/CM 0.1 SWEEP/CM 100 usec

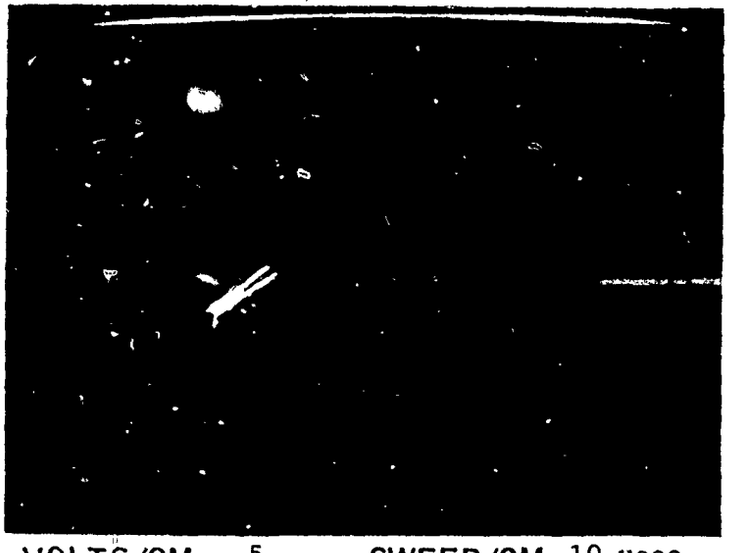

VOLTS/CM 5 SWEEP/CM 10 usec

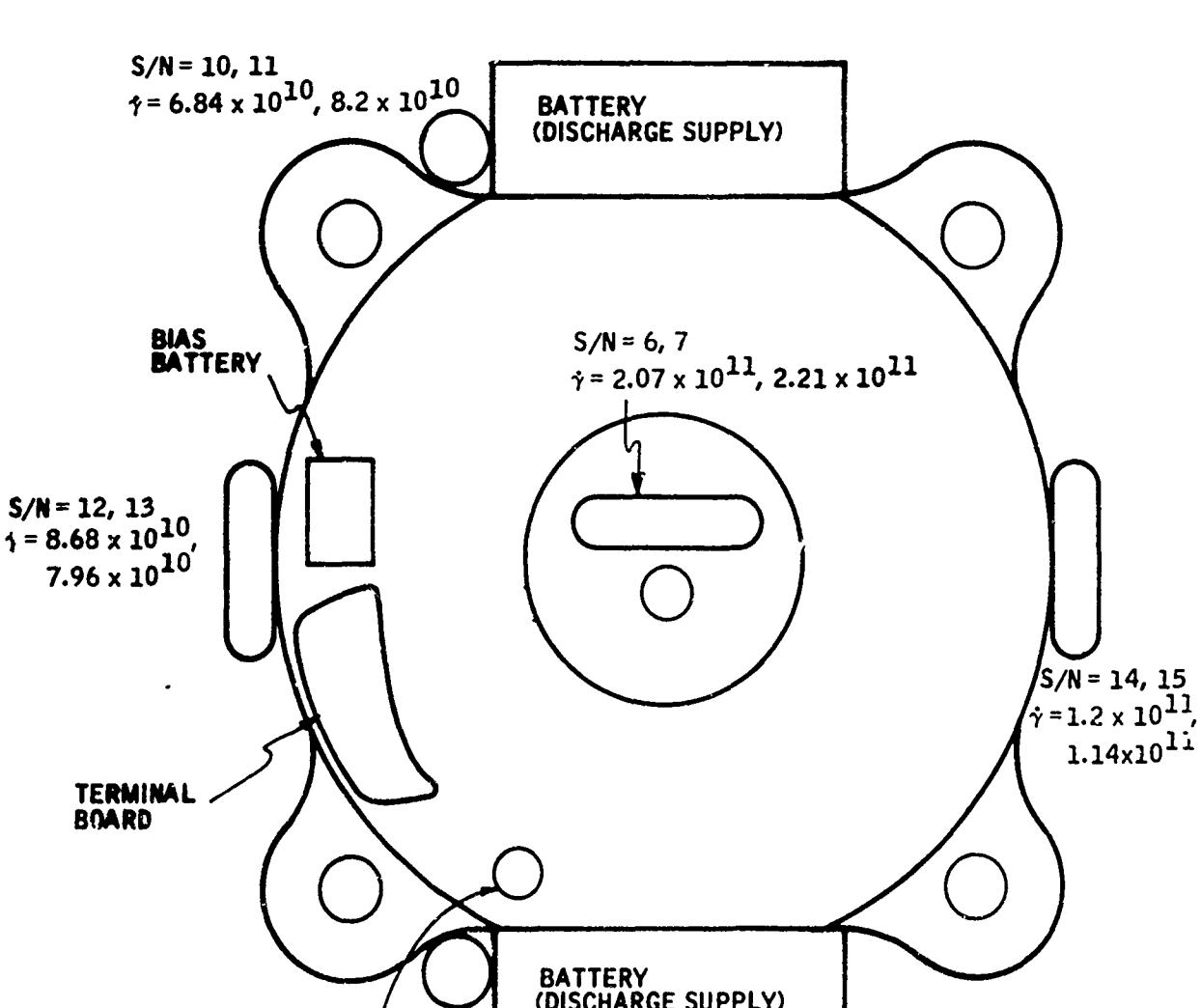

Gyro Test Shot No. 3 Dosimetry Data

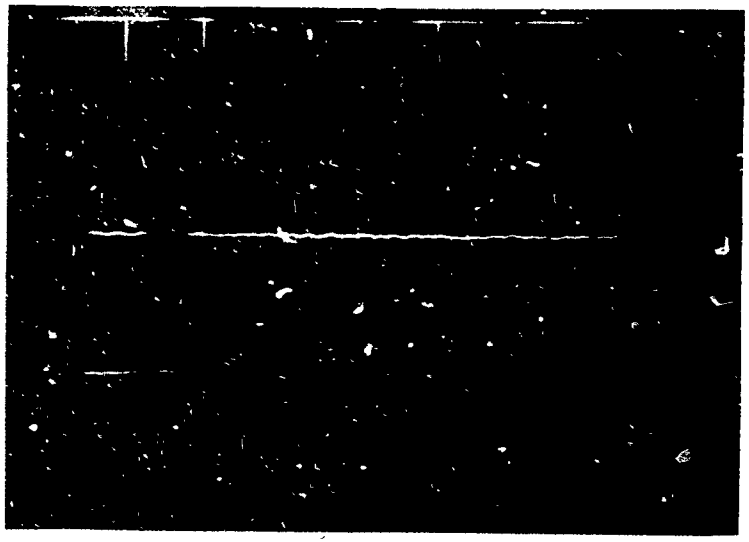

VOLTS/CM 1 SWEEP/CM 0.1 usec

VOLTS/CM 1 SWEEP/CM 1 usec

TEST NO. 3 - 1, 2, 3, 4: GYRO TEST - DISCHARGE CURRENTS

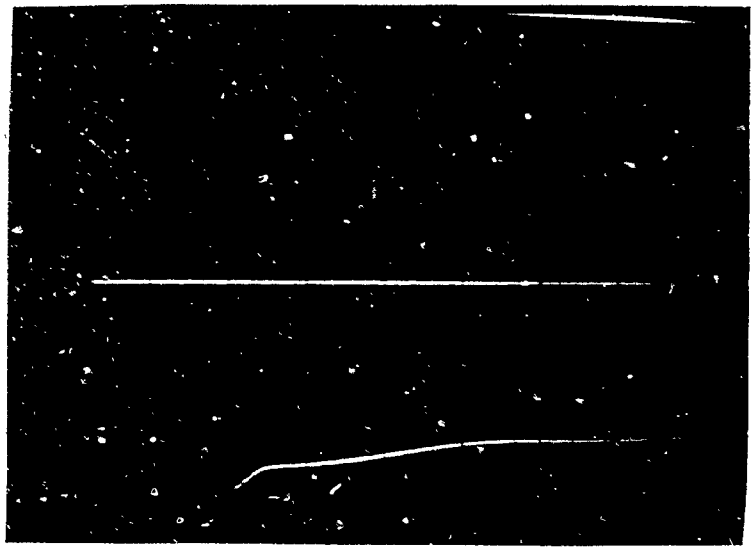

VOLTS/CM 1 SWEEP/CM 100 usec

VOLTS/CM 5 SWEEP/CM 10 usec

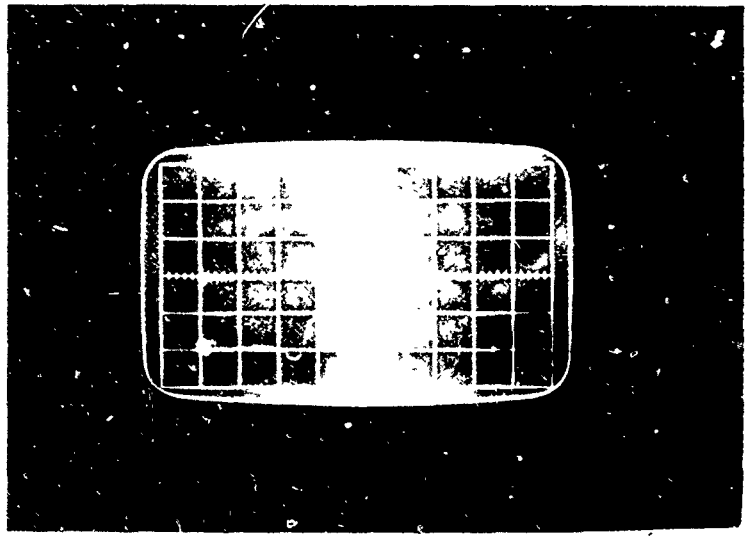

VOLTS/CM 1 SWEEP/CM 0.1 usec

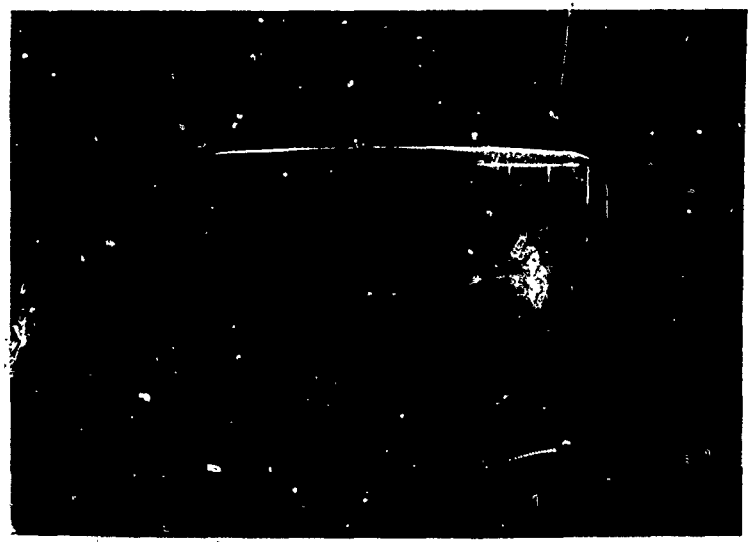

VOLTS/CM 1 SWEEP/CM 1 usec

TEST NO. 3 - 5, 6, 7, 8: GYRO TEST - DISCHARGE CURRENTS

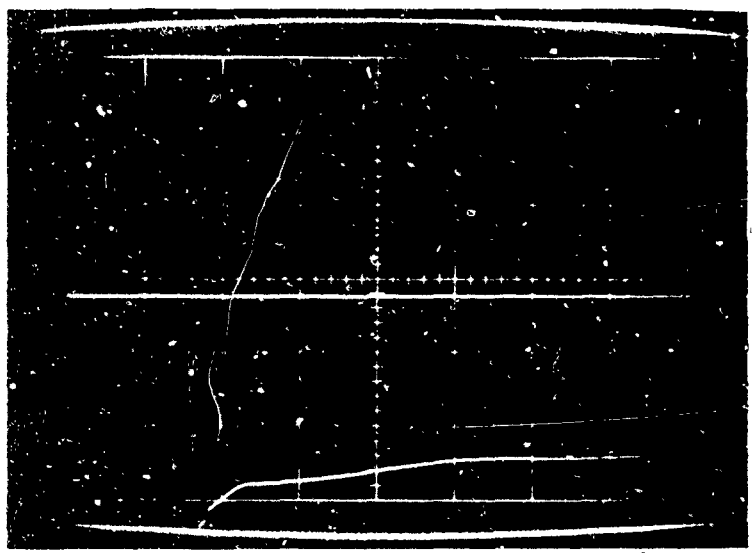

VOLTS/CM 1 SWEEP/CM 100 usec

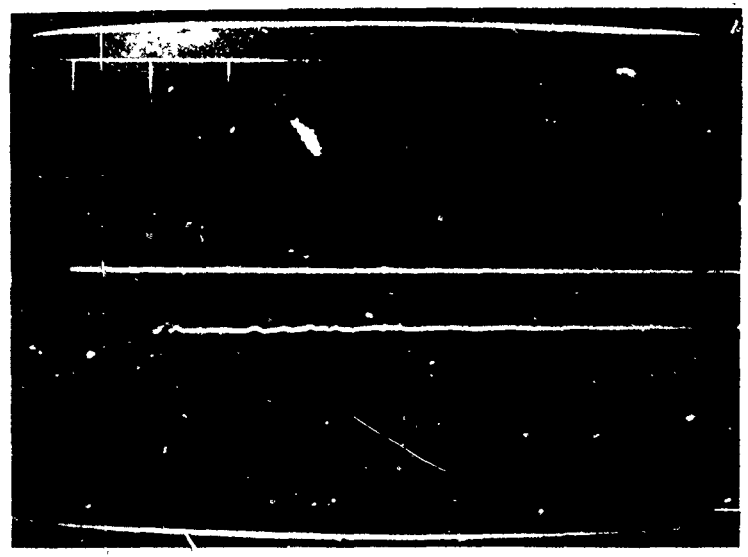

VOLTS/CM 5 SWEEP/CM 10 usec

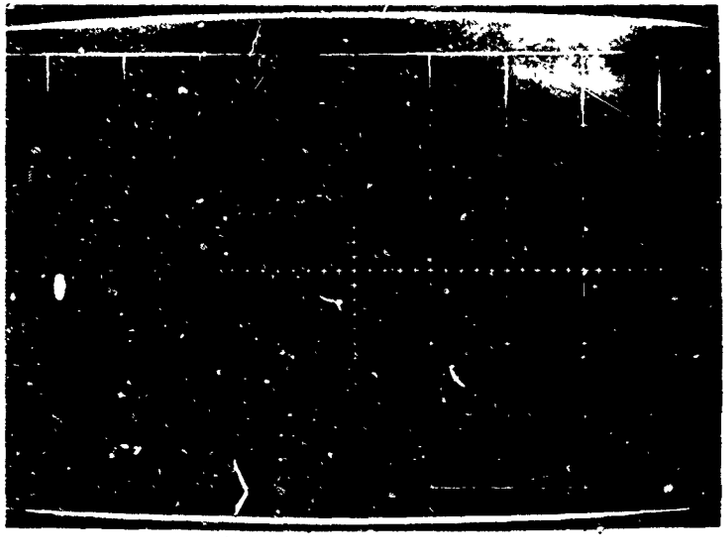

VOLTS/CM 1 SWEEP/CM 0.1 usec

VOLTS/CM 0.1 SWEEP/CM 1 usec

TEST NO. 3 - 9, 10, 11, 12: GYRO TEST - SENSOR OUTPUT

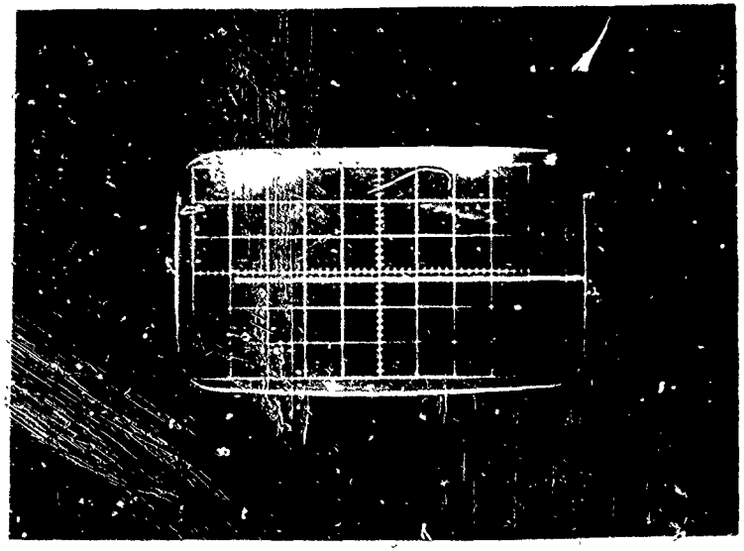

VOLTS/CM 0.1 SWEEP/CM 100 usec

VOLTS/CM 5 SWEEP/CM 10 usec

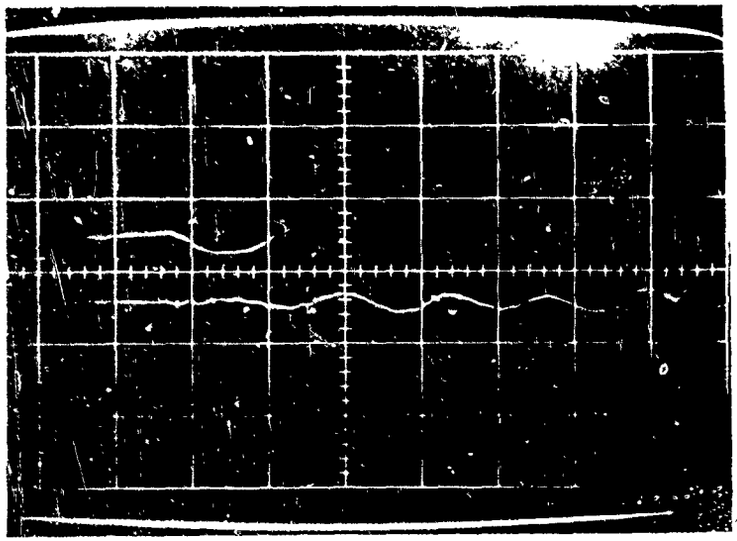

VOLTS/CM 1 SWEEP/CM .1 usec

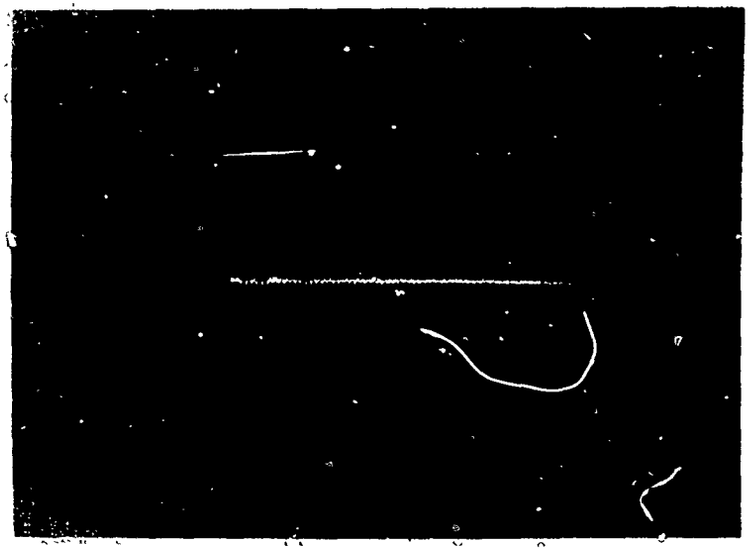

VOLTS/CM 0.1 SWEEP/CM 1 usec

TEST NO. 3 - 13, 14, 15, 16: GYRO TEST - SENSOR OUTPUT

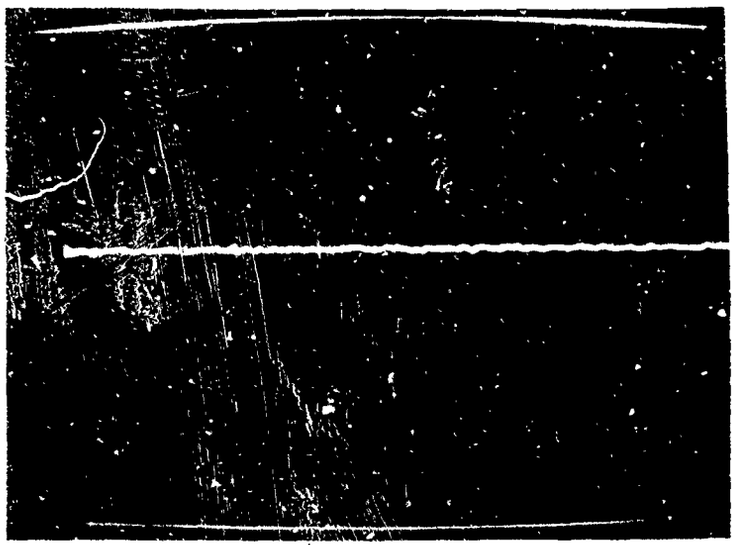

VOLTS/CM 0.1 SWEEP/CM 100 usec

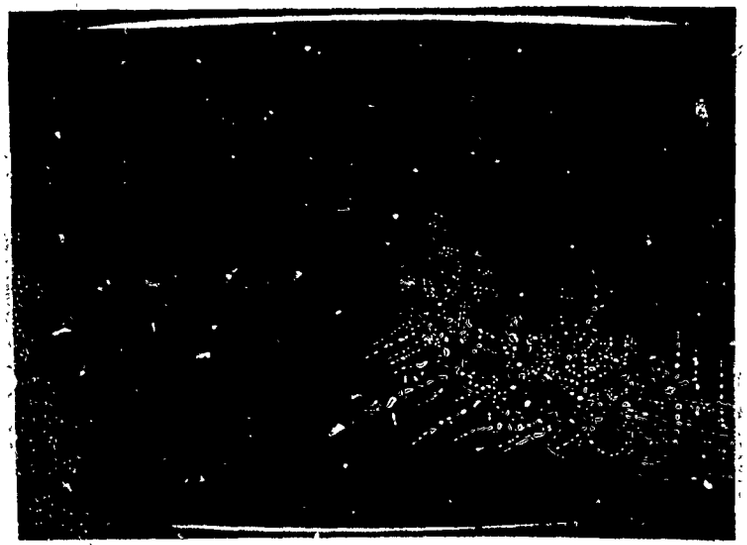

VOLTS/CM 5 SWEEP/CM 10 usec

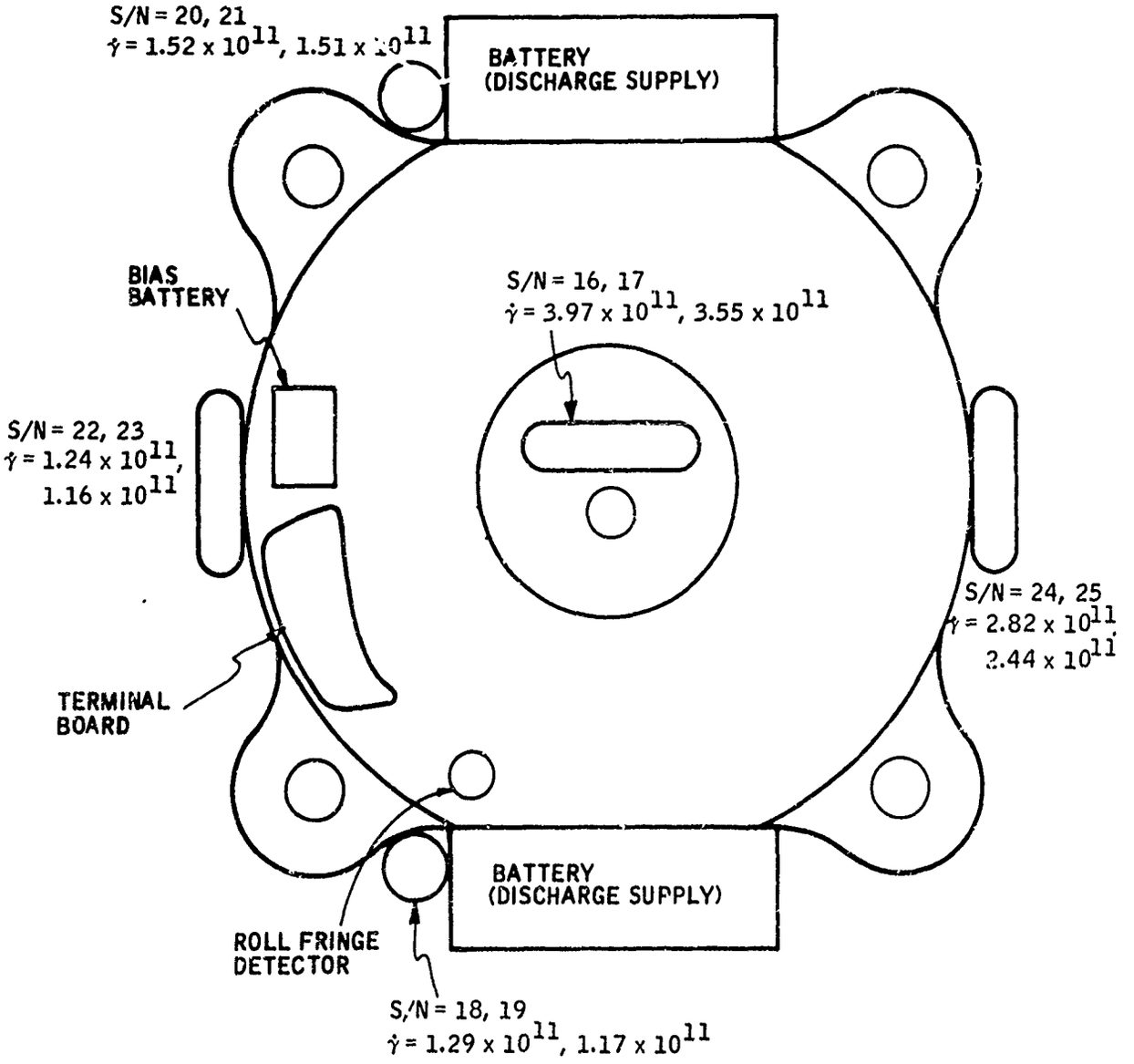

Gyro Test Shot No. 4 Dosimetry Data

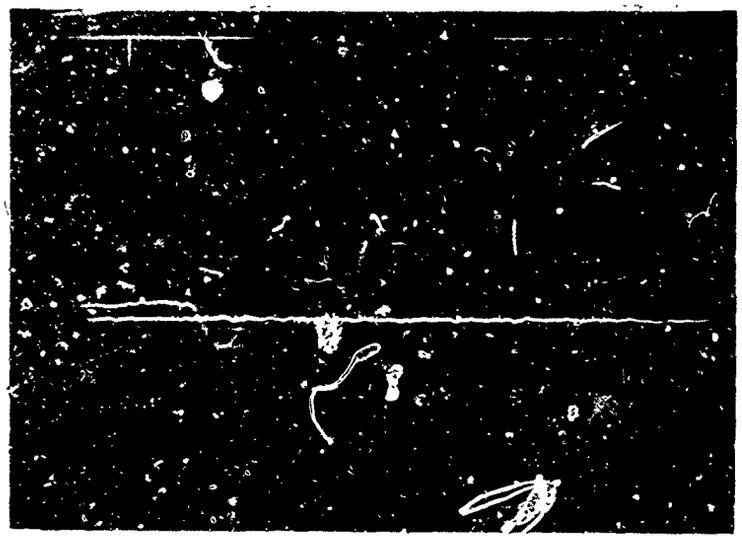

VOLTS/CM 1 SWEEP/CM 0.1 usec

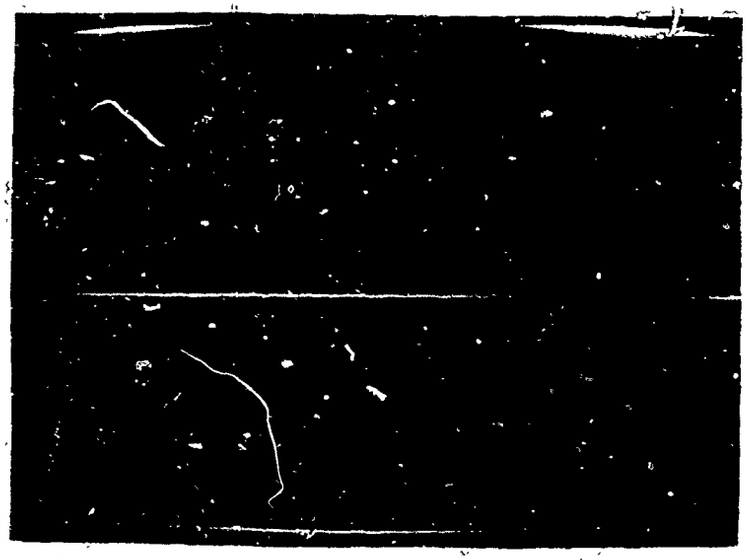

VOLTS/CM 1 SWEEP/CM 1 usec

TEST NO. 4 - 1, 2, 3, 4: GYRO TEST - DISCHARGE CURRENTS

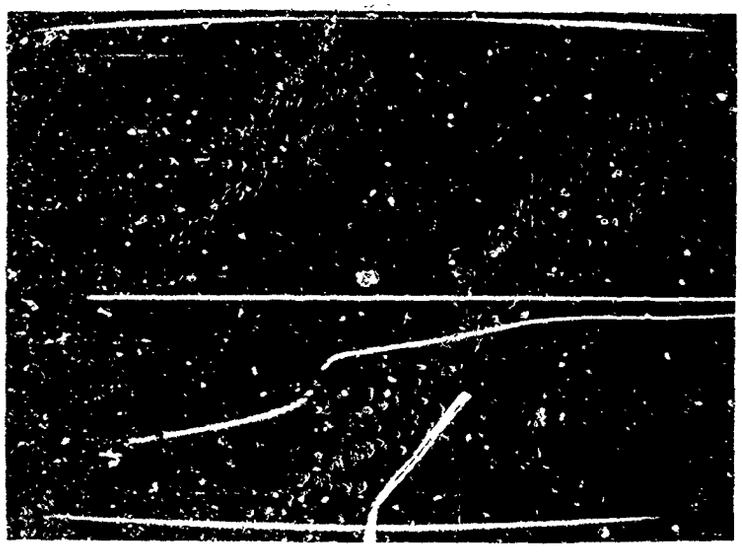

VOLTS/CM 1 SWEEP/CM 100 usec

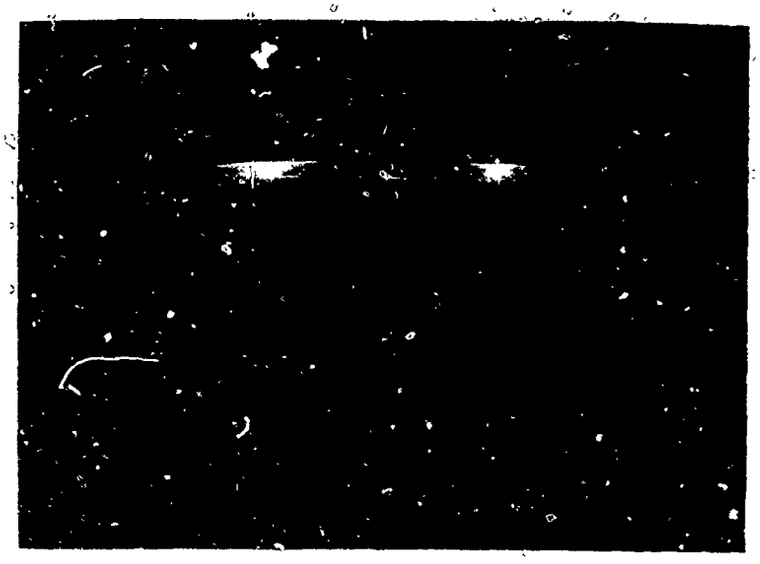

VOLTS/CM 5 SWEEP/CM 10 usec

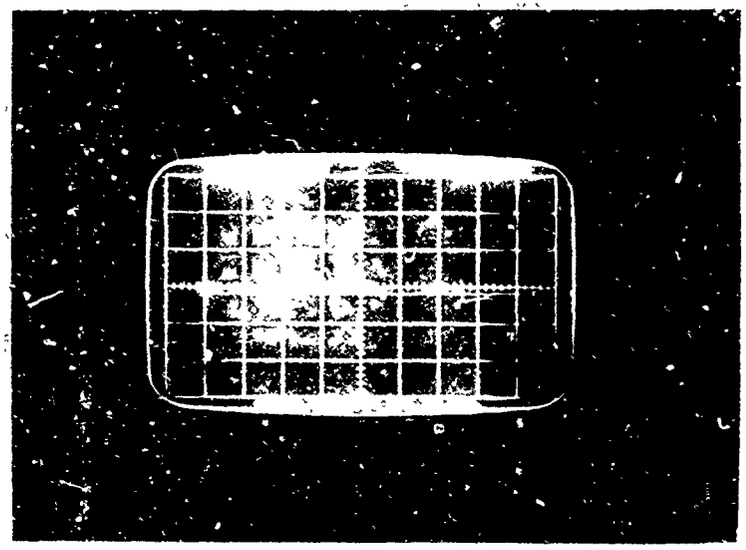

VOLTS/CM 1 SWEEP/CM 0.1 usec

VOLTS/CM 1 SWEEP/CM 1 usec

TEST NO. 4 - 5, 6, 7, 8: GYRO TEST - DISCHARGE CURRENTS

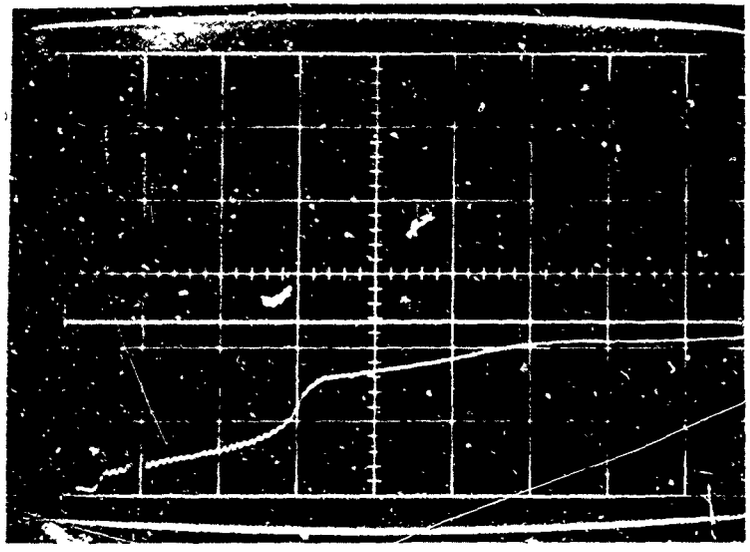

VOLTS/CM 1 SWEEP/CM 100 usec

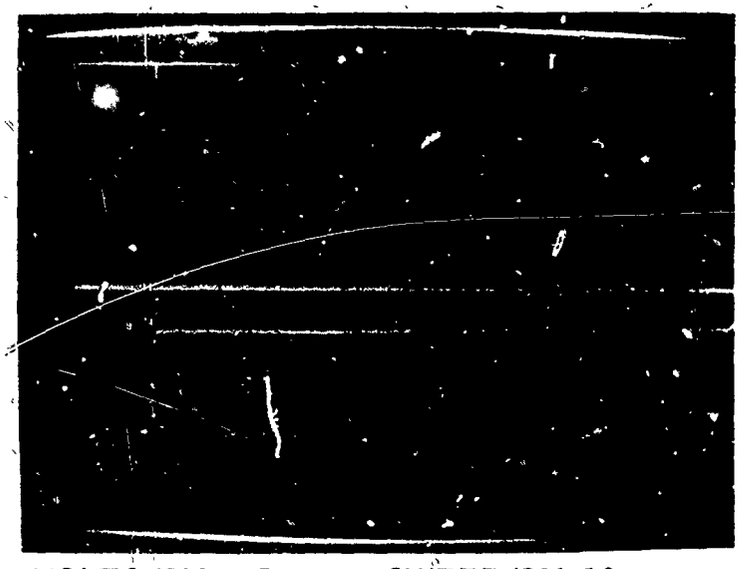

VOLTS/CM 5 SWEEP/CM 10 usec

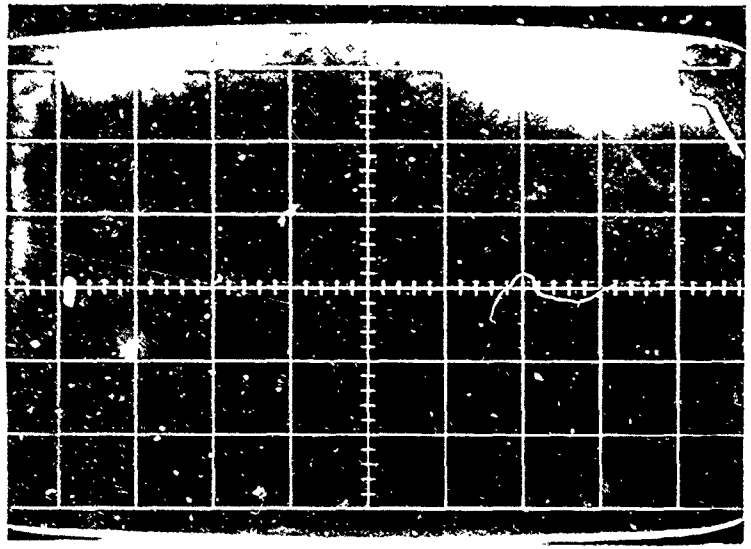

VOLTS/CM 1 SWEEP/CM 0.1 usec

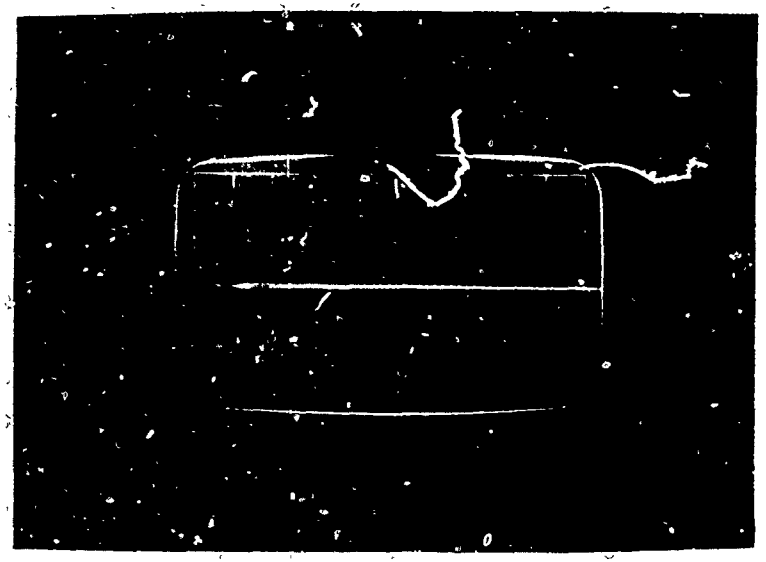

VOLTS/CM .1 SWEEP/CM 1 usec

TEST NO. 4 - 9, 10, 11, 12: GYRO TEST - SENSOR OUTPUT

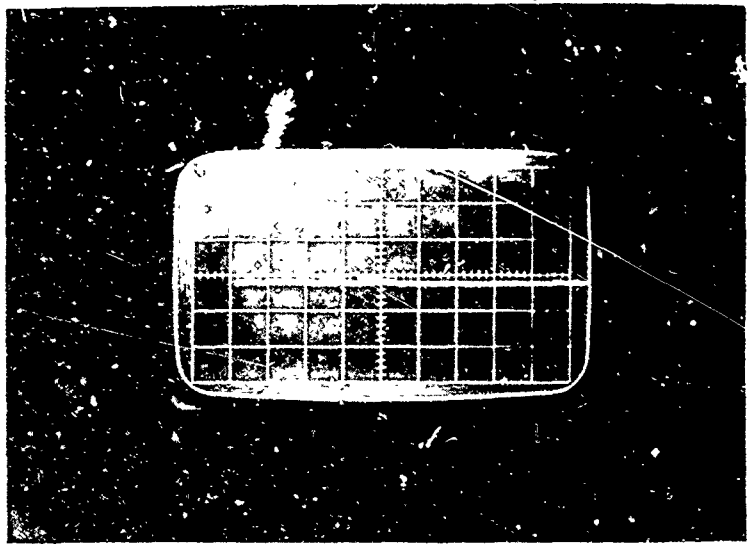

VOLTS/CM .1 SWEEP/CM 100 usec

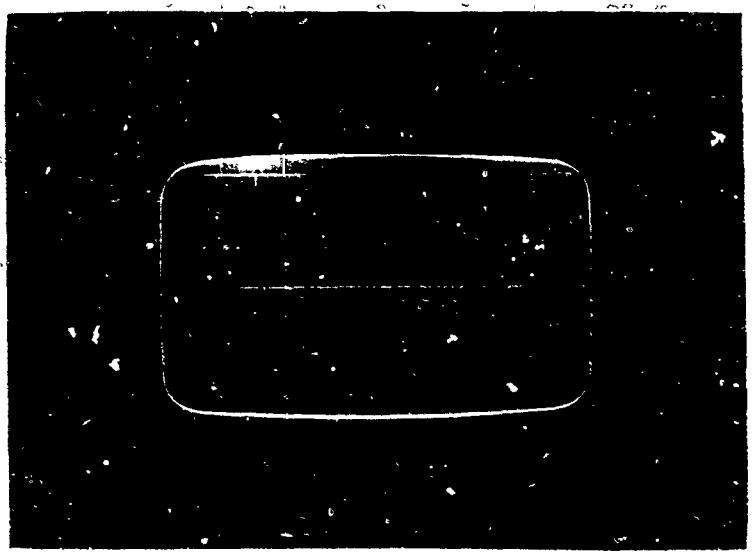

VOLTS/CM 5 SWEEP/CM 10 usec

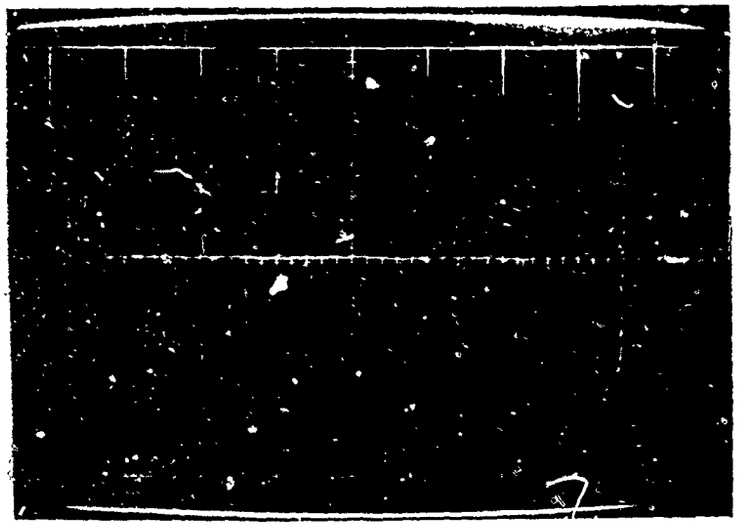

VOLTS/CM 1 SWEEP/CM 0.1 usec

VOLTS/CM .1 SWEEP/CM 1 usec

TEST NO. 4 - 13, 14, 15: GYRO TEST - SENSORU OUTPUT

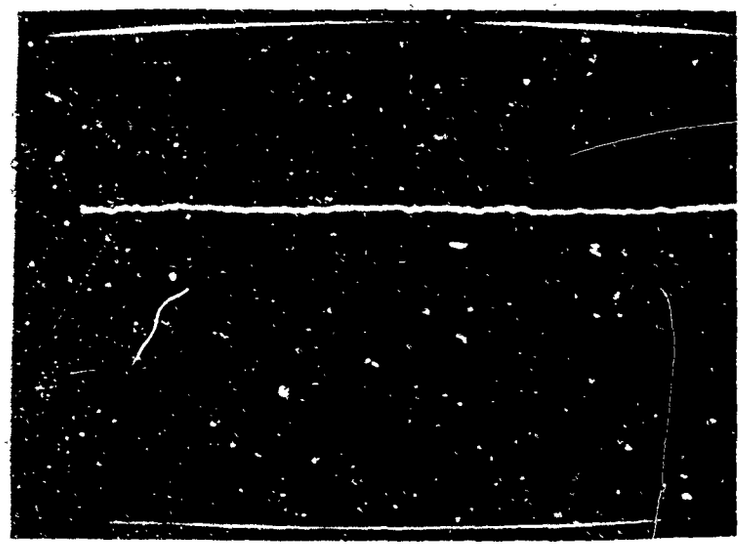

VOLTS/CM .1 SWEEP/CM 100 usec

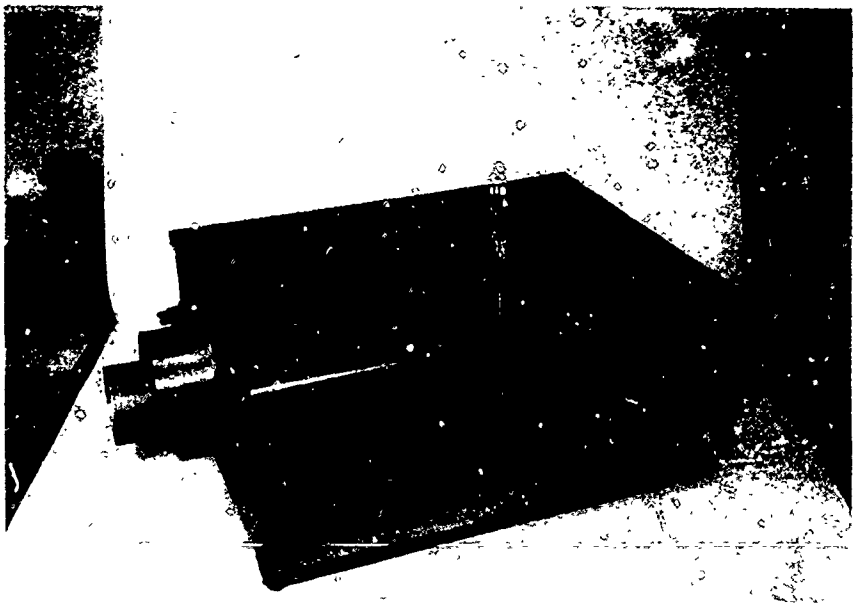

Circuits Test Cassette

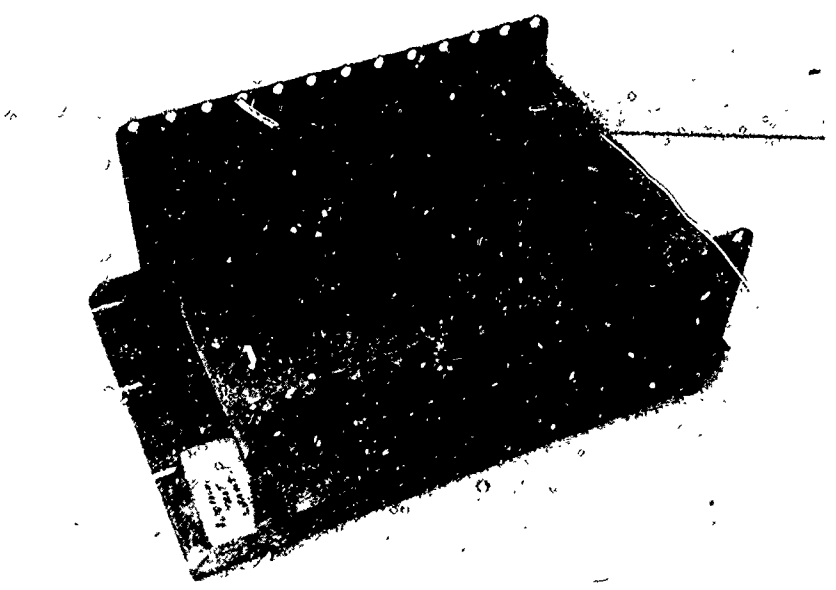

Digital Electronics Test Setup

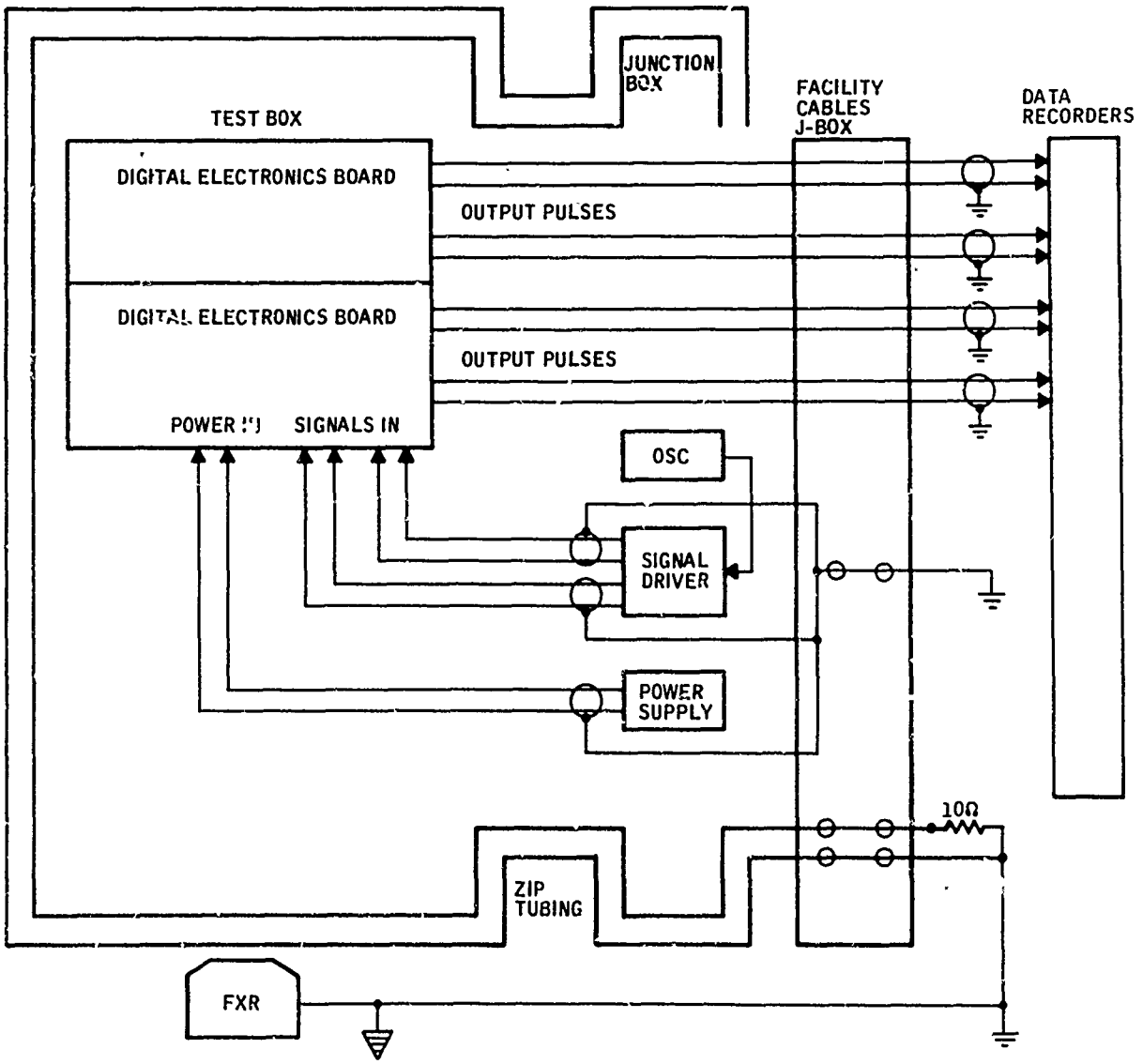

Digital Electronics Test

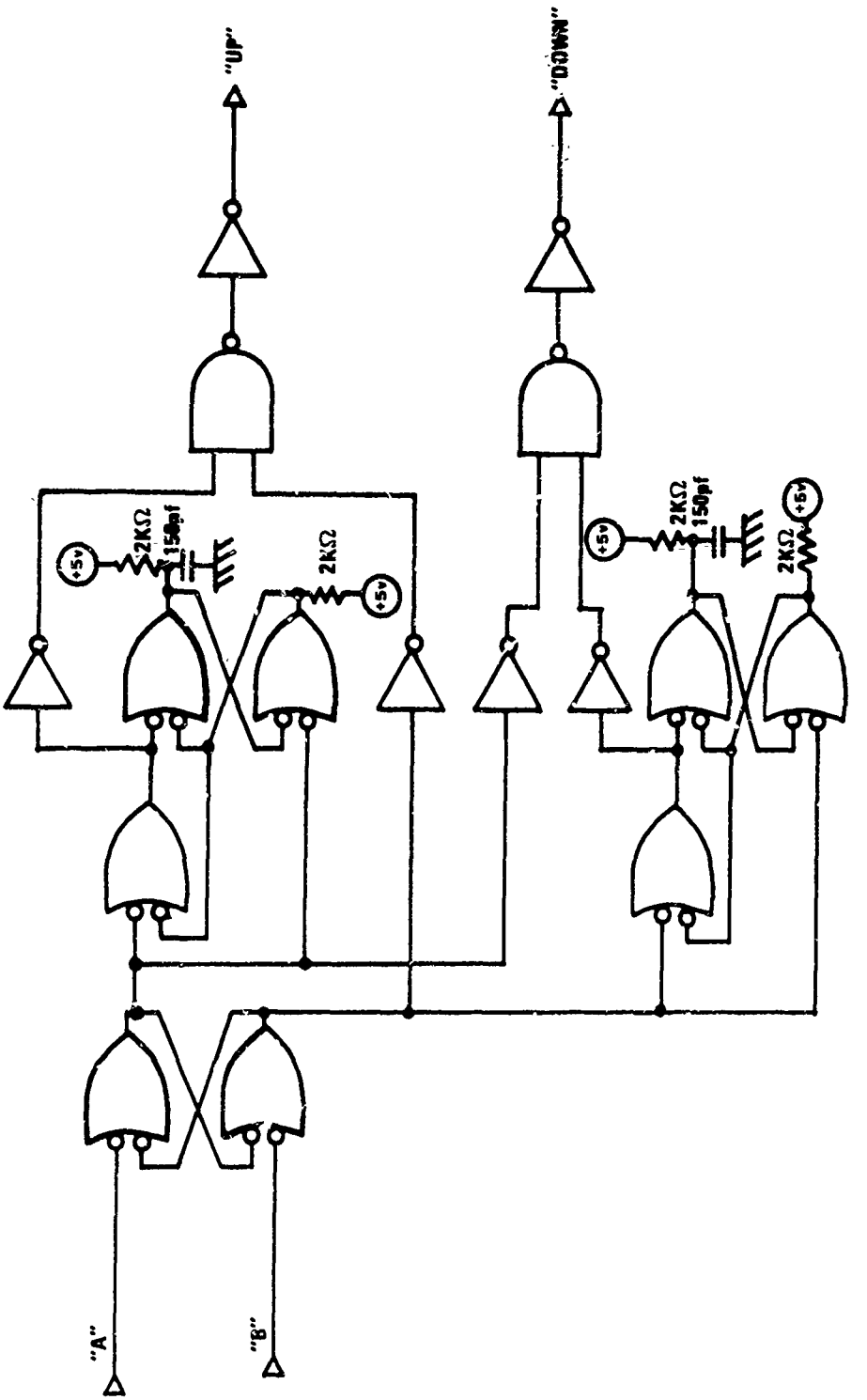

Direction Logic

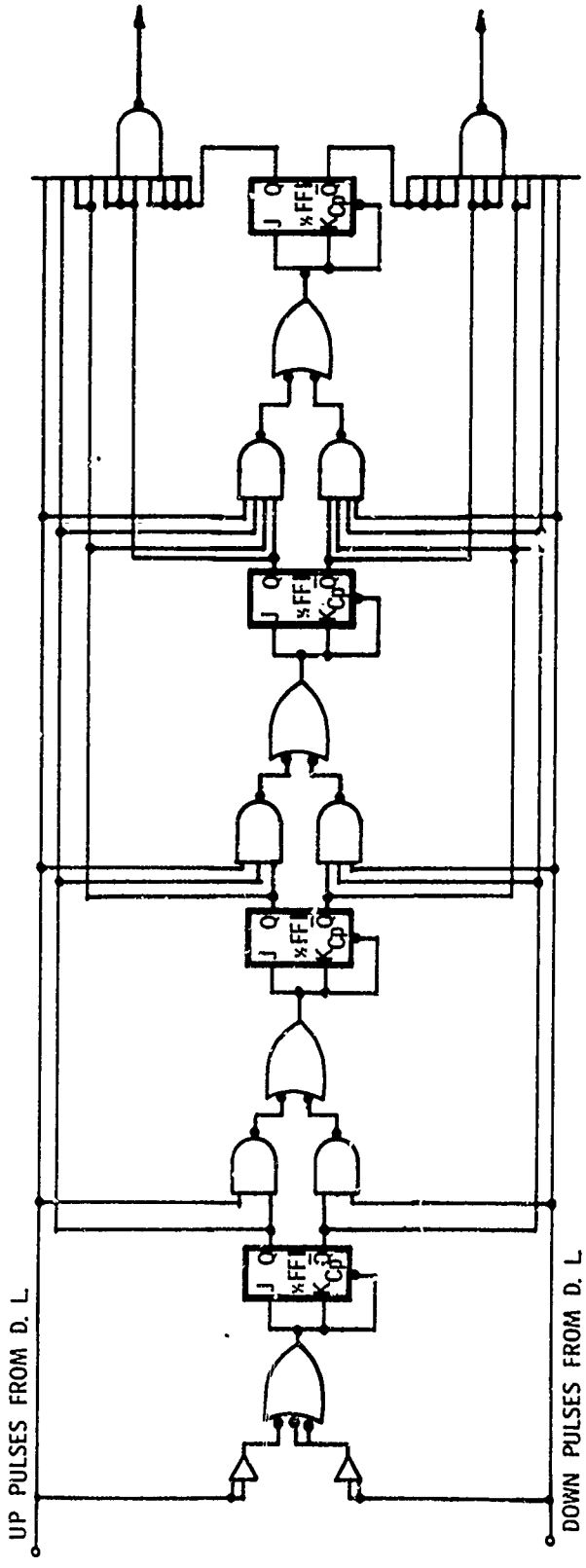

Up/Down Synchronous Counter

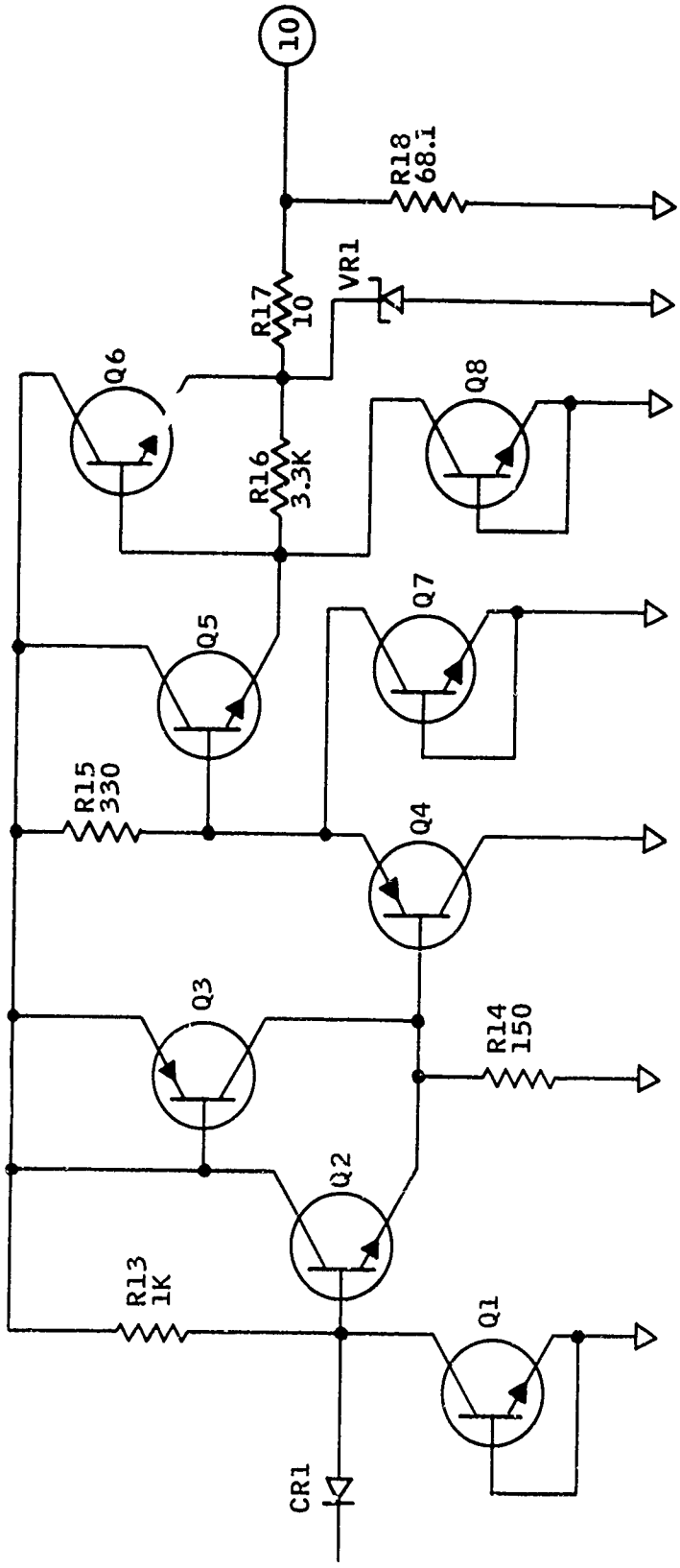

Digital Output Driver Circuit Diagram One-Half

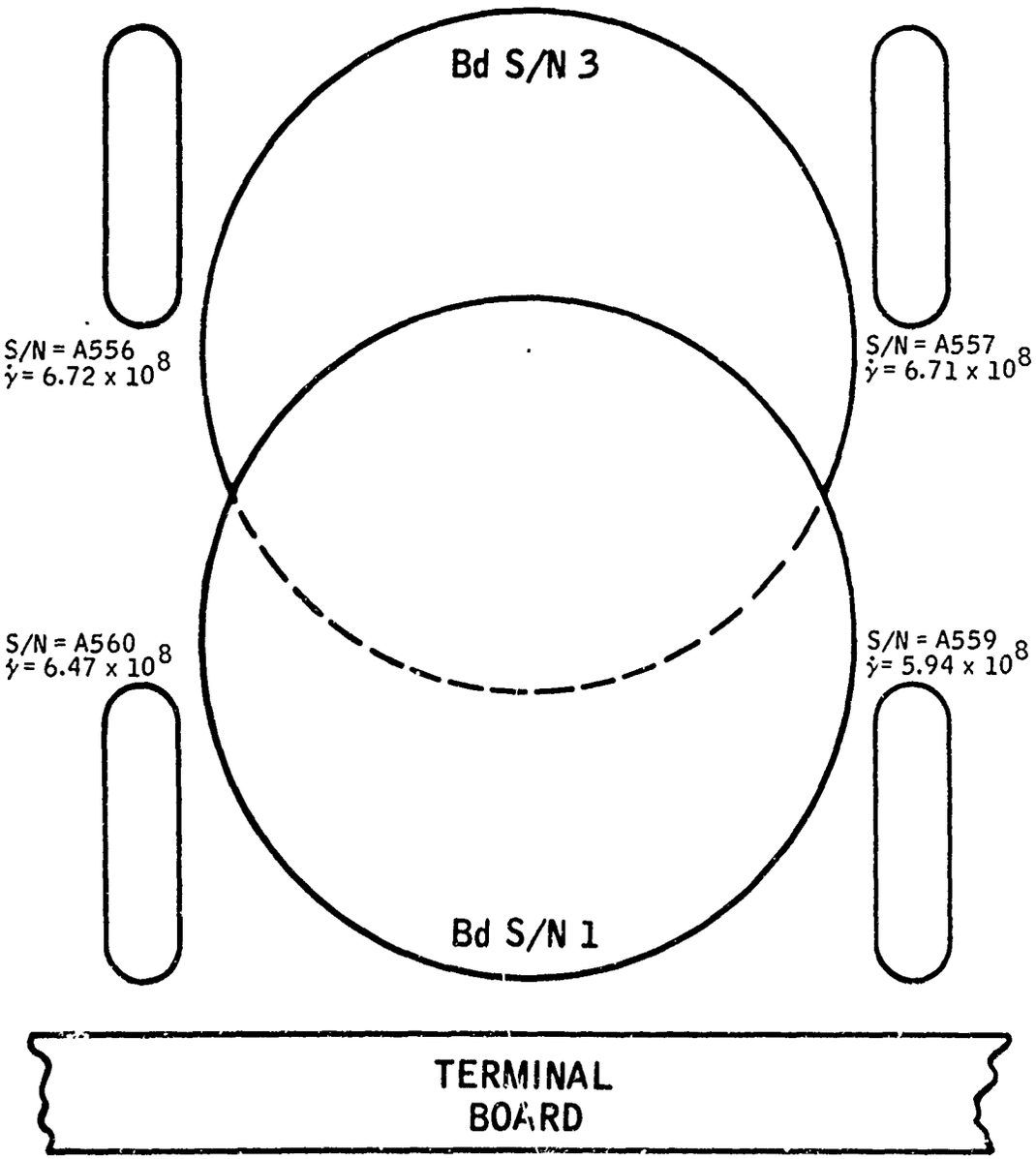

Digital Board Test Dosimetry Data (Shot No. 5)

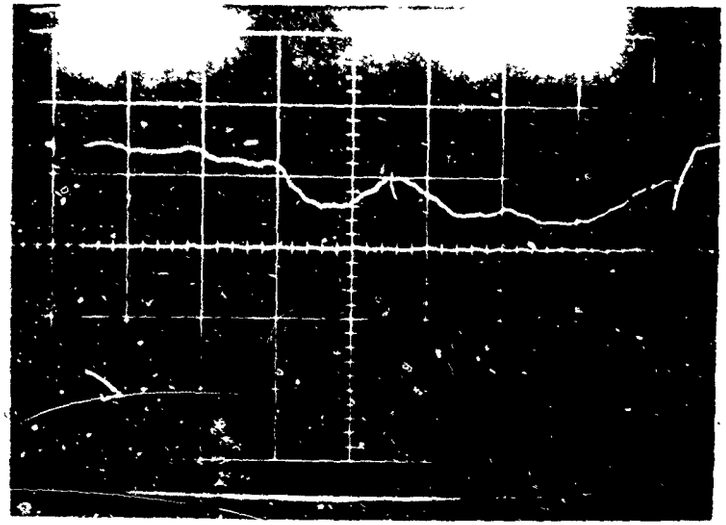

VOLTS/CM 2 SWEEP/CM 0.1 usec

VOLTS/CM 5 SWEEP/CM 0.1 usec

TEST NO. 5 - 1, 2, 3, 4: DIGITAL ELECTRONICS - FAST DIGITAL PLUSE

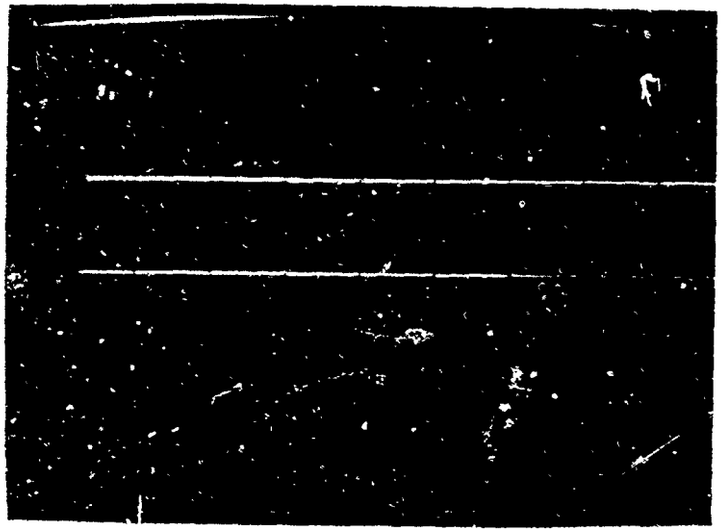

VOLTS/CM 2 SWEEP/CM .5 msec

VOLTS/CM 5 SWEEP/CM .5 msec

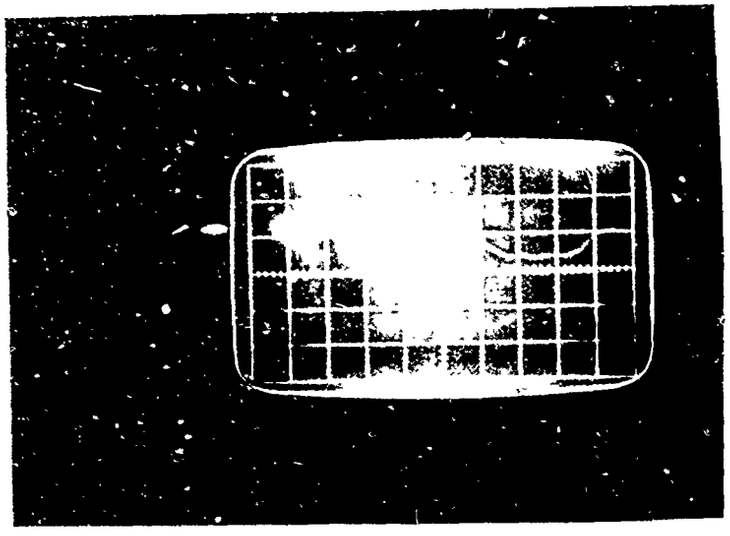

VOLTS/CM 2 SWEEP/CM 0.1 usec

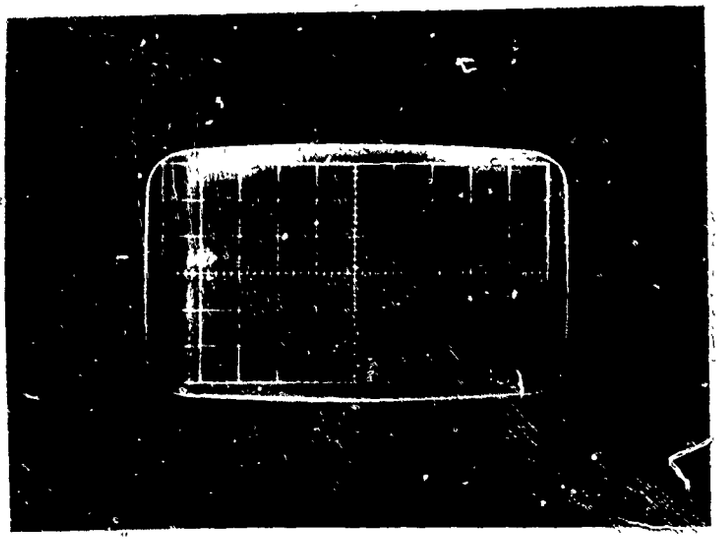

VOLTS/CM 5 SWEEP/CM 0.1 usec

TEST NO. 5 - 5, 6, 7, 8: DIGITAL ELECTRONICS - FAST DIGITAL PULSE

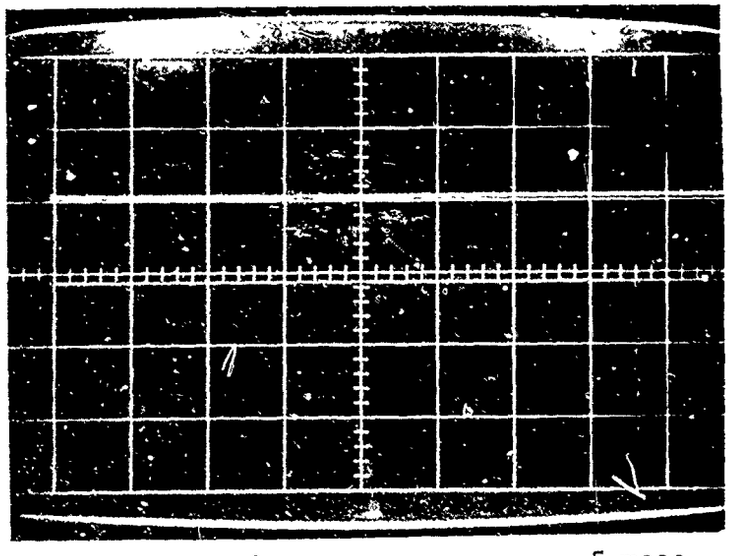

VOLTS/CM 2 SWEEP/CM .5 msec

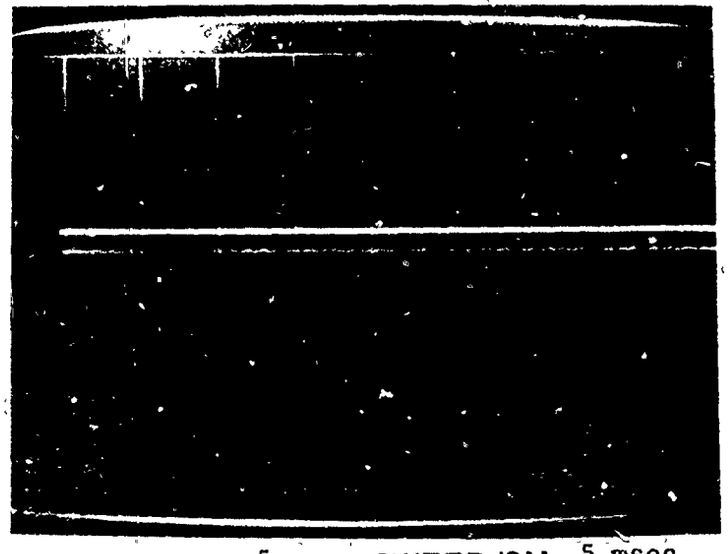

VOLTS/CM 5 SWEEP/CM .5 msec

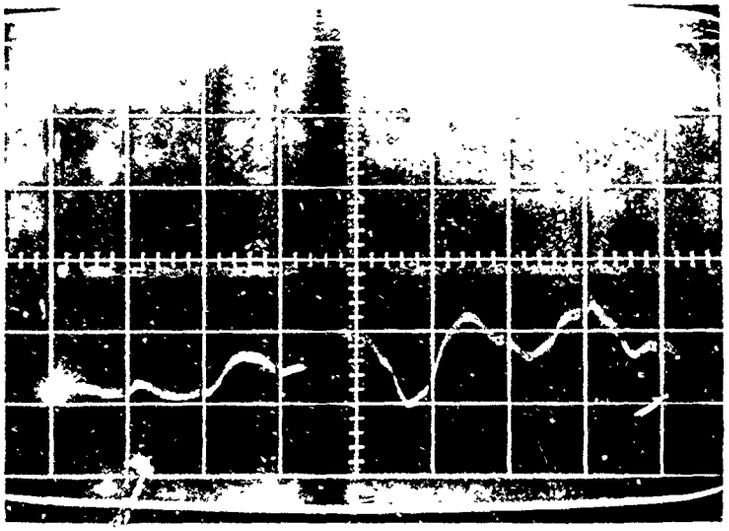

VOLTS/CM 2 SWEEP/CM 0.1 usec

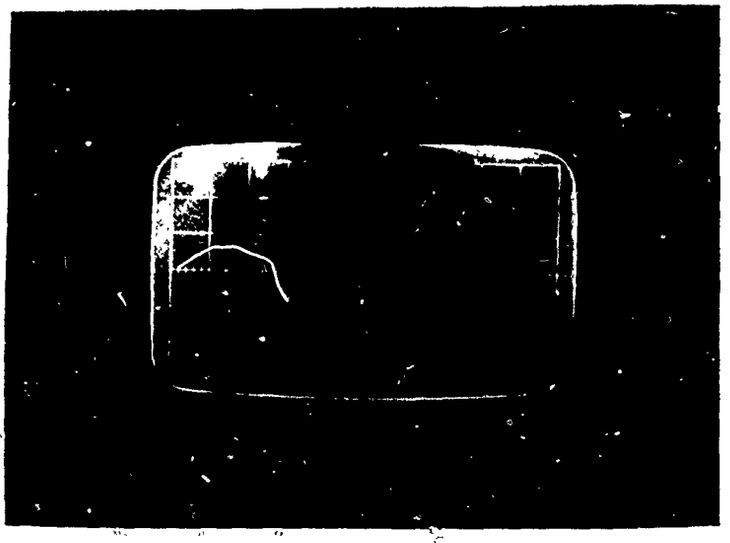

VOLTS/CM 5 SWEEP/CM 0.1 usec

TEST NO. 5 - 9, 10, 11, 12: DIGITAL ELECTRONICS - SLOW DIGITAL PULSE

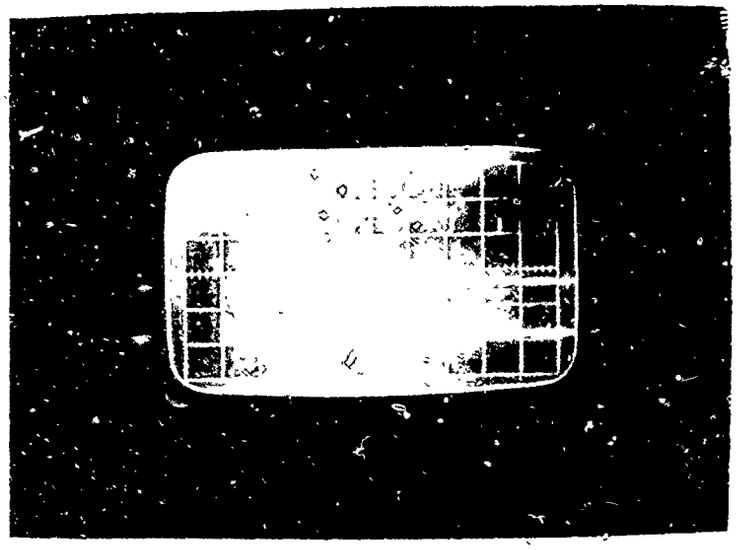

VOLTS/CM 2 SWEEP/CM .5 msec

VOLTS/CM 5 SWEEP/CM .5 msec

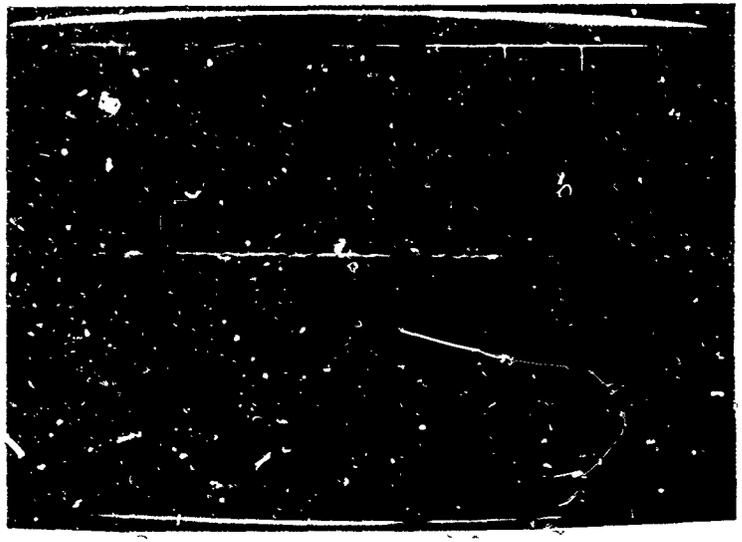

VOLTS/CM 2 SWEEP/CM 0.1 usec

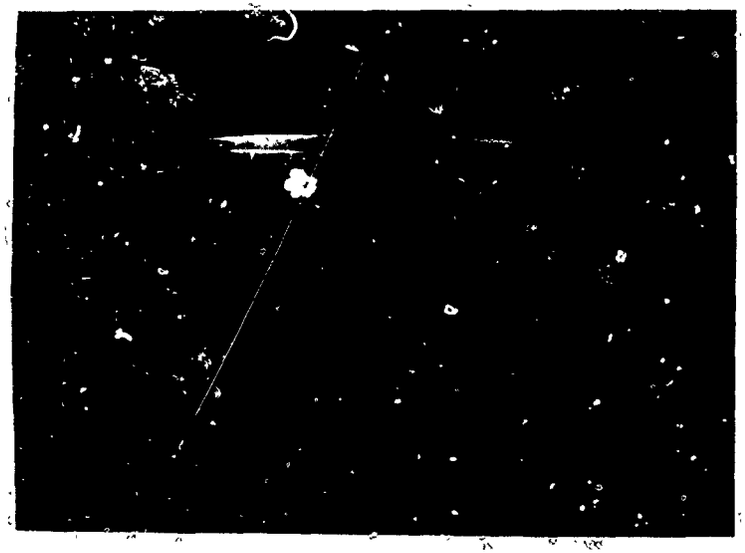

VOLTS/CM 5 SWEEP/CM 0.1 usec

TEST NO. 5 - 13, 14, 15: DIGITAL ELECTRONICS - SLOW DIGITAL PULSE

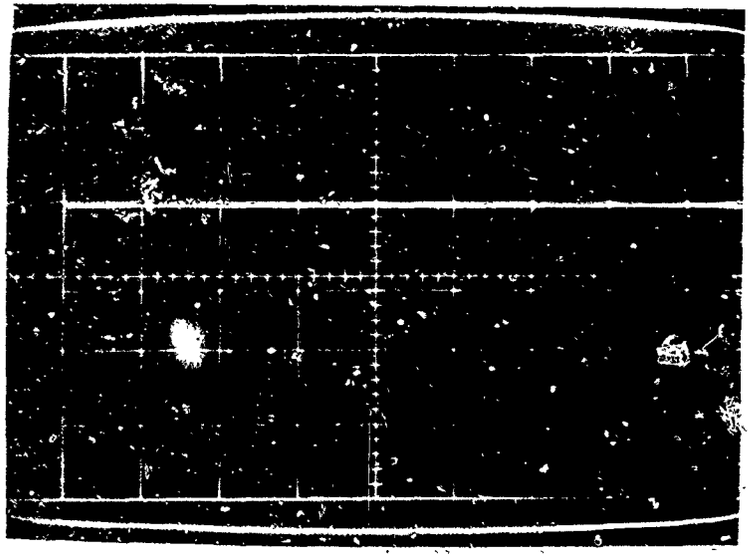

VOLTS/CM 2 SWEEP/CM .5 msec

VOLTS/CM _____ SWEEP/CM _____

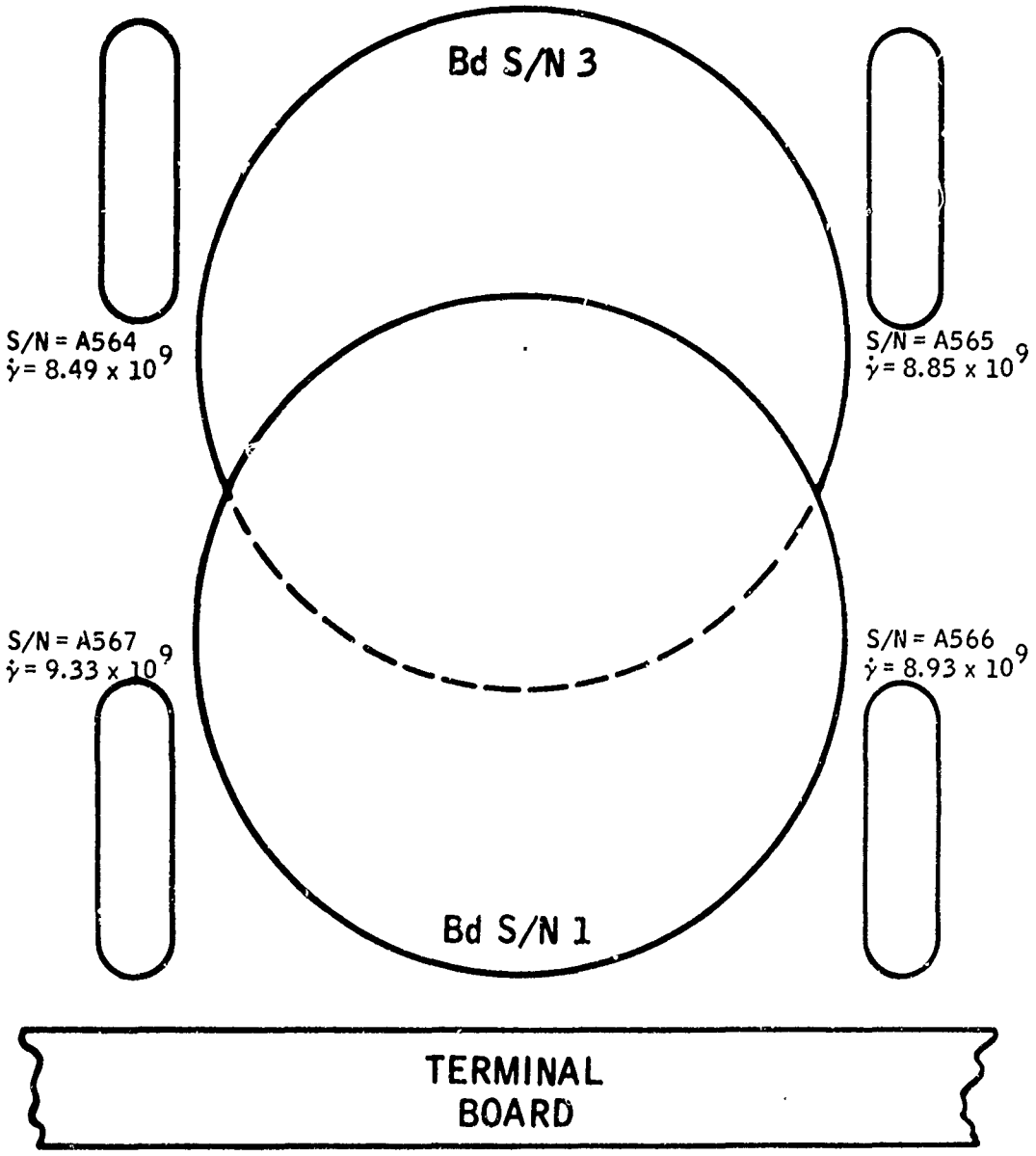

Digital Board Test - Dosimetry (Shot No. 6) - Sheet 1
Large Dosimeters

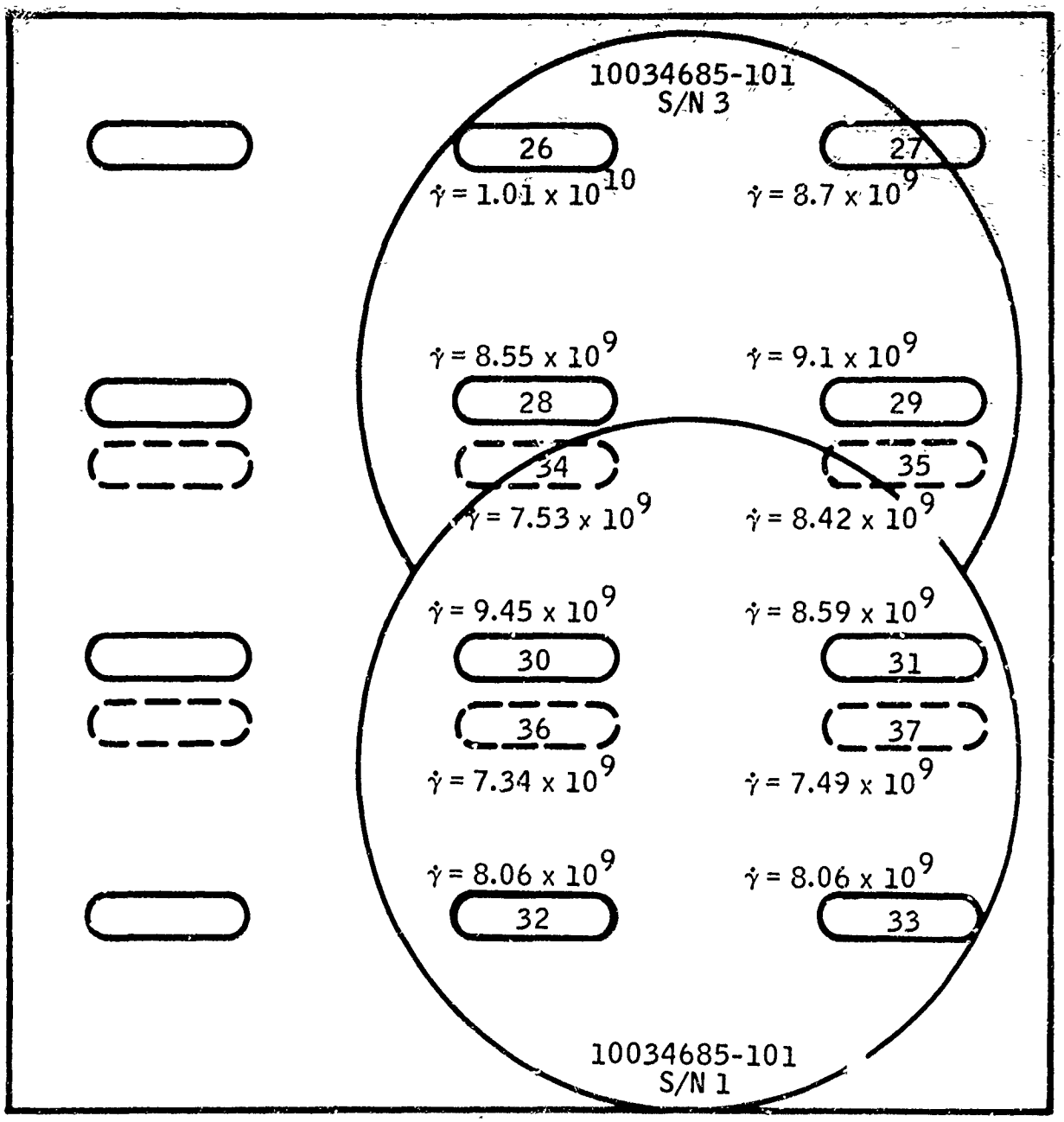

Digital Board Test - Dosimetry Data (Shot No. 6)
Sheet 2, Small Dosimeters

VOLTS/CM 2 SWEEP/CM 0.1 usec

VOLTS/CM 5 SWEEP/CM 0.1 usec

TEST NO. 6 - 1, 2, 3, 4: DIGITAL ELECTRONICS - FAST DIGITAL PULSE

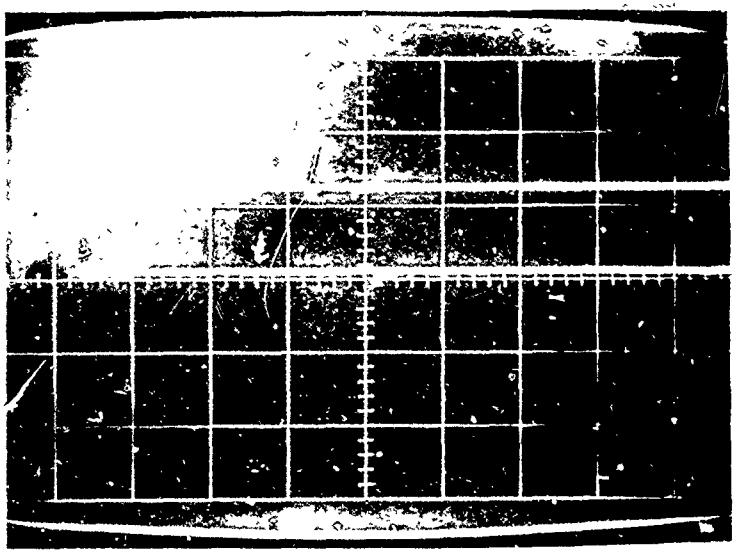

VOLTS/CM 2 SWEEP/CM .5 msec

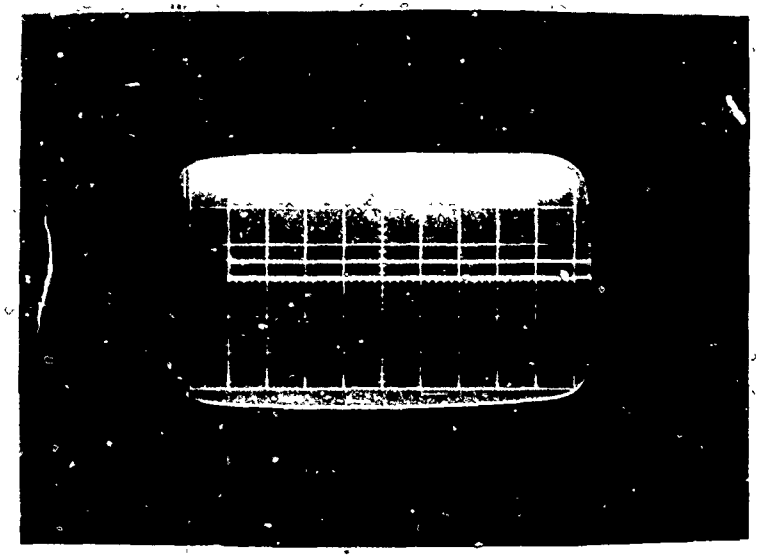

VOLTS/CM 5 SWEEP/CM .5 msec

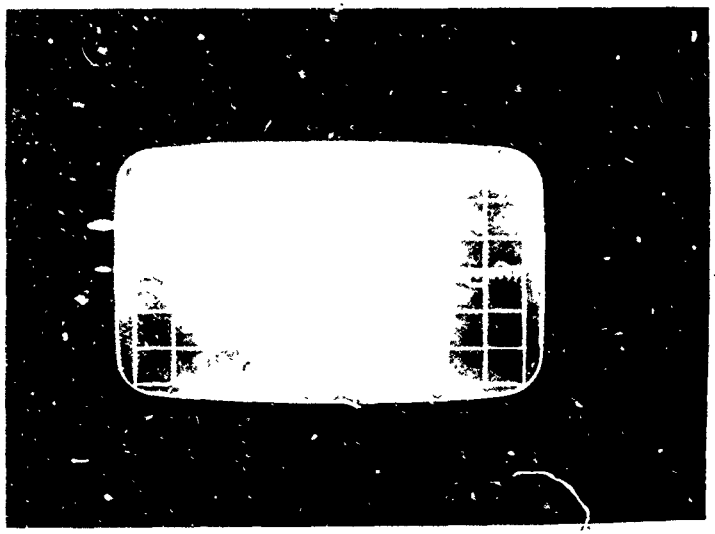

VOLTS/CM 2 SWEEP/CM 0.1 usec

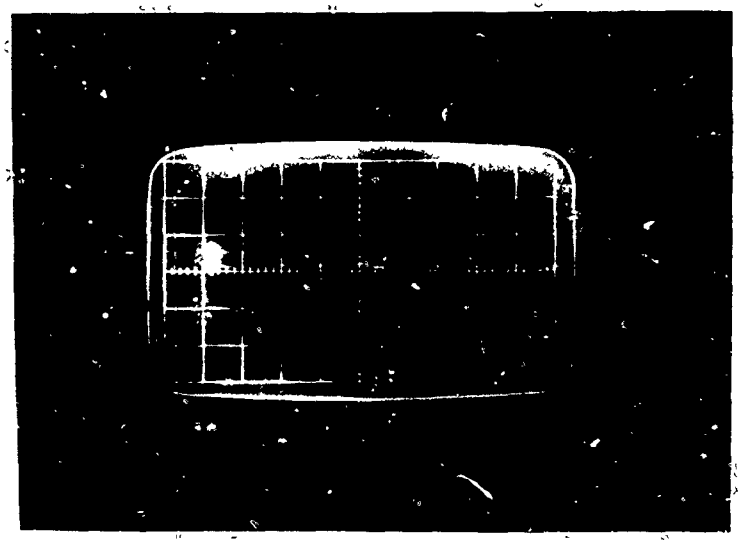

VOLTS/CM 5 SWEEP/CM 0.1 usec

TEST NO. 6 - 5, 6, 7, 8: DIGITAL ELECTRONICS - FAST DIGITAL PULSE

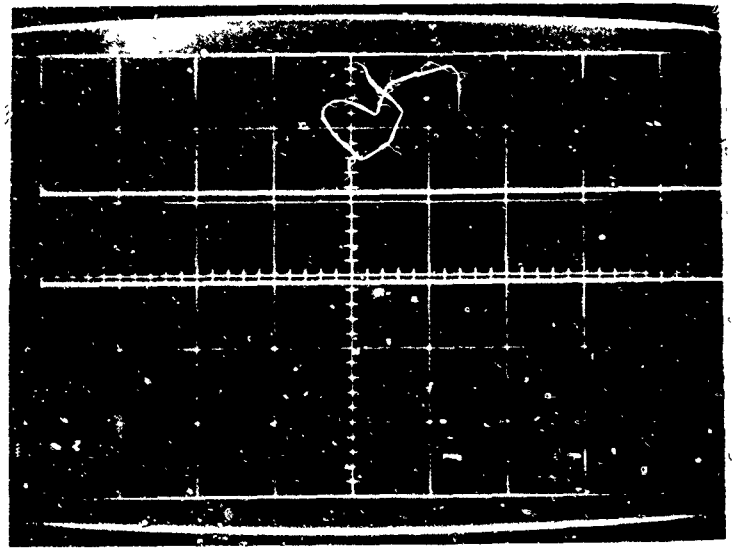

VOLTS/CM 2 SWEEP/CM .5 msec

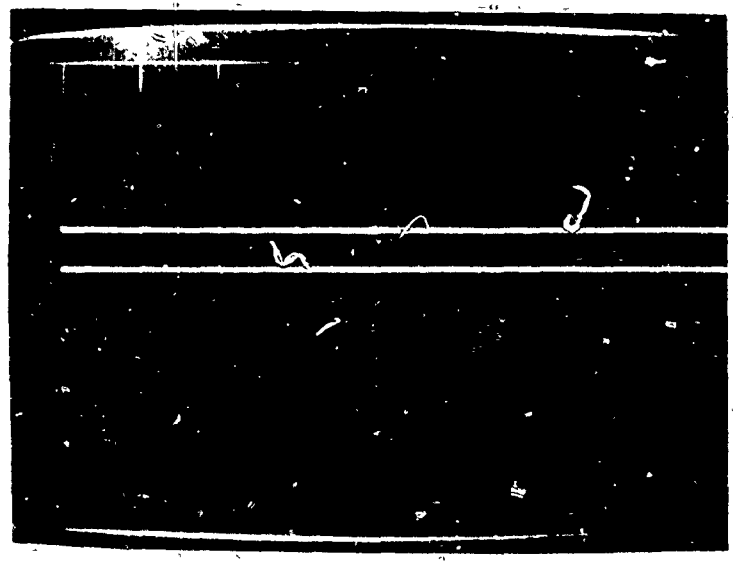

VOLTS/CM 5 SWEEP/CM .5 msec

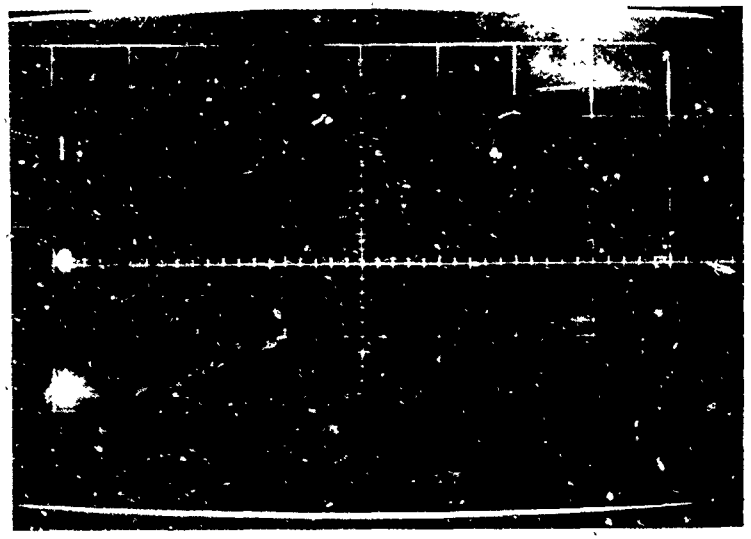

VOLTS/CM 2 SWEEP/CM 0.1 usec

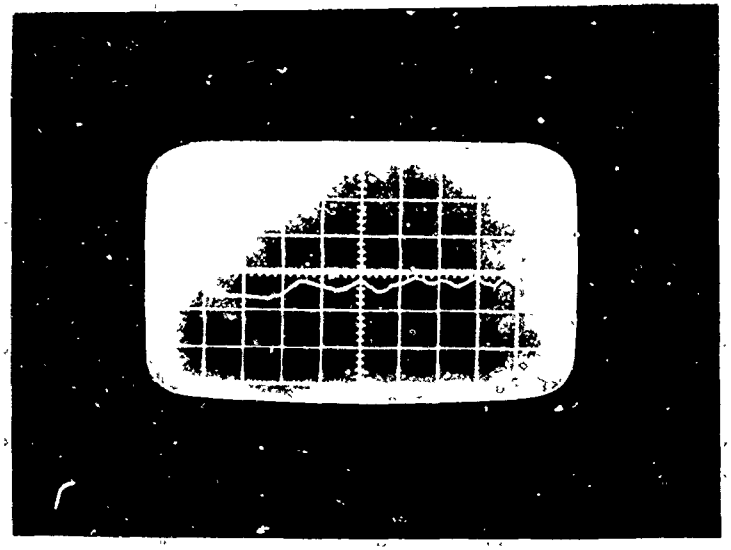

VOLTS/CM 5 SWEEP/CM 0.1 usec

TEST NO. 6 - 9, 10, 11, 12: DIGITAL ELECTRONICS - SLOW DIGITAL PULSE

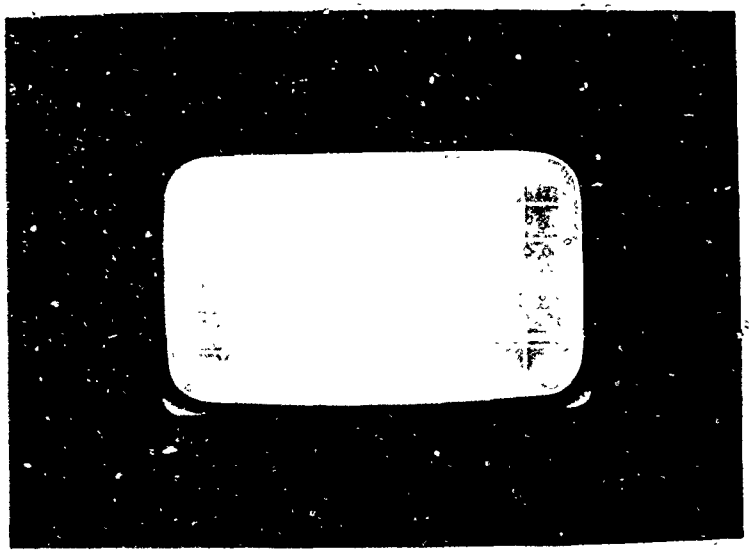

VOLTS/CM 2 SWEEP/CM .5 msec

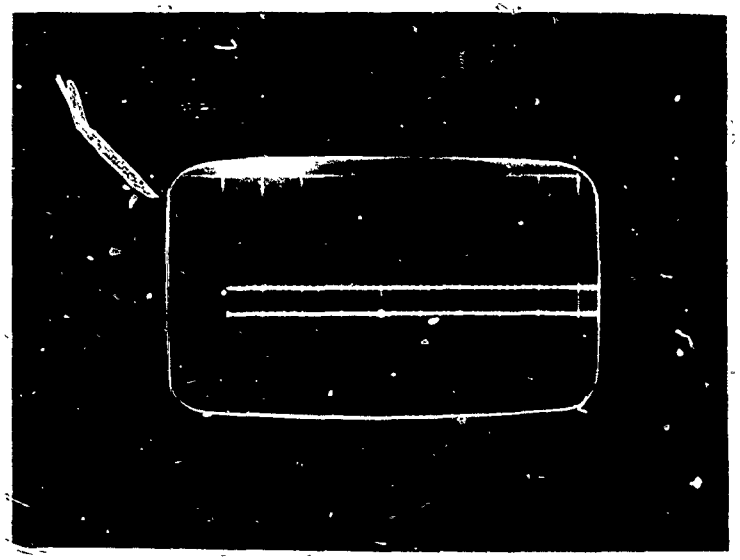

VOLTS/CM 5 SWEEP/CM .5 msec

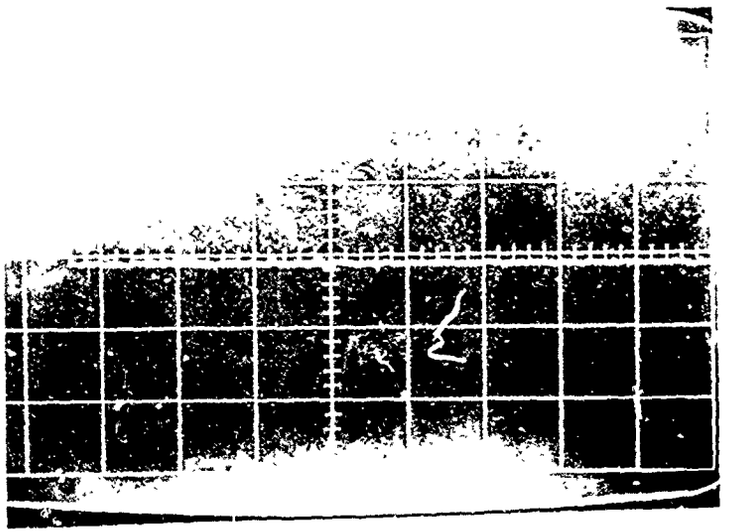

VOLTS/CM 2 SWEEP/CM .1 usec

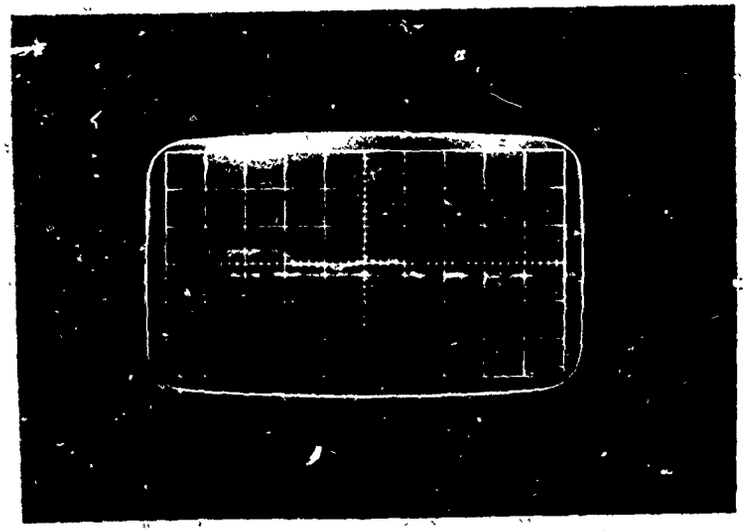

VOLTS/CM 5 SWEEP/CM .1 usec

TEST NO. 6 - 13, 14, 15: DIGITAL ELECTRONICS - SLOW DIGITAL PULSE

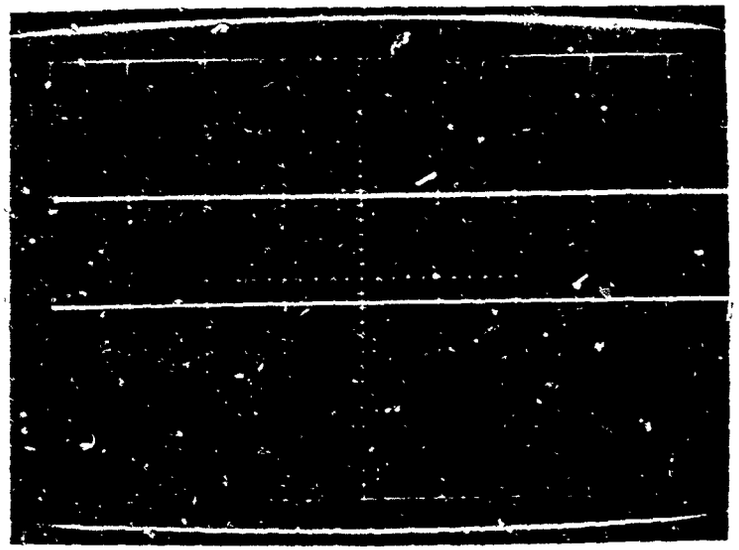

VOLTS/CM 2 SWEEP/CM .5 msec

VOLTS/CM _____ SWEEP/CM _____

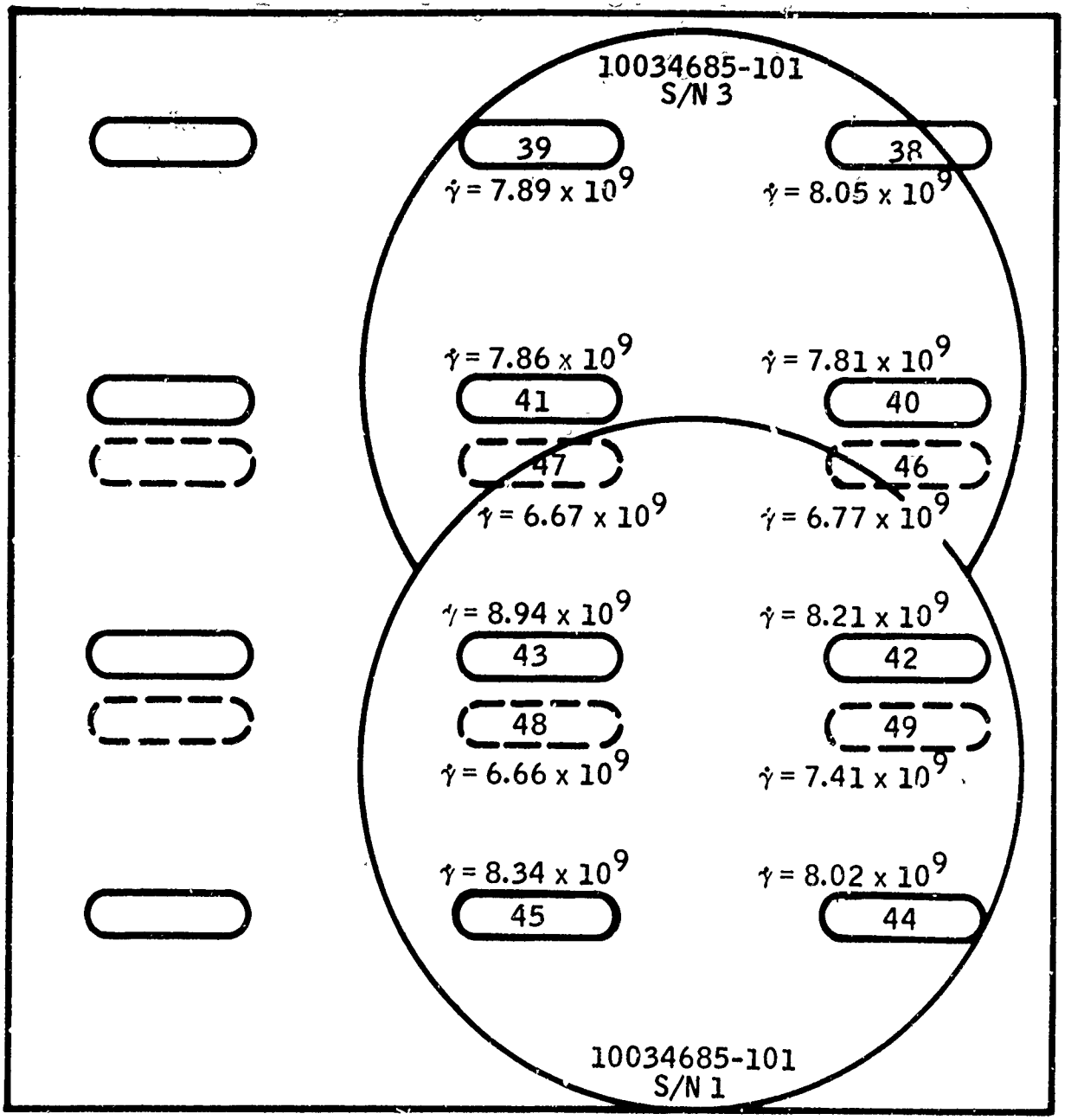

Digital Board Test - Dosimetry Data (Shot No. 7)

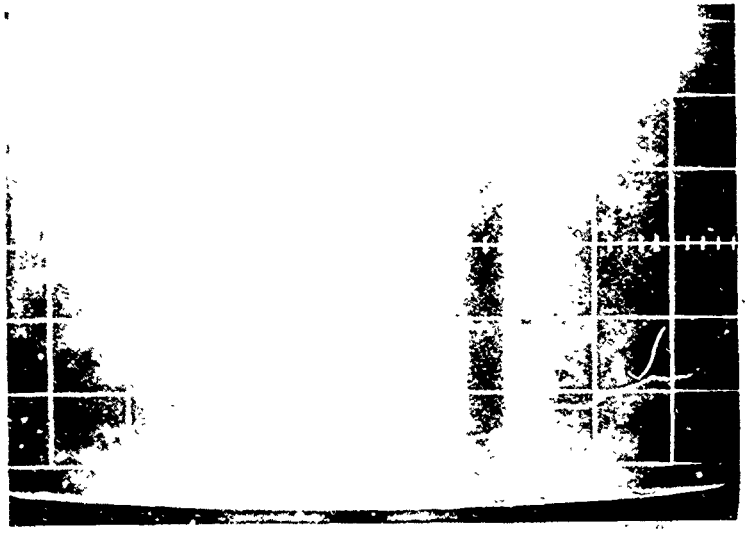

VOLTS/CM 2 SWEEP/CM 0.1 usec

VOLTS/CM 2 SWEEP/CM 1 usec

TEST NO. 7 - 1, 2, 3, 4: DIGITAL ELECTRONICS - FAST DIGITAL PULSE

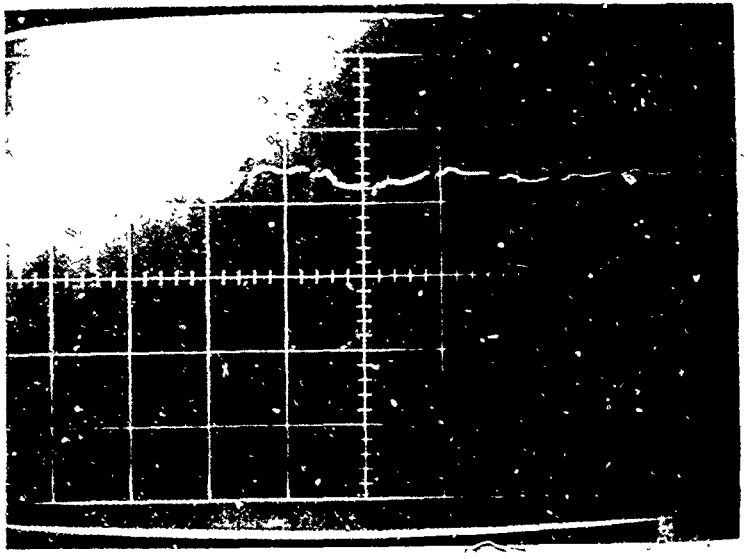

VOLTS/CM 2 SWEEP/CM 5 usec

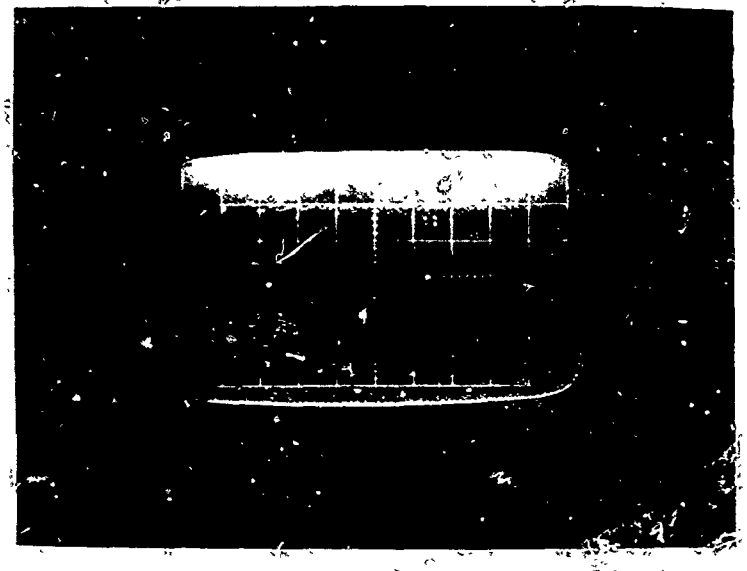

VOLTS/CM 2 SWEEP/CM 20 usec

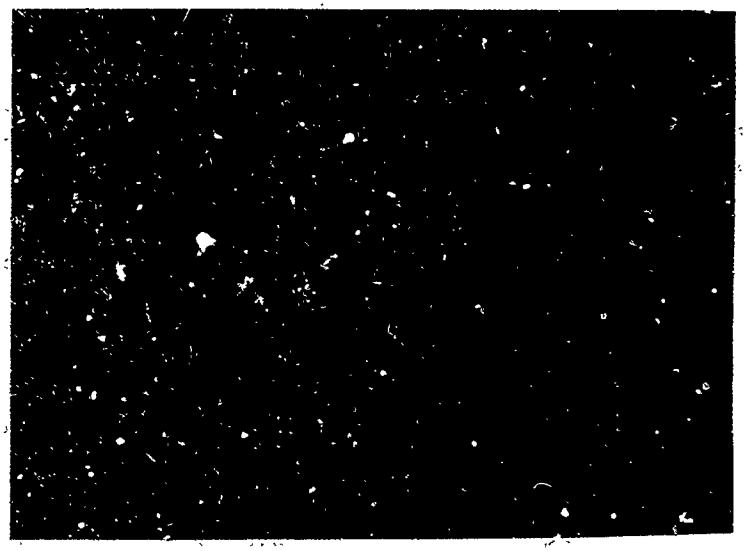

VOLTS/CM 2 SWEEP/CM 0.1 usec

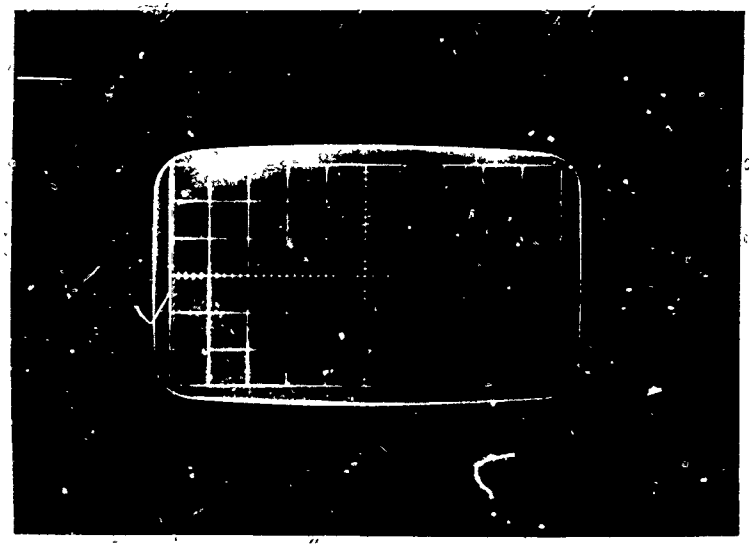

VOLTS/CM 2 SWEEP/CM 1 usec

TEST NO. 7 - 5, 6, 7, 8: DIGITAL ELECTRONICS - FAST DIGITAL PULSE

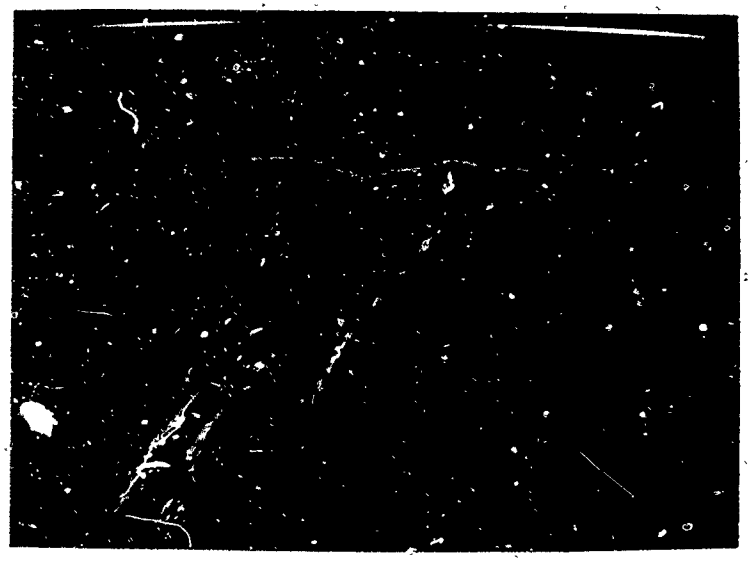

VOLTS/CM 2 SWEEP/CM 5 usec

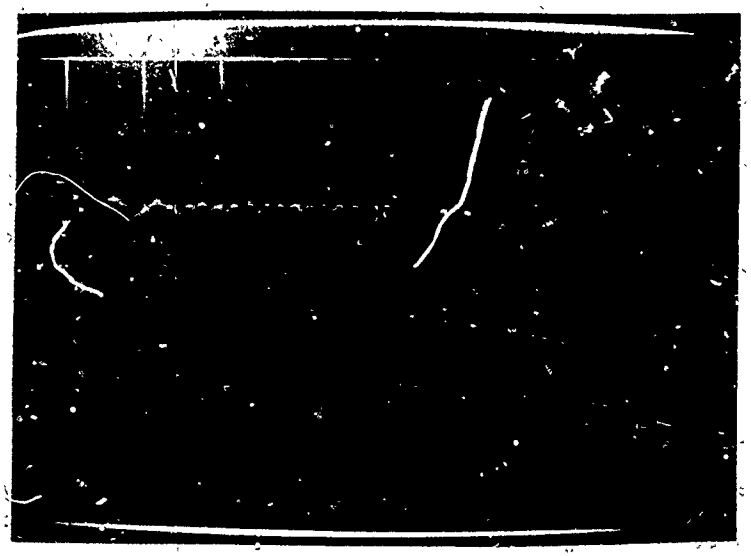

VOLTS/CM 2 SWEEP/CM 20 usec

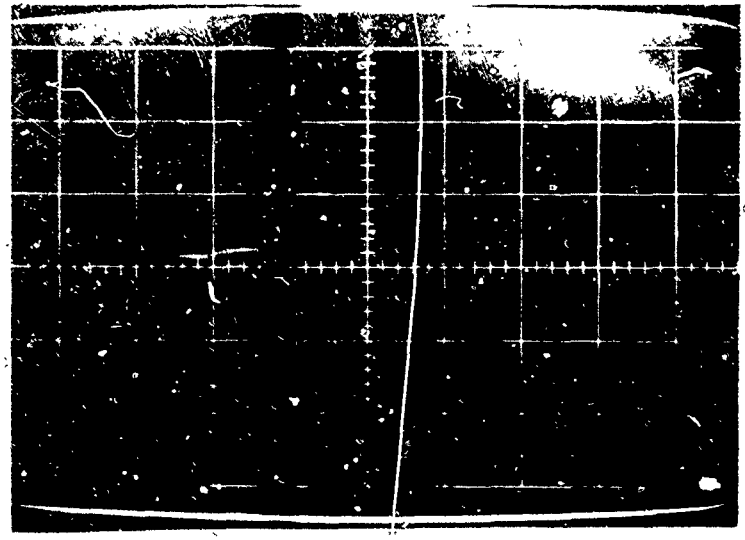

VOLTS/CM 5 SWEEP/CM 0.1 usec

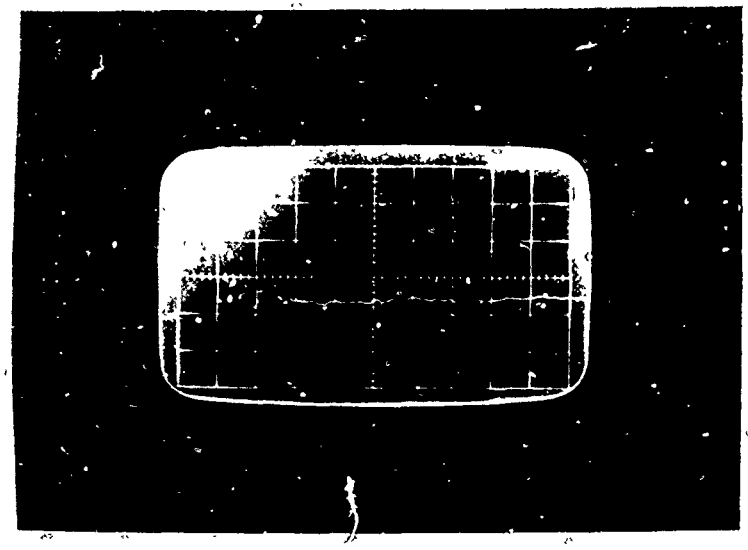

VOLTS/CM 5 SWEEP/CM 1 usec

TEST NO. 7 - 9, 10, 11, 12: DIGITAL ELECTRONICS - SLOW DIGITAL PULSE

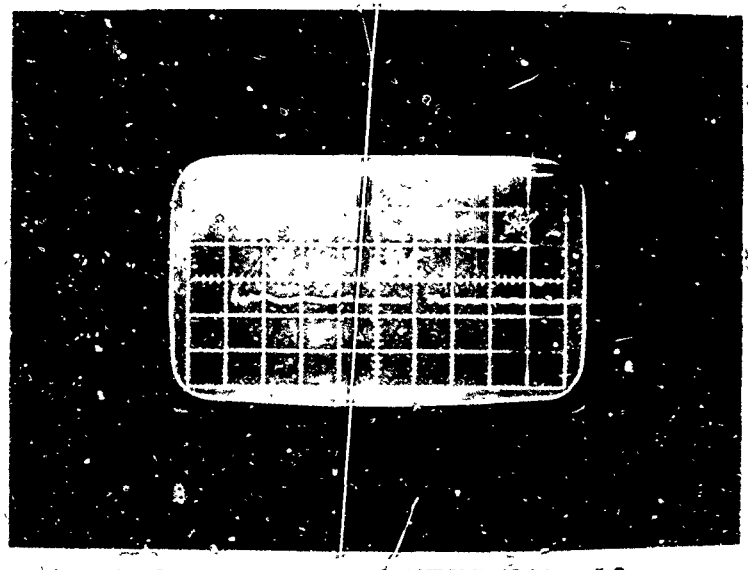

VOLTS/CM 5 SWEEP/CM 10 usec

VOLTS/CM 5 SWEEP/CM 100 usec

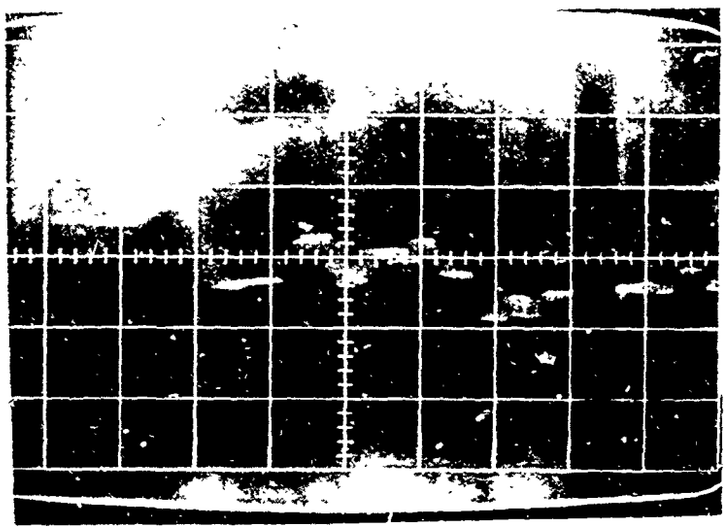

VOLTS/CM 5 SWEEP/CM 0.1 usec

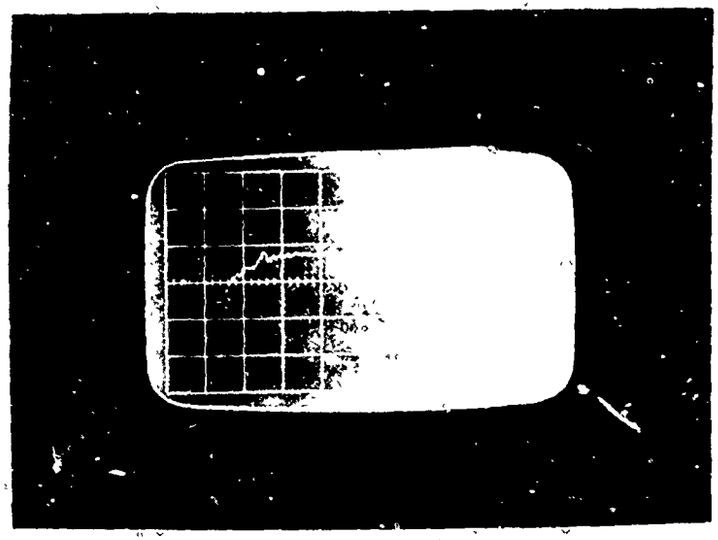

VOLTS/CM 5 SWEEP/CM 1 usec

TEST NO. 7 - 13, 14, 15, 16: DIGITAL ELECTRONICS - SLOW DIGITAL PULSE

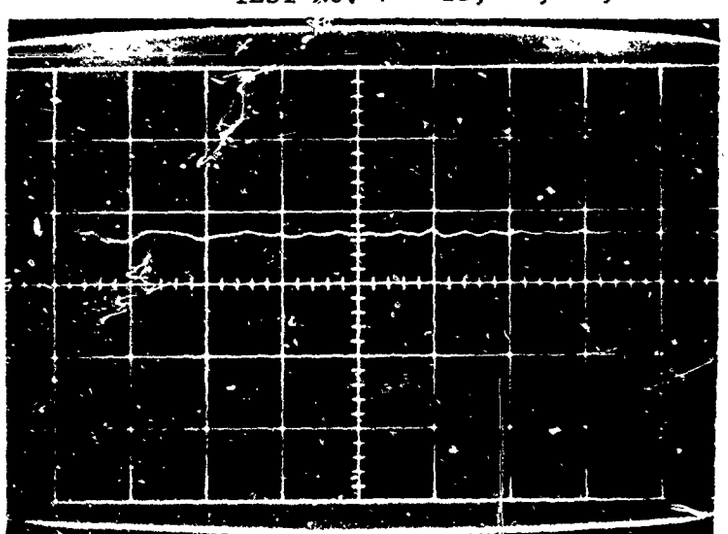

VOLTS/CM 5 SWEEP/CM 10 usec

VOLTS/CM 5 SWEEP/CM 100 usec

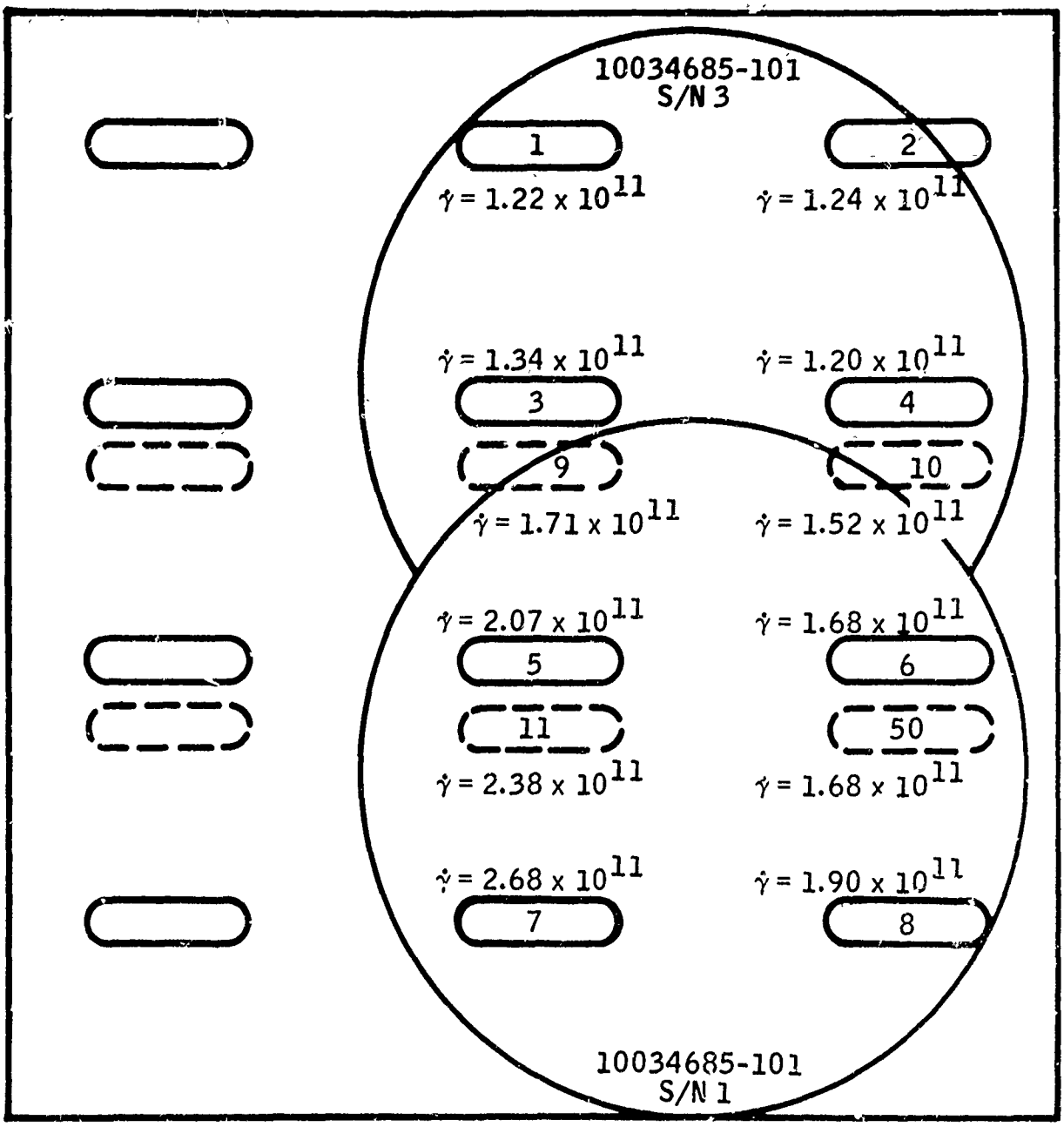

Digital Board Test - Dosimetry Data (Shot No. 8)

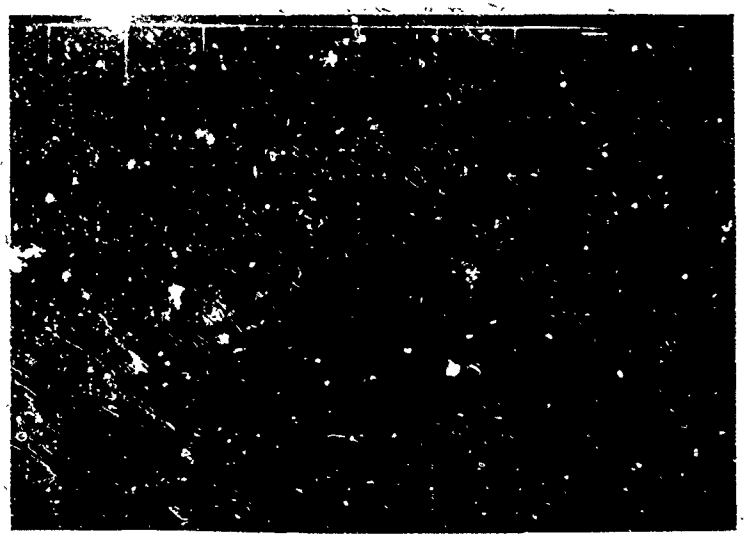

VOLTS/CM 2 SWEEP/CM 0.1 usec

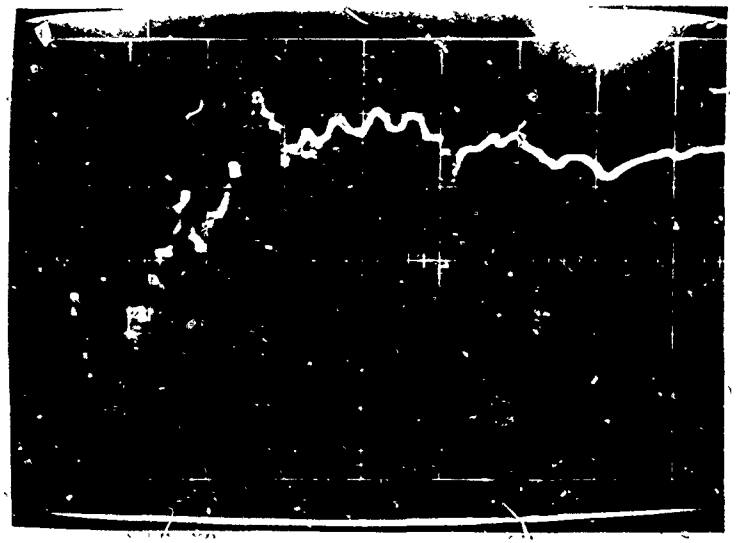

VOLTS/CM 2 SWEEP/CM 1 usec

TEST NO. 8 - 1, 2, 3, 4: DIGITAL ELECTRONICS - FAST DIGITAL PULSE

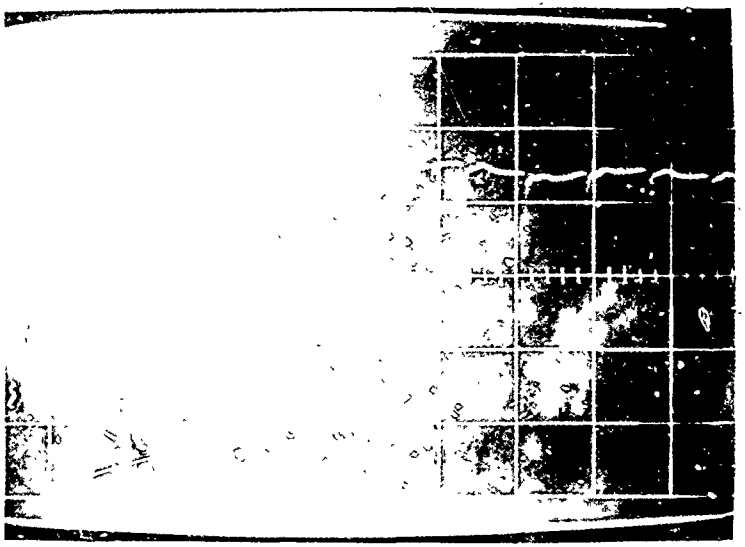

VOLTS/CM 2 SWEEP/CM 5 usec

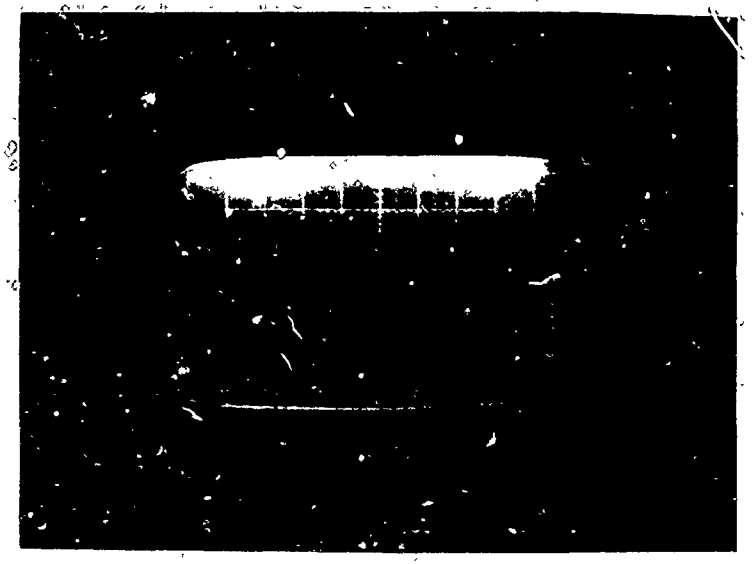

VOLTS/CM 2 SWEEP/CM 20 usec

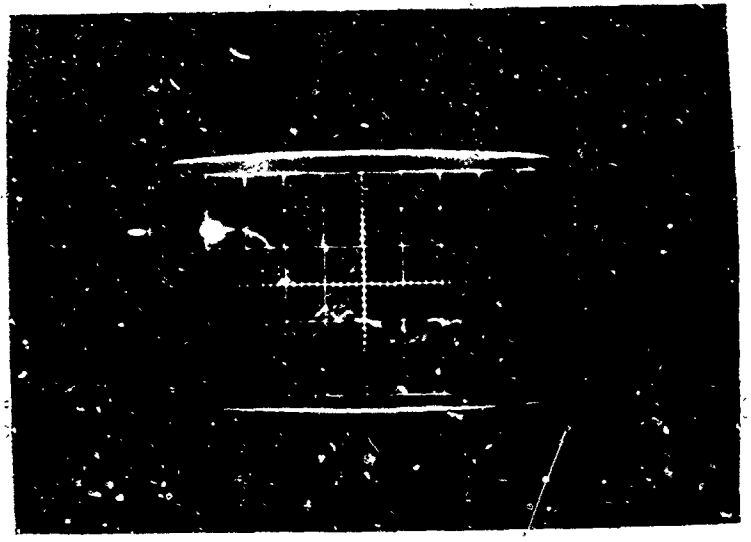

VOLTS/CM 2 SWEEP/CM 0.1 usec

VOLTS/CM 2 SWEEP/CM 1 usec

TEST NO. 8 - 5, 6, 7, 8: DIGITAL ELECTRONICS - FAST DIGITAL PULSE

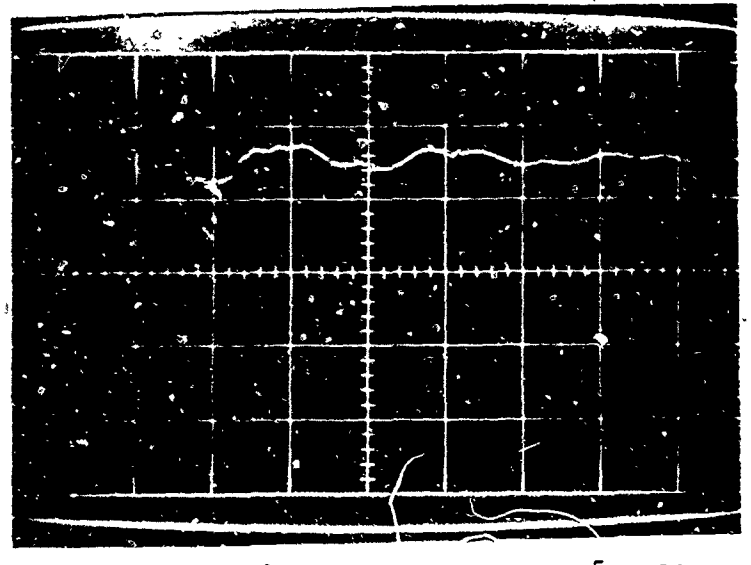

VOLTS/CM 2 SWEEP/CM 5 usec

VOLTS/CM 2 SWEEP/CM 20 usec

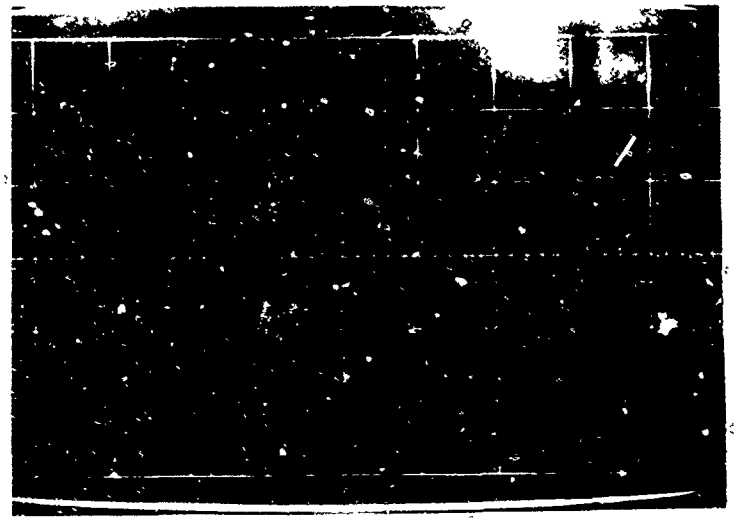

VOLTS/CM 5 SWEEP/CM 0.1 usec

VOLTS/CM 5 SWEEP/CM 1 usec

TEST NO. 8 - 9, 10, 11, 12: DIGITAL ELECTRONICS - SLOW DIGITAL PULSE

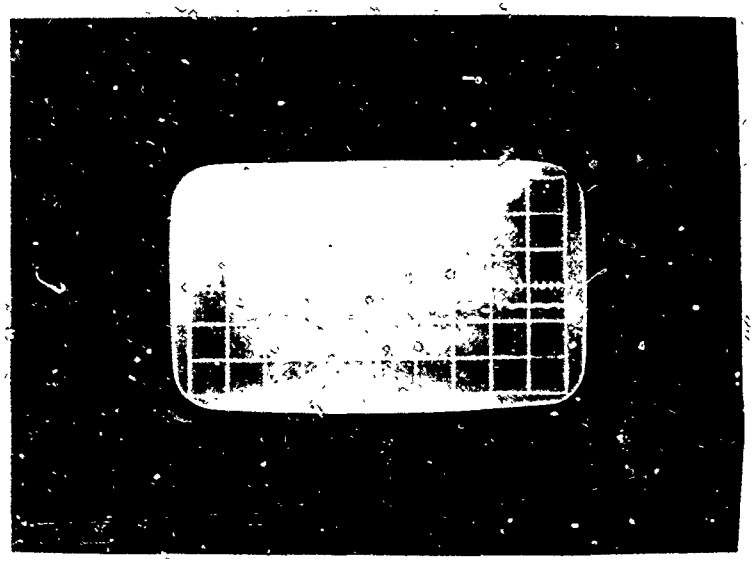

VOLTS/CM 5 SWEEP/CM 10 usec

VOLTS/CM 5 SWEEP/CM 100 usec

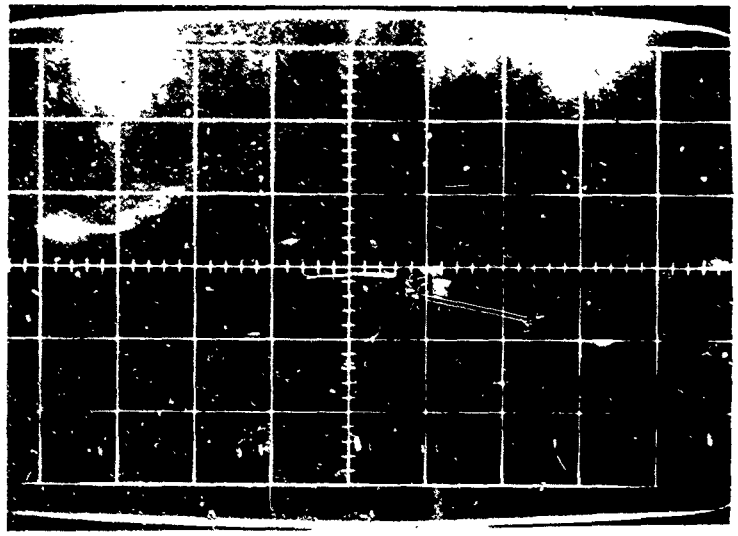

VOLTS/CM 5 SWEEP/CM 0.1 usec

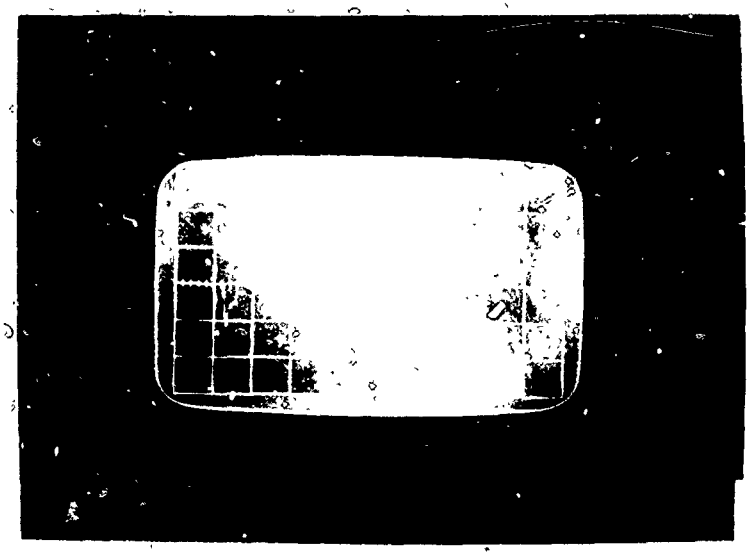

VOLTS/CM 5 SWEEP/CM 1 usec

TEST NO. 8 - 13, 14, 15, 16: DIGITAL ELECTRONICS - SLOW DIGITAL PULSE

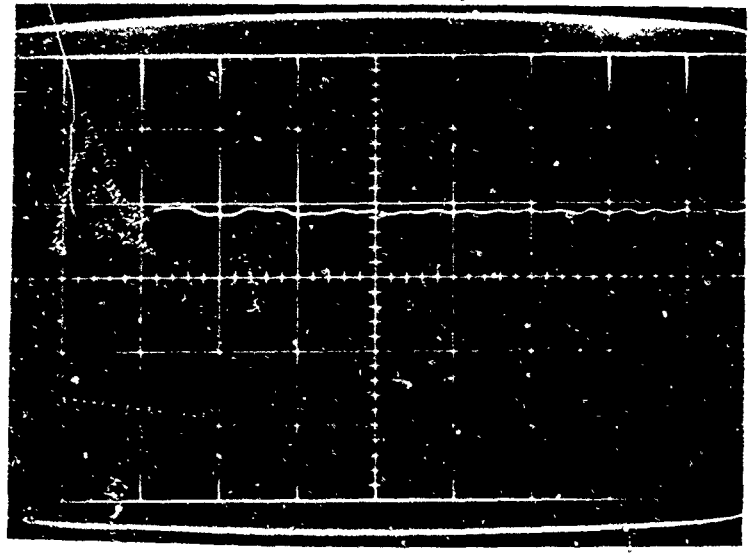

VOLTS/CM 5 SWEEP/CM 10 usec

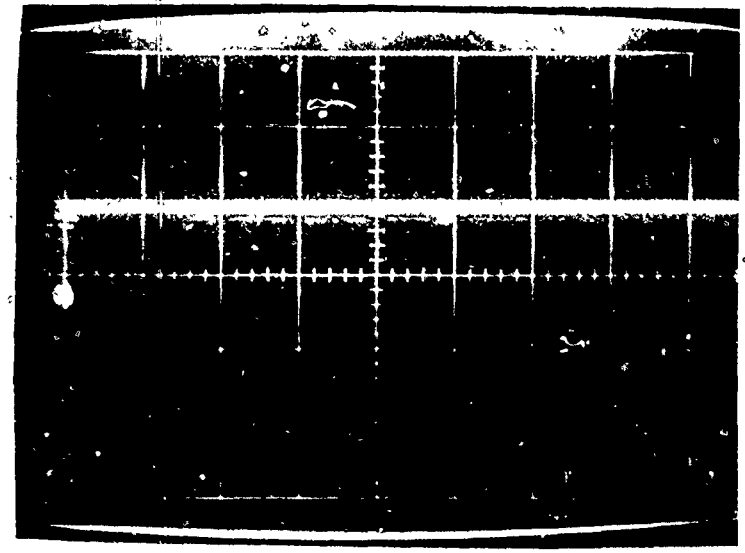

VOLTS/CM 5 SWEEP/CM 100 usec

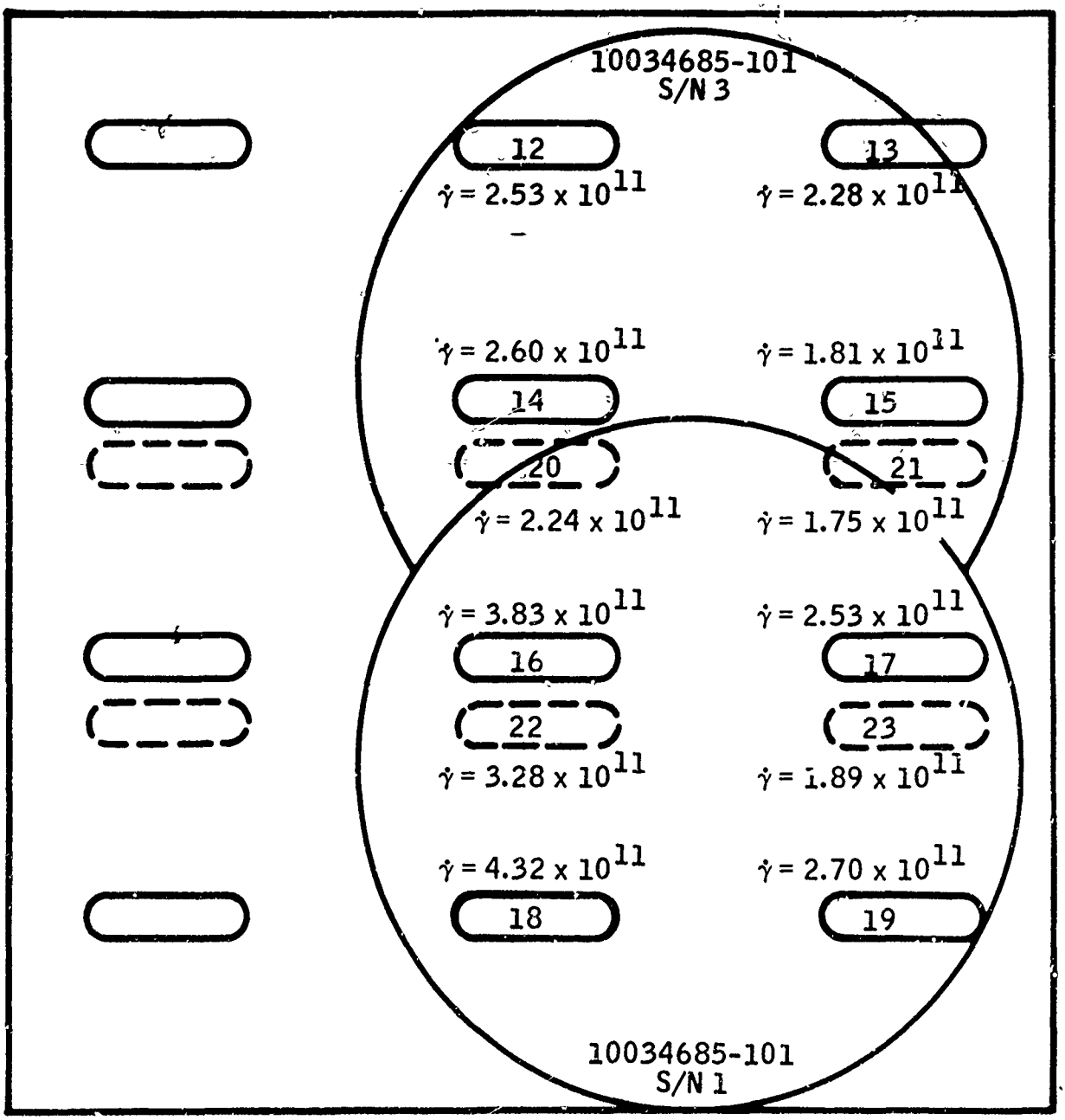

Digital Board Test - Dosimetry Data (Shot No. 9)

VOLTS/CM 2 SWEEP/CM 0.1 usec

VOLTS/CM 2 SWEEP/CM 1 usec

TEST NO. 9 - 1, 2, 3, 4: DIGITAL ELECTRONICS - FAST DIGITAL PULSE

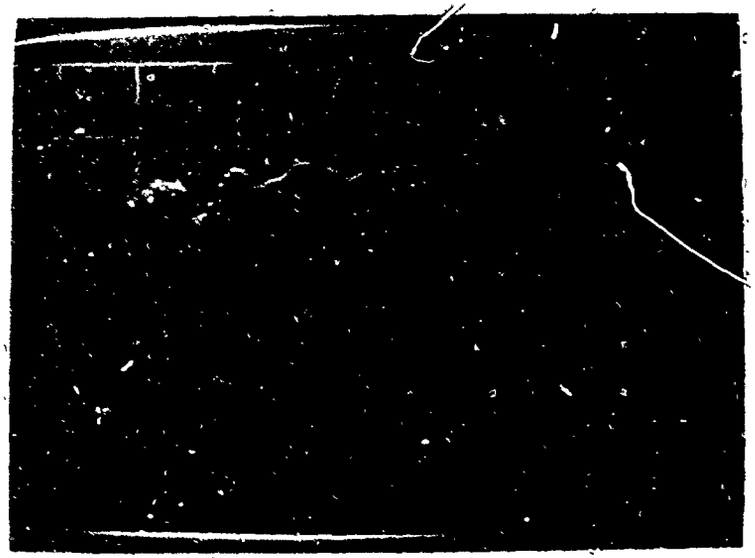

VOLTS/CM 2 SWEEP/CM 5 usec

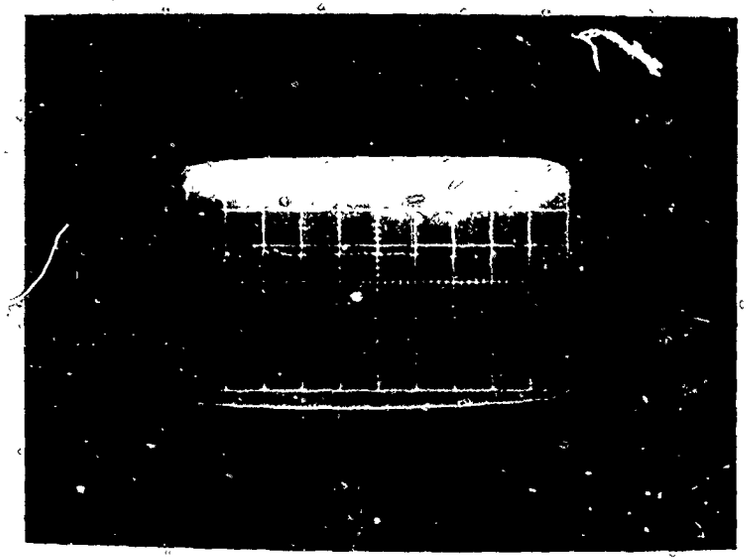

VOLTS/CM 2 SWEEP/CM 20 usec

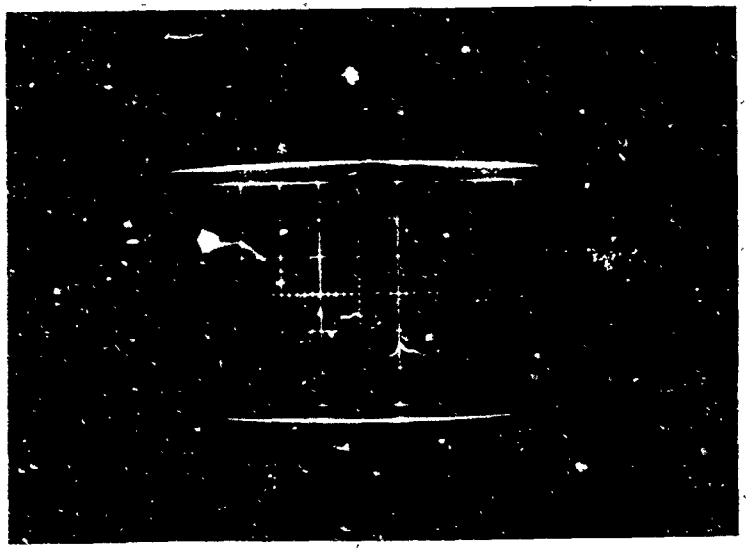

VOLTS/CM 2 SWEEP/CM 0.1 usec

VOLTS/CM 2 SWEEP/CM 1 usec

TEST NO. 9 - 5, 6, 7, 8: DIGITAL ELECTRONICS - FAST DIGITAL PULSE

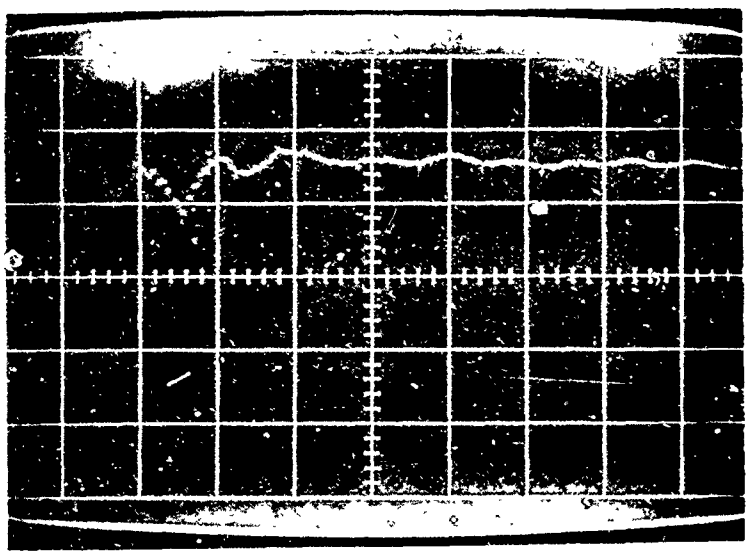

VOLTS/CM 2 SWEEP/CM 5 usec

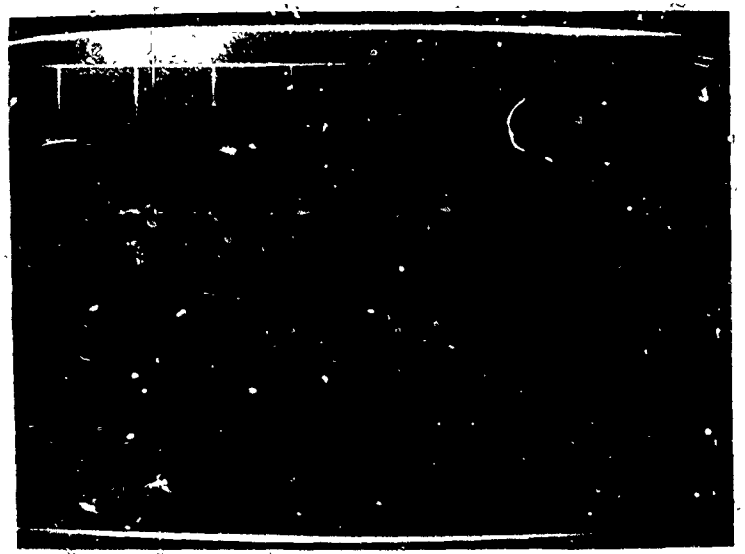

VOLTS/CM 2 SWEEP/CM 20 usec

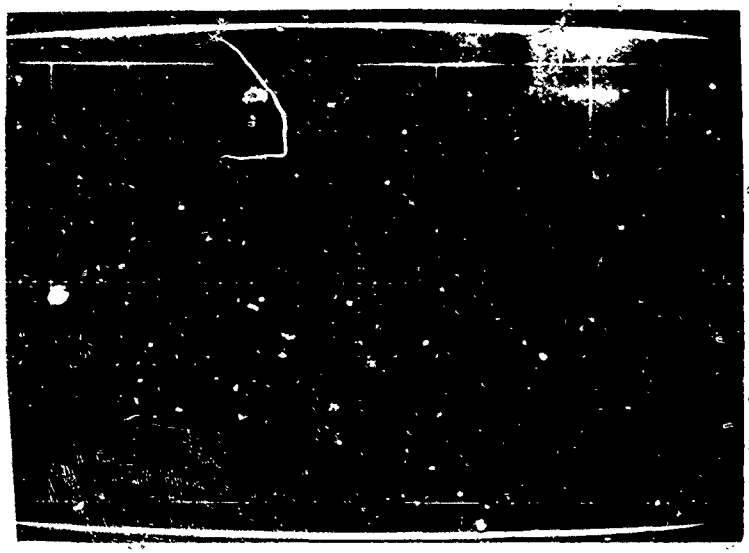

VOLTS/CM 5 SWEEP/CM 0.1 usec

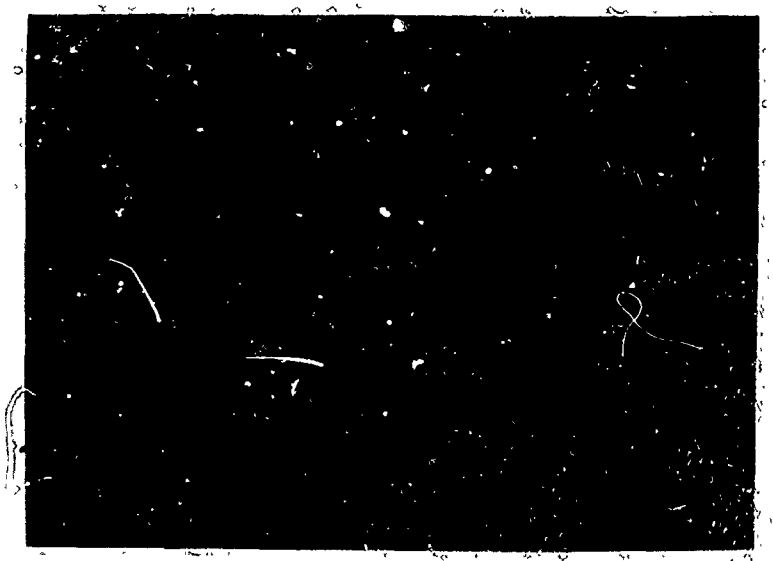

VOLTS/CM 5 SWEEP/CM 1 usec

TEST NO. 9 - 9, 10, 11, 12: DIGITAL ELECTRONICS - SLOW DIGITAL PULSE

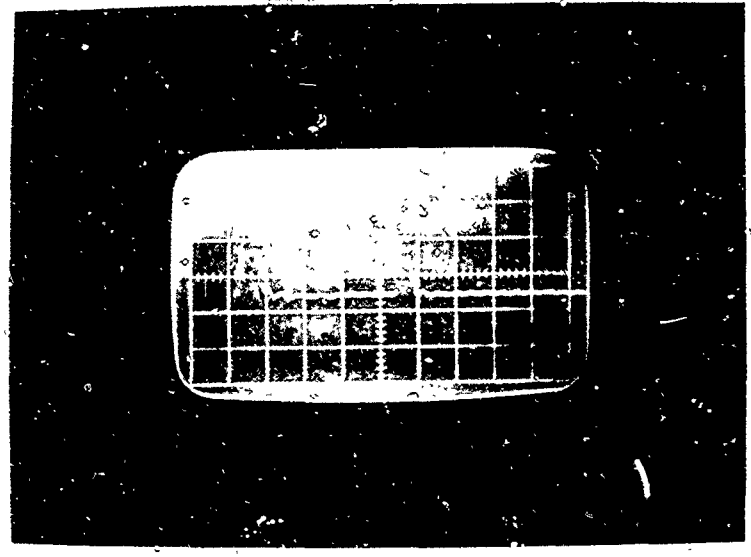

VOLTS/CM 5 SWEEP/CM 10 usec

VOLTS/CM 5 SWEEP/CM 100 usec

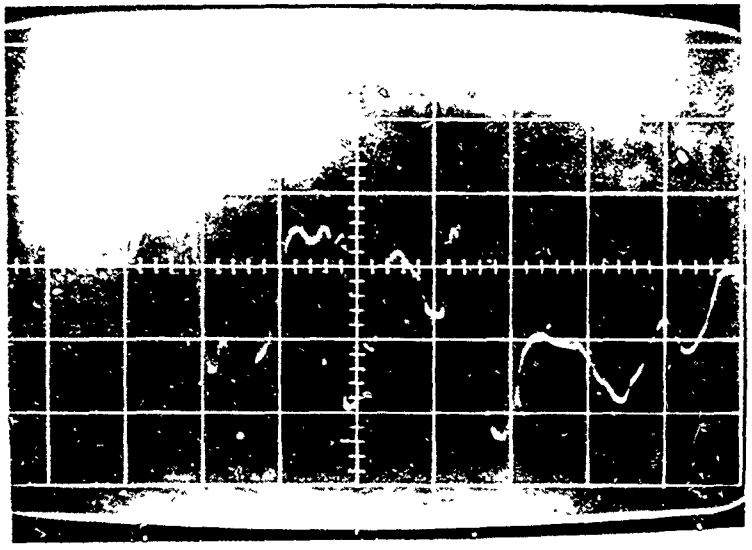

VOLTS/CM 5 SWEEP/CM 0.1 usec

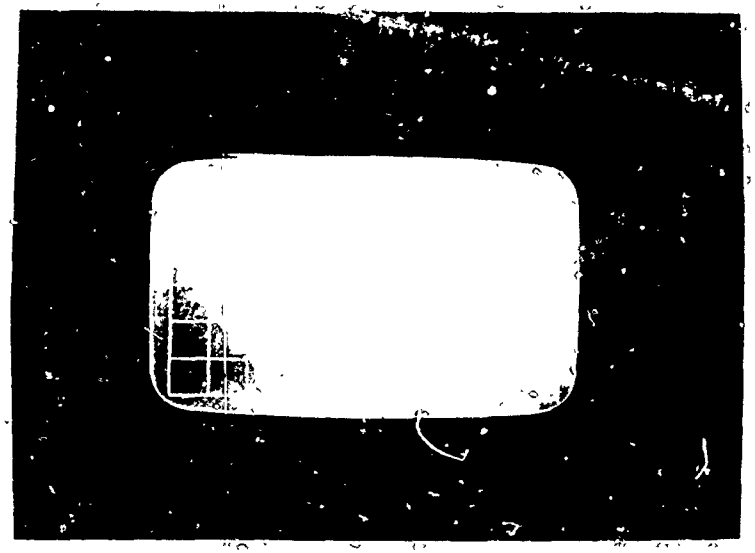

VOLTS/CM 5 SWEEP/CM 1 usec

TEST NO. 9 - 13, 14, 15, 16: DIGITAL ELECTRONICS - SLOW DIGITAL PULSE

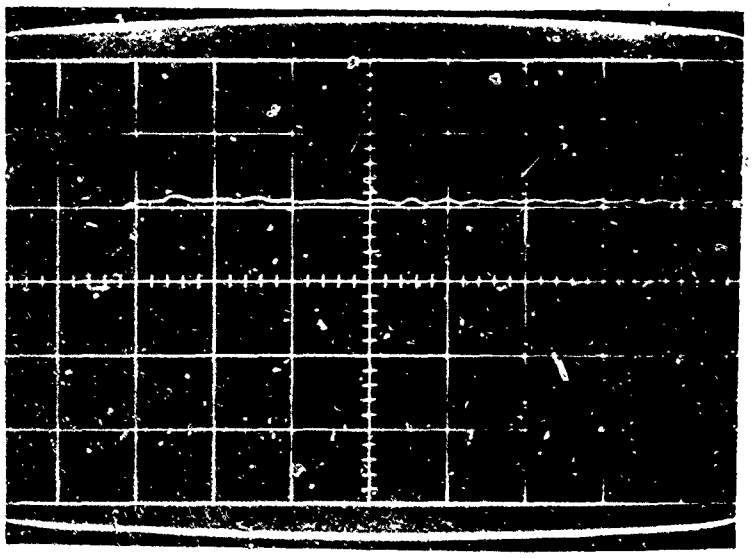

VOLTS/CM 5 SWEEP/CM 10 usec

VOLTS/CM 5 SWEEP/CM 100 usec

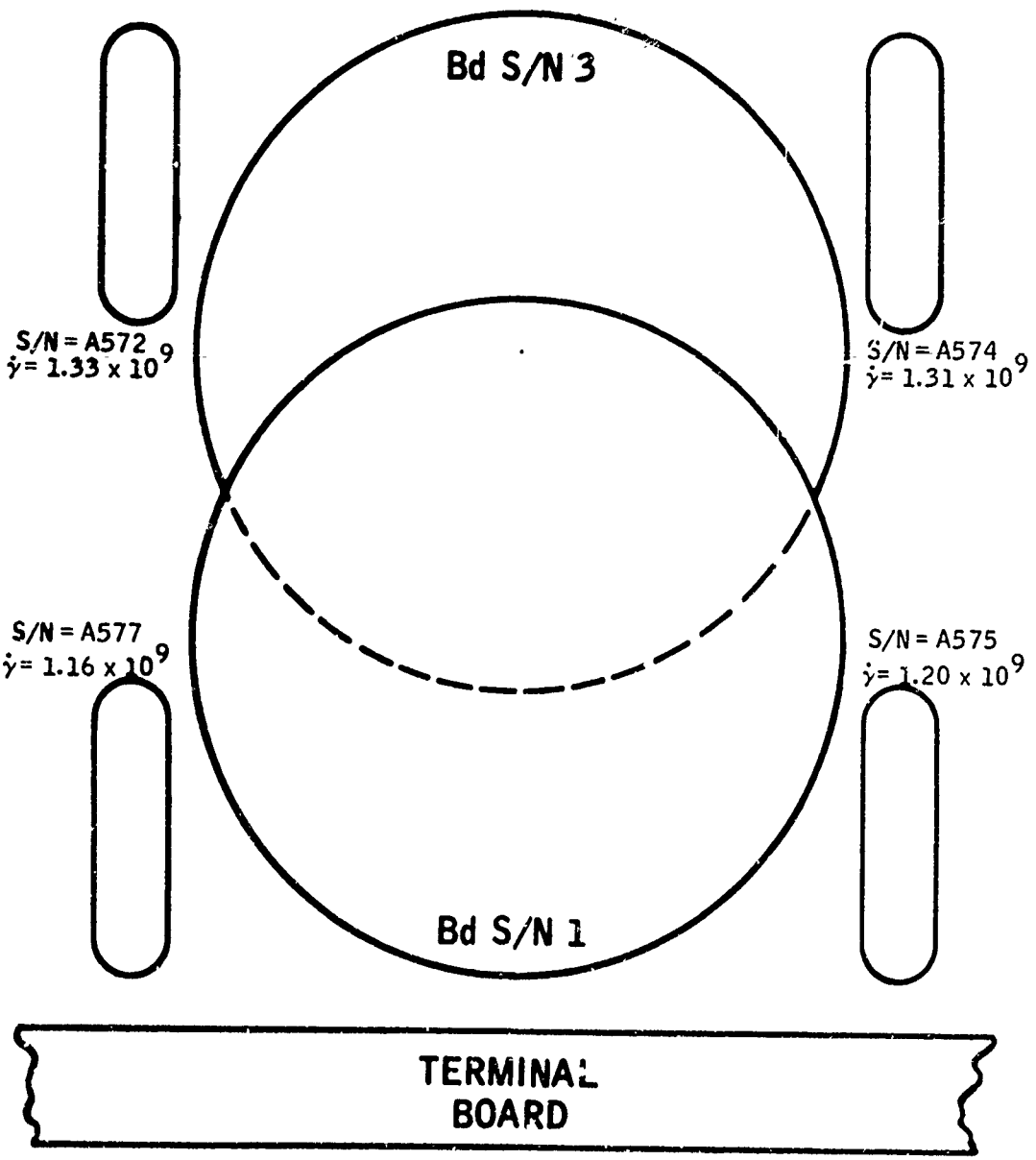

Digital Board Test - Dosimetry Data (Shot No. 10)

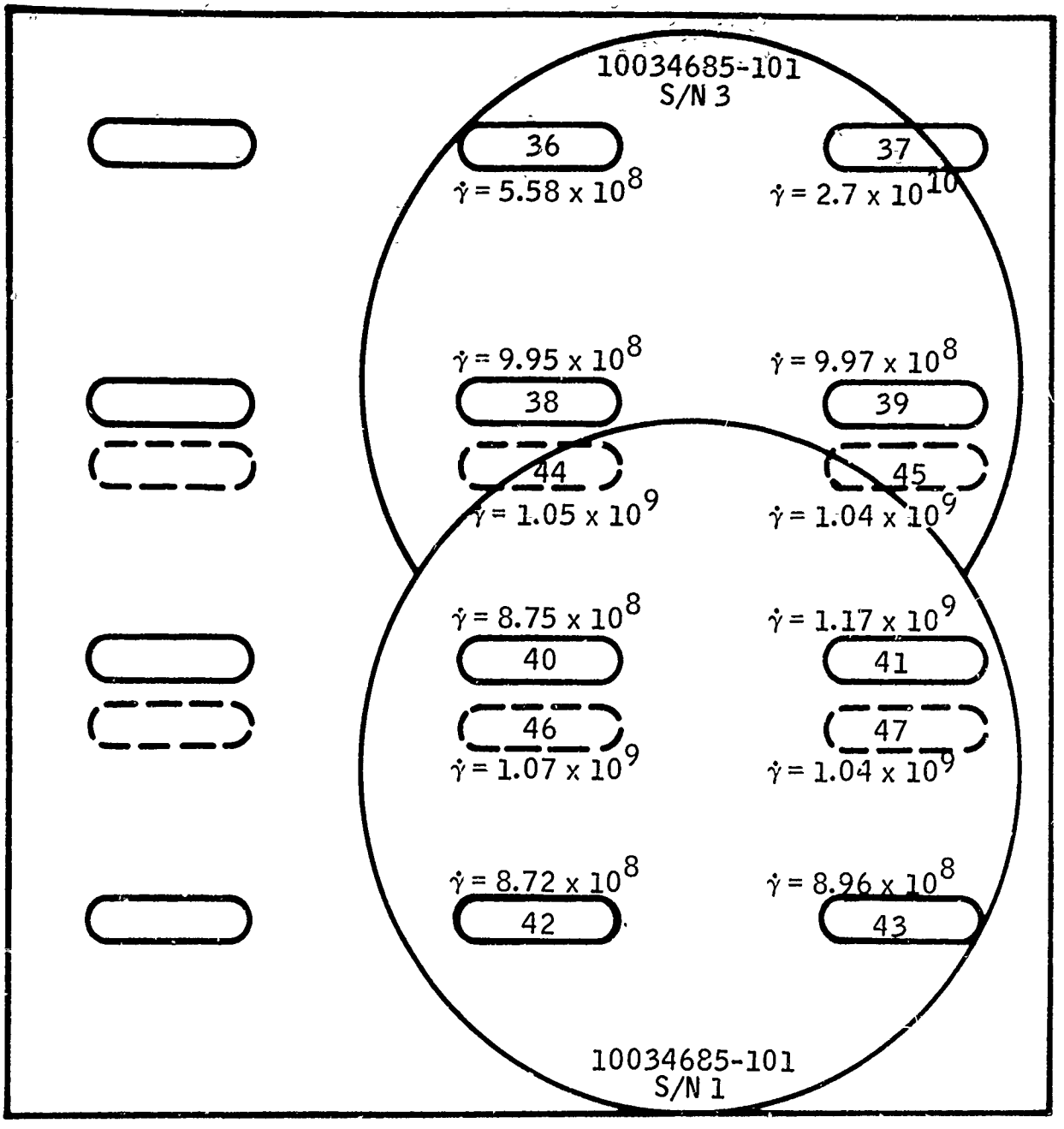

*This reading was considered to be in error and was omitted from Average Computation.

Digital Board Test - Dosimetry Data (Shot No. 11)
Sheet 1, Small Dosimeters

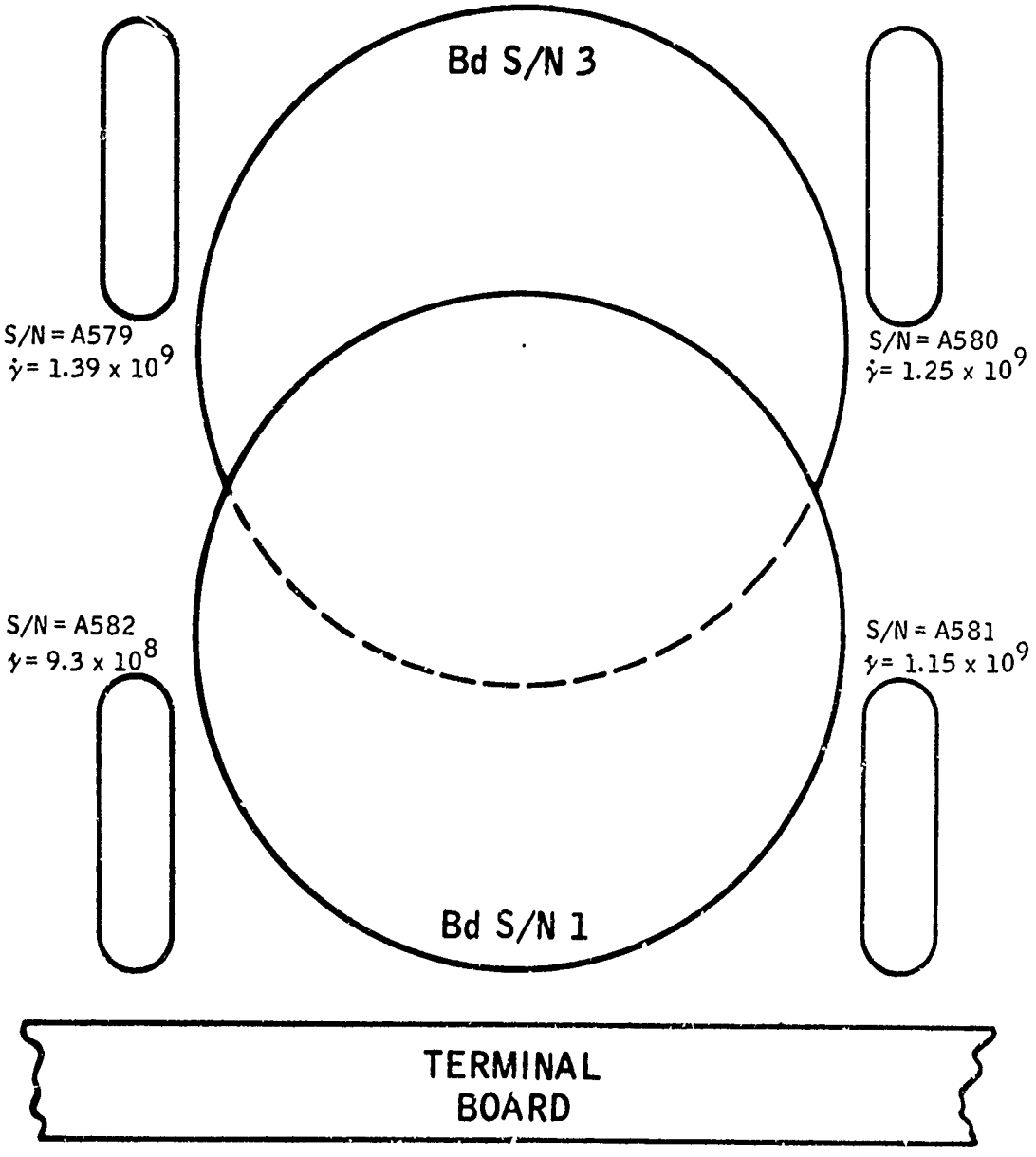

Digital Board Test - Dosimetry Data (Shot No. 11) - Sheet 2
Large Dosimeters

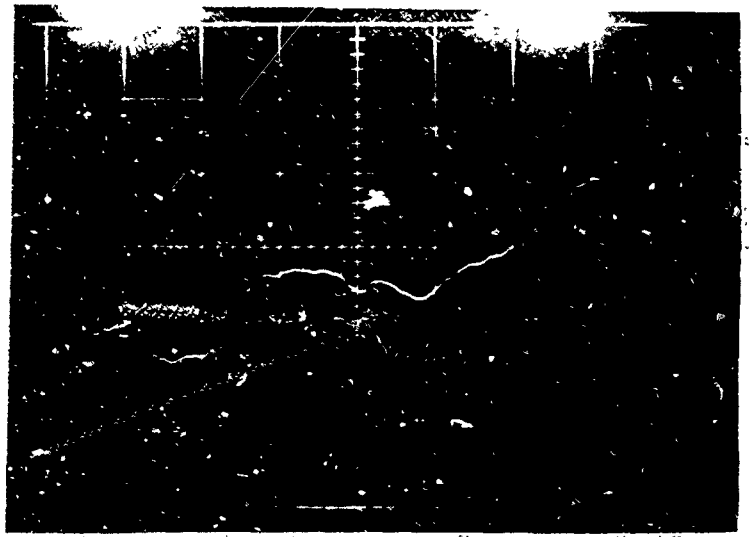

VOLTS/CM 2 SWEEP/CM 0.1 usec

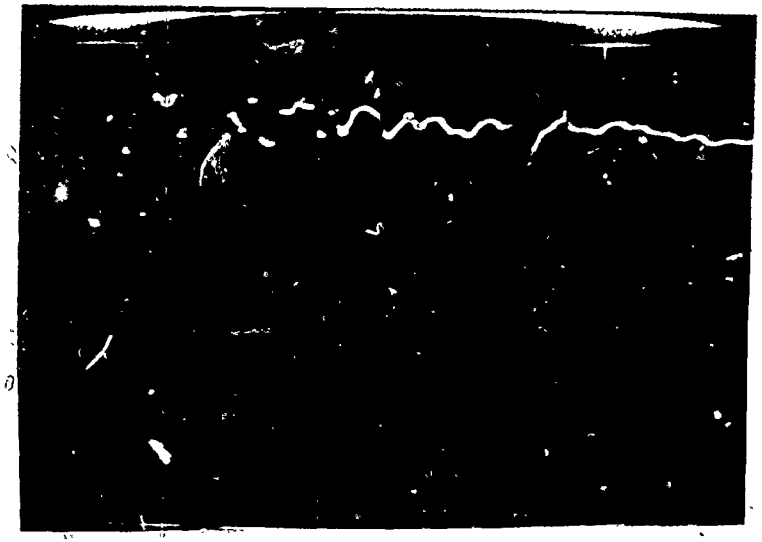

VOLTS/CM 2 SWEEP/CM 1 usec

TEST NO. 11 - 1, 2, 3, 4: DIGITAL ELECTRONICS - FAST DIGITAL PULSE

VOLTS/CM _____ SWEEP/CM _____

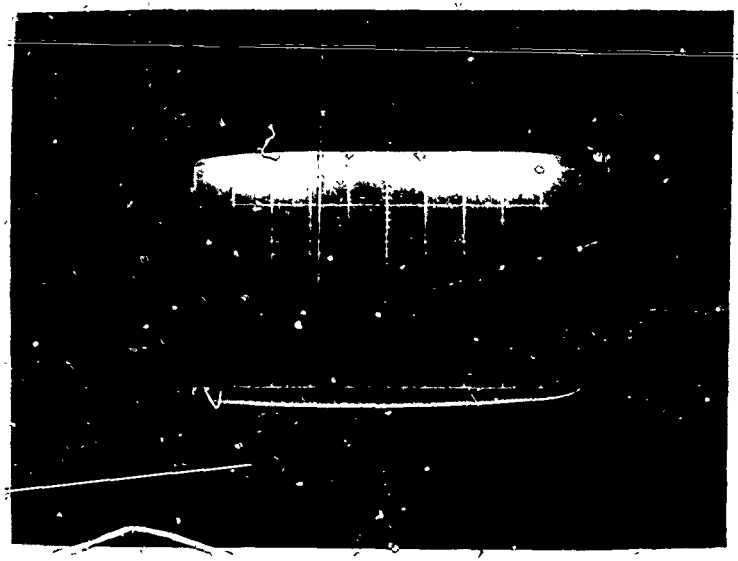

VOLTS/CM 2 SWEEP/CM 20 usec

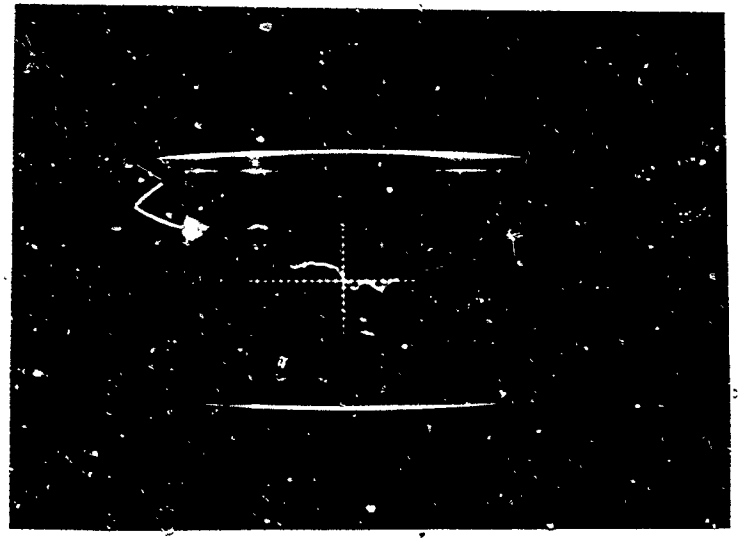

VOLTS/CM 2 SWEEP/CM .1 usec

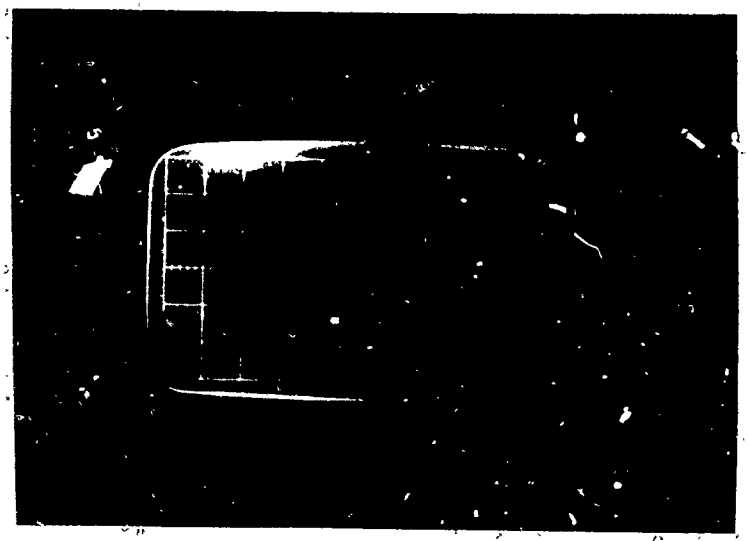

VOLTS/CM 2 SWEEP/CM 10 usec

TEST NO. 11 - 5, 6, 7, 8: DIGITAL ELECTRONICS - FAST DIGITAL PULSE

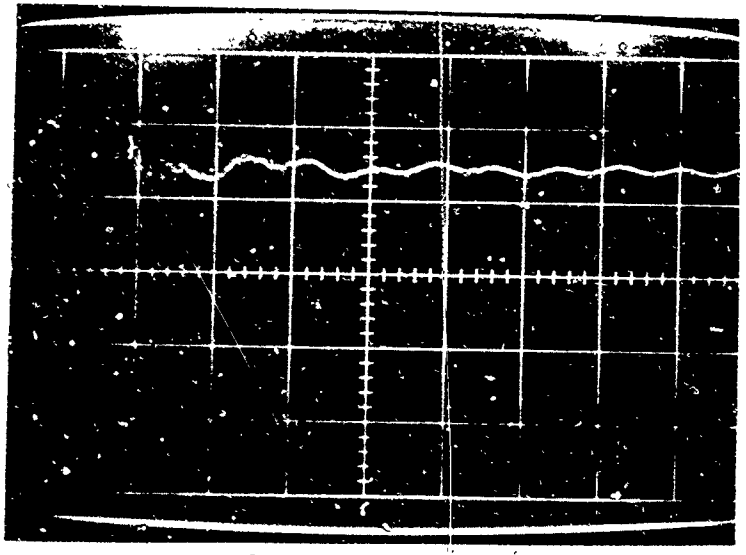

VOLTS/CM 2 SWEEP/CM 5 usec

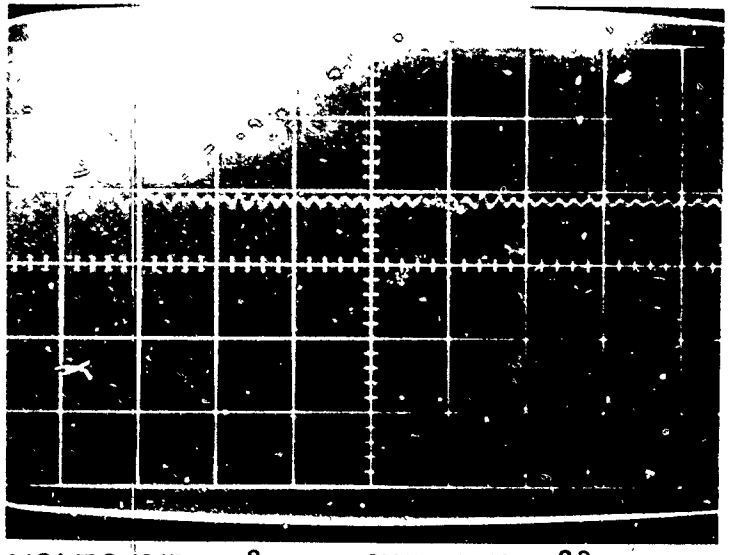

VOLTS/CM 2 SWEEP/CM 20 usec

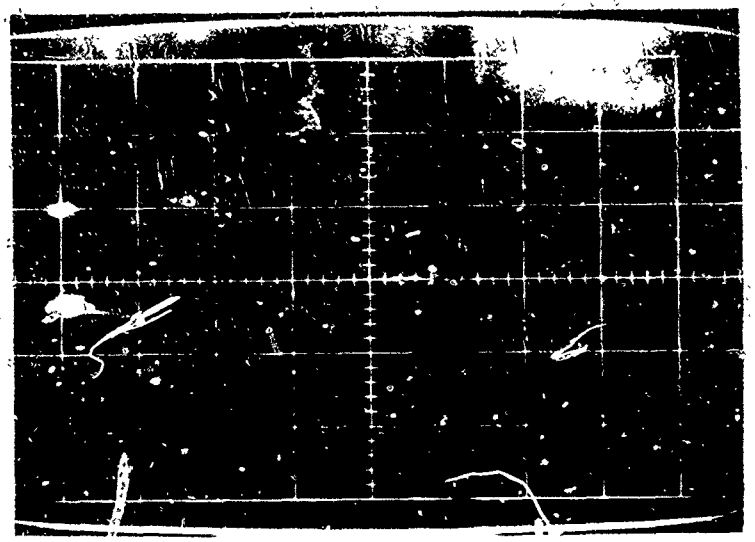

VOLTS/CM 5 SWEEP/CM .1 usec

VOLTS/CM 5 SWEEP/CM 1 usec

TEST NO. 11 - 9, 10, 11, 12: DIGITAL ELECTRONICS - SLOW DIGITAL PULSE

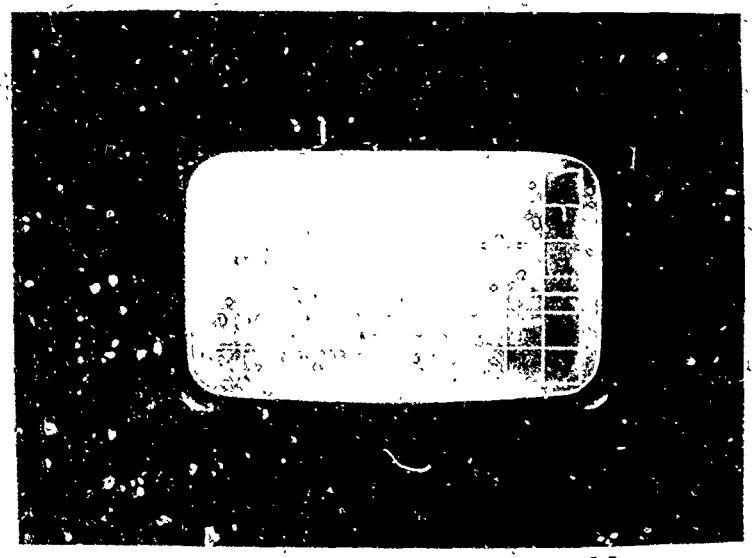

VOLTS/CM 5 SWEEP/CM 10 usec

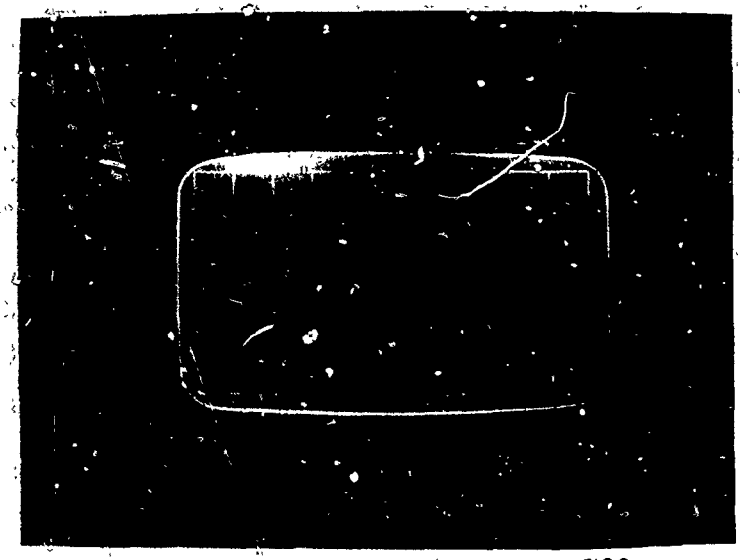

VOLTS/CM 5 SWEEP/CM 100 usec

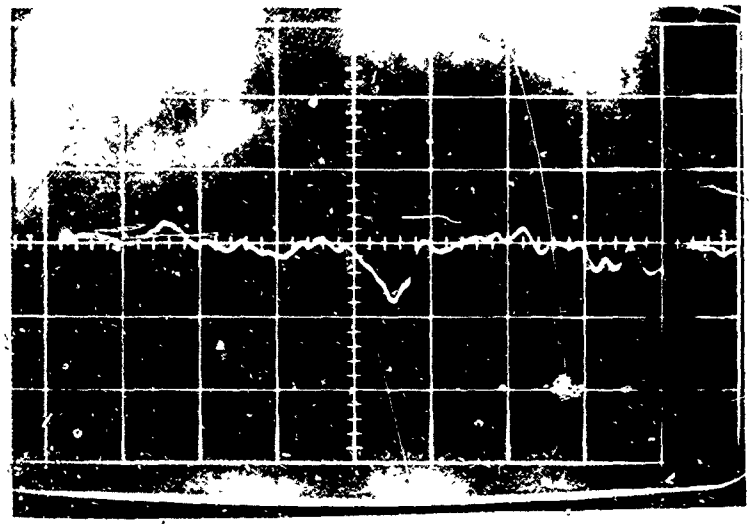

VOLTS/CM 5 SWEEP/CM .1 usec

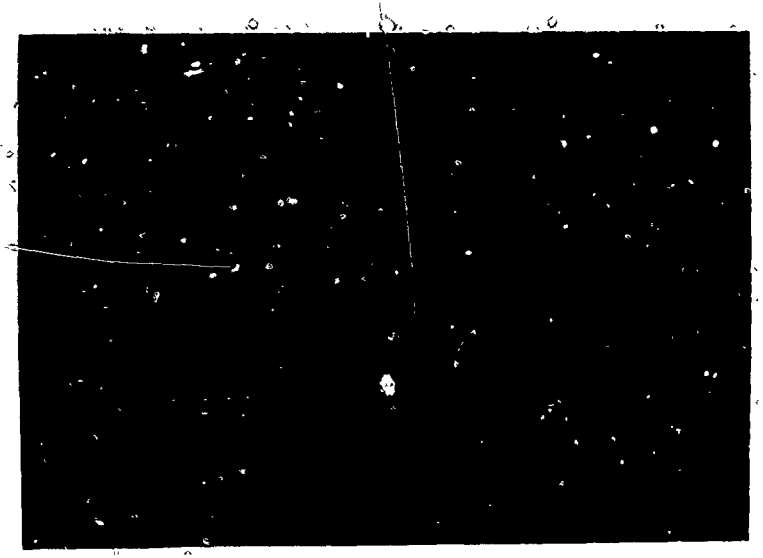

VOLTS/CM 5 SWEEP/CM 1 usec

TEST NO. 11 - 13, 14, 15, 16: DIGITAL ELECTRONICS - SLOW DIGITAL PULSE

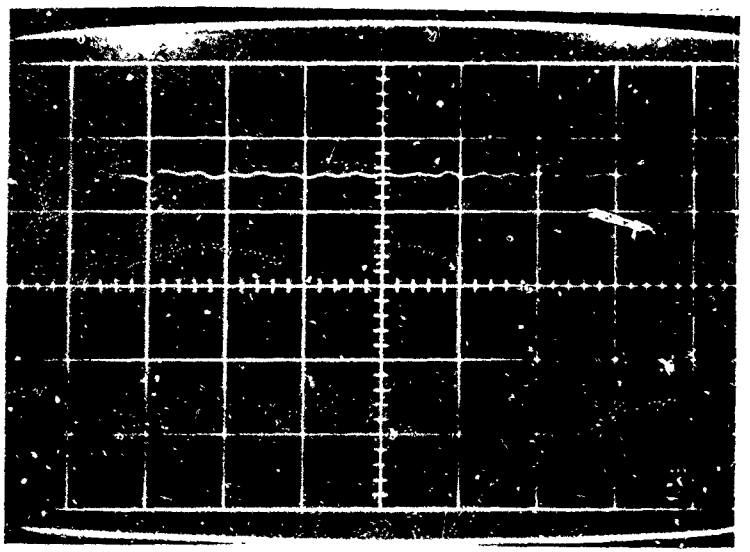

VOLTS/CM 5 SWEEP/CM 10 usec

VOLTS/CM 5 SWEEP/CM 100 usec

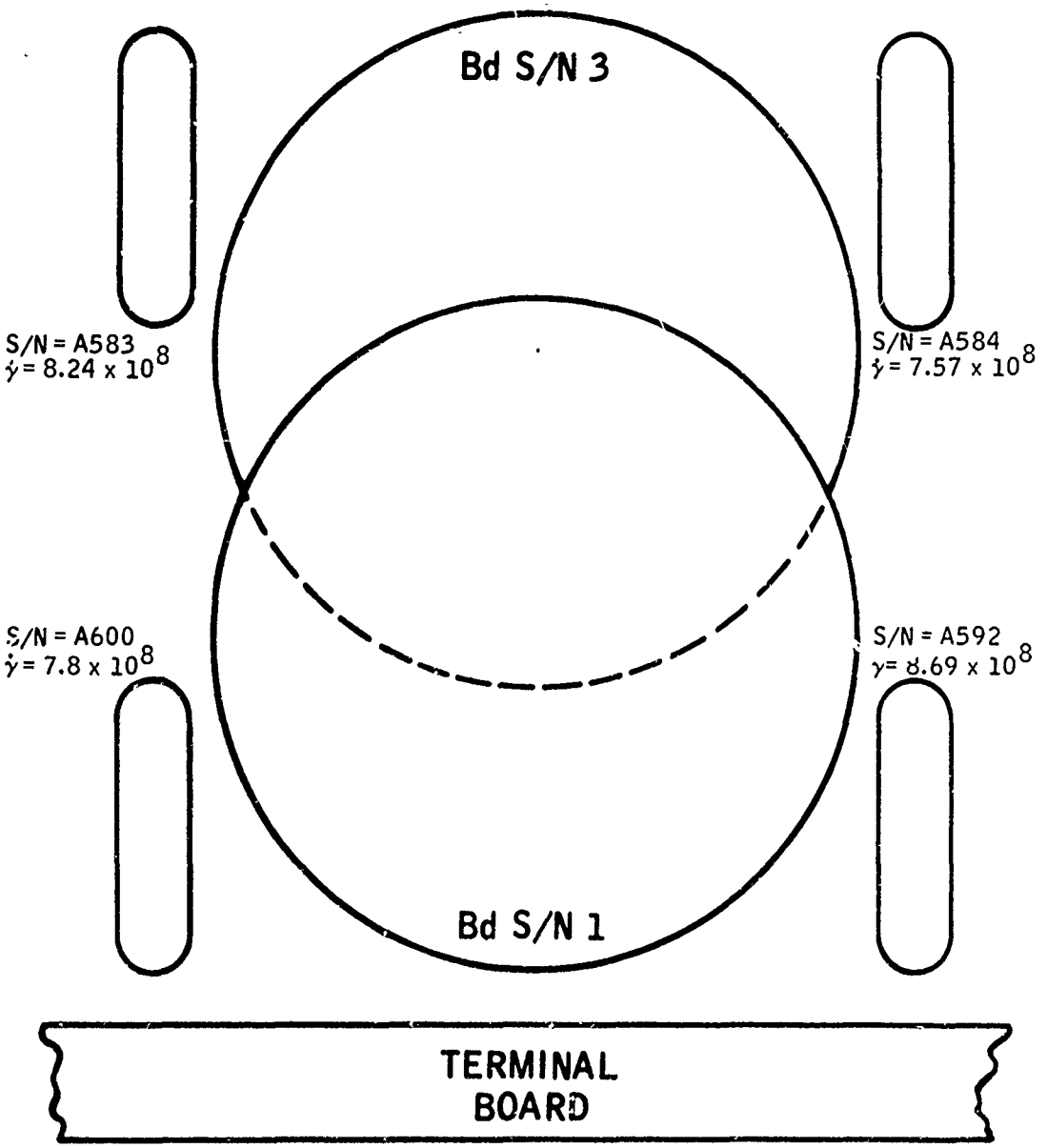

Digital Electronics Dosimetry (Shot No. 12)

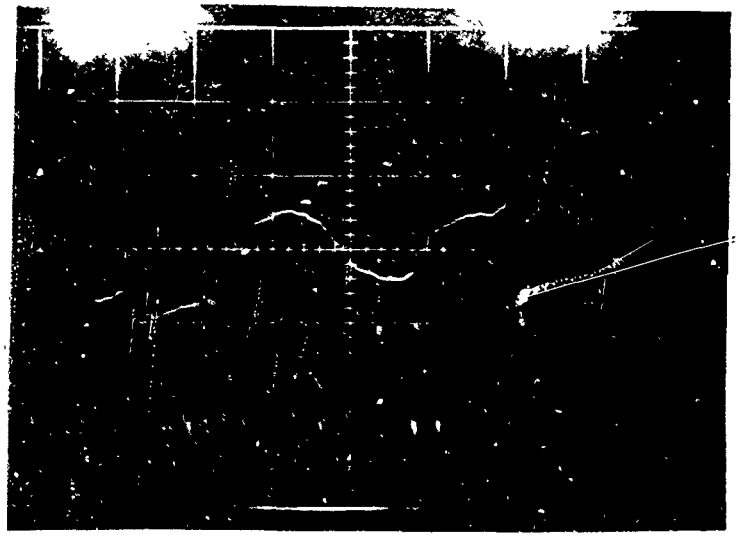

VOLTS/CM 2 SWEEP/CM 0.1 usec

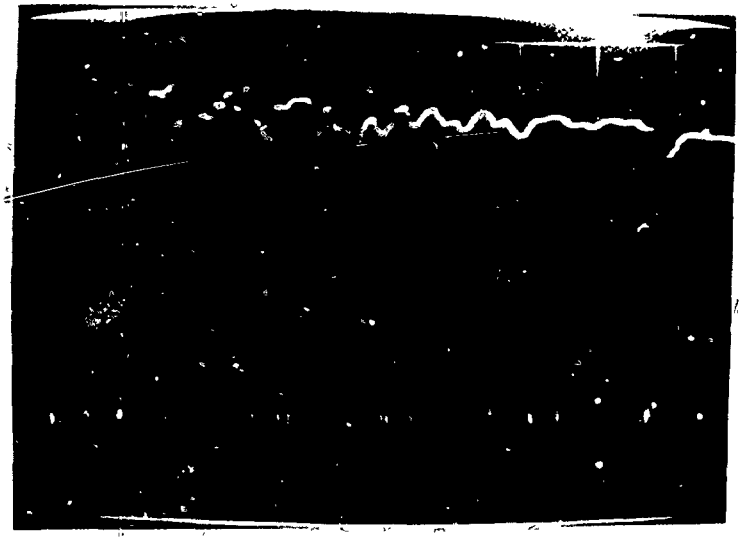

VOLTS/CM 2 SWEEP/CM 1 usec

TEST NO. 12 - 1, 2, 3, 4: DIGITAL ELECTRONICS - FAST DIGITAL PULSE

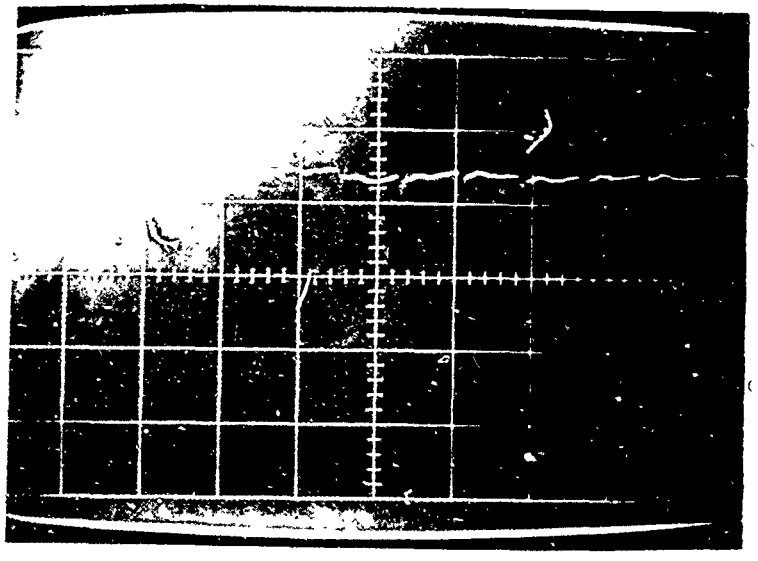

VOLTS/CM 2 SWEEP/CM 5 usec

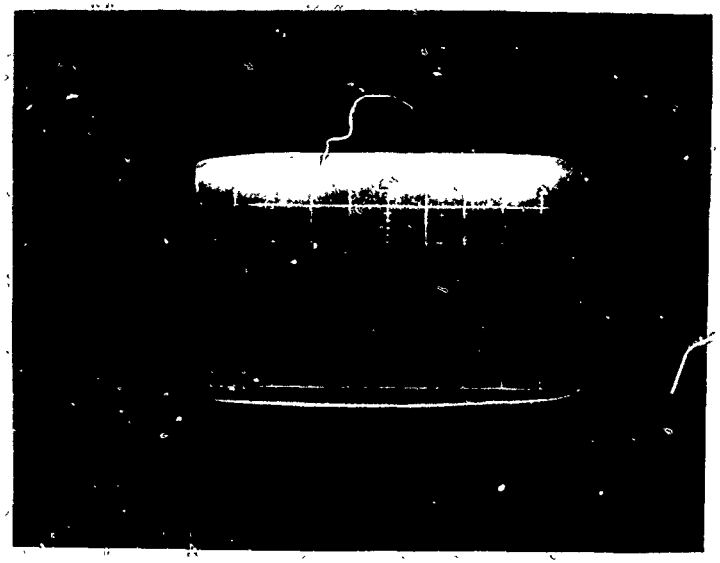

VOLTS/CM 2 SWEEP/CM 20 usec

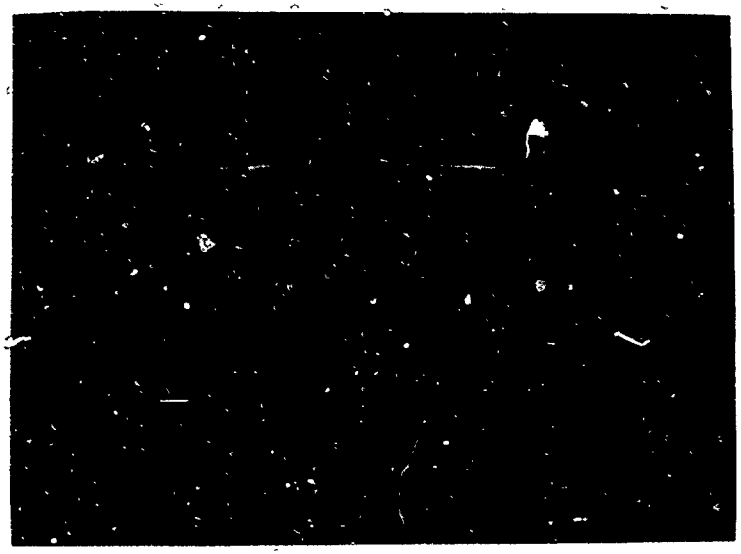

VOLTS/CM 2 SWEEP/CM 0.1 usec

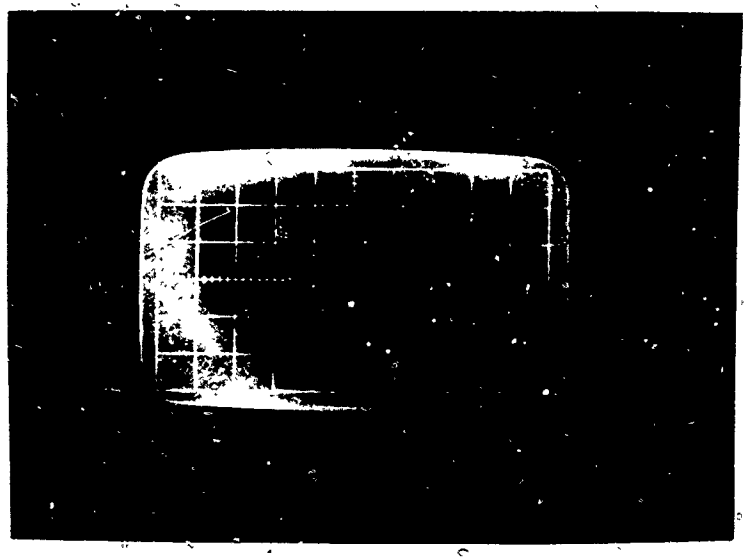

VOLTS/CM 2 SWEEP/CM 1 usec

TEST NO. 12 - 5, 6, 7, 8: DIGITAL ELECTRONICS - FAST DIGITAL PULSE

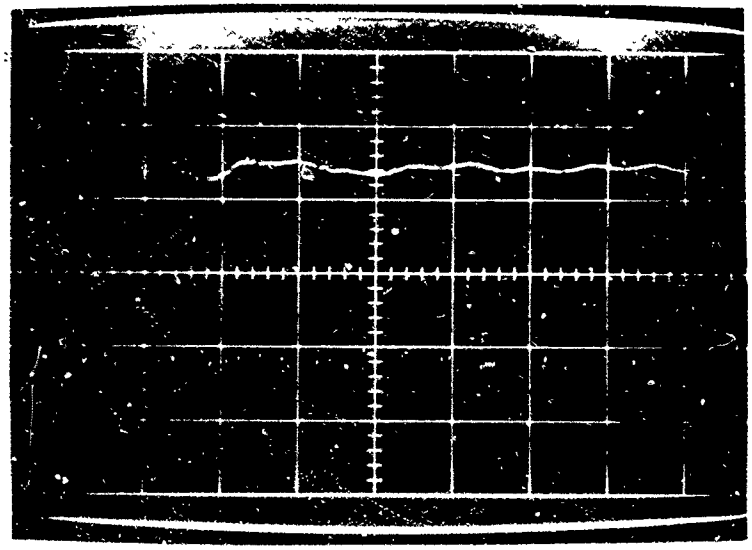

VOLTS/CM 2 SWEEP/CM 5 usec

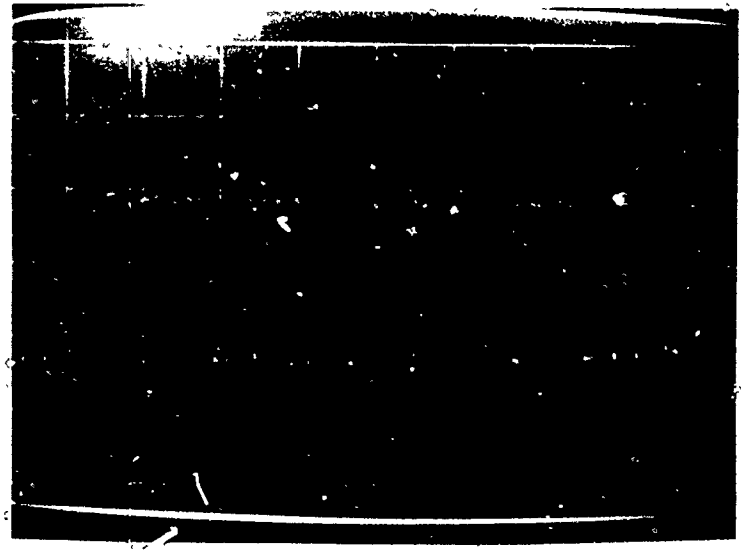

VOLTS/CM 2 SWEEP/CM 20 usec

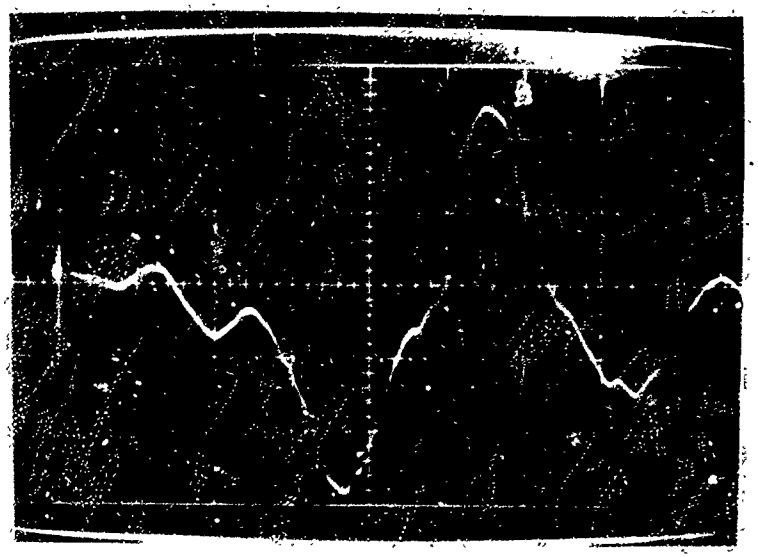

VOLTS/CM 5 SWEEP/CM 0.1 usec

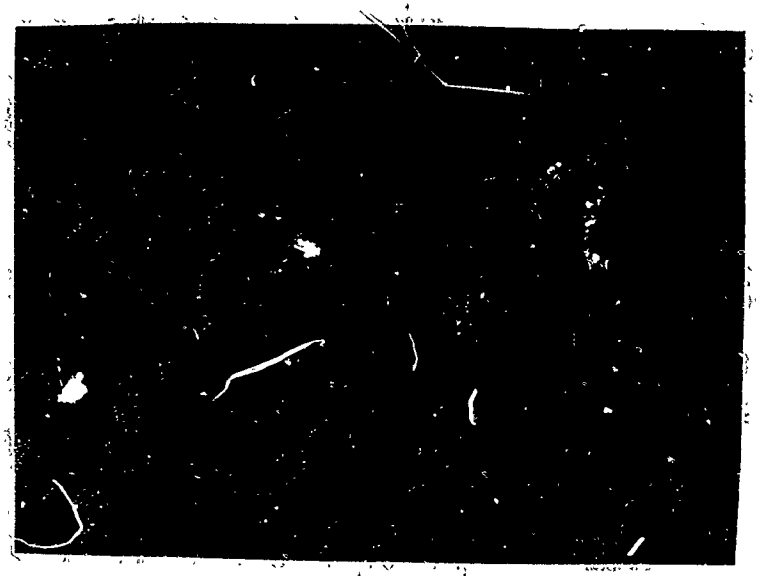

VOLTS/CM 5 SWEEP/CM 1 usec

TEST NO. 12 - 9, 10, 11, 12: DIGITAL ELECTRONICS - SLOW DIGITAL PULSE

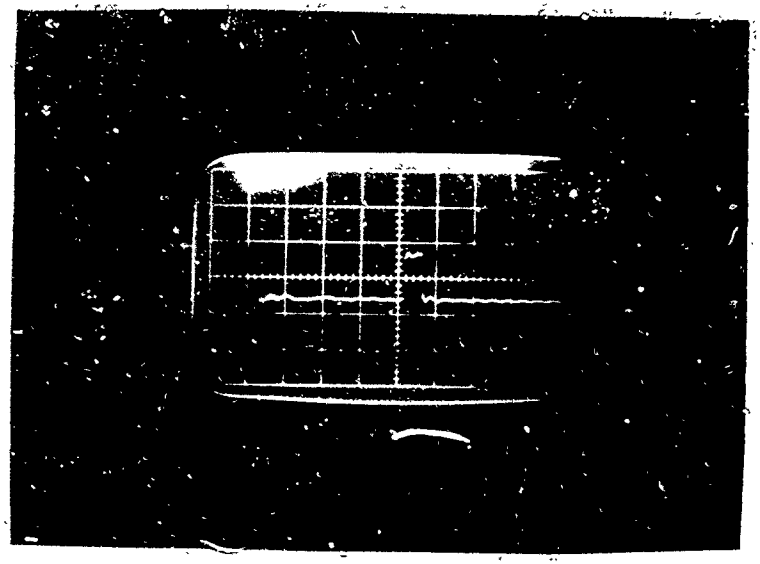

VOLTS/CM 5 SWEEP/CM 10 usec

VOLTS/CM 5 SWEEP/CM 100 usec

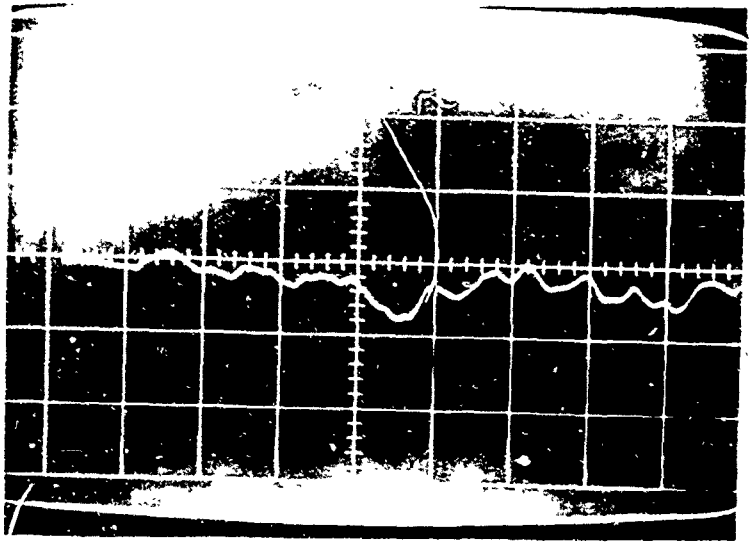

VOLTS/CM 5 SWEEP/CM 0.1 usec

VOLTS/CM 5 SWEEP/CM 1 usec

TEST NO. 12 - 13, 14, 15, 16: DIGITAL ELECTRONICS - SLOW DIGITAL PULSE

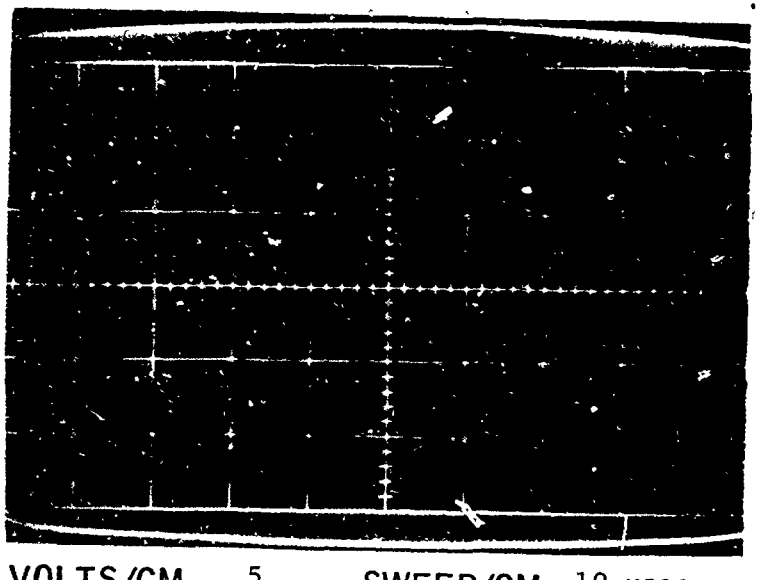

VOLTS/CM 5 SWEEP/CM 10 usec

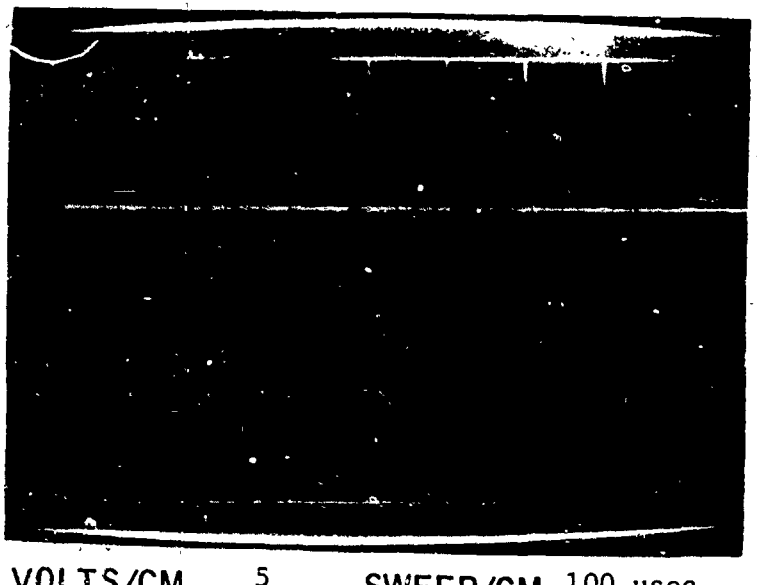

VOLTS/CM 5 SWEEP/CM 100 usec

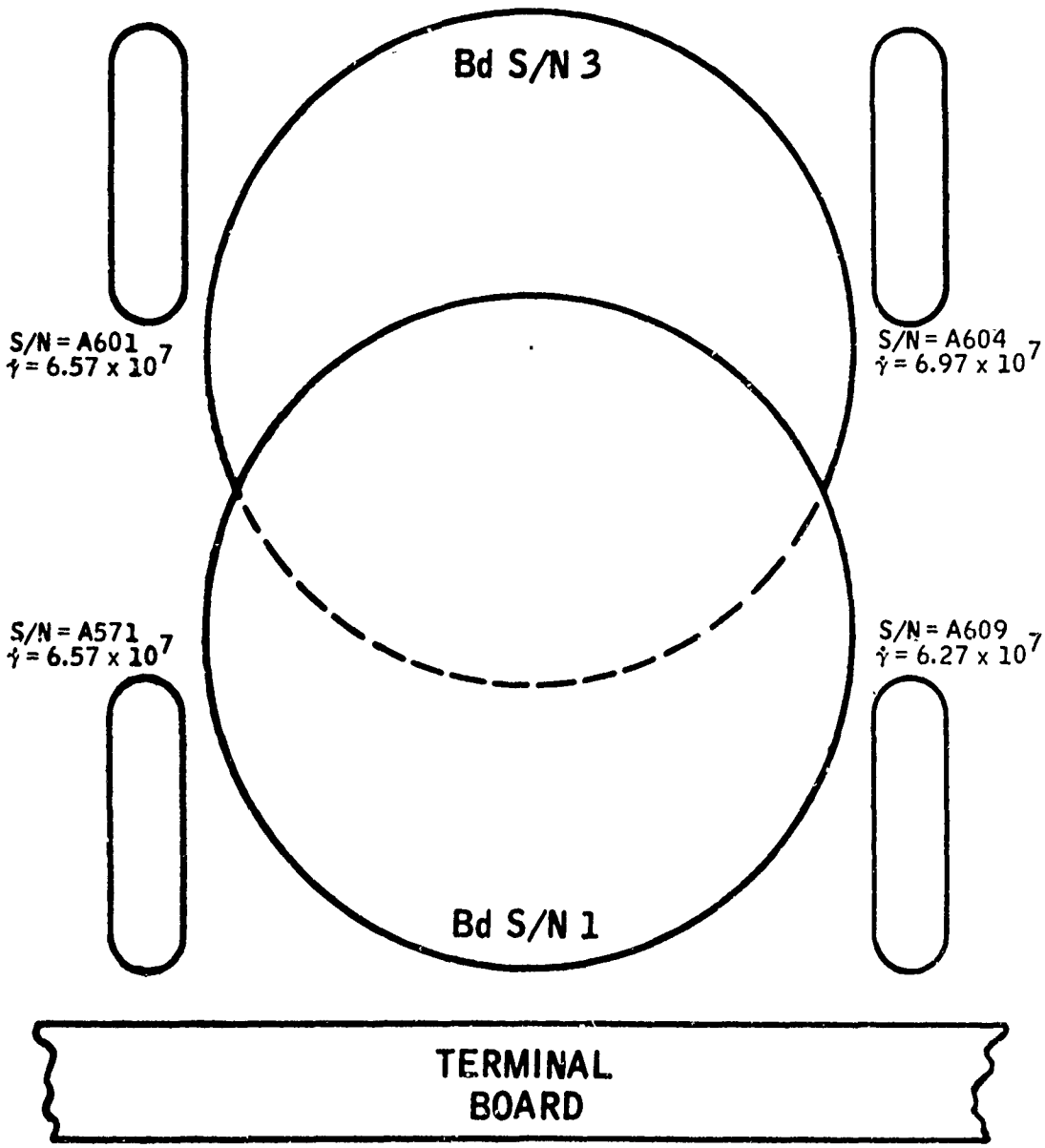

Digital Electronics Dosimetry (Shot No. 13)

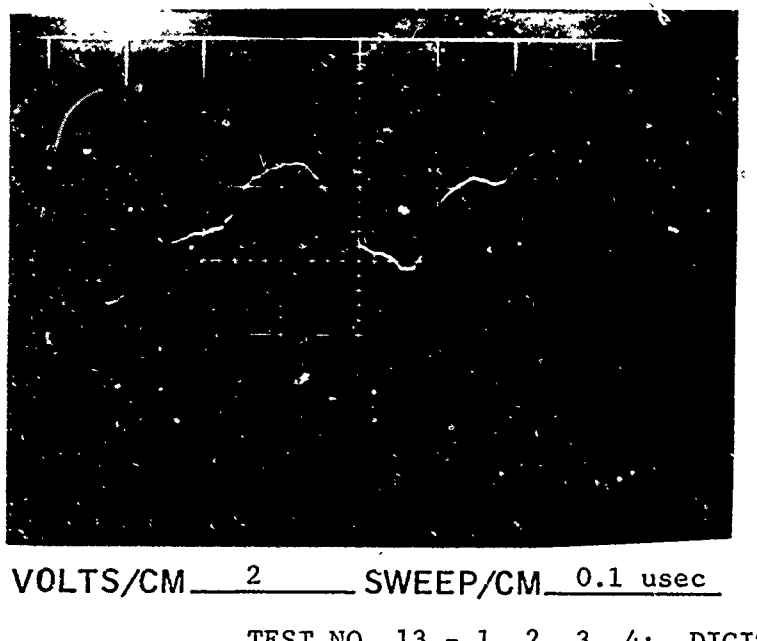

VOLTS/CM 2 SWEEP/CM 0.1 usec

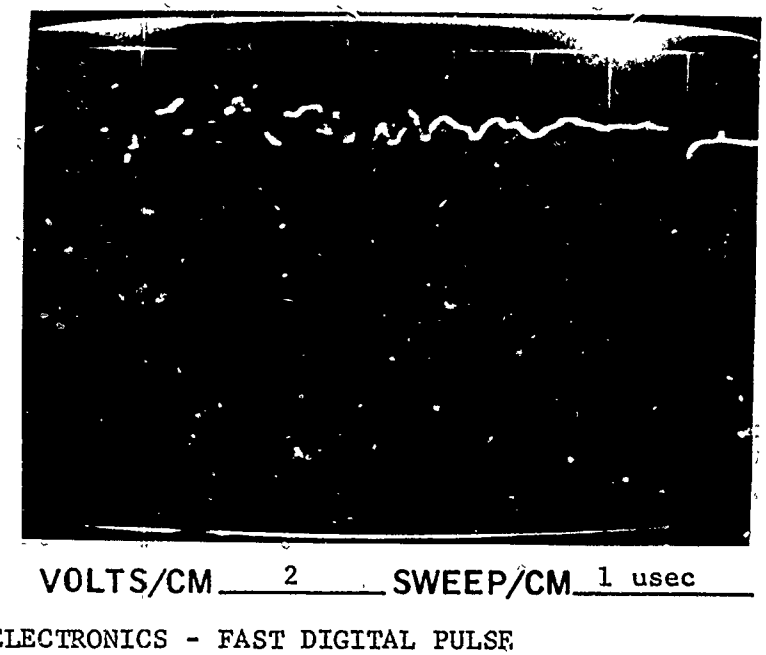

VOLTS/CM 2 SWEEP/CM 1 usec

TEST NO. 13 - 1, 2, 3, 4: DIGITAL ELECTRONICS - FAST DIGITAL PULSE

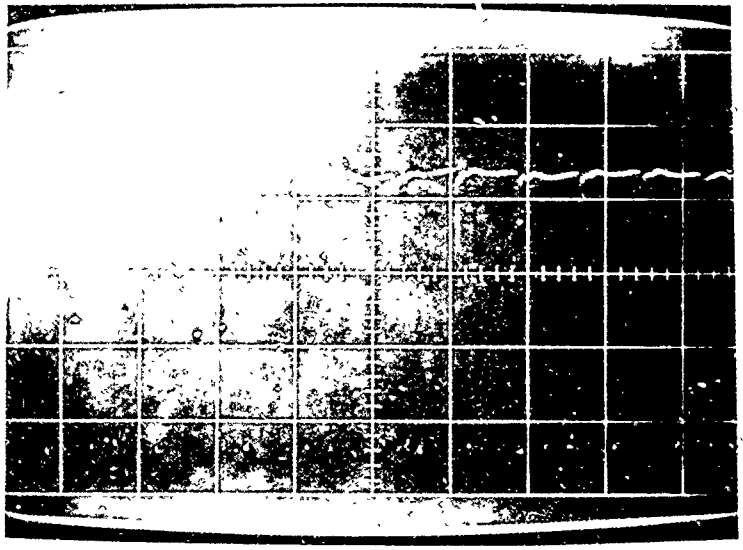

VOLTS/CM 2 SWEEP/CM 5 usec

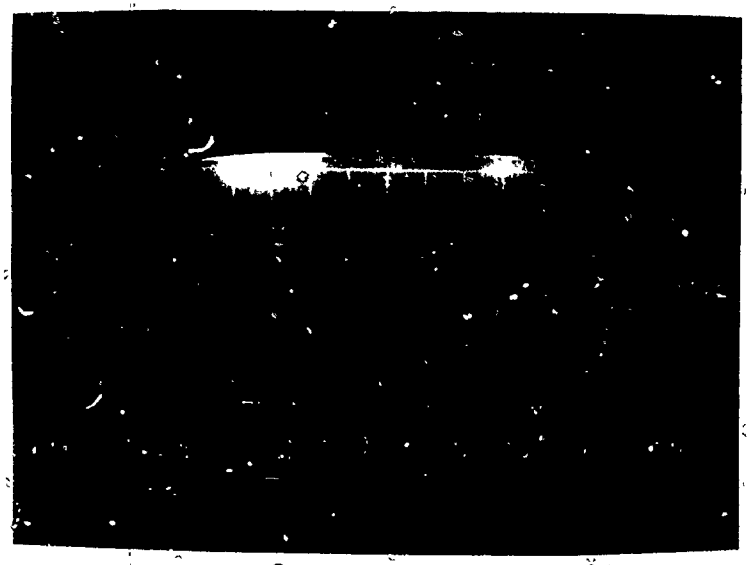

VOLTS/CM 2 SWEEP/CM 20 usec

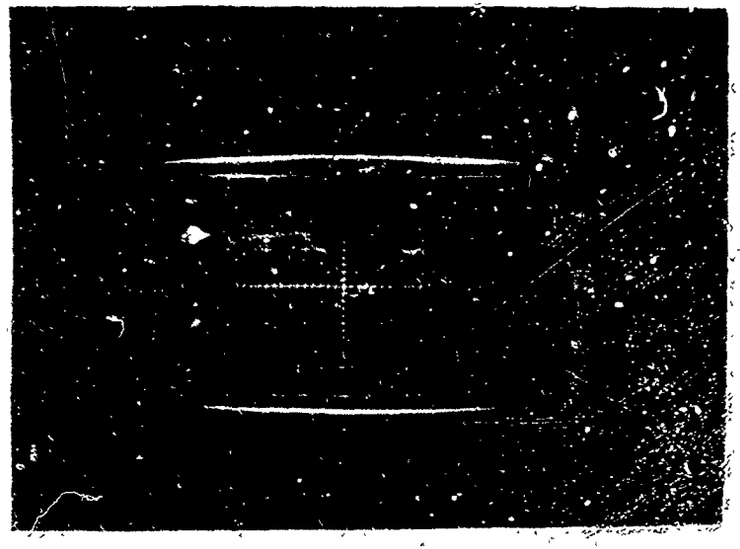

VOLTS/CM 2 SWEEP/CM 0.1 usec

VOLTS/CM 2 SWEEP/CM 1 usec

TEST NO. 13 - 5, 6, 7, 8: DIGITAL ELECTRONICS - FAST DIGITAL PULSE

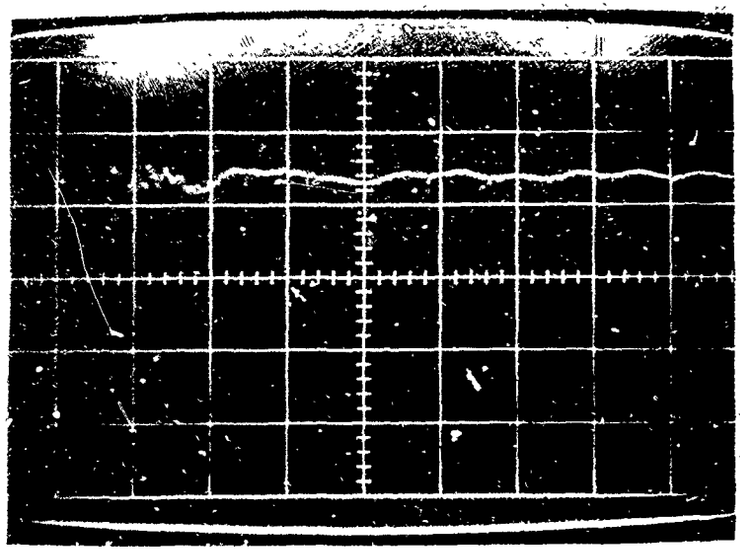

VOLTS/CM 2 SWEEP/CM 5 usec

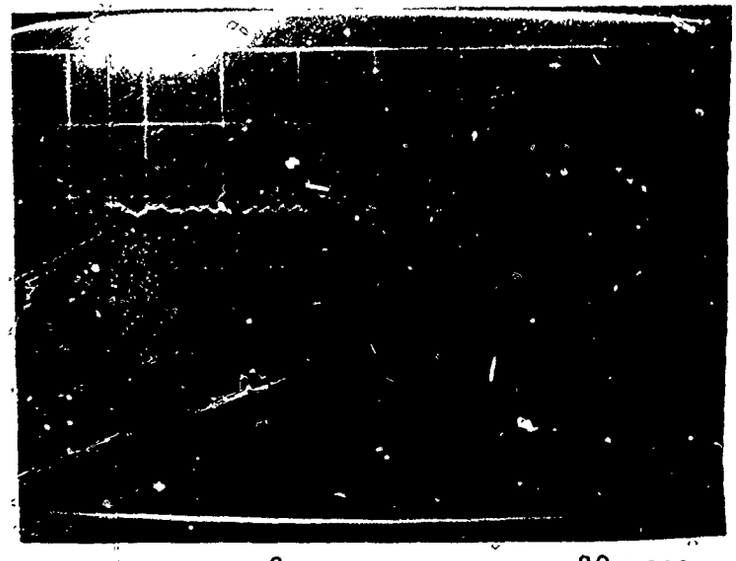

VOLTS/CM 2 SWEEP/CM 20 usec

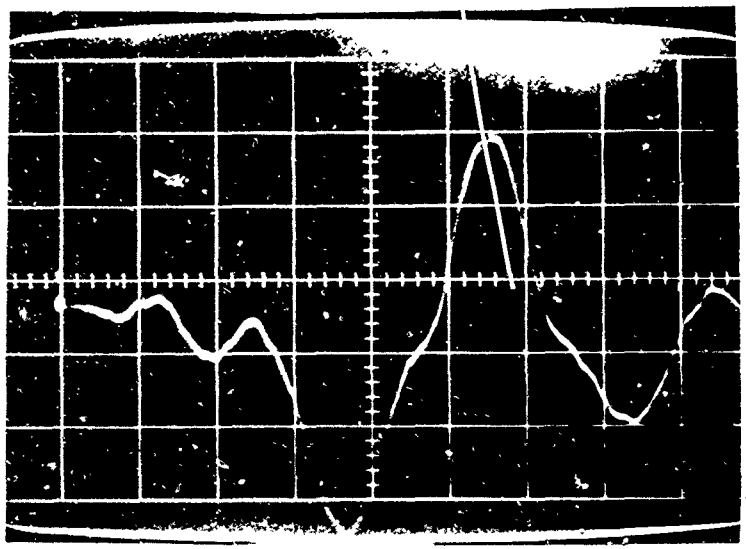

VOLTS/CM 5 SWEEP/CM 0.1 usec

VOLTS/CM 5 SWEEP/CM 1 usec

TEST NO. 13 - 9, 10, 11, 12: DIGITAL ELECTRONICS - SLOW DIGITAL PULSE

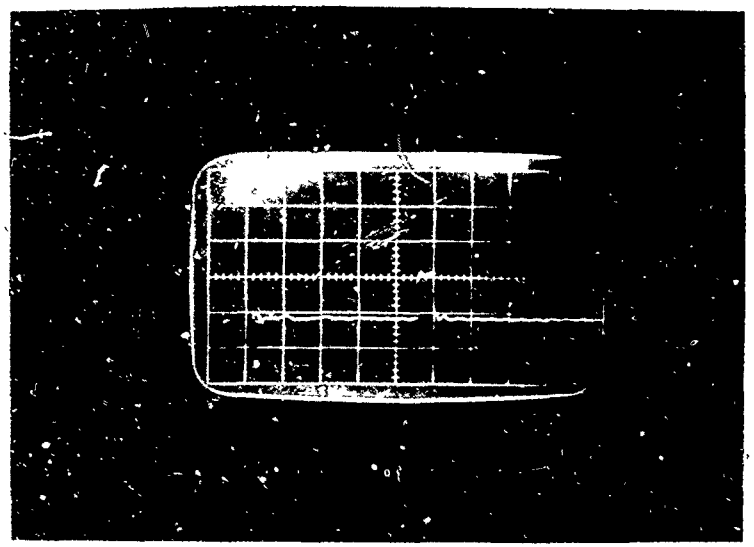

VOLTS/CM 5 SWEEP/CM 10 usec

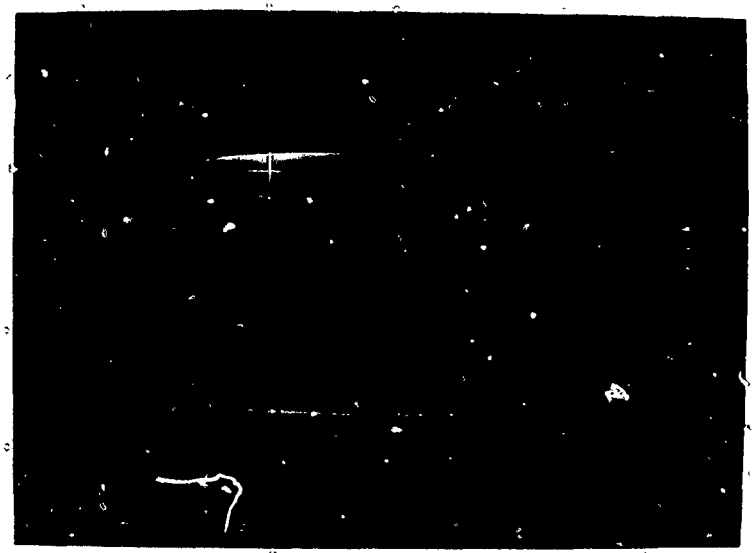

VOLTS/CM 5 SWEEP/CM 100 usec

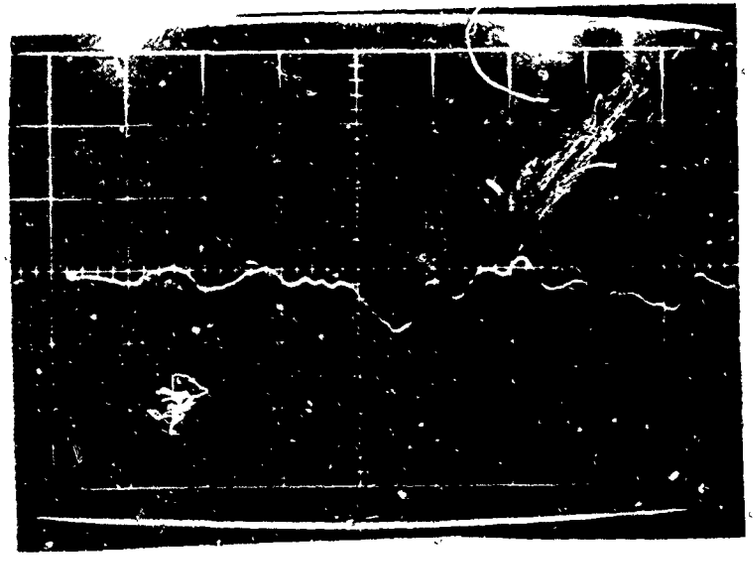

VOLTS/CM 5 SWEEP/CM 0.1 usec

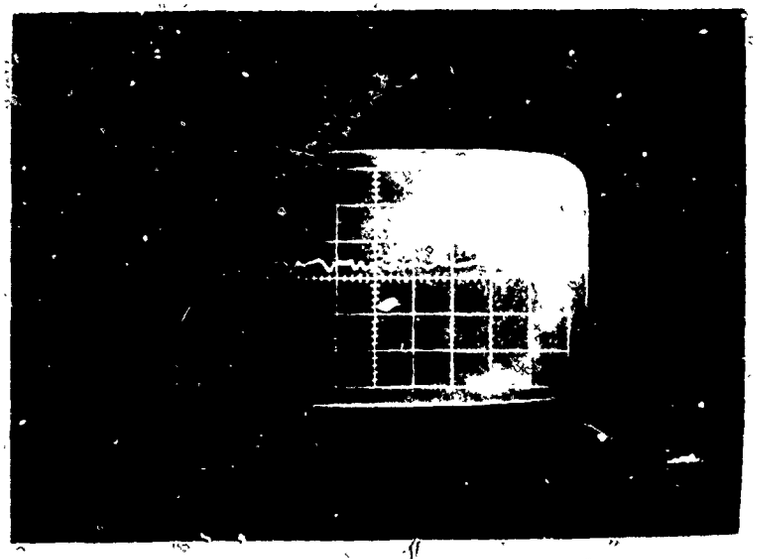

VOLTS/CM 5 SWEEP/CM 1 usec

TEST NO. 13 - 13, 14, 15, 16: DIGITAL ELECTRONICS - SLOW DIGITAL PULSE

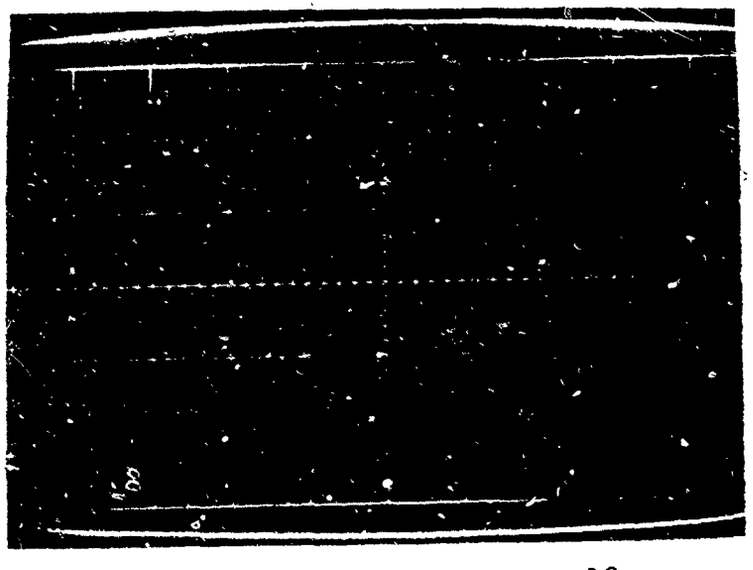

VOLTS/CM 5 SWEEP/CM 10 usec

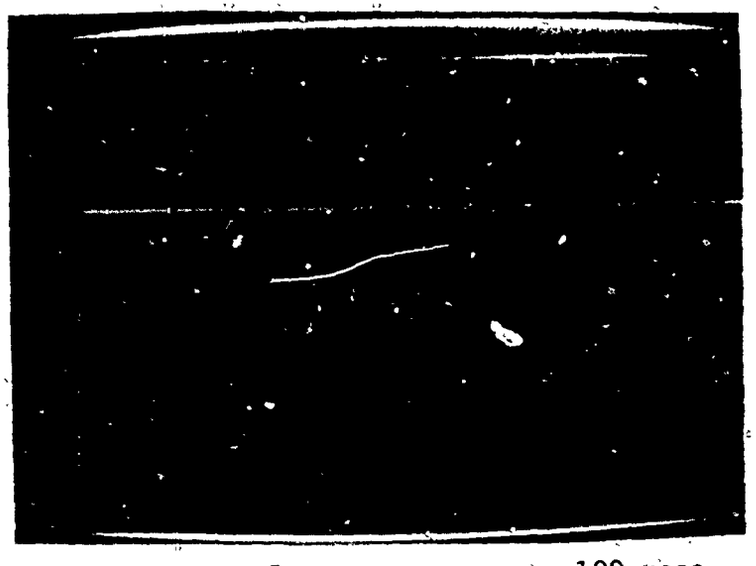

VOLTS/CM 5 SWEEP/CM 100 usec

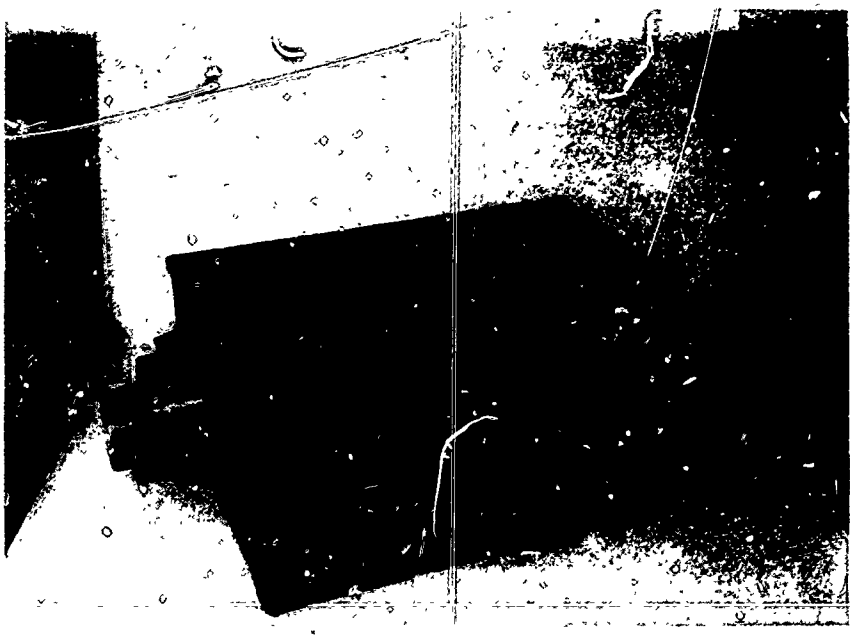

Circuits Test Cassette

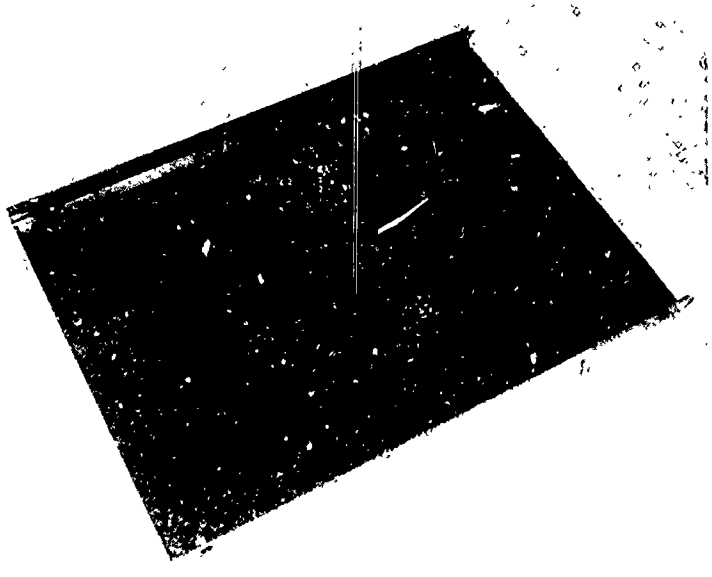

Circuits Test Setup (Partial Example)

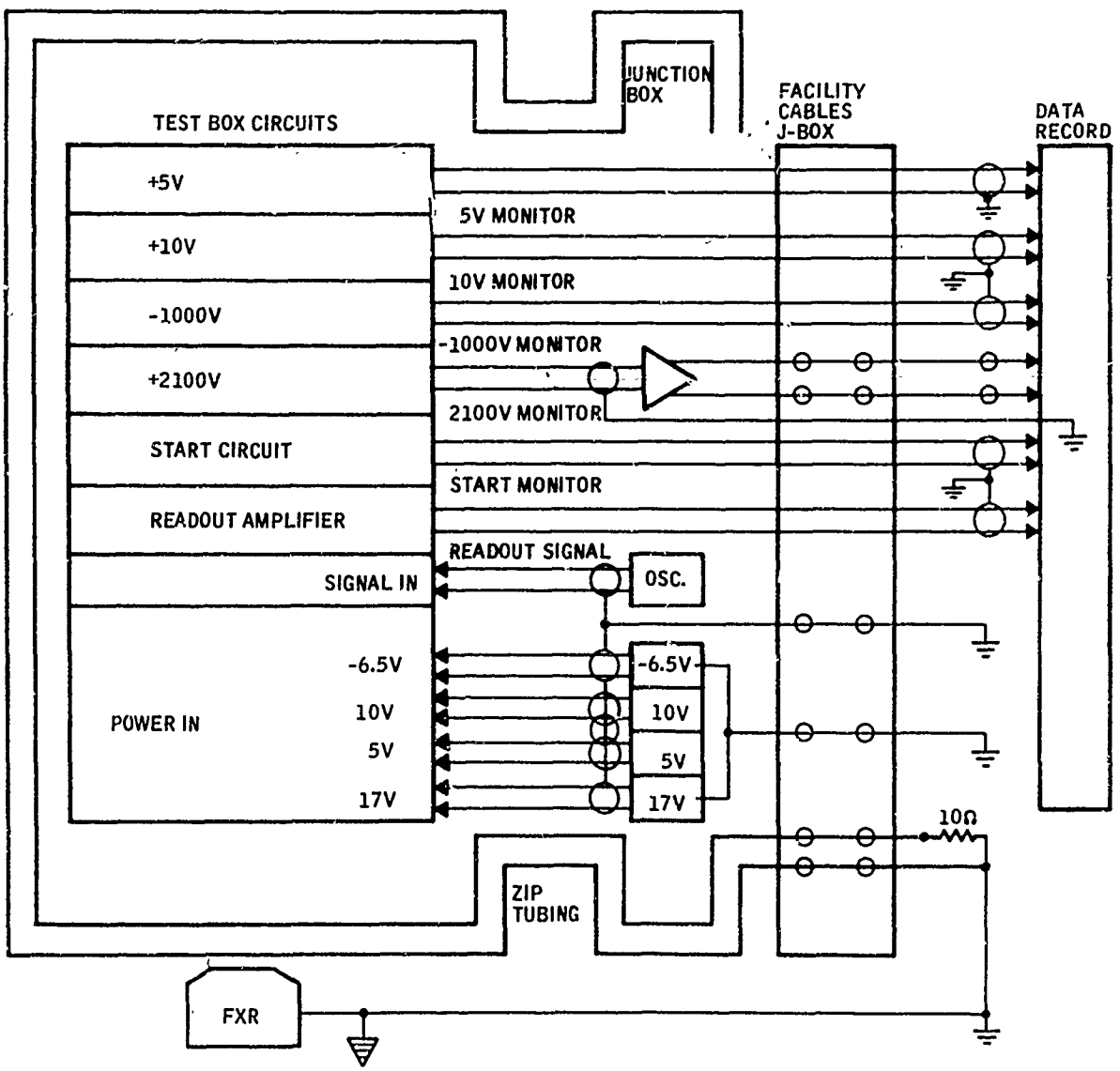

Circuit Test

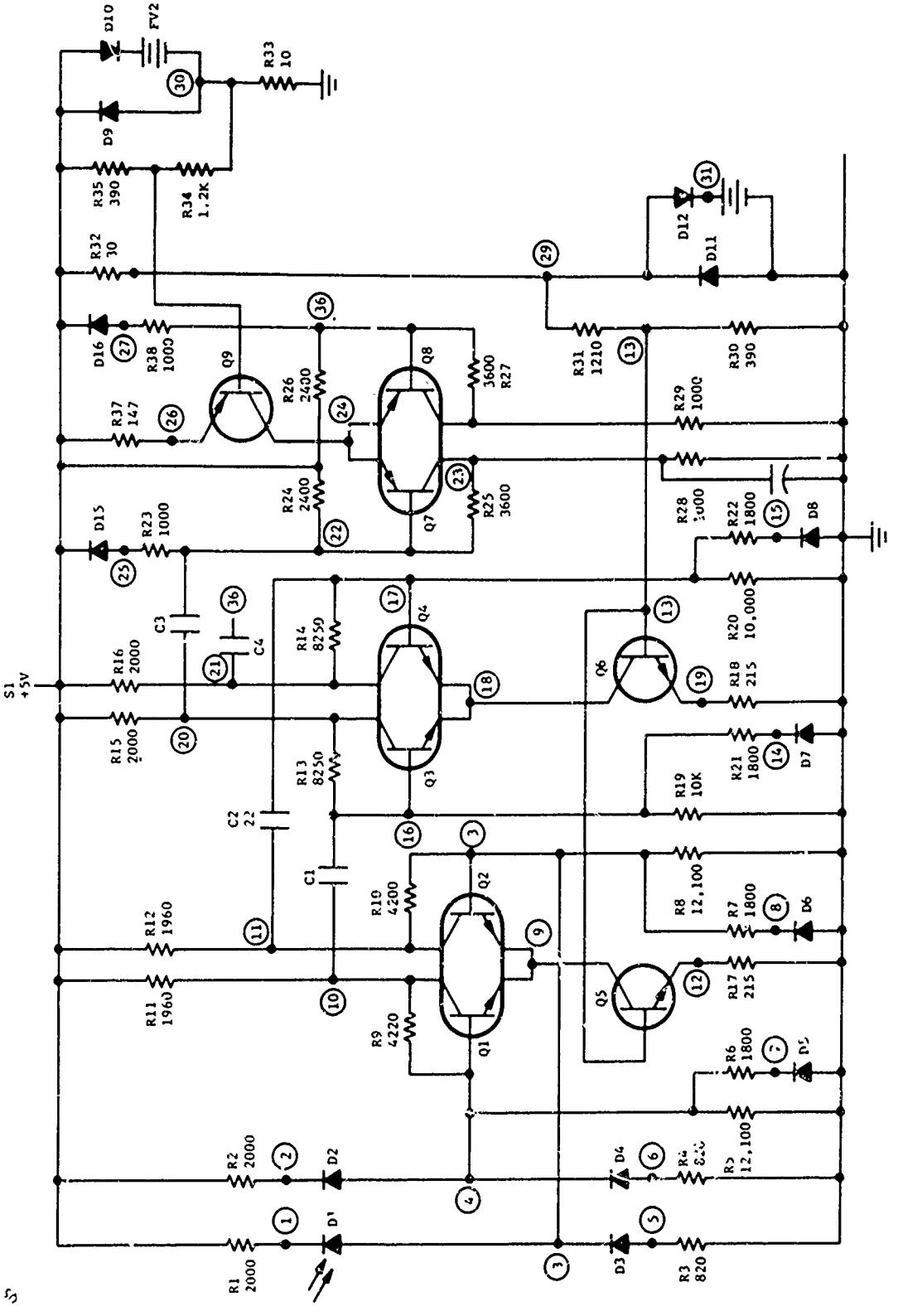

Readout Amplifier

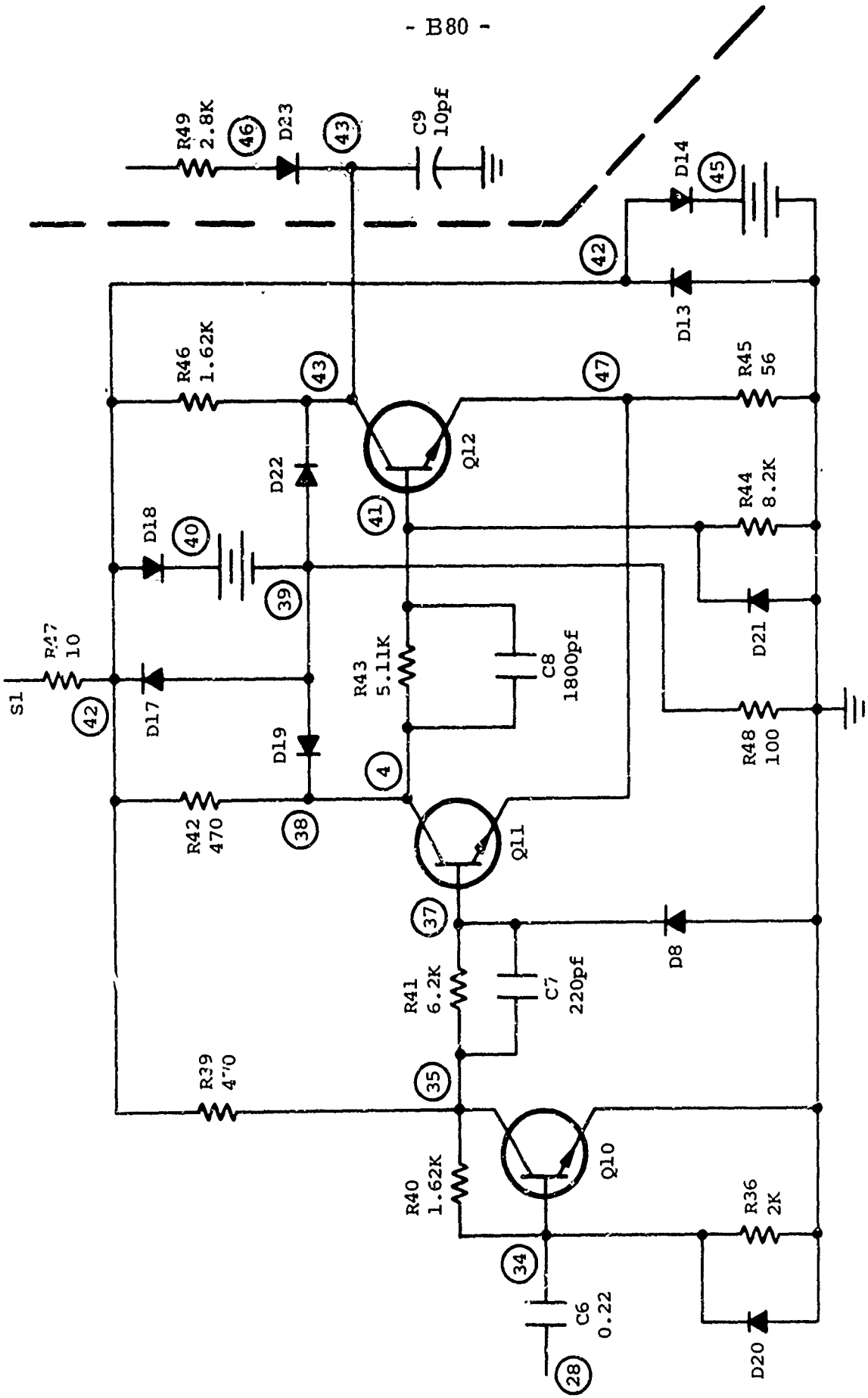

Readout Trigger Circuit

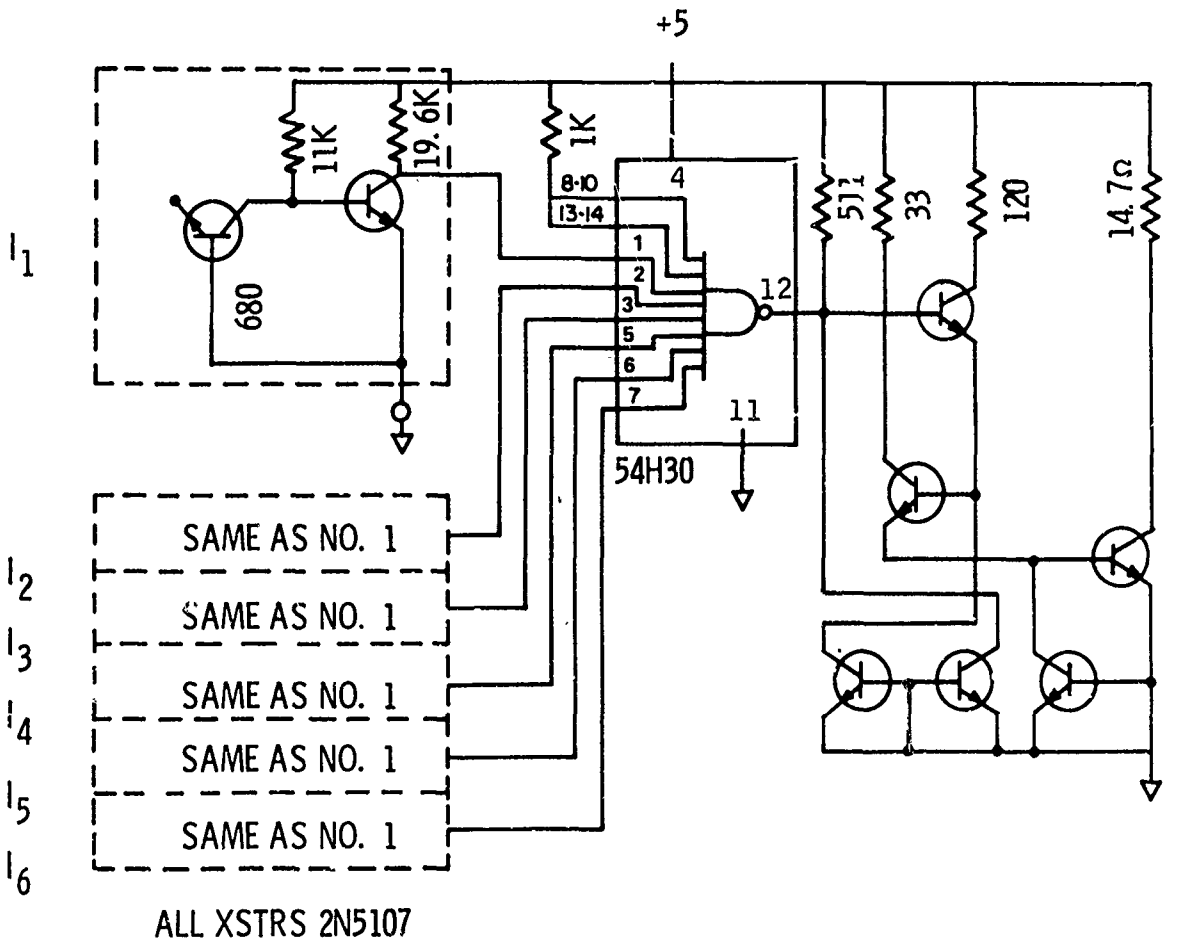

Laser Start/Restart Circuit

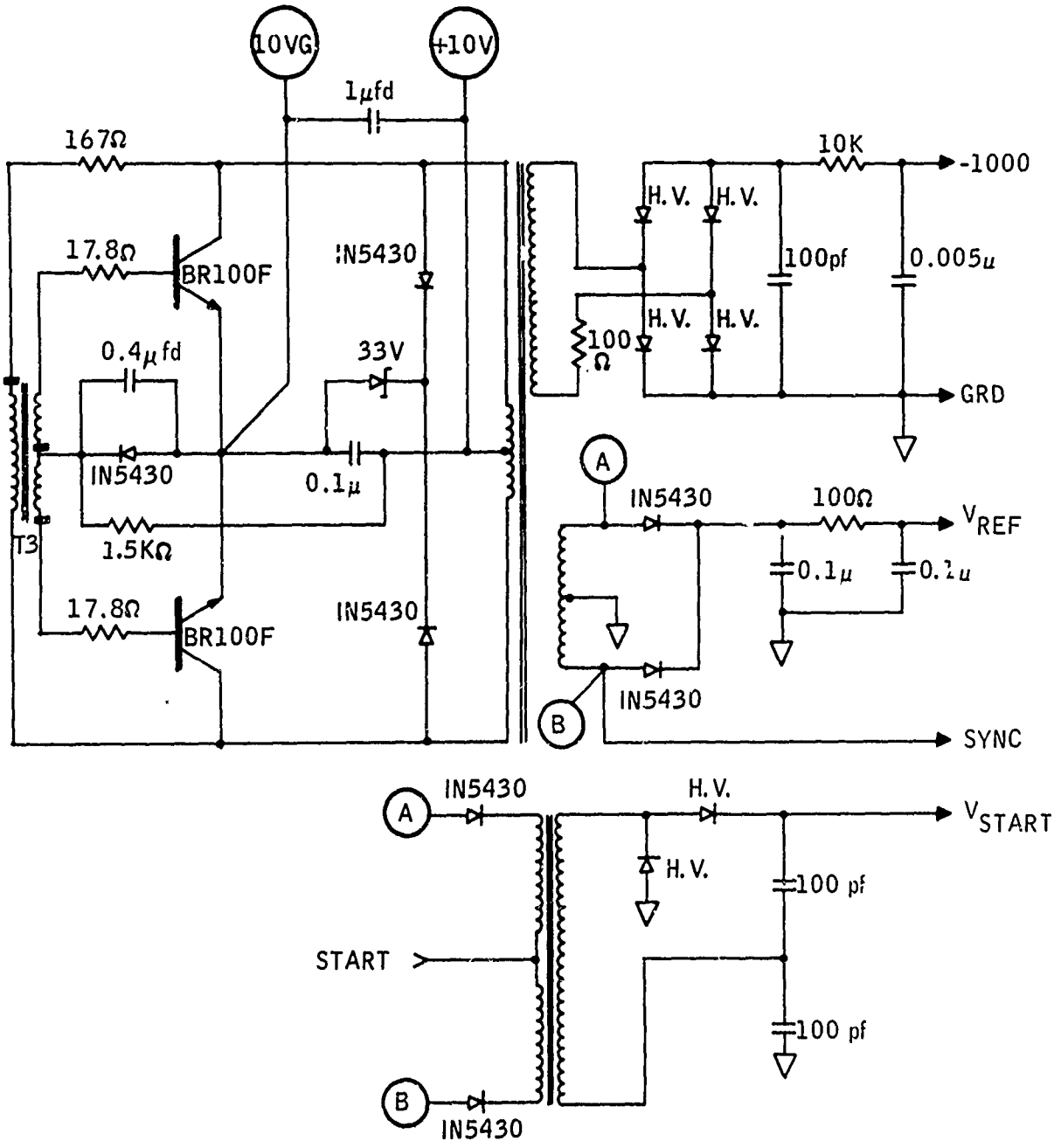

ALL DIODES MARKED H.V. ARE UNITRODE 652-745

High-Voltage D-C to D-C Converter

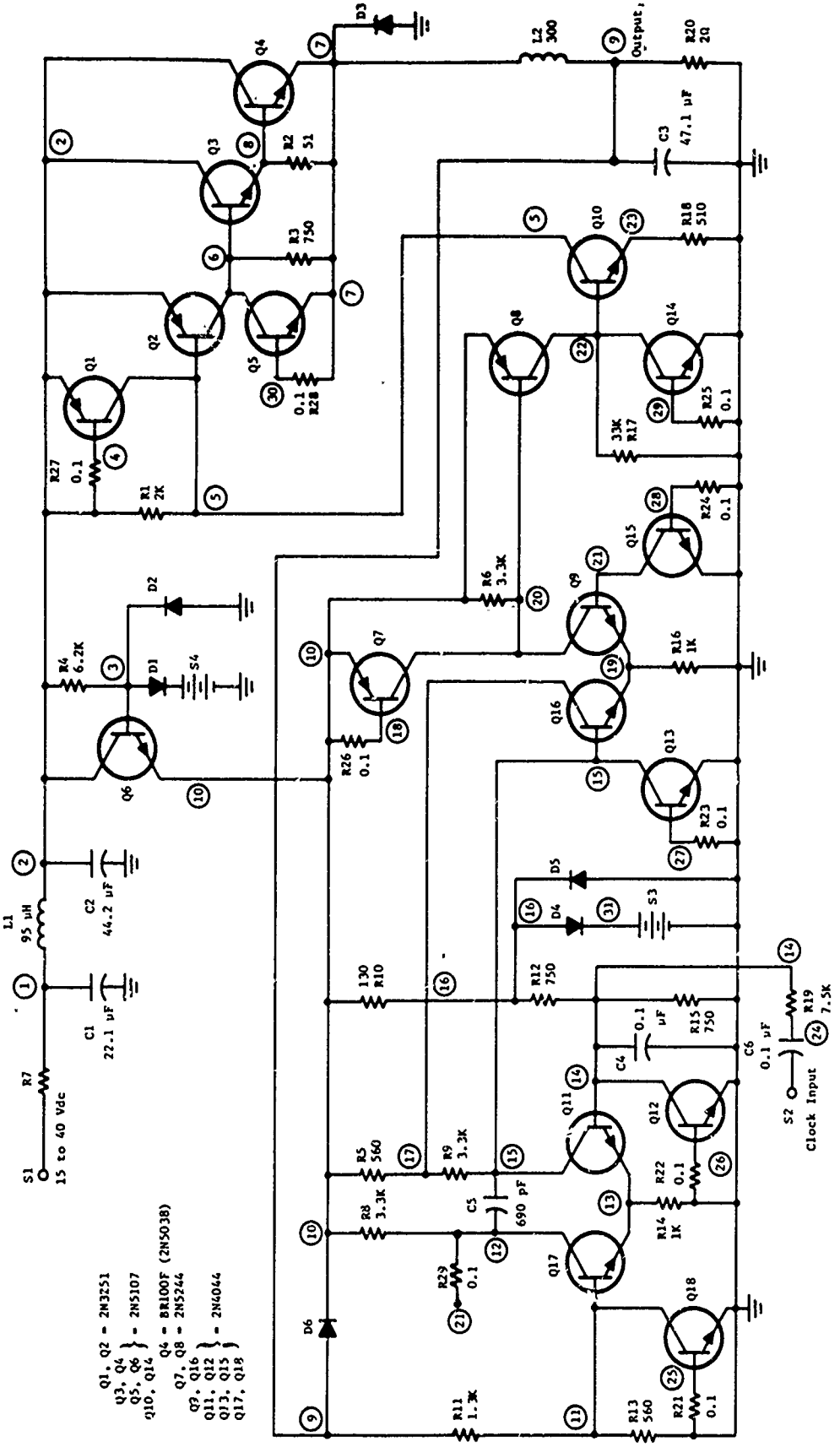

+5 Volt Switching Regulator

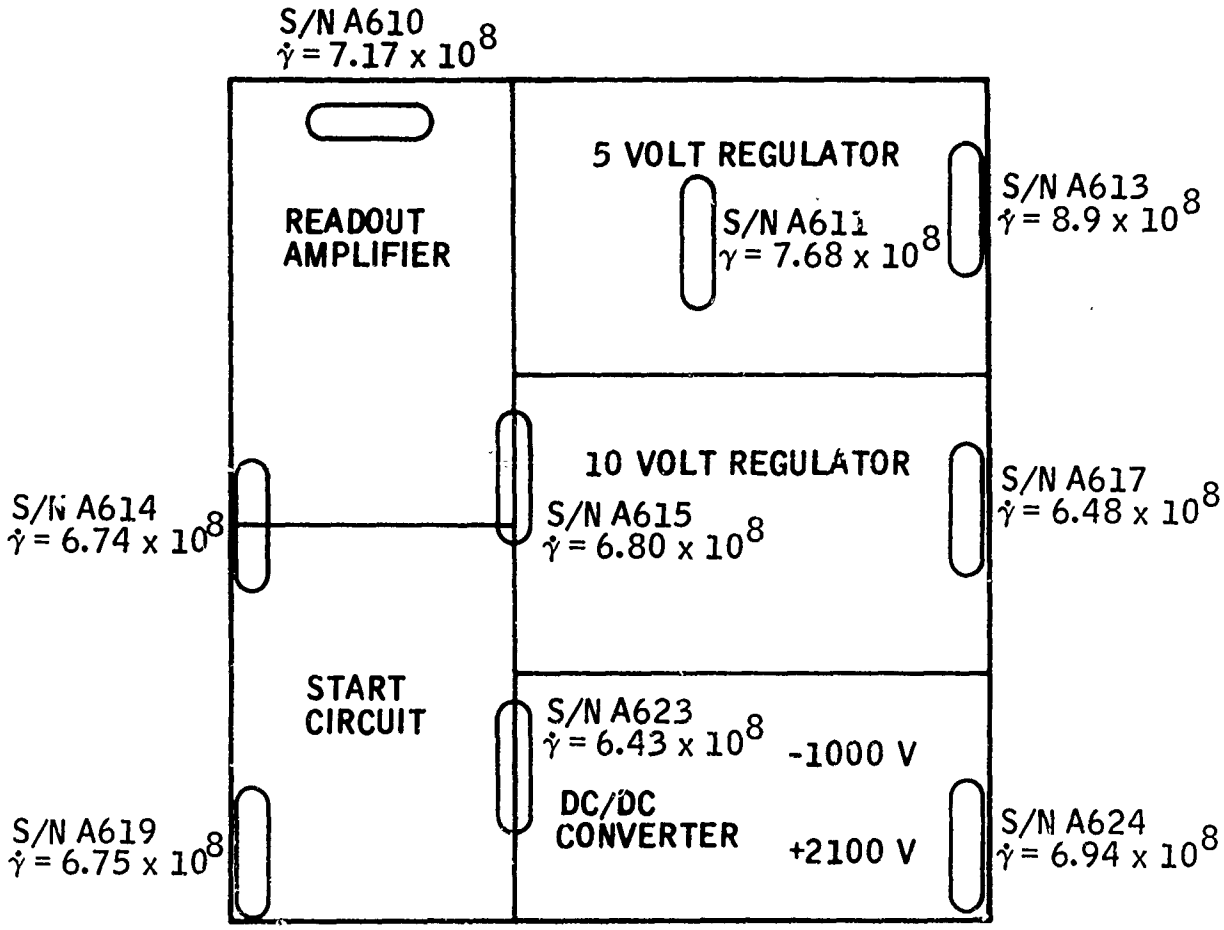

Circuits Test Dosimetry (Shot No. 19)

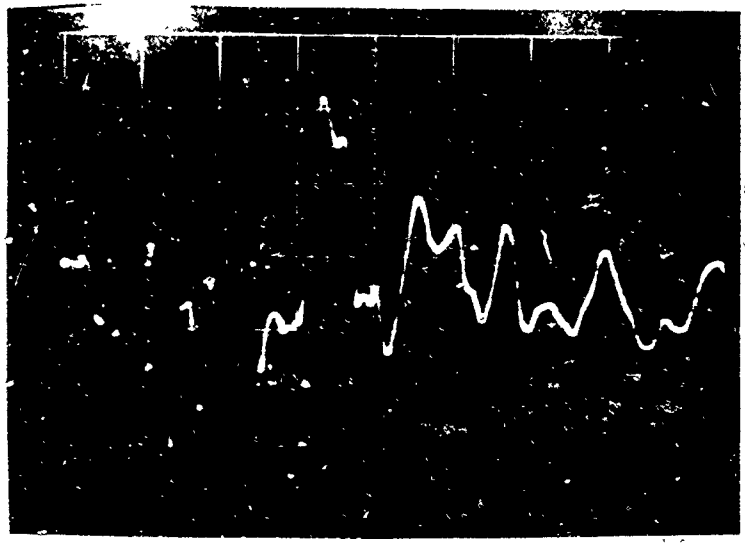

VOLTS/CM 2 SWEEP/CM 0.5 usec

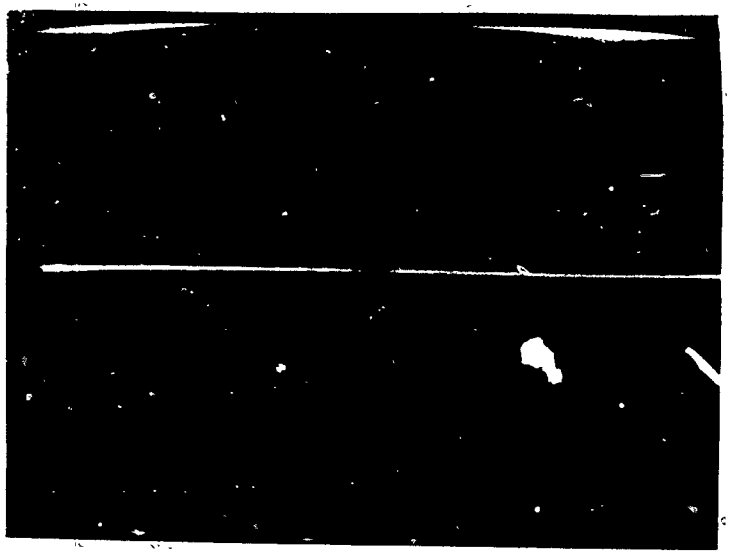

VOLTS/CM 2 SWEEP/CM 5 usec

TEST NO. 19 - 1, 2, 3: CIRCUITS TEST - 5 VOLT MONITOR

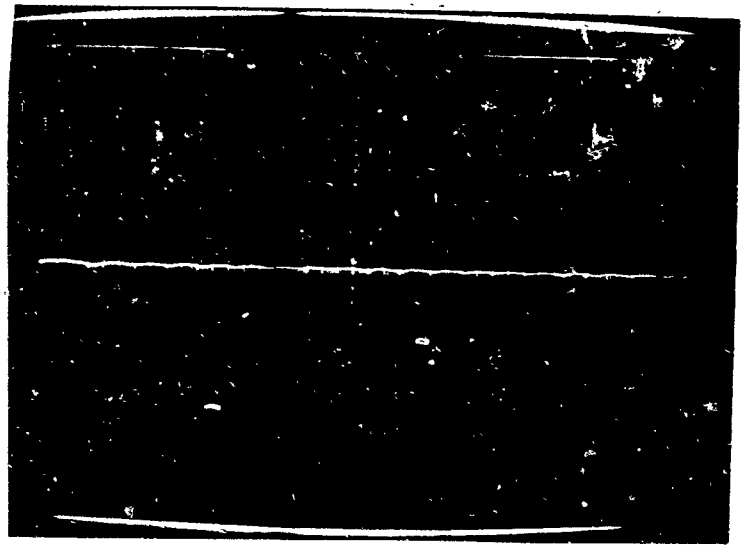

VOLTS/CM 2 SWEEP/CM 50 usec

VOLTS/CM _____ SWEEP/CM _____

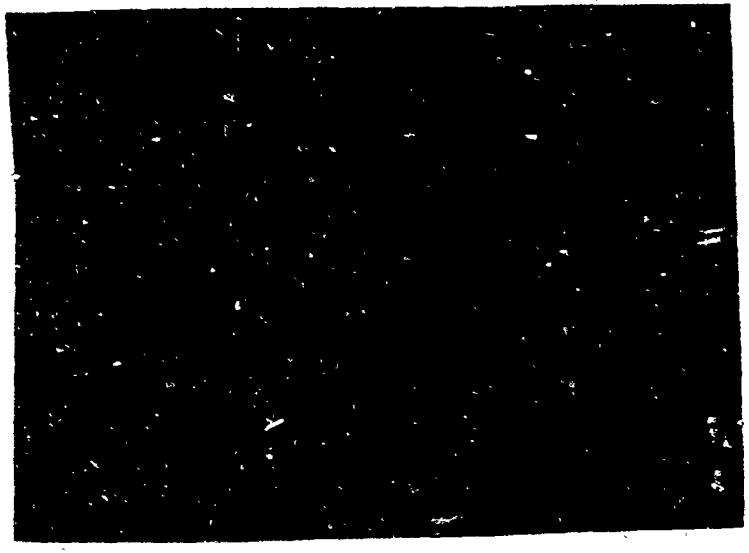

VOLTS/CM 5 SWEEP/CM .5 usec

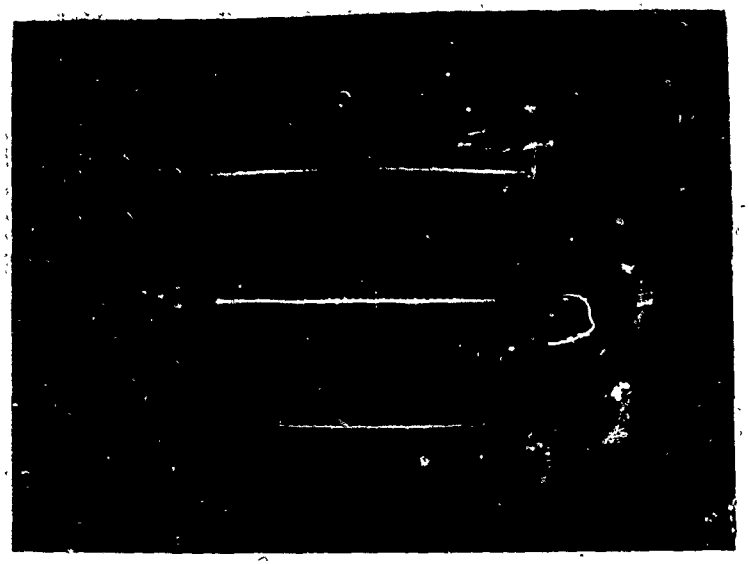

VOLTS/CM 5 SWEEP/CM 5 usec

TEST NO. 19 - 4, 5, 6: CIRCUITS TEST - 10 VOLT MONITOR

VOLTS/CM 5 SWEEP/CM 50 usec

VOLTS/CM _____ SWEEP/CM _____

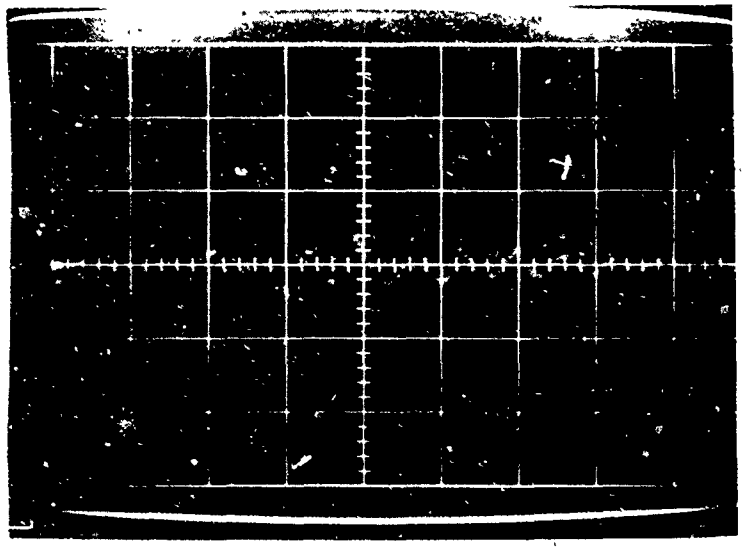

VOLTS/CM .2 SWEEP/CM .5 usec

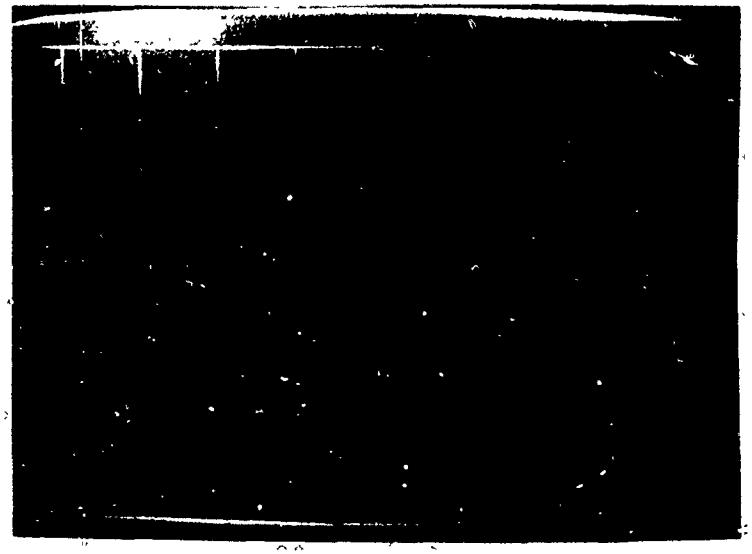

VOLTS/CM .2 SWEEP/CM 5 usec

TEST NO. 19 - 7, 8, 9: CIRCUITS TEST - 2100 VCLT MONITOR

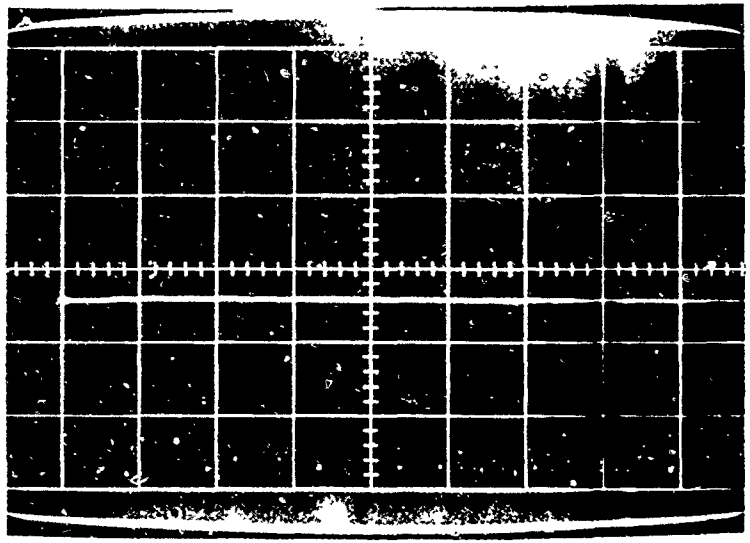

VOLTS/CM 0.2 SWEEP/CM 50 usec

VOLTS/CM _____ SWEEP/CM _____

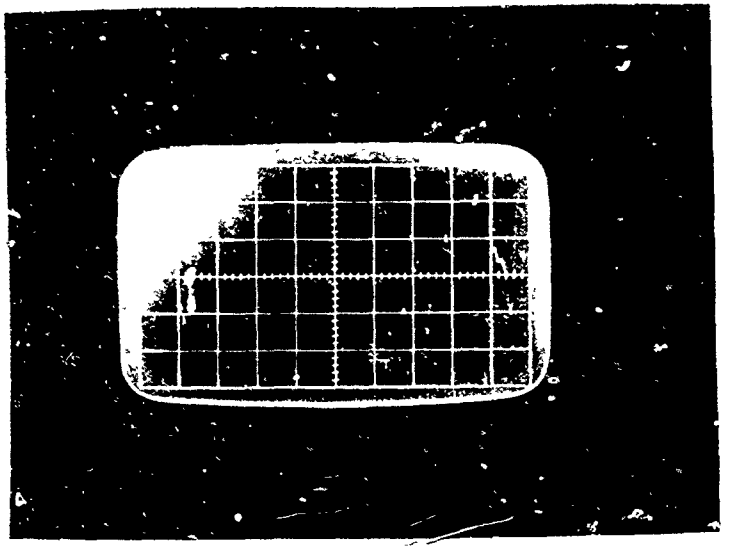

VOLTS/CM 0.2 SWEEP/CM 0.5 usec

VOLTS/CM 0.2 SWEEP/CM 5 usec

TEST NO. 19 - 10, 11, 12: CIRCUITS TEST - 1000 VOLT MONITOR

VOLTS/CM .2 SWEEP/CM 50 usec

VOLTS/CM _____ SWEEP/CM _____

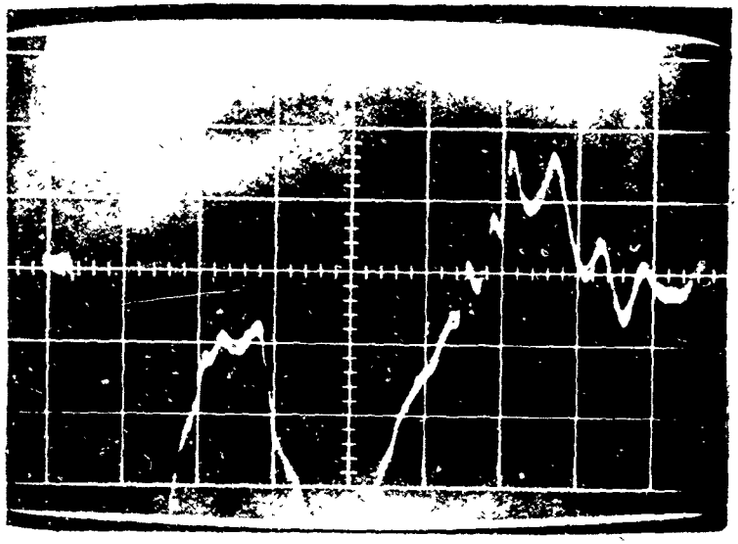

VOLTS/CM 2 SWEEP/CM 0.5 usec

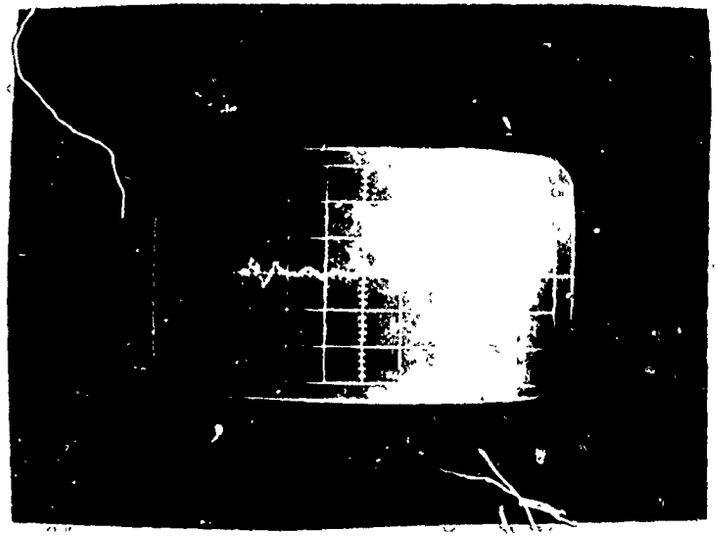

VOLTS/CM 2 SWEEP/CM 5 usec

TEST NO. 19 - 13, 14, 15: CIRCUITS TEST - START MONITOR

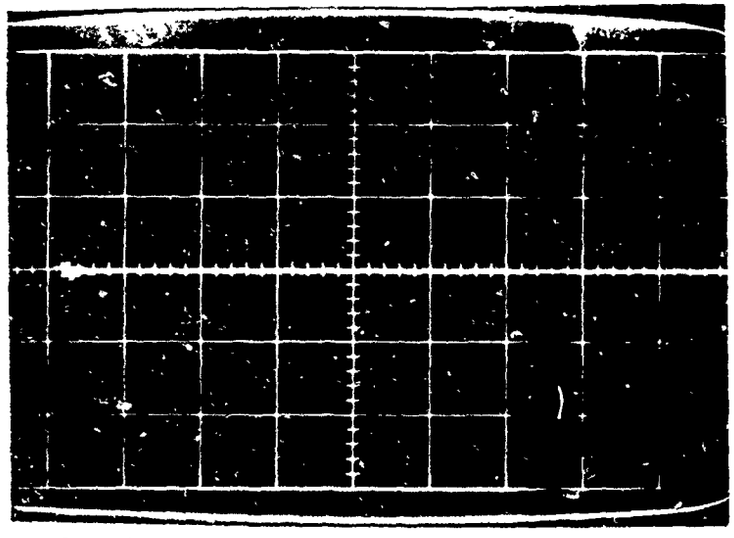

VOLTS/CM 2 SWEEP/CM 50 usec

VOLTS/CM _____ SWEEP/CM _____

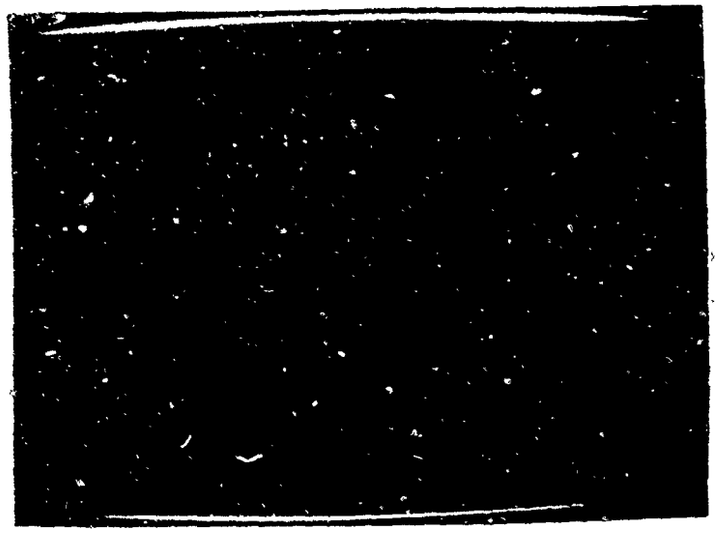

VOLTS/CM 50 mv SWEEP/CM .5 usec

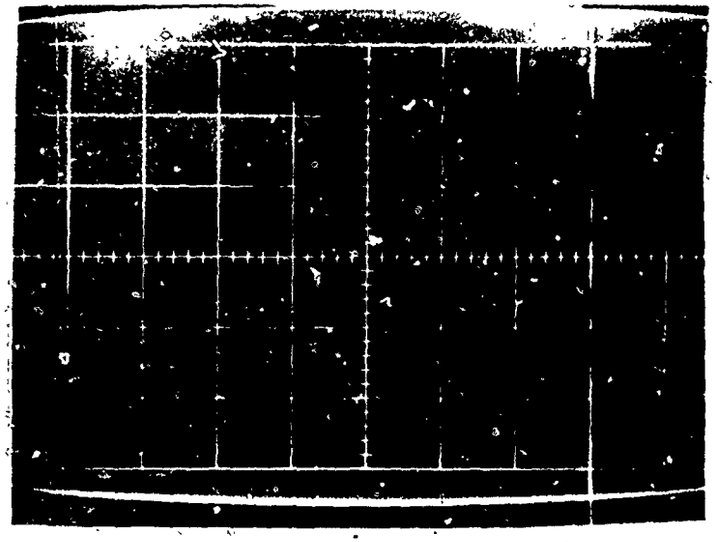

VOLTS/CM 50 mv SWEEP/CM 5 usec

TEST NO. 19 - 16, 17, 18: CIRCUITS TEST - READOUT MONITOR

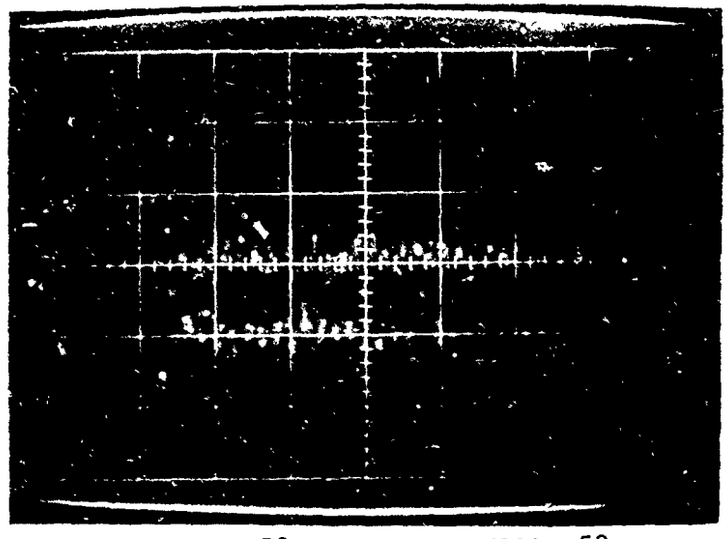

VOLTS/CM 50 mv SWEEP/CM 50 usec

VOLTS/CM _____ SWEEP/CM _____

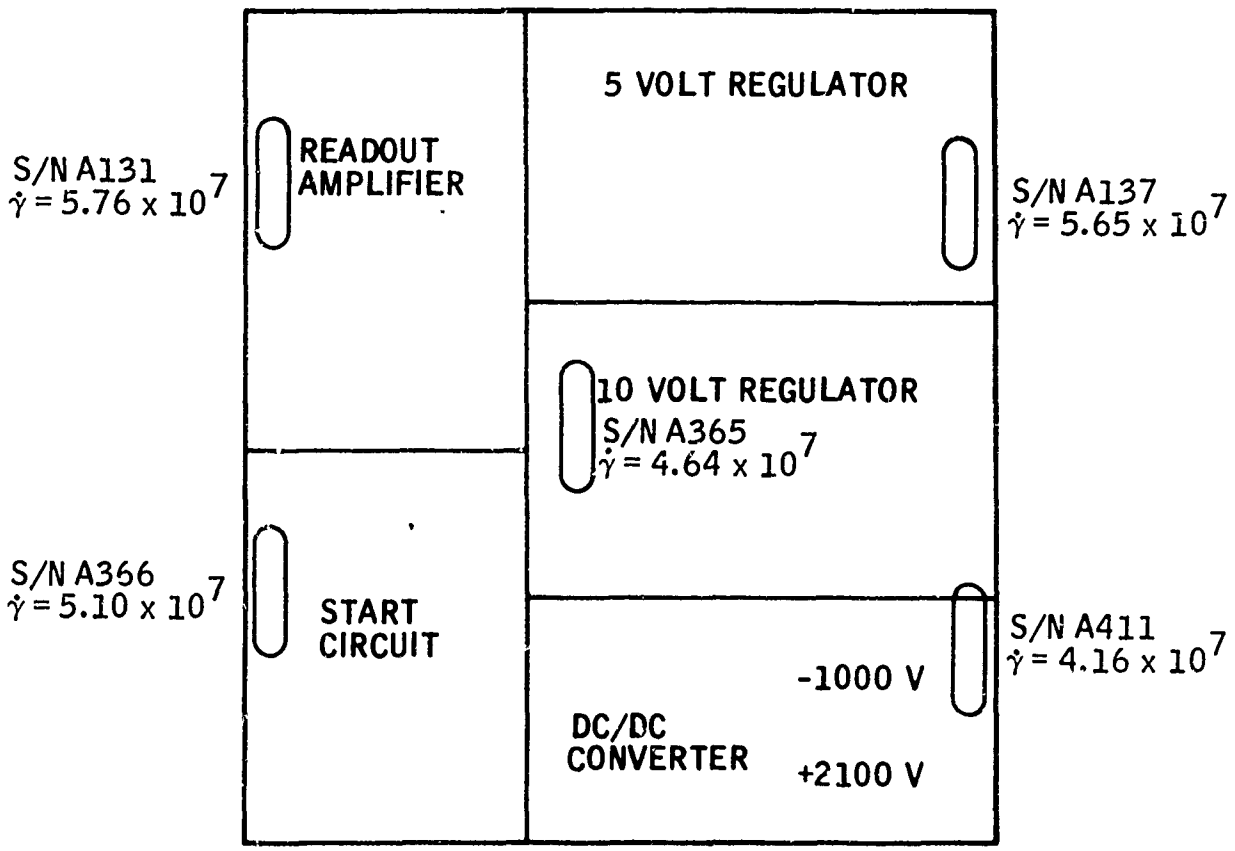

Circuits Test Dosimetry (Shot No. 20)

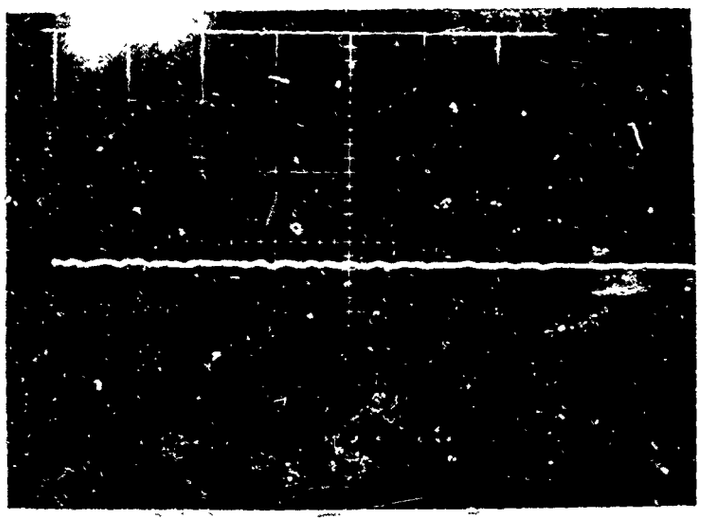

VOLTS/CM 2 SWEEP/CM 0.5 usec

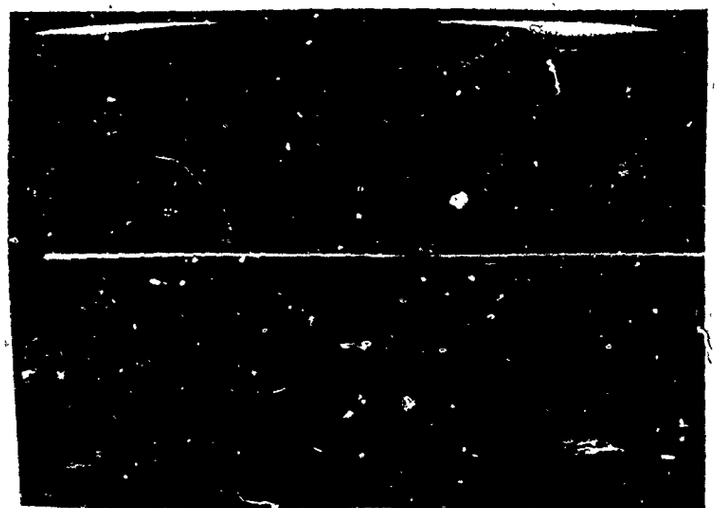

VOLTS/CM 2 SWEEP/CM 5 usec

TEST NO. 20 - 1, 2, 3: CIRCUITS TEST - 5 VOLT MONITOR

VOLTS/CM _____ SWEEP/CM _____

VOLTS/CM _____ SWEEP/CM _____

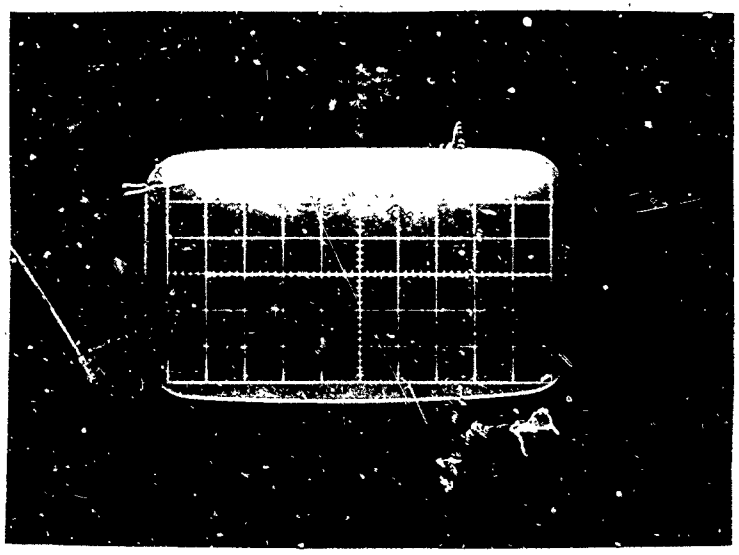

VOLTS/CM 5 SWEEP/CM .5 usec

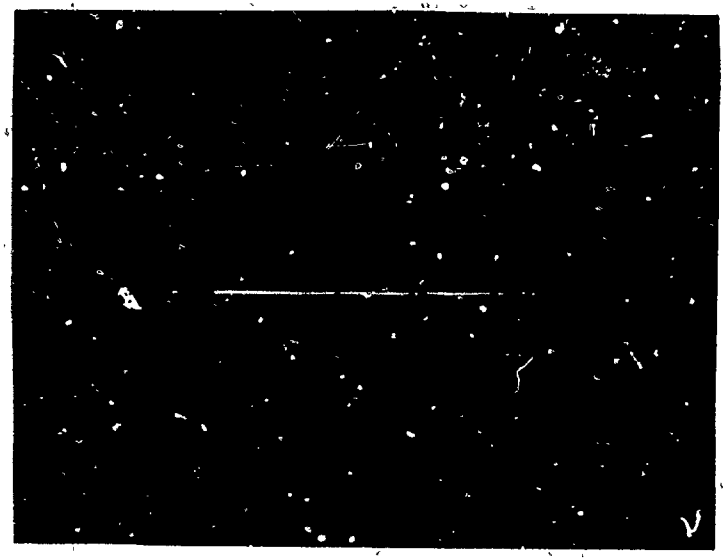

VOLTS/CM 5 SWEEP/CM 5 usec

TEST NO. 20 - 4, 5, 6: CIRCUITS TEST - 10 VOLT MONITOR

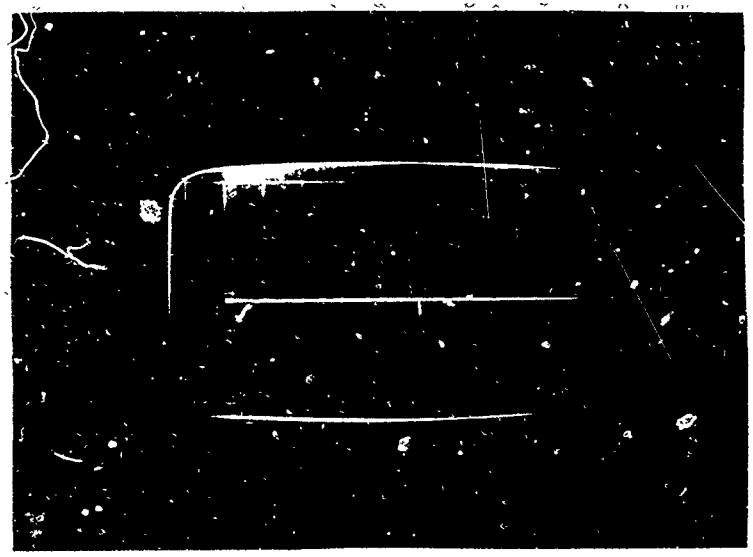

VOLTS/CM 5 SWEEP/CM 20 usec

VOLTS/CM _____ SWEEP/CM _____

VOLTS/CM _____ SWEEP/CM _____

VOLTS/CM .2 SWEEP/CM 5 usec

TEST NO. 20 - 7, 8, 9: CIRCUITS TEST - 2100 VOLT MONITOR

VOLTS/CM _____ SWEEP/CM _____

VOLTS/CM _____ SWEEP/CM _____

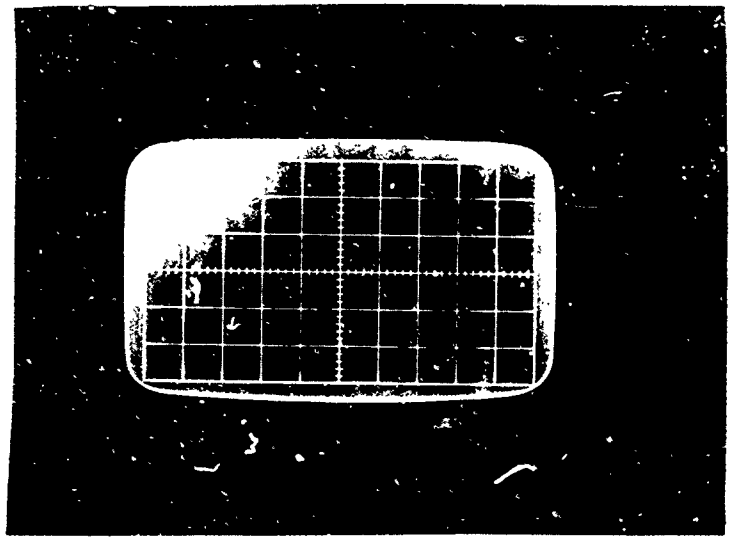

VOLTS/CM 0.2 SWEEP/CM 0.5 usec

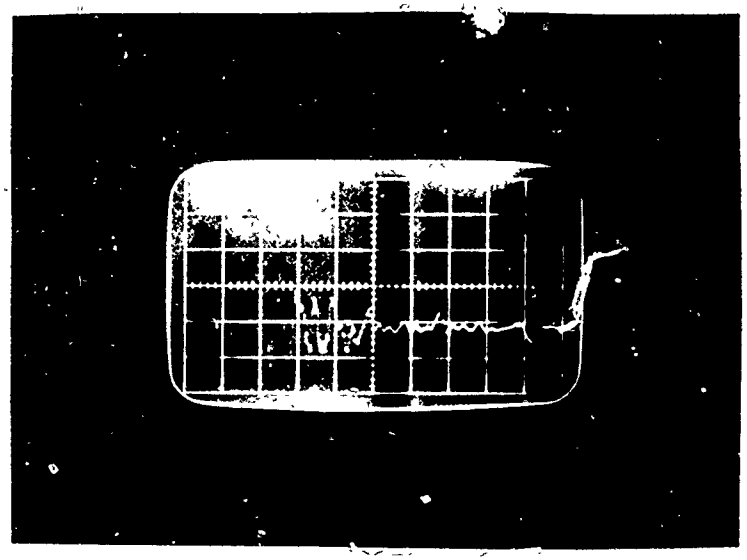

VOLTS/CM 0.2 SWEEP/CM 5 usec

TEST NO. 20 - 10, 11, 12: CIRCUITS TEST - 1000 VOLT MONITOR

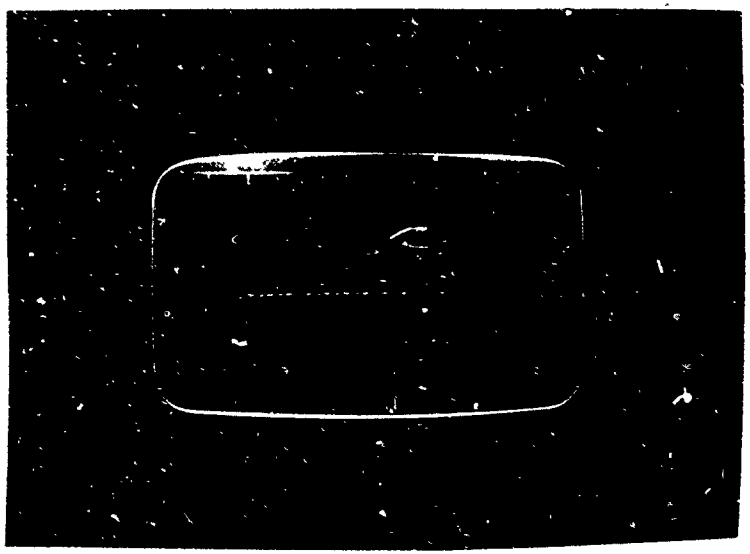

VOLTS/CM .2 SWEEP/CM 50 usec

VOLTS/CM _____ SWEEP/CM _____

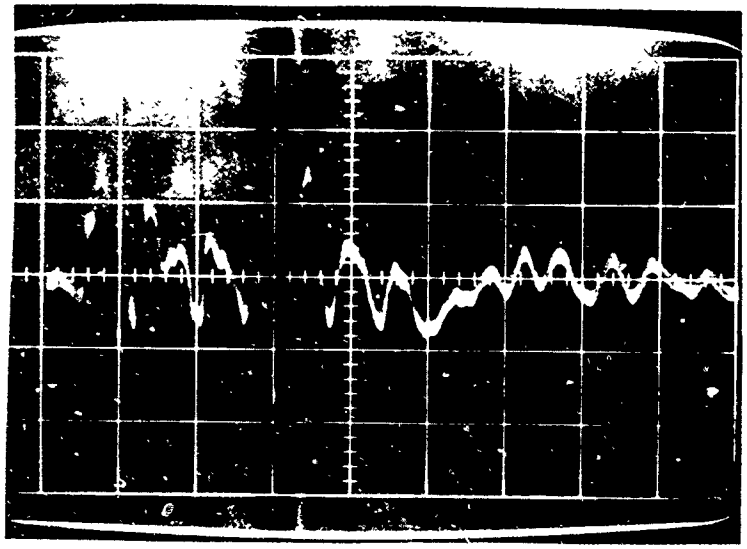

VOLTS/CM 2 SWEEP/CM 0.5 usec

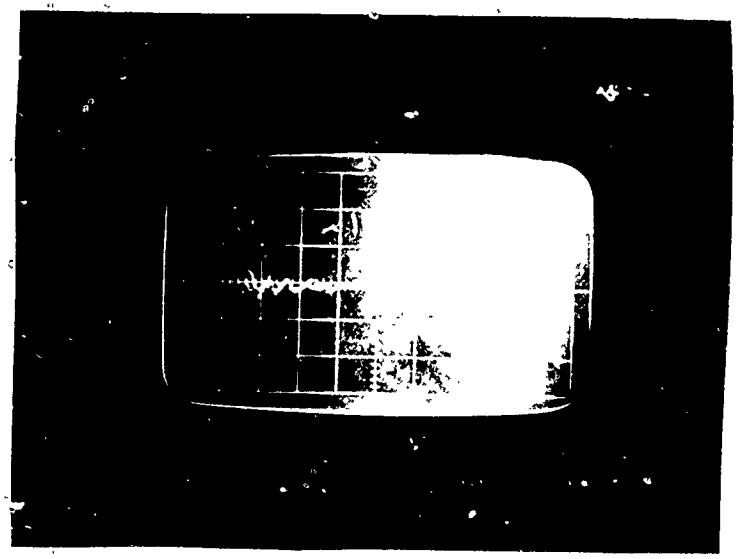

VOLTS/CM 2 SWEEP/CM 5 usec

TEST NO. 20 - 13, 14, 15: CIRCUITS TEST - START MONITOR

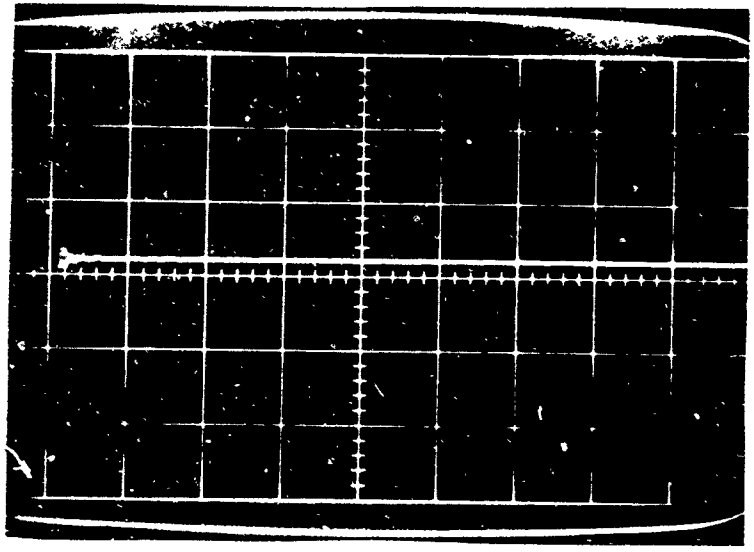

VOLTS/CM 2 SWEEP/CM 50 usec

VOLTS/CM _____ SWEEP/CM _____

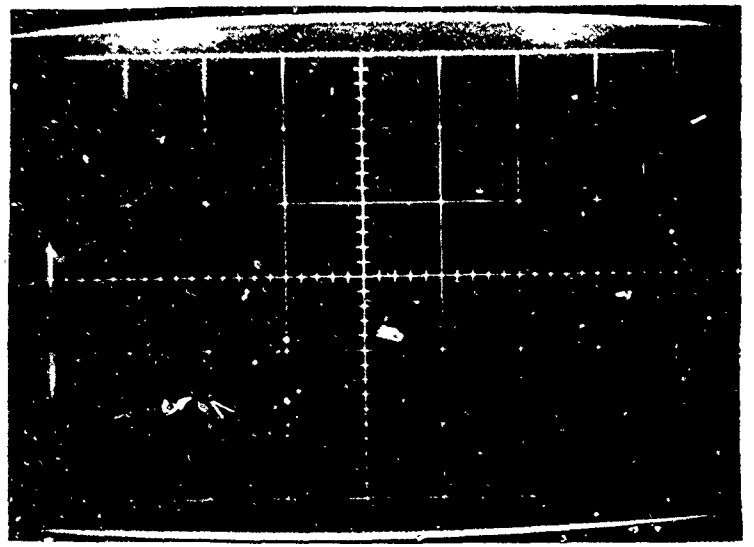

VOLTS/CM 50 mv SWEEP/CM .5 usec

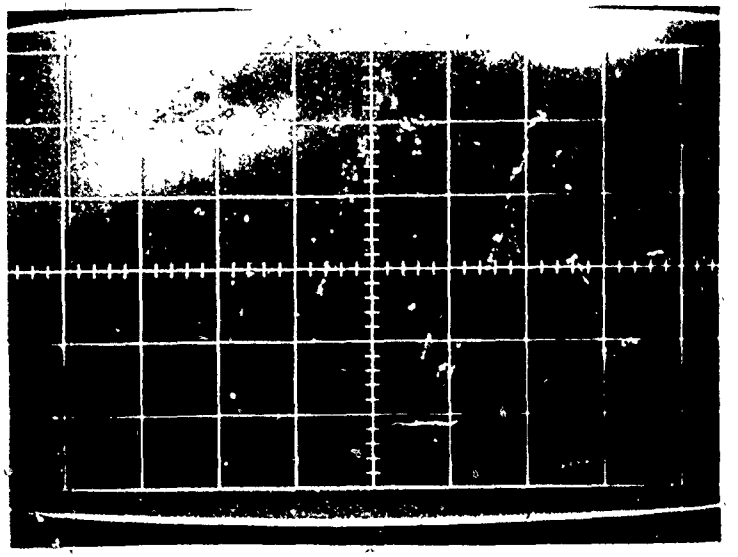

VOLTS/CM 50 mv SWEEP/CM 5 usec

TEST NO. 20 - 16, 17, 18: CIRCUITS TEST - READOUT AMPLIFIER

VOLTS/CM 50 mv SWEEP/CM 50 usec

VOLTS/CM _____ SWEEP/CM _____

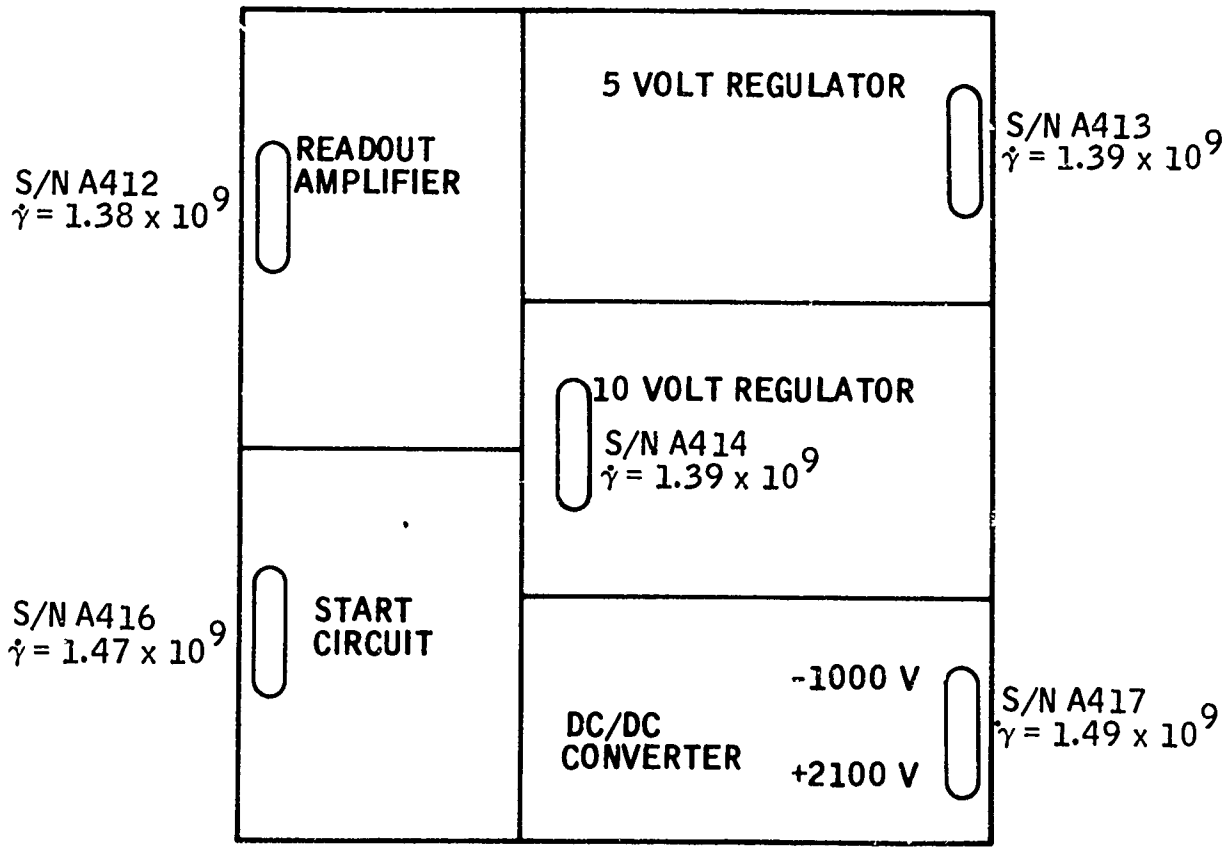

Circuits Test Dosimetry (Shot No. 21)
Sheet 1, Large Dosimeters

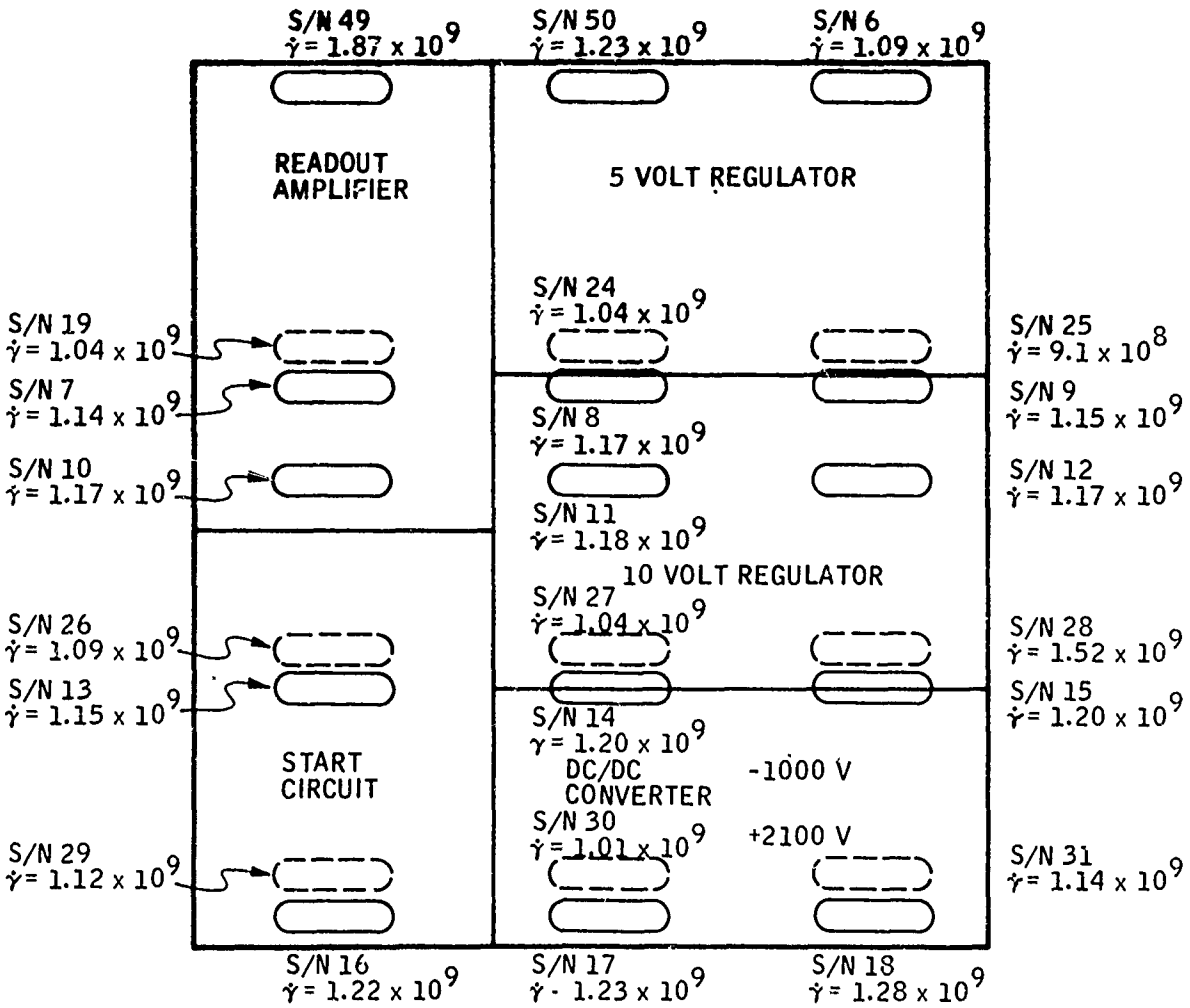

Circuits Test Dosimetry (Shot No. 21)
Sheet 2 of 2 Small Dosimeters

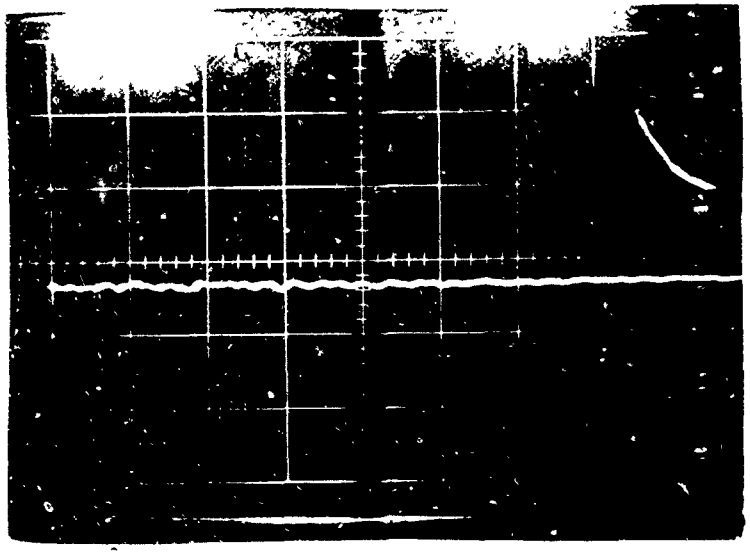

VOLTS/CM 2 SWEEP/CM 0.5 usec

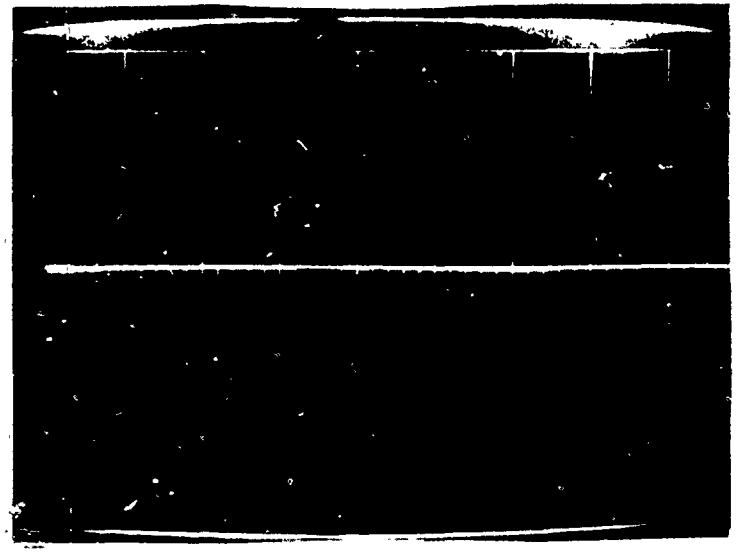

VOLTS/CM 2 SWEEP/CM 5 usec

TEST NO. 21 - 1, 2, 3: CIRCUITS TEST - 5 VOLT MONITOR

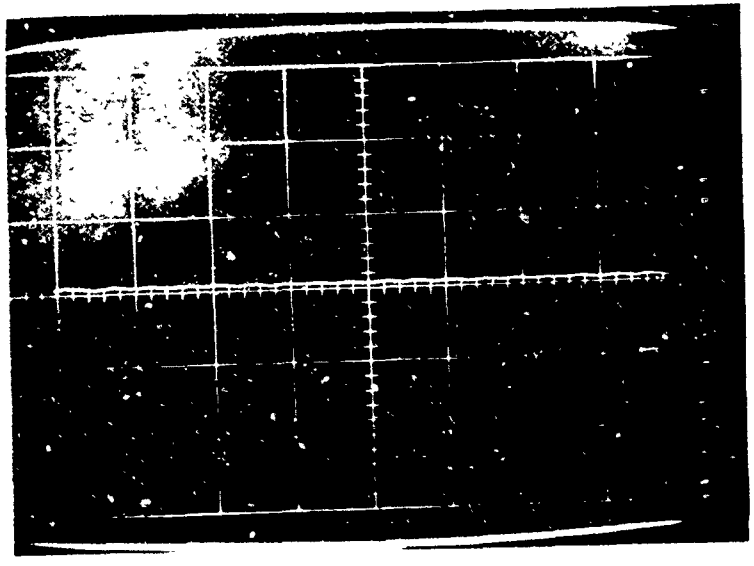

VOLTS/CM 2 SWEEP/CM 50 usec

VOLTS/CM _____ SWEEP/CM _____

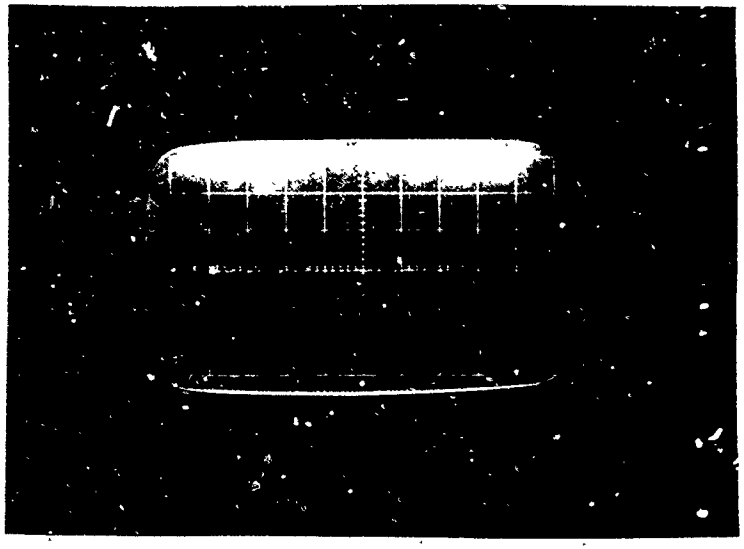

VOLTS/CM 5 SWEEP/CM .5 usec

VOLTS/CM 5 SWEEP/CM 5usec

TEST NO. 21 - 4, 5, 6: CIRCUITS TEST - 10 VOLT MONITOR

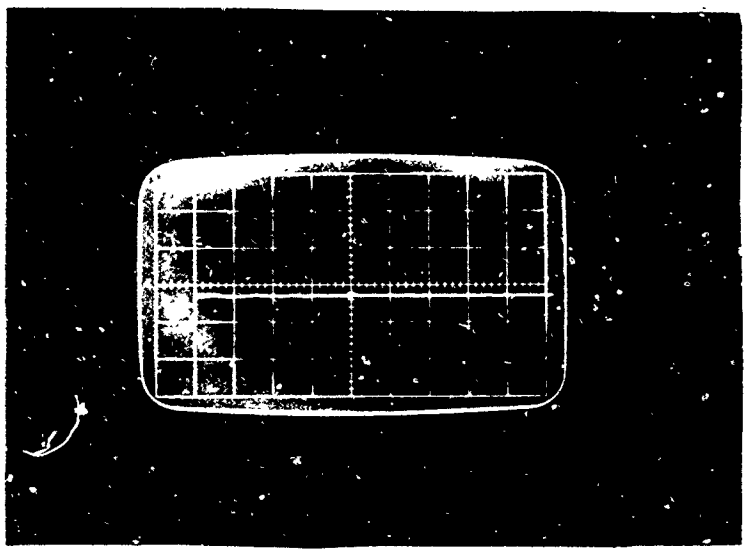

VOLTS/CM 5 SWEEP/CM 5 usec

VOLTS/CM _____ SWEEP/CM _____

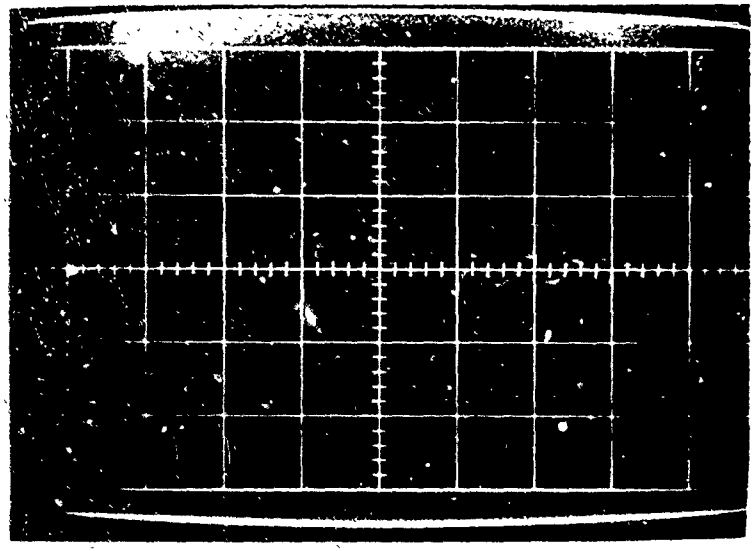

VOLTS/CM .2 SWEEP/CM .5 usec

VOLTS/CM .2 SWEEP/CM 5 usec

TEST NO. 21 - 7, 8, 9: CIRCUITS TEST - 2100 VOLT MONITOR

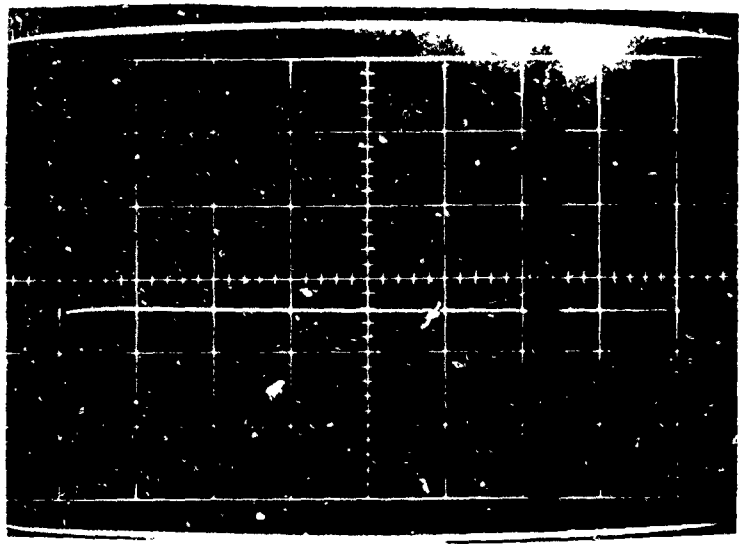

VOLTS/CM 0.2 SWEEP/CM 50 usec

VOLTS/CM _____ SWEEP/CM _____

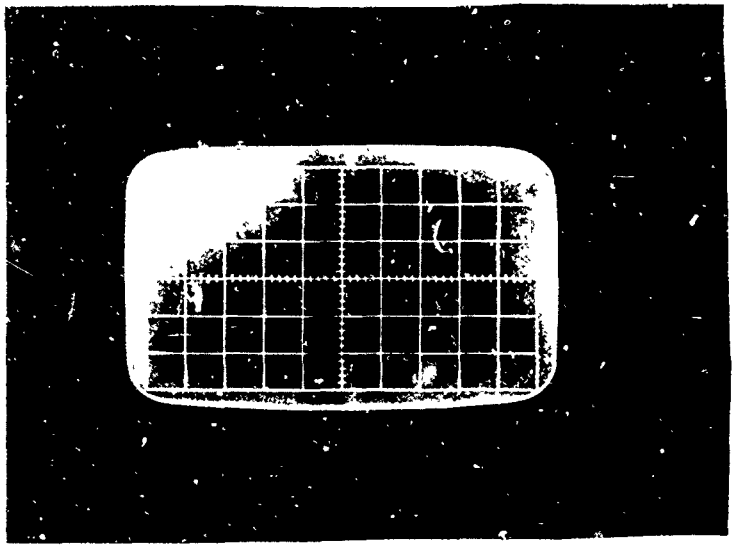

VOLTS/CM 0.2 SWEEP/CM 0.5 usec

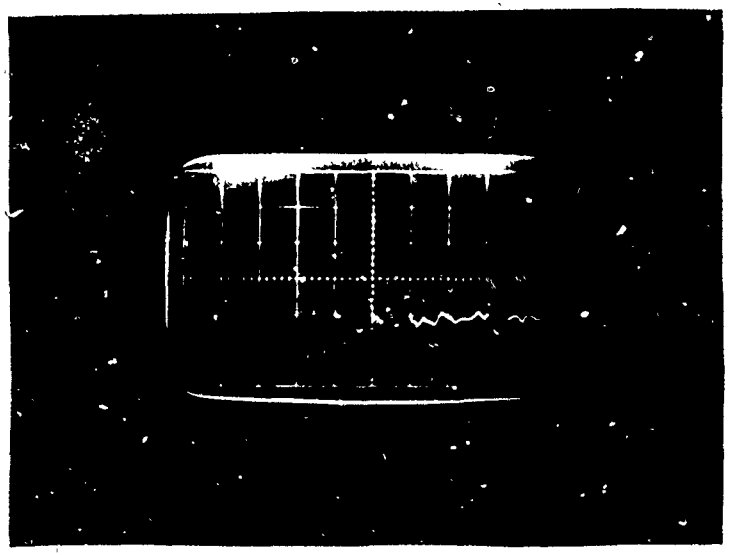

VOLTS/CM 0.2 SWEEP/CM 5 usec

TEST NO. 21 - 10, 11, 12: CIRCUITS TEST - 1000 VOLT MONITOR

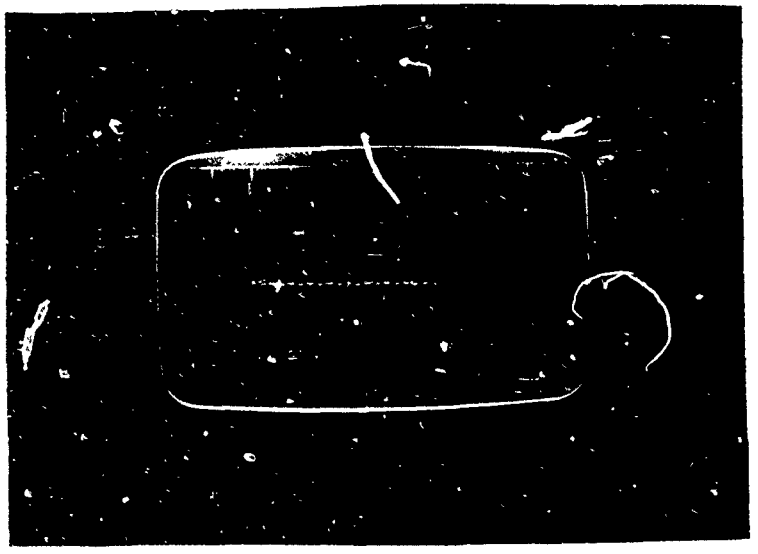

VOLTS/CM .2 SWEEP/CM 50 usec

VOLTS/CM _____ SWEEP/CM _____

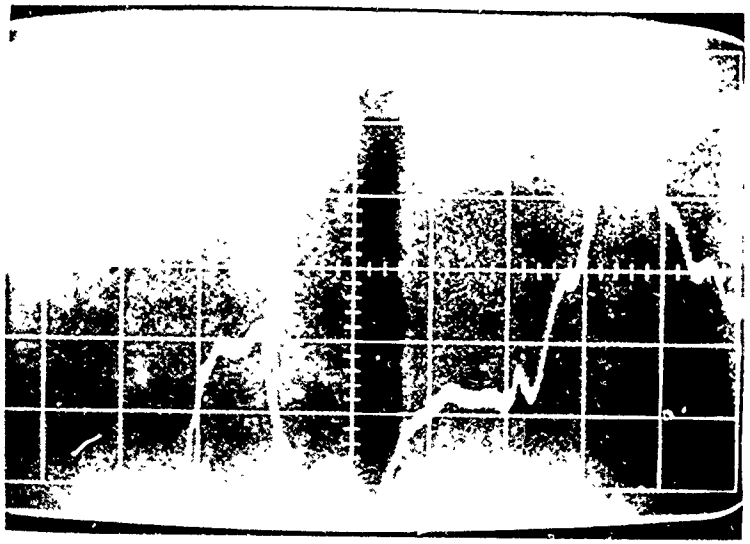

VOLTS/CM 2 SWEEP/CM 0.5 usec

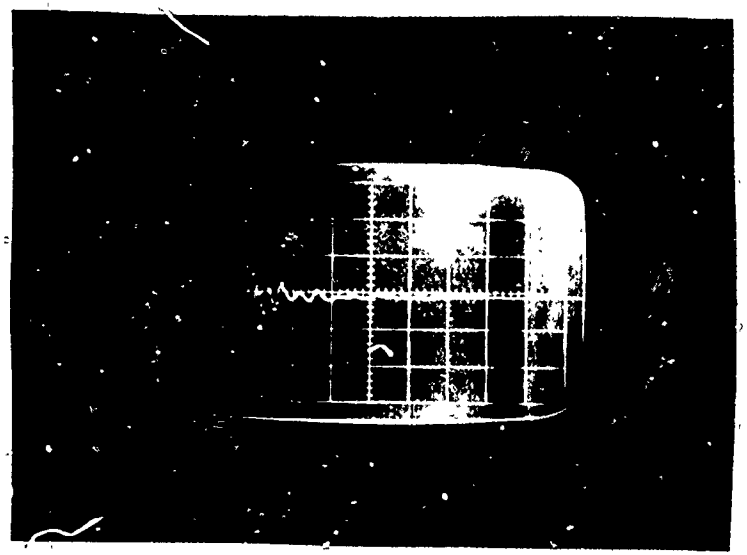

VOLTS/CM 2 SWEEP/CM 5 usec

TEST NO. 21 - 13, 14, 15: CIRCUITS TEST - START MONITOR

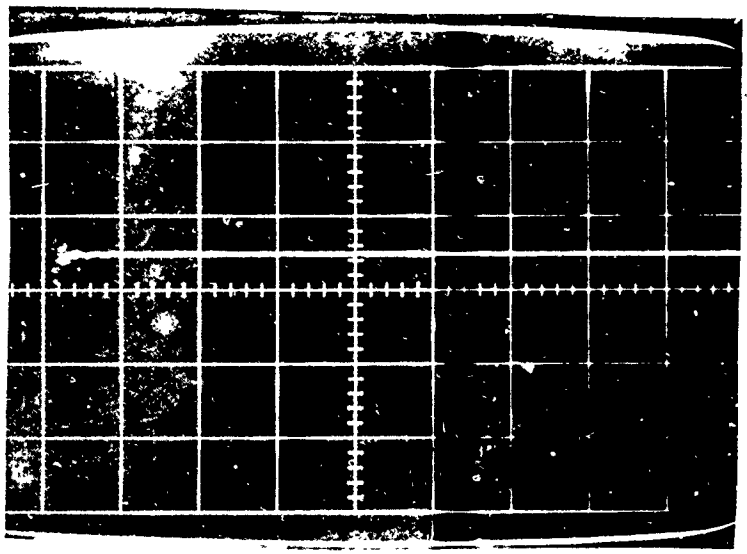

VOLTS/CM 2 SWEEP/CM 50 usec

VOLTS/CM _____ SWEEP/CM _____

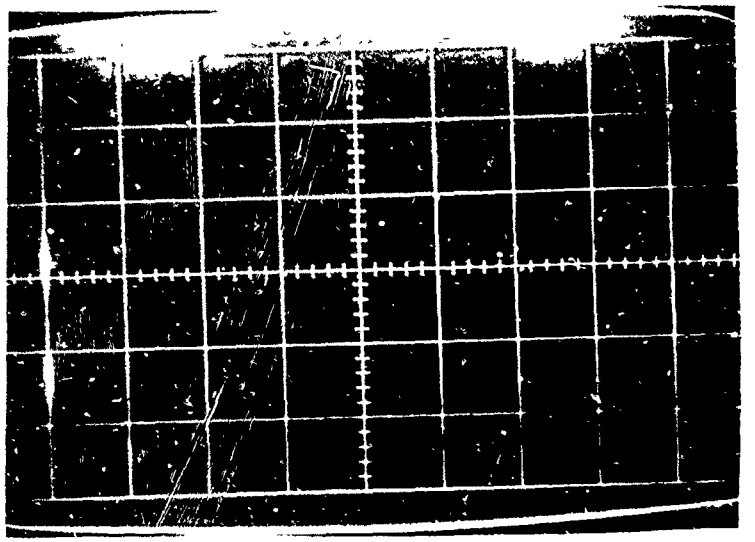

VOLTS/CM 50 mv SWEEP/CM .5 usec

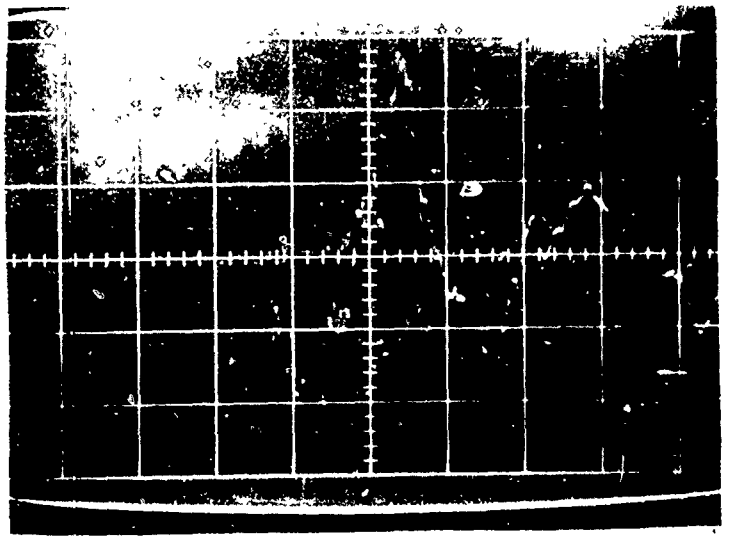

VOLTS/CM 50 mv SWEEP/CM 5 usec

TEST NO. 21 - 16, 17, 18: CIRCUITS TEST - READOUT AMPLIFIER

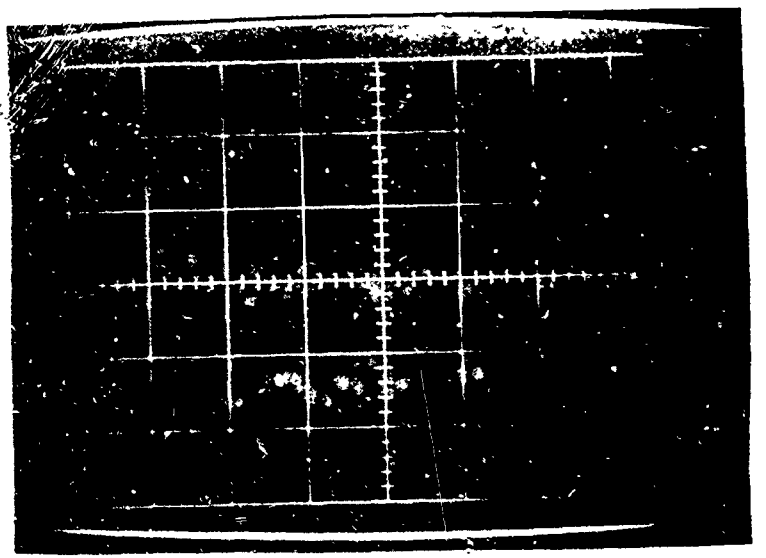

VOLTS/CM 50 mv SWEEP/CM 50 usec

VOLTS/CM _____ SWEEP/CM _____

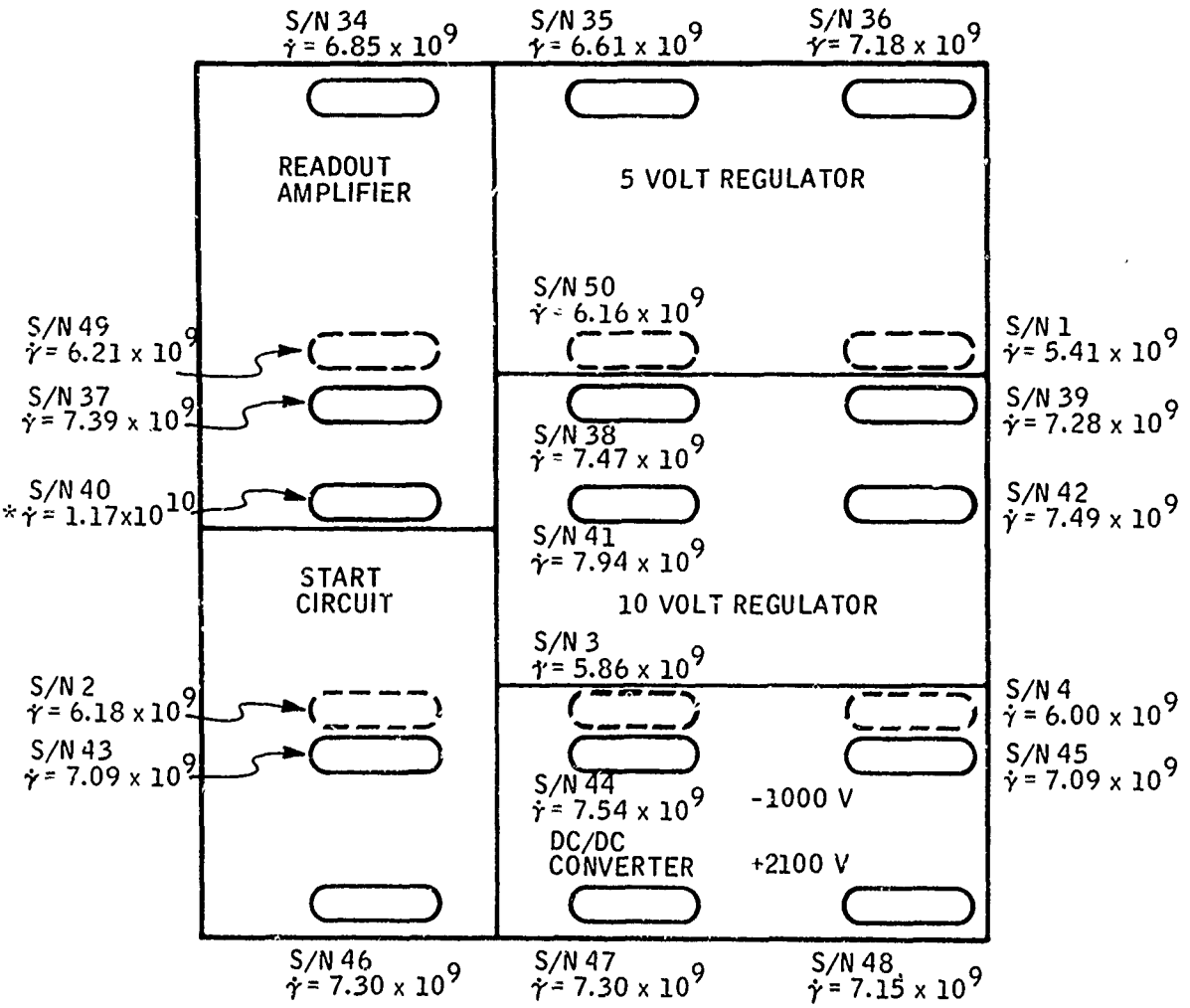

*Assumed to be in error - not included in average dose or dose rate calculations.

Circuits Test Dosimetry (Shot No. 22)

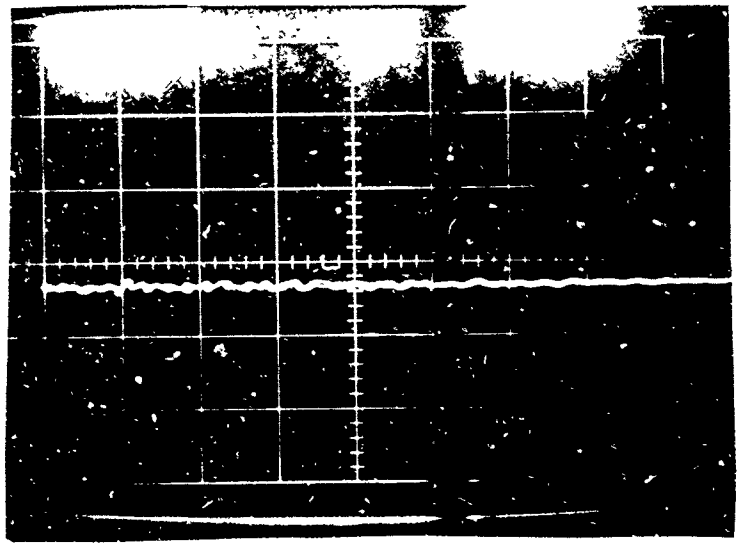

VOLTS/CM 2 SWEEP/CM 0.5 usec

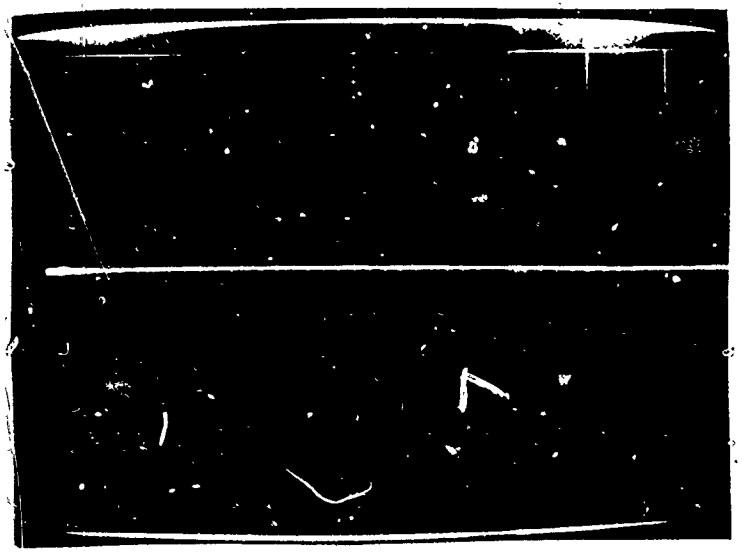

VOLTS/CM 2 SWEEP/CM 5 usec

TEST NO. 22 - 1, 2, 3: CIRCUITS TEST - 5 VOLT MONITOR

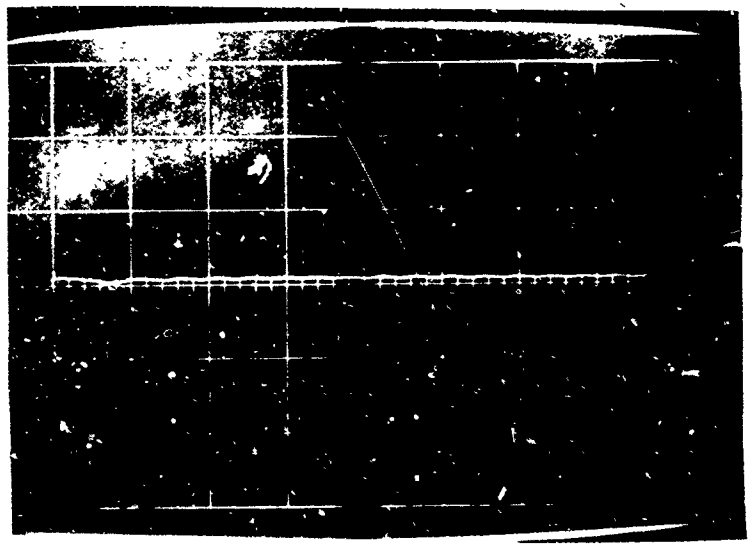

VOLTS/CM 2 SWEEP/CM 50 usec

VOLTS/CM _____ SWEEP/CM _____

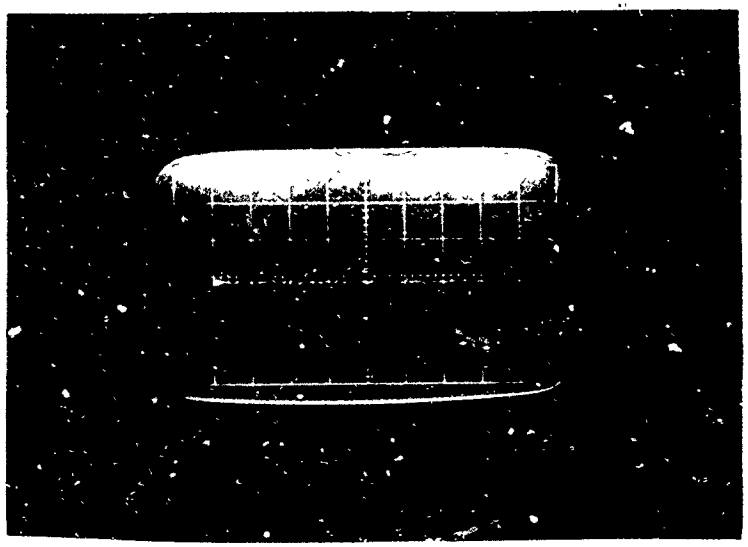

VOLTS/CM 5 SWEEP/CM .5 usec

VOLTS/CM 5 SWEEP/CM 5 usec

TEST NO. 22 - 4, 5, 6: CIRCUITS TEST - 10 VOLT MONITOR

VOLTS/CM 5 SWEEP/CM 50 usec

VOLTS/CM _____ SWEEP/CM _____

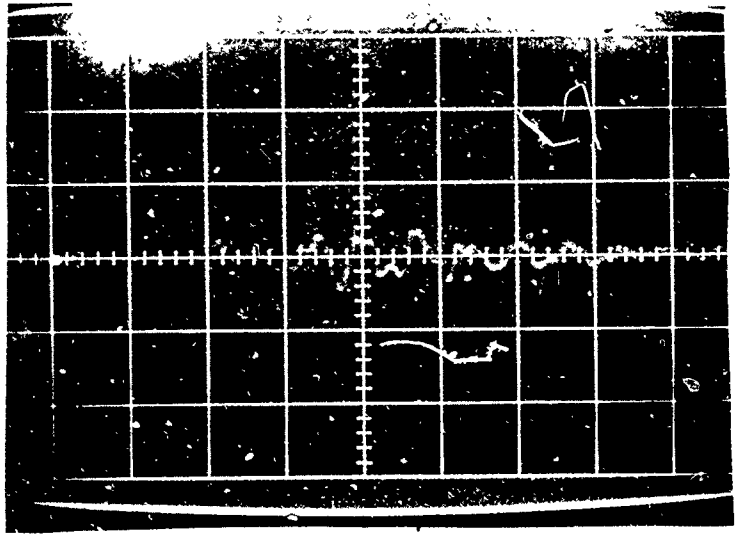

VOLTS/CM .2 SWEEP/CM .5 usec

VOLTS/CM .2 SWEEP/CM 5 usec

TEST NO. 22 - 7, 8, 9: CIRCUITS TEST - 2100 VOLT MONITOR

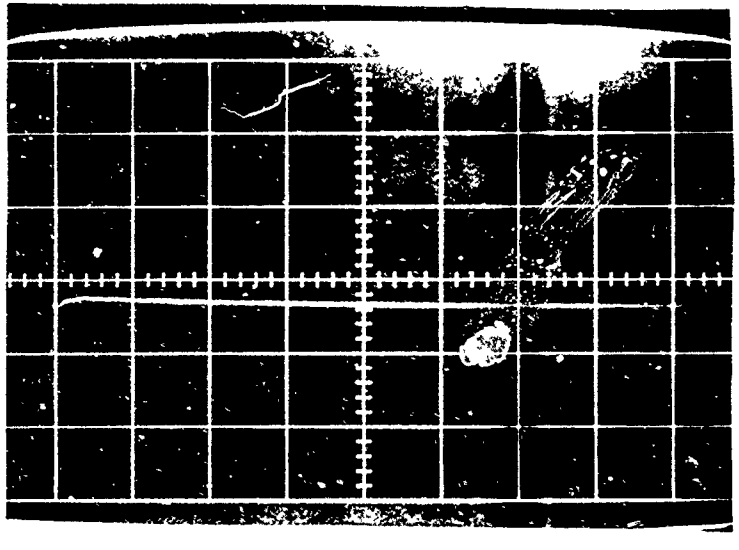

VOLTS/CM 0.2 SWEEP/CM 50 usec

VOLTS/CM _____ SWEEP/CM _____

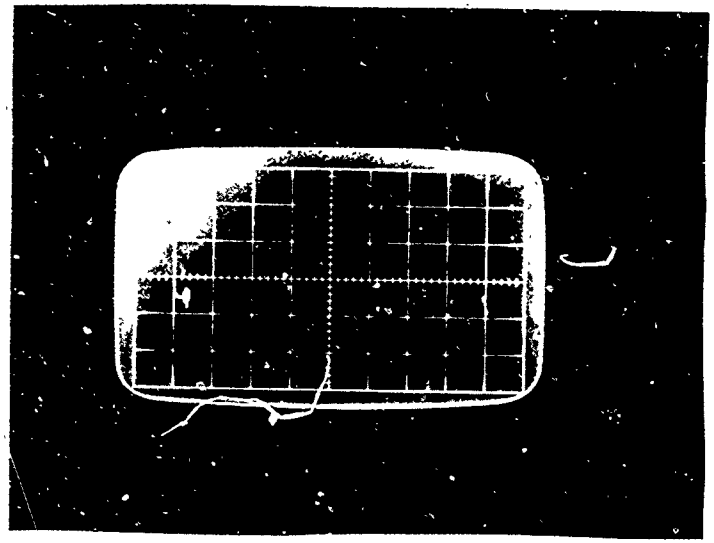

VOLTS/CM 0.2 SWEEP/CM 0.5 usec

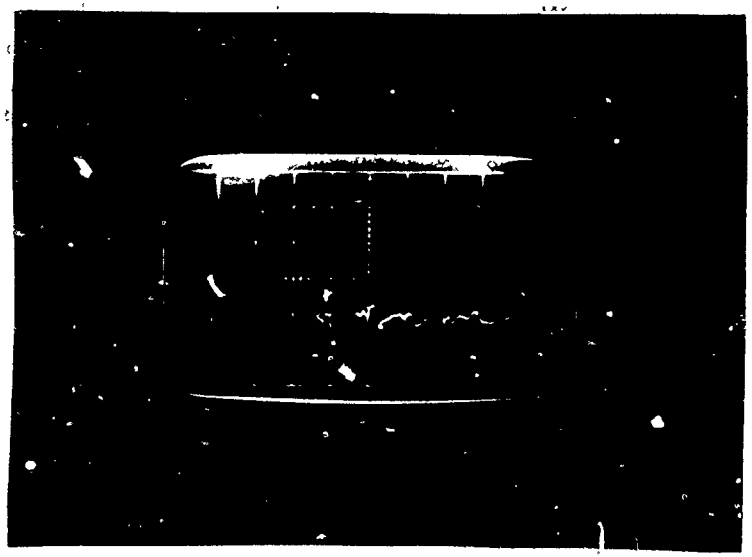

VOLTS/CM 0.2 SWEEP/CM 5 usec

TEST NO. 22 - 10, 11, 12: CIRCUITS TEST - 1000 VOLT MONITOR

VOLTS/CM .2 SWEEP/CM 50 usec

VOLTS/CM _____ SWEEP/CM _____

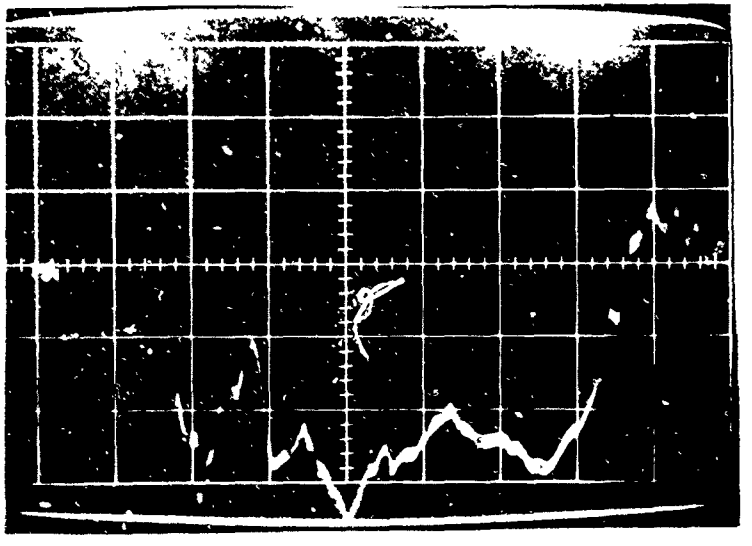

VOLTS/CM 2 SWEEP/CM .5 usec

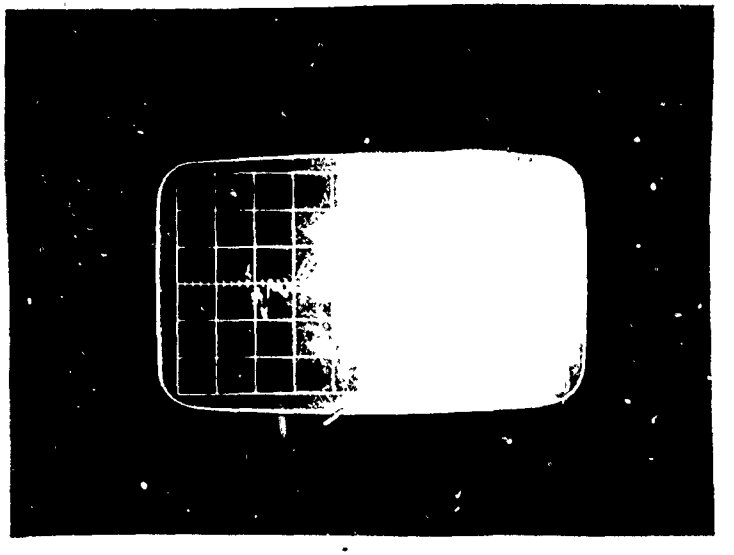

VOLTS/CM 2 SWEEP/CM 5 usec

TEST NO. 22 - 13, 14, 15: CIRCUITS TEST - START MONITOR

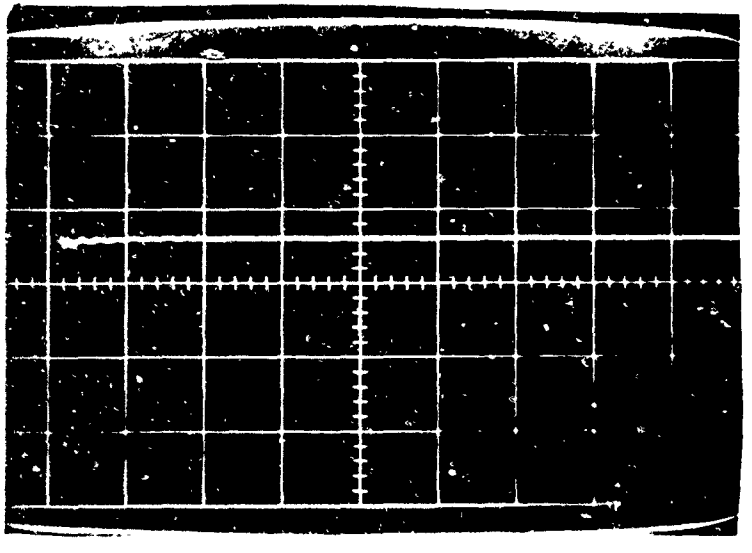

VOLTS/CM 2 SWEEP/CM 50 usec

VOLTS/CM _____ SWEEP/CM _____

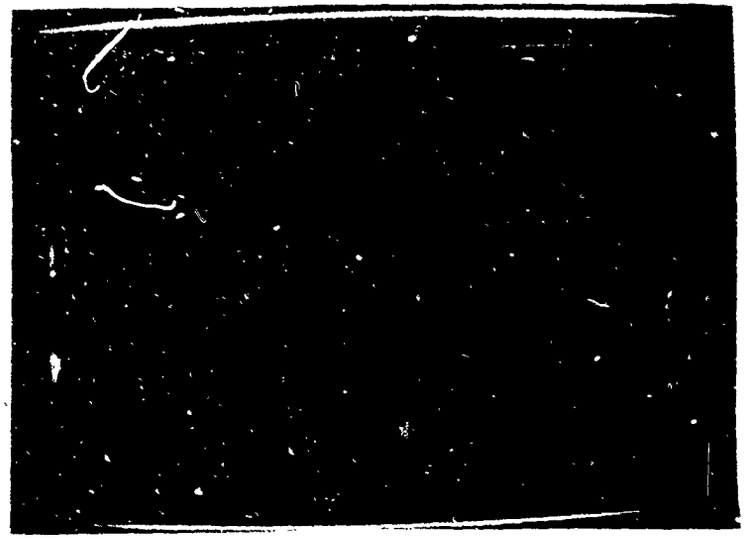

VOLTS/CM 50 mv SWEEP/CM .5 usec

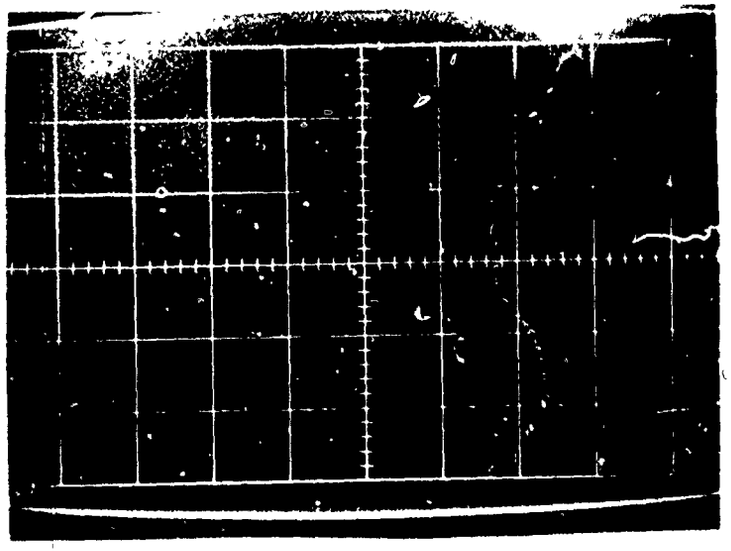

VOLTS/CM 50 mv SWEEP/CM 5 usec

TEST NO. 22 - 16, 17, 18: CIRCUITS TEST - READOUT AMPLIFIER

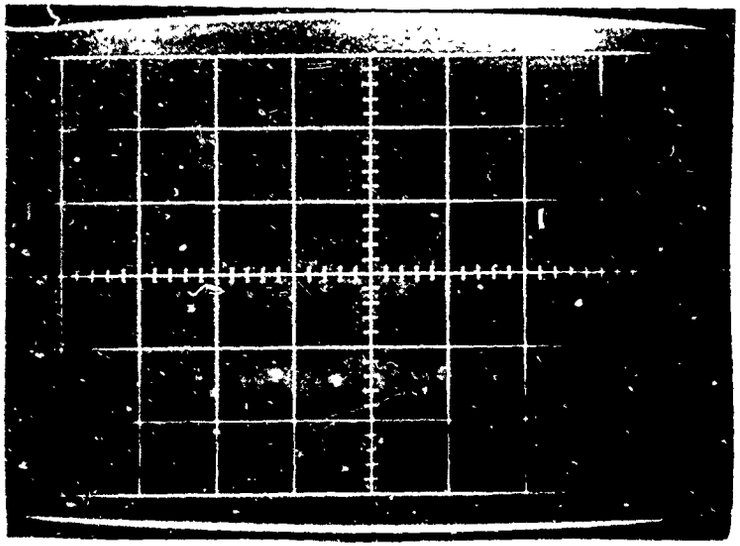

VOLTS/CM 50 mv SWEEP/CM 50 usec

VOLTS/CM _____ SWEEP/CM _____

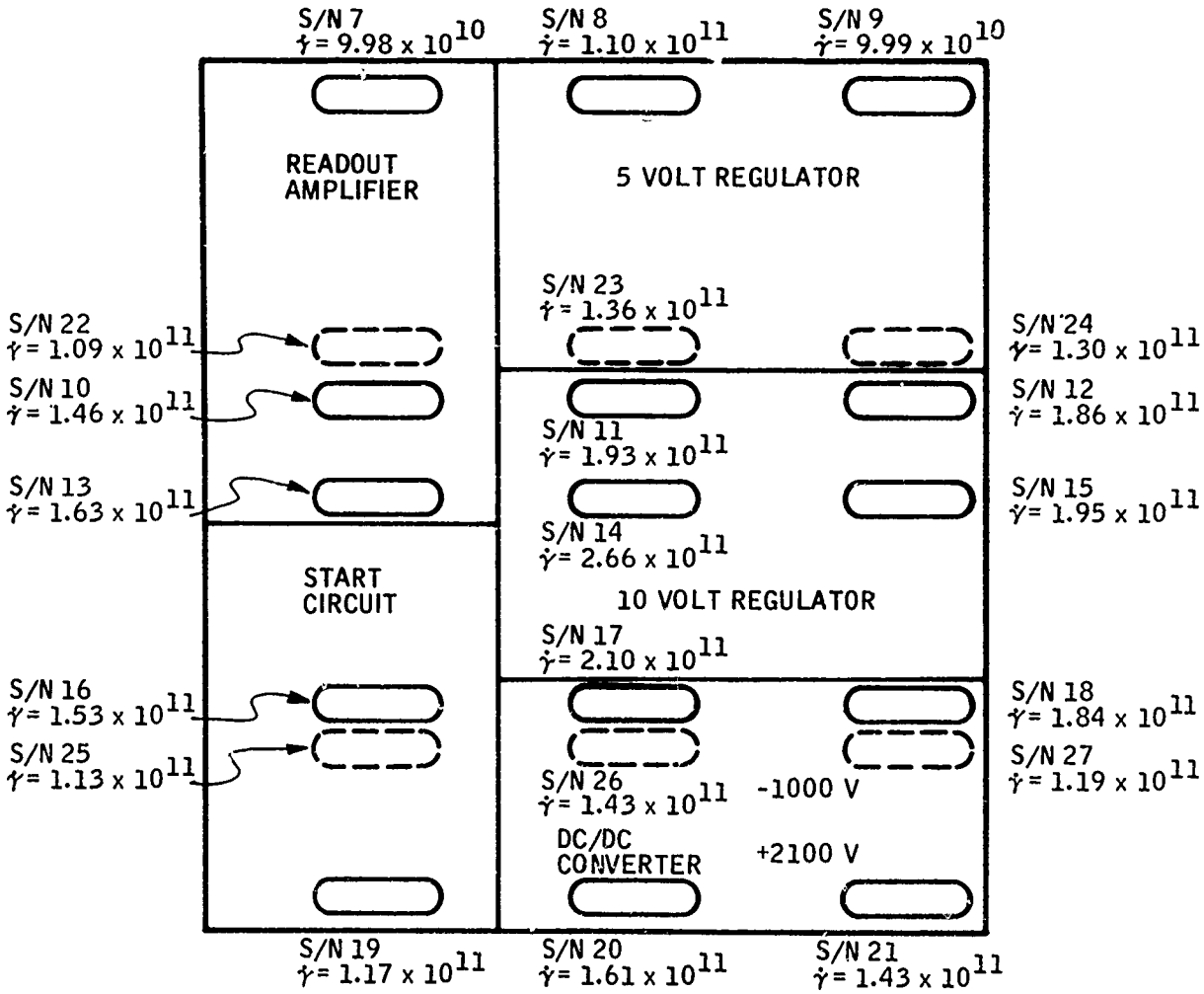

Circuits Test Dosimetry (Shot No. 23)

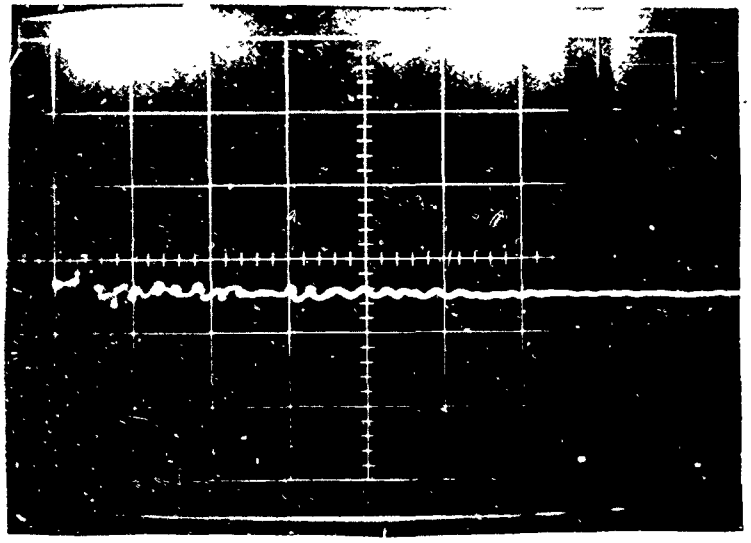

VOLTS/CM 2 SWEEP/CM .5 usec

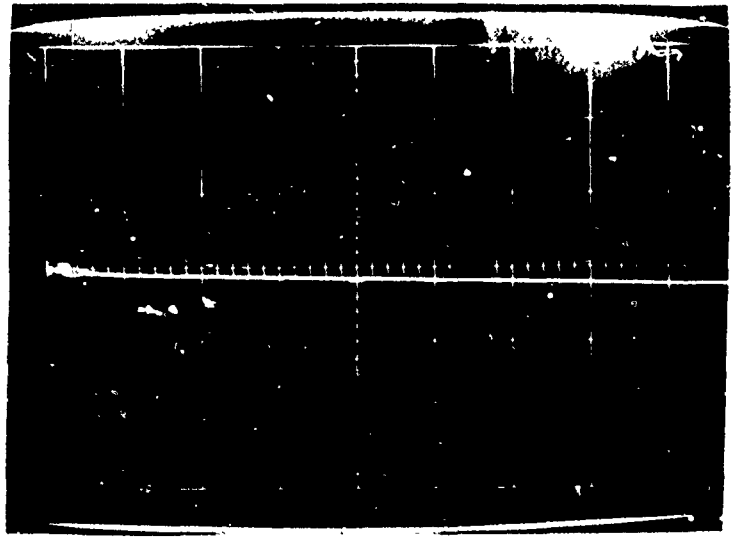

VOLTS/CM 2 SWEEP/CM 5 usec

TEST NO. 23 - 1, 2, 3: CIRCUITS TEST - 5 VOLT MONITOR

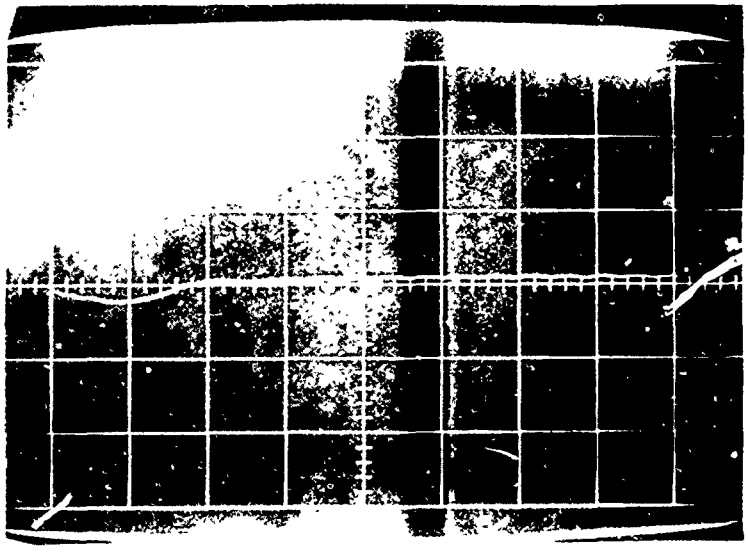

VOLTS/CM 2 SWEEP/CM 50 usec

VOLTS/CM _____ SWEEP/CM _____

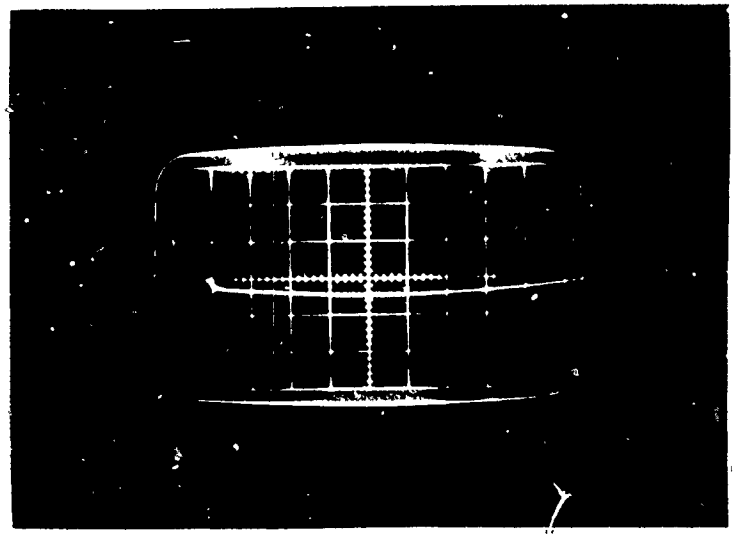

VOLTS/CM_____ SWEEP/CM_____

VOLTS/CM 5 SWEEP/CM 5 usec

TEST NO. 23 - 4, 5, 6: CIRCUITS TEST - 10 VOLT MONITOR

VOLTS/CM 5 SWEEP/CM 50 usec

VOLTS/CM_____ SWEEP/CM_____

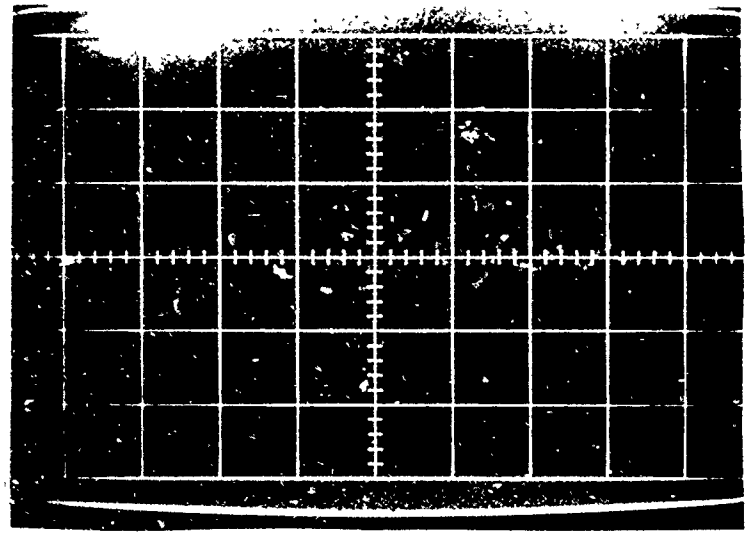

VOLTS/CM .2 SWEEP/CM .5 usec

VOLTS/CM _____ SWEEP/CM _____

TEST NO. 23 - 7, 8, 9: CIRCUITS TEST - 2100 VOLT MONITOR

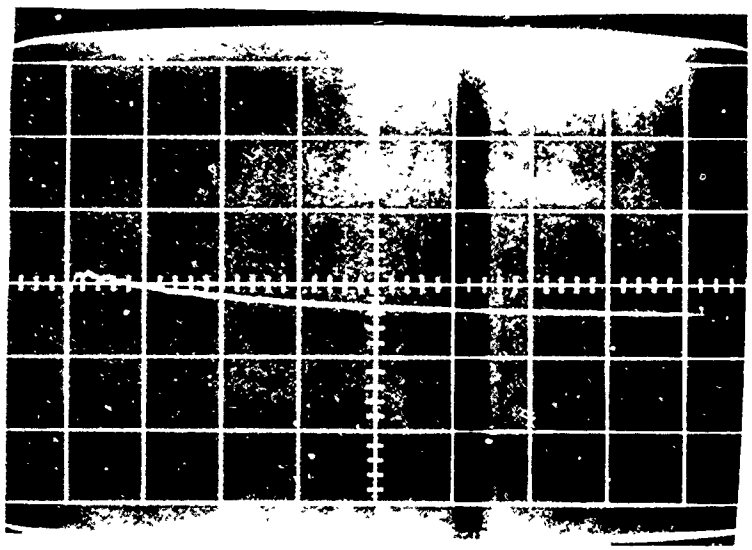

VOLTS/CM 0.2 SWEEP/CM 50 usec

VOLTS/CM _____ SWEEP/CM _____

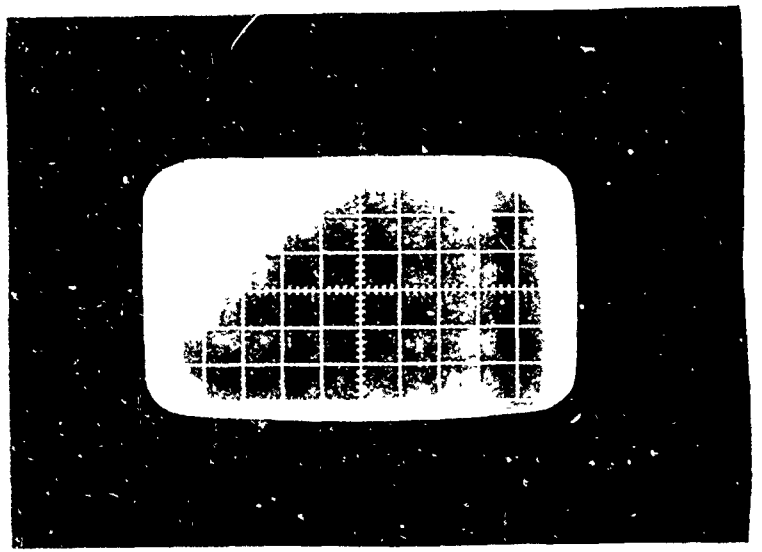

VOLTS/CM 0.2 SWEEP/CM 0.5 usec

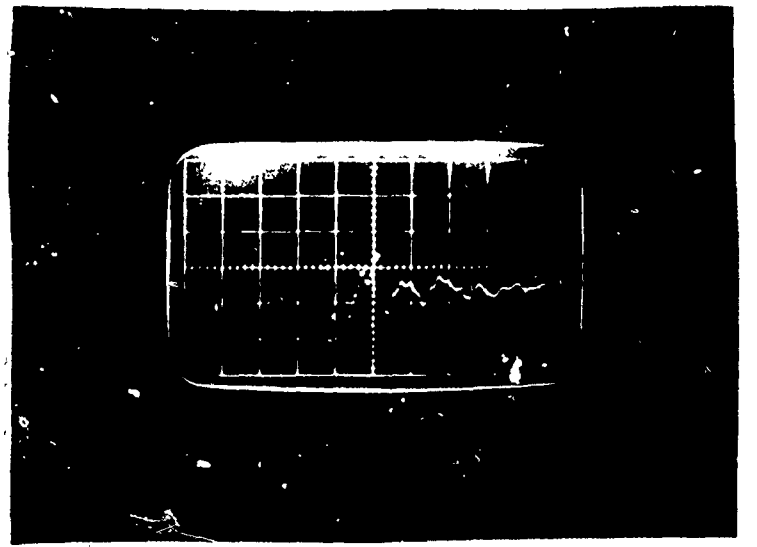

VOLTS/CM 0.2 SWEEP/CM 5 usec

TEST NO. 23 - 10, 11, 12 - CIRCUITS TEST - 1000 VOLT MONITOR

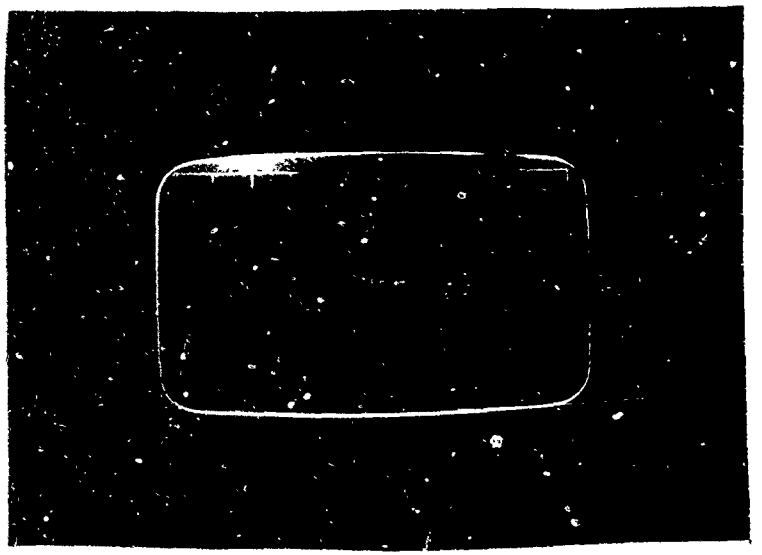

VOLTS/CM .2 SWEEP/CM 50 usec

VOLTS/CM _____ SWEEP/CM _____

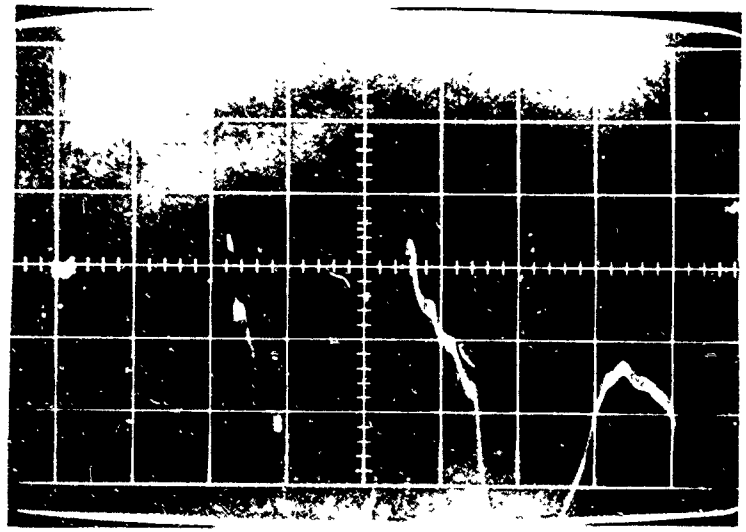

VOLTS/CM 2 SWEEP/CM 0.5 usec

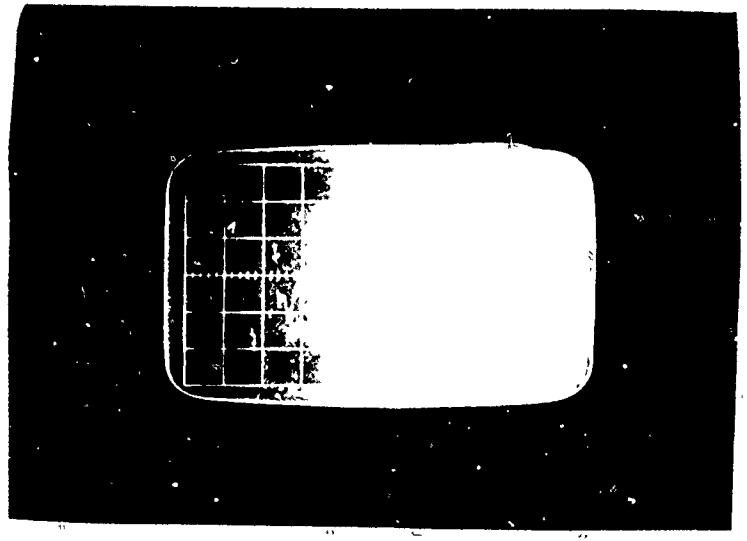

VOLTS/CM 2 SWEEP/CM 5 usec

TEST NO. 23 - 13, 14, 15: CIRCUITS TEST - START MONITOR

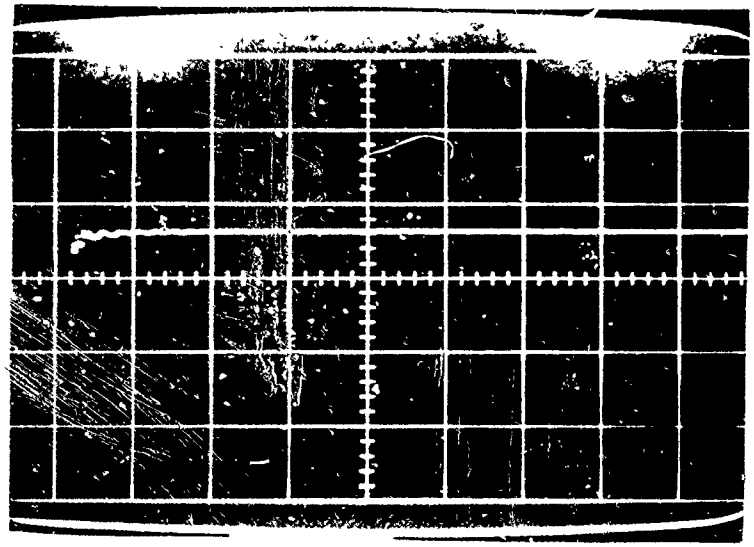

VOLTS/CM 2 SWEEP/CM 50 usec

VOLTS/CM _____ SWEEP/CM _____

VOLTS/CM 50 mv SWEEP/CM .5 usec

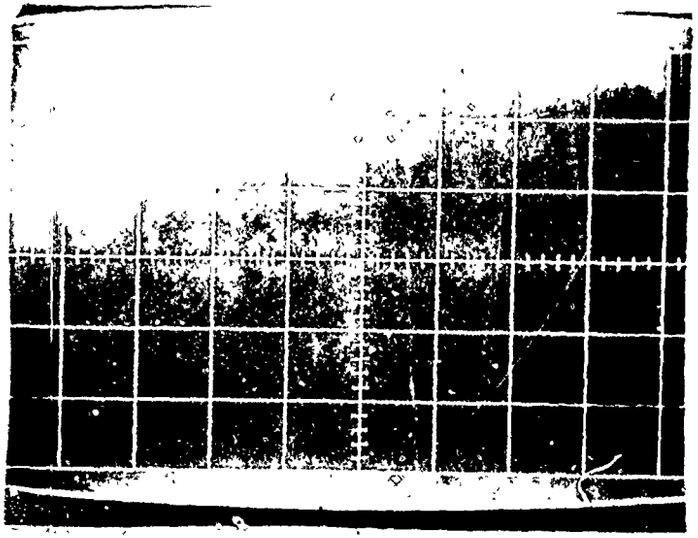

VOLTS/CM 50 mv SWEEP/CM 5 usec

TEST NO. 23 - 16, 17, 18 - CIRCUITS TESTS - READOUT MONITOR

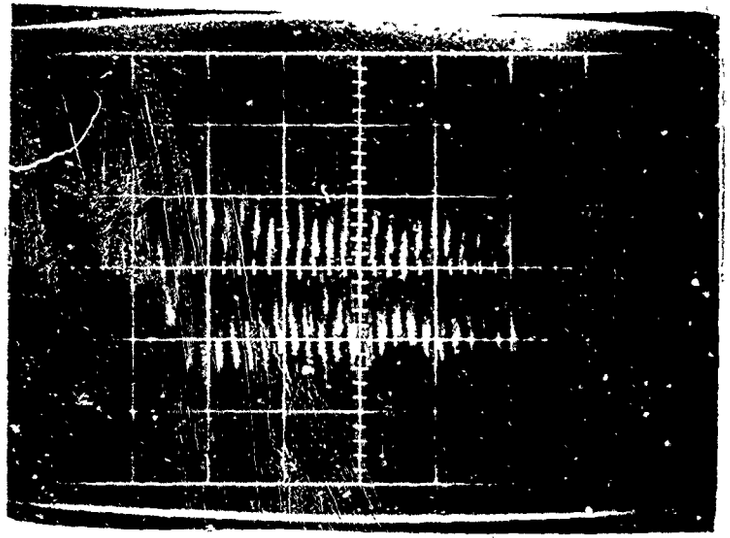

VOLTS/CM 50 mv SWEEP/CM 50 usec

VOLTS/CM _____ SWEEP/CM _____

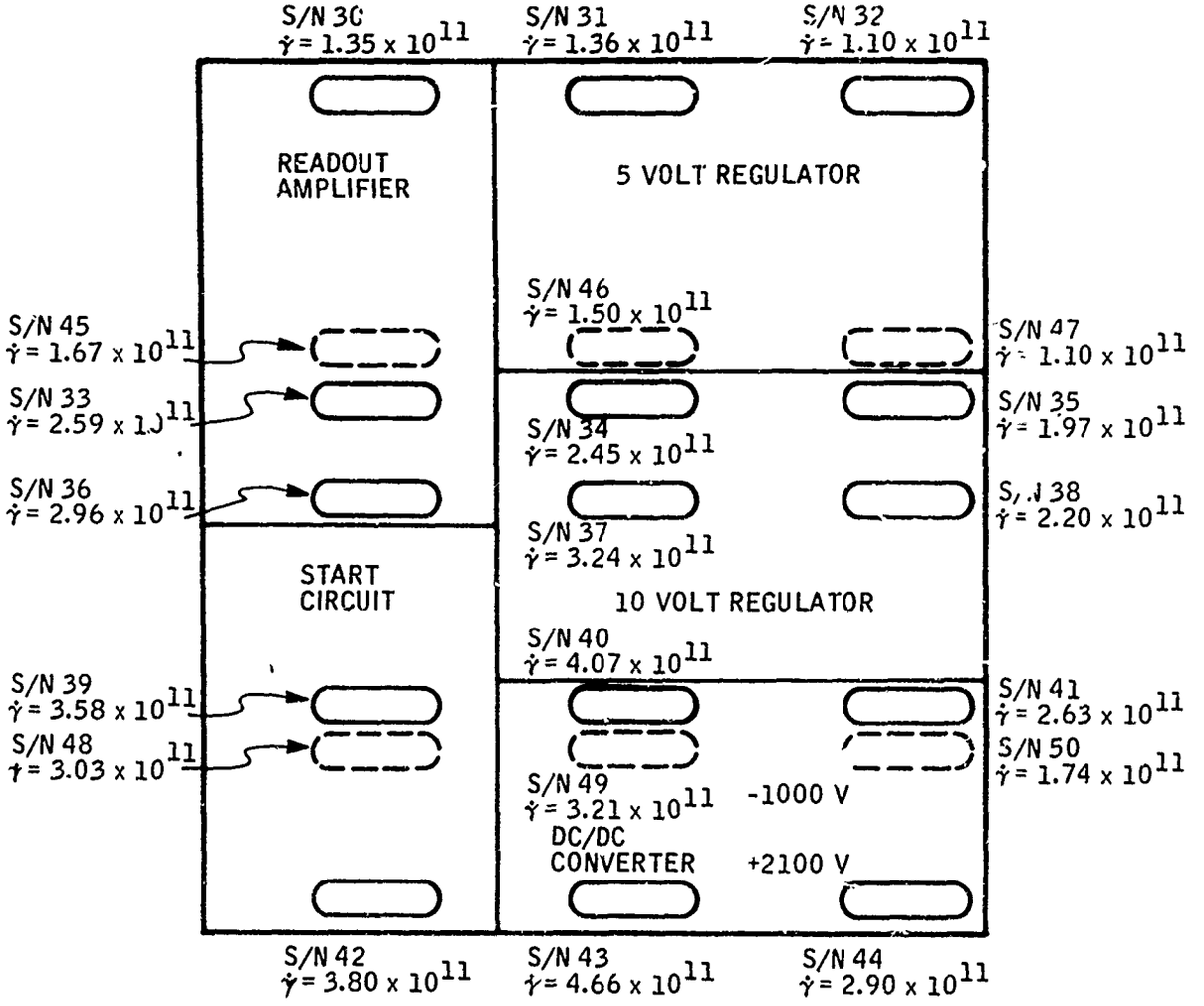

Circuits Test Dosimetry (Shot No. 24)

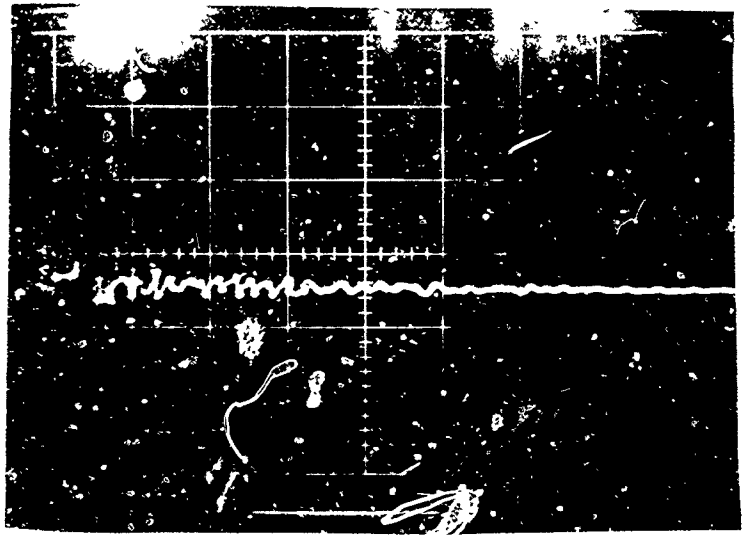

VOLTS/CM 2 SWEEP/CM 0.5 usec

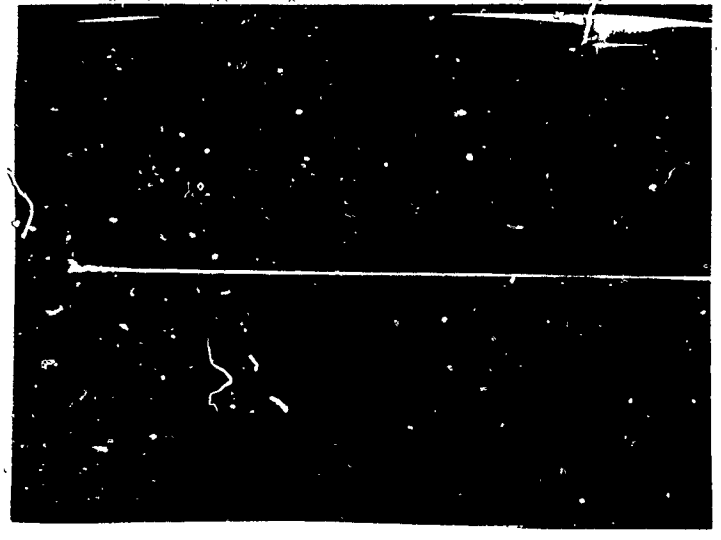

VOLTS/CM 2 SWEEP/CM 5 usec

TEST NO. 24 - 1, 2, 3: CIRCUITS TEST - 5 VOLT MONITOR

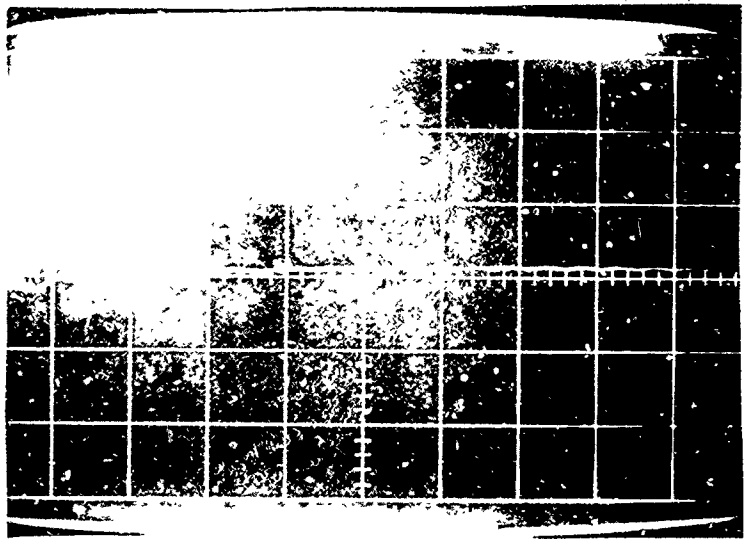

VOLTS/CM 2 SWEEP/CM 50 usec

VOLTS/CM _____ SWEEP/CM _____

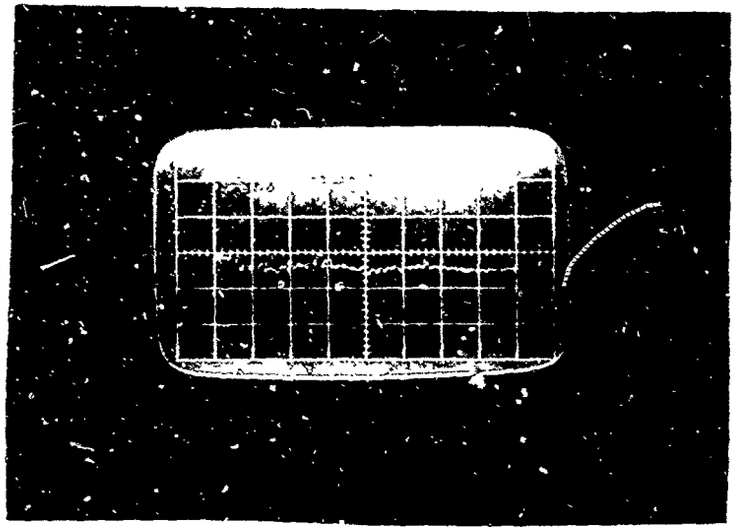

VOLTS/CM 5 SWEEP/CM .5 usec

VOLTS/CM 5 SWEEP/CM 5 usec

TEST NO. 24 - 4, 5, 6: CIRCUITS TEST - 10 VOLT MONITOR

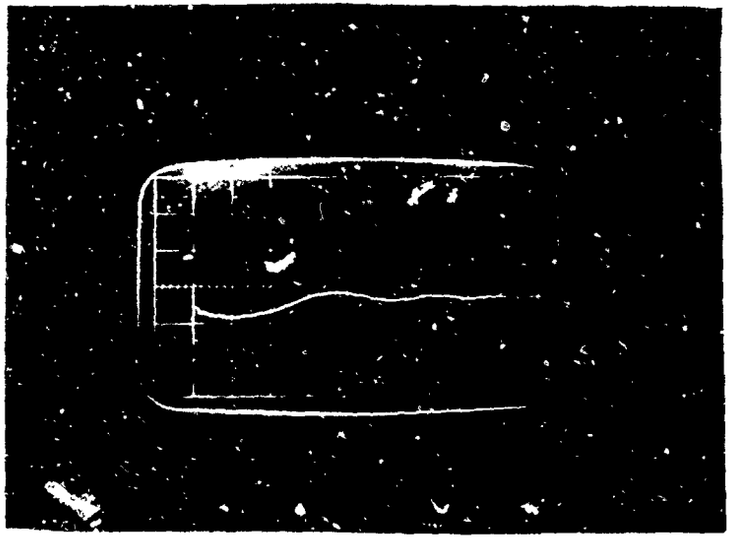

VOLTS/CM 5 SWEEP/CM 50 usec

VOLTS/CM _____ SWEEP/CM _____

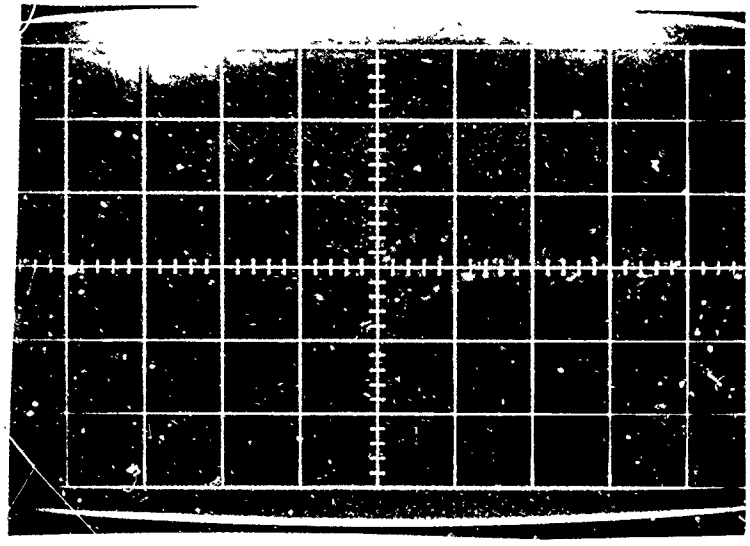

VOLTS/CM .2 SWEEP/CM .5 usec

VOLTS/CM .2 SWEEP/CM 5 usec

TEST NO. 24 - 7, 8, 9: CIRCUITS TEST - 2100 VOLT MONITOR

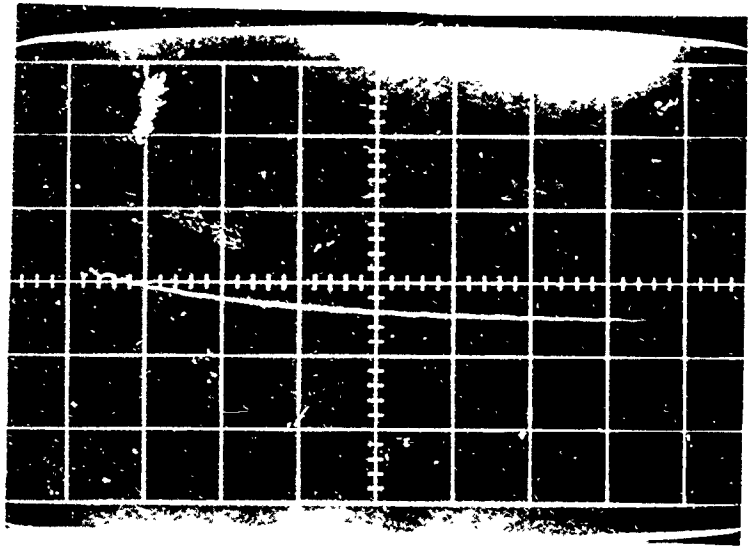

VOLTS/CM 0.2 SWEEP/CM 50 usec

VOLTS/CM _____ SWEEP/CM _____

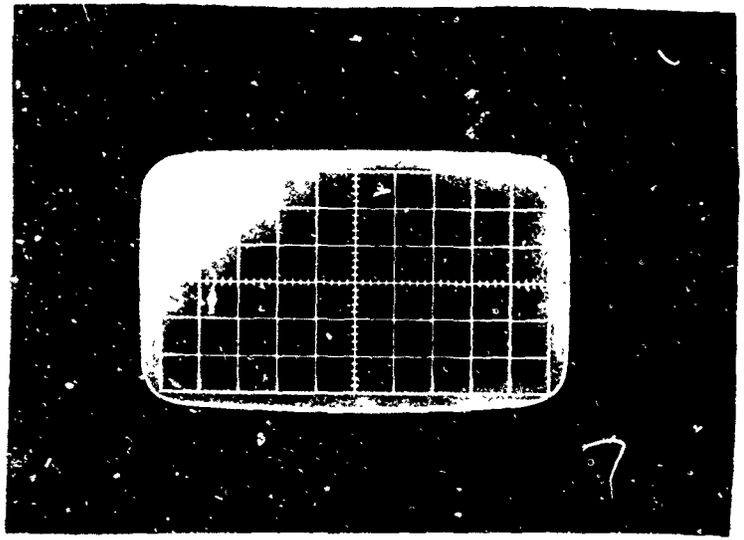

VOLTS/CM 0.2 SWEEP/CM 0.5 usec

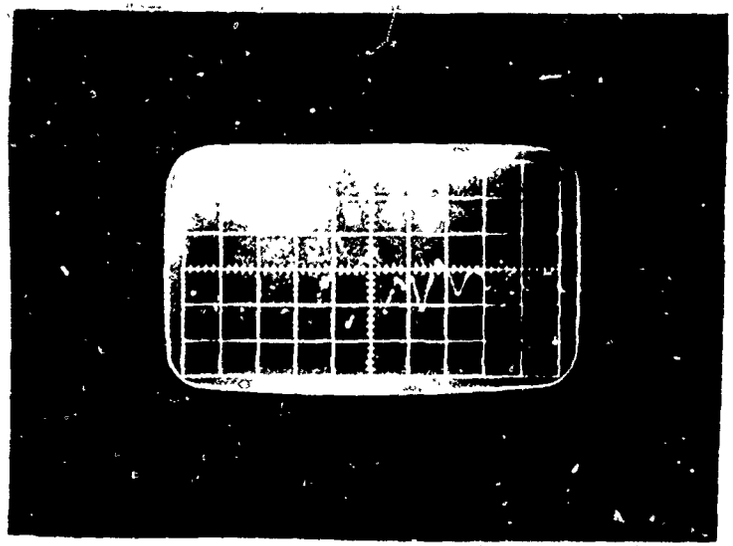

VOLTS/CM 0.2 SWEEP/CM 5 usec

TEST NO. 24 - 10, 11, 12: CIRCUITS TEST - 1000 VOLT MONITOR

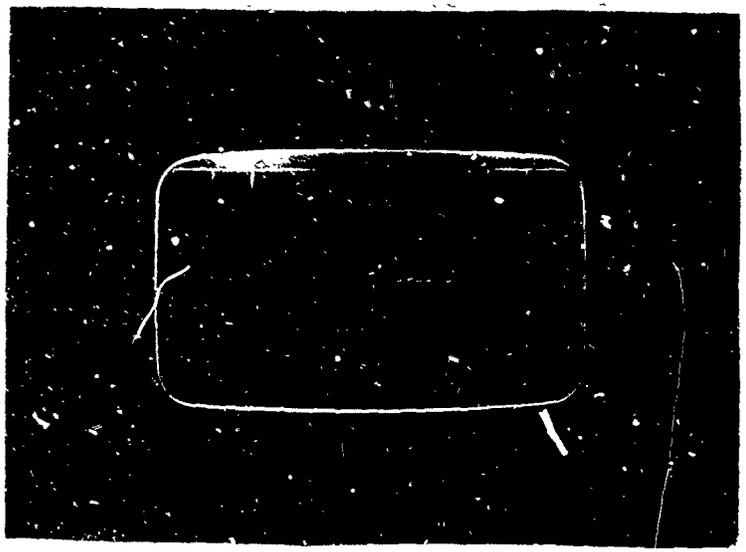

VOLTS/CM .2 SWEEP/CM 50 usec

VOLTS/CM _____ SWEEP/CM _____

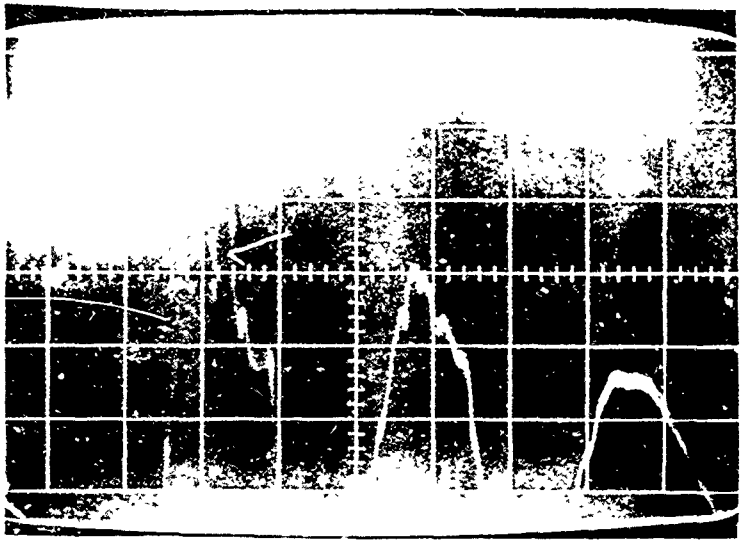

VOLTS/CM 2 SWEEP/CM 0.5 usec

VOLTS/CM 2 SWEEP/CM 5 usec

TEST NO. 24 - 13, 14, 15: CIRCUITS TEST - START MONITOR

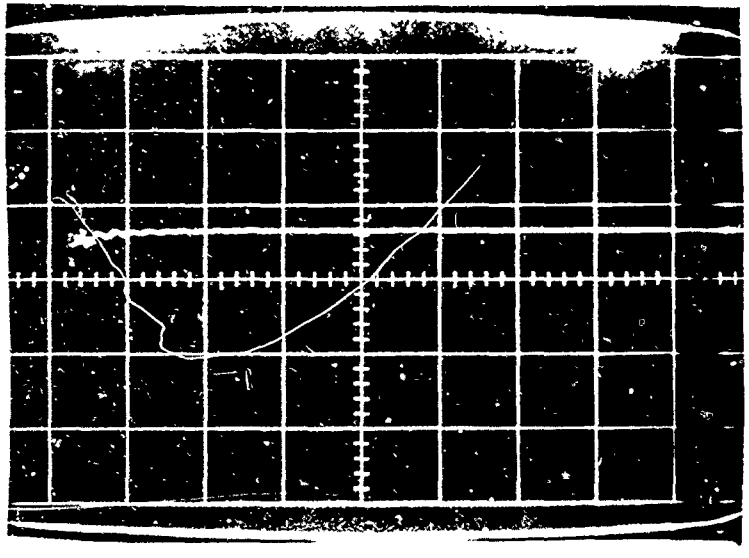

VOLTS/CM 2 SWEEP/CM 50 usec

VOLTS/CM _____ SWEEP/CM _____

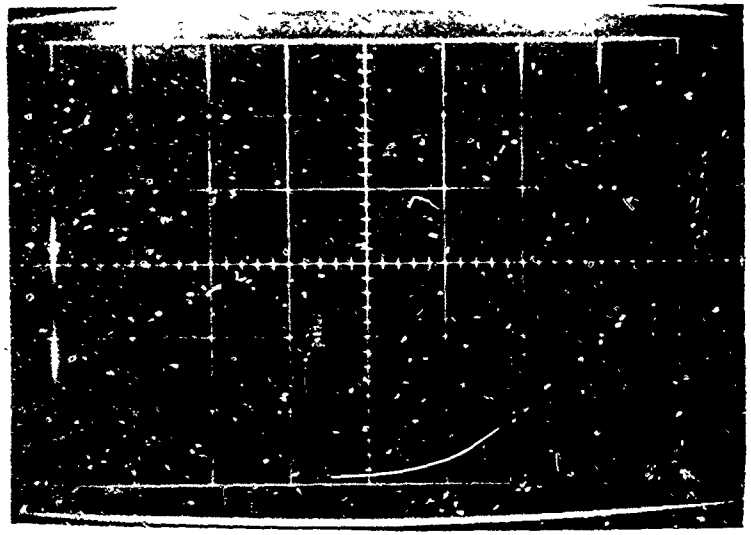

VOLTS/CM 50 mv SWEEP/CM .5 usec

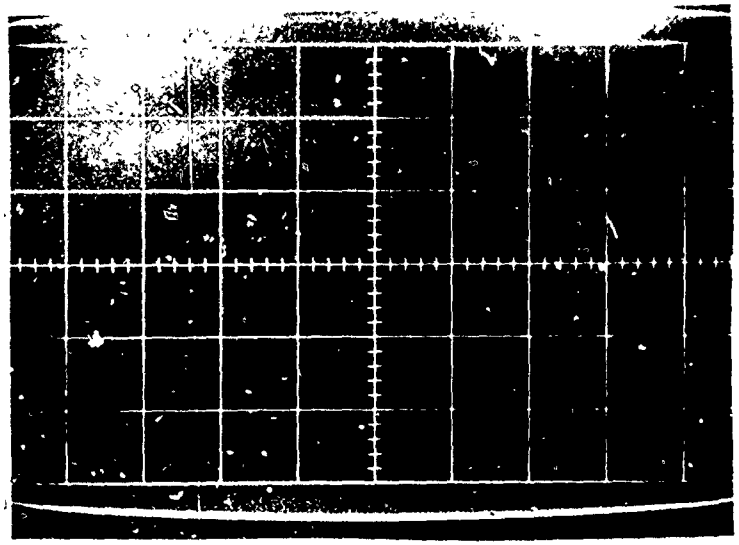

VOLTS/CM 50 mv SWEEP/CM 5 usec

TEST NO. 24 - 16, 17, 18: CIRCUITS TEST - READOUT AMPLIFIER

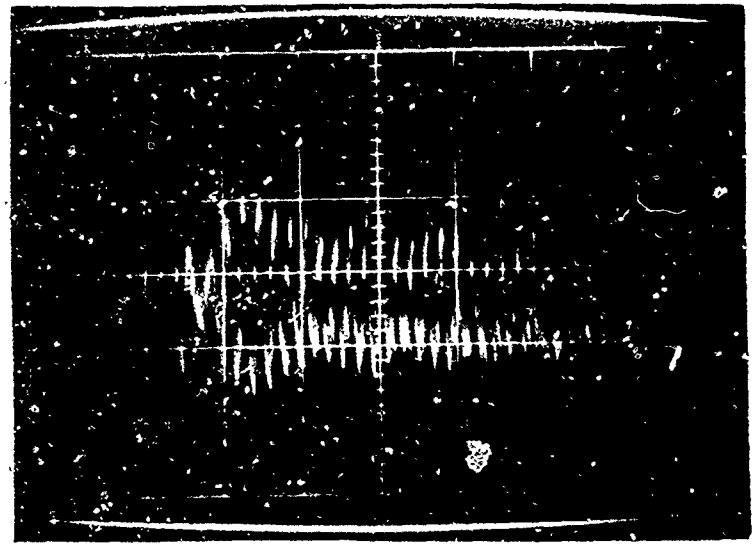

VOLTS/CM 50 mv SWEEP/CM 50 usec

VOLTS/CM _____ SWEEP/CM _____

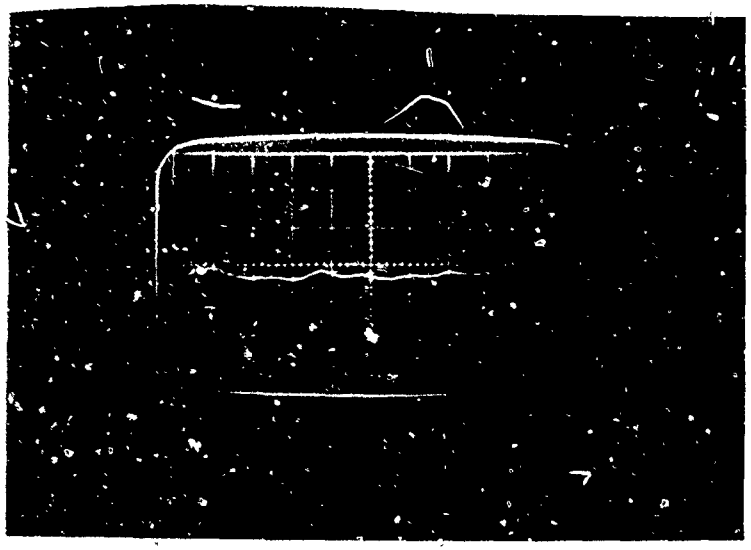

VOLTS/CM 10 SWEEP/CM 100 nsec

TEST NO. 20 - 37: SHIELD CURRENT MONITOR

VOLTS/CM 5 SWEEP/CM 500 nsec

TEST NO. 21 - 37: SHIELD CURRENT MONITOR

VOLTS/CM 5 SWEEP/CM .5 usec

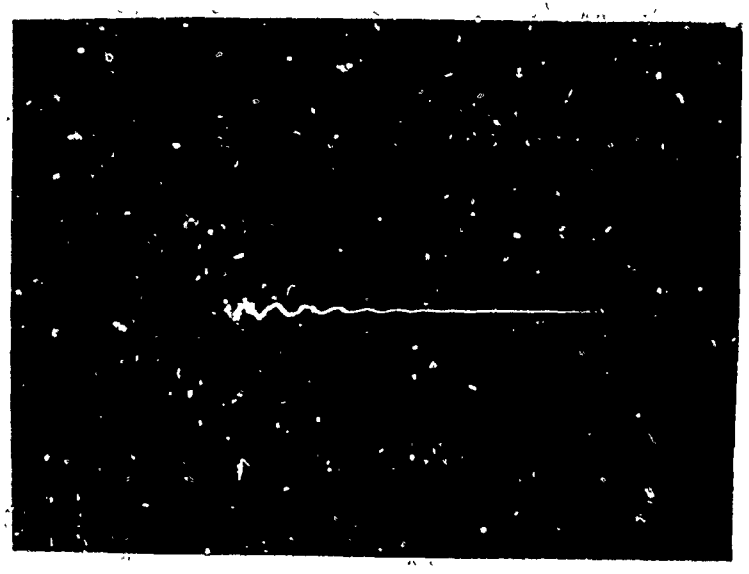

VOLTS/CM 5 SWEEP/CM 5 usec

TEST NO. 22 - 37, 38: SHIELD CURRENT MONITOR

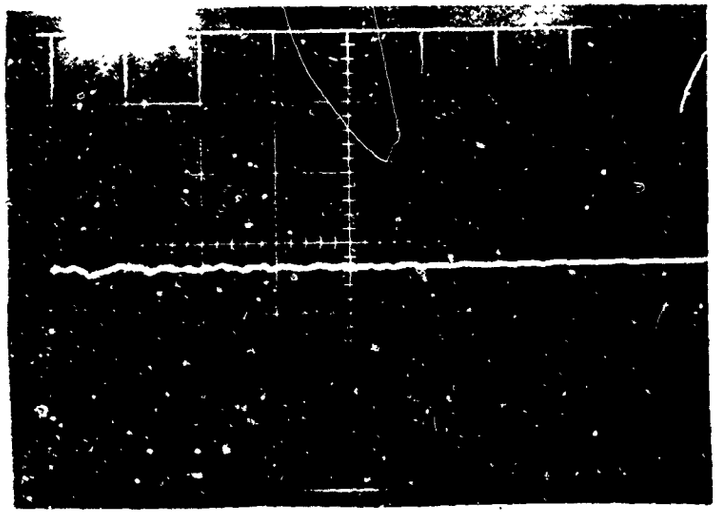

VOLTS/CM 2 SWEEP/CM 0.5 usec

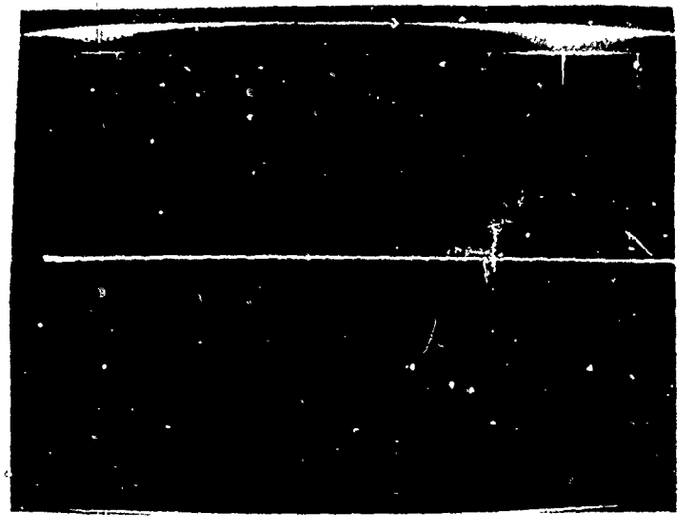

VOLTS/CM 2 SWEEP/CM 5 usec

TEST NO. 25 - 1, 2, 3: SUPPORT ELECTRONICS TEST - 5 VOLT MONITOR

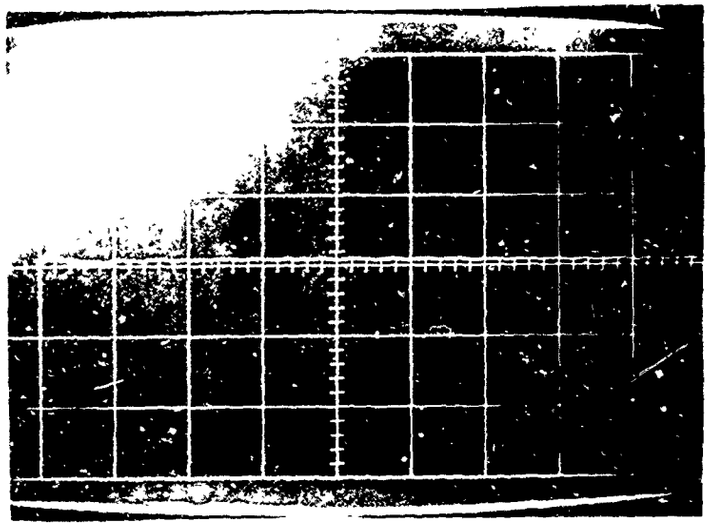

VOLTS/CM 2 SWEEP/CM 50 usec

VOLTS/CM _____ SWEEP/CM _____

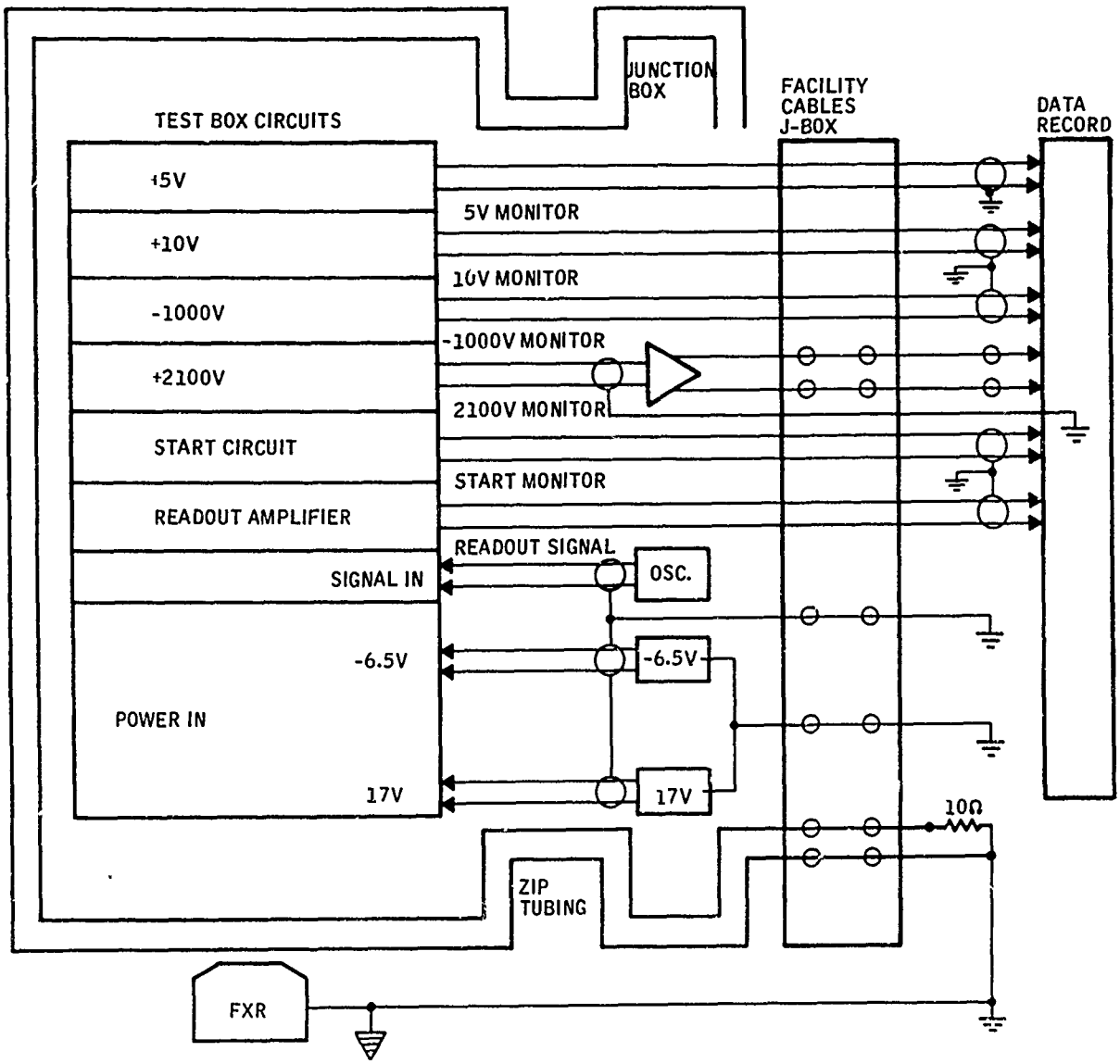

Support Electronics Test

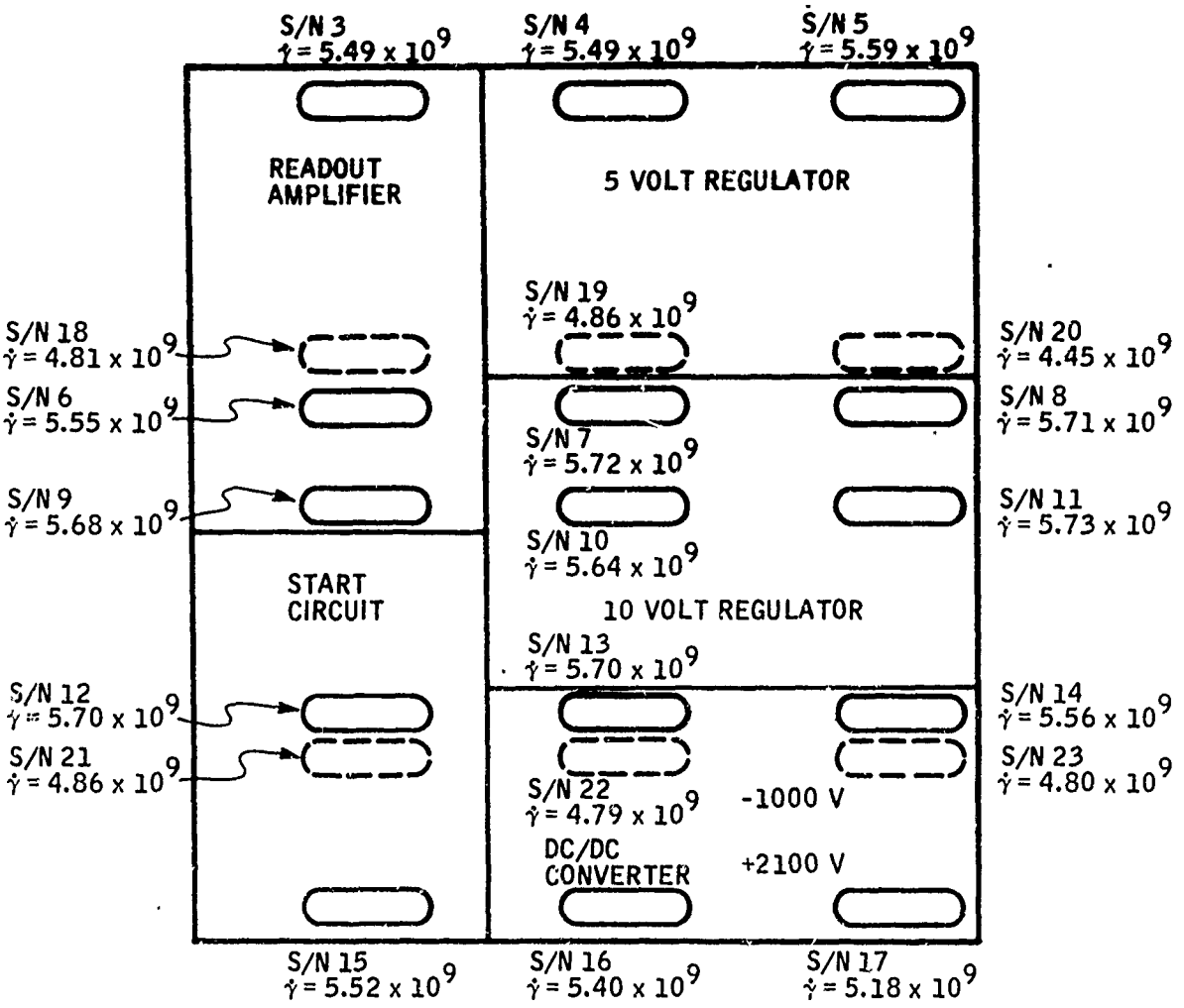

Support Electronics Dosimetry (Shot No. 25)

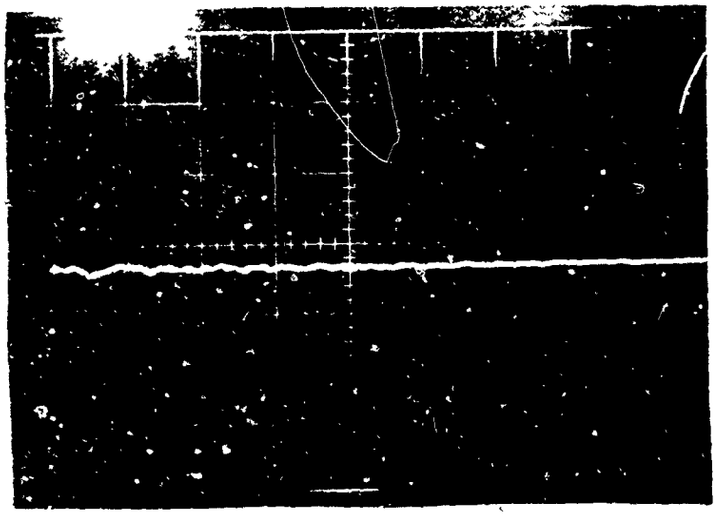

VOLTS/CM 2 SWEEP/CM 0.5 usec

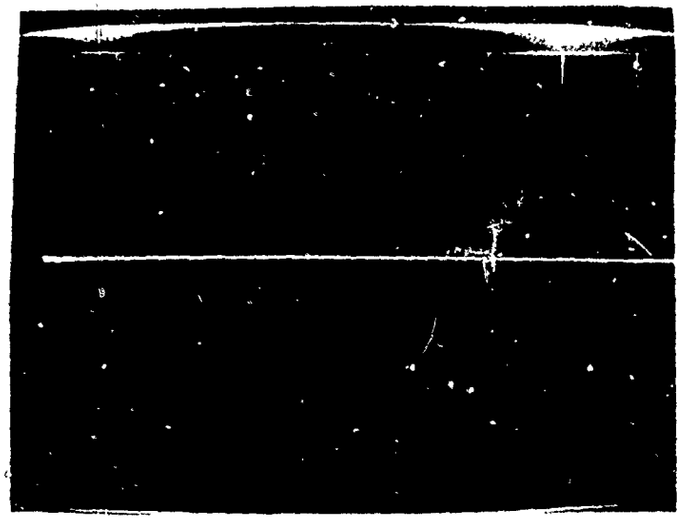

VOLTS/CM 2 SWEEP/CM 5 usec

TEST NO. 25 - 1, 2, 3: SUPPORT ELECTRONICS TEST - 5 VOLT MONITOR

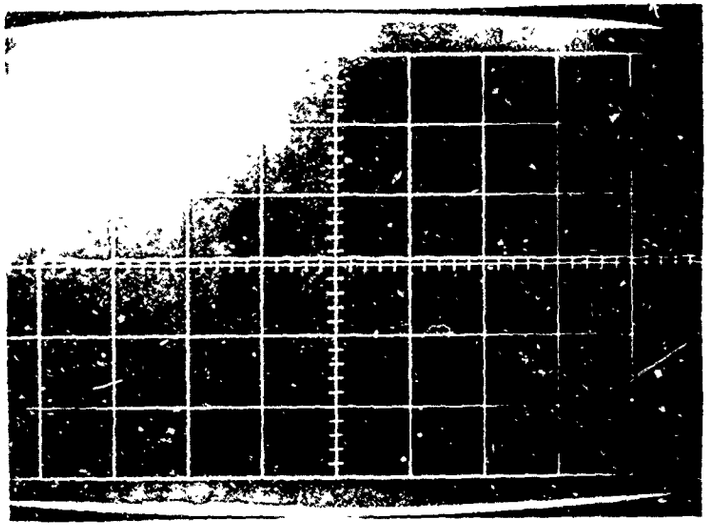

VOLTS/CM 2 SWEEP/CM 50 usec

VOLTS/CM _____ SWEEP/CM _____

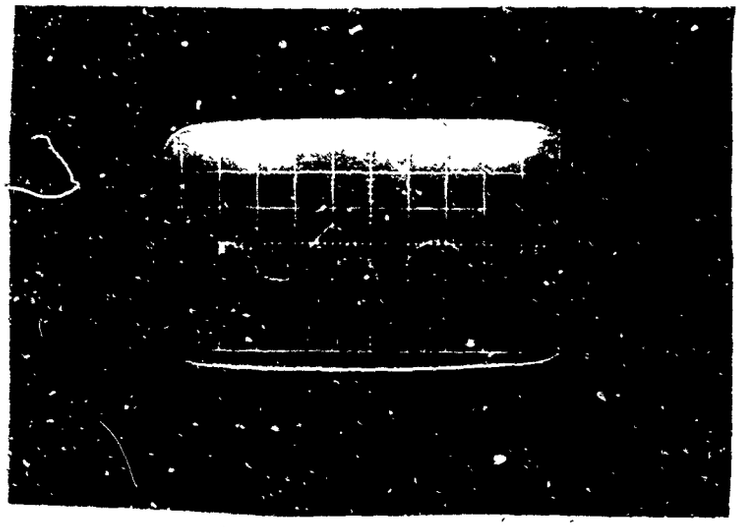

VOLTS/CM 5 SWEEP/CM .5 usec

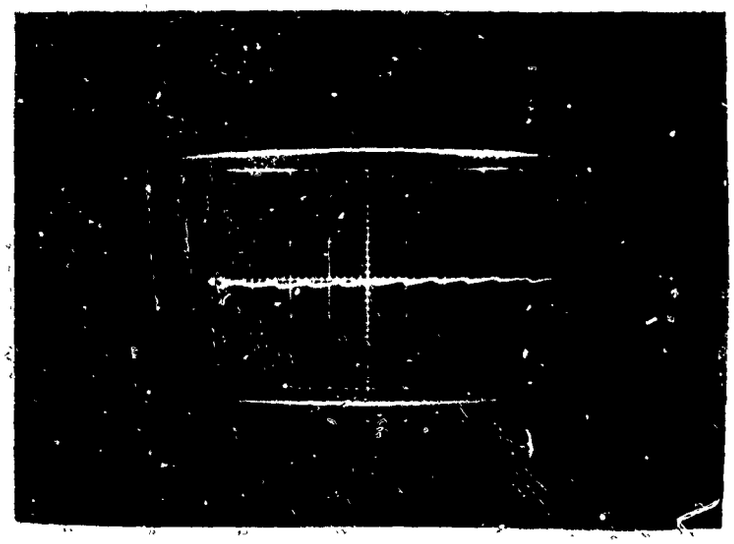

VOLTS/CM 5 SWEEP/CM 5 usec

TEST NO. 25 - 4, 5, 6: SUPPORT ELECTRONICS TEST - 10 VOLT MONITOR

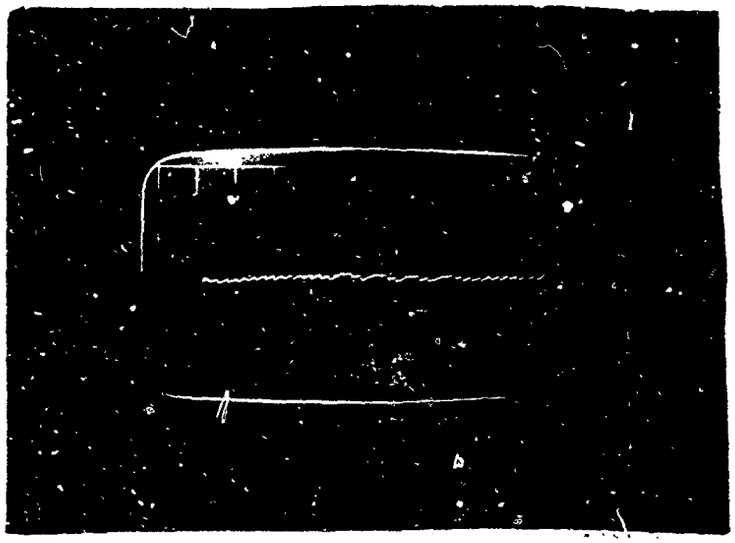

VOLTS/CM 5 SWEEP/CM 50 usec

VOLTS/CM _____ SWEEP/CM _____

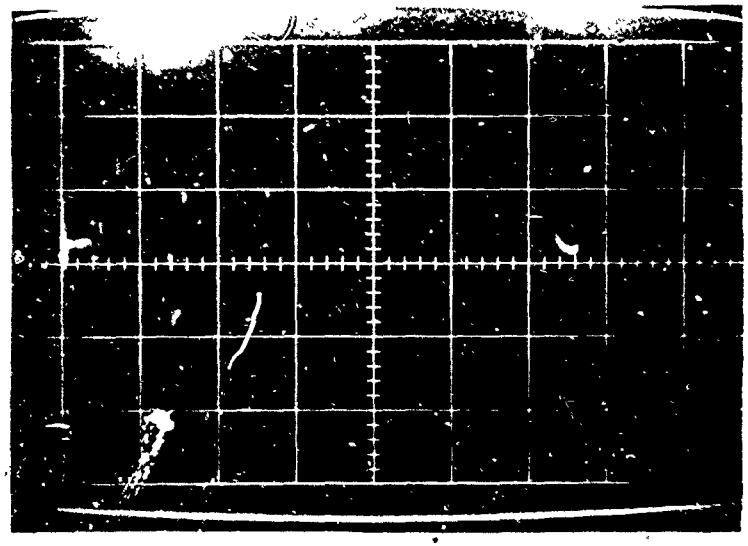

VOLTS/CM .2 SWEEP/CM .5 usec

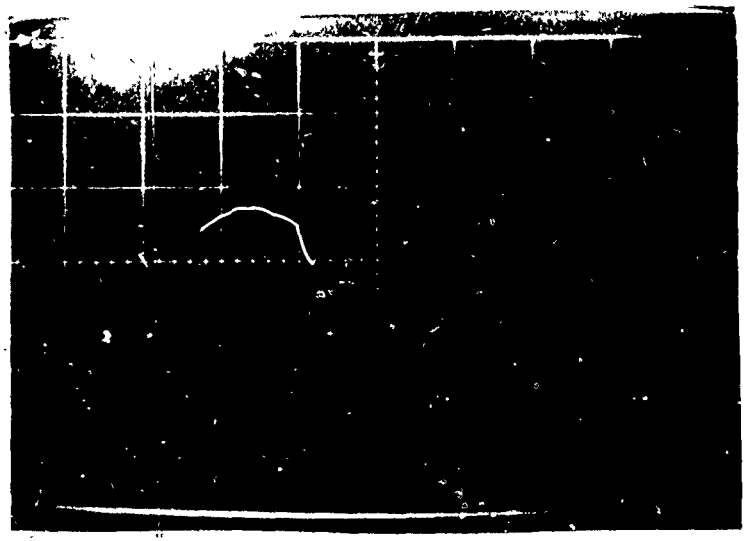

VOLTS/CM .2 SWEEP/CM 5 usec

TEST NO. 25 - 7, 8, 9: SUPPORT ELECTRONICS TEST - 2100 VOLT MONITOR

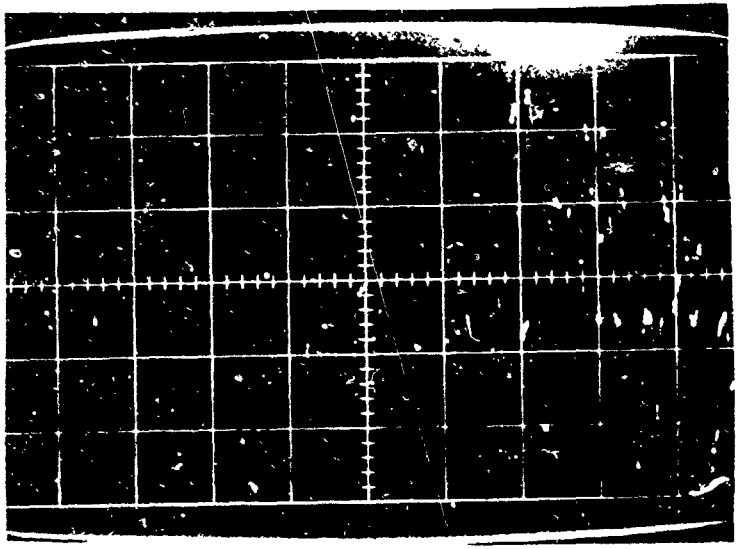

VOLTS/CM 0.2 SWEEP/CM 5 usec

VOLTS/CM _____ SWEEP/CM _____

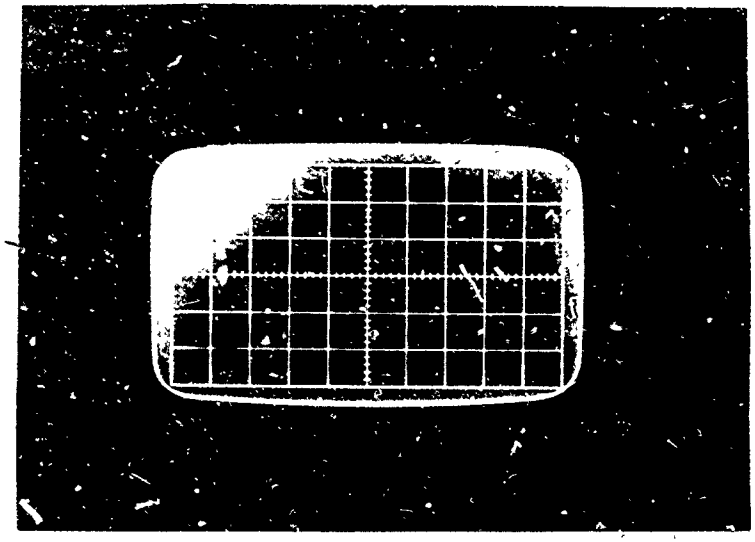

VOLTS/CM 0.2 SWEEP/CM 0.5 usec

VOLTS/CM 0.2 SWEEP/CM 5 usec

TEST NO. 25 - 10, 11, 12: SUPPORT ELECTRONICS TEST - 1000 VOLT MONITOR

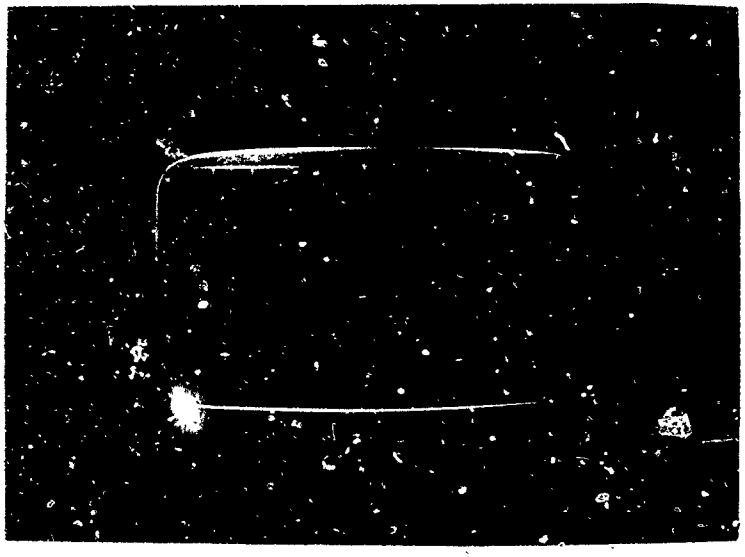

VOLTS/CM .2 SWEEP/CM 50 usec

VOLTS/CM _____ SWEEP/CM _____

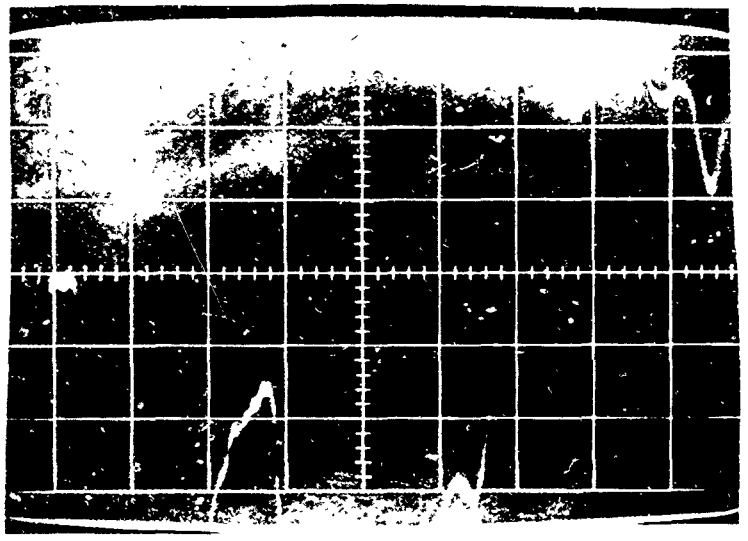

VOLTS/CM 2 SWEEP/CM 0.5 usec

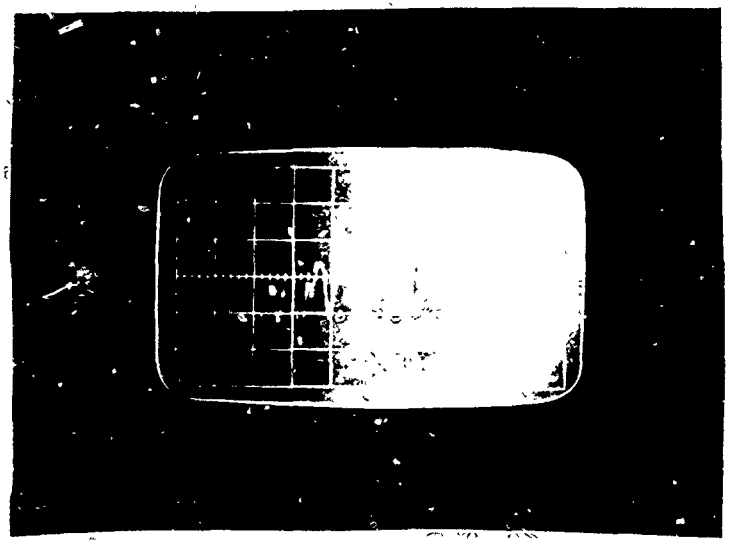

VOLTS/CM 2 SWEEP/CM 5 usec

TEST NO. 25 - 13, 14, 15: SUPPORT ELECTRONICS TEST - START MONITOR

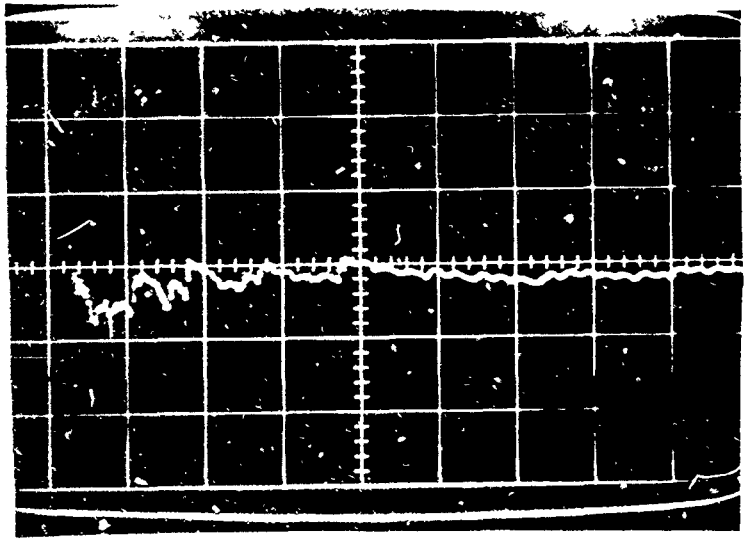

VOLTS/CM 2 SWEEP/CM 50 usec

VOLTS/CM _____ SWEEP/CM _____

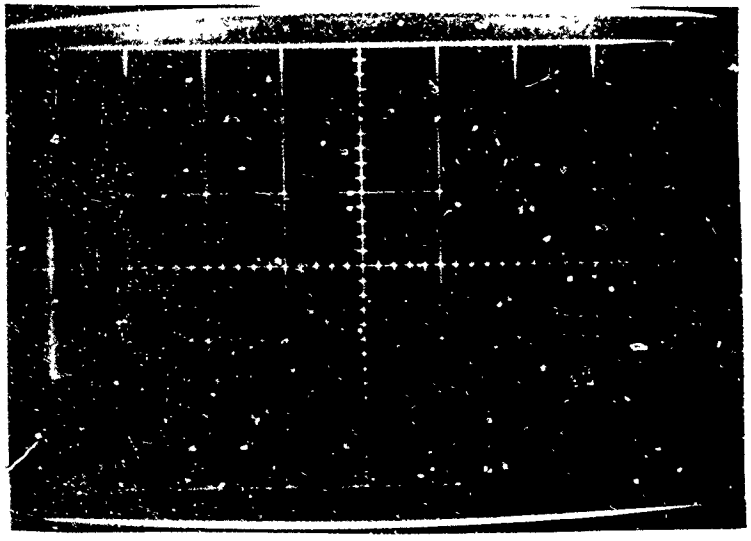

VOLTS/CM 50 mv SWEEP/CM .5 usec

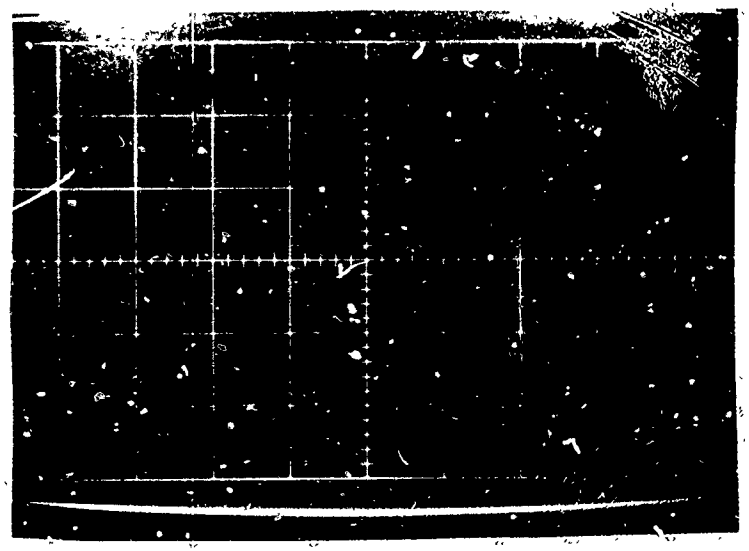

VOLTS/CM 50 mv SWEEP/CM 5 usec

TEST NO. 25 - 16, 17, 18: SUPPORT ELECTRONICS TEST - READOUT AMPLIFIER

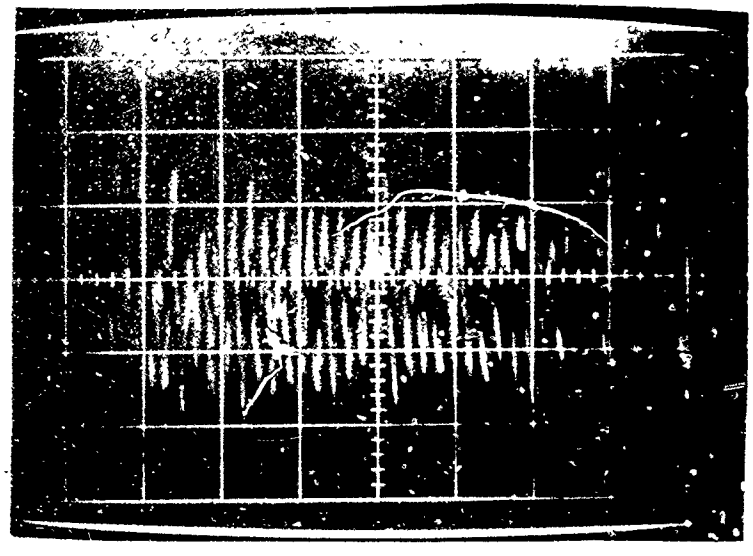

VOLTS/CM 50 mv SWEEP/CM 50 usec

VOLTS/CM _____ SWEEP/CM _____

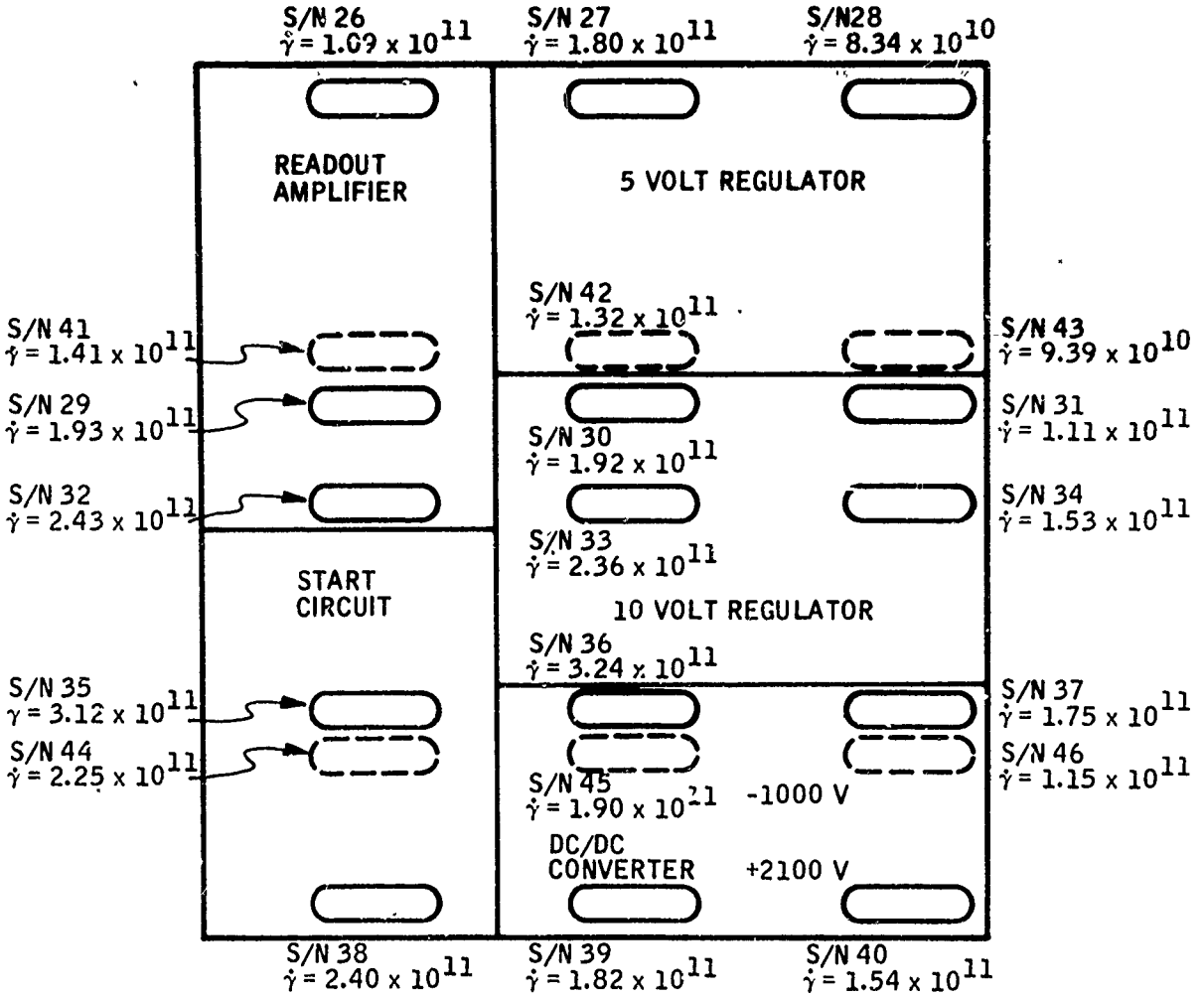

Support Electronics Dosimetry (Shot No. 26)

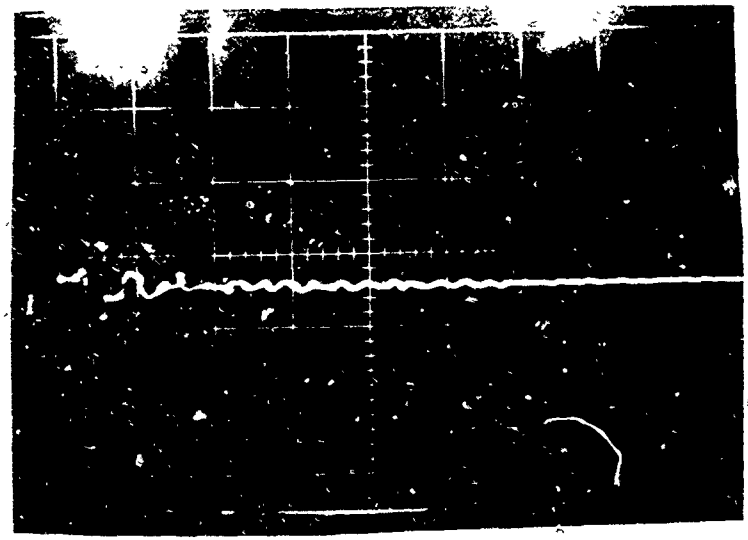

VOLTS/CM 2 SWEEP/CM 0.5 usec

VOLTS/CM 2 SWEEP/CM 5 usec

TEST NO. 26 - 1, 2, 3: SUPPORT ELECTRONICS TEST - 5 VOLT MONITOR

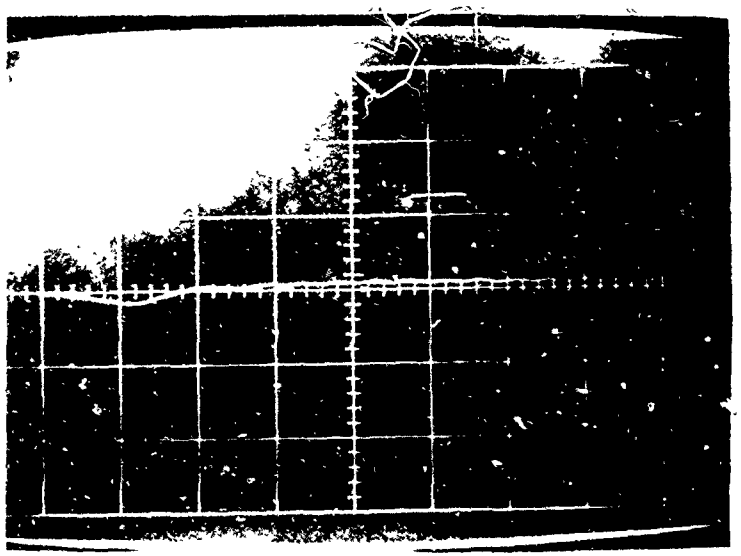

VOLTS/CM 2 SWEEP/CM 50 usec

VOLTS/CM _____ SWEEP/CM _____

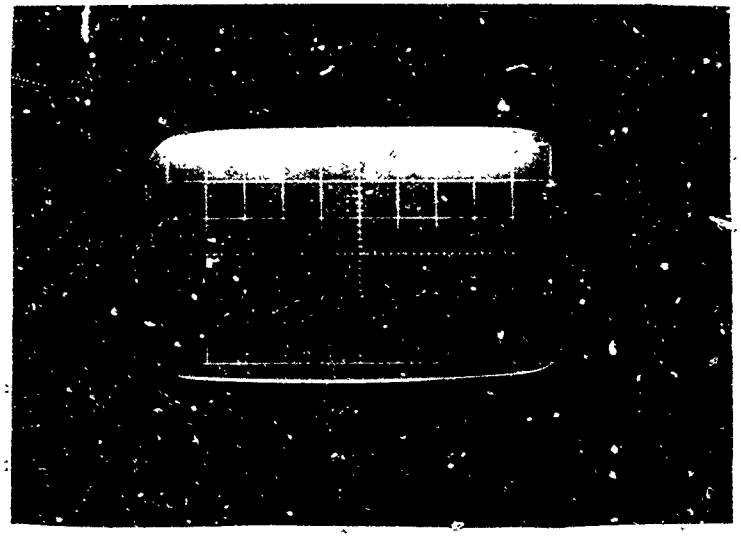

VOLTS/CM 5 SWEEP/CM .5 usec

VOLTS/CM 5 SWEEP/CM 5 usec

TEST NO. 26 - 4, 5, 6: SUPPORT ELECTRONICS TEST - 10 VOLT MONITOR

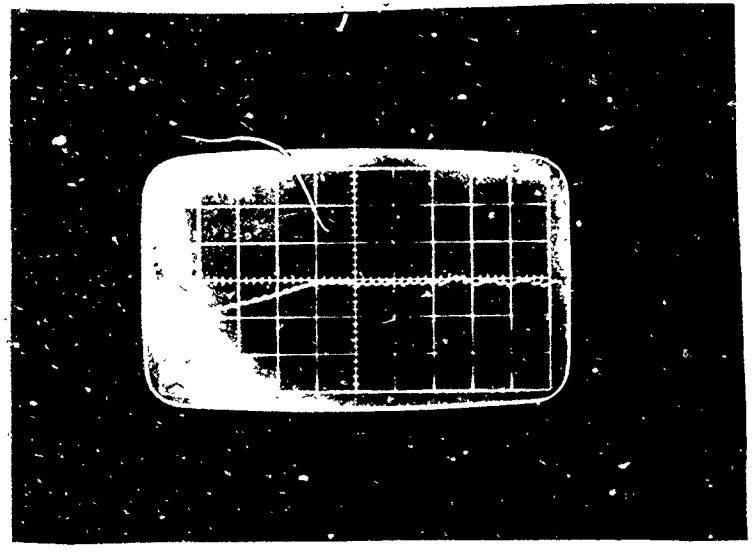

VOLTS/CM 5 SWEEP/CM 50 usec

VOLTS/CM _____ SWEEP/CM _____

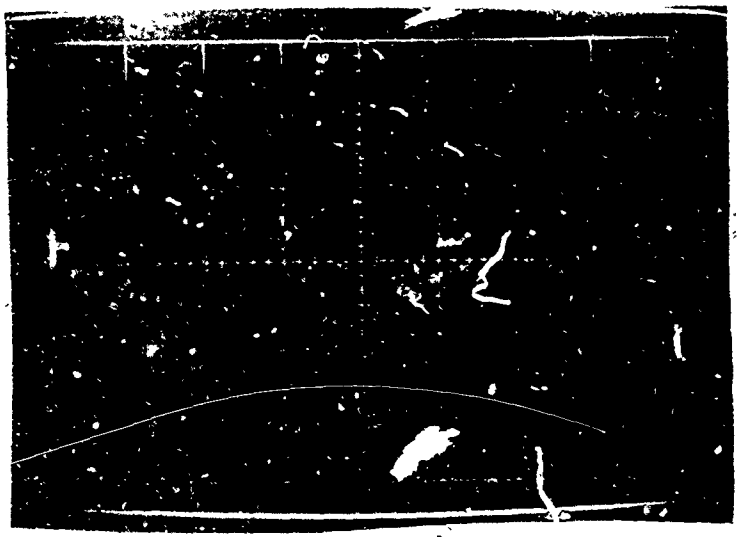

VOLTS/CM .2 SWEEP/CM .5 usec

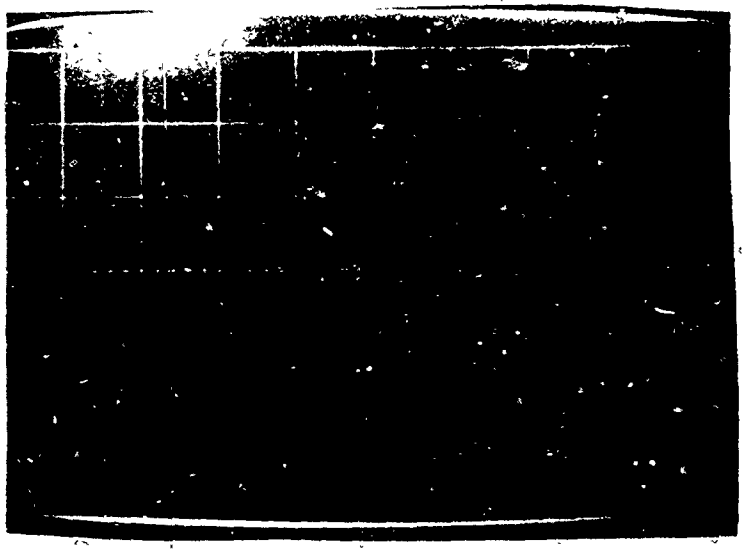

VOLTS/CM .2 SWEEP/CM 5 usec

TEST NO. 26 - 7, 8, 9: SUPPORT ELECTRONICS TEST - 2100 VOLT MONITOR

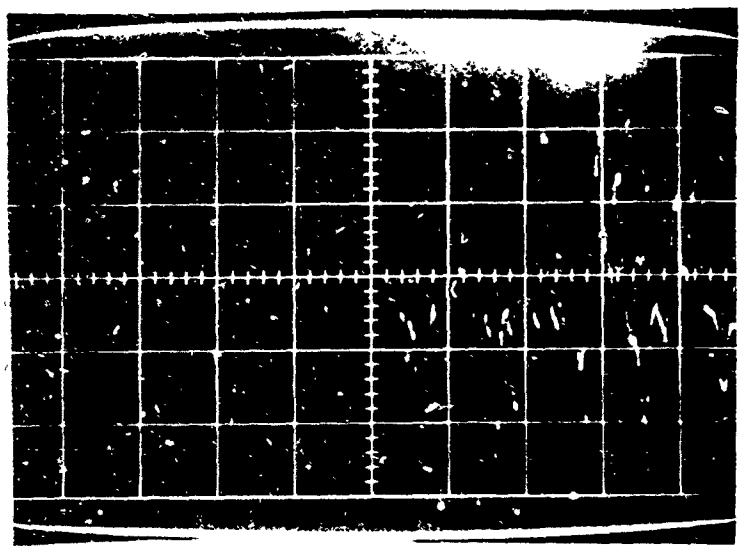

VOLTS/CM 0.2 SWEEP/CM 5 usec

VOLTS/CM _____ SWEEP/CM _____

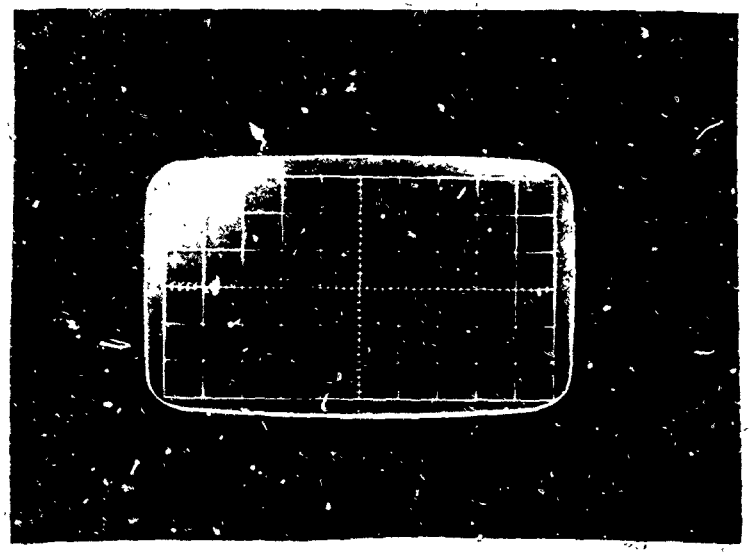

VOLTS/CM 0.2 SWEEP/CM 0.5 usec

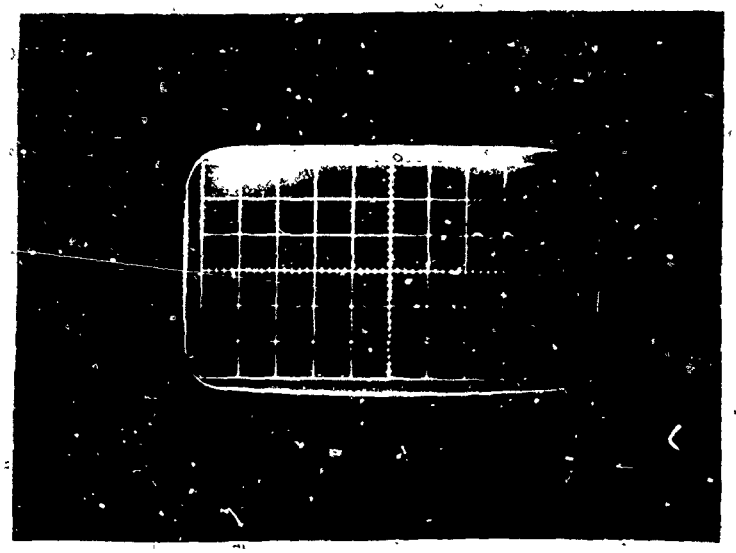

VOLTS/CM 0.2 SWEEP/CM 5 usec

TEST NO. 26 - 10, 11, 12: SUPPORT ELECTRONICS TEST - 1000 VOLT MONITOR

VOLTS/CM .2 SWEEP/CM 50 usec

VOLTS/CM _____ SWEEP/CM _____

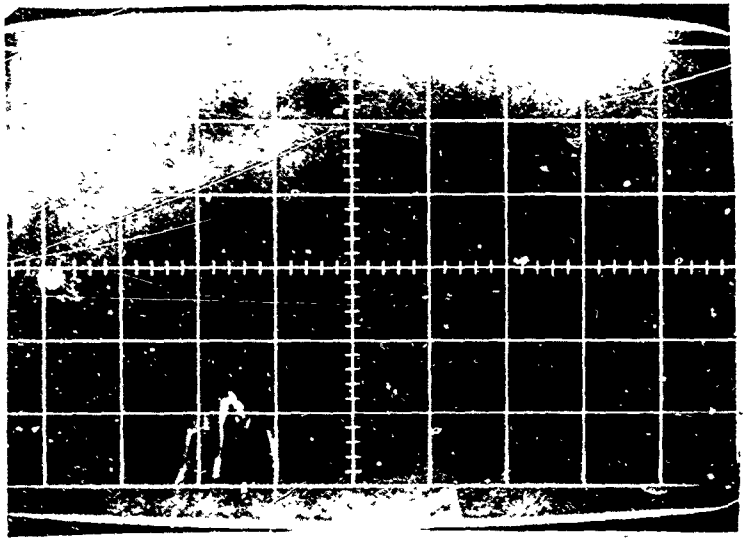

VOLTS/CM 2 SWEEP/CM 0.5 usec

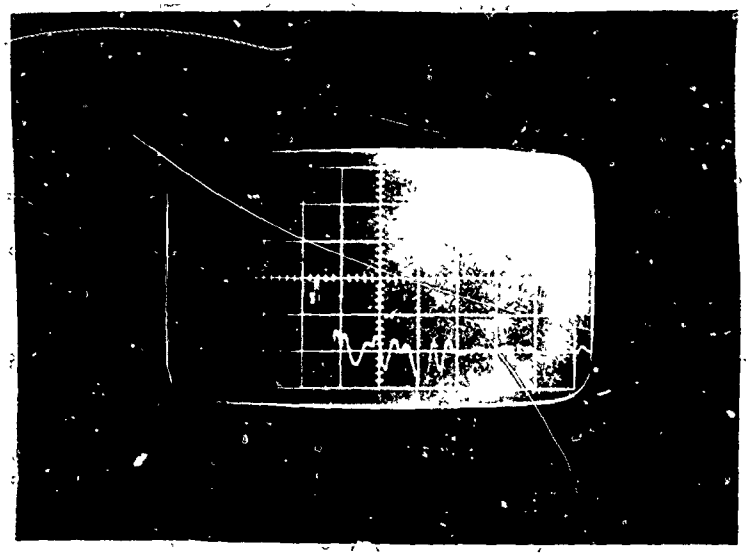

VOLTS/CM 2 SWEEP/CM 5 usec

TEST NO. 26 - 13, 14, 15: SUPPORT ELECTRONICS TEST - START MONITOR

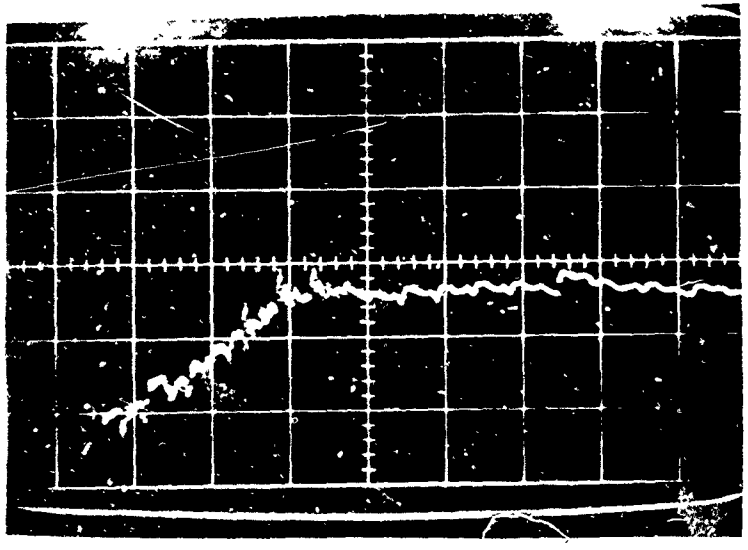

VOLTS/CM 2 SWEEP/CM 50 usec

VOLTS/CM _____ SWEEP/CM _____

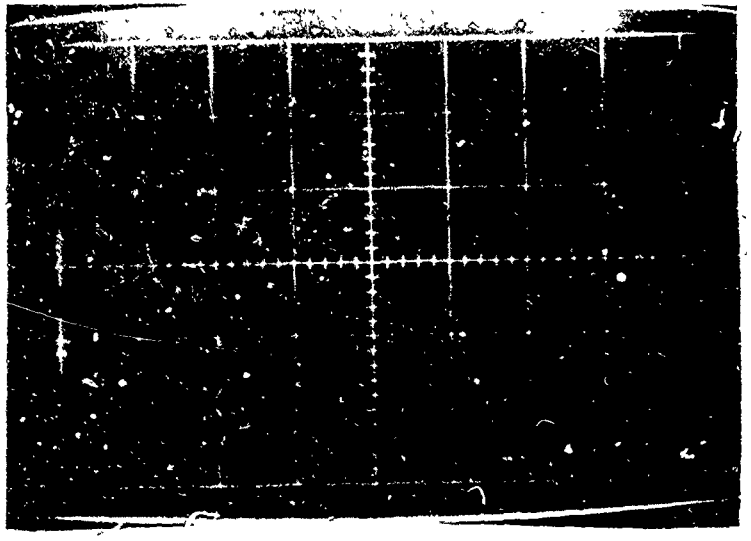

VOLTS/CM 50 mv SWEEP/CM .5 usec

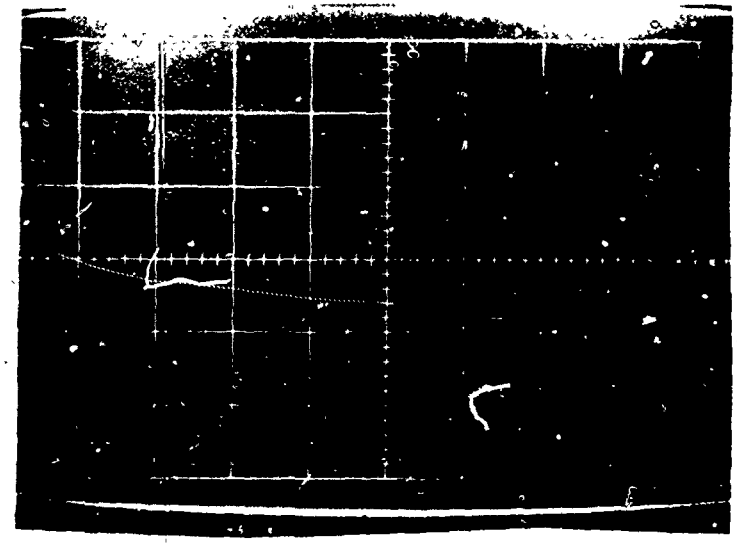

VOLTS/CM 50 mv SWEEP/CM 5 usec

TEST NO. 26 - 16, 17, 18: SUPPORT ELECTRONICS TEST - READOUT AMPLIFIER

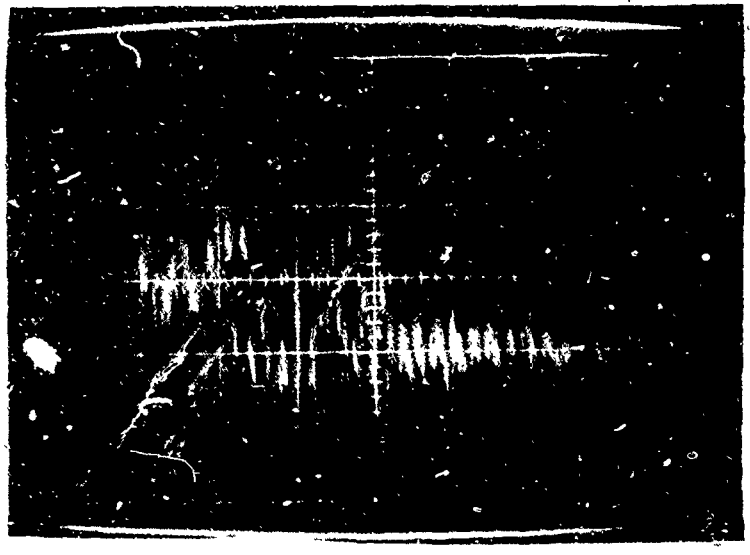

VOLTS/CM 50 mv SWEEP/CM 50 usec

VOLTS/CM _____ SWEEP/CM _____

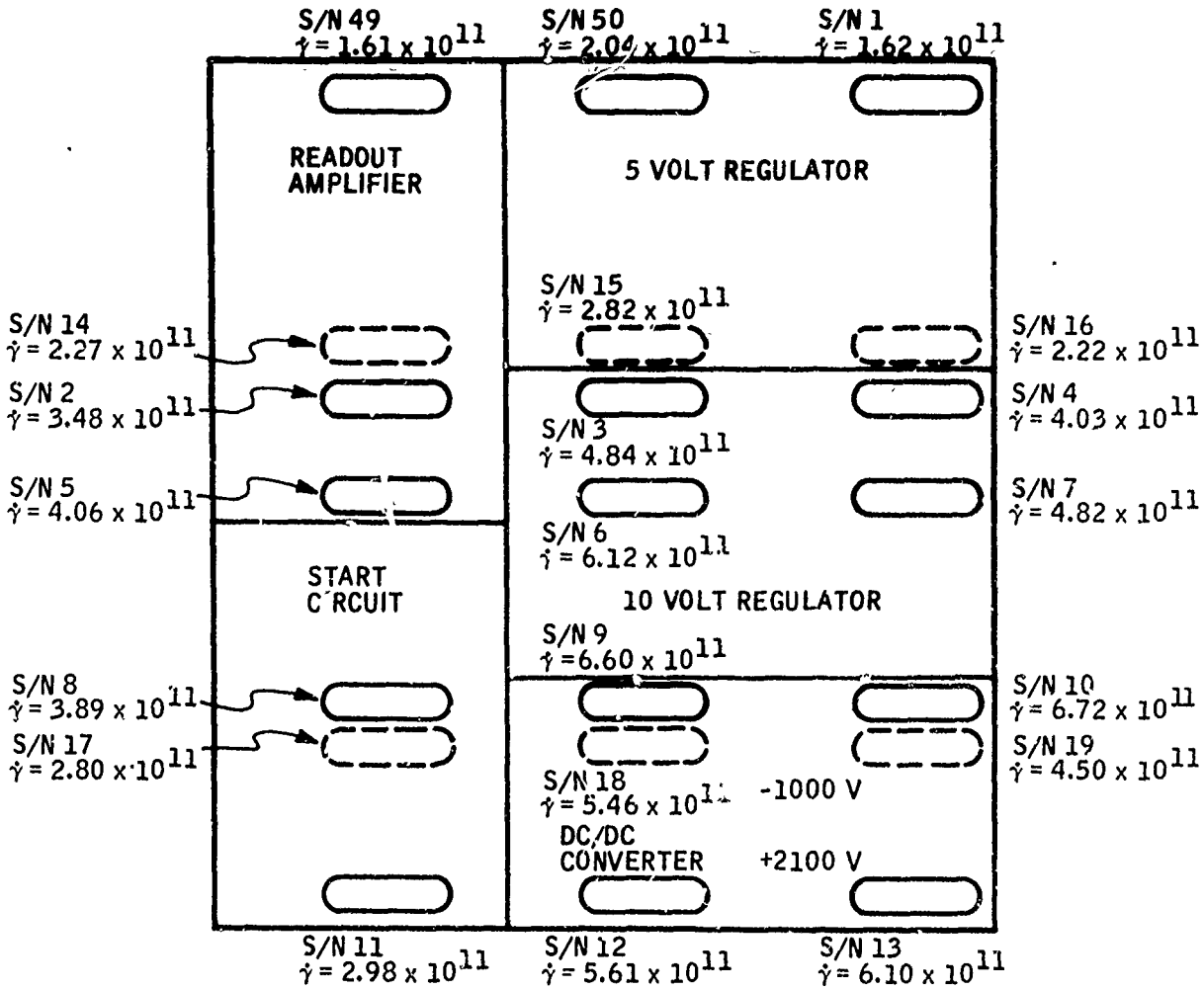

Support Electronics Dosimetry (Shot No. 27)

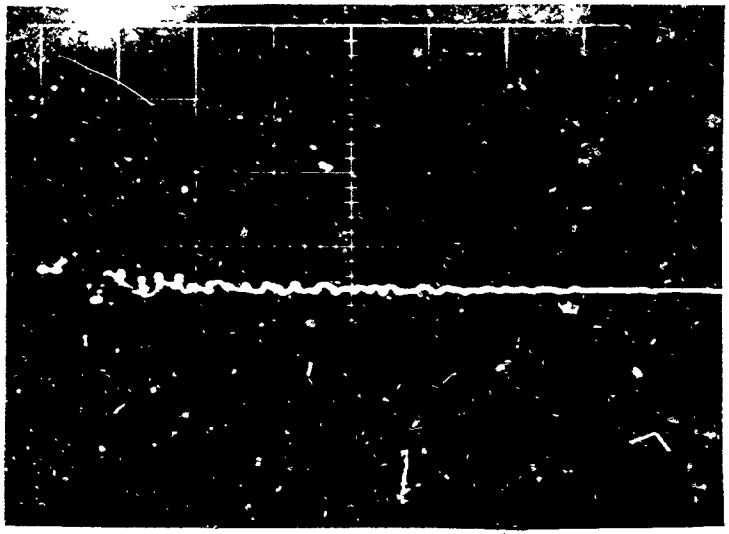

VOLTS/CM 2 SWEEP/CM 0.5 usec

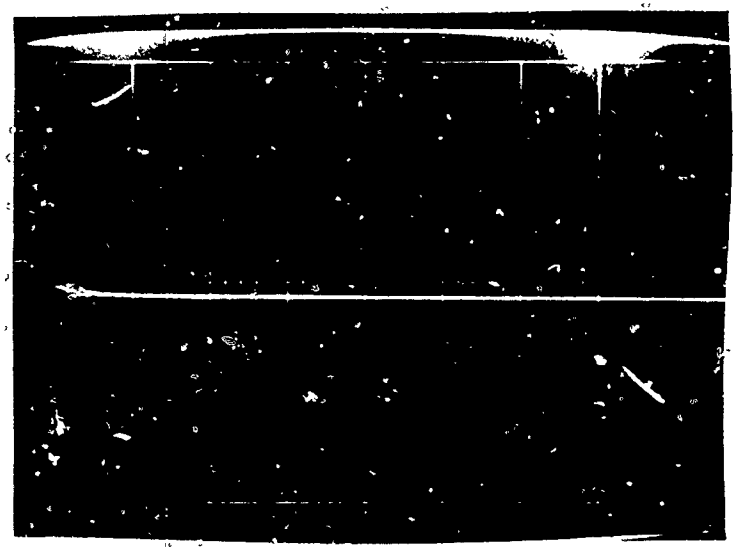

VOLTS/CM 2 SWEEP/CM 5 usec

TEST NO. 27 - 1, 2, 3: SUPPORT ELECTRONICS TEST - 5 VOLT MONITOR

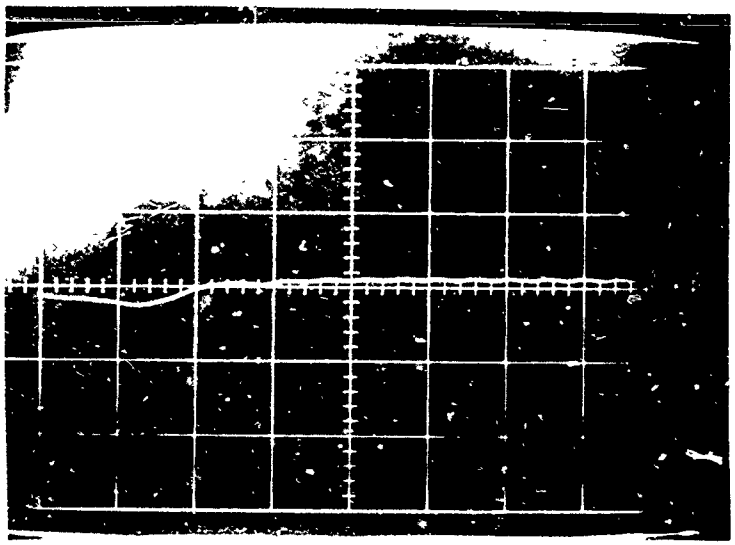

VOLTS/CM 2 SWEEP/CM 5 usec

VOLTS/CM _____ SWEEP/CM _____

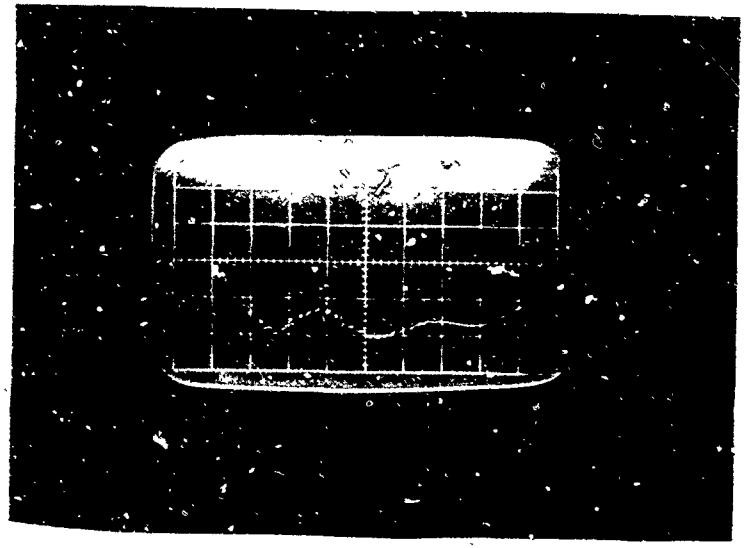

VOLTS/CM 5 SWEEP/CM .5 usec

VOLTS/CM 5 SWEEP/CM 5 usec

TEST NO. 27 - 4, 5, 6: SUPPORT ELECTRONICS TEST - 10 VOLT MONITOR

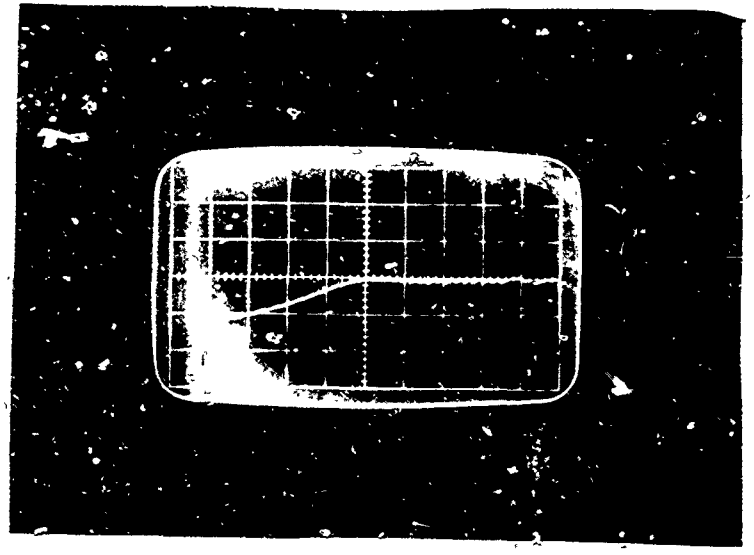

VOLTS/CM 5 SWEEP/CM 50 usec

VOLTS/CM _____ SWEEP/CM _____

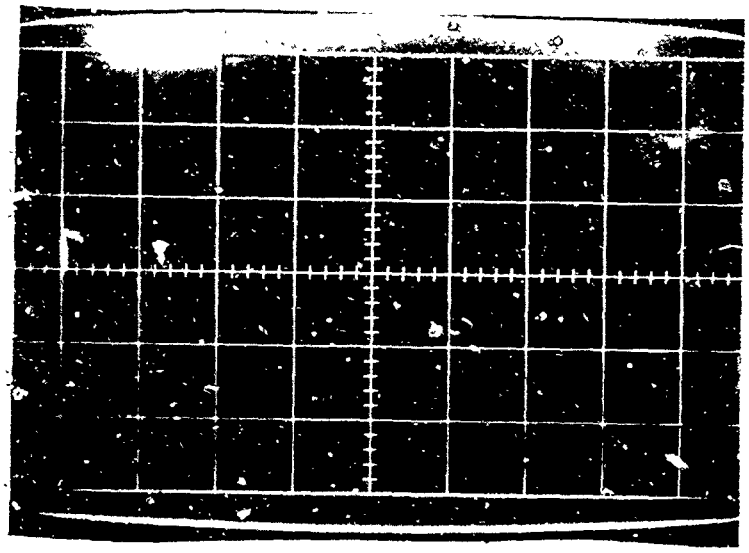

VOLTS/CM .2 SWEEP/CM .5 usec

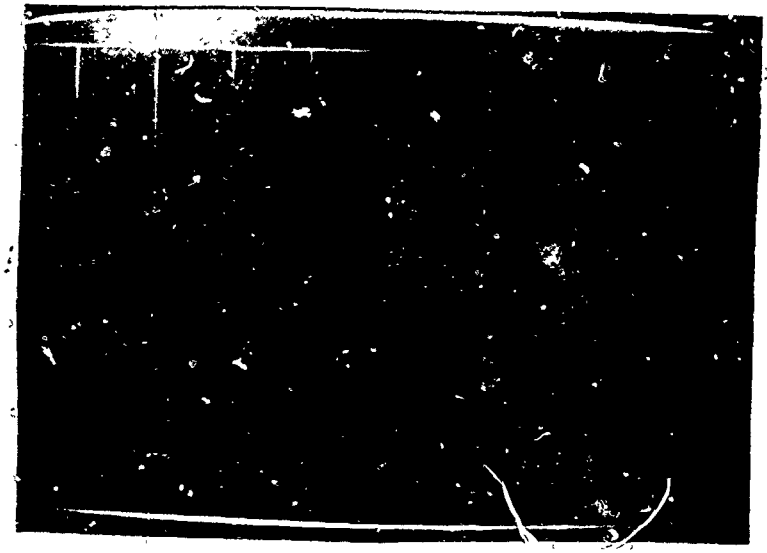

VOLTS/CM .2 SWEEP/CM .5 usec

TEST NO. 27 - 7, 8, 9: SUPPORT ELECTRONICS TESTS - 2100 VOLTS MONITOR

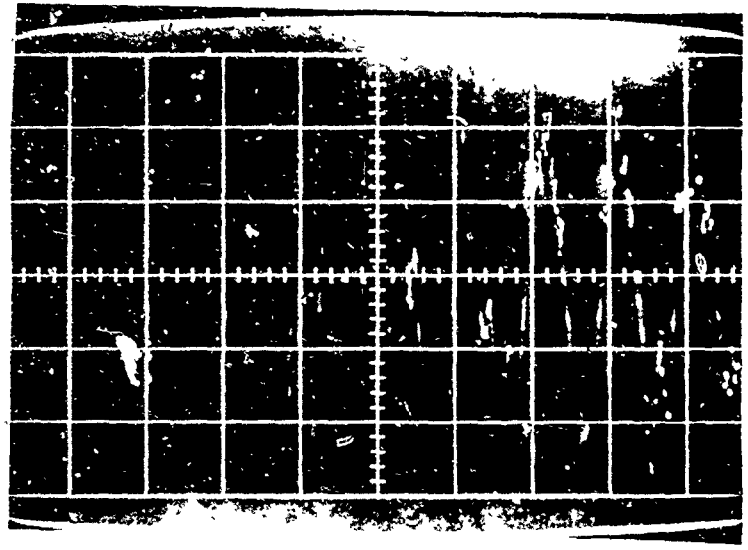

VOLTS/CM 0.2 SWEEP/CM .5 usec

VOLTS/CM _____ SWEEP/CM _____

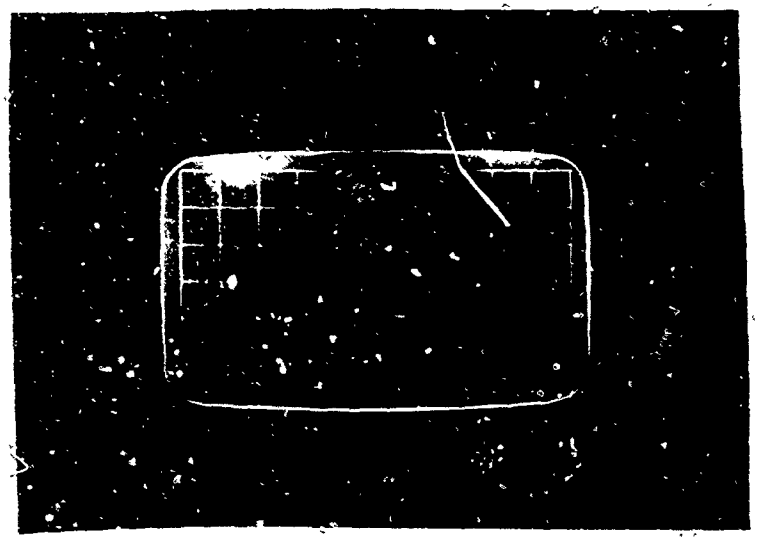

VOLTS/CM 0.2 SWEEP/CM 0.5 usec

VOLTS/CM 0.2 SWEEP/CM 5 usec

TEST NO. 27 - 10, 11, 12: SUPPORT ELECTRONICS TEST - 1000 VOLT MONITOR

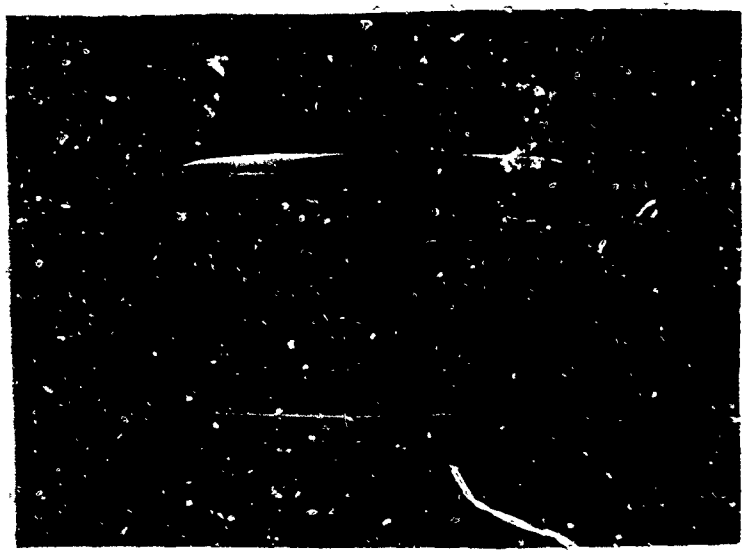

VOLTS/CM .2 SWEEP/CM 50 usec

VOLTS/CM _____ SWEEP/CM _____

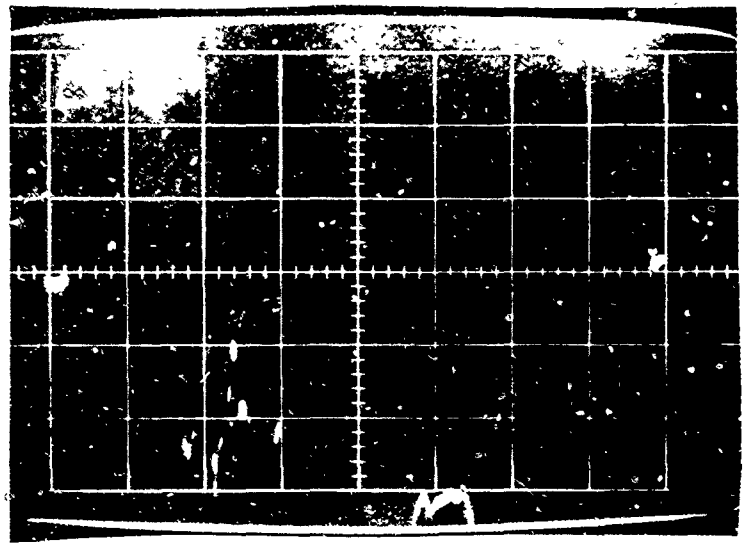

VOLTS/CM 2 SWEEP/CM 0.5 usec

VOLTS/CM 2 SWEEP/CM 5 usec

TEST NO. 27 - 13, 14, 15: SUPPORT ELECTRONICS TEST - START MONITOR

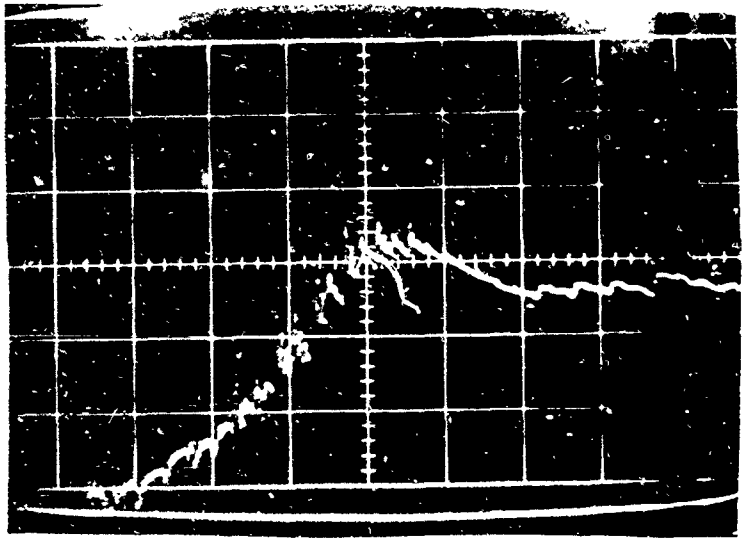

VOLTS/CM 2 SWEEP/CM 50 usec

VOLTS/CM_____ SWEEP/CM_____

VOLTS/CM 50 mv SWEEP/CM .5 usec

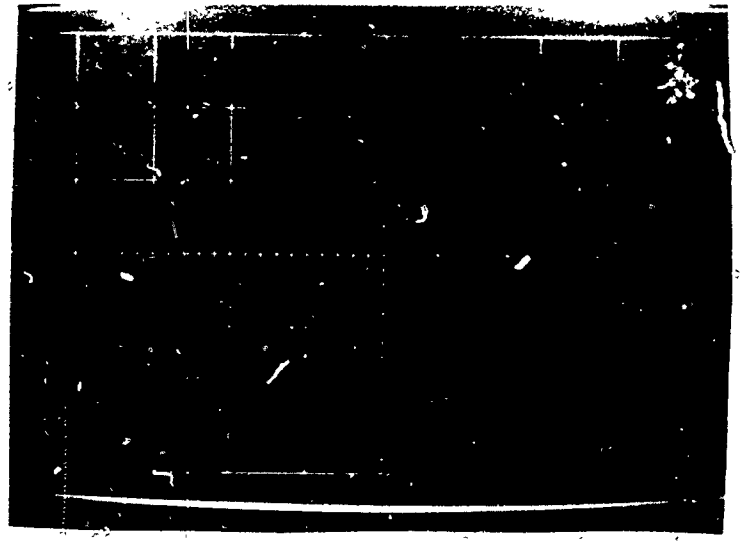

VOLTS/CM 50 mv SWEEP/CM 5 usec

TEST NO. 27 - 16, 17, 18: SUPPORT ELECTRONICS TEST - READOUT AMPLIFIER

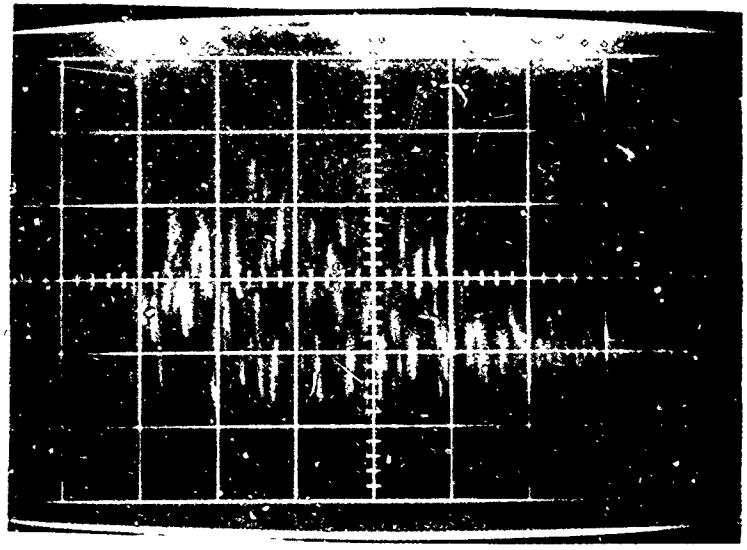

VOLTS/CM 50 mv SWEEP/CM 50 usec

VOLTS/CM _____ SWEEP/CM _____

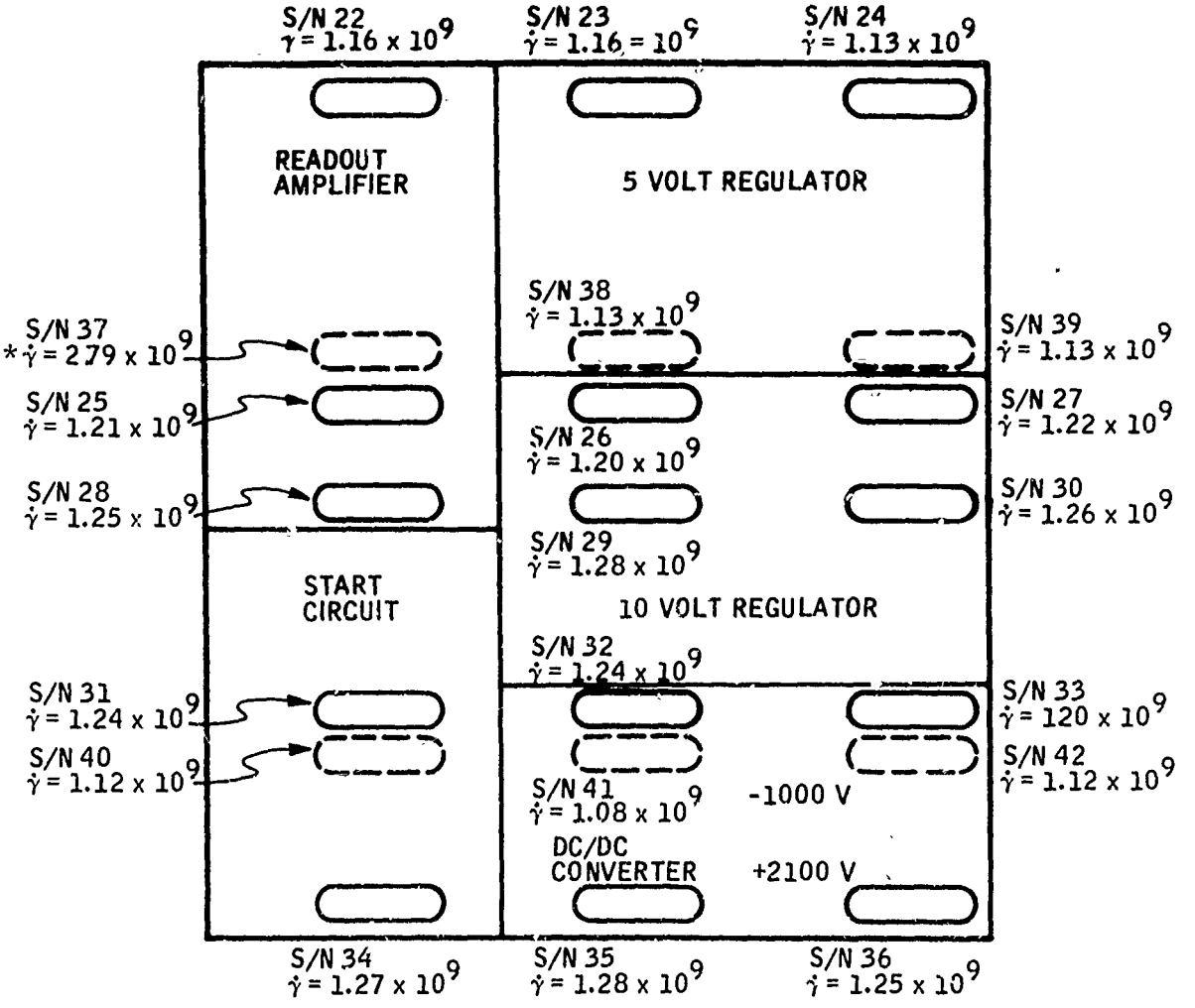

* THIS READING CONSIDERED TO BE IN ERROR AND WAS NOT INCLUDED IN DOSE AND DOSE RATE CALCULATIONS.

Support Electronics Dosimetry (Shot No. 28)

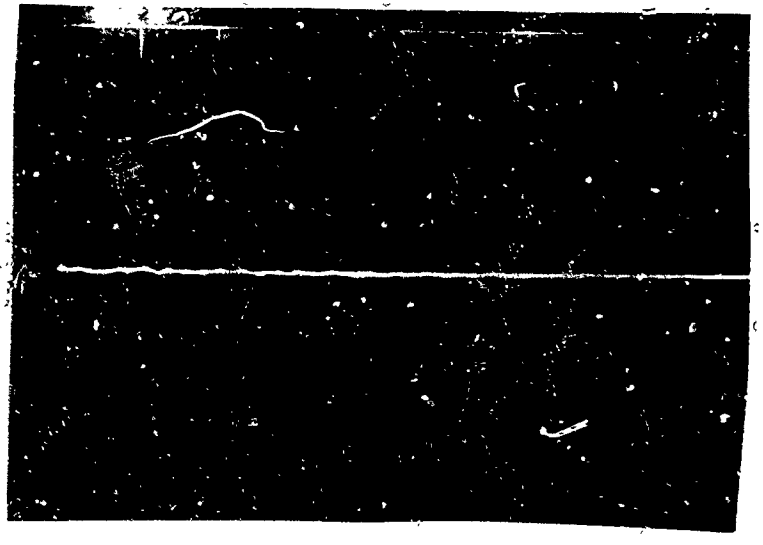

VOLTS/CM 2 SWEEP/CM 0.5 usec

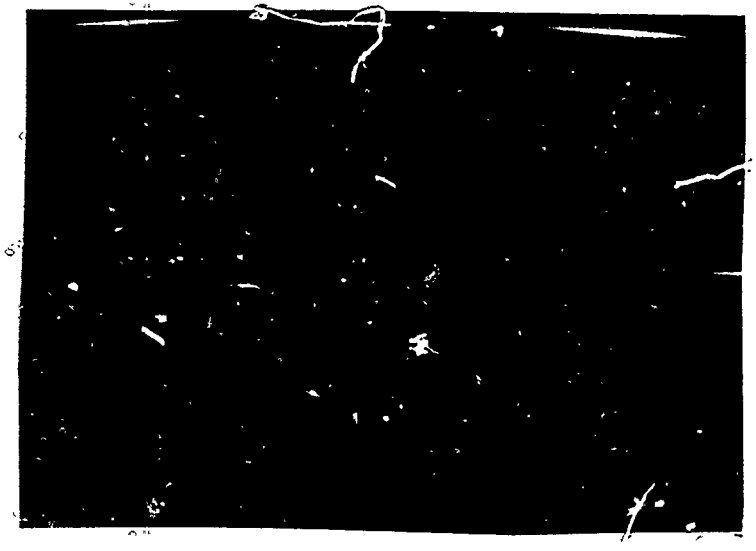

VOLTS/CM 2 SWEEP/CM 5 usec

TEST NO. 28 - 1, 2, 3: SUPPORT ELECTRONICS TEST - 5 VOLT MONITOR

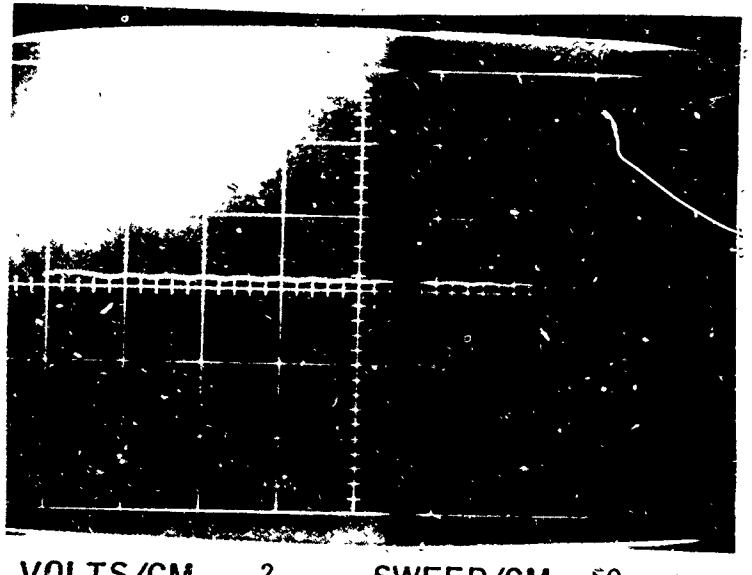

VOLTS/CM 2 SWEEP/CM 50 usec

VOLTS/CM _____ SWEEP/CM _____

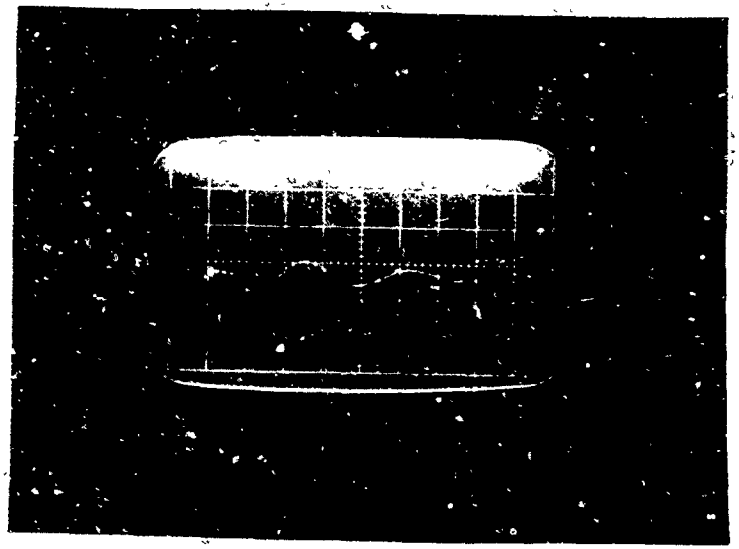

VOLTS/CM 5 SWEEP/CM .5 usec

VOLTS/CM 5 SWEEP/CM 5usec

TEST NO. 28 - 4, 5, 6: SUPPORT ELECTRONICS TEST - 10 VOLT MONITOR

VOLTS/CM 5 SWEEP/CM 50 usec

VOLTS/CM _____ SWEEP/CM _____

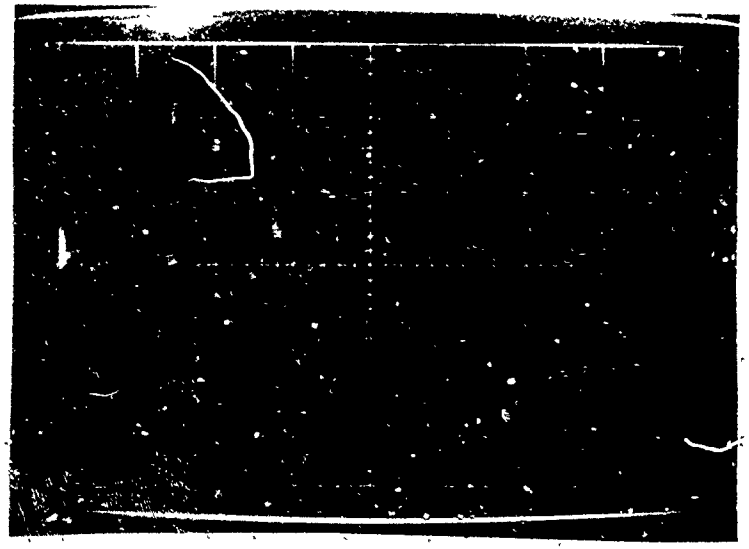

VOLTS/CM .2 SWEEP/CM .5 usec

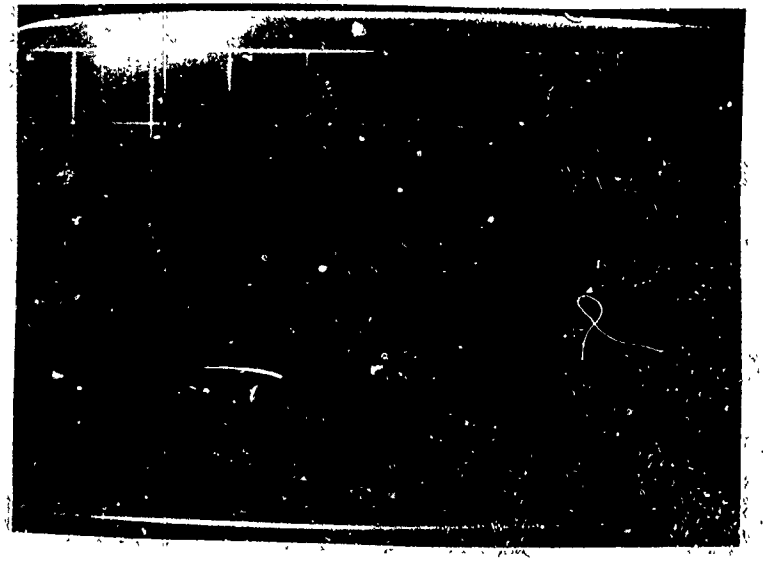

VOLTS/CM .2 SWEEP/CM 5 usec

TEST NO. 28 - 7, 8, 9: SUPPORT ELECTRONICS TEST - 2100 VOLT MONITOR

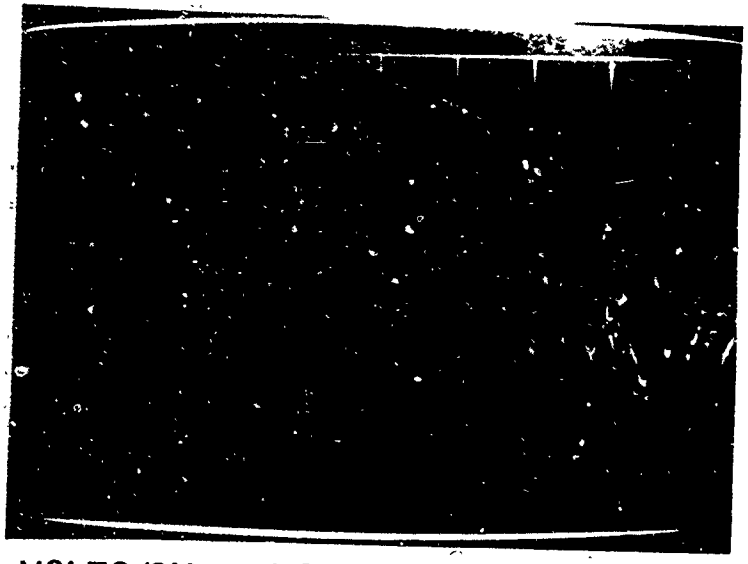

VOLTS/CM 0.2 SWEEP/CM 5 usec

VOLTS/CM _____ SWEEP/CM _____

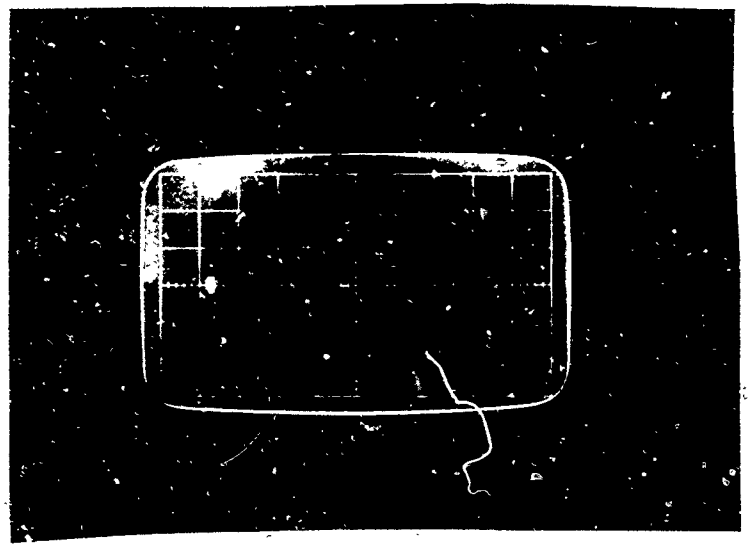

VOLTS/CM 2 SWEEP/CM 0.5 usec

VOLTS/CM 0.2 SWEEP/CM 5 usec

TEST NO. 28 - 10, 11, 12: SUPPORT ELECTRONICS TEST - 1000 VOLT MONITOR

VOLTS/CM .2 SWEEP/CM 50 usec

VOLTS/CM _____ SWEEP/CM _____

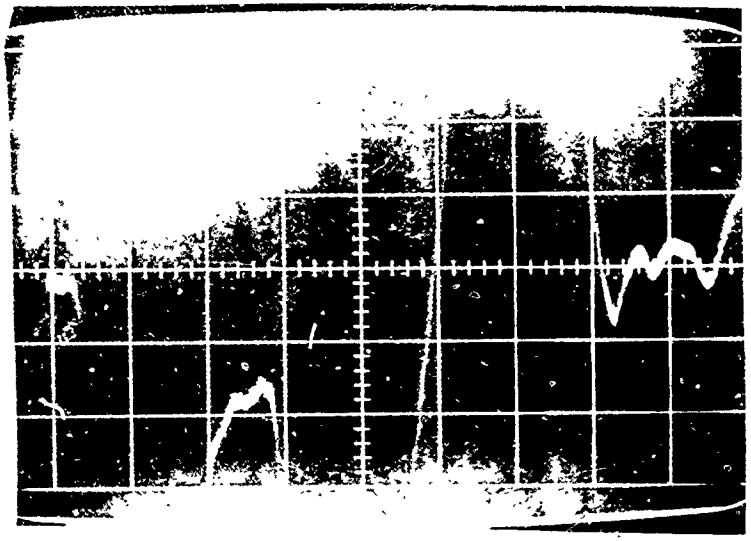

VOLTS/CM 2 SWEEP/CM 0.5 usec

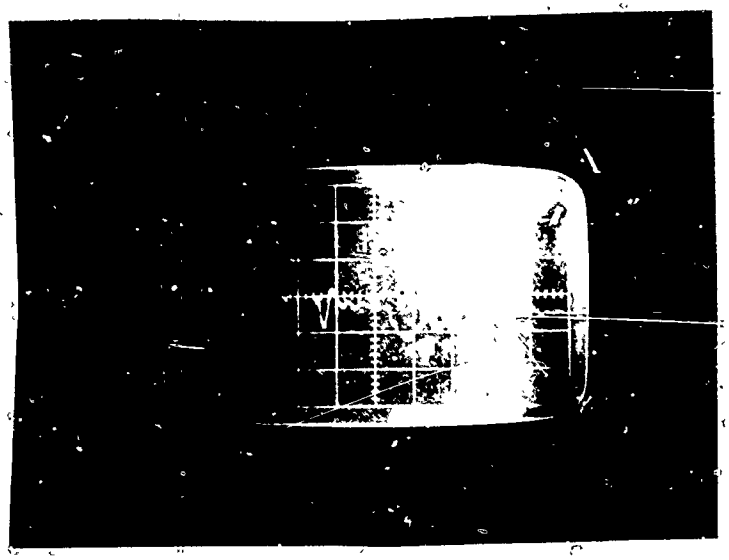

VOLTS/CM 2 SWEEP/CM 5 usec

TEST NO. 28 - 13, 14, 15: SUPPORT ELECTRONICS TEST - START MONITOR

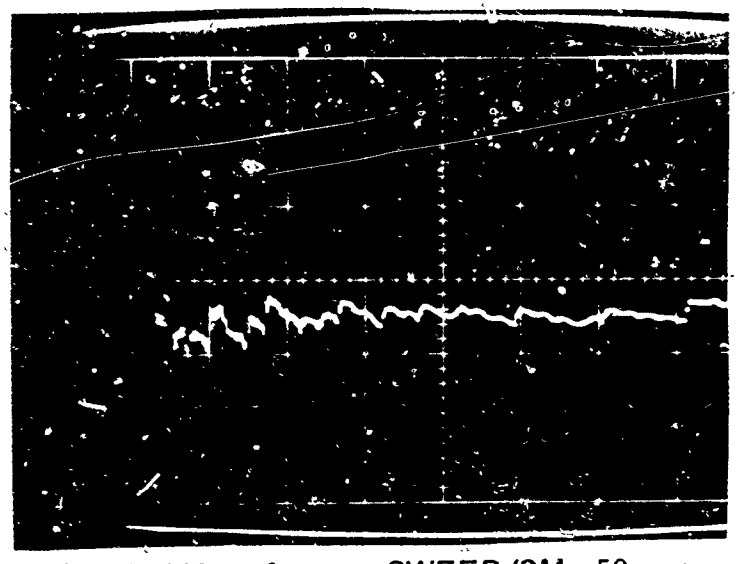

VOLTS/CM 2 SWEEP/CM 50 usec

VOLTS/CM _____ SWEEP/CM _____

VOLTS/CM 50 mv SWEEP/CM .5 usec

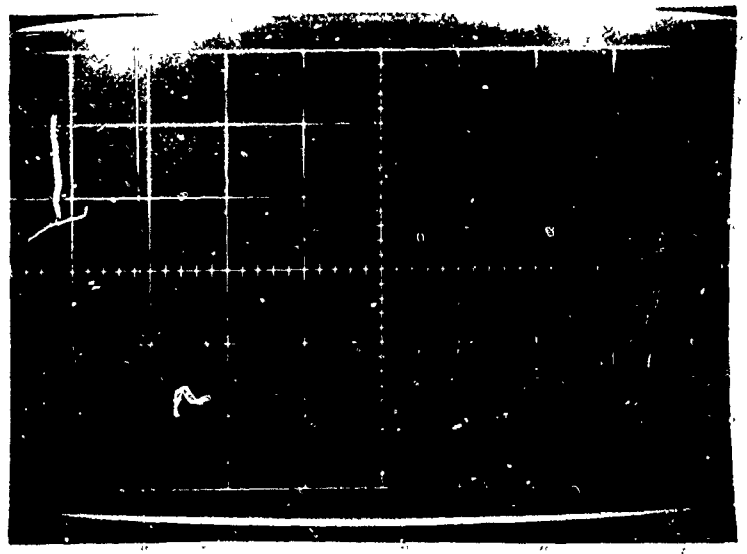

VOLTS/CM 50 mv SWEEP/CM 5 usec

TEST NO. 28 - 16, 17, 18: SUPPORT ELECTRONICS TEST - READOUT AMPLIFIER

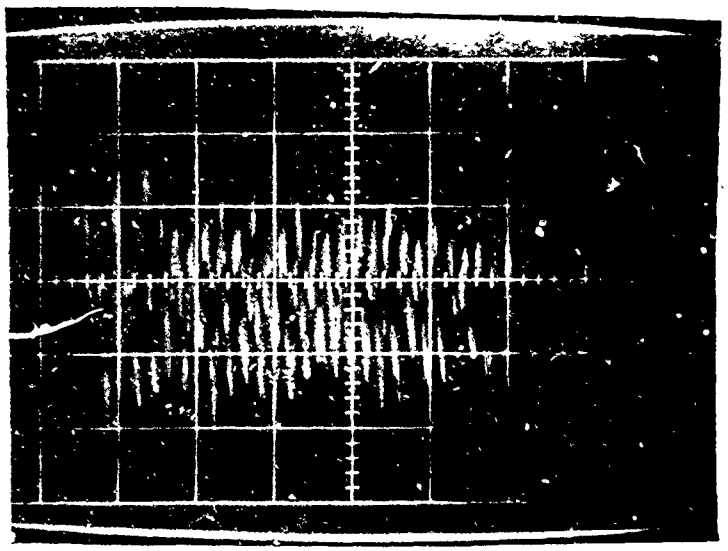

VOLTS/CM 50 mv SWEEP/CM 50 usec

VOLTS/CM _____ SWEEP/CM _____

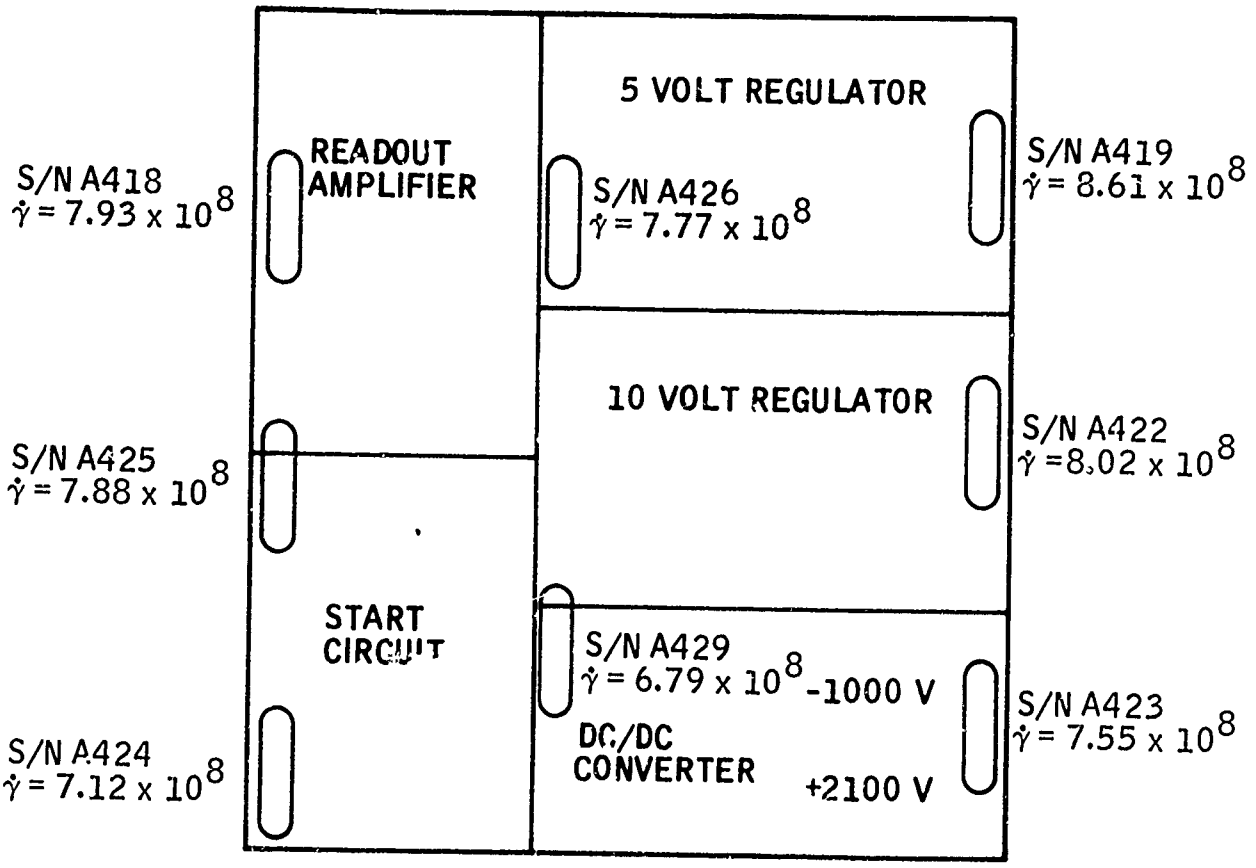

Support Electronics Dosimetry (Shot No. 29)

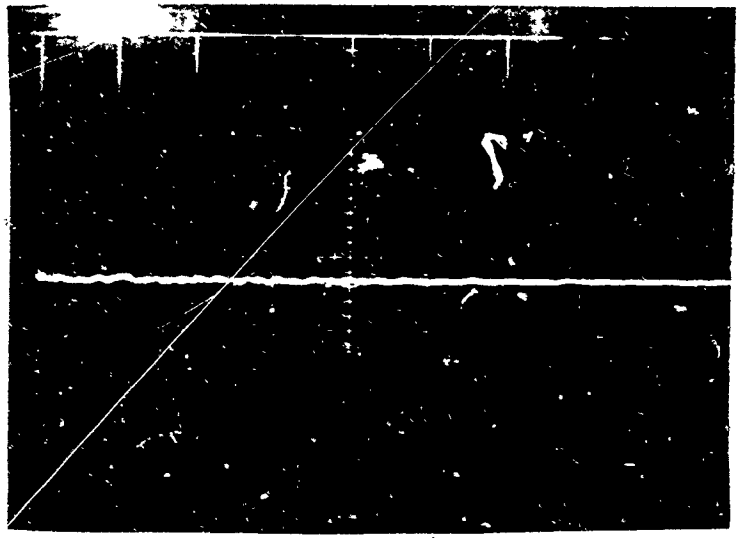

VOLTS/CM 2 SWEEP/CM 0.5 usec

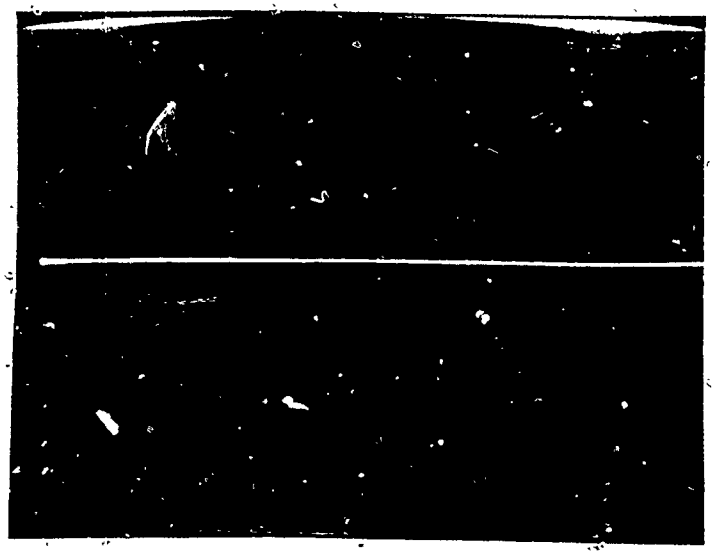

VOLTS/CM 2 SWEEP/CM 5 usec

TEST NO. 29 - 1, 2, 3: SUPPORT ELECTRONICS TEST - 5 VOLT MONITOR

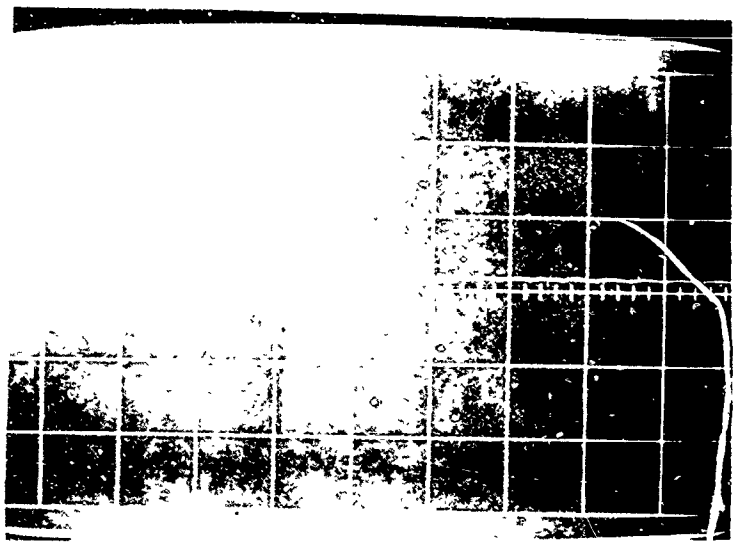

VOLTS/CM 2 SWEEP/CM 50 usec

VOLTS/CM _____ SWEEP/CM _____

VOLTS/CM 5 SWEEP/CM .5 usec

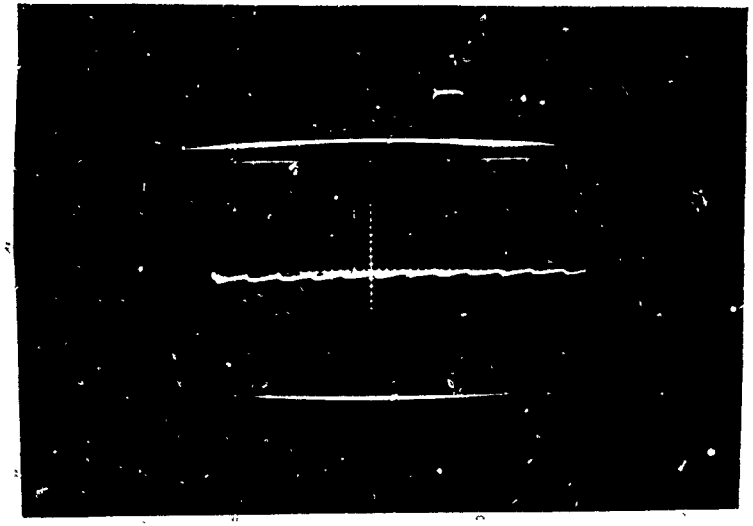

VOLTS/CM 5 SWEEP/CM 5 usec

TEST NO. 29 - 4, 5, 6: SUPPORT ELECTRONICS TEST - 10 VOLT MONITOR

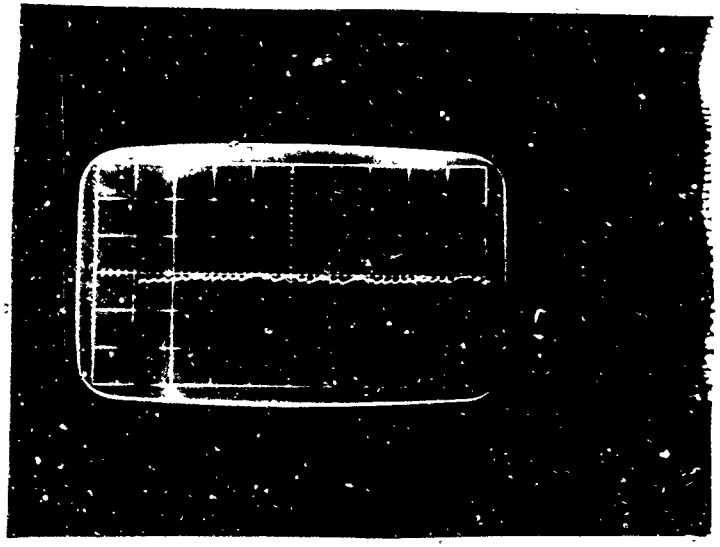

VOLTS/CM 5 SWEEP/CM 50 usec

VOLTS/CM _____ SWEEP/CM _____

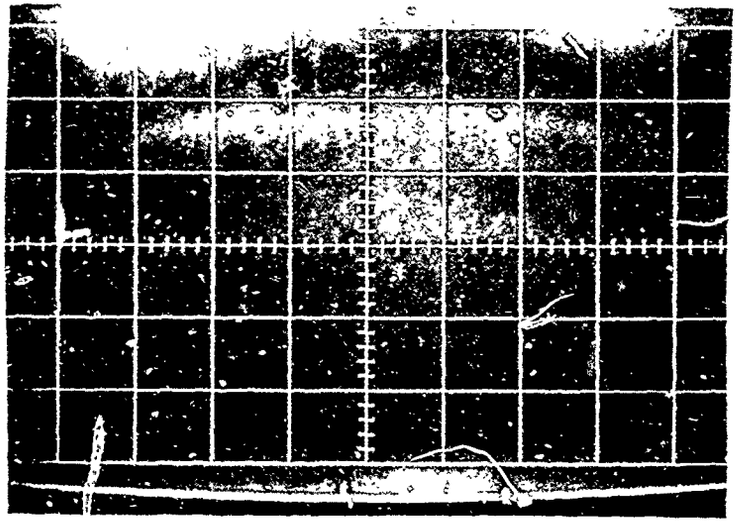

VOLTS/CM .2 SWEEP/CM .5 usec

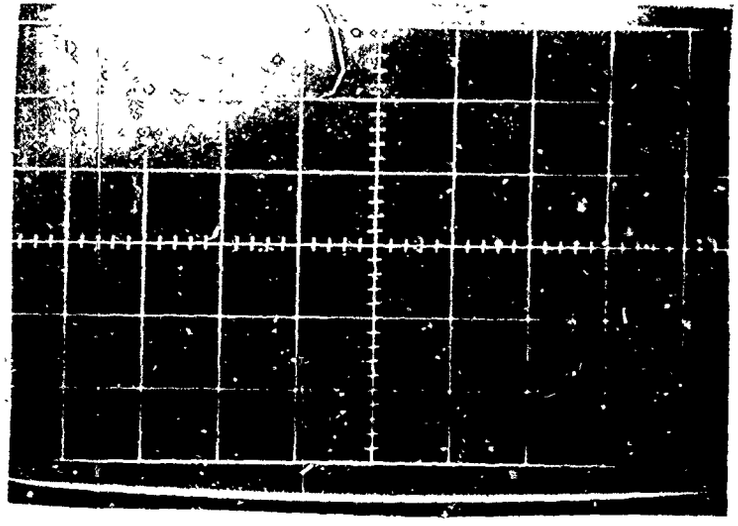

VOLTS/CM .2 SWEEP/CM 5 usec

TEST NO. 29 - 7, 8, 9: SUPPORT ELECTRONICS TEST - 2100 VOLT MONITOR

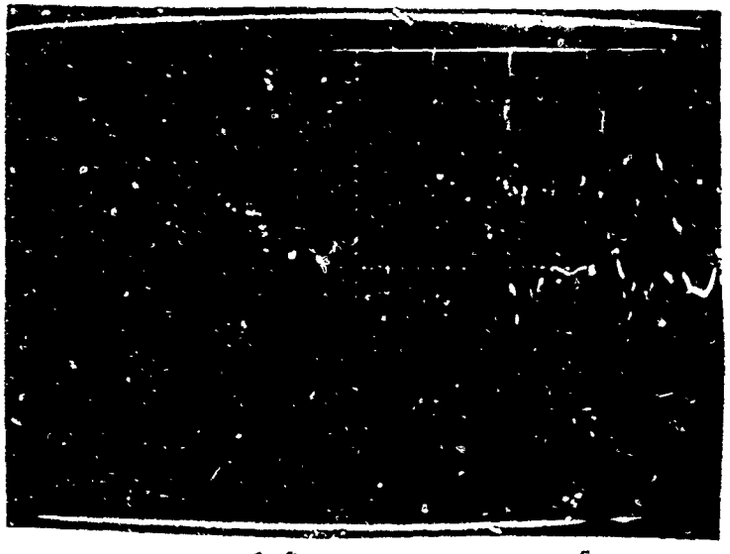

VOLTS/CM 0.2 SWEEP/CM 5 usec

VOLTS/CM _____ SWEEP/CM _____

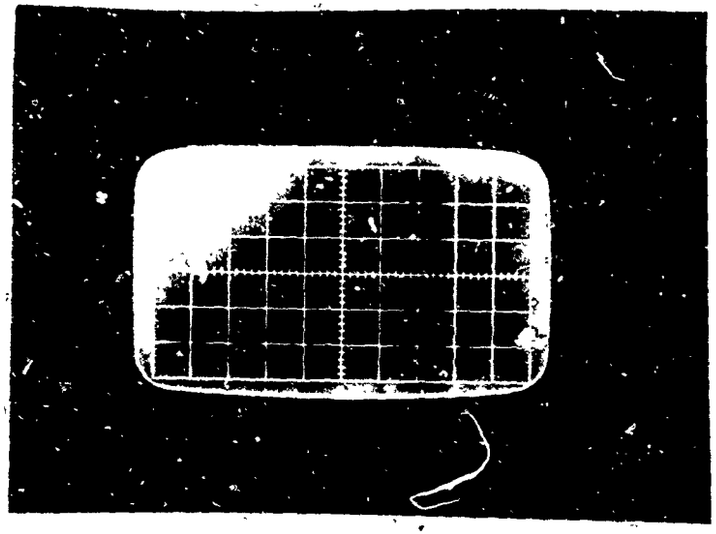

VOLTS/CM 0.2 SWEEP/CM 5 usec

VOLTS/CM 0.2 SWEEP/CM 5 usec

TEST NO. 29 - 10, 11, 12: SUPPORT ELECTRONICS TEST - 1000 VOLT MONITOR

VOLTS/CM .2 SWEEP/CM 50 usec

VOLTS/CM _____ SWEEP/CM _____

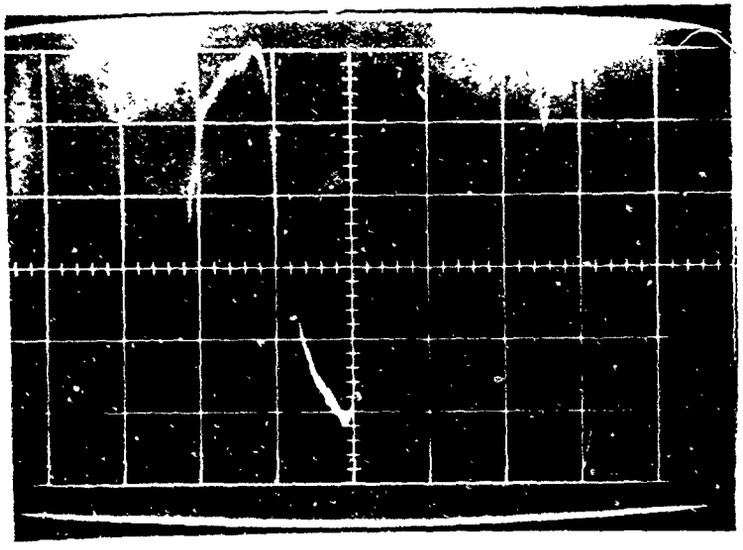

VOLTS/CM 2 SWEEP/CM 0.5 usec

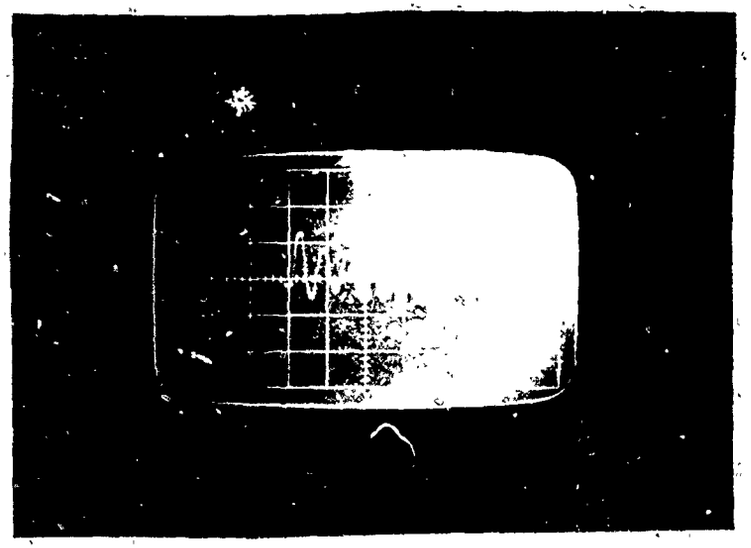

VOLTS/CM 2 SWEEP/CM 5 usec

TEST NO. 29 - 13, 14, 15: SUPPORT ELECTRONICS TEST - START MONITOR

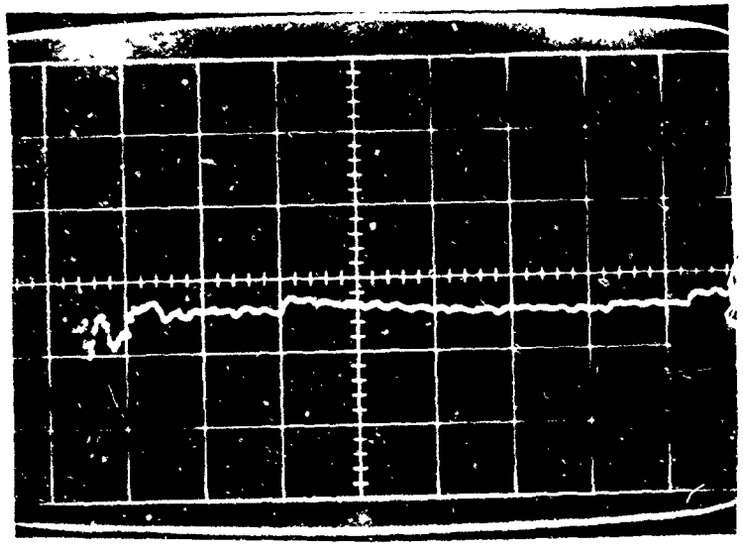

VOLTS/CM 2 SWEEP/CM 50 usec

VOLTS/CM _____ SWEEP/CM _____

VOLTS/CM 50 mv SWEEP/CM .5 usec

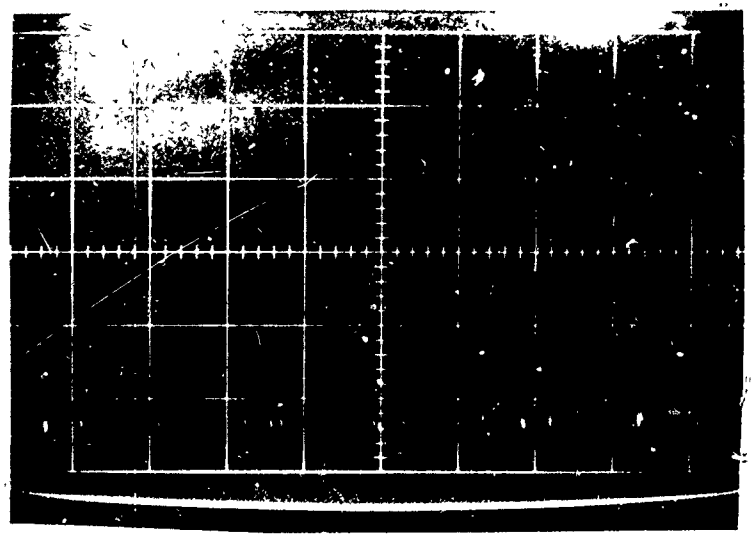

VOLTS/CM 50 mv SWEEP/CM 5 usec

TEST NO. 29 - 16, 17, 18: SUPPORT ELECTRONICS TEST - READOUT AMPLIFIER

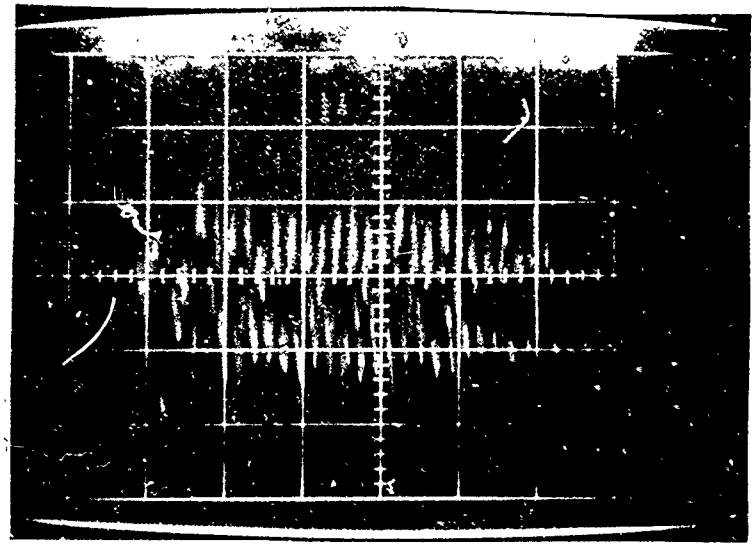

VOLTS/CM 50 mv SWEEP/CM 50 usec

VOLTS/CM _____ SWEEP/CM _____

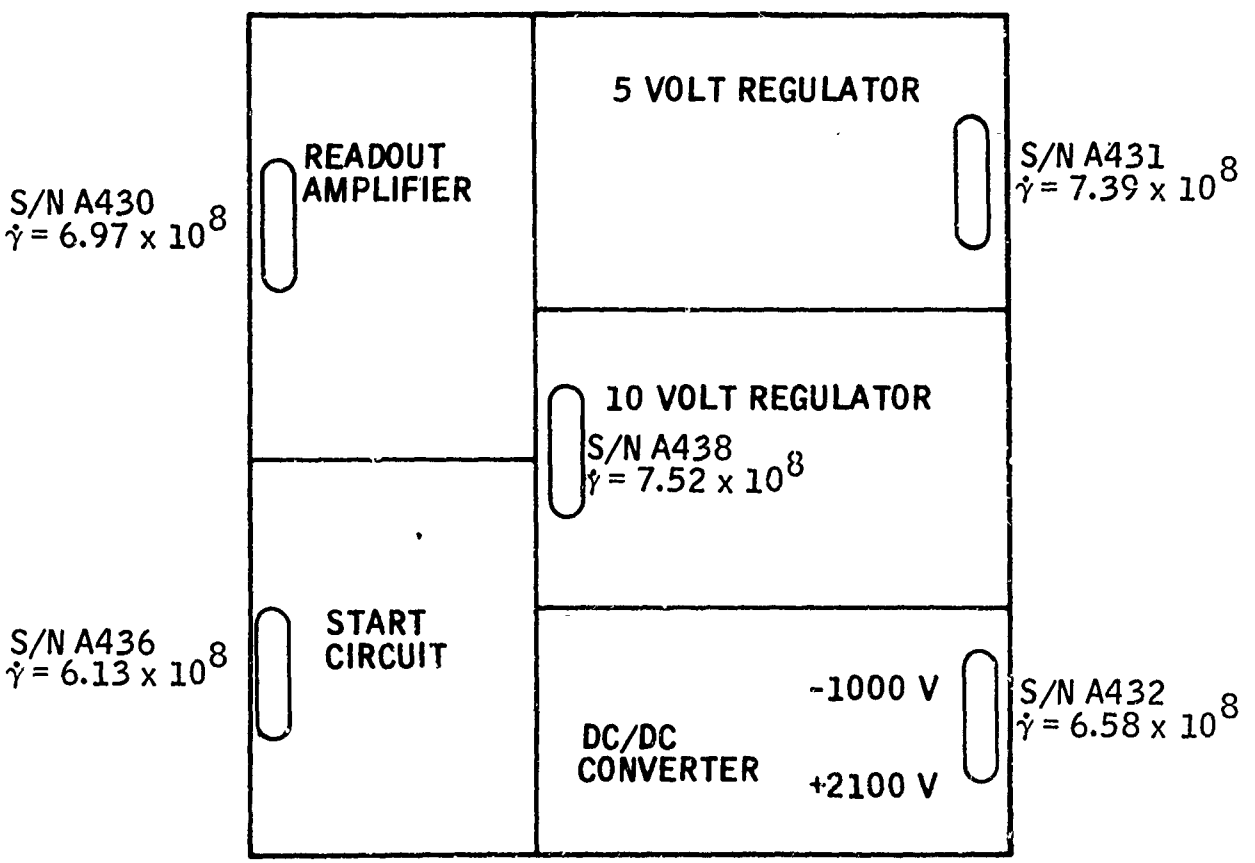

Support Electronics Dosimetry (Shot No. 30)

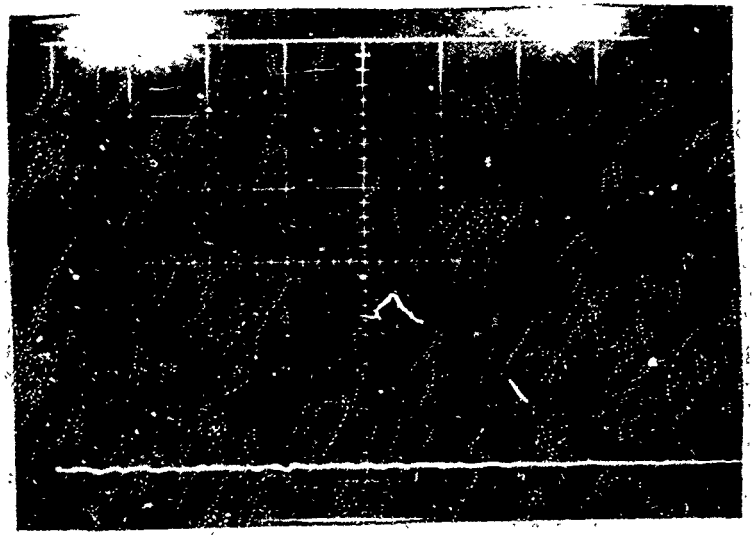

VOLTS/CM 2 SWEEP/CM 0.5 usec

VOLTS/CM 2 SWEEP/CM 5 usec

TEST NO. 30 - 1, 2, 3: SUPPORT ELECTRONICS TEST - 5 VOLT MONITOR

VOLTS/CM 2 SWEEP/CM 50 usec

VOLTS/CM _____ SWEEP/CM _____

VOLTS/CM 5 SWEEP/CM .5 usec

VOLTS/CM 5 SWEEP/CM 5usec

TEST NO. 30 - 4, 5, 6: SUPPORT ELECTRONICS TEST - 10 VOLT MONITOR

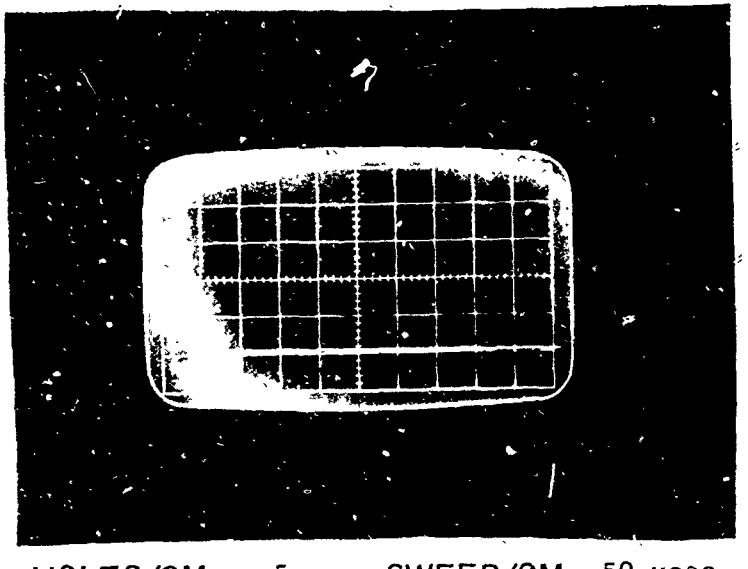

VOLTS/CM 5 SWEEP/CM 50 usec

VOLTS/CM _____ SWEEP/CM _____

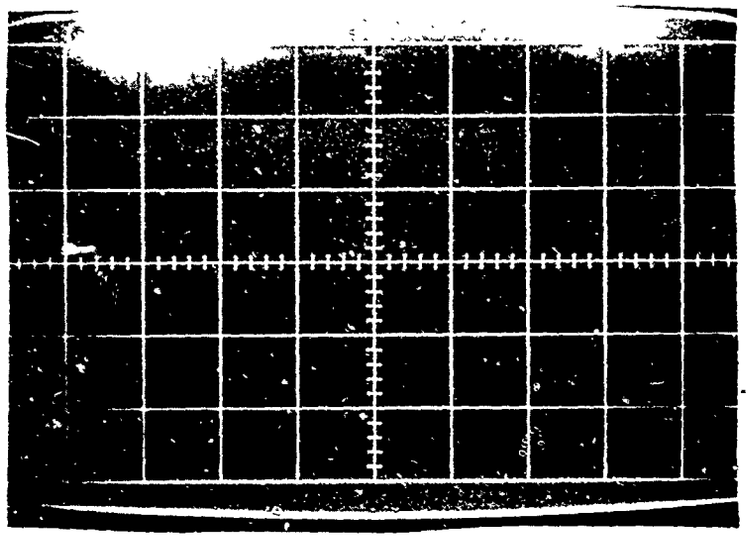

VOLTS/CM .2 SWEEP/CM .5 usec

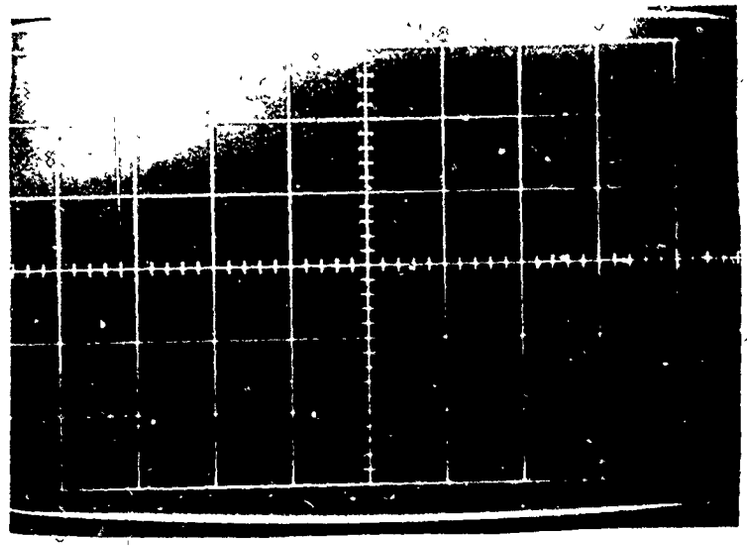

VOLTS/CM .2 SWEEP/CM 5 usec

TEST NO. 30 - 7, 8, 9: SUPPORT ELECTRONICS TESTS - 2100 VOLT MONITOR

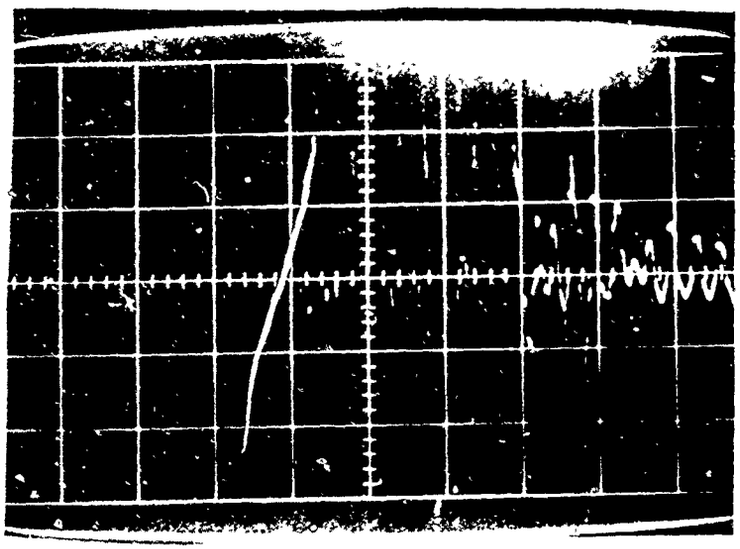

VOLTS/CM 0.2 SWEEP/CM 5 usec

VOLTS/CM _____ SWEEP/CM _____

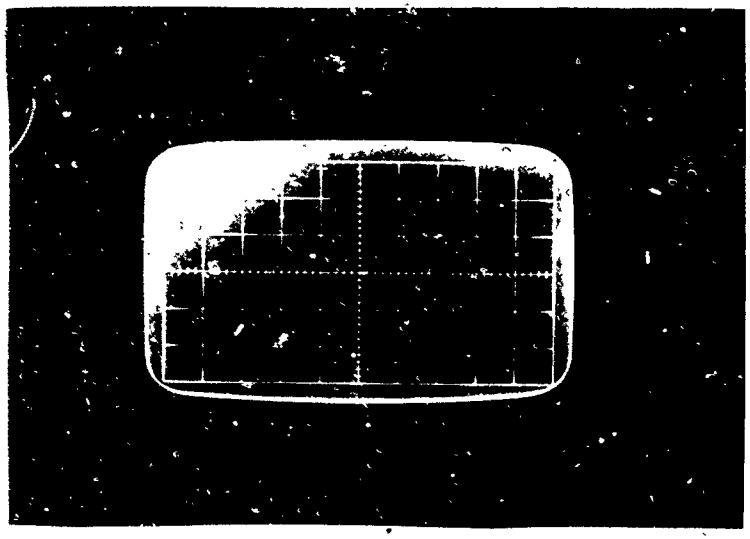

VOLTS/CM 0.2 SWEEP/CM 0.5 usec

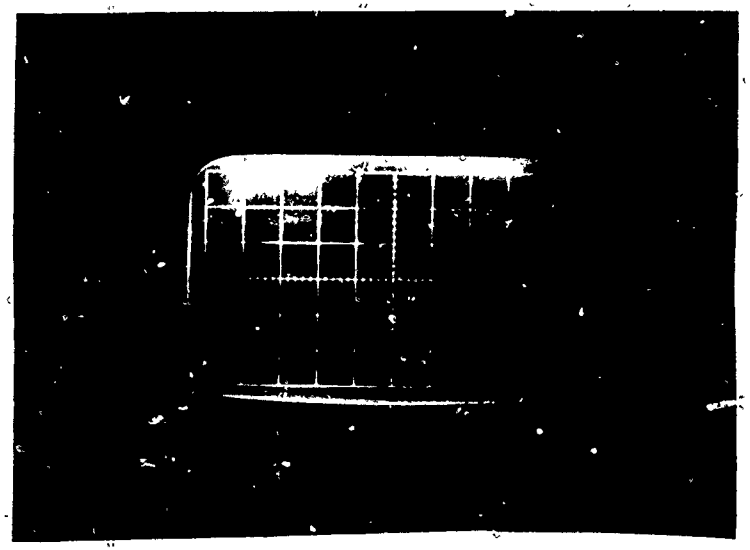

VOLTS/CM 0.2 SWEEP/CM 5 usec

TEST NO. 30 - 10, 11, 12: SUPPORT ELECTRONICS TEST - 1000 VOLT MONITOR

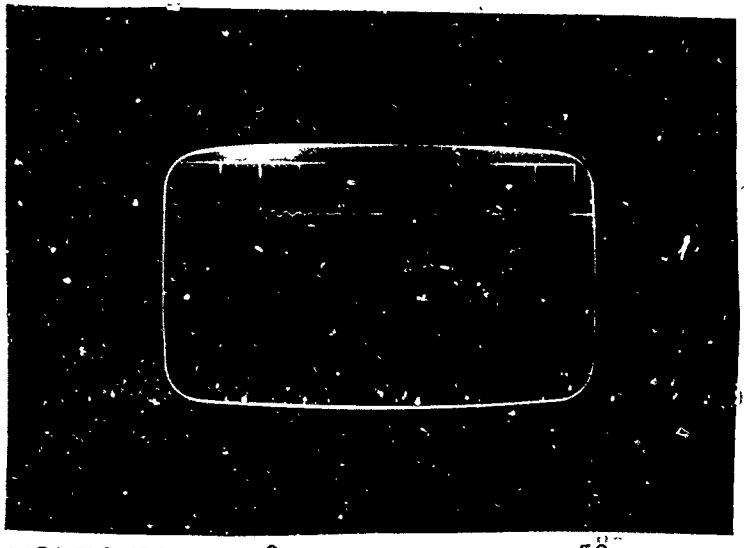

VOLTS/CM .2 SWEEP/CM 50 usec

VOLTS/CM _____ SWEEP/CM _____

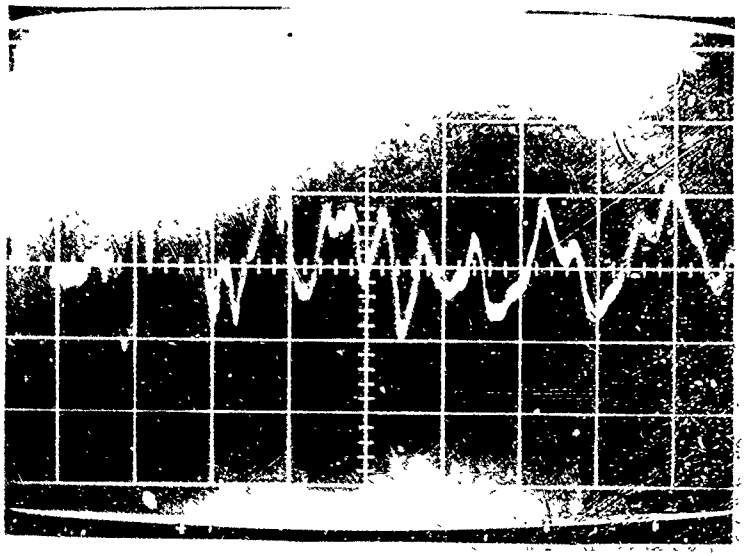

VOLTS/CM 2 SWEEP/CM 0.5 usec

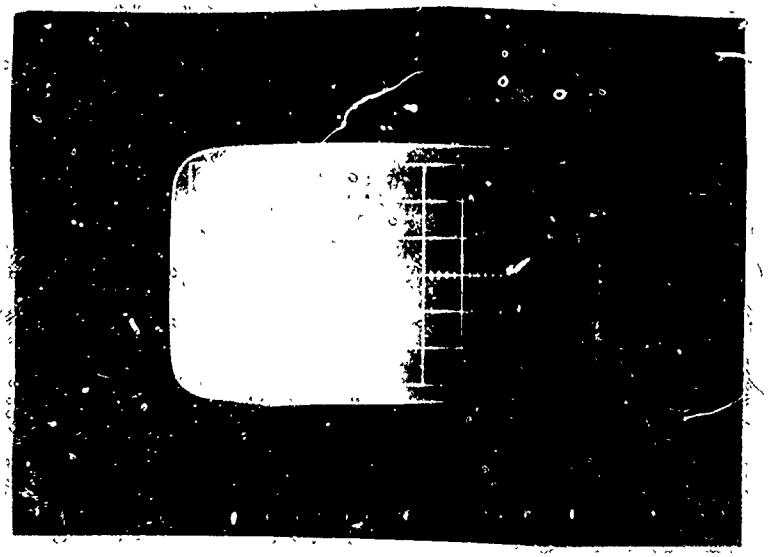

VOLTS/CM 2 SWEEP/CM 5 usec

TEST NO. 30 - 13, 14, 15: SUPPORT ELECTRONICS TEST - START MONITOR

VOLTS/CM _____ SWEEP/CM _____

VOLTS/CM _____ SWEEP/CM _____

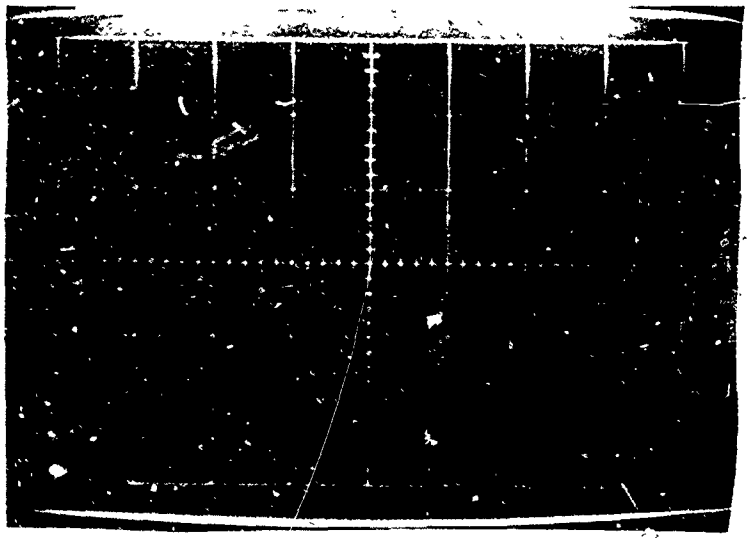

VOLTS/CM 50 mv SWEEP/CM .5 usec

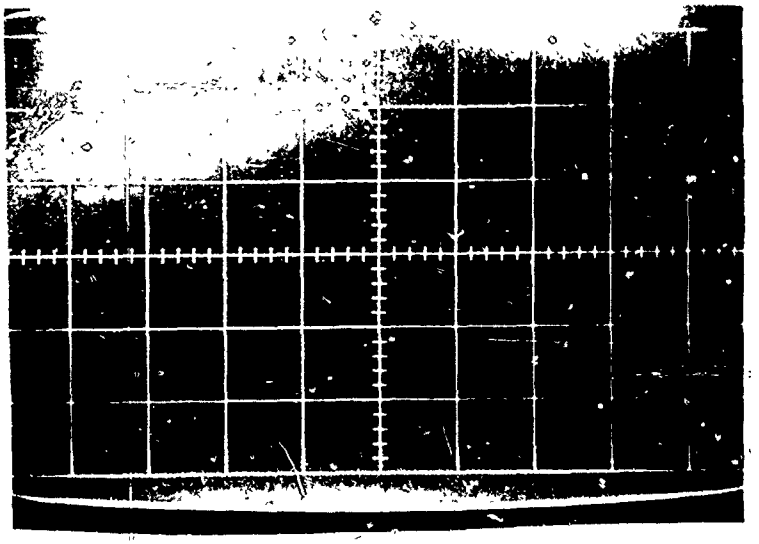

VOLTS/CM 50 mv SWEEP/CM 5 usec

TEST NO. 30 - 16, 17, 18: SUPPORT ELECTRONICS TEST - READOUT AMPLIFIER

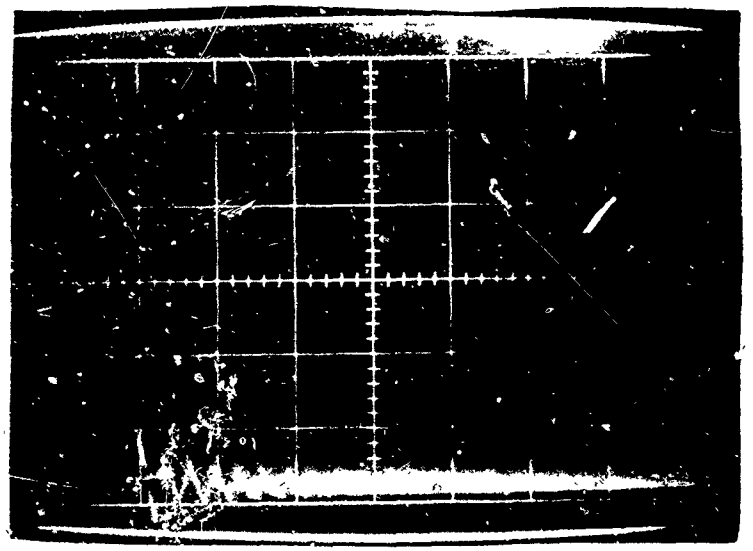

VOLTS/CM 50 mv SWEEP/CM 50 usec

VOLTS/CM _____ SWEEP/CM _____

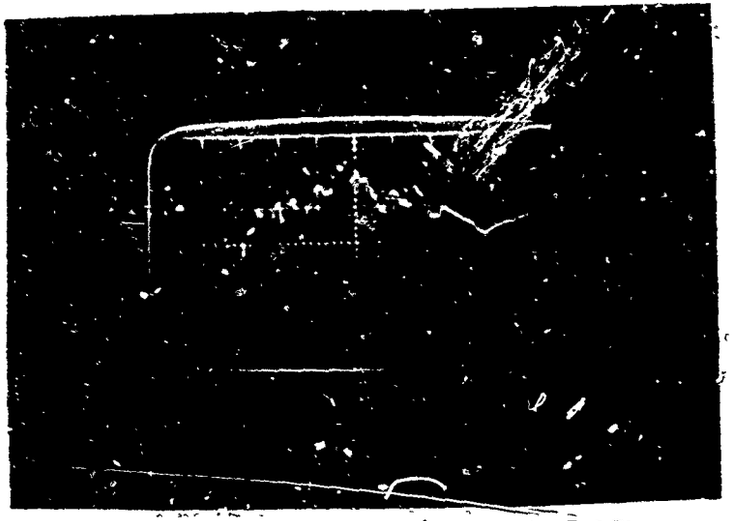

VOLTS/CM 2 SWEEP/CM .5 usec

VOLTS/CM 2 SWEEP/CM 5 usec

TEST NO. 25 - 37, 38: SHIELD CURRENT MONITOR

VOLTS/CM 5 SWEEP/CM .5 usec

VOLTS/CM 5 SWEEP/CM 5 usec

TEST NO. 26 - 37, 38: SHIELD CURRENT MONITOR

VOLTS/CM 5 SWEEP/CM .5 usec

VOLTS/CM 5 SWEEP/CM 5 usec

TEST NO. 27 - 37, 38: SHIELD CURRENT MONITOR

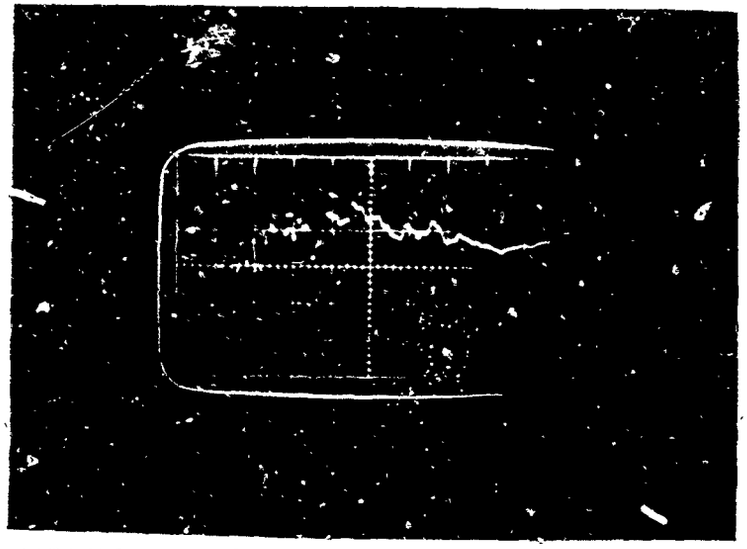

VOLTS/CM 2 SWEEP/CM .5 usec

VOLTS/CM 2 SWEEP/CM 5 usec

TEST NO. 28 - 37, 38: SHIELD CURRENT MONITOR

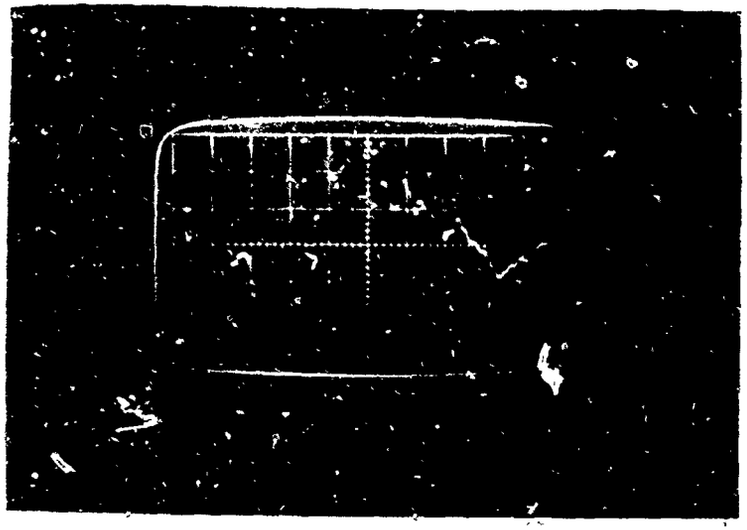

VOLTS/CM 1 SWEEP/CM .5 usec

VOLTS/CM 1 SWEEP/CM 5 usec

TEST NO. 29 - 37, 38: SHIELD CURRENT MONITOR

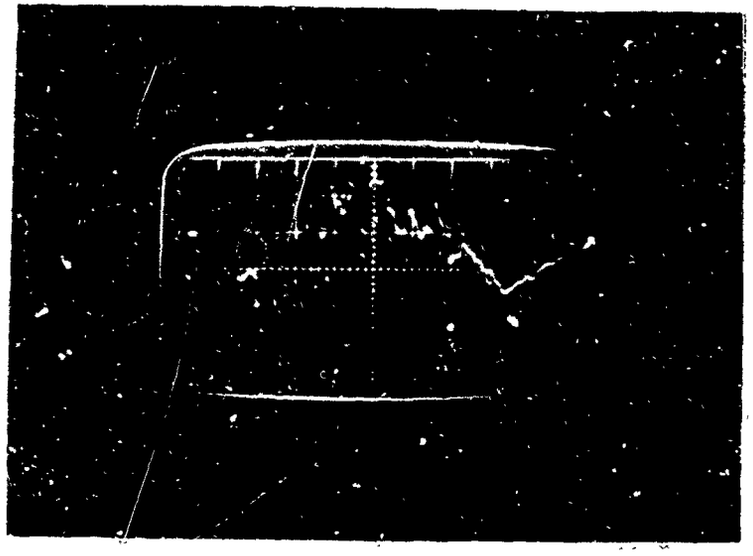

VOLTS/CM 1 SWEEP/CM .5 usec

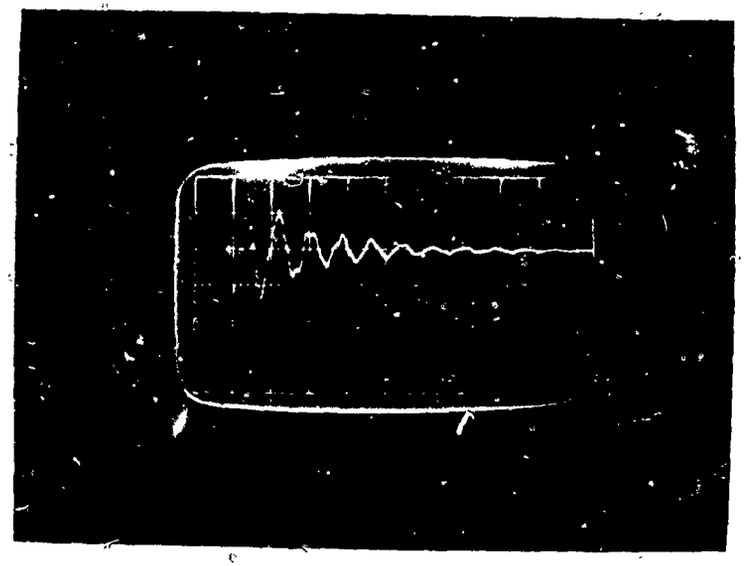

VOLTS/CM 1 SWEEP/CM 5 usec

TEST NO. 30 - 37, 38: SHIELD CURRENT MONITOR

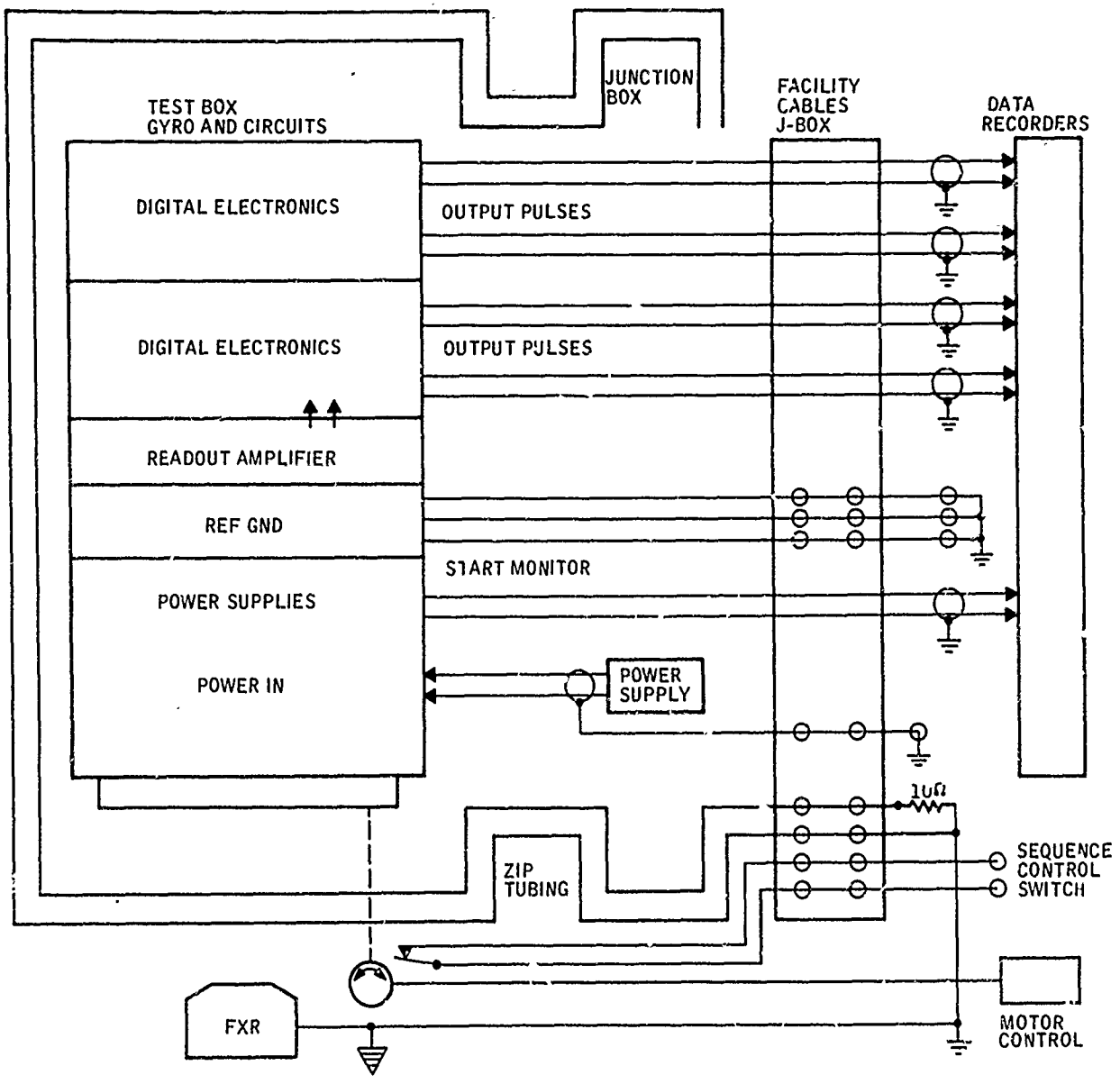
JUNCTION BOX
TEST BOX
GYRO AND CIRCUITS
FACILITY CABLES J-BOX
DATA RECORDERS
DIGITAL ELECTRONICS
OUTPUT PULSES
DIGITAL ELECTRONICS
OUTPUT PULSES
READOUT AMPLIFIER
REF GND
START MONITOR
POWER SUPPLIES
POWER IN
POWER SUPPLY
1uΩ
SEQUENCE CONTROL SWITCH
ZIP TUBING
FXR
MOTOR CONTROL

System Test

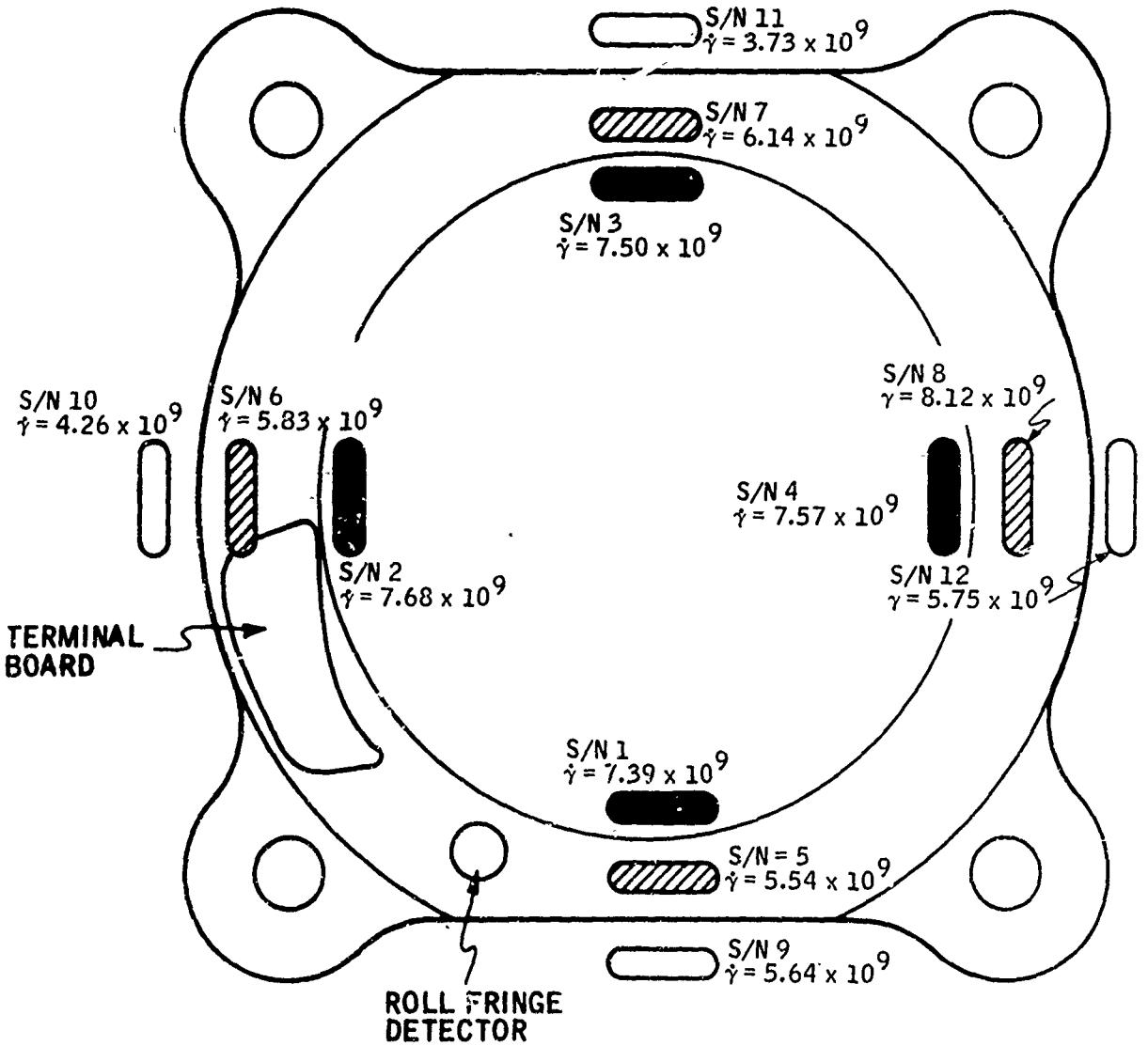

DOSIMETER LOCATED AT FRONT SURFACE ON DIGITAL BOARD

DOSIMETER LOCATED AT GYRO FLANGE (2 3/8 IN. BACK)

DOSIMETER LOCATED AT TABLE TOP (6 3/8 IN. BACK)

System Test Shot No. 31 Dosimetry Data

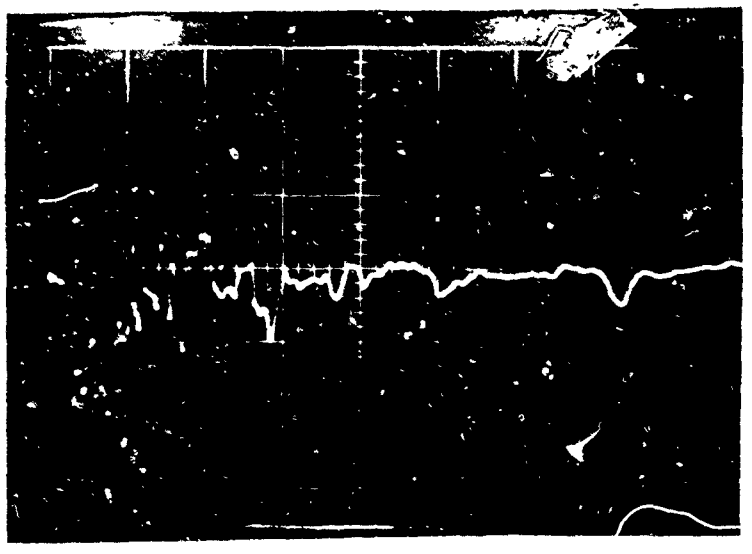

VOLTS/CM 2 SWEEP/CM .5 usec

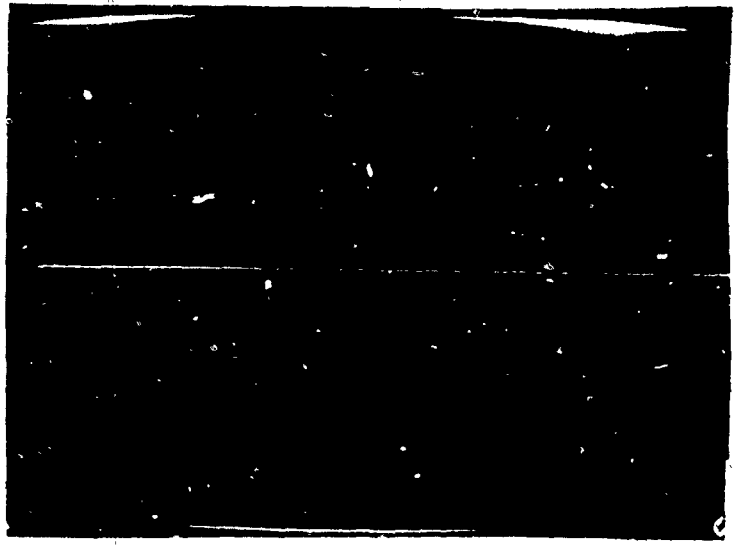

VOLTS/CM 2 SWEEP/CM 5 usec

TEST NO. 31 - 1, 2, 3: SYSTEM TEST - FAST DIGITAL PULSE

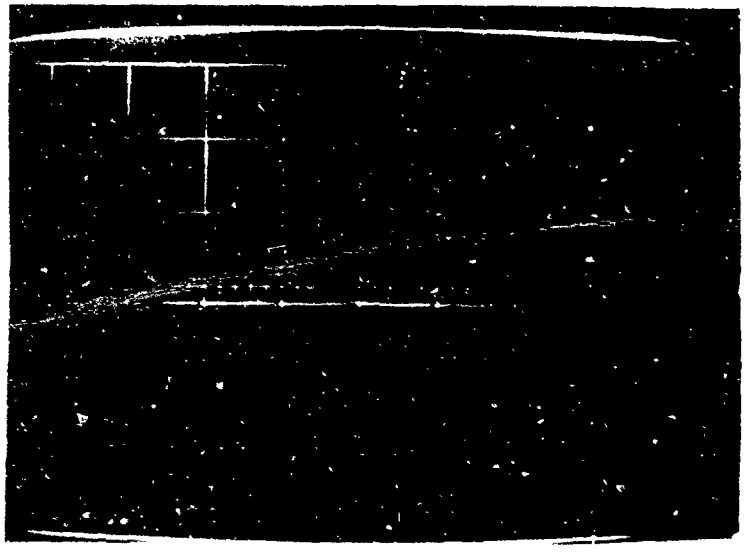

VOLTS/CM 2 SWEEP/CM 50 usec

VOLTS/CM _____ SWEEP/CM _____

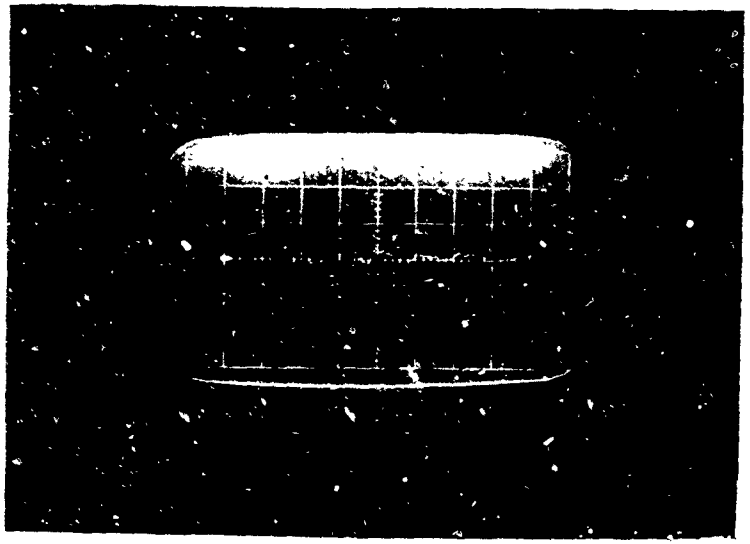

VOLTS/CM 2 SWEEP/CM 0.5 usec

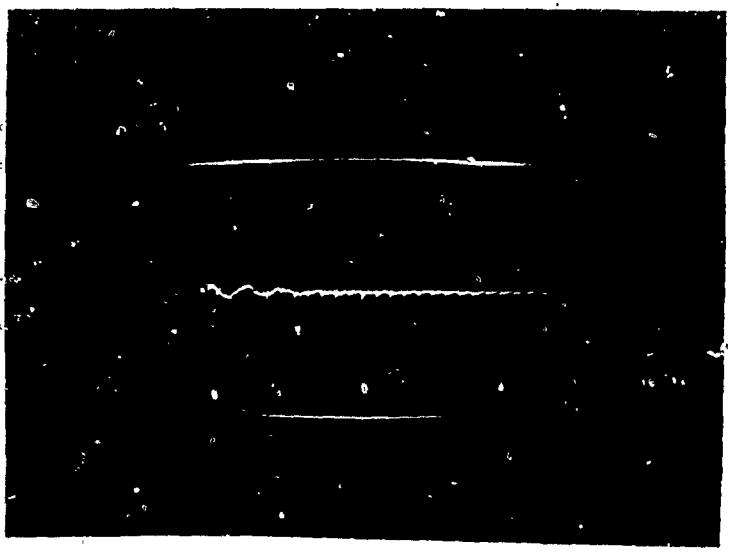

VOLTS/CM 2 SWEEP/CM 5 usec

TEST NO. 31 - 4, 5, 6: SYSTEM TEST - FAST DIGITAL PULSE

VOLTS/CM 2 SWEEP/CM 50 usec

VOLTS/CM _____ SWEEP/CM _____

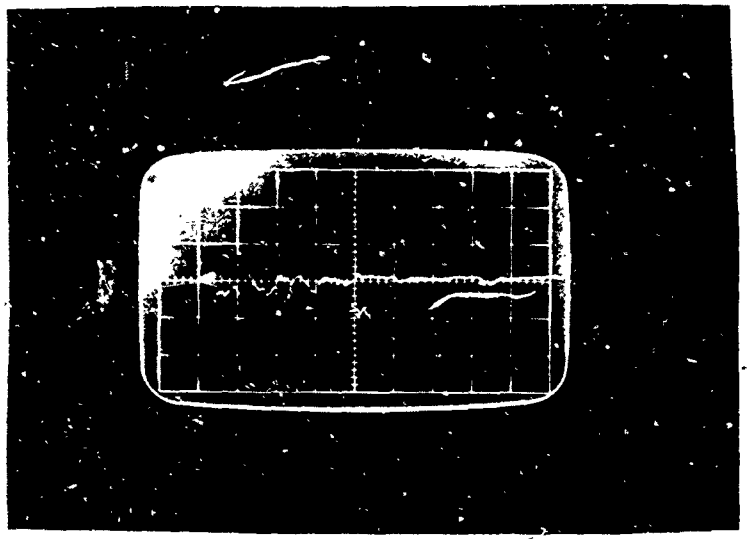

VOLTS/CM 5 SWEEP/CM .5 usec

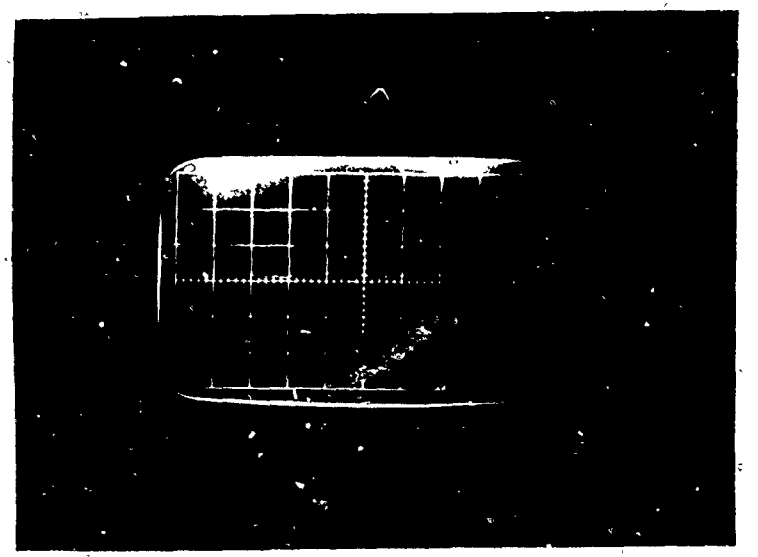

VOLTS/CM 5 SWEEP/CM 5 usec

TEST NO. 31 - 10, 11, 12: SYSTEM TEST - SLOW DIGITAL PULSE

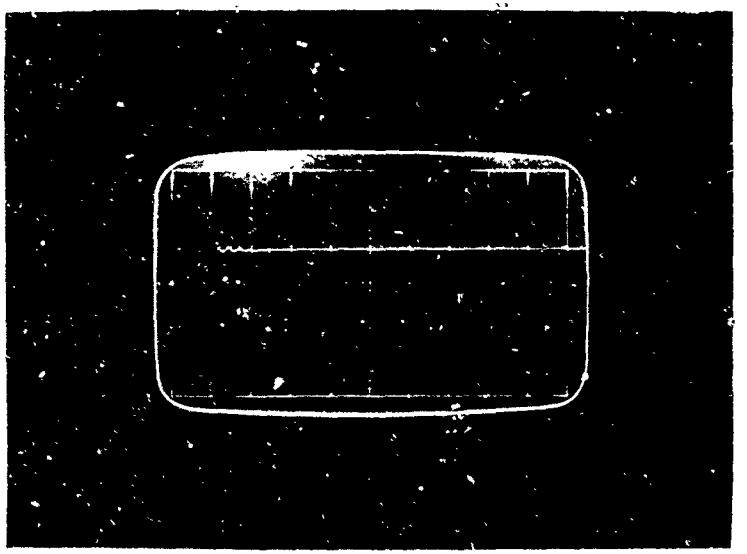

VOLTS/CM 5 SWEEP/CM 50 usec

VOLTS/CM _____ SWEEP/CM _____

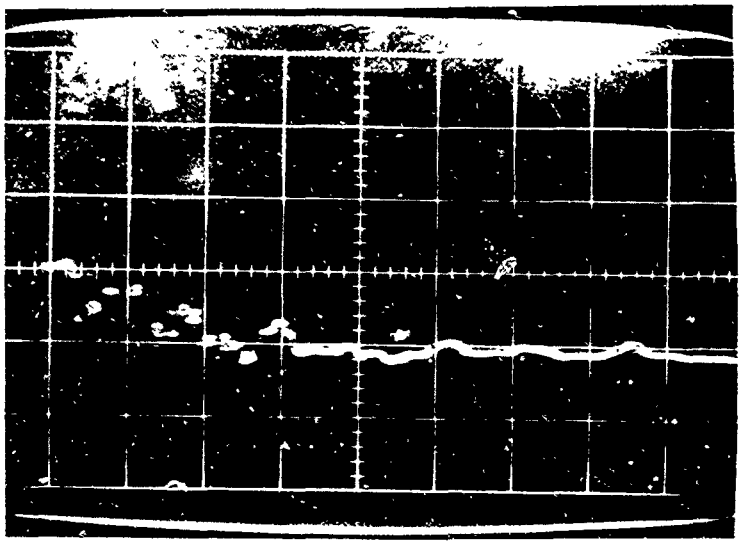

VOLTS/CM 5 SWEEP/CM .5 usec

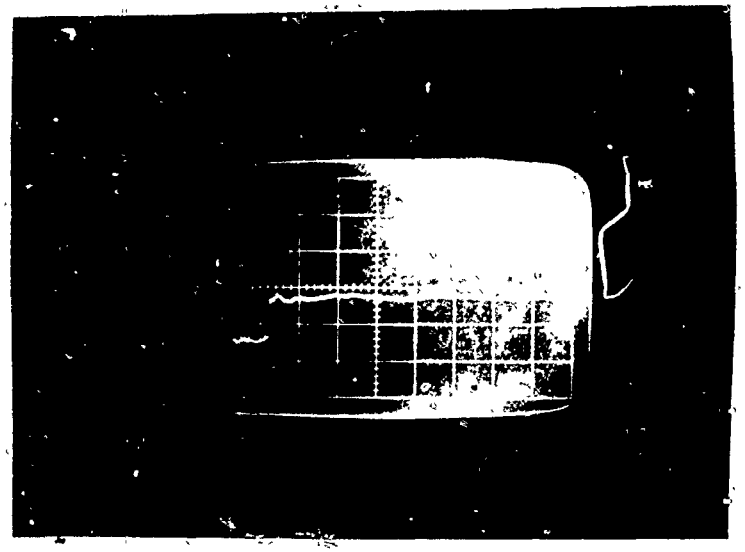

VOLTS/CM 5 SWEEP/CM 5 usec

TEST NO. 31 - 13, 14, 15: SYSTEM TEST - SLOW DIGITAL PULSE

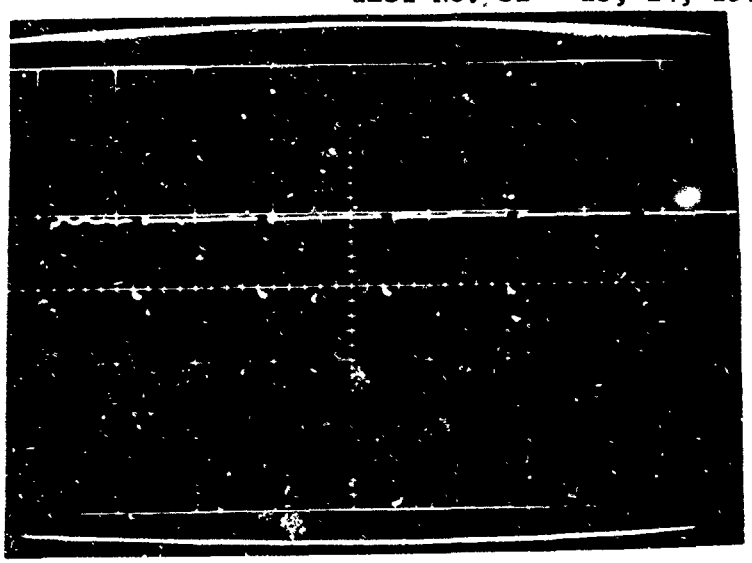

VOLTS/CM 5 SWEEP/CM 50 usec

VOLTS/CM _____ SWEEP/CM _____

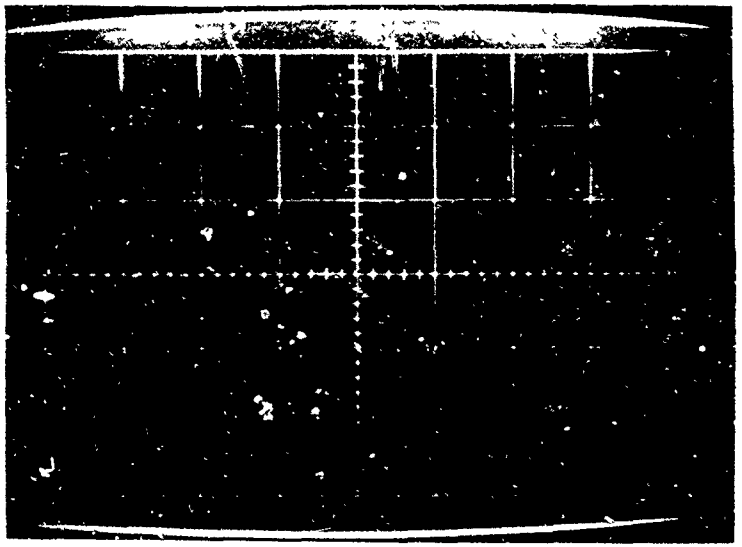

VOLTS/CM 0.2 SWEEP/CM 0.5 usec

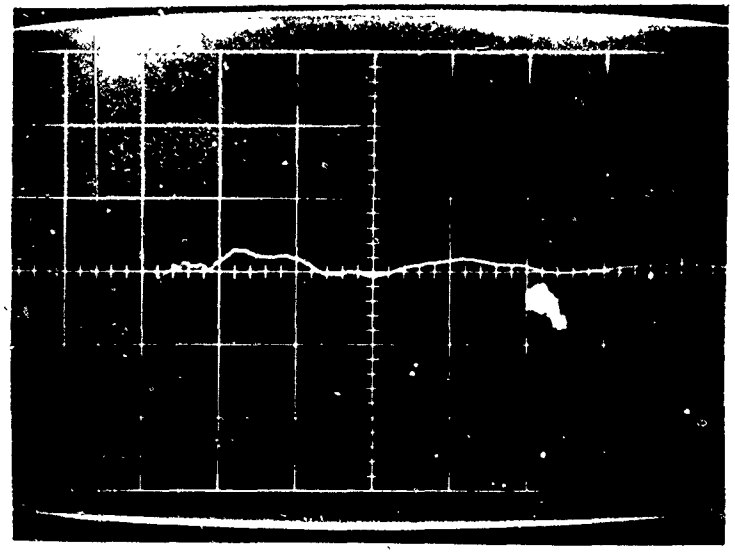

VOLTS/CM 0.2 SWEEP/CM 5 usec

TEST NO. 31 - 16, 17, 18: SYSTEM TEST - START MONITOR

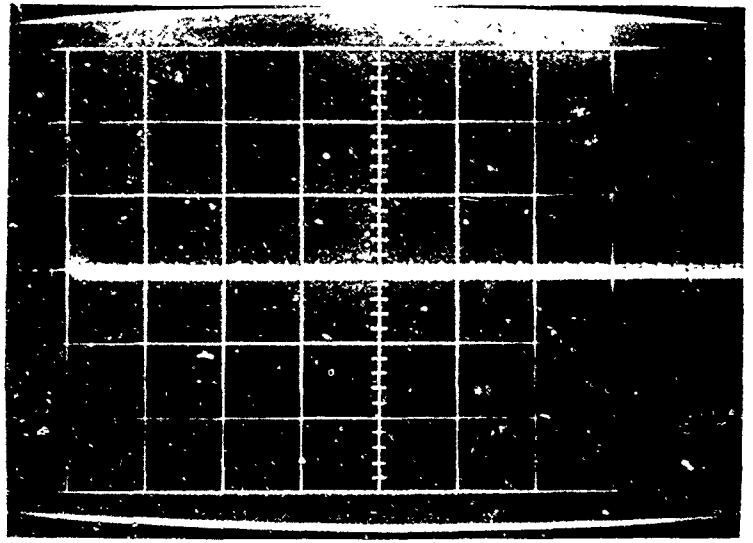

VOLTS/CM 0.2 SWEEP/CM 50 usec

VOLTS/CM _____ SWEEP/CM _____

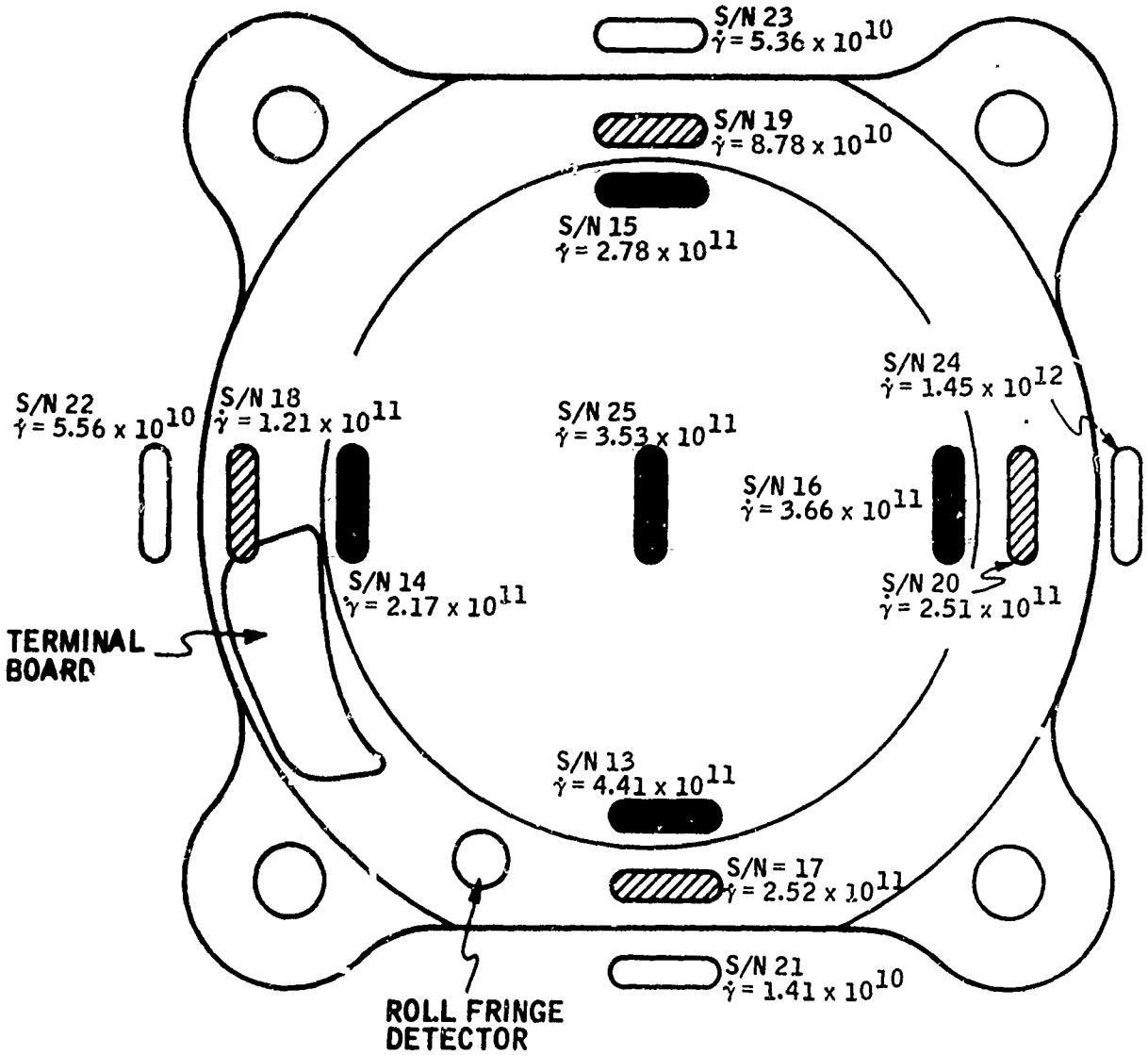

DOSIMETER LOCATED AT FRONT SURFACE ON DIGITAL BOARD

DOSIMETER LOCATED AT GYRO FLANGE (2 3/8 IN. BACK)

DOSIMETER LOCATED AT TABLE TOP (6 3/8 IN. BACK)

System Test Shot No. 32 Dosimetry Data

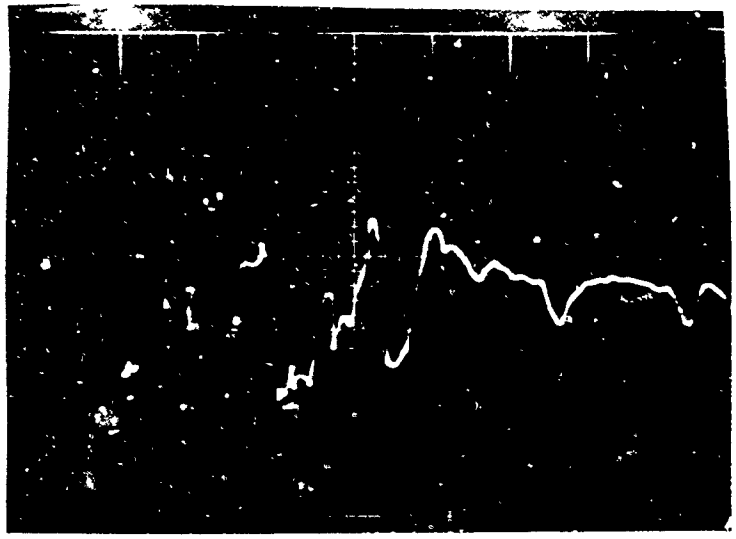

VOLTS/CM 2 SWEEP/CM .5 usec

VOLTS/CM 2 SWEEP/CM 5 usec

TEST NO. 32 - 1, 2, 3: SYSTEM TEST - FAST DIGITAL PULSE

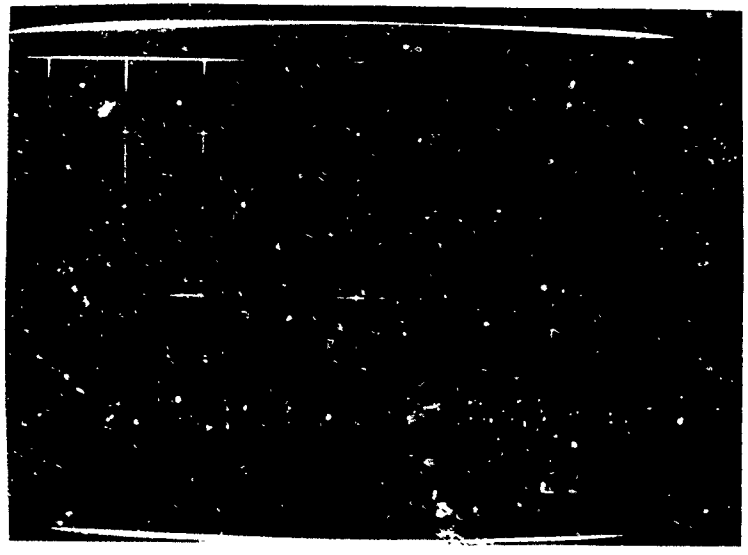

VOLTS/CM 2 SWEEP/CM 50 usec

VOLTS/CM _____ SWEEP/CM _____

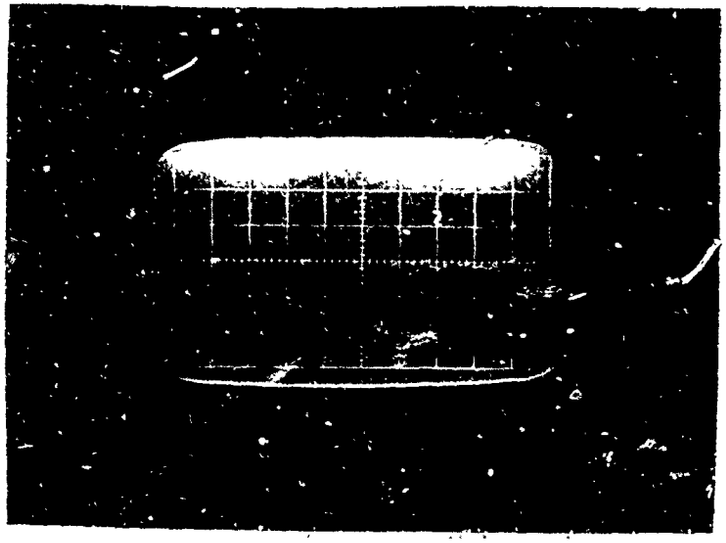

VOLTS/CM 2 SWEEP/CM 0.5 usec

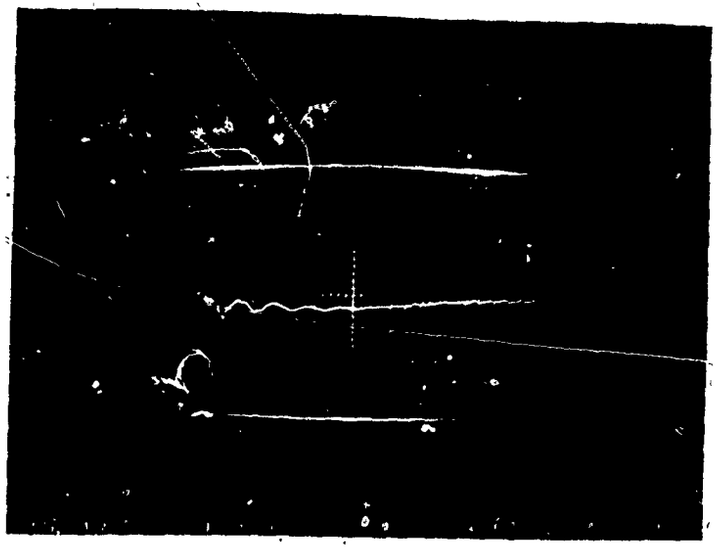

VOLTS/CM 2 SWEEP/CM 5 usec

TEST NO. 32 - 4, 5, 6: SYSTEM TEST - FAST DIGITAL PULSE

VOLTS/CM 2 SWEEP/CM 50 usec

VOLTS/CM _____ SWEEP/CM _____

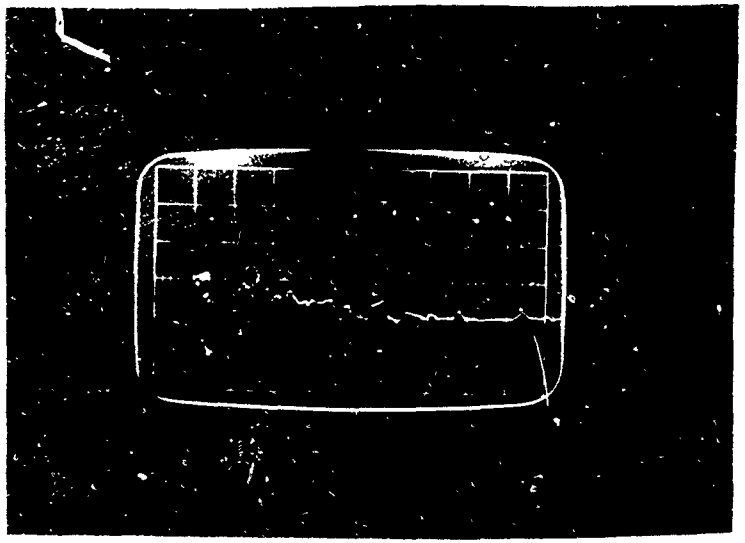

VOLTS/CM 5 SWEEP/CM .5 usec

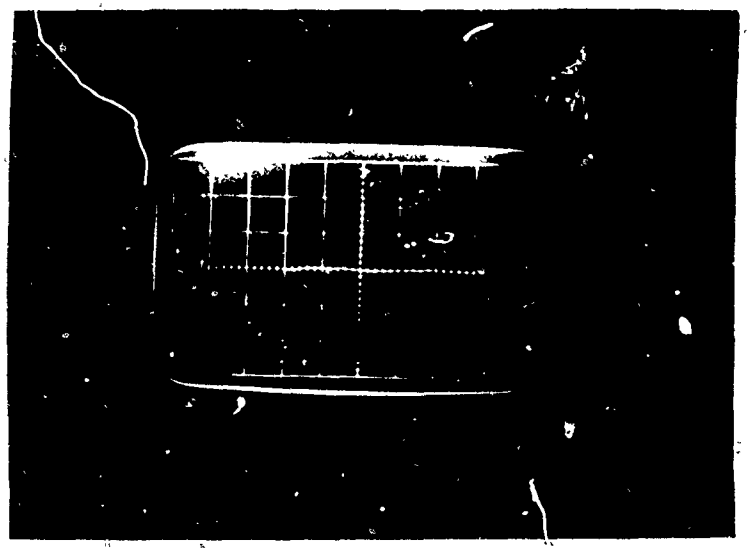

VOLTS/CM 5 SWEEP/CM 5 usec

TEST NO. 32 - 10, 11, 12: SYSTEM TEST - SLOW DIGITAL PULSE

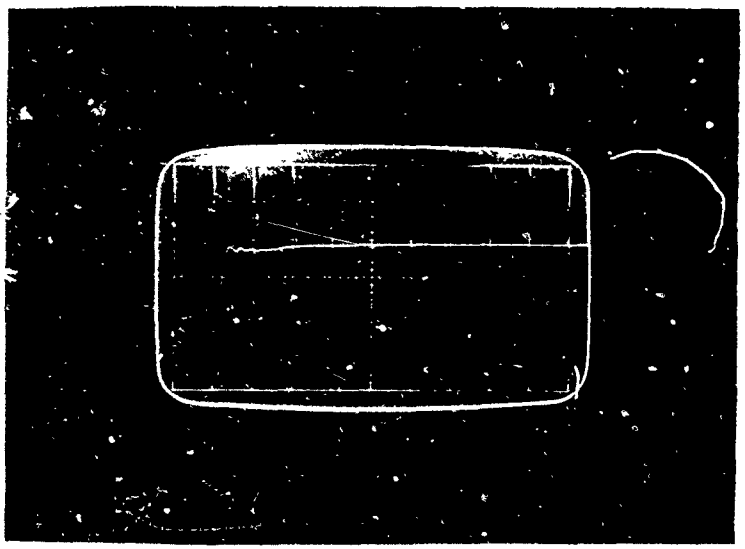

VOLTS/CM 5 SWEEP/CM 50 usec

VOLTS/CM _____ SWEEP/CM _____

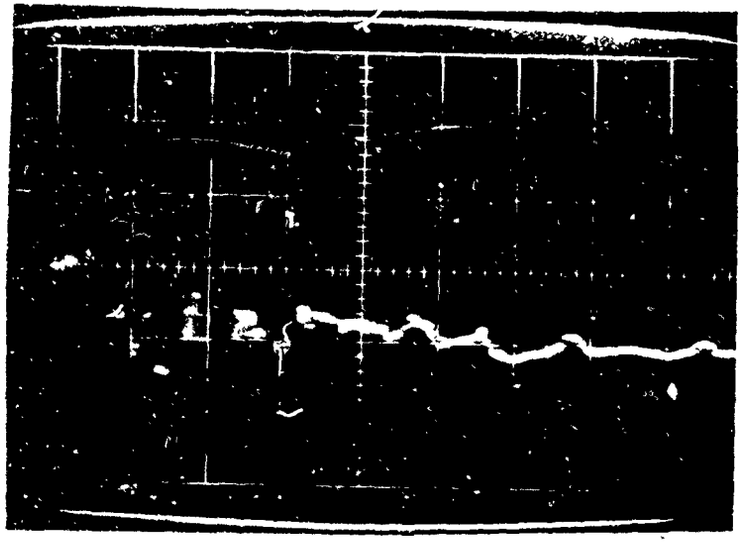

VOLTS/CM 5 SWEEP/CM .5 usec

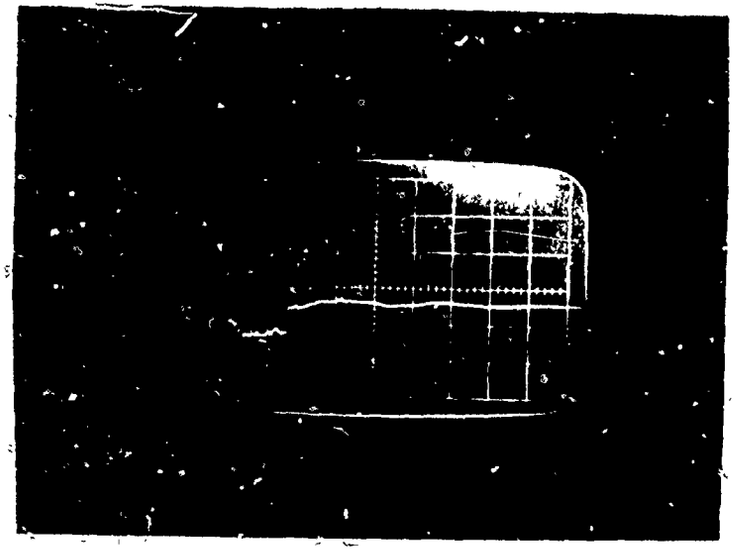

VOLTS/CM 5 SWEEP/CM 5 usec

TEST NO. 32 - 13, 14 15: SYSTEM TEST - SLOW DIGITAL PULSE

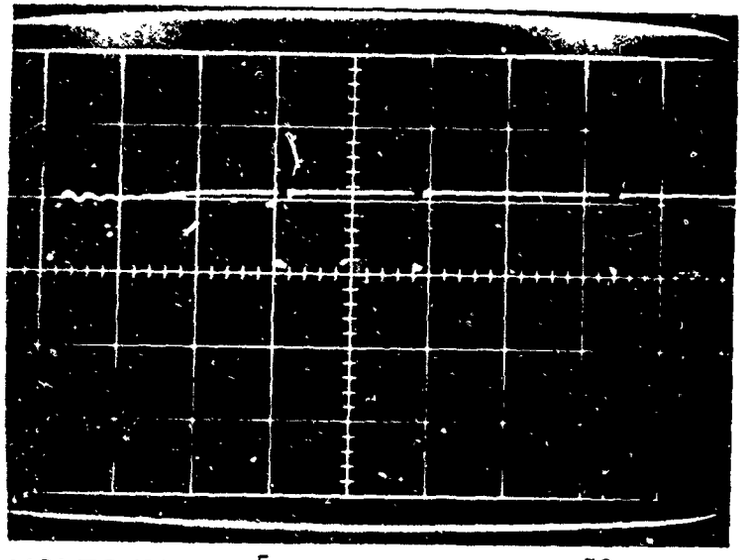

VOLTS/CM 5 SWEEP/CM 50 usec

VOLTS/CM _____ SWEEP/CM _____

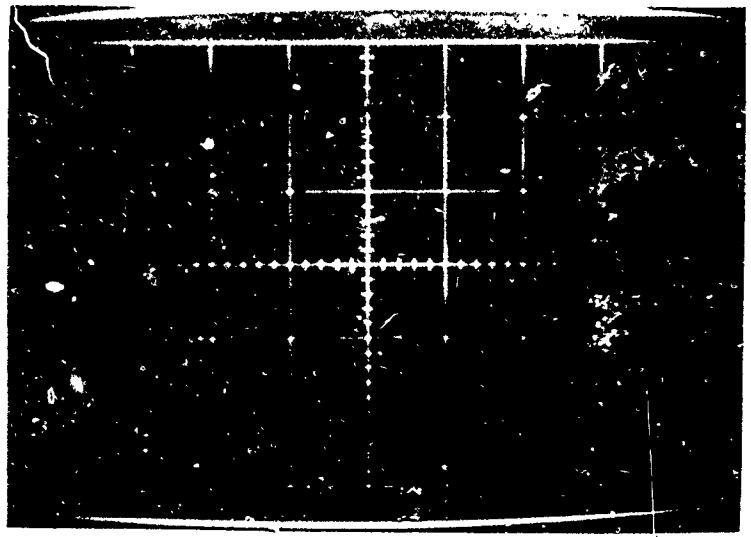

VOLTS/CM 0.2 SWEEP/CM 0.5 usec

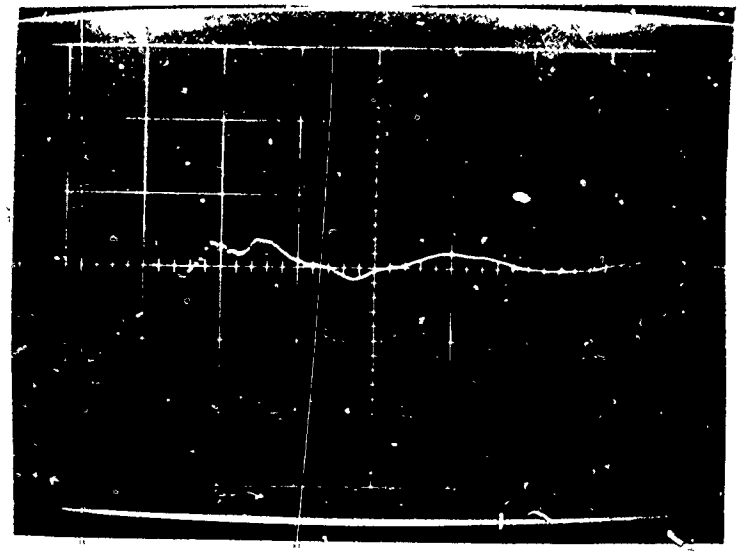

VOLTS/CM 0.2 SWEEP/CM 5 usec

TEST NO. 32 - 16, 17, 18: SYSTEM TEST - START MONITOR

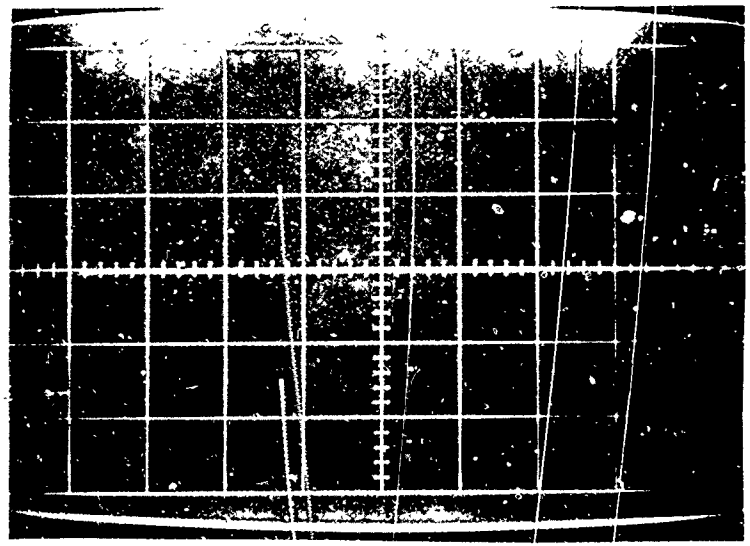

VOLTS/CM 0.2 SWEEP/CM 50 usec

VOLTS/CM _____ SWEEP/CM _____

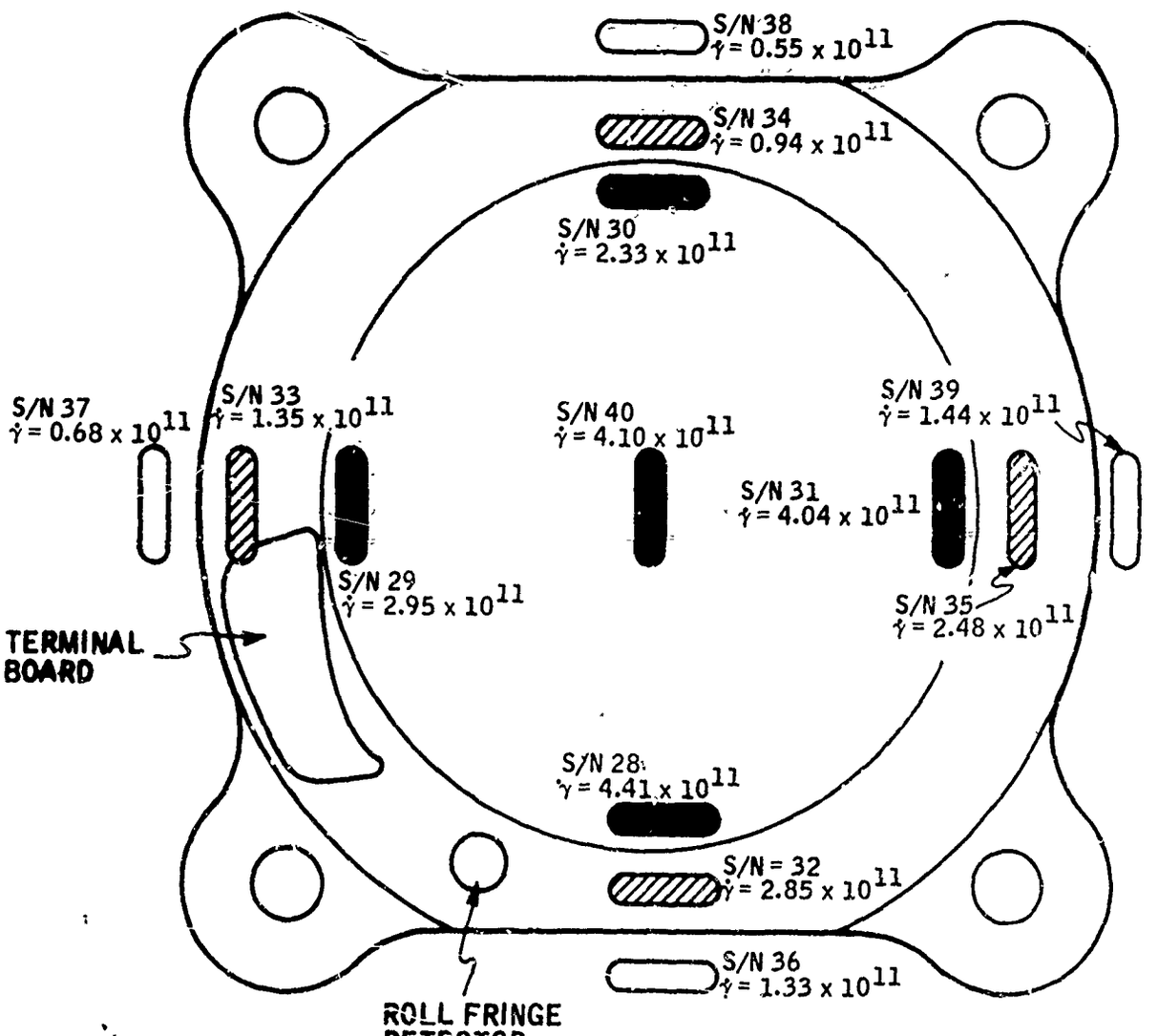

System Test Shot No. 33 Dosimetry Data

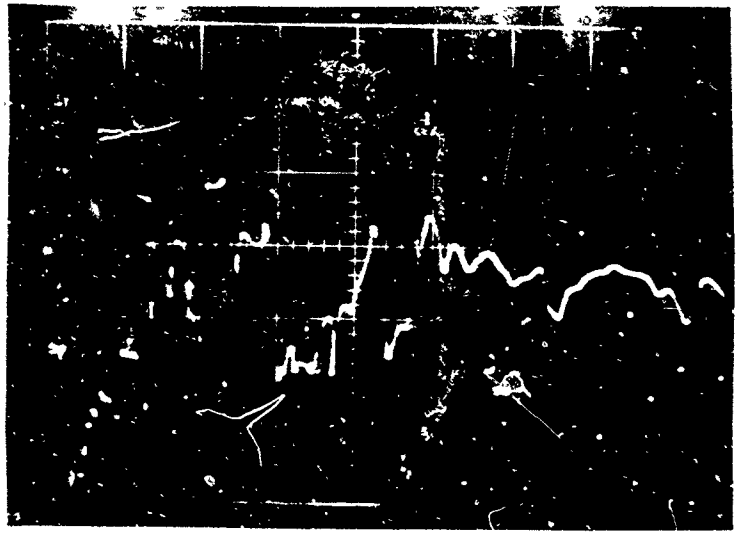

VOLTS/CM 2 SWEEP/CM .5 usec

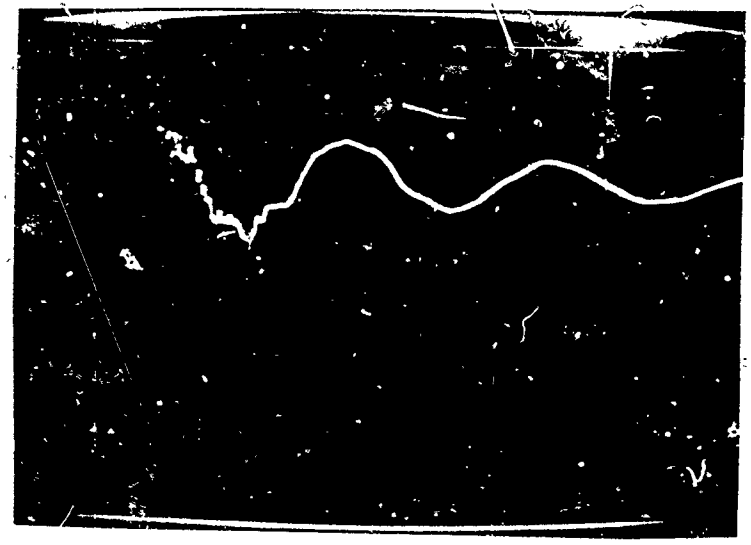

VOLTS/CM 2 SWEEP/CM 5 usec

TEST NO. 33 - 1, 2, 3: SYSTEM TEST - FAST DIGITAL PULSE

VOLTS/CM _____ SWEEP/CM _____

VOLTS/CM _____ SWEEP/CM _____

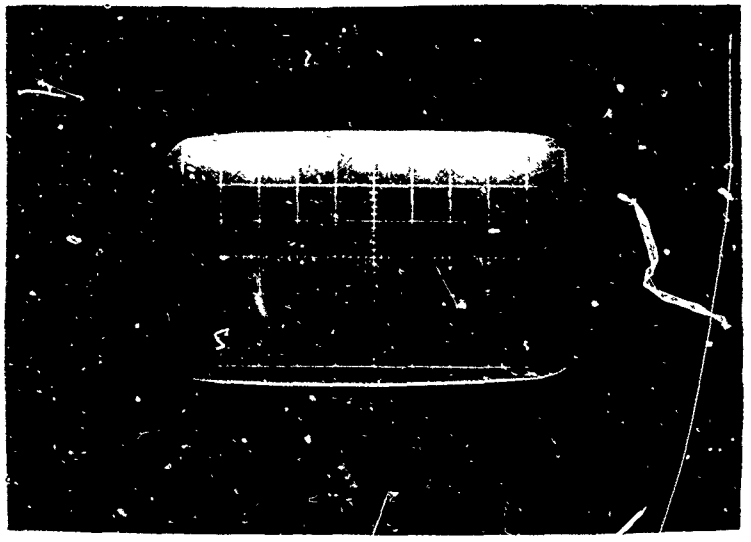

VOLTS/CM 2 SWEEP/CM 0.5 usec

VOLTS/CM 2 SWEEP/CM 5 usec

TEST NO. 33 - 4, 5, 6: SYSTEM TEST - FAST DIGITAL PULSE

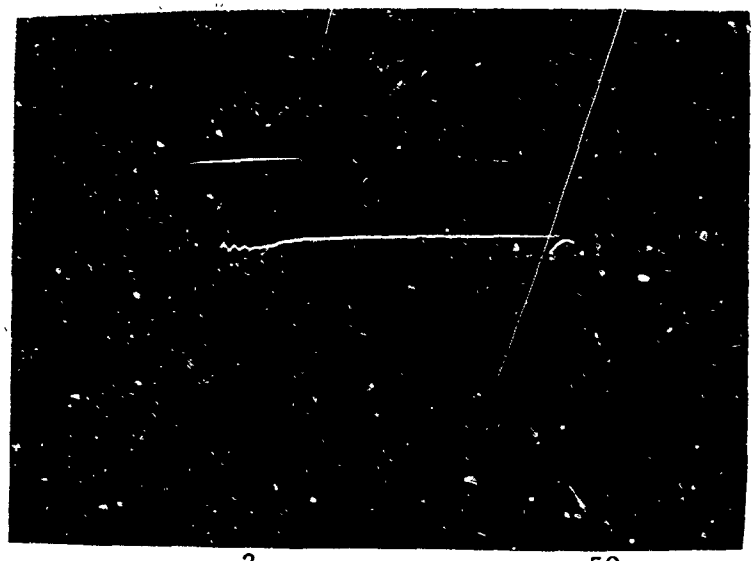

VOLTS/CM 2 SWEEP/CM 50 usec

VOLTS/CM _____ SWEEP/CM _____

VOLTS/CM 5 SWEEP/CM .5 usec

VOLTS/CM 5 SWEEP/CM 5 usec

TEST NO. 33 - 10, 11, 12: SYSTEM TEST - SLOW DIGITAL PULSE

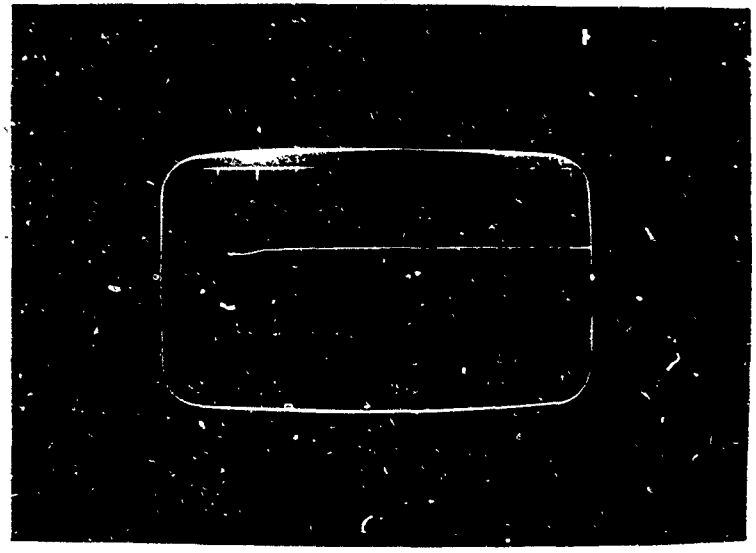

VOLTS/CM 5 SWEEP/CM 100 usec

VOLTS/CM _____ SWEEP/CM _____

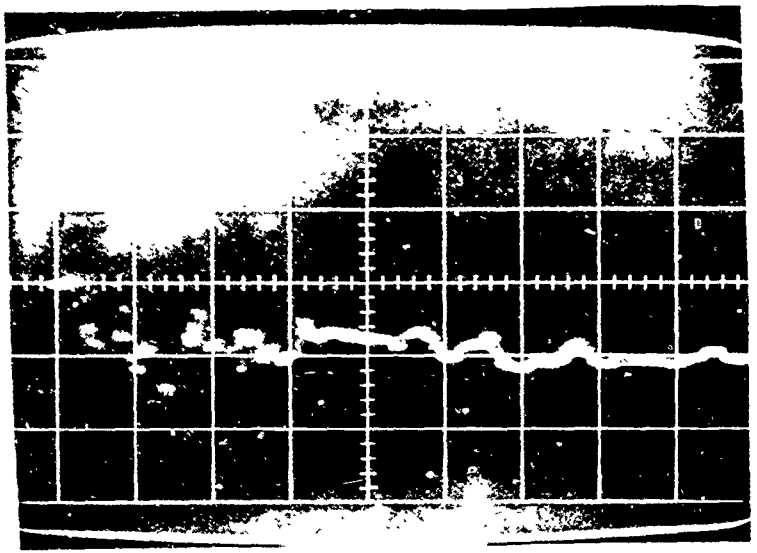

VOLTS/CM 5 SWEEP/CM .5 usec

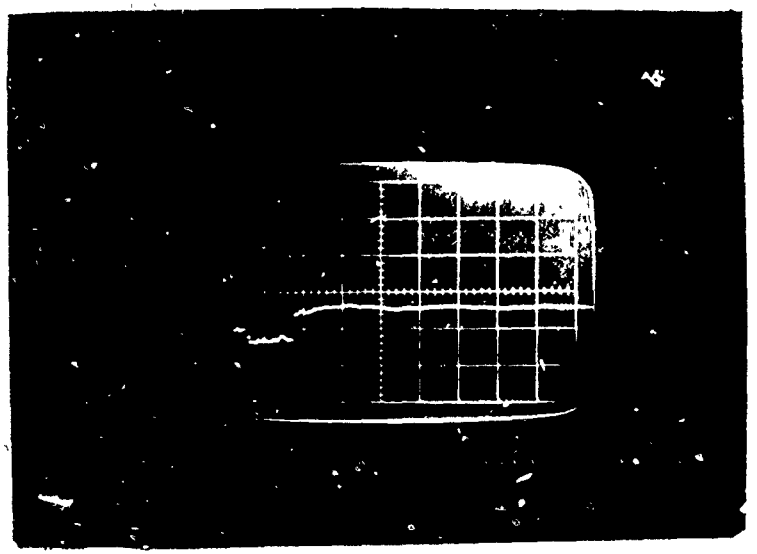

VOLTS/CM 5 SWEEP/CM 5 usec

TEST NO. 33 - 13, 14, 15: SYSTEM TEST - SLOW DIGITAL PULSE

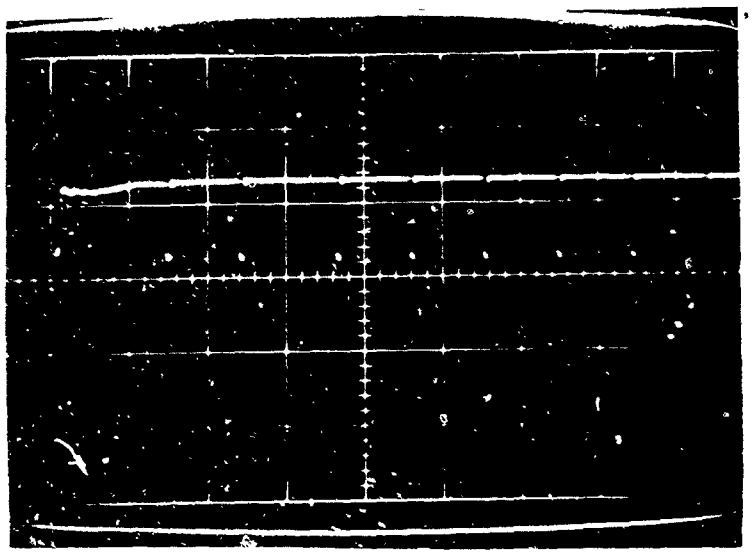

VOLTS/CM 5 SWEEP/CM .1 msec

VOLTS/CM _____ SWEEP/CM _____

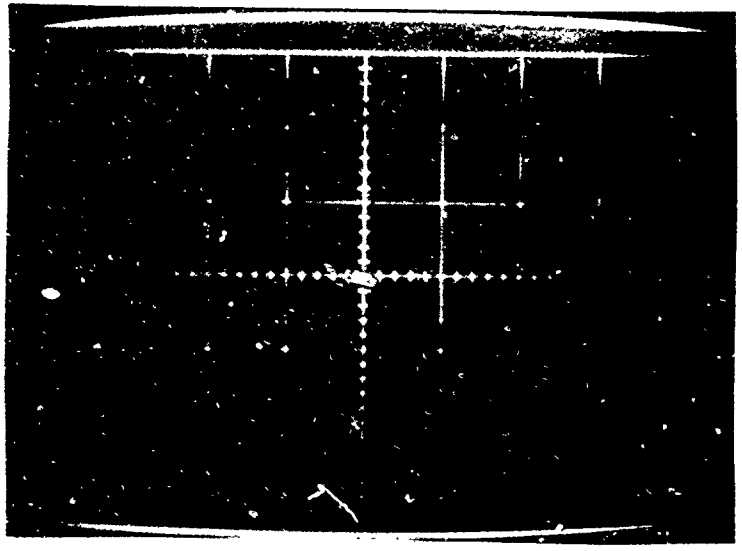

VOLTS/CM 0.2 SWEEP/CM 0.5 usec

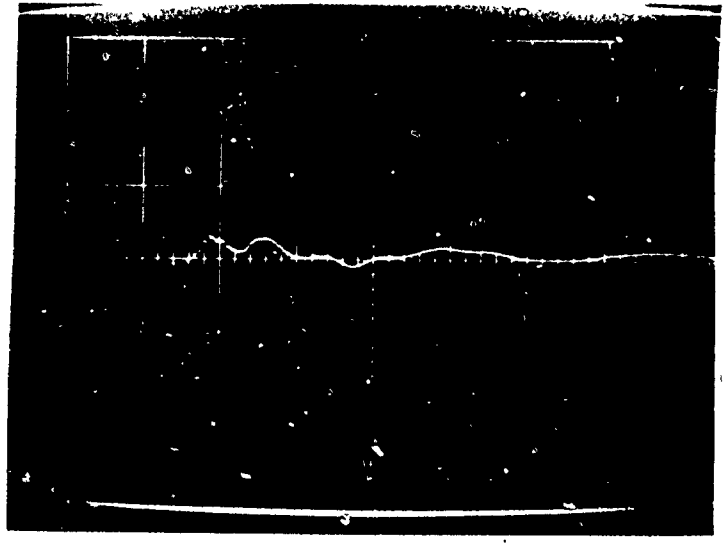

VOLTS/CM 0.2 SWEEP/CM 5 usec

TEST NO. 33 - 16, 17, 18: SYSTEM TEST - START MONITOR

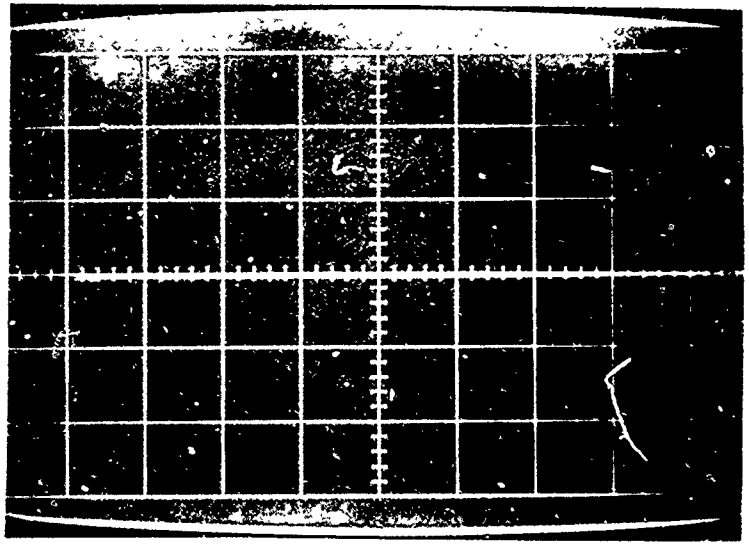

VOLTS/CM 0.2 SWEEP/CM 50 usec

VOLTS/CM _____ SWEEP/CM _____

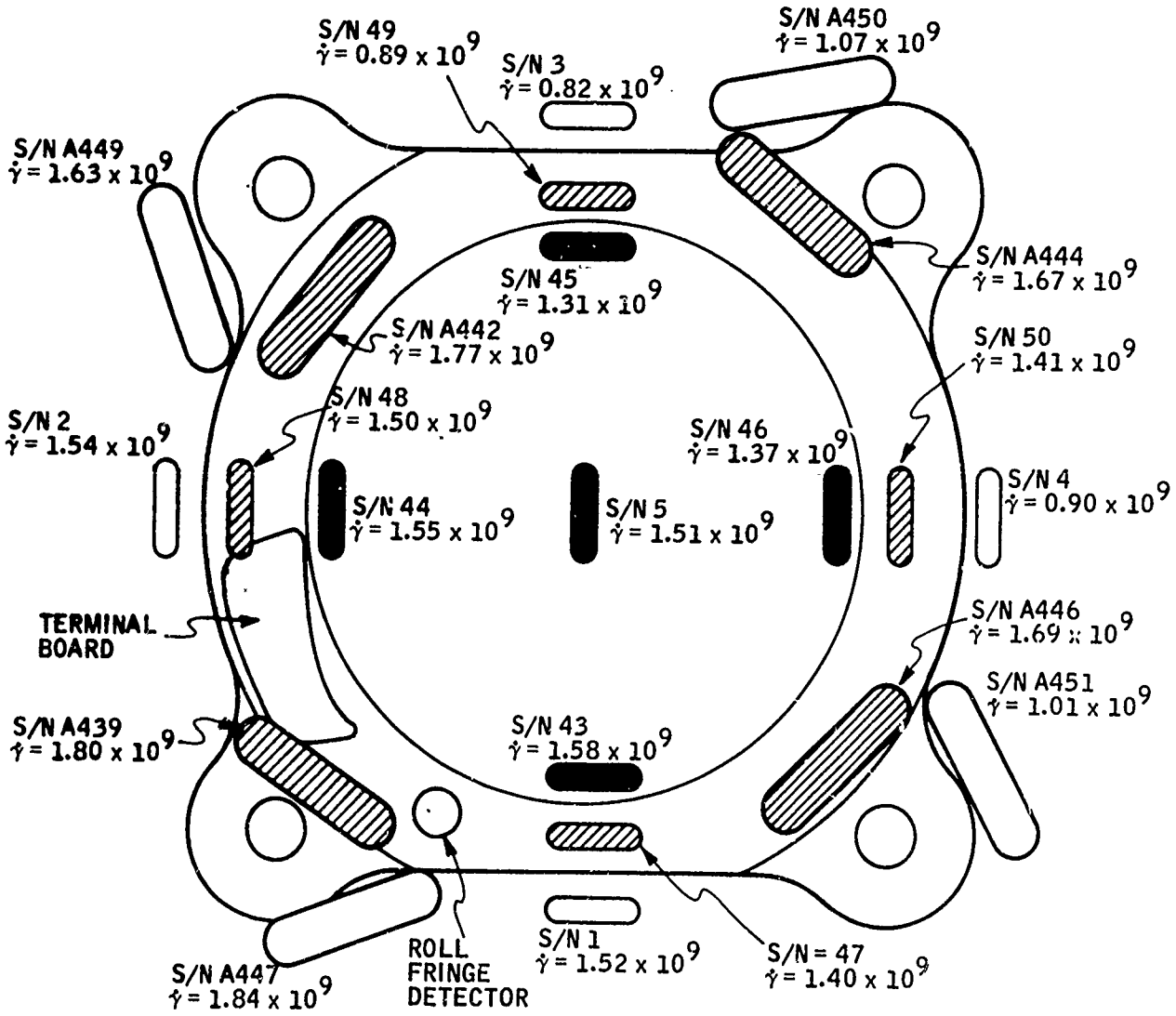

System Test Shot No. 34 Dosimetry Data

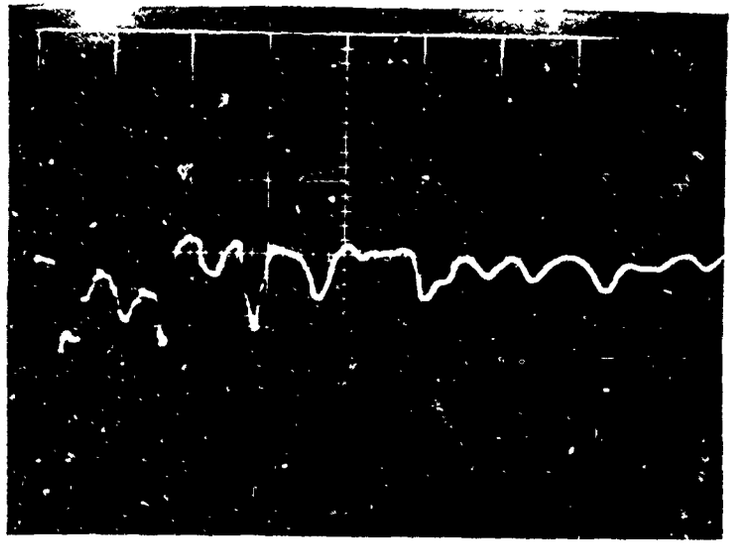

VOLTS/CM 2 SWEEP/CM 0.5 usec

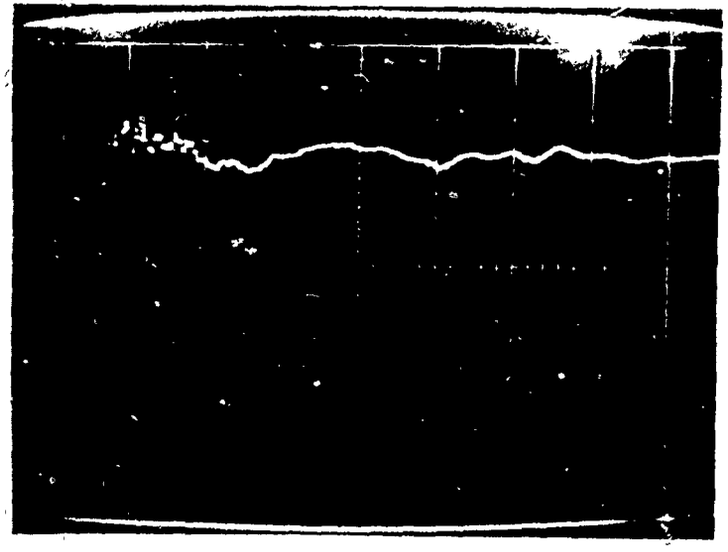

VOLTS/CM 2 SWEEP/CM 5 usec

TEST NO. 34 - 1, 2, 3: SYSTEM TEST - FAST DIGITAL PULSE

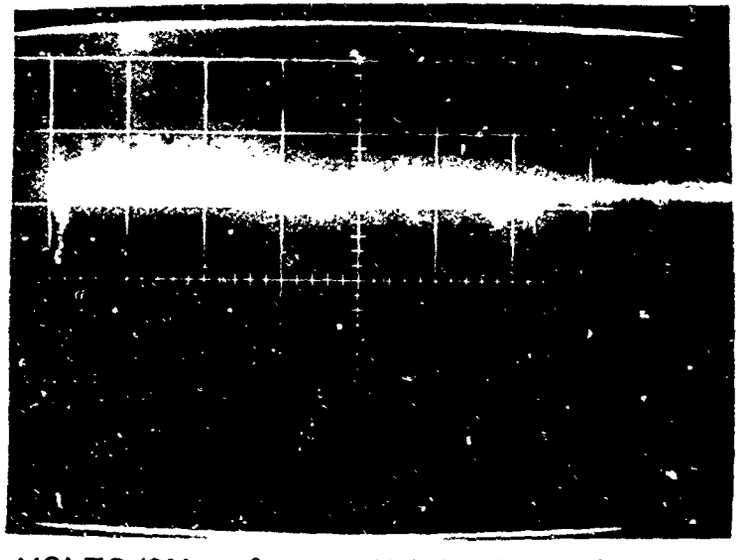

VOLTS/CM 2 SWEEP/CM 50 usec

VOLTS/CM _____ SWEEP/CM _____

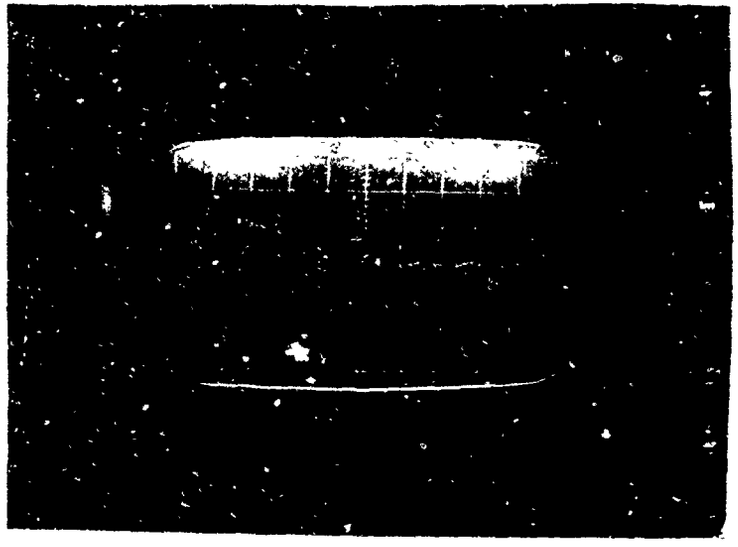

VOLTS/CM 2 SWEEP/CM .5 usec

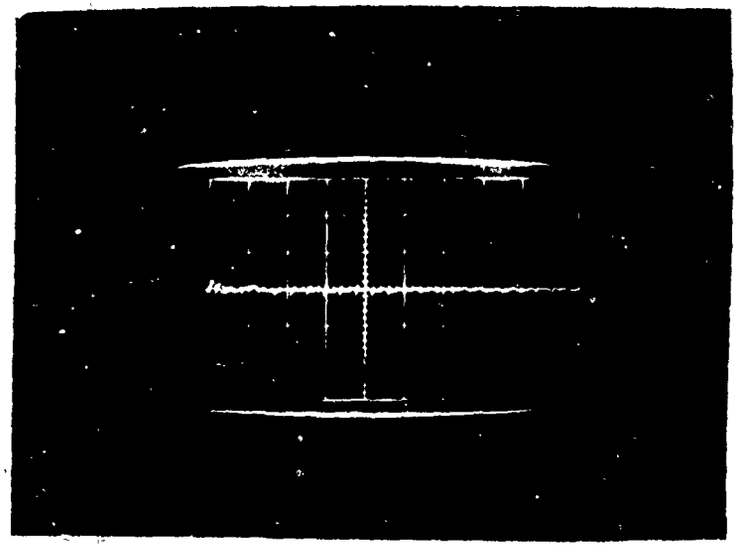

VOLTS/CM 2 SWEEP/CM 5 usec

TEST NO. 34 - 4, 5, 6: SYSTEM TEST - FAST DIGITAL PULSE

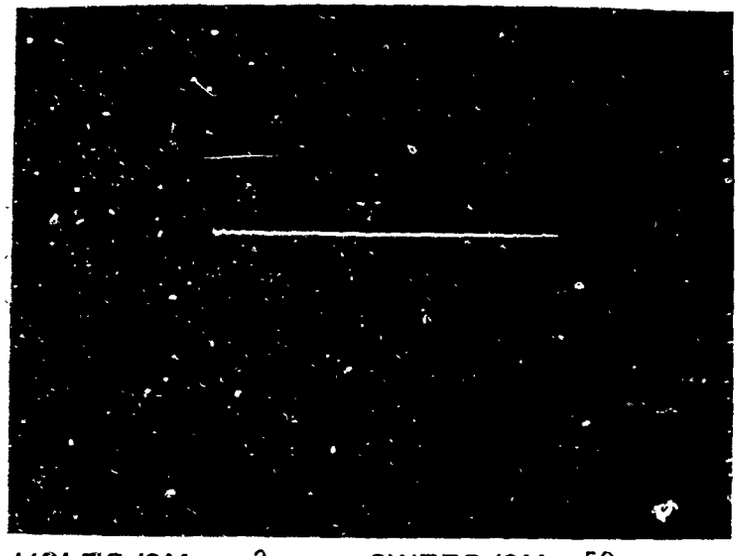

VOLTS/CM 2 SWEEP/CM 50 usec

VOLTS/CM _____ SWEEP/CM _____

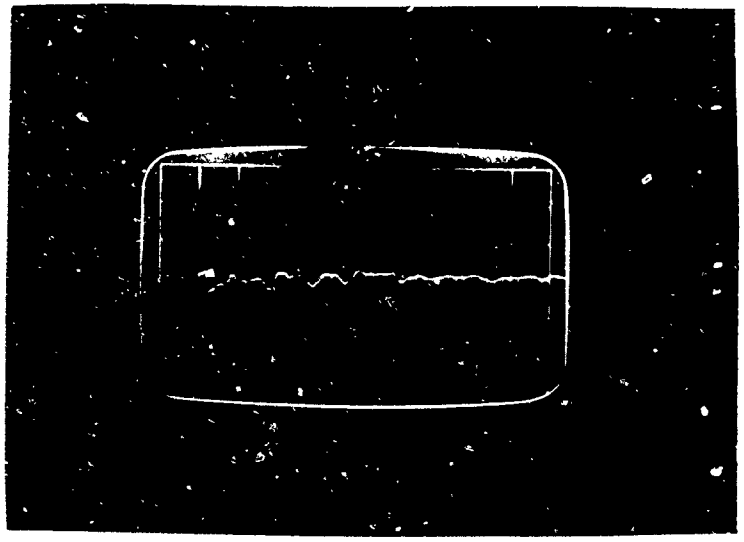

VOLTS/CM 5 SWEEP/CM 0.5 usec

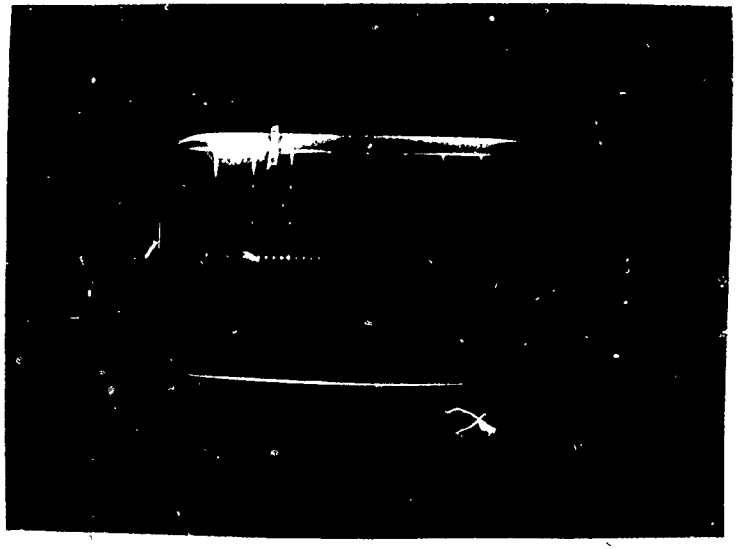

VOLTS/CM 5 SWEEP/CM 5 usec

TEST NO. 34 - 10, 11, 12: SYSTEM TEST - SLOW DIGITAL PULSE

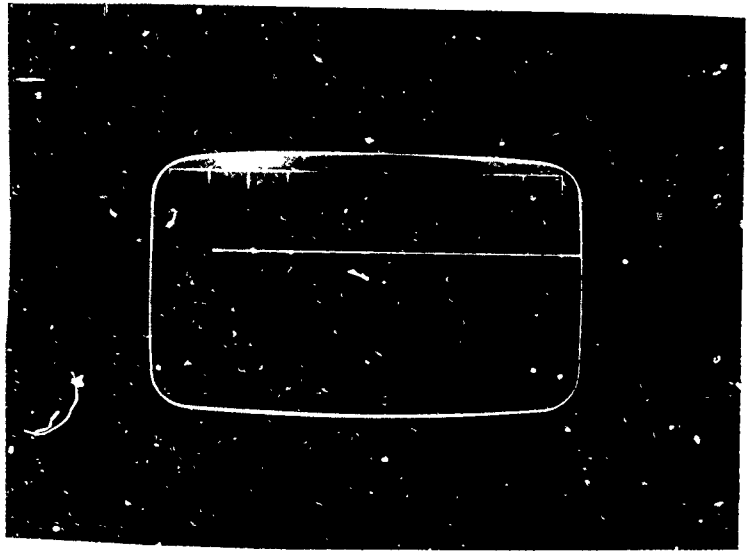

VOLTS/CM 2 SWEEP/CM 5 usec

VOLTS/CM _____ SWEEP/CM _____

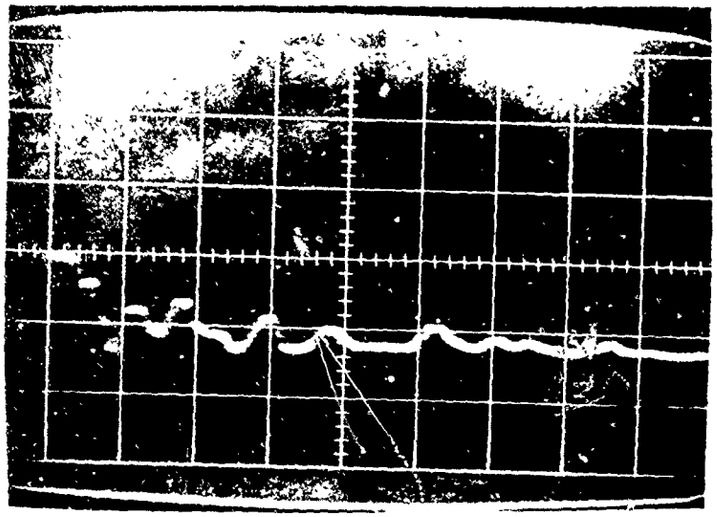

VOLTS/CM 5 SWEEP/CM 0.5 usec

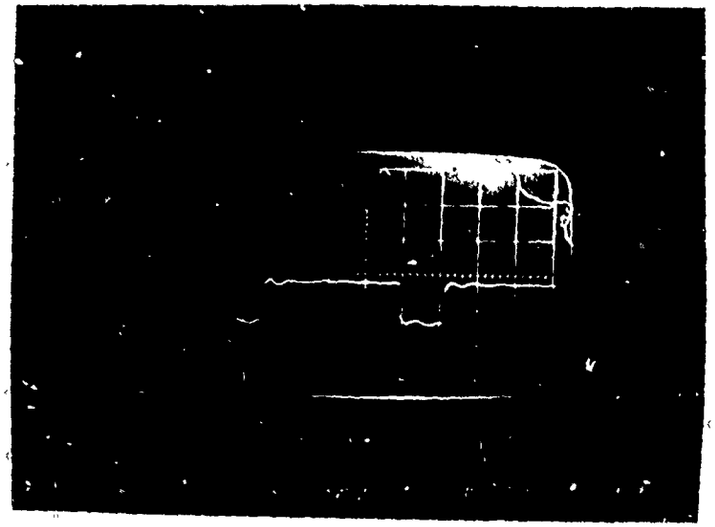

VOLTS/CM 5 SWEEP/CM 5 usec

TEST NO. 34 - 13, 14, 15: SYSTEM TEST - SLOW DIGITAL PULSE

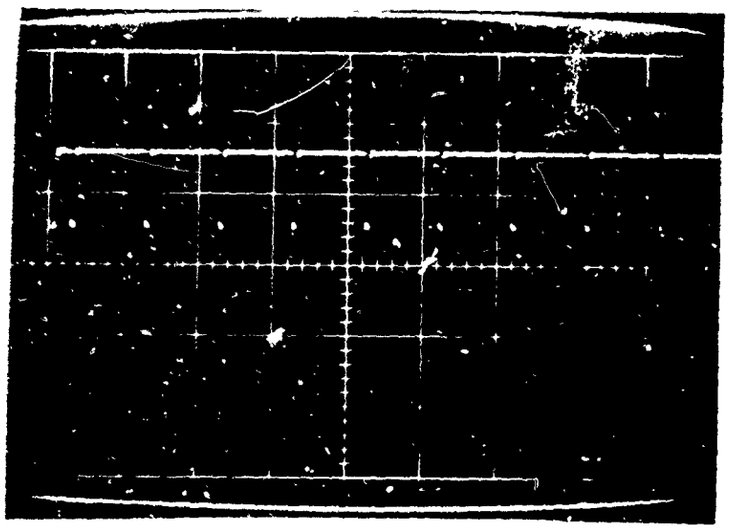

VOLTS/CM 5 SWEEP/CM 100 usec

VOLTS/CM _____ SWEEP/CM _____

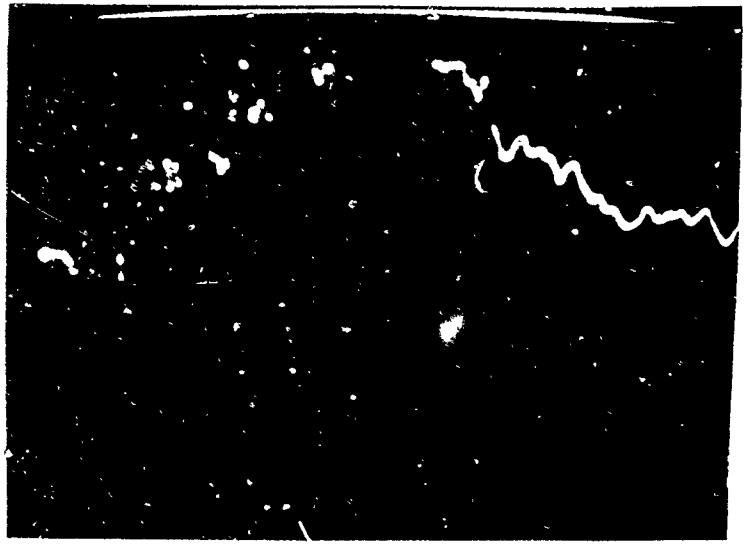

VOLTS/CM 2 SWEEP/CM 0.5 usec

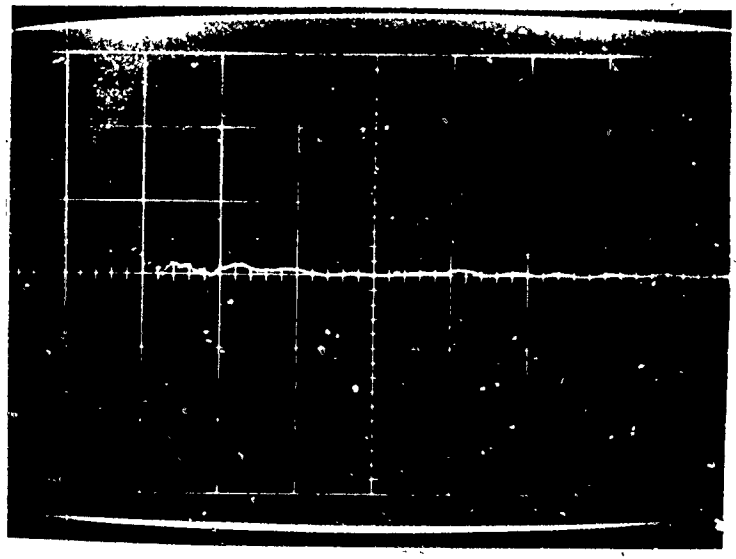

VOLTS/CM .2 SWEEP/CM .5 usec

TEST NO. 34 - 16, 17, 18: SYSTEM TEST - START MONITOR

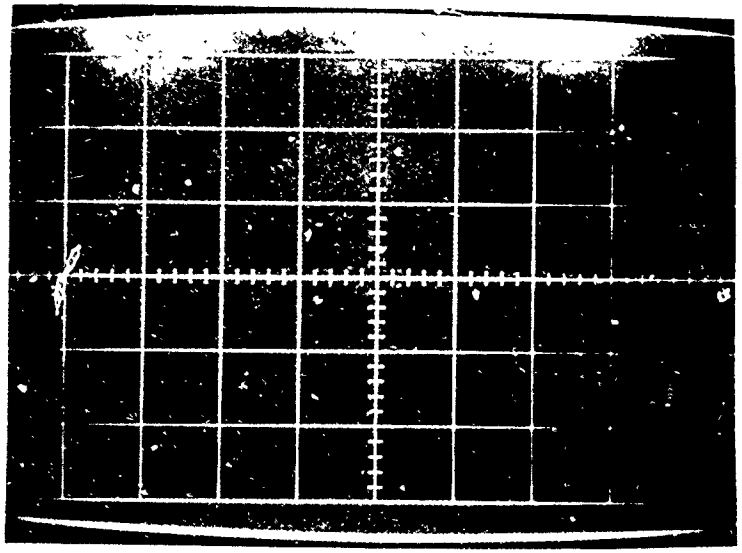

VOLTS/CM .2 SWEEP/CM 50 usec

VOLTS/CM _____ SWEEP/CM _____

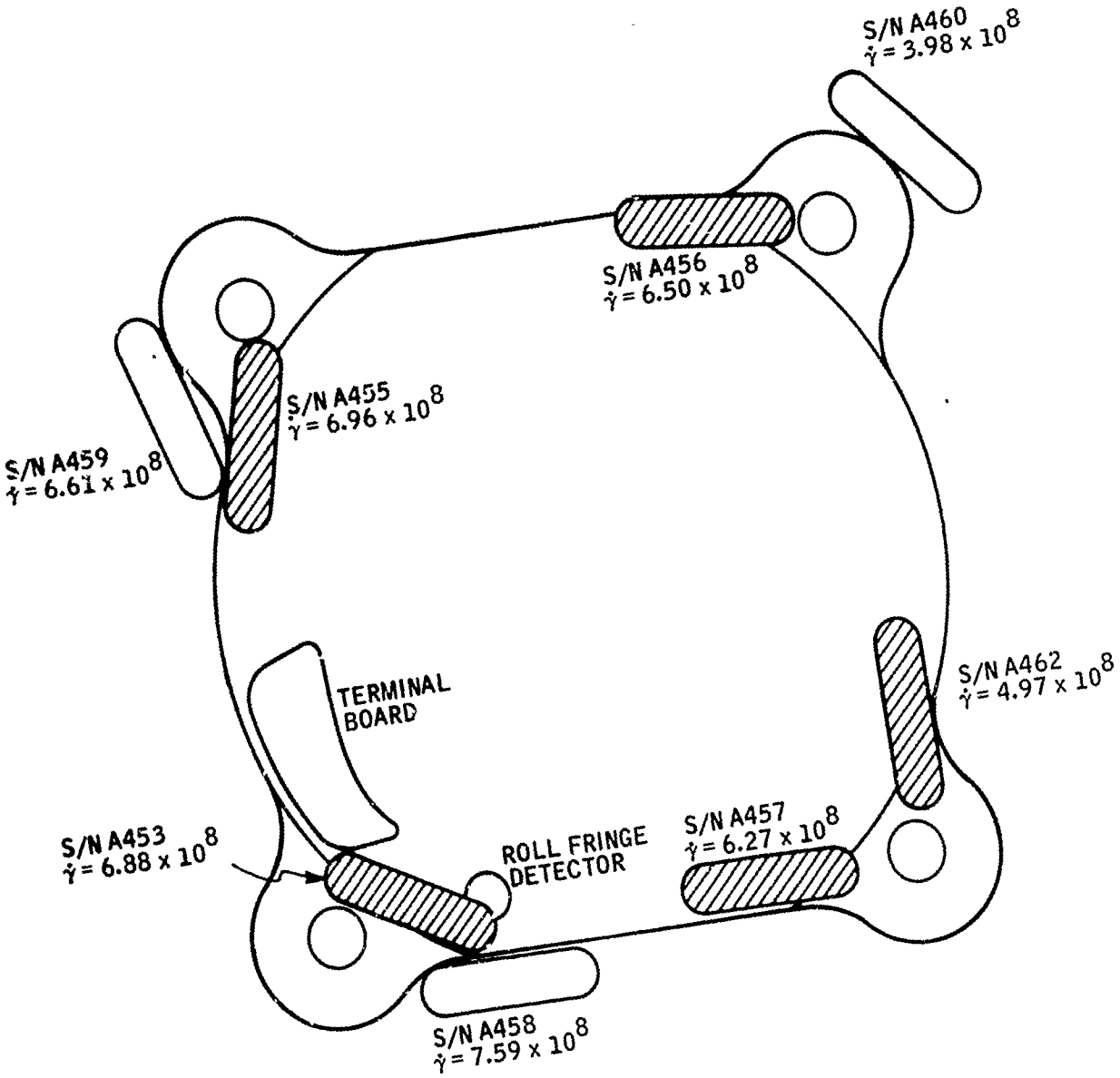

DOSIMETER ON GYRO FLANGE

DOSIMETER ON BASEPLATE

System Test Shot No. 35 Dosimetry Data

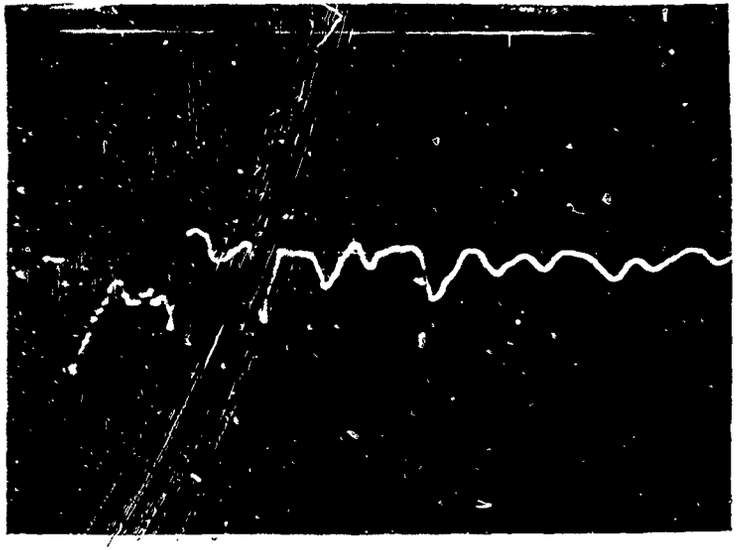

VOLTS/CM 2 SWEEP/CM 0.5 usec

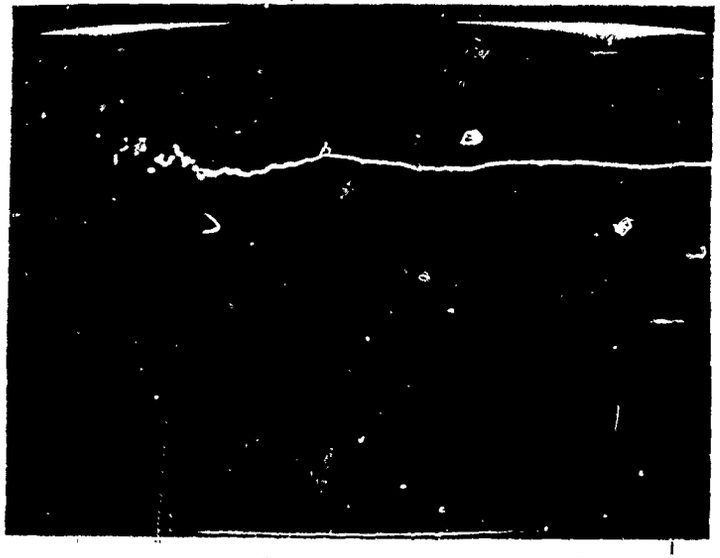

VOLTS/CM 2 SWEEP/CM 5 usec

TEST NO. 35 - 1, 2, 3: SYSTEM TEST - FAST DIGITAL PULSE

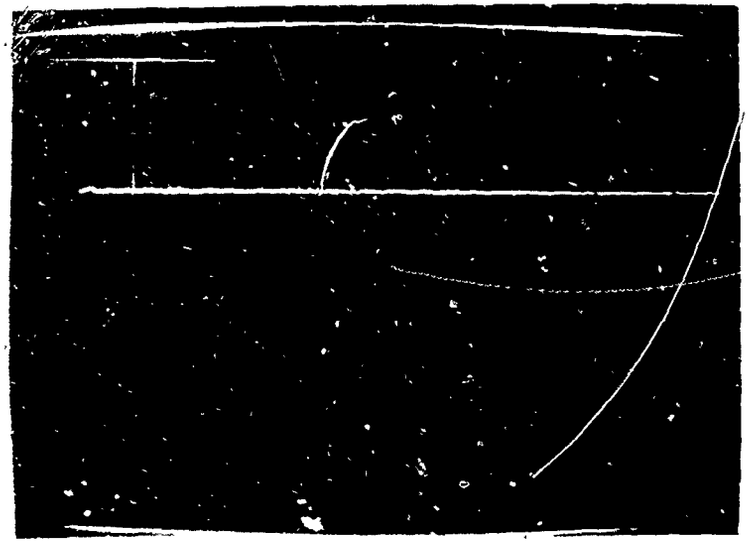

VOLTS/CM 2 SWEEP/CM 50 usec

VOLTS/CM _____ SWEEP/CM _____

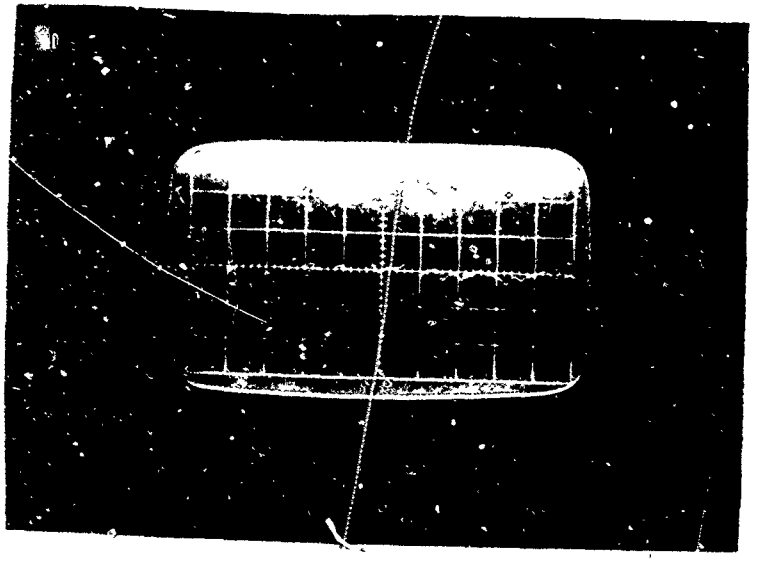

VOLTS/CM 2 SWEEP/CM .5 usec

VOLTS/CM 2 SWEEP/CM 5 usec

TEST NO. 35 - 4, 5, 6: SYSTEM TEST - FAST DIGITAL PULSE

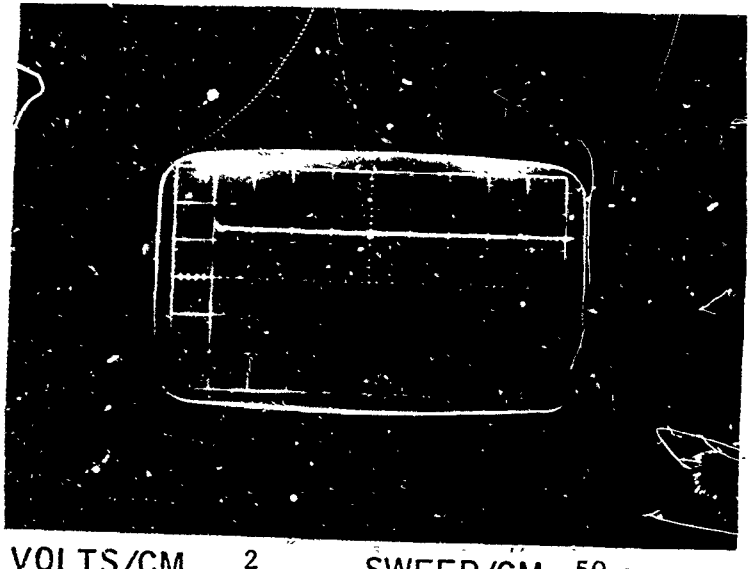

VOLTS/CM 2 SWEEP/CM 50 usec

VOLTS/CM _____ SWEEP/CM _____

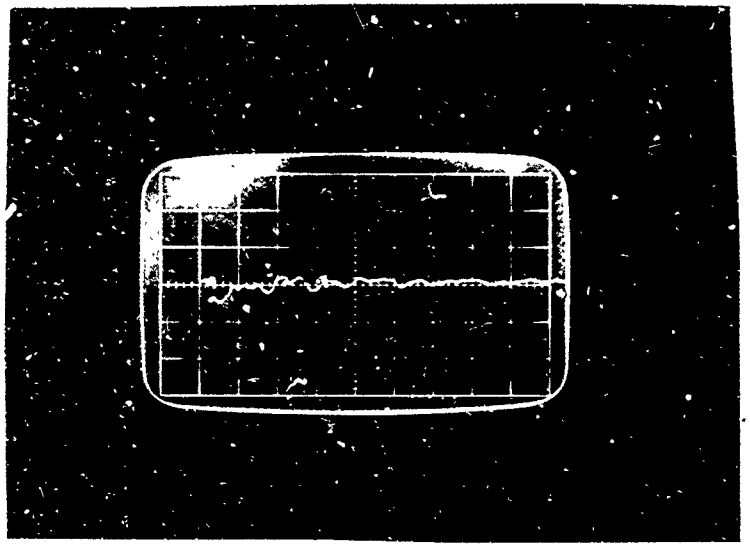

VOLTS/CM 5 SWEEP/CM .5 usec

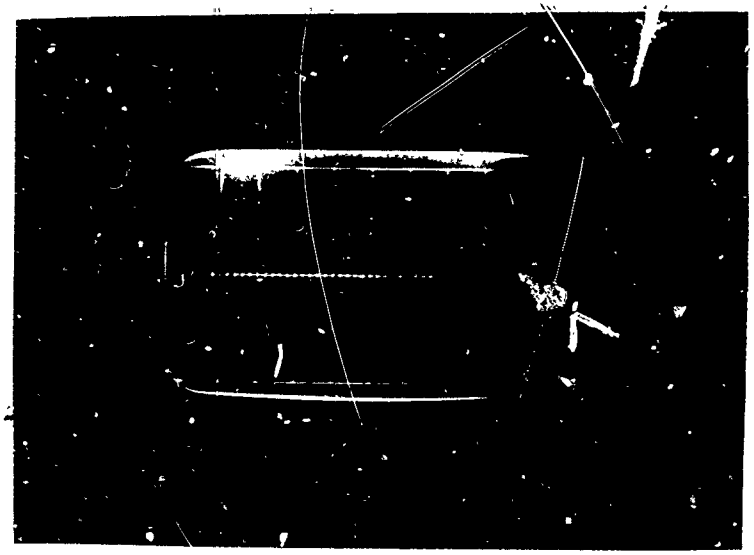

VOLTS/CM 5 SWEEP/CM 5 usec

TEST NO. 35 - 10, 11, 12: SYSTEM TEST - SLOW DIGITAL PULSE

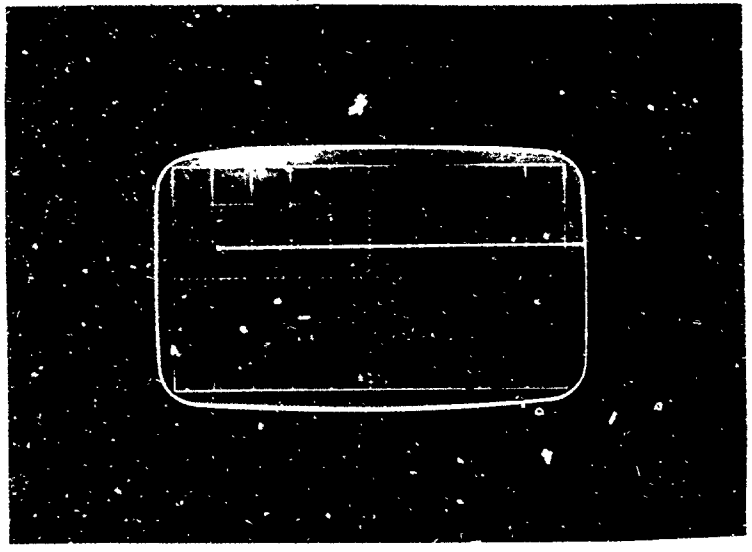

VOLTS/CM 2 SWEEP/CM 100 usec

VOLTS/CM _____ SWEEP/CM _____

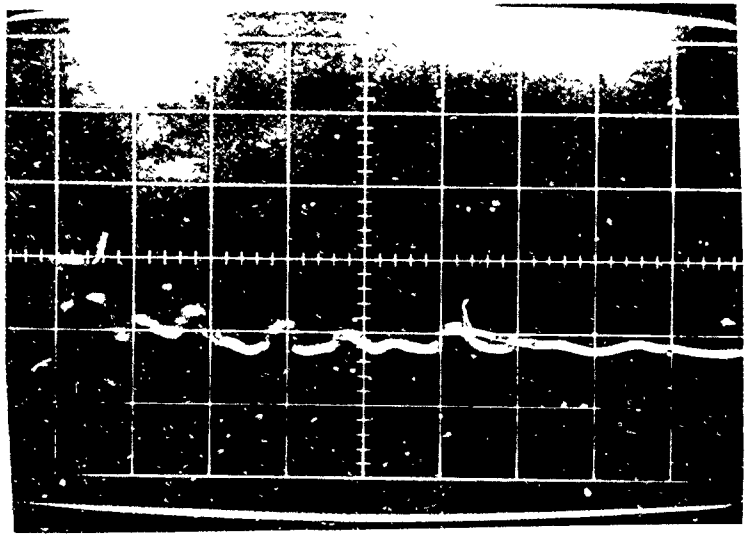

VOLTS/CM 5 SWEEP/CM .5 usec

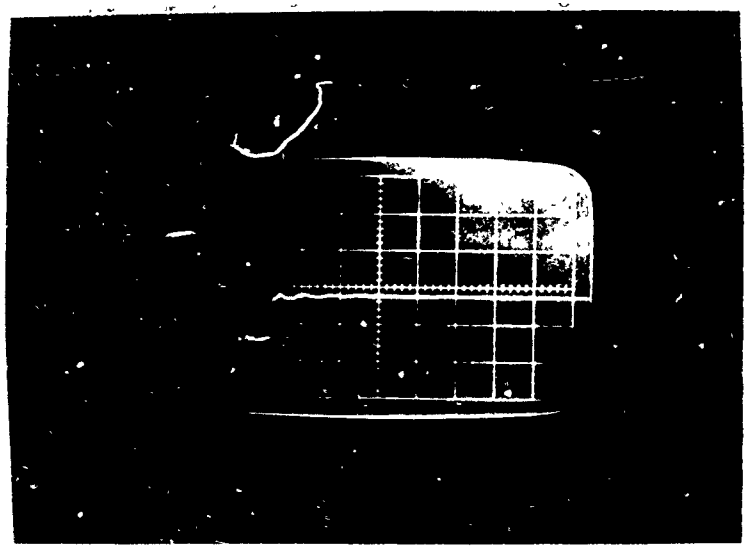

VOLTS/CM 5 SWEEP/CM 5 usec

TEST NO. 35 - 13, 14, 15: SYSTEM TEST - SLOW DIGITAL PULSE

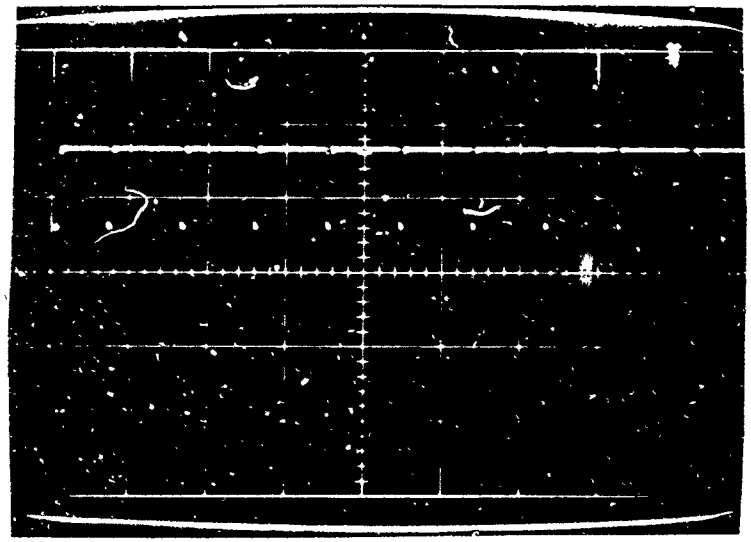

VOLTS/CM 5 SWEEP/CM .1 msec

VOLTS/CM _____ SWEEP/CM _____

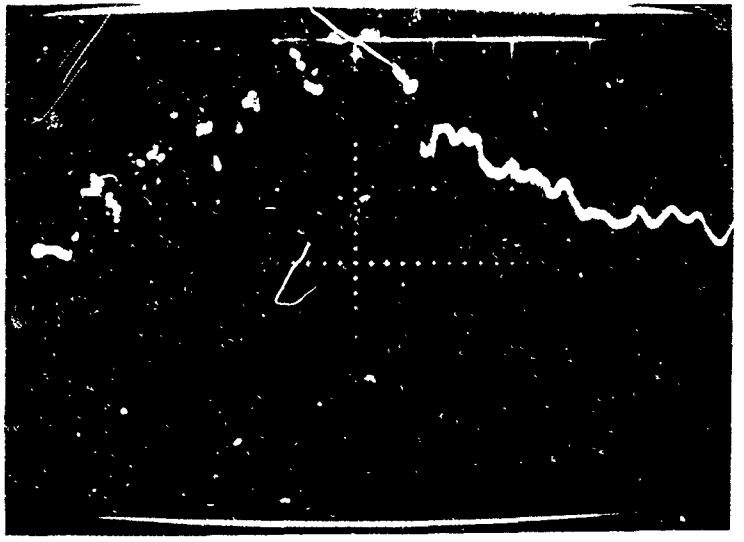

VOLTS/CM .2 SWEEP/CM .5 usec

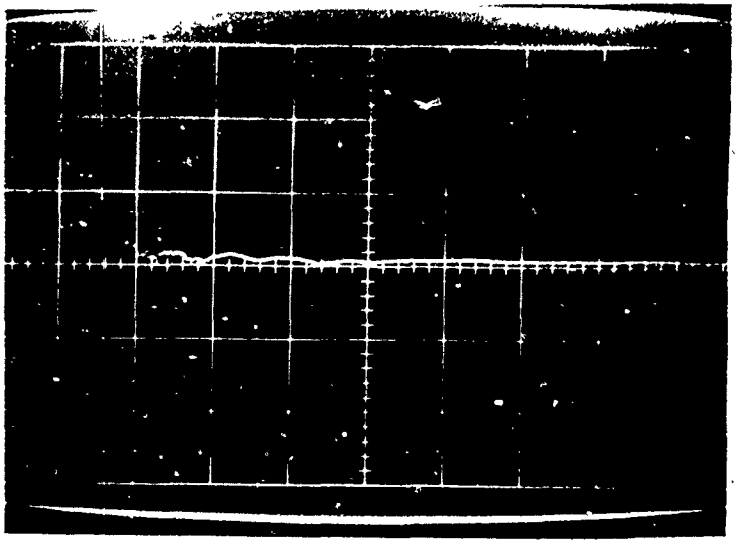

VOLTS/CM .2 SWEEP/CM 5 usec

TEST NO. 35 - 16, 17, 18: SYSTEM TEST - START MONITOR

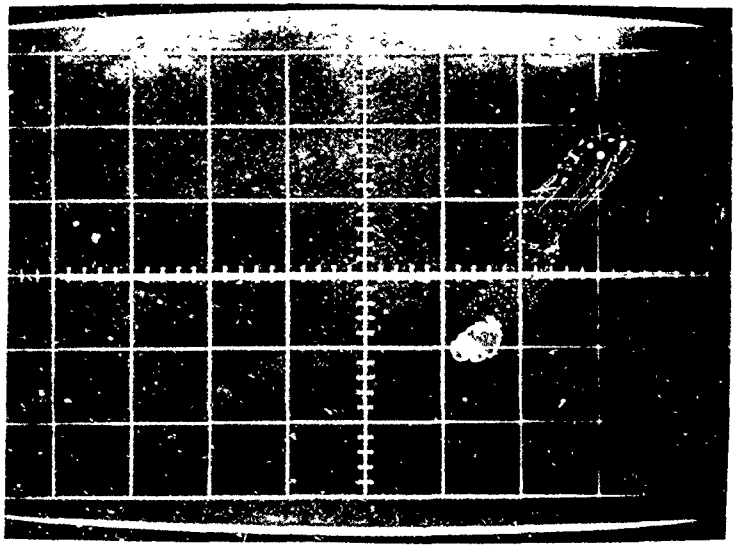

VOLTS/CM .2 SWEEP/CM 50 usec

VOLTS/CM _____ SWEEP/CM _____

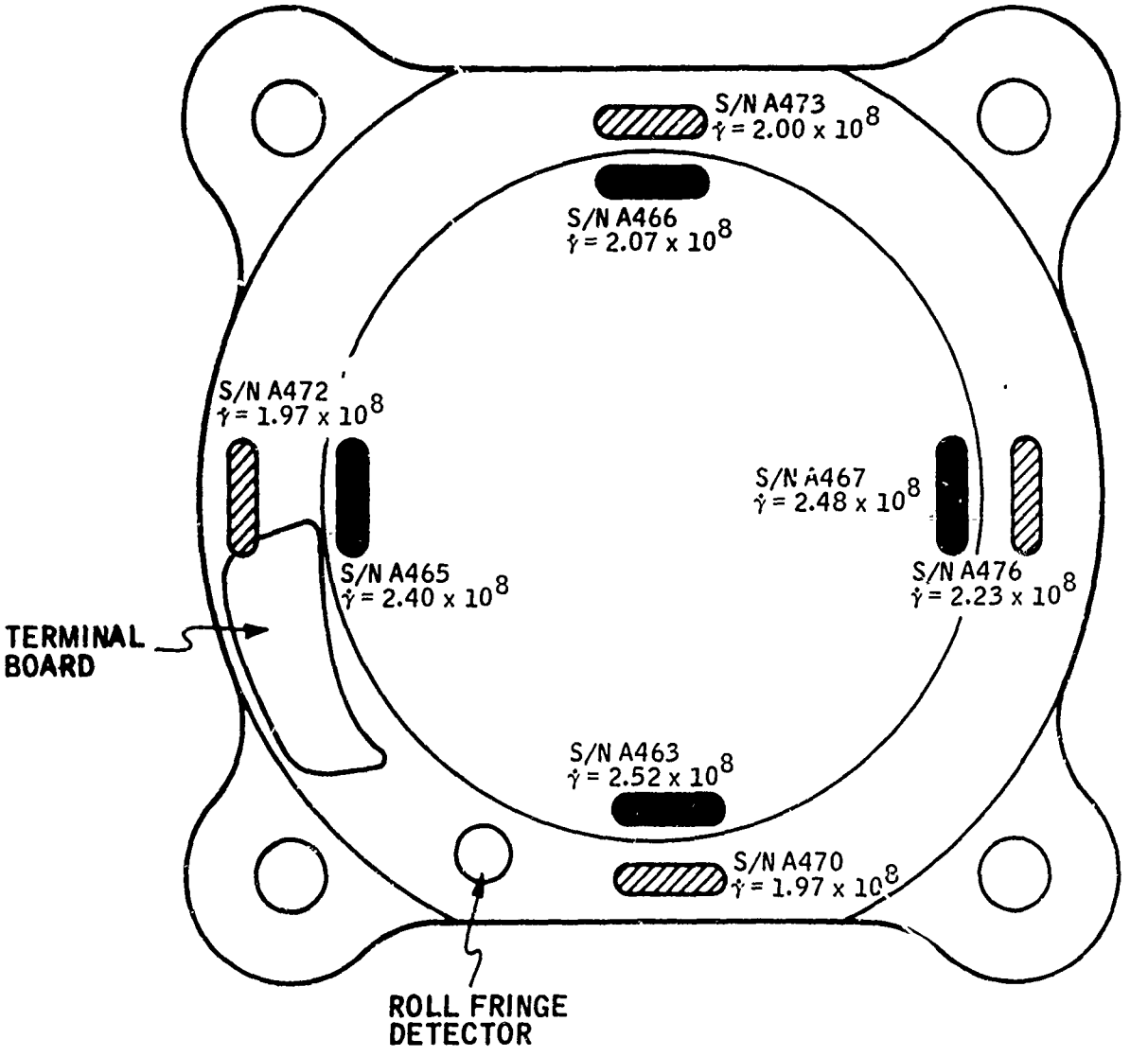

DOSIMETER LOCATED AT FRONT SURFACE ON DIGITAL BOARD

DOSIMETER LOCATED AT GYRO FLANGE (2 3/8 IN. BACK)

System Test Shot No. 36 Dosimetry Data

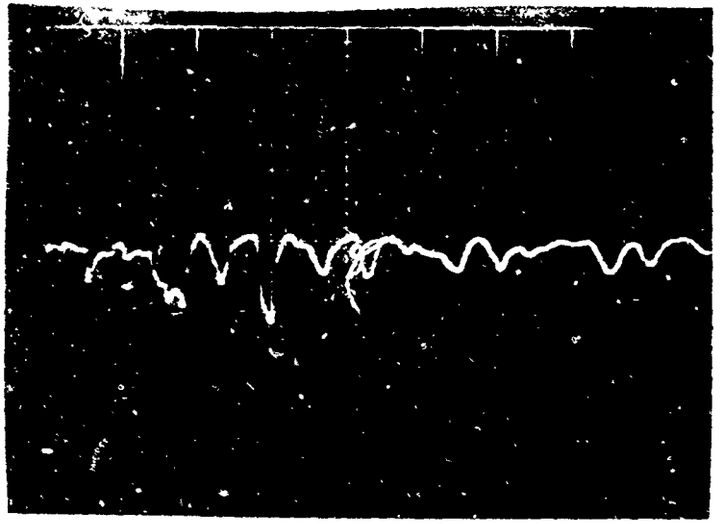

VOLTS/CM 2 SWEEP/CM 0.5 usec

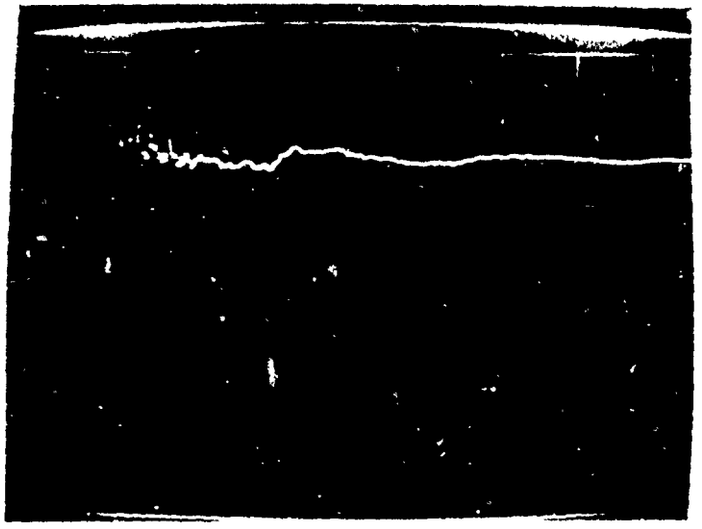

VOLTS/CM 2 SWEEP/CM 5 usec

TEST NO. 36 - 1, 2, 3: SYSTEM TEST - FAST DIGITAL PULSE

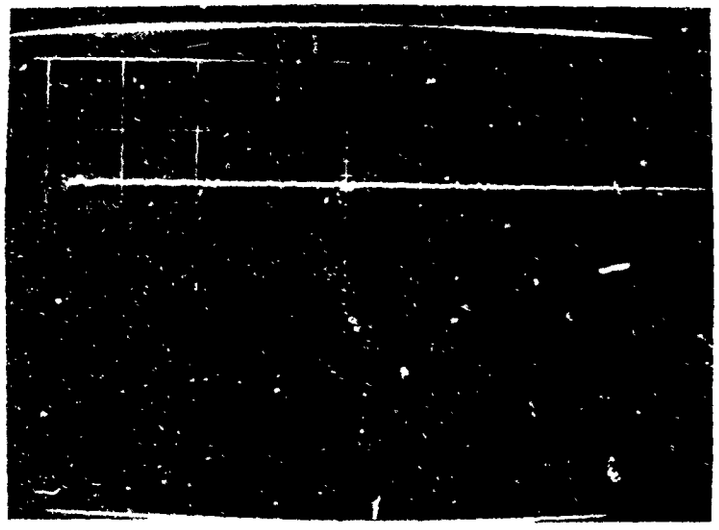

VOLTS/CM 2 SWEEP/CM 50 usec

VOLTS/CM _____ SWEEP/CM _____

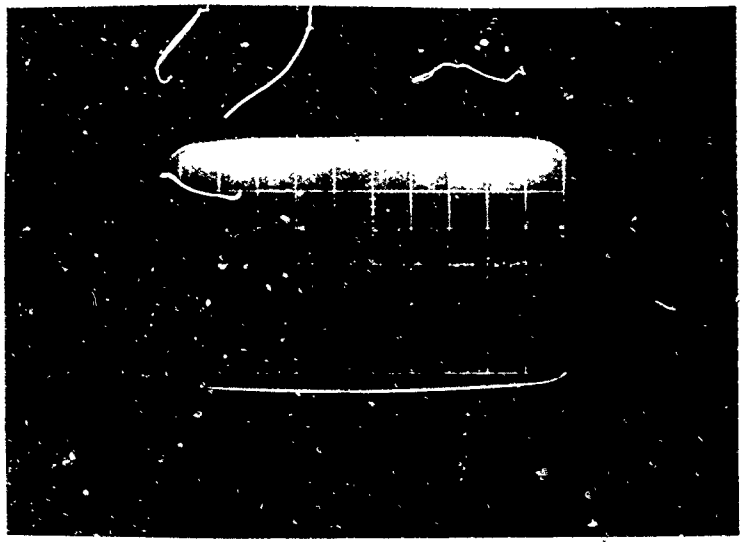

VOLTS/CM 2 SWEEP/CM .5 usec

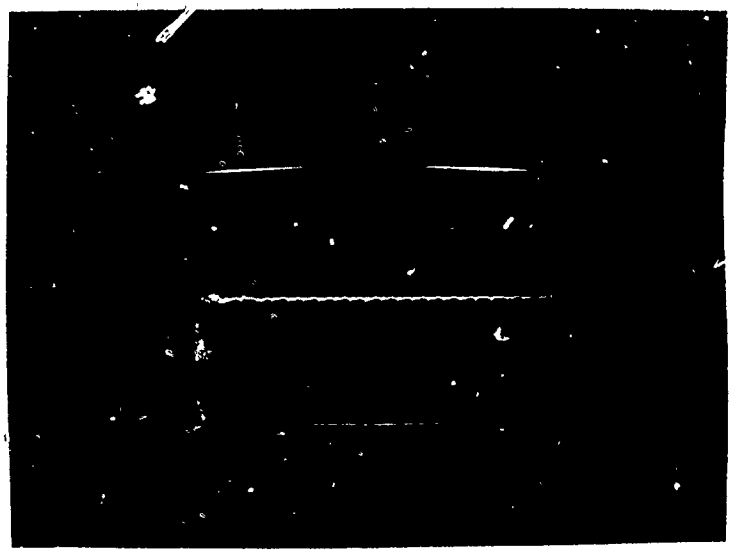

VOLTS/CM 2 SWEEP/CM 5 usec

TEST NO. 36 - 4, 5, 6: SYSTEM TEST - FAST DIGITAL PULSE

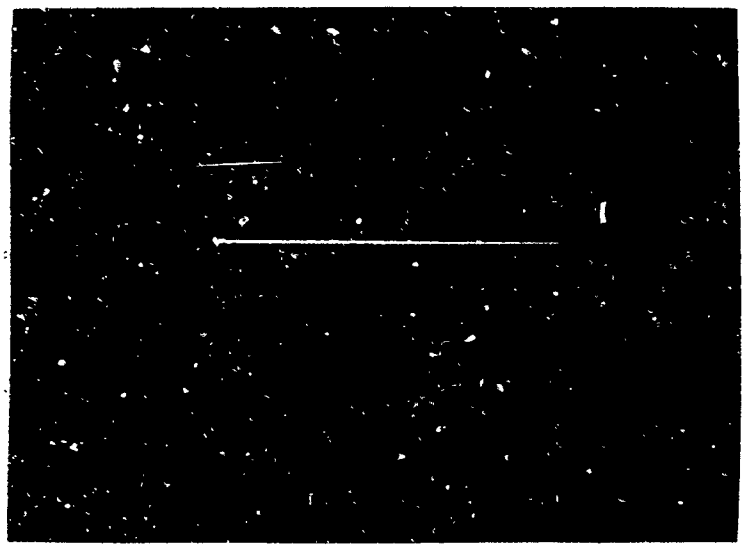

VOLTS/CM 2 SWEEP/CM 50 usec

VOLTS/CM _____ SWEEP/CM _____

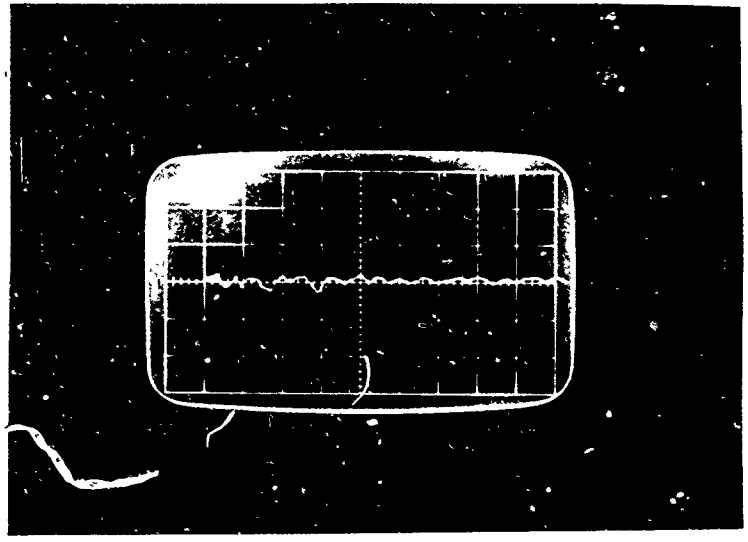

VOLTS/CM 5 SWEEP/CM 0.5 usec

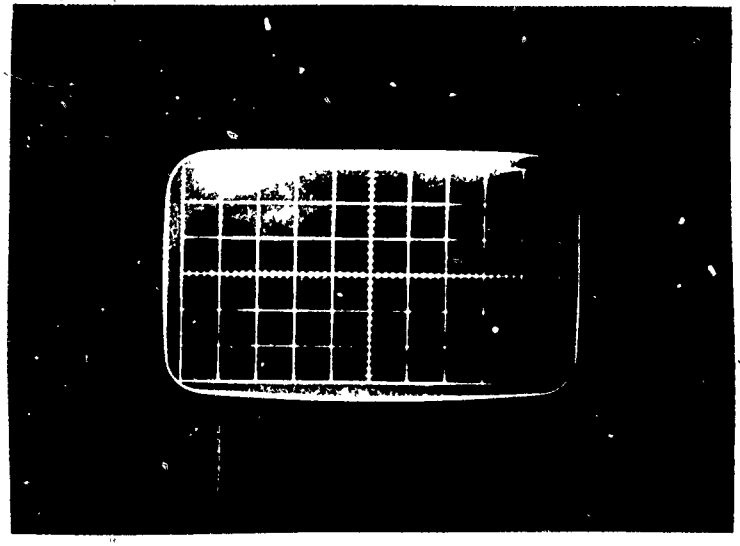

VOLTS/CM 5 SWEEP/CM 5 usec

TEST NO. 36 - 10, 11, 12: SYSTEM TEST - SLOW LIGITAL PULSE

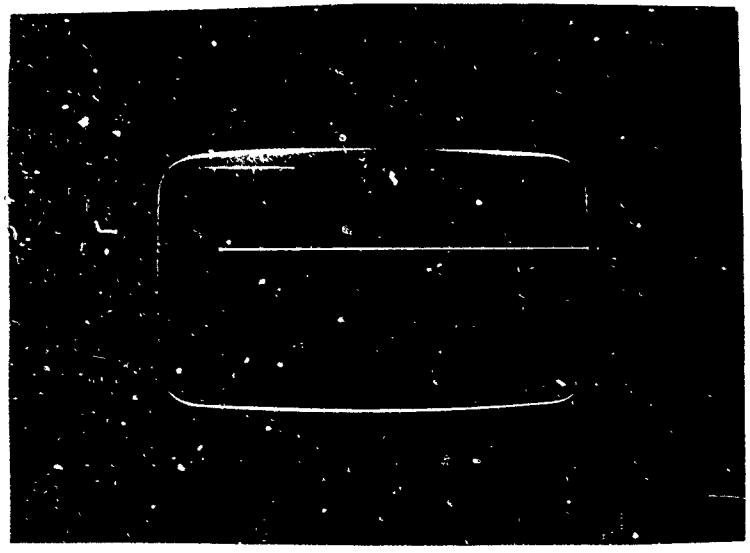

VOLTS/CM 2 SWEEP/CM 100 usec

VOLTS/CM _____ SWEEP/CM _____

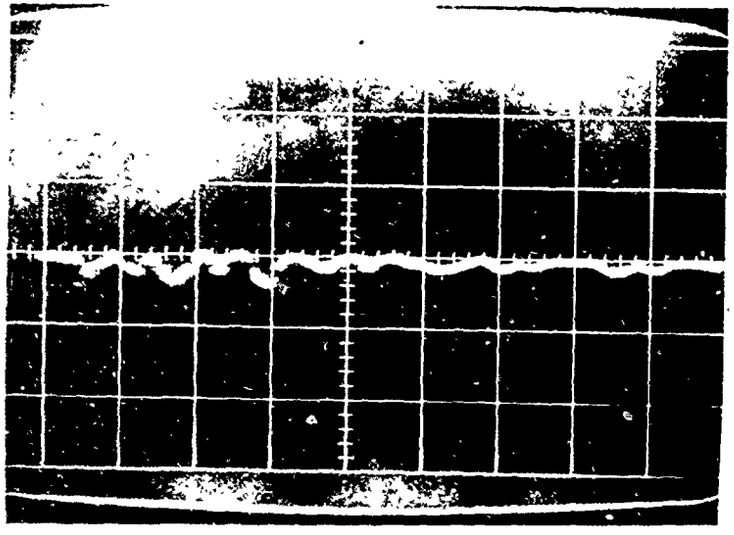

VOLTS/CM 5 SWEEP/CM 0.5 usec

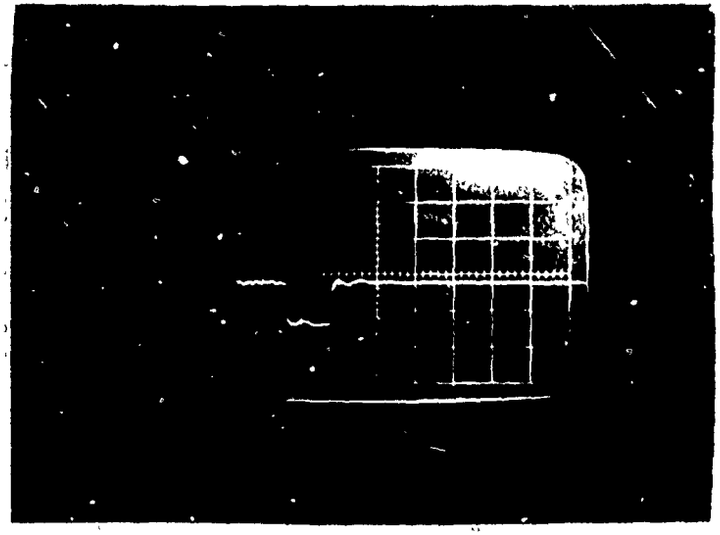

VOLTS/CM 5 SWEEP/CM 5 usec

TEST NO. 36 - 13, 14, 15: SYSTEM TEST - SLOW DIGITAL PULSE

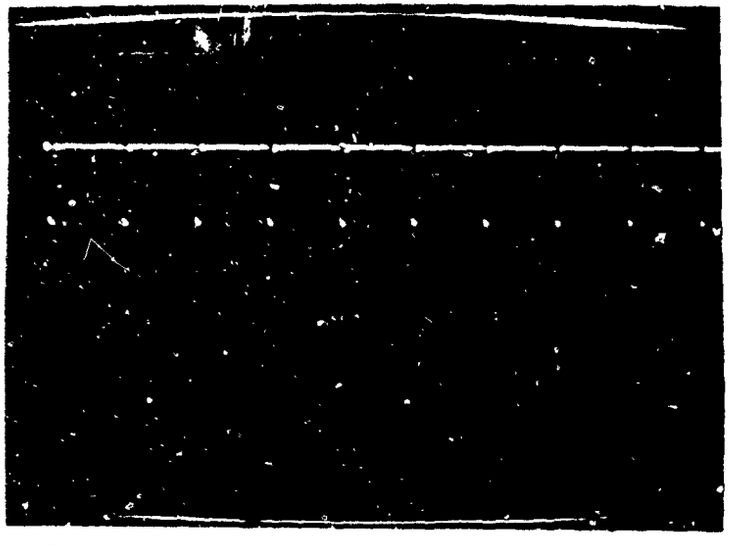

VOLTS/CM 5 SWEEP/CM 100 usec

VOLTS/CM _____ SWEEP/CM _____

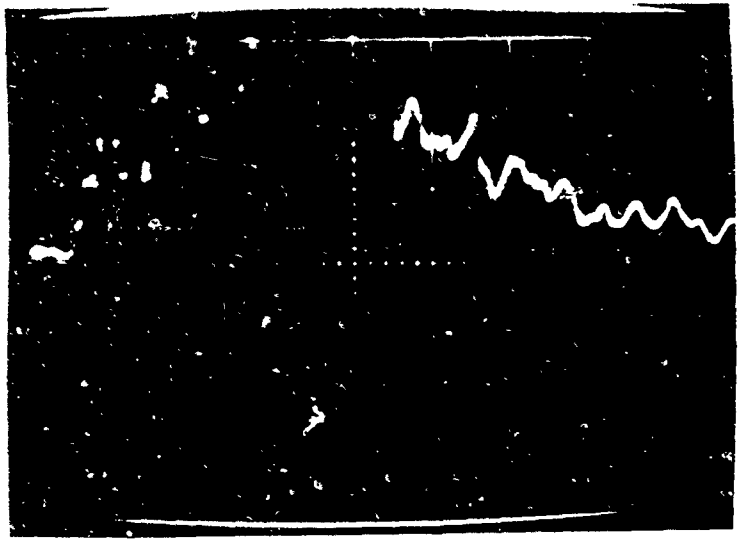

VOLTS/CM 0.2 SWEEP/CM 0.5 usec

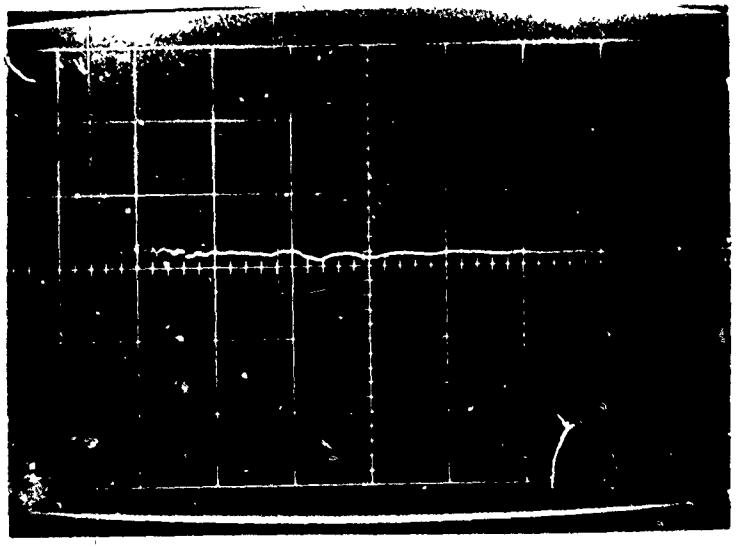

VOLTS/CM .2 SWEEP/CM 5 usec

TEST NO. 36 - 16, 17, 18: SYSTEM TEST - START MONITOR

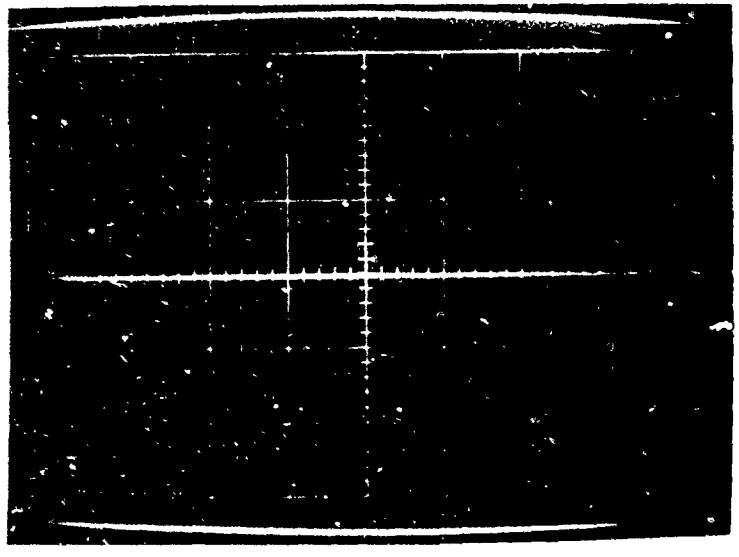

VOLTS/CM .2 SWEEP/CM 50 usec

VOLTS/CM _____ SWEEP/CM _____

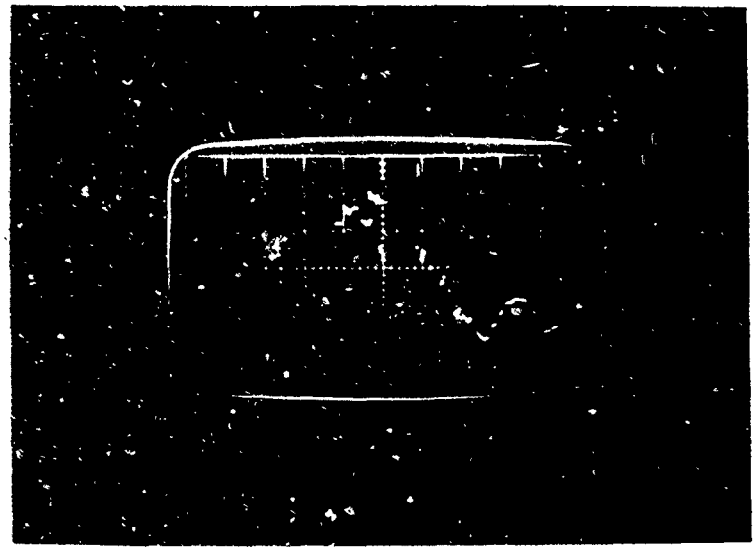

VOLTS/CM 1V SWEEP/CM .5 usec

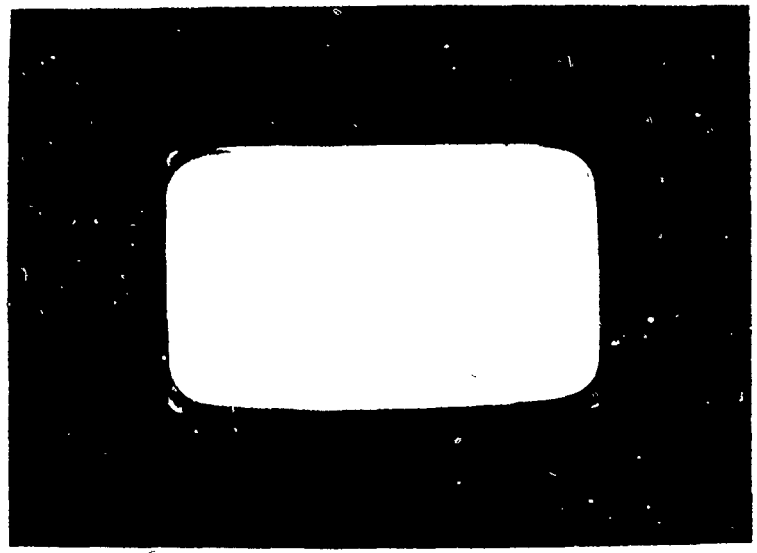

VOLTS/CM 1 SWEEP/CM 5 usec

TEST NO. 31 - 37, 38: SHIELD CURRENT MONITOR

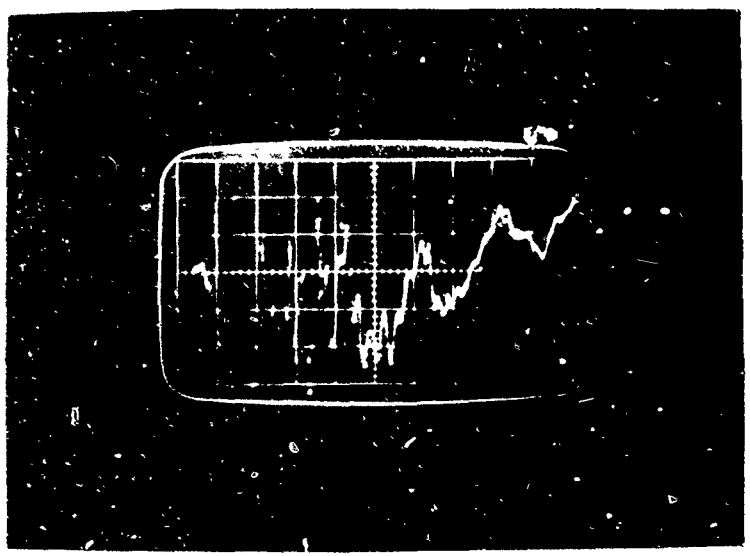

VOLTS/CM 2 SWEEP/CM .5 usec

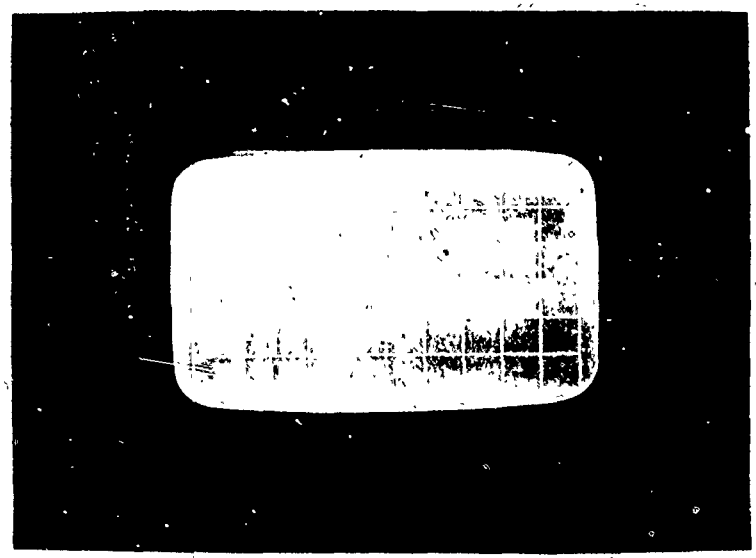

VOLTS/CM 2 SWEEP/CM 5 usec

TEST NO. 33 - 37, 38: SHIELD CURRENT MONITOR

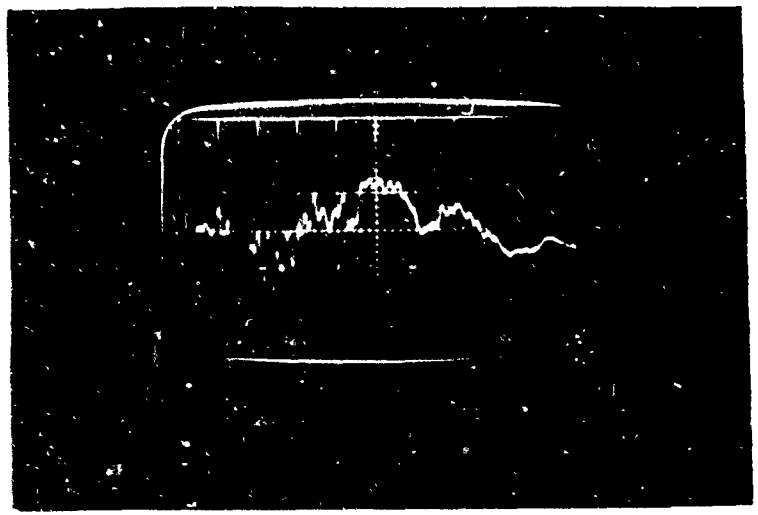

VOLTS/CM 2 SWEEP/CM .5 usec

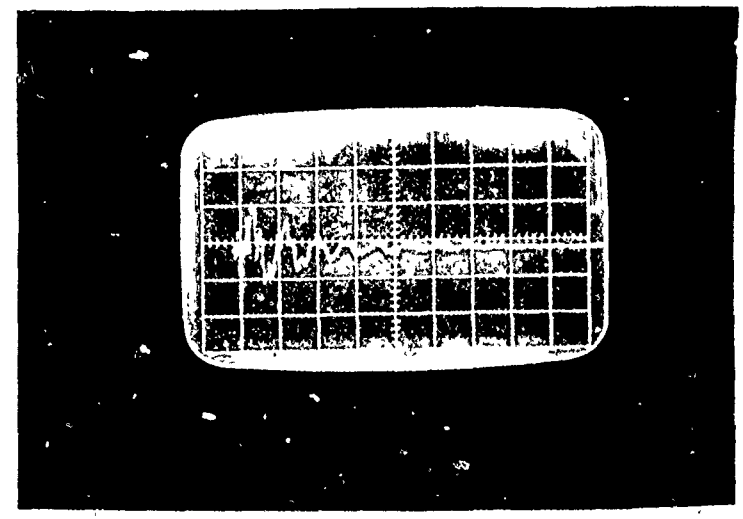

VOLTS/CM 2 SWEEP/CM 5 usec

TEST NO. 34 - 37, 38: SHIELD CURRENT MONITOR

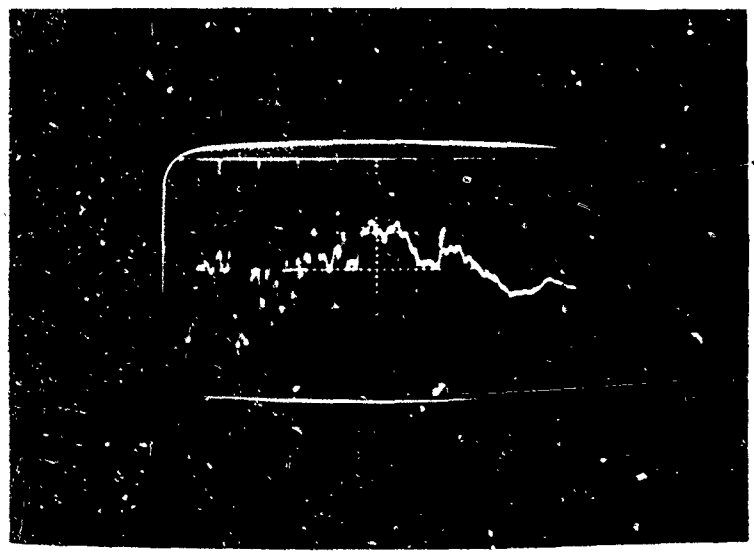

VOLTS/CM 2 SWEEP/CM .5 usec

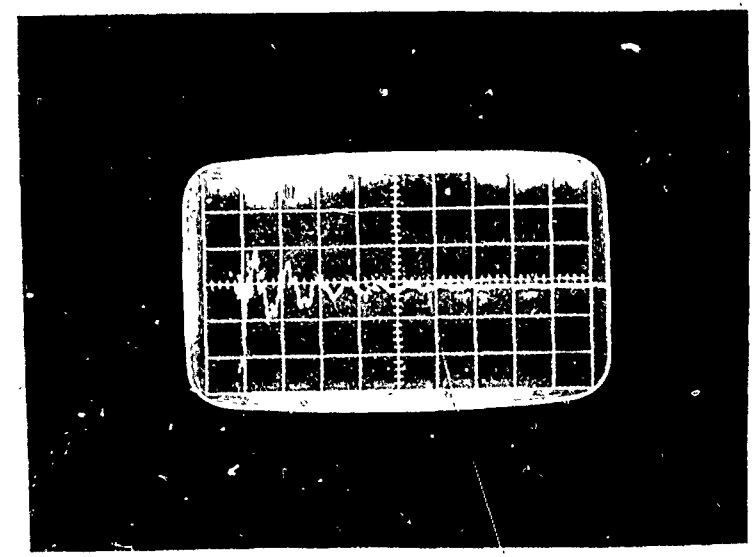

VOLTS/CM 2 SWEEP/CM 5 usec

TEST NO. 35 - 37, 38: SHIELD CURRENT MONITOR

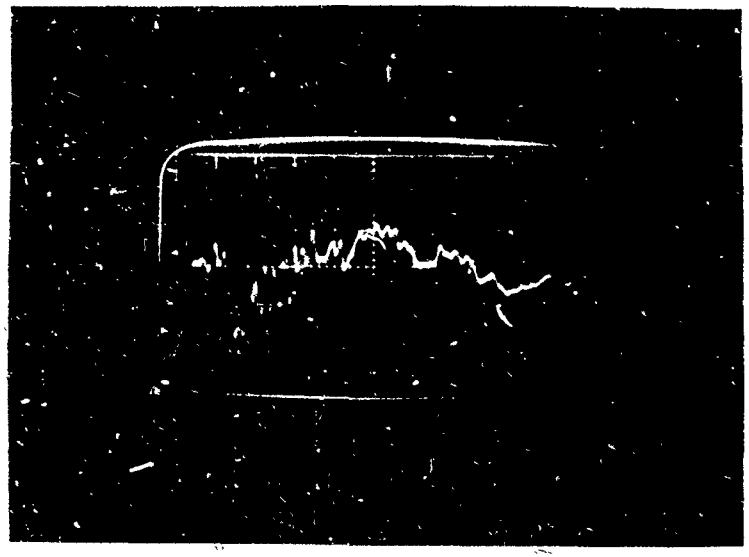

VOLTS/CM 2 SWEEP/CM .5 usec

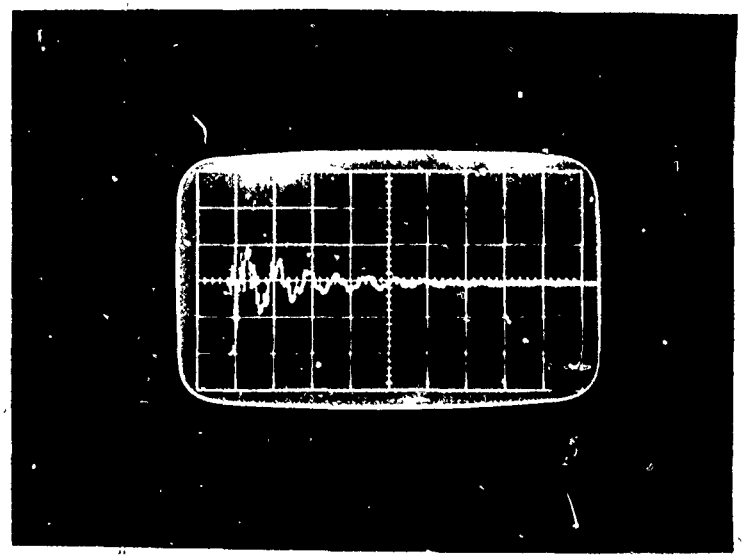

VOLTS/CM 2 SWEEP/CM 5 usec

TEST NO. 36 - 37, 38: SHIELD CURRENT MONITOR

VOLTS/CM _____ SWEEP/CM _____

VOLTS/CM _____ SWEEP/CM _____

APPENDIX C
HARDENED LASER ANGULAR RATE SENSOR

21695-PR10

15 November 1971

Monthly Progress Report

HARDENED LASER ANGULAR RATE SENSOR

Prepared for:

U.S. Army Advanced Ballistic Missile Defense Agency
Huntsville, Alabama

Contract No. DAHC60-71-C-0041

Prepared by:

R.R. Johnson
Sr. Development Engineer

Approved by:

M.F. Demos
Project Engineer

T.A. Thompson
Contract Administrator

Honeywell Inc.
Government and Aeronautical Products Division
2600 Ridgway Parkway N.E.
Minneapolis, Minnesota 55413

CONTENTS

		Page
SECTION I	INTRODUCTION AND SUMMARY	1
	Introduction	1
	Summary	1
SECTION II	PROGRAM ACTIVITIES	3
	Fast-Burst Reactor (FBR) Test	3
	Testing	6
	FBR Post-Test Analysis	6
	Summary	6
	5-Volt Input Regulator	8
	HV D-C/D-C Converter	11
	Laser Start/Restart Circuit	13
	Fringe Pattern Detector	15
	Prototype Design	16
SECTION III	FUTURE PLANS	17
APPENDIX A	FAST-BURST REACTOR TEST DATA, WHITE SANDS MISSILE RANGE 8/16/71 TO 8/20/71	

SECTION I
INTRODUCTION AND SUMMARY

INTRODUCTION

This is the tenth progress report submitted to the U.S. Army Advanced Ballistic Missile Defense Agency, under Contract No. DAHC60-71-C-0041 for the development, fabrication, radiation laboratory proof testing, and delivery of a radiation-hardened laser angular rate sensor (LARS). The hardened LARS will feature a three-axis ring laser, with power supplies, laser starting and control electronics, readout detectors and amplifiers, and digital signal processing electronics.

Emphasis of the program is to demonstrate the feasibility of hardening the electronics essential to the implementation of the ring laser gyro as a sensor subsystem. With the UPSTAGE LTRG design as a base, the primary circuits will be redesigned and hardened electronic components used in an effort to achieve the desired hardness for the LARS. The program entails the design, fabrication, and laboratory radiation proof testing of breadboard and prototype electronics, together with a ring laser, as shown in the program milestone schedule (Figure 1).

SUMMARY

During October the emphasis was on the prototype layouts and the post-FBR testing. The fourth oral program review was conducted in Washington, D.C. on 7 October 1971.

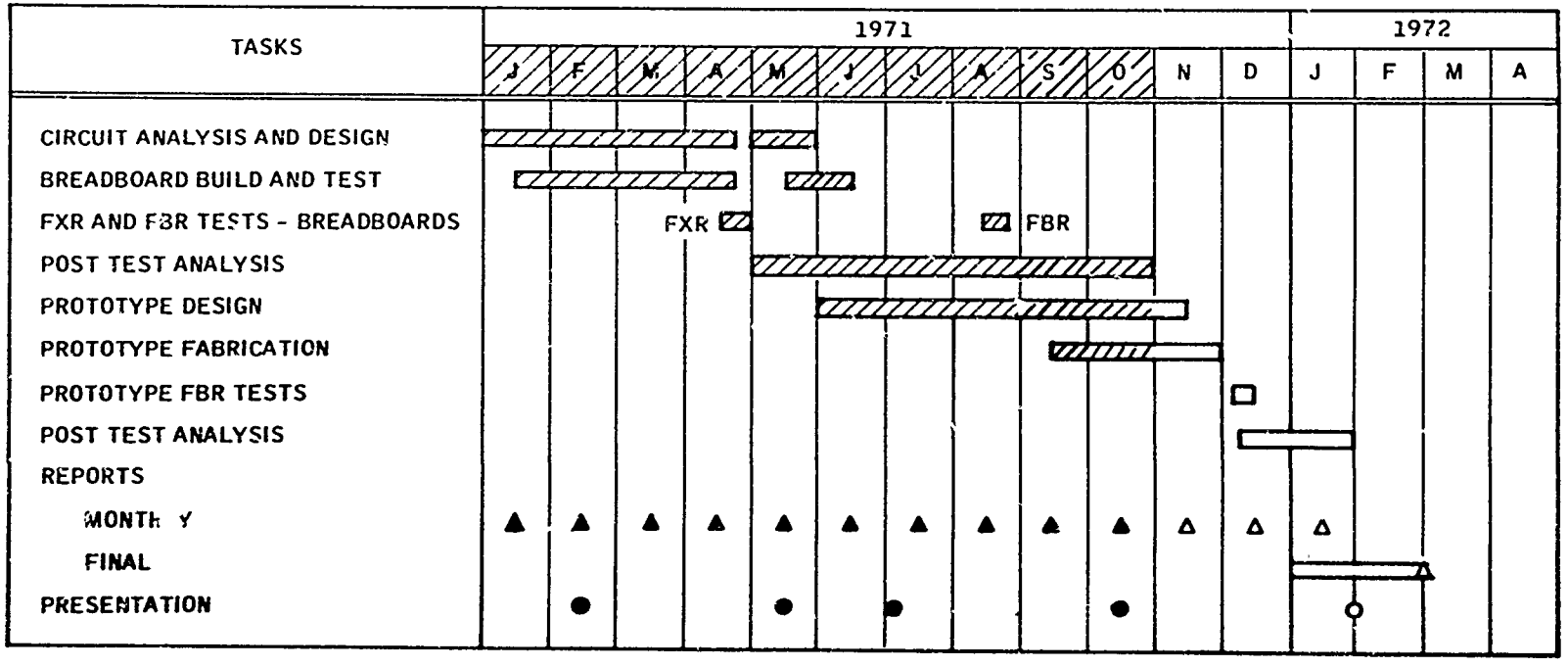

Figure 1. Program Milestone Schedule

SECTION II
PROGRAM ACTIVITIES

This section details the activities in the tasks that are currently in progress. The tasks discussed are fast-burst reactor test, future test plans, and prototype design.

FAST-BURST REACTOR (FBR) TEST

Two sets of breadboards were constructed to permit testing of each circuit function individually, and then, interconnected with the laser gyro in an operational single-axis system as shown in Figure 2. Additional tests outside of the system included an alternate amplifier/trigger circuit and a Germanium fringe pattern detector (to measure photocurrent response for computer modeling purposes). All tests were set up with cabling prewired to connectors to reduce the setup and teardown time. Three test setups were used:

1) the digital electronics (Figure 3a)
2) the individual circuits with the sensor photocurrent (Figure 3b)
3) the laser gyro system with the sensor photocurrent test (Figure 3c)

All setups were assembled on a mockup and evaluated in the lab prior to the field tests.

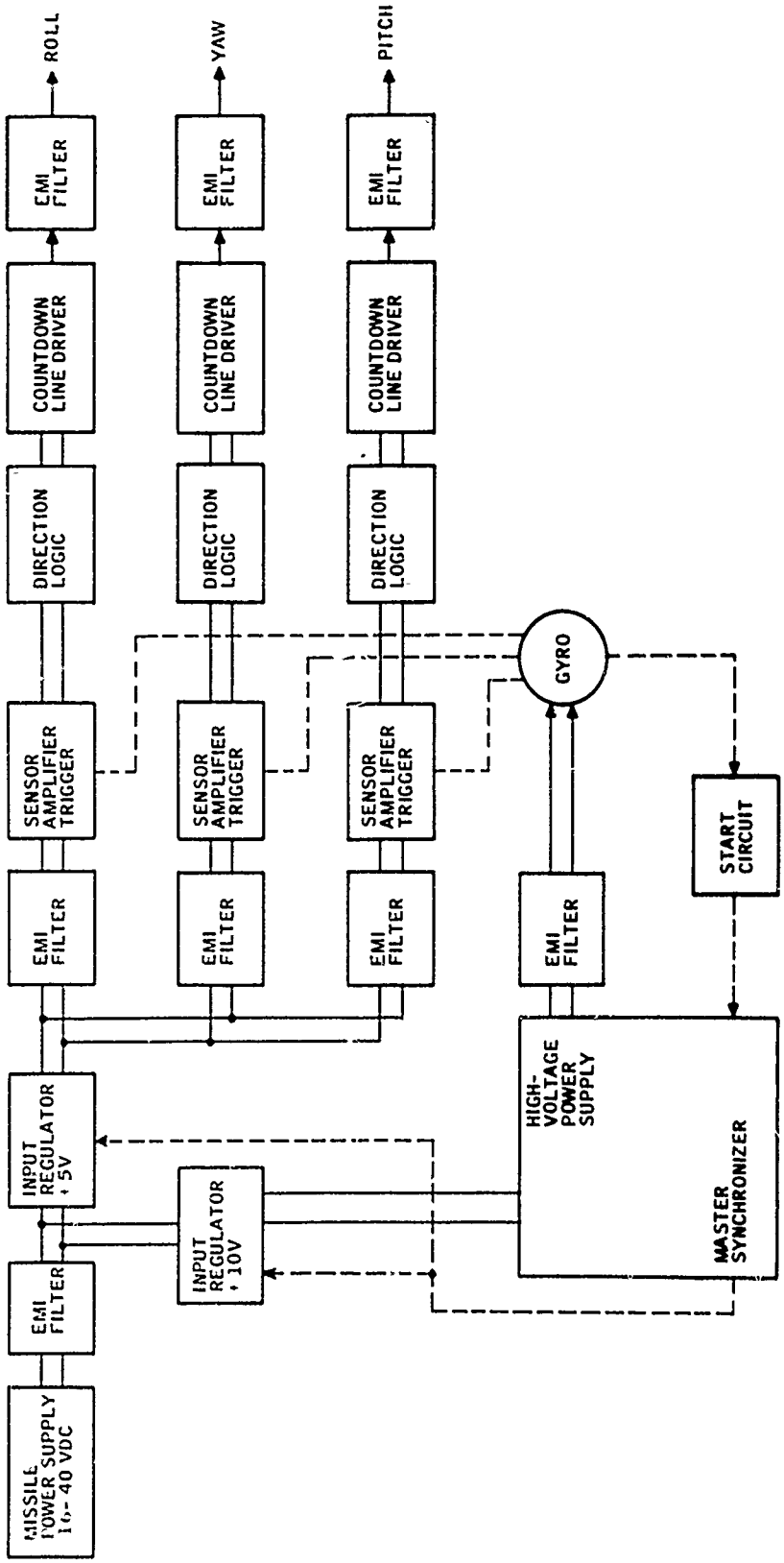

Figure 2. Hardened Laser Angular Rate Sensor Block Diagram

b

c

a

Figure 3. FBR Test Setups for Laser Gyro

TESTING

The test gear was transported to the FBR at White Sands Missile Range (WSMR) 15 August and set up on 16 August. August 17 the digital boards received four bursts, with operation normal. The individual circuits test was set up that afternoon. Testing proceeded with three bursts 18 August and the fourth the morning of 19 August. That afternoon the laser gyro system received two bursts, with two additional bursts 20 August before teardown and packing for shipment.

FBR POST-TEST ANALYSIS

Fast-burst reactor (FBR) post-test analysis has proceeded slowly due to a heavy prototype design load. The dosimetry data was received and reduced and indicated that the reactor neutron dosage/burst was 50 percent higher than was anticipated. This improves the redesign status somewhat since the circuit designs previously considered marginal at he estimated level of interest now appear acceptable. The phases of the FBR post-test analysis that have the most severe program impact are completed and presented in this report along with Appendix A, which presents the FBR test data. Further analysis results will be published when available and summarized in the Final Report.

Summary

During the FBR testing at White Sands Missile Range (WSMR), several on-site observations were made as briefly stated below:

1) Digital boards - normal operation - design complete

2) Germanium photosensor - large photocurrents observed

3) Readout/trigger operated normally

4) One 5-volt regulator failed

5) High-voltage d-c/d-c converter-output voltage dropped

6) Difficulty keeping the discharge "lit" during bursts

7) Loss of fringe pattern detector signal to one amplifier

8) Start/restart circuit functioned normally

Appendix A presents the actual photographic test data and some laboratory photos depicting the changes seen in some of the electronic components. Using the data included in the photos with the on-site observations and post-test measurements, the following conclusions were drawn.

1) Digital circuitry - use as is in prototype

2) The Germanium detector shows a 3.15 ma at 1×10^7 rad(Si)/sec photocurrent response plus a 10-fold permanent increase in reverse bias leakage current. The photocurrent response is a problem and should be compensated. The reverse current leakage increase is well within the common-mode rejection capabilities of the differential amplifier and presents no problem.

3) The readout/trigger circuit design is ready for the prototype.

4) The 5-volt regulator analysis is incomplete and will be reported later.

5) As expected, the voltage feedbacks and synchronizing signals with a redesigned transformer compensate for the permanent damage in the d-c/d-c converter and "heal" the radiation damage, making the high-voltage supplies operational with the irradiated parts. Some transient testing remains on the high-voltage supplies but the outcome looks good.

6) The gyro shows no degradation. The difficulty in keeping the discharge "lit" during bursts is due to the "soft" high-voltage supply.

7) The loss of fringe pattern detector output has not been verified. The detector leads will be examined when the ball is removed from the frame for installation of the pitch and yaw prisms and detectors.

8) The start/restart circuit functioned normally but test data reduction showed excessive photocurrent responses. Compensation is considered desirable and is being incorporated into the prototype.

Presented in the following paragraphs are detailed circuit-by-circuit descriptions of how the circuit performance was evaluated and what corrections can be made in the prototype design.

5-Volt Input Regulator

Since the Serial No. 1 5-volt regulator went through both the SFXR and the FBR without failure and performed according to computer predictions, the analysis of the Serial No. 2 failure has had less priority and is not complete at this writing. The computer predictions (Figure 4) and the measured performance (pages A39, A46, A53 and A59 of Appendix A) of Serial No. 1 5-volt regulator (Figure 5) indicate a problem that has two supplementary causes:

a) The Q1, 2, 3 and 5 photocurrent responses

b) The Q4 and Q15 photocurrent response

Q1 is a photocurrent compensator for Q2 in that it prevents the turn-on of Q2 due to Q2 primary photocurrent. The Q1 and Q2 primary photocurrents pass through the Q1 and Q2 collector-base junctions in a series circuit that completes

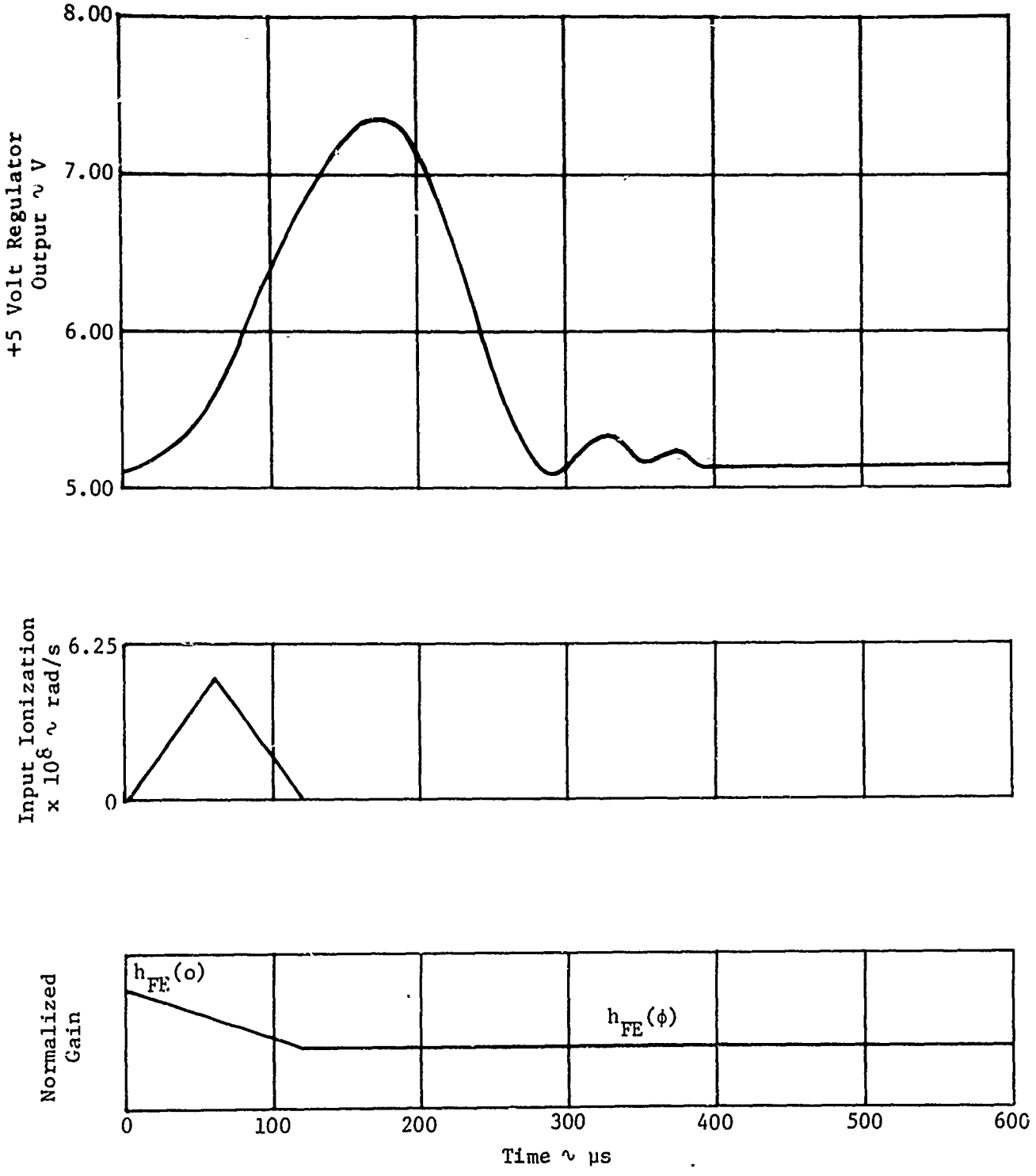

Figure 4. Predicted Response of +5-Volt Regulator at FBR

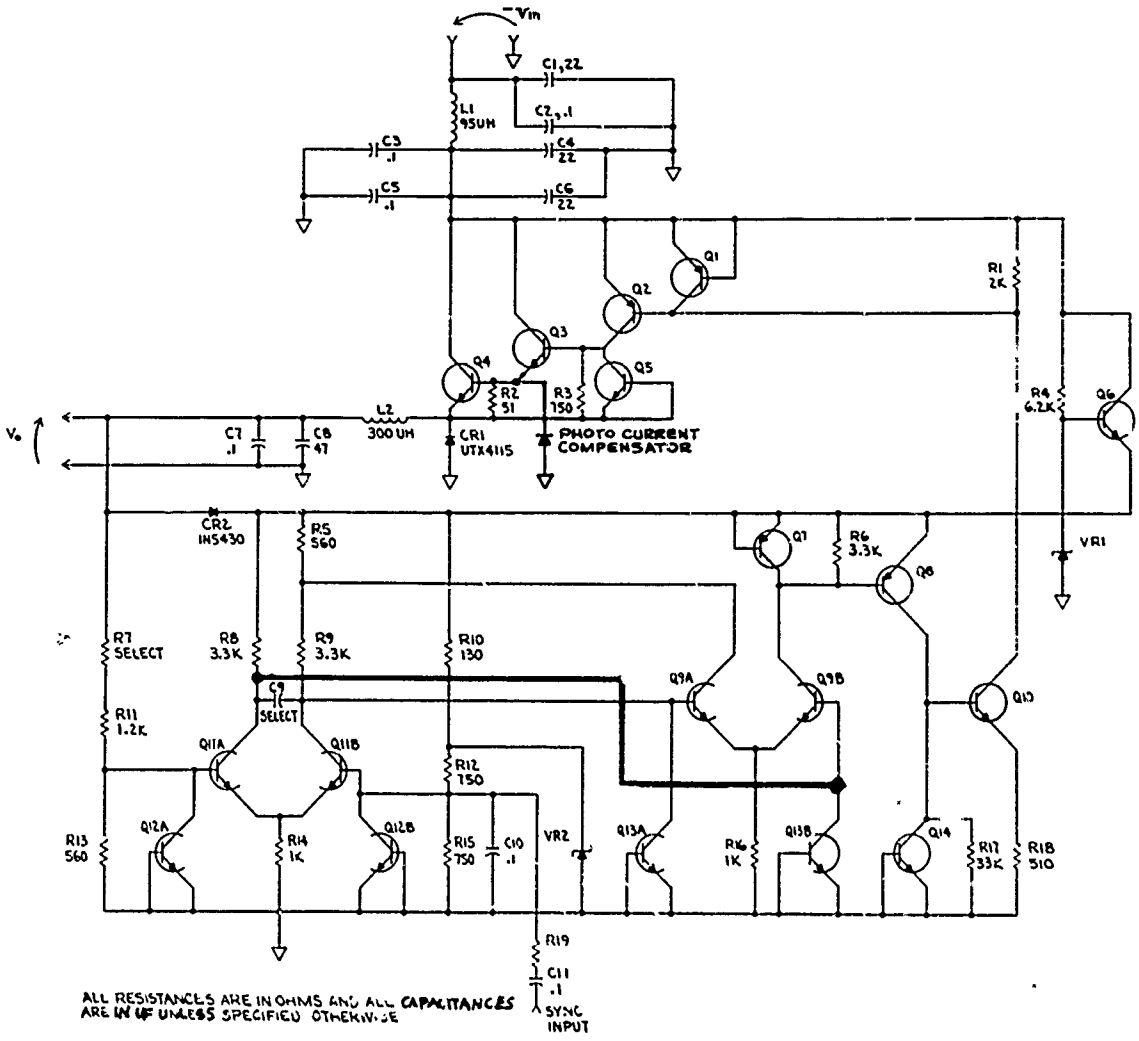

Figure 5. 5-Volt Input Regulator

Q4 photocurrent is compensated by Q15 except that the bias voltages are different (Q4, V_{CB} = 35 volts and Q15, V_{CB} = 5 volts when the input voltage is at 40 volts). Replacing the Q15 (BR100F) transistor with a diode that has a 10-percent greater photocurrent response than the BR100F will ensure that Q4 remains in the "off" mode during a gamma exposure.

Both of the above changes have been incorporated into the prototype circuits.

HV D-C/D-C Converter

The high-voltage d-c/d-c converter (Figure 6) survived four bursts in the individual circuit testing. The output voltage dropped at each burst, going from an initial -845 volts to -790 volts in three shots. The 10-volt switching regulator (Figure 7) showed a corresponding decrease in output. Since the 10-volt regulator and the HV d-c/d-c converter were connected "open loop", the high voltage should drop along with the 10-volt regulator. Laboratory tests with the 10-volt regulator and the HV d-c/d-c converter connected "closed loop" indicate that the power supply would have maintained the -845 volts throughout the four bursts.

Computer analyses indicate that the rise in output voltage (Figures A9, A16, A22, and A28 of Appendix A) during the burst is caused by photocurrents in the switching transistor. The two 2N3251s are adding a photocurrent to that of the switching transistor and the switching transistor compensator (BR100F Q15) cannot compensate for both currents. The substitution of a 11178122 diode for the BR100F compensating transistor will overcompensate the switching transistor and ensure its remaining off during transient radiation. The computer also indicates that the power dissipation in the BR100F converter transistors will approach 120 watts for a short time due to uncompensated photocurrents in the converter transistors. Adding the 11178122 diodes should compenate the converter. These compensation elements are included in the prototype circuits.

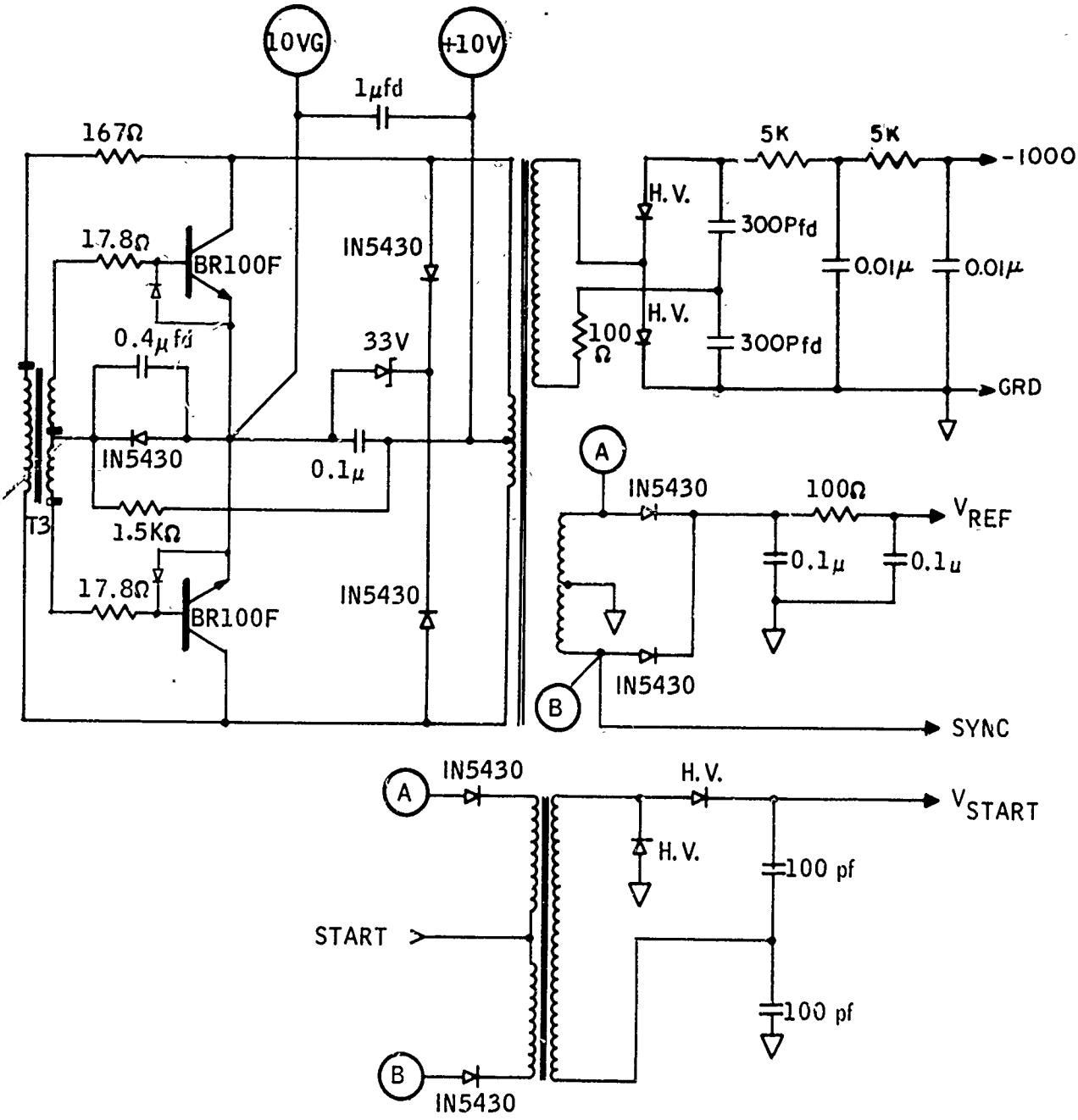

ALL DIODES MARKED H.V. ARE UNITRODE 652-745

Figure 6. High-Voltage D-C/D-C Converter

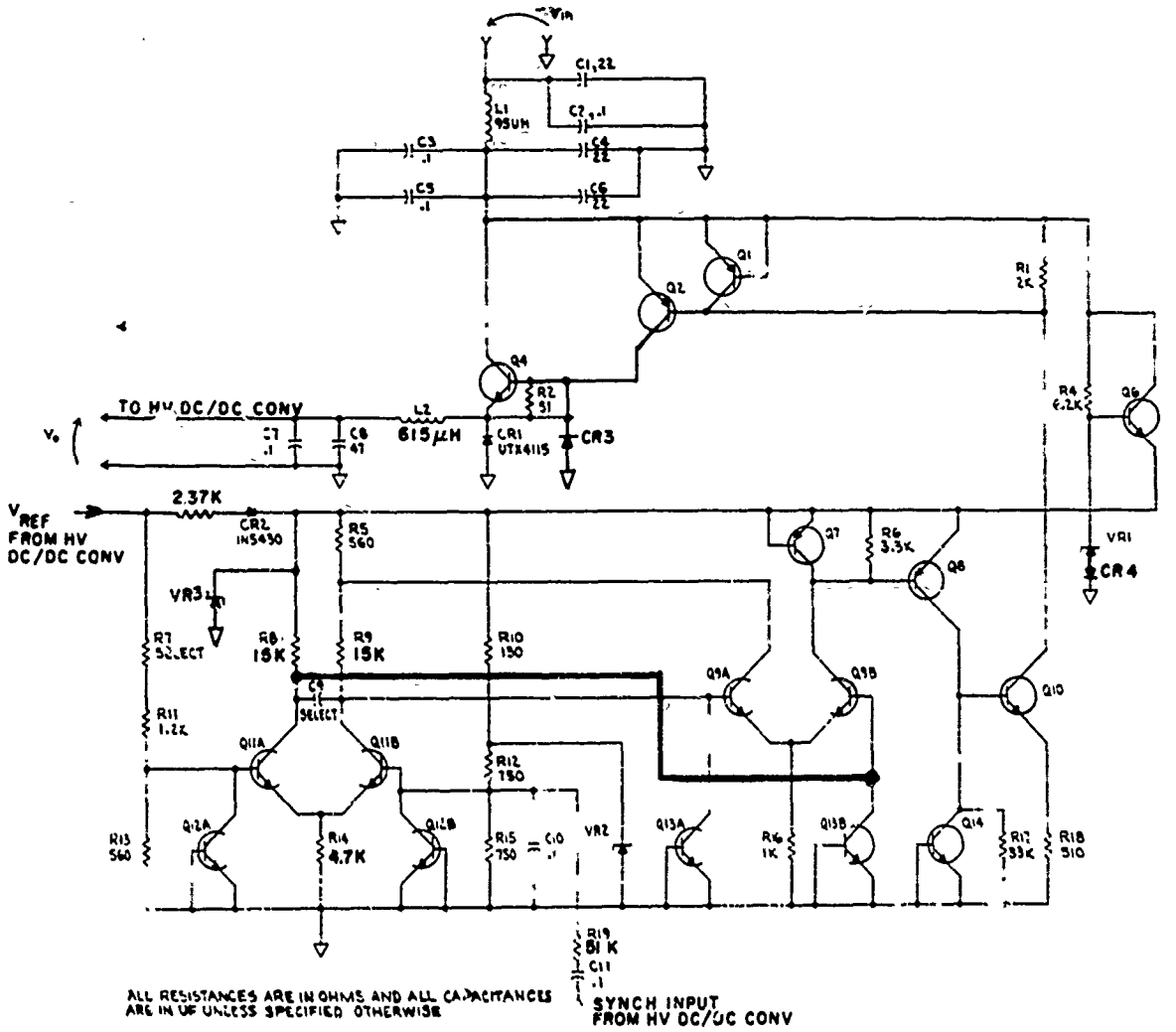

Figure 7. 10-Volt Input Regulator

Laser Start/Restart Circuit

Figure 8 shows the start/restart circuit including the added photocurrent compensator to prevent the photocurrents from Q1 and Q2 from providing an "O" input to the 54H31 gate. Previous analysis indicated that the photocurrent in Q8 would energize the start function at levels above 1×10^9 rad(Si)/sec of gamma input. Pages A11, A18, A24, and A30 of Appendix A show the start circuit energizing at much lower levels. This low-level "turn-on" of the start

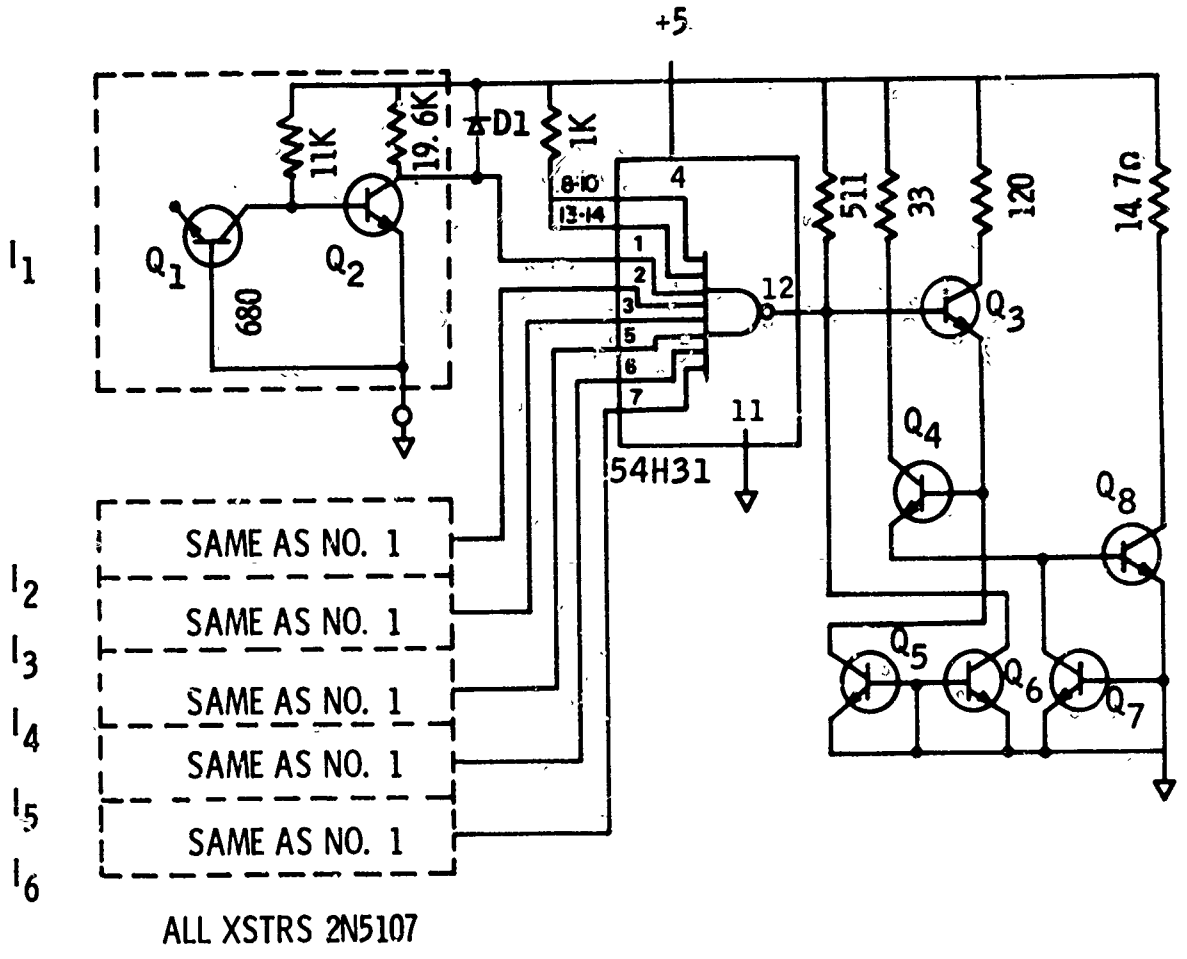

Figure 8. Laser Start/Restart Circuit

circuit is caused by photocurrent in Q2 providing an "O" to the logic gate which then calls for a start function. When the start circuit "turns on" the +2000 volts are applied to the discharge, increasing the load on the d-c/d-c converter. The increased load lowers the run voltage (-1000 volts) and increases the ripple content of the run voltage. The lowered run voltage and the increased ripple may (depending on the ability of the voltage feedback to compensate for these changes) cause a degradation of the gyro performance. It is desirable, if not necessary, to prevent any gyro performance degradation at levels below 1×10^9 rad(Si)/sec.

Fringe Pattern Detector

The fringe pattern detector has a high [3.15 ma at 1×10^7 rad(Si)/sec] photocurrent response, that if uncompensated, drives the detector into a circuit-connected current limiting saturation at levels as low as 3×10^6 rad(Si)/sec. The recovery time is extended by this type of saturation to as much as 150 μsec, depending on the input radiation level. The addition of a compensating diode will limit the saturation and reduce the recovery time to 1 μsec and if ideally compensated may permit operation through the gamma input. A 10-percent error in photocurrent compensation would allow the differential amplifier to read the detector output without error at gamma input levels up to 3×10^7 rad(Si)/sec. A linear compensation with 10-percent accuracy is improbable if not impossible since the gamma saturation level of the detector (Germanium) and compensator (silicon) are different. If the compensator remains linear to higher levels than the detector the differential amplifier will see a high common-mode voltage at the input. The amplifier can read through a 1-volt increase in common-mode voltage. The Germanium detector appears to saturate at 6.6×10^7 rad(Si)/sec probably due to exhausting the population of electrons in the energy levels below the photon energy of the gamma. This type of saturation has a fast recovery time. At this point the differential amplifier is shut off by the input common-mode voltage going to zero. The compensator continues to increase its photocurrent as gamma increases turning on the differential amplifier at 1.1×10^8 rad(Si)/sec. The differential amplifier remains on until 2×10^8 rad(Si)/sec, where the common-mode input voltage exceeds 3.5 volts. At levels above 2×10^8 the differential amplifier is off but all time constants are minimized and the readout will be back "on the air" within 1 μsec of the end of the gamma input.

Prototype Design

Figure 9 shows an assembly drawing of the prototype GG1331 Radiation-Tolerant Laser Triad Rate Gyro (LTRG). The electronics during this neutron and gamma test phase are built using discrete components mounted on two-layer fiberglass printed circuit boards. Twisted-pair wiring is used exclusively for the electronics interconnections. Ground planes are utilized in the critical circuit areas in the switching regulators and the converter.

A novel feature of the GG1331 is the treatment of the EMI filter pin connecters, (Figures 9a and 9b). Past experience with this type of connector dictates that 1) signal lines and power lines must be well separated, and 2) the RF path to chassis must be short and well defined. Isolation of signal and power is accomplished by keeping all signal lines in one connecter (Figure 9a) and mounting the connecter at the opposite side of the flange from the power input connecter (Figure 9b).

The plastic spacers (Figures 9c and 9d) provide a low-capacitance separation between the filter pin assemblies and the dust cover, thus defining the EMI path to chassis by reducing the RF current flow in the dust cover.

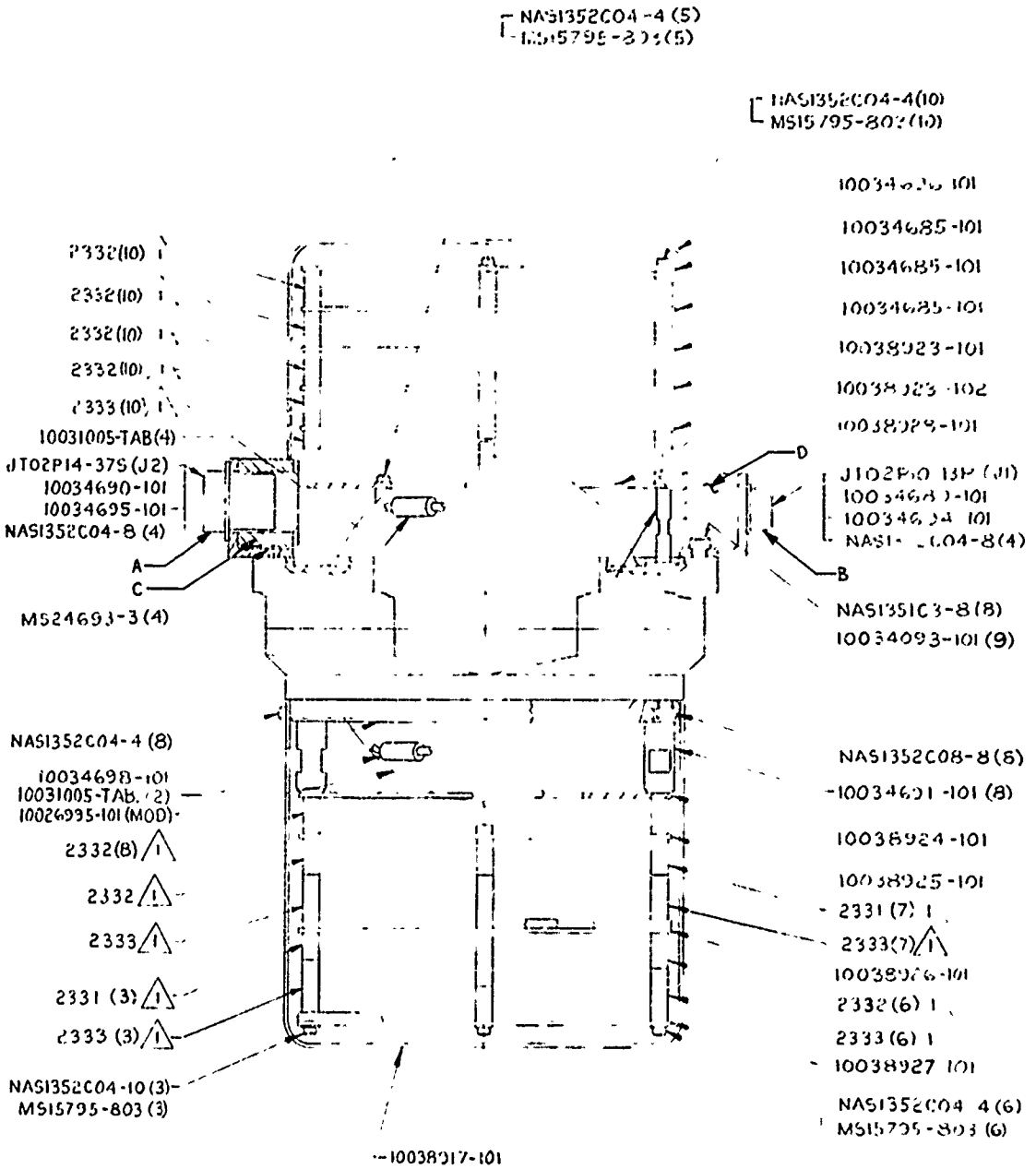

3 - C13707AA02

2 - DR14228

1 - USE 4-40 SETSCREWS AS REQD TO CREATE THREADED STANDOFF

LTRG - RADIATION TOLERANT LO 57980 G (HI-6002)

Figure 9. Prototype GG1231 Radiation-Tolerant Laser Triad Rate Gyro

SECTION III
FUTURE PLANS

- Update circuitry to correct performance errors from first FBR testing
- Assemble prototype GG1331
- Test prototype at FBR 12/6/71 to 12/10/71

APPENDIX A

FAST-BURST REACTOR TEST DATA
WHITE SANDS MISSILE RANGE 8/16/71 TO 8/20/71

FBR test data is as follows:

Page No.	Burst No.	Device Tested
Digital Boards A2-A7	1-4	
Individual Circuits		
A8, A15	5, 6	5-volt regulator (failed in burst No. 6)
A9, A16, A22, A28	5, 6	10-volt regulator
A10, A17, A23, A29	5, 6, 7, 8	-1000-volt converter
A11, A18, A24, A30	5, 6, 7, 8	Start monitor
A12, A19, A25, A31	5, 6, 7, 8	Readout-trigger S/N 4 (new design)
A13, A20, A26, A32	5, 6, 7, 8	Readout-trigger S/N 3 (old design)
A14, A21, A27, A33	5, 6, 7, 8	Germanium photodetector S/N XV
System Testing		
A34, A41, A48, A55	9, 10, 11, 12	Slow digital pulses (up direction)
A35, A42, A49 scope failed	9, 10, 11, 12	Slow digital pulses (down direction)
A36, A43, A50, A56	9, 10, 11, 12	Fast digital pulses (up direction)
A37, A44, A51, A57	9, 10, 11, 12	Fast digital pulses (down direction)
A38, A45, A52, A58	9, 10, 11 12	Start monitor
A39, A46, A53, A59	9, 10, 11, 12	10-volt regulator = upper trace; 5-volt regulator = lower trace
A40, A47, A54, A60	9, 10, 11, 12	Germanium photodetector S/N XV
Component Variations		
A61	5-8	TI Germanium photodetector I/V characteristics
A62	8-12	TI Germanium photodetector reverse-current I/V characteristics
A63	8-12	TI Germanium photodetector I/V characteristics
A64	9-12	Philco-Ford Germanium photosensor reverse-current I/V characteristics
A65	9-12	Philco-Ford Germanium photodetector forward-current I/V characteristics
A66	9-12	1N748A zener diode reverse-current I/V characteristics
A67	9-12	1N746A zener diode reverse-current I/V characteristics
A68	---	Low-voltage avalanche zener diode reverse-current I/V characteristics
A69	9-12	BR100F collector I/V characteristics
A70	9-12	2N4878 collector I/V characteristics

H = 50 sec/cm
V = 5 Volt/cm

UP COUNT LINE

H = 500 sec/cm
V = 5 Volt/cm

BEFORE BURST

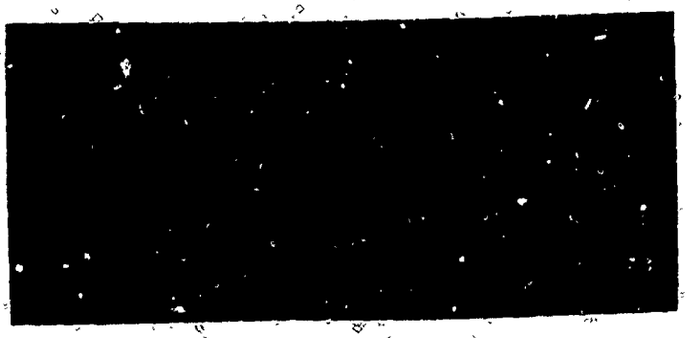

H = 50 sec/cm
V = 5 Volt/cm

DOWN COUNT LINE

H = 500 sec/cm
V = 5 Volt/cm

H = 50 sec/cm
V = 5 Volt/cm

UP COUNT LINE

H = 500 sec/cm
V = 5 Volt/cm

DURING BURST

H = 50 sec/cm
V = 5 Volt/cm

DOWN COUNT LINE

H = 500 sec/cm
V = 5 Volt/cm

BURST # 1 DATE 8/17/71

FUNCTION Slow Digital Pulses

H = 1 sec/cm
V = 5 Volt/cm

UP COUNT LINE

H = 200 sec/cm
V = 5 Volt/cm

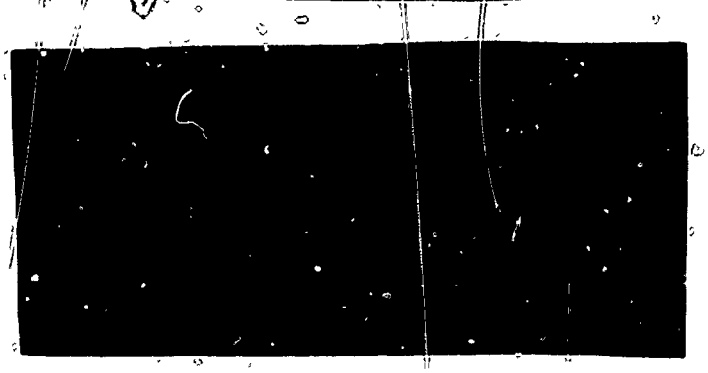

BEFORE BURST

H = 1 sec/cm
V = 5 Volt/cm

DOWN COUNT LINE

H = 200 sec/cm
V = 5 Volt/cm

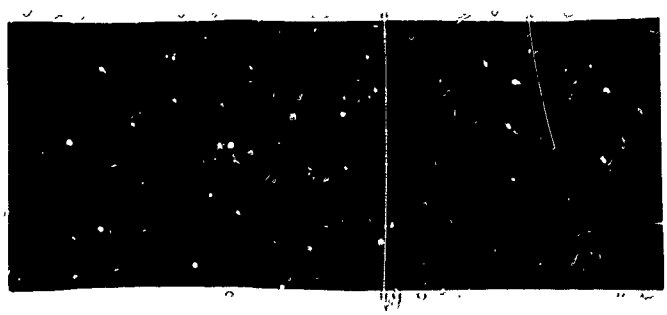

H = 1 sec/cm
V = 5 Volt/cm

UP COUNT LINE

H = 200 sec/cm
V = 5 Volt/cm

DURING BURST

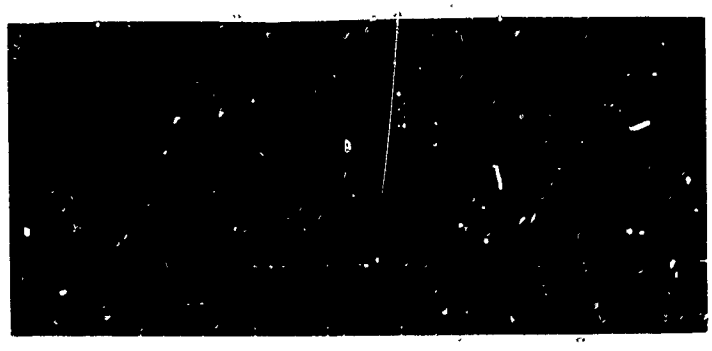

H = 1 sec/cm
V = 5 Volt/cm

DOWN COUNT LINE

H = 200 sec/cm
V = 5 Volt/cm

BURST # 1 DATE 8/17/71

FUNCTION Fast Digital Pulse Outputs

- C 24 -

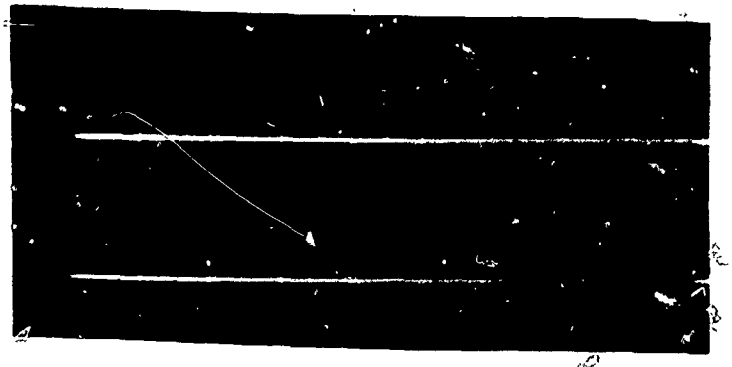

H = 50 sec/cm
V = 5 Volt/cm

UP COUNT LINE

H = 500 sec/cm
V = 5 Volt/cm

BEFORE BURST

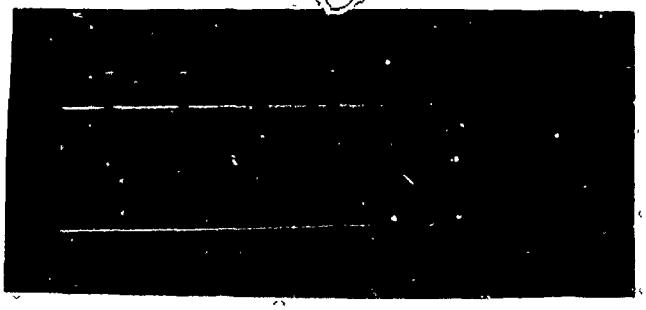

H = 50 sec/cm
V = 5 Volt/cm

DOWN COUNT LINE

H = 500 sec/cm
V = 5 Volt/cm

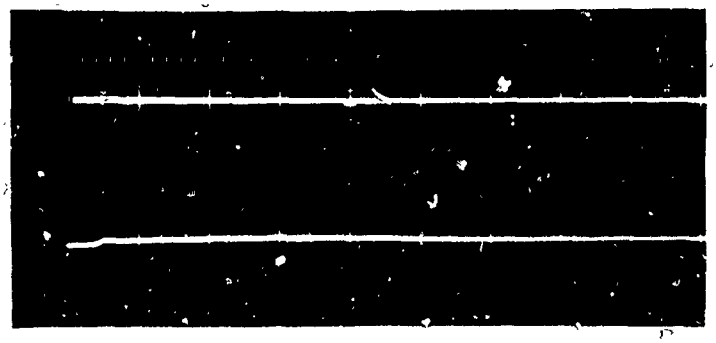

H = 50 sec/cm
V = 5 Volt/cm

UP COUNT LINE

H = 500 sec/cm
V = 5 Volt/cm

DURING BURST

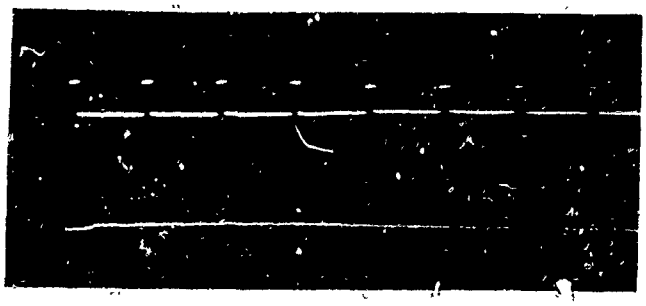

H = 50 sec/cm
V = 5 Volt/cm

DOWN COUNT LINE

H = 500 sec/cm
V = 5 Volt/cm

BURST # 2 DATE 8/17/71

FUNCTION Slow Digital Pulses

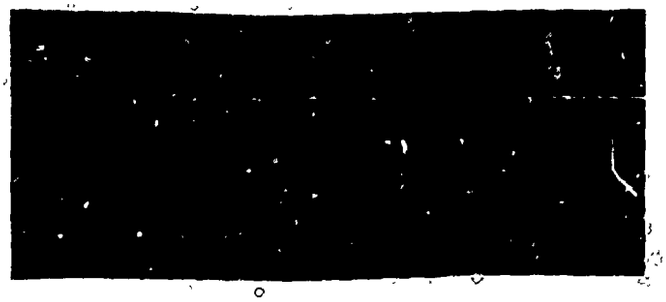

H = 20 sec/cm
V = 5 Volt/cm

UP COUNT LINE

H = 200 sec/cm
V = 5 Volt/cm

BEFORE BURST

H = 20 sec/cm
V = 5 Volt/cm

DOWN COUNT LINE

H = 200 sec/cm
V = 5 Volt/cm

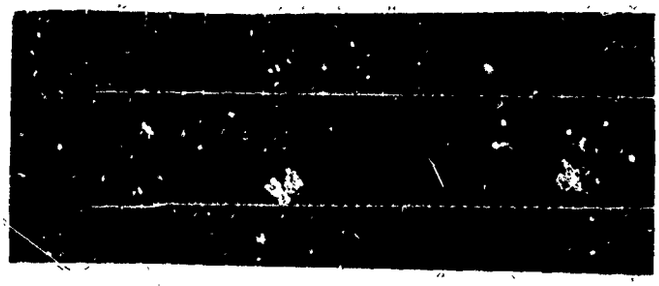

H = 20 sec/cm
V = 5 Volt/cm

UP COUNT LINE

H = 200 sec/cm
V = 5 Volt/cm

DURING BURST

H = 20 sec/cm
V = 5 Volt/cm

DOWN COUNT LINE

H = 200 sec/cm
V = 5 Volt/cm

BURST # 2 DATE 8/17/71

FUNCTION Fast Digital Pulses

H = 50 sec/cm
V = 5 Volt/cm

UP COUNT LINE

H = 500 sec/cm
V = 5 Volt/cm

SLOW DIGITAL PULSES

H = 50 sec/cm
V = 5 Volt/cm

DOWN COUNT LINE

H = 500 sec/cm
V = 5 Volt/cm

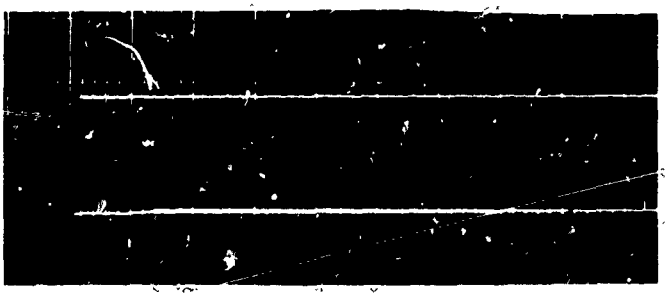

H = 20 sec/cm
V = 5 Volt/cm

UP COUNT LINE

H = 200 sec/cm
V = 5 Volt/cm

FAST DIGITAL PULSES

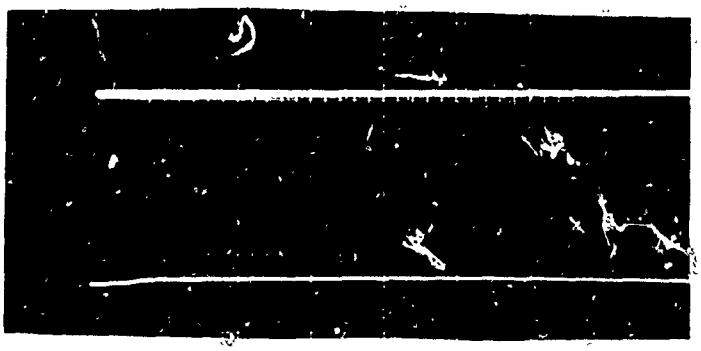

H = 20 sec/cm
V = 5 Volt/cm

DOWN COUNT LINE

H = 200 sec/cm
V = 5 Volt/cm

BURST # 3 DATE 8/17/71

FUNCTION Digital Pulse Performance During Burst

H = 50 sec/cm
V = 5 Volt/cm

UP COUNT LINE

H = 500 sec/cm
V = 5 Volt/cm

SLOW DIGITAL PULSES

H = 50 sec/cm
V = 5 Volt/cm

DOWN COUNT LINE

H = 500 sec/cm
V = 5 Volt/cm

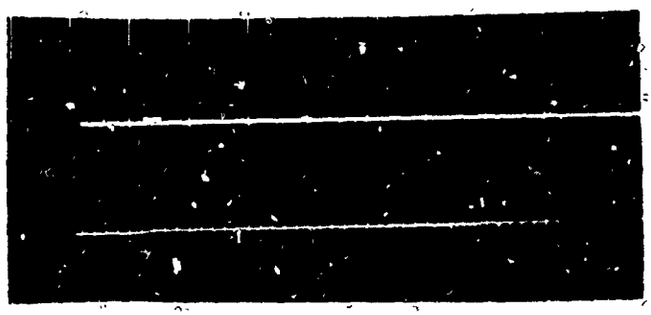

H = 20 sec/cm
V = 5 Volt/cm

UP COUNT LINE

H = 200 sec/cm
V = 5 Volt/cm

FAST DIGITAL PULSES

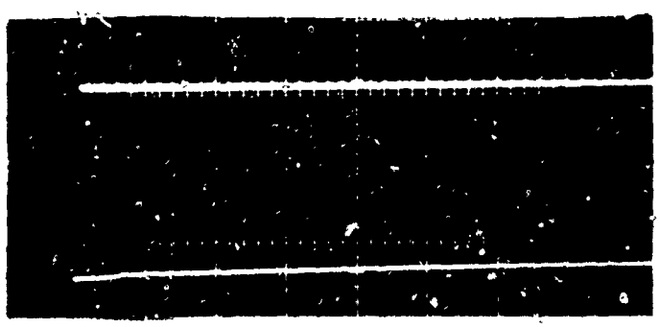

H = 20 sec/cm
V = 5 Volt/cm

DOWN COUNT LINE

H = 200 sec/cm
V = 5 Volt/cm

BURST # 4 DATE 8/17/71

FUNCTION Digital Pulse Performance During Burst

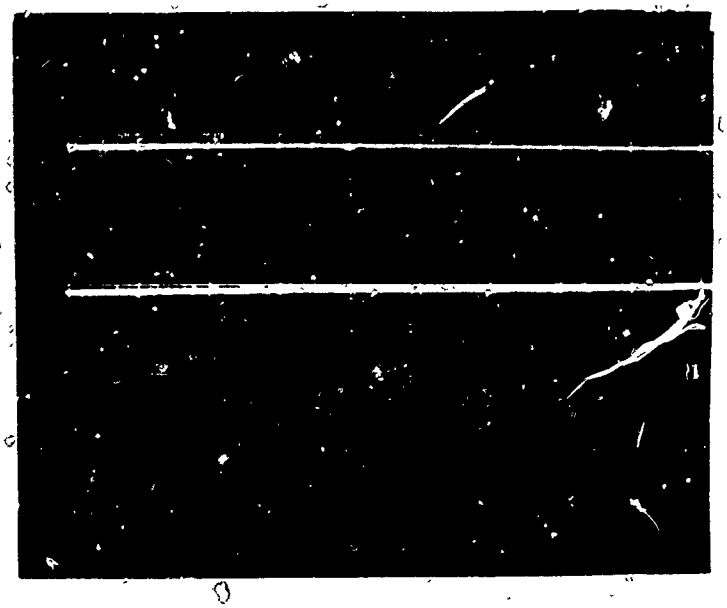

Horizontal 50 μ sec/ cm

Vertical 5 Volt/ cm

BEFORE

Horizontal 500 μ sec /cm

Vertical 5 Volt /cm

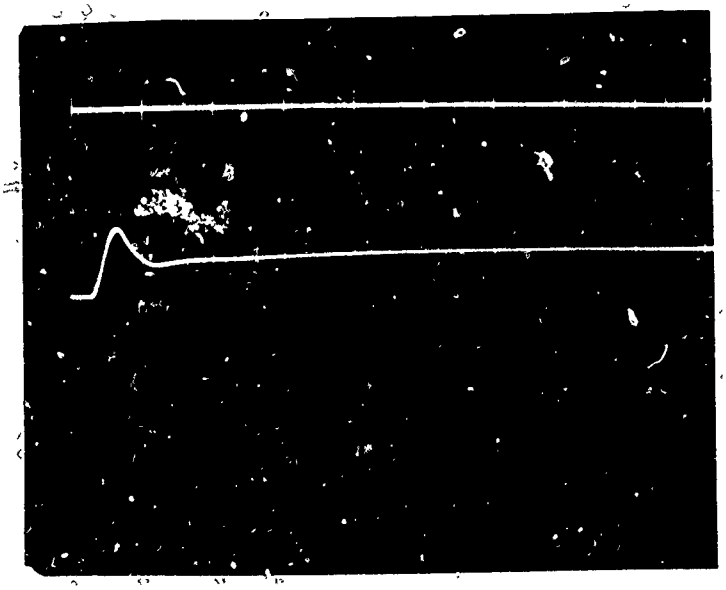

Horizontal 50 μ sec /cm

Vertical 5 Volt /cm

DURING

Horizontal 500 μ sec /cm

Vertical 5 Volt /cm

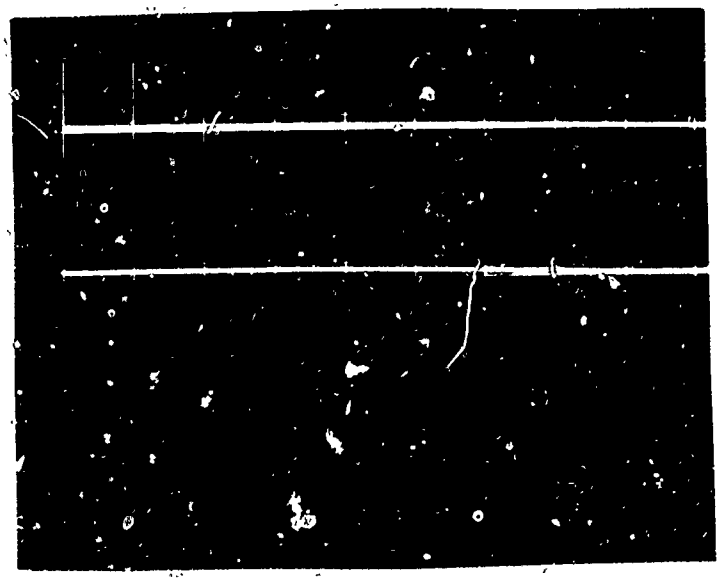

Horizontal 50 μ sec /cm

Vertical 5 Volt /cm

AFTER

Horizontal 500 μ sec/ cm

Vertical 5 Volt/ cm

BURST # 5 DATE 8/18/71

FUNCTION 5 Volt Regulator

Horizontal 50 μsec/ cm

Vertical 10 Volt/ cm

BEFORE

Horizontal 500 μsec /cm

Vertical 10 Volt /cm

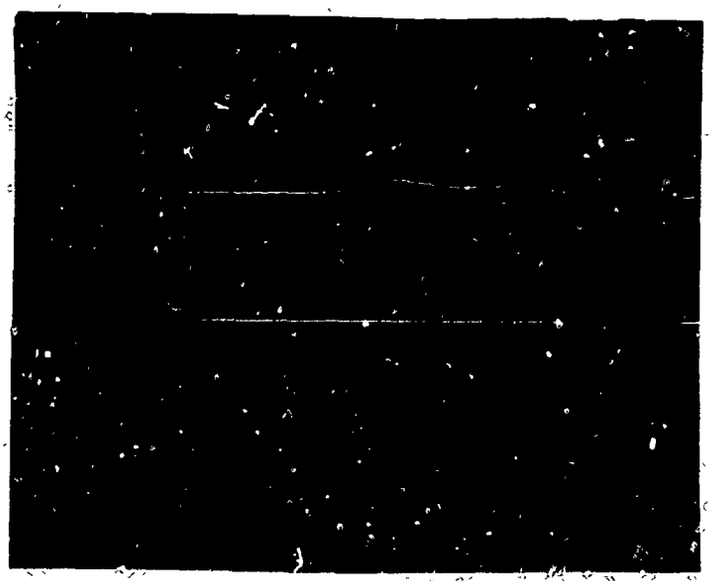

Horizontal 50 μsec /cm

Vertical 10 Volt /cm

DURING

Horizontal 500 μsec /cm

Vertical 10 Volt /cm

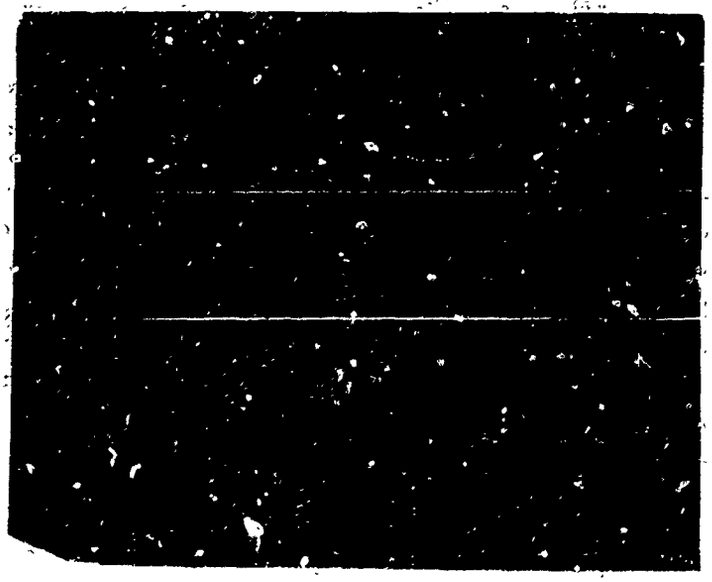

Horizontal 50 μsec /cm

Vertical 10 Volt /cm

AFTER

Horizontal 500 μsec/ cm

Vertical 10 Volt/ cm

BURST # 5 DATE 8/18/71

FUNCTION 10 Volt Regulator

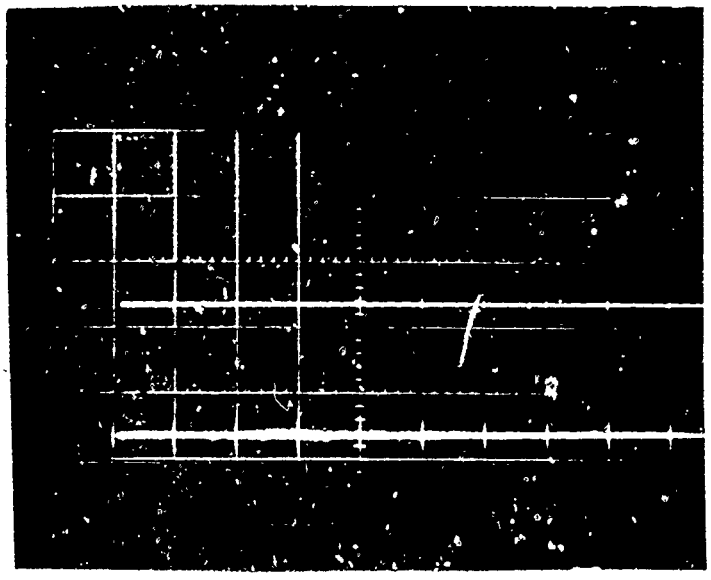

Horizontal 50 μsec/ cm

Vertical 0.5 Volt/ cm

BEFORE

Horizontal 500 μsec /cm

Vertical 0.5 Volt /cm

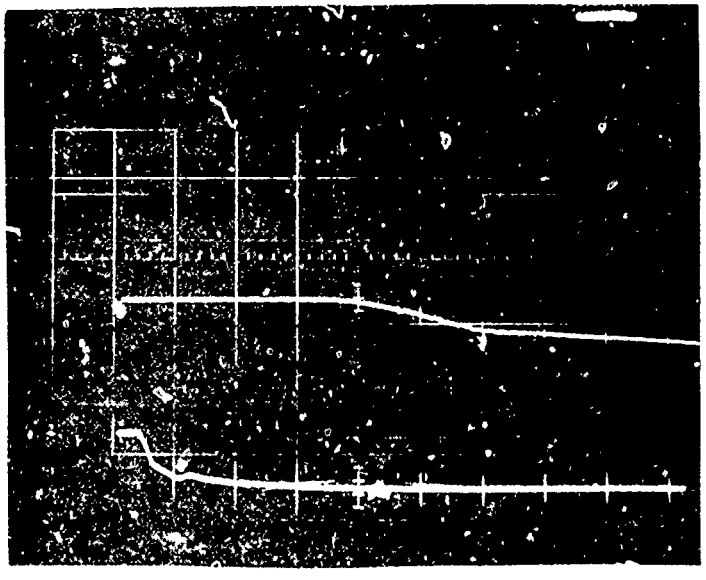

Horizontal 50 μsec /cm

Vertical 0.5 Volt /cm

DURING

Horizontal 500 μsec /cm

Vertical 0.5 Volt /cm

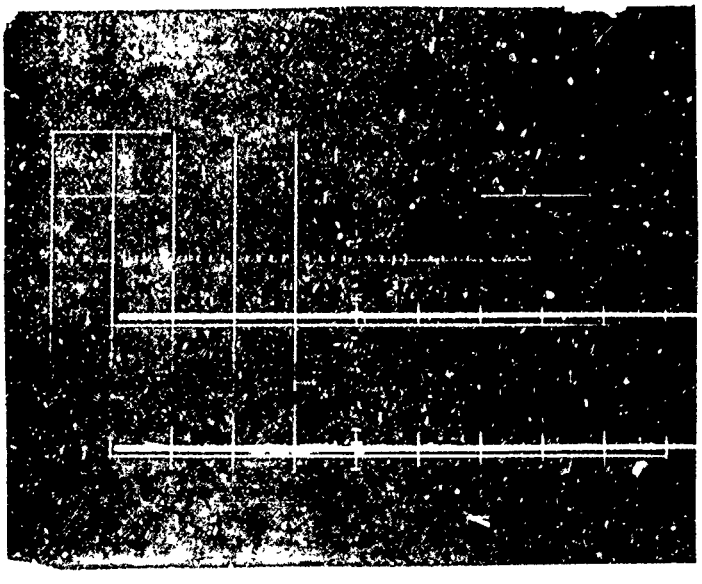

Horizontal 50 μsec /cm

Vertical 0.5 Volt /cm

AFTER

Horizontal 500 μsec/ cm

Vertical 0.5 Volt / cm

5 DATE 8/18/71

V Power Supply

Horizontal 50 μsec/ cm

Vertical 0.5 Volt/ cm

BEFORE

Horizontal 500 μsec /cm

Vertical 0.5 Volt /cm

Horizontal 50 μsec /cm

Vertical 0.5 Volt /cm

DURING

Horizontal 500 μsec /cm

Vertical 0.5 Volt /cm

Horizontal 50 μsec /cm

Vertical 0.5 Volt /cm

AFTER

Horizontal 500 μsec/ cm

Vertical 0.5 Volt/ cm

BURST # 5 DATE 8/18/71

FUNCTION Start Monitor

Horizontal 50 μ sec/ cm

Vertical 1 Volt/ cm

BEFORE

Horizontal 500 μ sec /cm

Vertical 1 Volt /cm

Horizontal 50 μ sec /cm

Vertical 1 Volt /cm

DURING

Horizontal 500 μ sec /cm

Vertical 1 Volt /cm

Horizontal 50 μ sec /cm

Vertical 1 Volt /cm

AFTER

Horizontal 500 μ sec/ cm

Vertical 1 Volt/ cm

BURST # 5 DATE 8/18/71

FUNCTION Readout/Trigger Serial #4

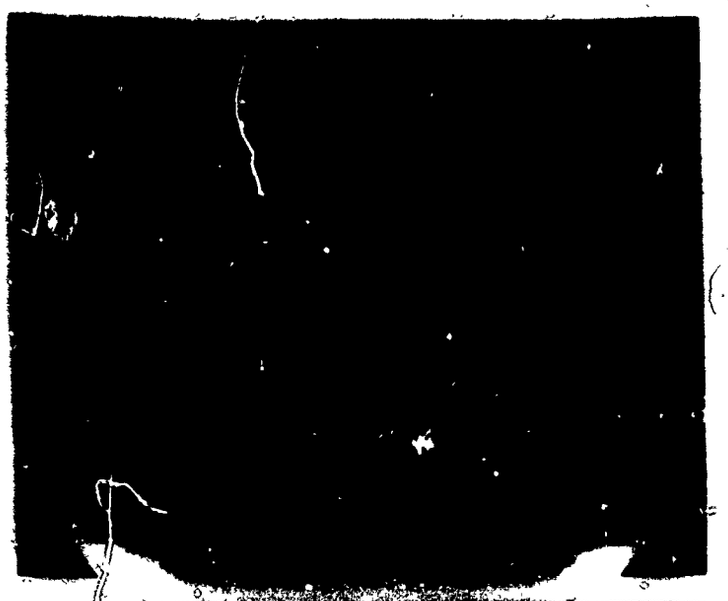

Horizontal 50 μsec/ cm

Vertical 1 Volt/ cm

BEFORE

Horizontal 500 μsec /cm

Vertical 1 Volt /cm

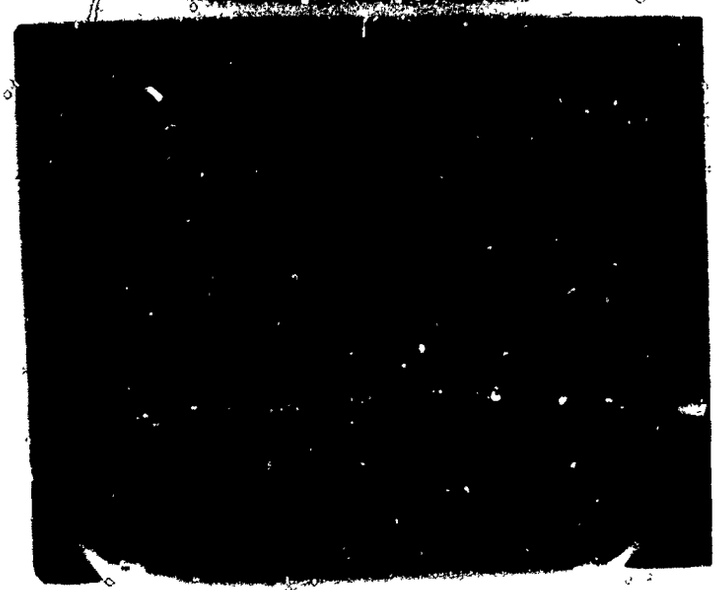

Horizontal 50 μ sec /cm

Vertical 1 Volt /cm

DURING

Horizontal 500 μ sec /cm

Vertical 1 Volt /cm

Horizontal 50 μ sec /cm

Vertical 1 Volt /cm

AFTER

Horizontal 500 μ sec / cm

Vertical 1 Volt / cm

BURST # 5 DATE 8/18/71

FUNCTION Readout/Trigger Serial #3

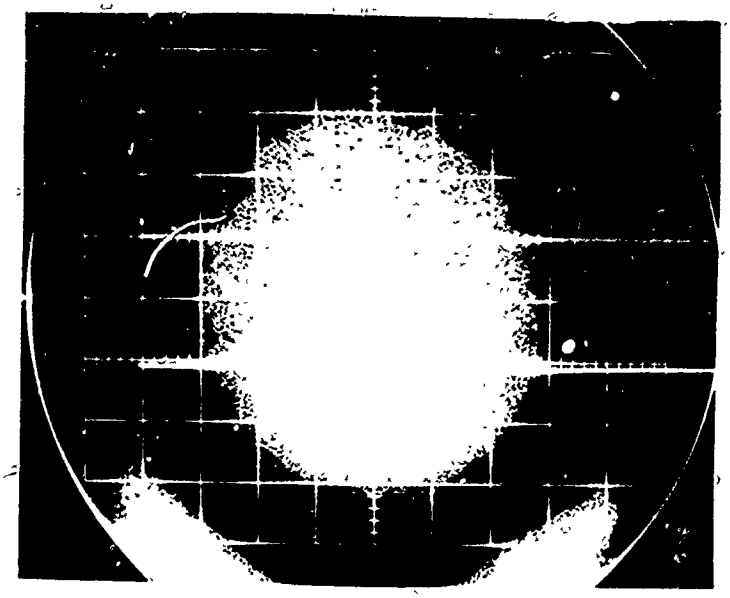

Horizontal 500 μsec/ cm

Vertical 1 Volt/ cm

BEFORE

Horizontal 500 μsec /cm

Vertical 1 Volt /cm

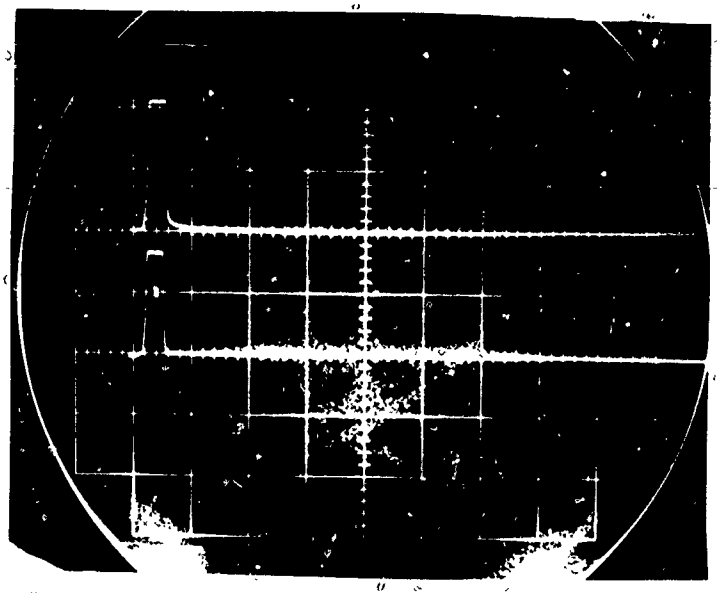

Horizontal 500 μsec /cm

Vertical 1 Volt /cm

DURING

Horizontal 500 μsec /cm

Vertical 1 Volt /cm

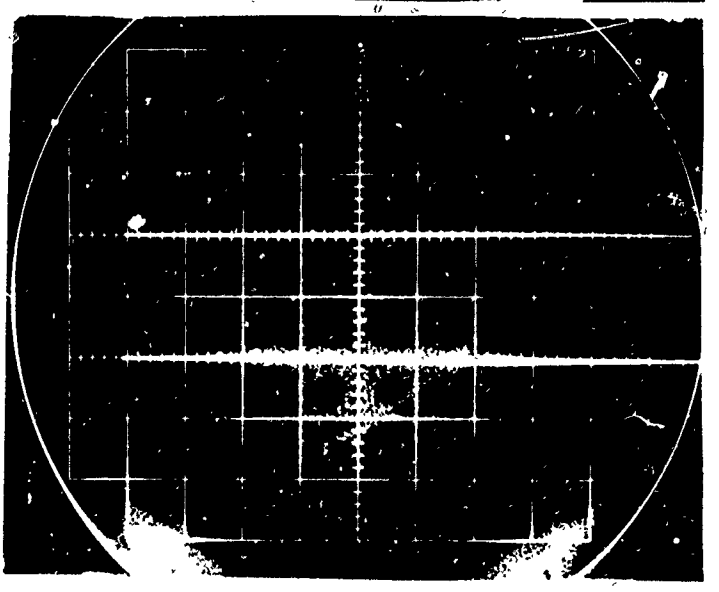

Horizontal 500 μsec /cm

Vertical 1 Volt /cm

AFTER

Horizontal 500 μsec cm

Vertical 1 Volt cm

BURST # 5 DATE 8/18/71

FUNCTION Germanium Photodetector

Same as "After" photo on page A8

Horizontal 50 μsec/ cm

Vertical 5 Volt/ cm

BEFORE

Horizontal 500 μsec /cm

Vertical 5 Volt /cm

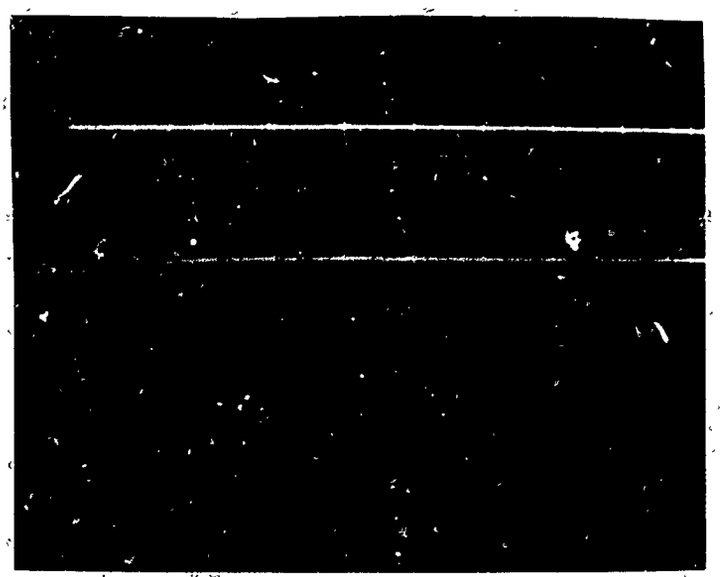

Horizontal 50 μsec /cm

Vertical 5 Volt /cm

DURING

Horizontal 500 μsec /cm

Vertical 5 Volt /cm

Horizontal 50 μsec /cm

Vertical 5 Volt /cm

AFTER

Horizontal 500 μsec cm

Vertical 5 Volt cm

BURST # 6 DATE 8/18/71

FUNCTION 5 Volt Regulator

Same as "After" photo on page A9

Horizontal 50 μ sec / cm

Vertical 10 volt / cm

BEFORE

Horizontal 500 μ sec /cm

Vertical 10 volt /cm

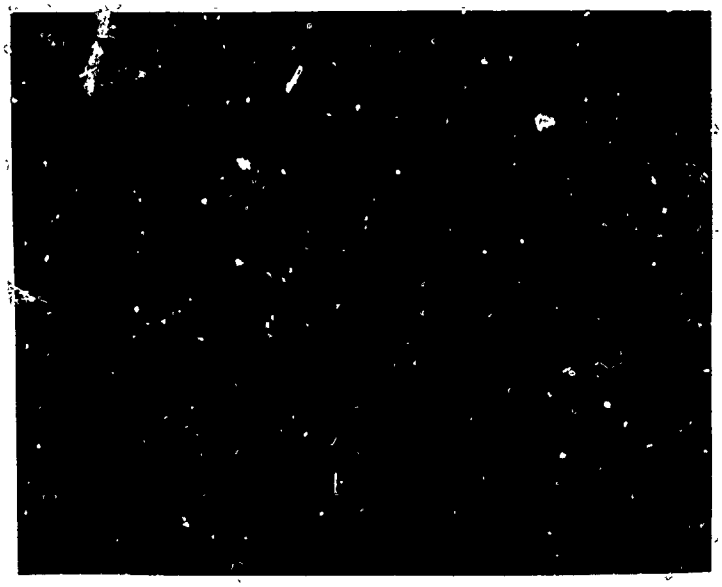

Horizontal 50 μ sec /cm

Vertical 10 volt /cm

DURING

Horizontal 500 μ sec /cm

Vertical 10 volt /cm

Horizontal 50 μ sec /cm

Vertical 10 volt /cm

AFTER

Horizontal 500 μ sec/ cm

Vertical 10 volt/ cm

BURST # 6 DATE 8/18/71

FUNCTION 10 Volt Regulator

Same as "After" photo on page A10

Horizontal 50 μ sec / cm

Vertical 0.5 volt / cm

BEFORE

Horizontal 500 μ sec /cm

Vertical 0.5 volt /cm

Horizontal 50 μ sec /cm

Vertical 0.5 volt /cm

DURING

Horizontal 500 μ sec /cm

Vertical 0.5 volt /cm

Horizontal 50 μ sec /cm

Vertical 0.5 volt /cm

AFTER

Horizontal 500 μ sec / cm

Vertical 0.5 volt / cm

BURST # 6 DATE 8/18/71

FUNCTION -1000 volt Supply

Same as "After" photo on page A11

Horizontal 50 μ sec / cm

Vertical 0.5 volt/ cm

BEFORE

Horizontal 500 μ sec /cm

Vertical 0.5 volt /cm

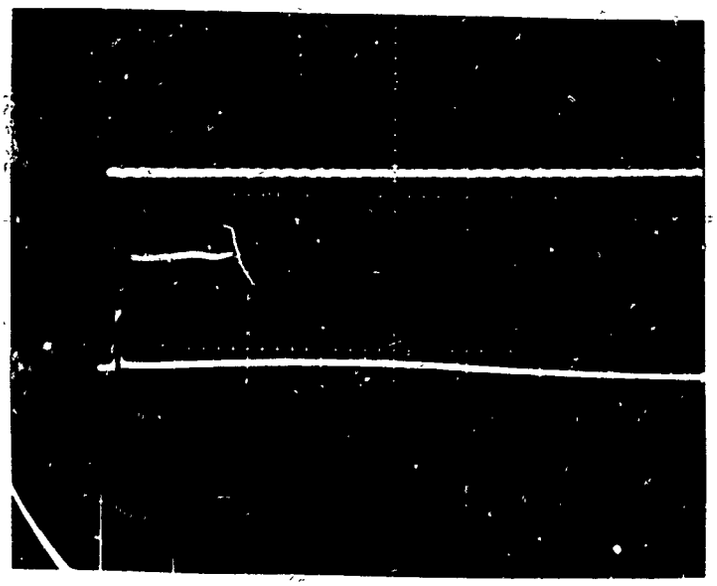

Horizontal 50 μ sec /cm

Vertical 0.5 volt /cm

DURING

Horizontal 500 μ sec /cm

Vertical 0.5 volt /cm

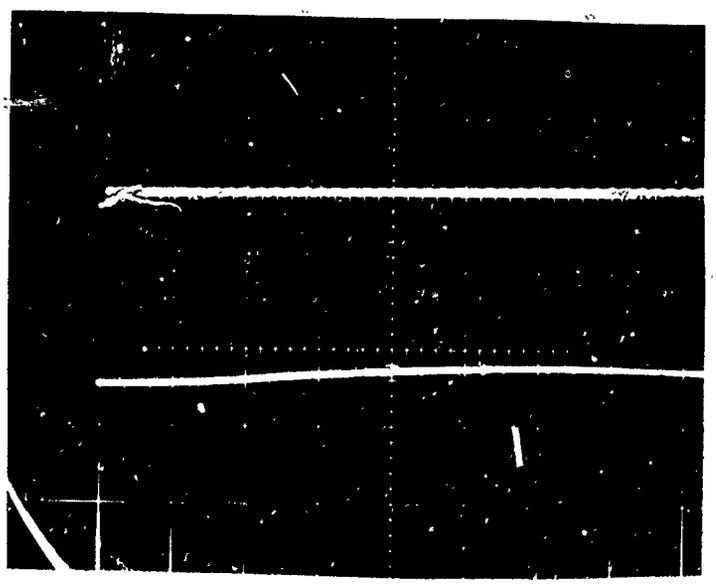

Horizontal 50 μ sec /cm

Vertical 0.5 volt /cm

AFTER

Horizontal 500 μ sec / cm

Vertical 0.5 volt / cm

BURST # 6 DATE 8/18/71

FUNCTION Start Monitor

Same as "After" photo on page A12

Horizontal 50 μsec/ cm

Vertical 1 Volt / cm

BEFORE

Horizontal 500 μsec -m

Vertical 1 Volt 1 /cm

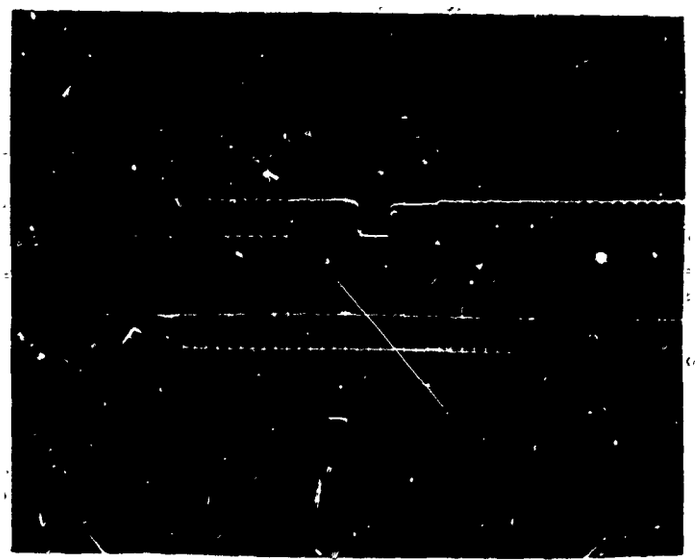

Horizontal 50μsec /cm

Vertical 1 Volt 1 /cm

DURING

Horizontal 500μsec /cm

Vertical 1 Volt 1 /cm

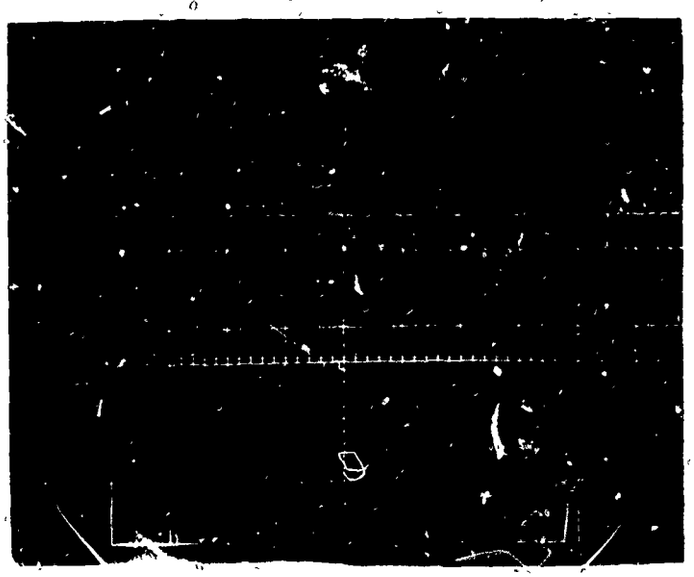

Horizontal 50μsec /cm

Vertical 1 Volt 1 /cm

AFTER

Horizontal 500μsec / cm

Vertical 1 Volt / cm

BURST # 6 DATE 8/18/71

FUNCTION Readout Trigger S/N 4

Same as "After" photo on page A13

Horizontal 50 μ sec/ cm

Vertical 1 Volt/ cm

BEFORE

Horizontal 500 μ sec /cm

Vertical 1 Volt /cm

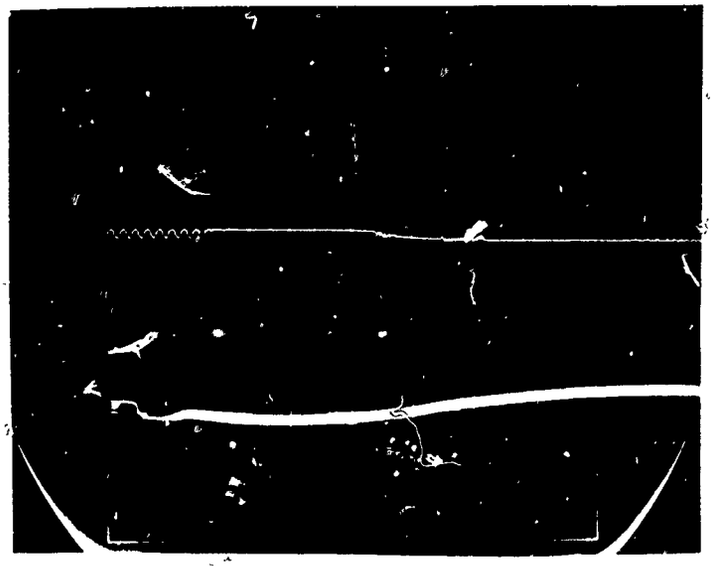

Horizontal 50 μ sec /cm

Vertical 1 Volt /cm

DURING

Horizontal 500 μ sec /cm

Vertical 1 Volt /cm

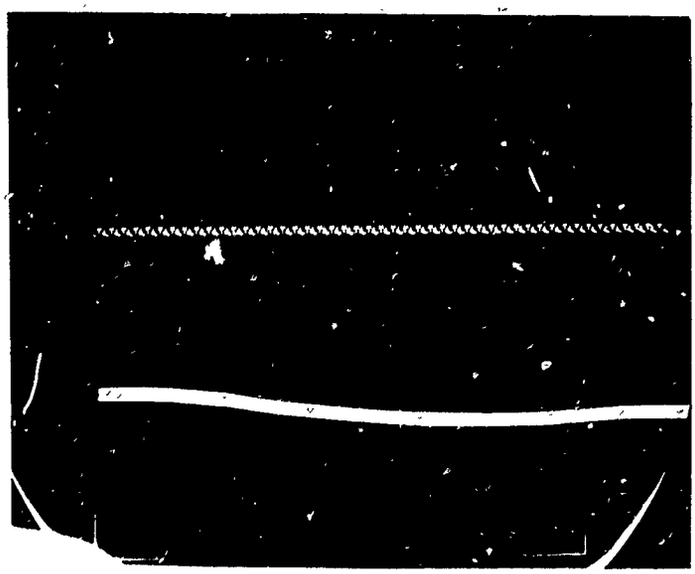

Horizontal 50 μ sec /cm

Vertical 1 Volt /cm

AFTER

Horizontal 500 μ sec/ cm

Vertical 1 Volt / cm

BURST # 6 DATE 8/18/71

FUNCTION Readout/Trigger S/N 3

Same as "After" photo on page A14

Horizontal 500 μ sec/ cm

Vertical 1 Volt/ cm

BEFORE

Horizontal 500 μ sec /cm

Vertical 1 Volt /cm

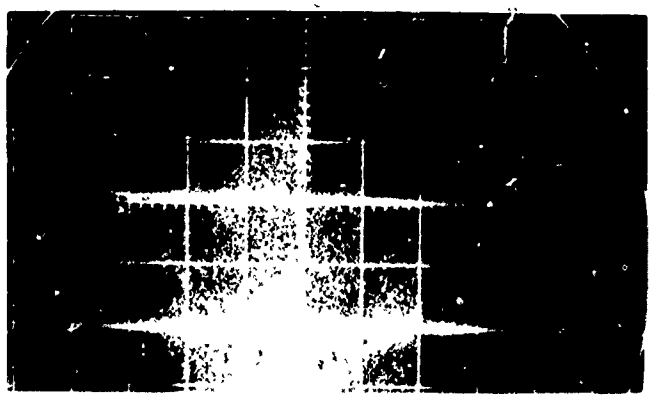

Horizontal 500 μ sec /cm

Vertical 1 Volt /cm

DURING

Horizontal 500 μ sec /cm

Vertical 1 Volt /cm

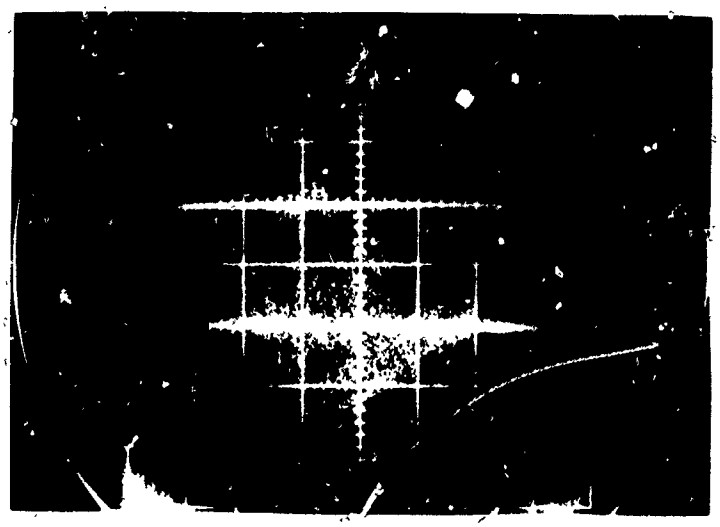

Horizontal 500 μ sec /cm

Vertical 1 Volt /cm

AFTER

Horizontal 500 μ sec / cm

Vertical 1 Volt / cm

BURST # 6 DATE 8/18/71

FUNCTION Germanium Photodetector

Same as "After" photo on page A16

Horizontal 50 μ sec/ cm

Vertical 10 Volt/ cm

BEFORE

Horizontal 500 μ sec /cm

Vertical 10 Volt /cm

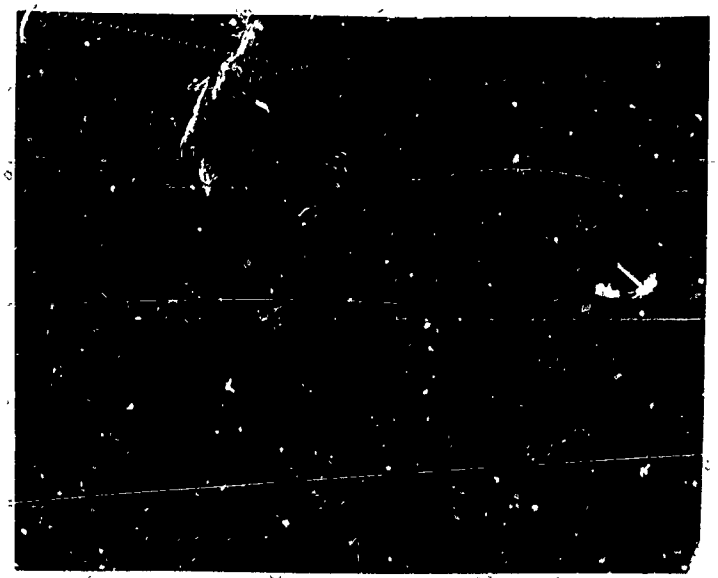

Horizontal 50 μ sec /cm

Vertical 10 Volt /cm

DURING

Horizontal 500 μ sec /cm

Vertical 10 Volt /cm

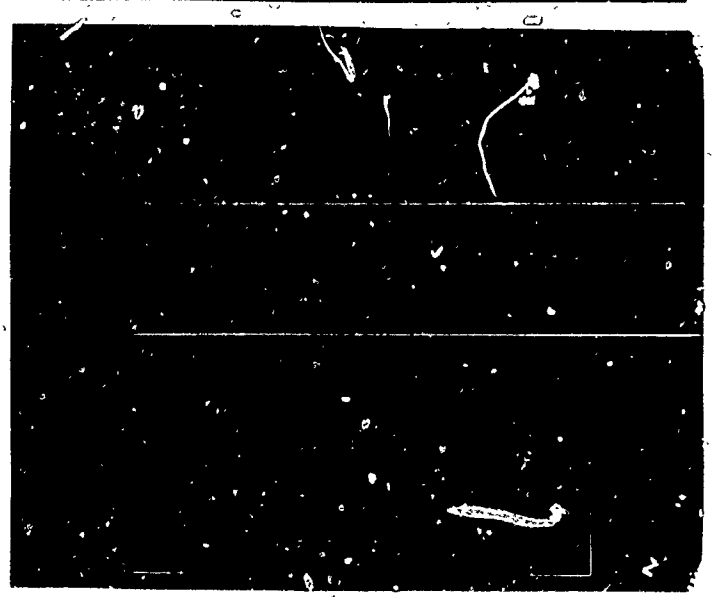

Horizontal 50 μ sec /cm

Vertical 10 Volt /cm

AFTER

Horizontal 500 μ sec cm

Vertical 10 Volt cm

BURST # 7 DATE 8/18/71

FUNCTION 10 Volt Regulator

Same as "After" photo on page A17

Horizontal 50 μsec/ cm

Vertical 0.5 Volt/ cm

BEFORE

Horizontal 500 μsec /cm

Vertical 0.5 Volt /cm

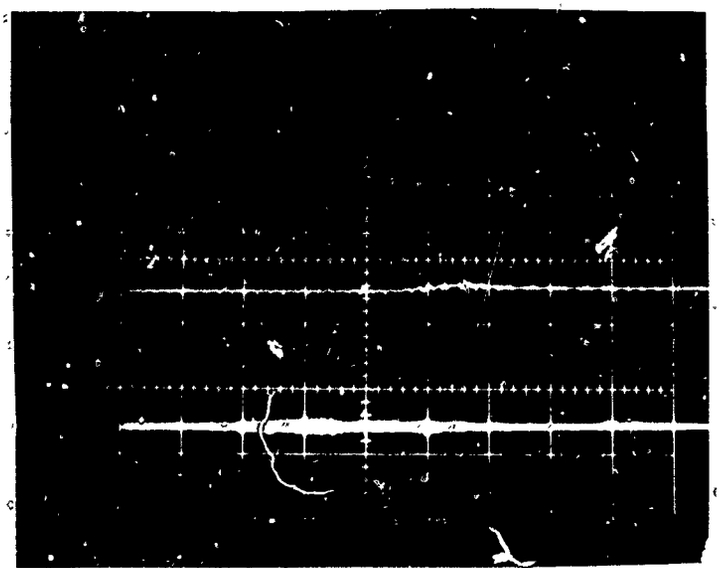

Horizontal 50 μsec /cm

Vertical 0.5 Volt /cm

DURING

Horizontal 500 μsec /cm

Vertical 0.5 Volt /cm

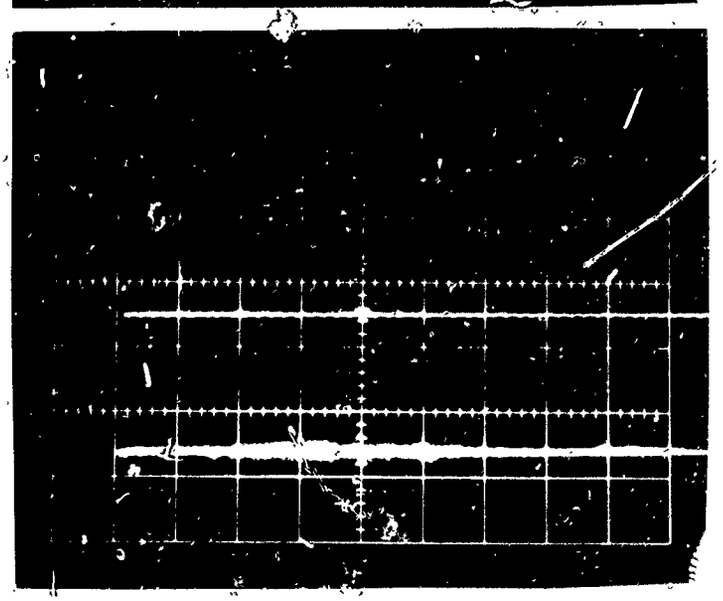

Horizontal 50 μsec /cm

Vertical 0.5 Volt /cm

AFTER

Horizontal 500 μsec cm

Vertical 0.5 Volt cm

BURST # 7 DATE 8/18/71

FUNCTION - 1000 Volt Supply

Same as the "After" photo on page A18

Horizontal 50 μ sec/ cm

Vertical 0.5 Volt/ cm

BEFORE

Horizontal 500 μ sec /cm

Vertical 0.5 Volt /cm

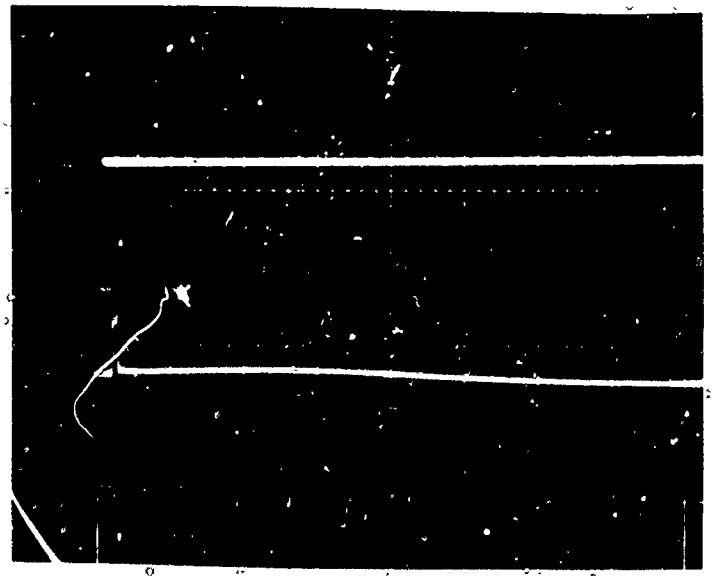

Horizontal 50 μ sec /cm

Vertical 0.5 Volt /cm

DURING

Horizontal 500 μ sec /cm

Vertical 0.5 Volt /cm

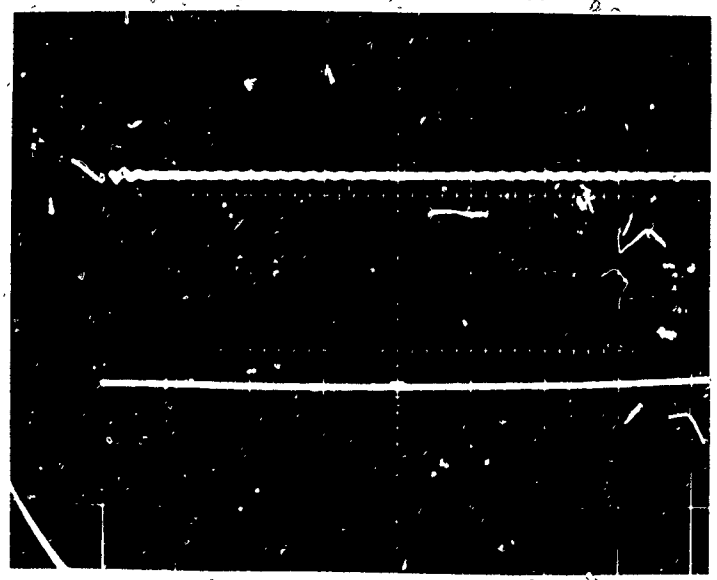

Horizontal 50 μ sec /cm

Vertical 0.5 Volt /cm

AFTER

Horizontal 500 μ sec cm

Vertical 0.5 Volt cm

BURST # 7 DATE 8/18/71

FUNCTION Start Monitor

Same as the "After" photo on page A19

Horizontal 50 μ sec/ cm

Vertical 1 Volt/ cm

BEFORE

Horizontal 500 μ sec /cm

Vertical 1 Volt /cm

Horizontal 50 μ sec /cm

Vertical 1 Volt /cm

DURING

Horizontal 500 μ sec /cm

Vertical 1 Volt /cm

Horizontal 50 μ sec /cm

Vertical 1 Volt /cm

AFTER

Horizontal 500 μ sec cm

Vertical 1 Volt cm

BURST # 7 DATE 8/18/71

FUNCTION Readout/Trigger Serial #4

Same as the "After" photo on page A20

Horizontal 50 μ sec/ cm

Vertical 1 Volt/ cm

BEFORE

Horizontal 500 μ sec /cm

Vertical 1 Volt /cm

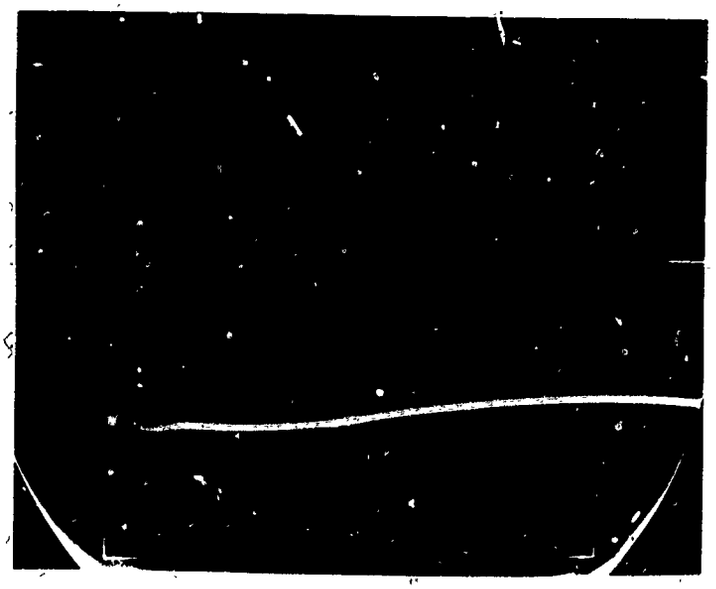

Horizontal 50 μ sec /cm

Vertical 1 Volt /cm

DURING

Horizontal 500 μ sec /cm

Vertical 1 Volt /cm

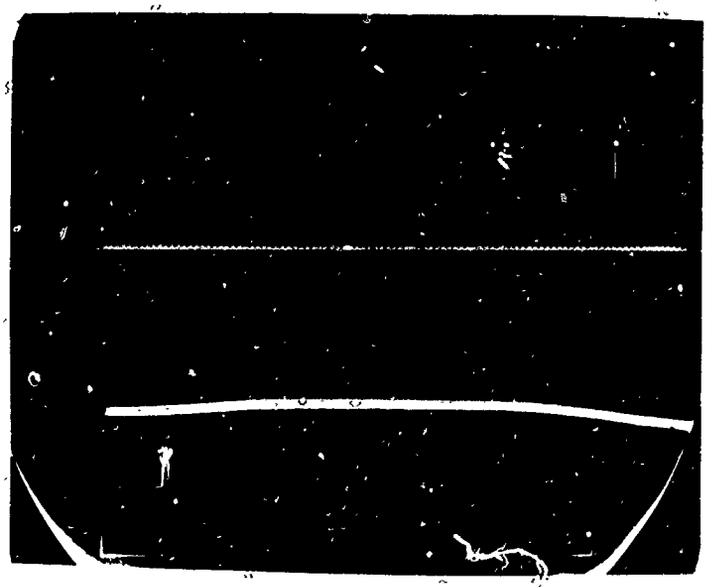

Horizontal 50 μ sec /cm

Vertical 1 Volt /cm

AFTER

Horizontal 500 μ sec cm

Vertical 1 Volt cm

BURST # 7 DATE 8/18/71

FUNCTION Readout/Trigger Serial #3

Same as the "After" photo on page A21

Horizontal 500 μsec/ cm

Vertical 0.1 Volt/ cm

BEFORE

Horizontal 500 μsec /cm

Vertical 0.1 Volt /cm

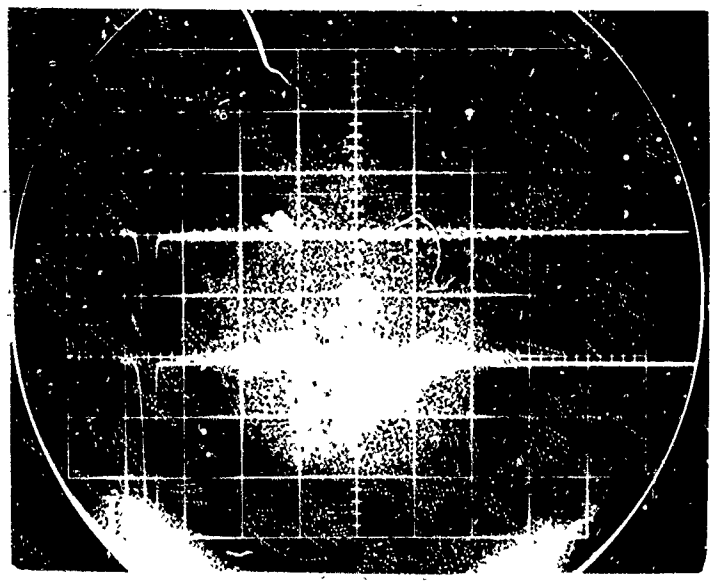

Horizontal 500 μsec /cm

Vertical 0.1 Volt /cm

DURING

Horizontal 500 sec /cm

Vertical 0.1 Volt /cm

Horizontal 500 μsec /cm

Vertical 0.1 Volt /cm

AFTER

Horizontal 500 μsec cm

Vertical 0.1 Volt cm

BURST # 7 DATE 8/18/71

FUNCTION Germanium Photodetector

Horizontal 50 μsec/ cm

Vertical 10 Volt/ cm

BEFORE

Horizontal 500 μsec /cm

Vertical 10 Volt /cm

Horizontal 50 μsec /cm

Vertical 10 Volt /cm

DURING

Horizontal 500 μsec /cm

Vertical 10 Volt /cm

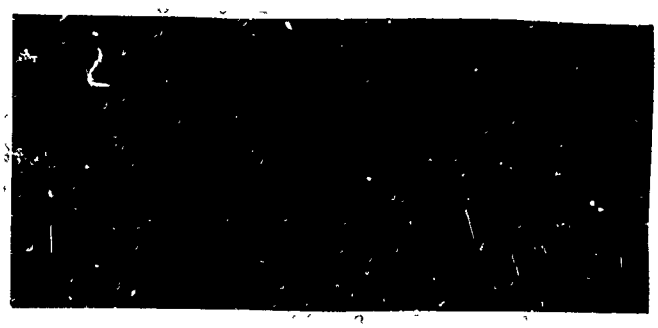

Horizontal 50 μsec /cm

Vertical 10 Volt /cm

AFTER

Horizontal 500 μsec cm

Vertical 10 Volt cm

BURST # 8 DATE 8/19/71

FUNCTION 10 Volt Regulator

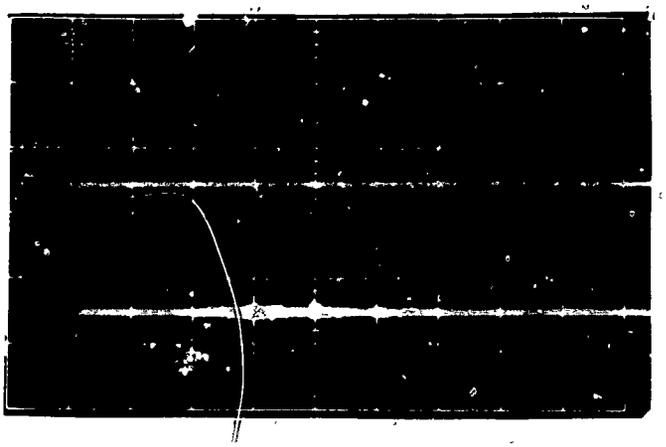

Horizontal 50 μ sec/ cm

Vertical 0.5 Volt/ cm

BEFORE

Horizontal 500 μ sec /cm

Vertical 0.5 Volt /cm

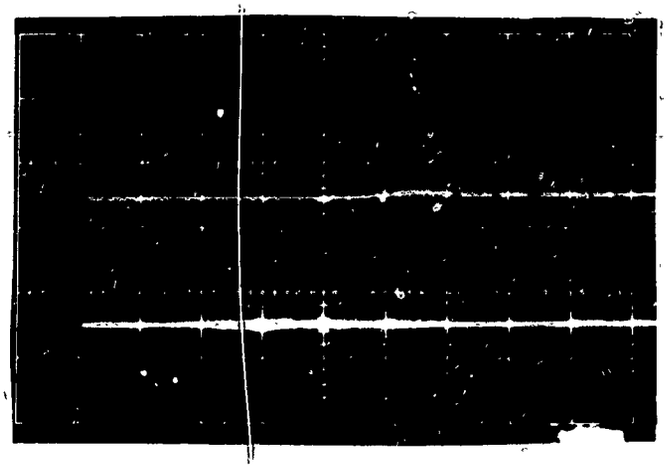

Horizontal 50 μ sec /cm

Vertical 0.5 Volt /cm

DURING

Horizontal 500 μ sec /cm

Vertical 0.5 Volt /cm

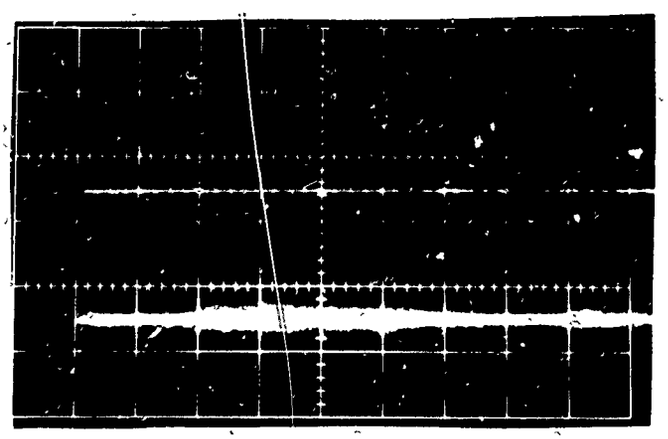

Horizontal 50 μ sec /cm

Vertical 0.5 Volt /cm

AFTER

Horizontal 500 μ sec/ cm

Vertical 0.5 Volt/ cm

BURST # 8 DATE 8/19/71

FUNCTION -1000 Volt Supply

Horizontal 50 μ sec/ cm

Vertical 0.5 Volt/ cm

BEFORE

Horizontal 500 μ sec /cm

Vertical 0.5 Volt /cm

Horizontal 50 μ sec /cm

Vertical 0.5 Volt /cm

DURING

Horizontal 500 μ sec /cm

Vertical 0.5 Volt /cm

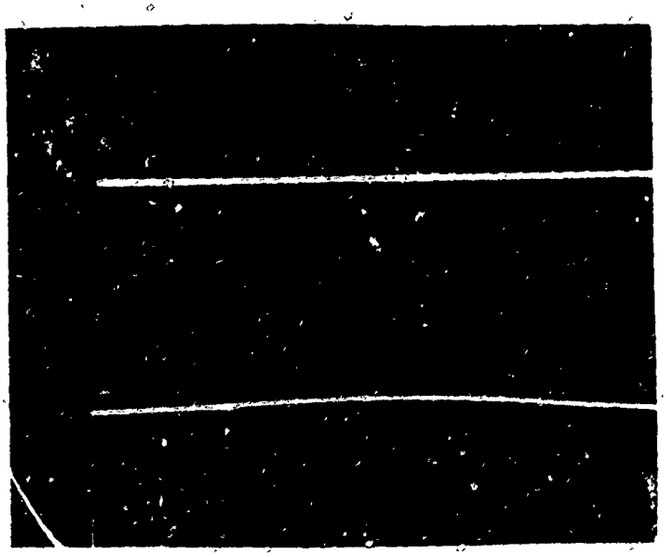

Horizontal 50 μ sec /cm

Vertical 0.5 Volt /cm

AFTER

Horizontal 500 μ sec/ cm

Vertical 0.5 Volt/ cm

BURST # 8 DATE 8/19/71

FUNCTION Start Monitor

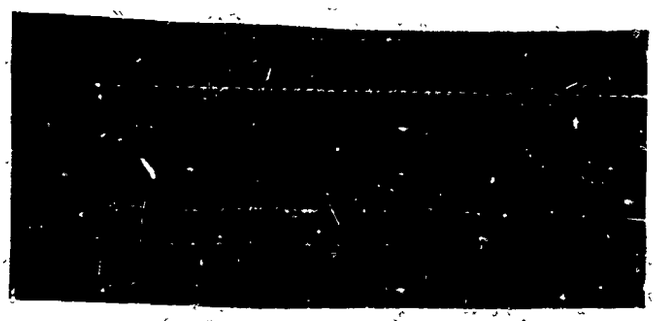

Horizontal 50 μsec/ cm

Vertical 1 Volt/ cm

BEFORE

Horizontal 500 μsec /cm

Vertical 1 Volt /cm

Horizontal 50 μ sec /cm

Vertical 1 Volt /cm

DURING

Horizontal 500 μsec /cm

Vertical 1 Volt /cm

Horizontal 50 μ sec /cm

Vertical 1 Volt /cm

AFTER

Horizontal 500 μsec cm

Vertical 1 Volt cm

BURST # 8 DATE 8/19/71

FUNCTION Readout/Trigger Serial #4

Horizontal 50 μ sec/ cm

Vertical 1 Volt/ cm

BEFORE

Horizontal 500 μsec/ /cm

Vertical 1 Volt /cm

Horizontal 50 μ sec /cm

Vertical 1 Volt /cm

DURING

Horizontal 500 μsec /cm

Vertical 1 Volt /cm

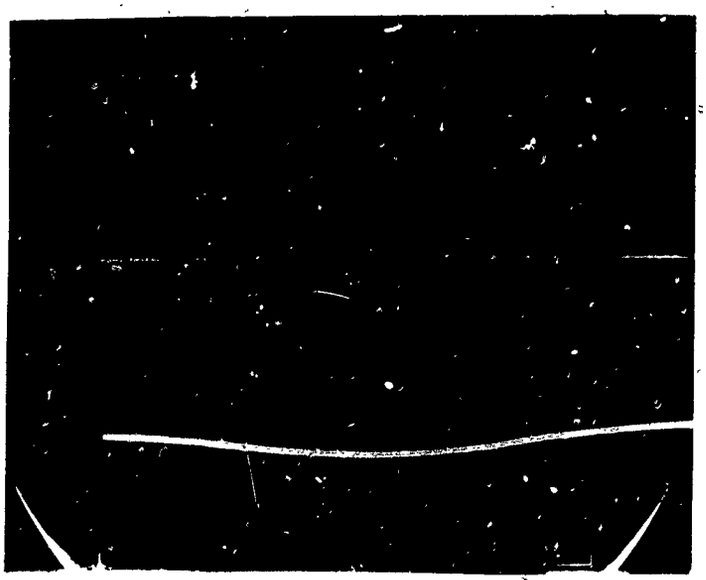

Horizontal 50 μ sec /cm

Vertical 1 Volt /cm

AFTER

Horizontal 500 μsec/ cm

Vertical 1 Volt/ cm

BURST # 8 DATE 8/19/71

FUNCTION Readout/Trigger Serial #3

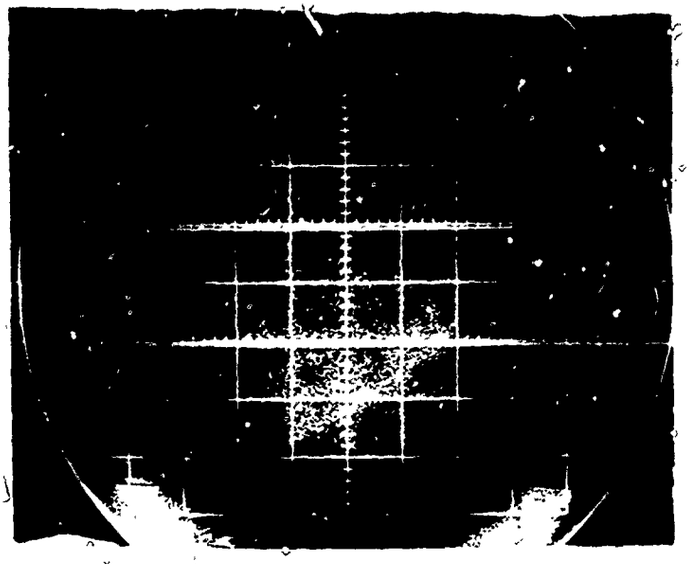

Horizontal 100 μ sec/ cm

Vertical 0.5 Volt/ cm

BEFORE

Horizontal 100 μ sec /cm

Vertical 0.5 Volt /cm

Horizontal 100 μ sec /cm

Vertical 0.5 Volt /cm

DURING

Horizontal 100 μ sec /cm

Vertical 0.5 Volt /cm

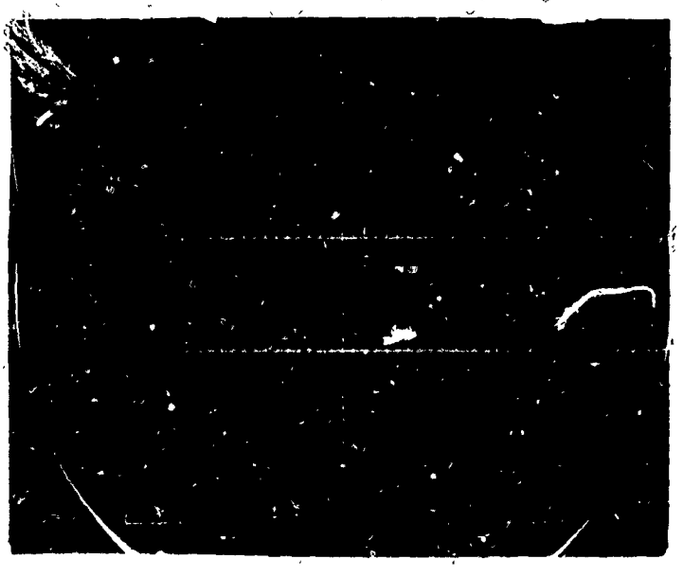

Horizontal 100 μ sec /cm

Vertical 0.5 Volt /cm

AFTER

Horizontal 100 μ sec/ cm

Vertical 0.5 Volt/ cm

BURST # 8 DATE 8/19/71

FUNCTION Germanium Photodetector

Horizontal 50 μsec/ cm

Vertical 5 Volt/ cm

BEFORE

Horizontal 500 μsec /cm

Vertical 5 Volt /cm

Horizontal 50 μsec /cm

Vertical 5 Volt /cm

DURING

Horizontal 500 μsec /cm

Vertical 5 Volt /cm

Horizontal 50 μsec /cm

Vertical 5 Volt /cm

AFTER

Horizontal 500 μsec/ cm

Vertical 5 Volt/ cm

BURST # 9 DATE 8/19/71

FUNCTION Slow Digital Pulses (Up)

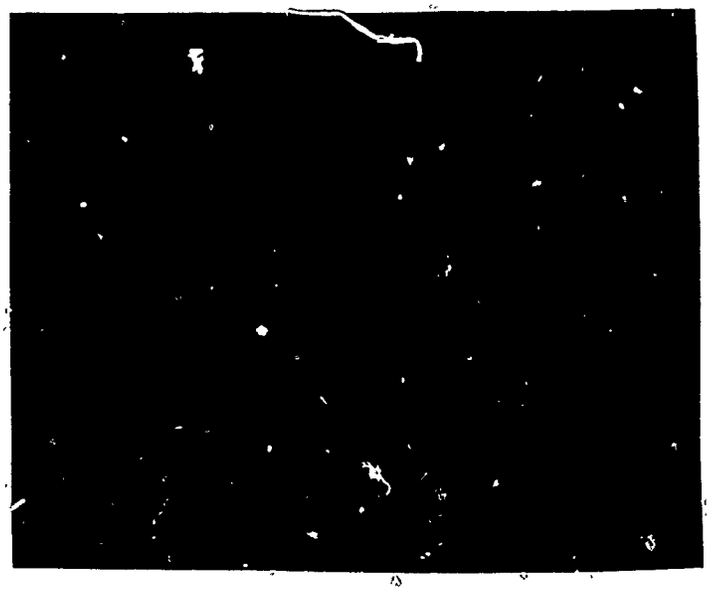

Horizontal 50 μ sec/ cm

Vertical 5 Volt/ cm

BEFORE

Horizontal 500 μ sec /cm

Vertical 5 Volt /cm

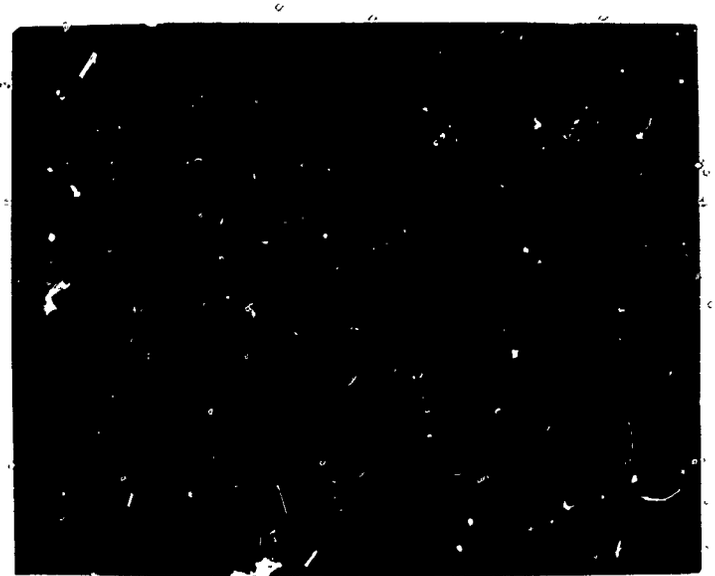

Horizontal 50 μ sec /cm

Vertical 5 Volt /cm

DURING

Horizontal 500 μ sec /cm

Vertical 5 Volt /cm

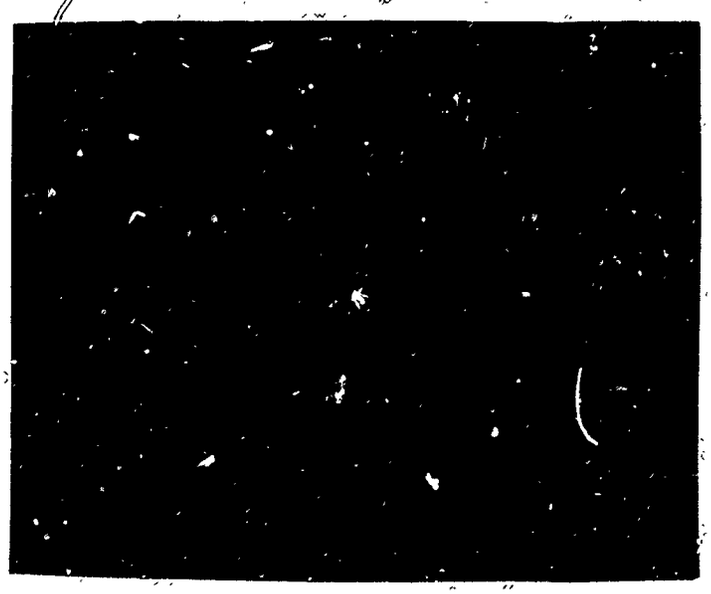

Horizontal 50 μ sec /cm

Vertical 5 Volt /cm

AFTER

Horizontal 500 μ sec/ cm

Vertical 5 Volt/ cm

BURST # 9 DATE 8/19/71

FUNCTION Slow Digital Pulses (Down)

Horizontal 20 μsec/ cm

Vertical 2 Volt/ cm

BEFORE

Horizontal 200 μsec /cm

Vertical 2 Volt /cm

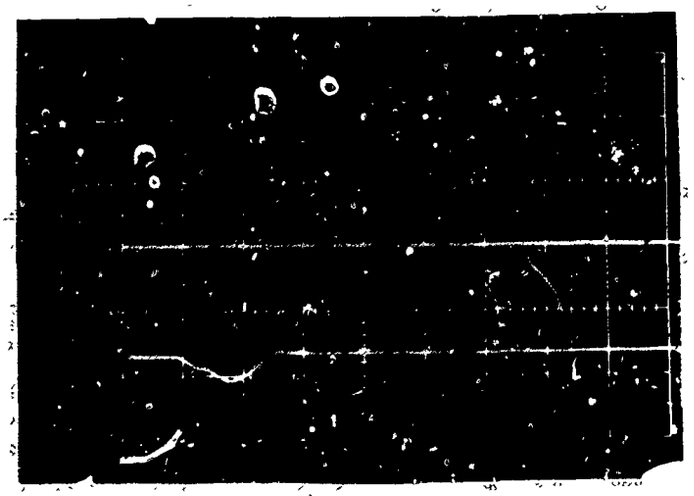

Horizontal 20 μ sec /cm

Vertical 2 Volt /cm

DURING

Horizontal 200 μsec /cm

Vertical 2 Volt /cm

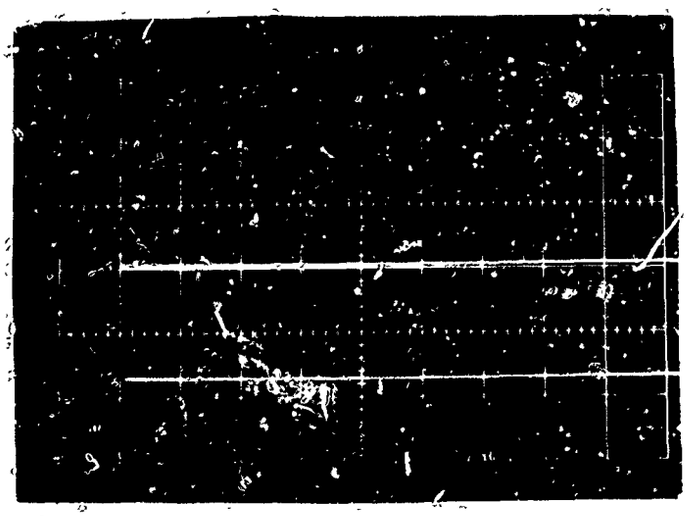

Horizontal 20 μ sec /cm

Vertical 2 Volt /cm

AFTER

Horizontal 200 μ sec/ cm

Vertical 2 Volt/ cm

BURST # 9 DATE 8/19/71

FUNCTION Fast Digital Pulses (Up)

Horizontal 20 μsec/ cm

Vertical 2 Volt/ cm

BEFORE

Horizontal 200 μsec /cm

Vertical 2 Volt /cm

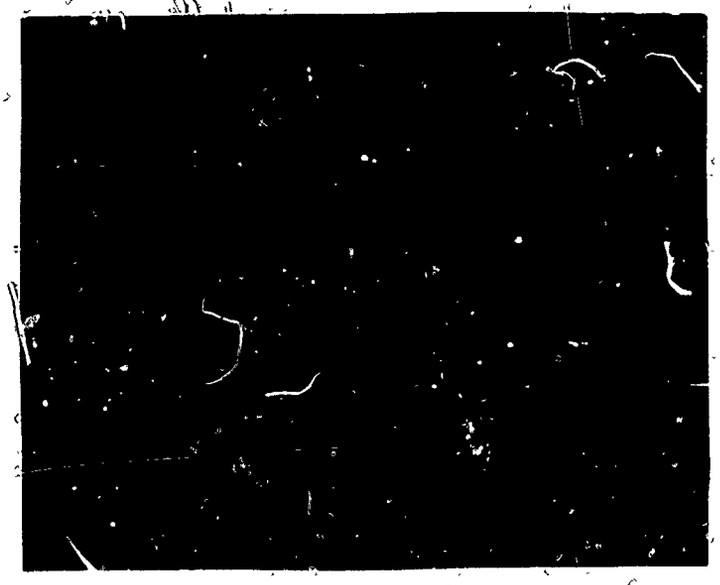

Horizontal 20 μsec /cm

Vertical 2 Volt /cm

DURING

Horizontal 200 μsec /cm

Vertical 2 Volt /cm

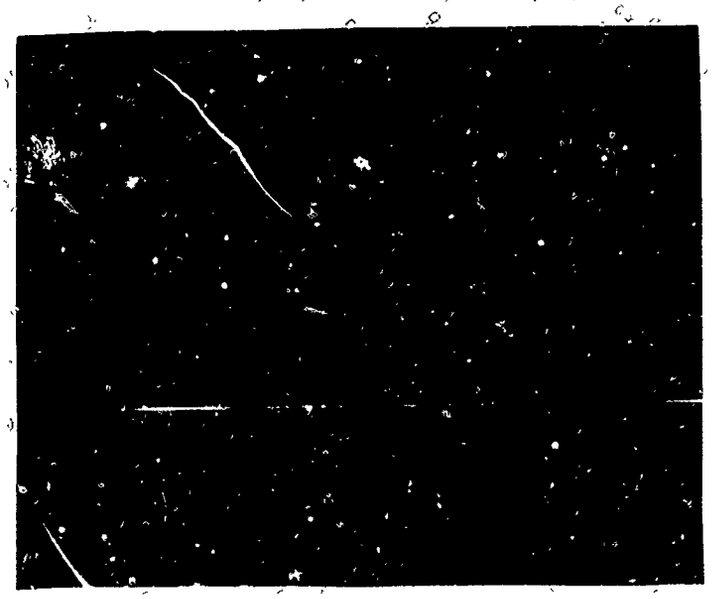

Horizontal 20 μsec /cm

Vertical 2 Volt /cm

AFTER

Horizontal 200 μsec/ cm

Vertical 2 Volt/ cm

BURST # 9 DATE 8/19/71

FUNCTION Fast Digital Pulses (Down)

Horizontal 50 μ sec/ cm

Vertical 1 Volt/ cm

BEFORE

Horizontal 500 μ sec /cm

Vertical 1 Volt /cm

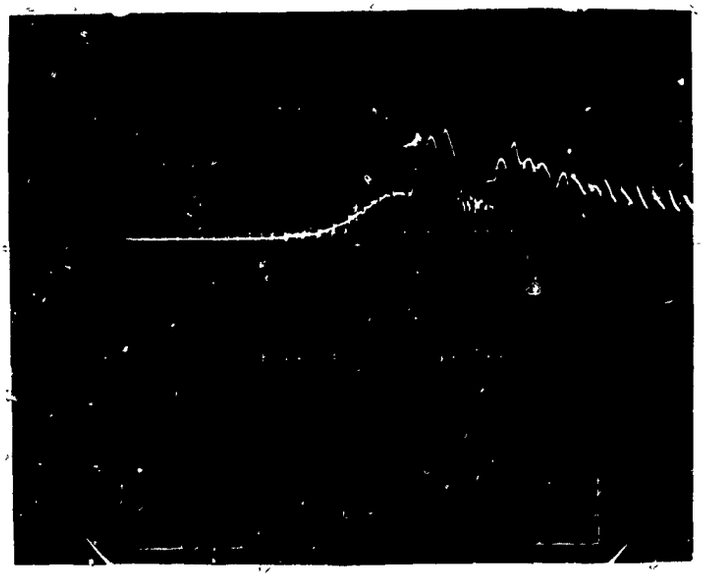

Horizontal 50 μ sec /cm

Vertical 1 Volt /cm

DURING

Horizontal 500 μ sec /cm

Vertical 1 Volt /cm

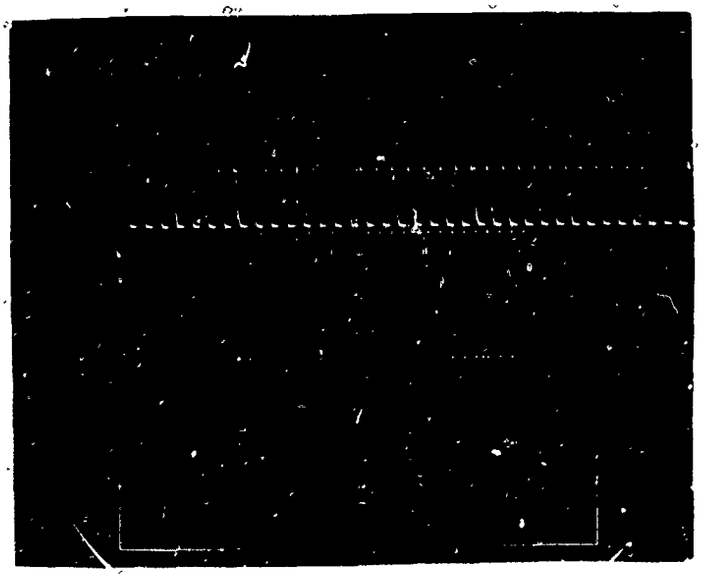

Horizontal 50 μ sec /cm

Vertical 1 Volt /cm

AFTER

Horizontal 500 μ sec/ cm

Vertical 1 Volt/ cm

BURST # 9 DATE 8/19/71

FUNCTION Start Monitor

Horizontal 500 μsec/ cm

Vertical 10 Volt/ cm

BEFORE

Horizontal 500 μ sec /cm

Vertical 5 Volt /cm

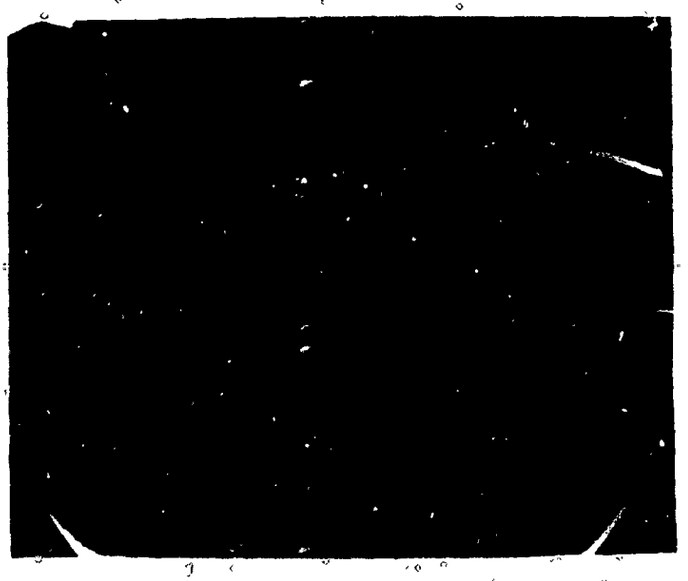

Horizontal 500 μ sec /cm

Vertical 10 Volt /cm

DURING

Horizontal 500 μ sec /cm

Vertical 5 Volt /cm

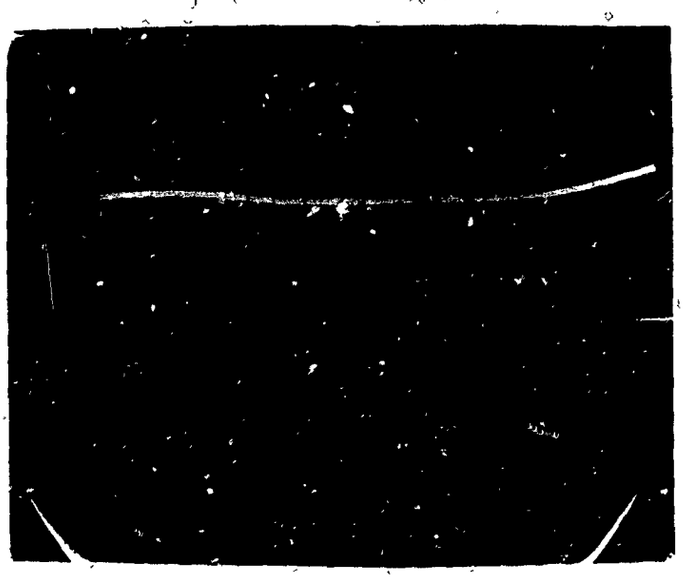

Horizontal 500 μ sec /cm

Vertical 10 Volt /cm

AFTER

Horizontal 500 μ sec/ cm

Vertical 5 Volt/ cm

BURST # 9 DATE 8/19/71

FUNCTION Upper Trace 10V; Lower 5V Supplies

Horizontal 100 μ sec/ cm

Vertical 0.5 Volt/ cm

BEFORE

Horizontal 100 μ sec /cm

Vertical 0.5 Volt /cm

Horizontal 100 μ sec /cm

Vertical 0.5 Volt /cm

DURING

Horizontal 100 μ sec /cm

Vertical 0.5 Volt /cm

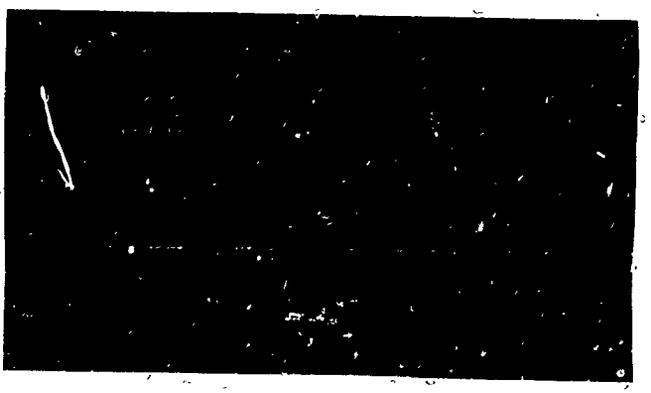

Horizontal 100 μ sec /cm

Vertical 0.5 Volt /cm

AFTER

Horizontal 100 μ sec/ cm

Vertical 0.5 Volt/ cm

BURST # 9 DATE 8/19/71

FUNCTION Germanium Photodetector

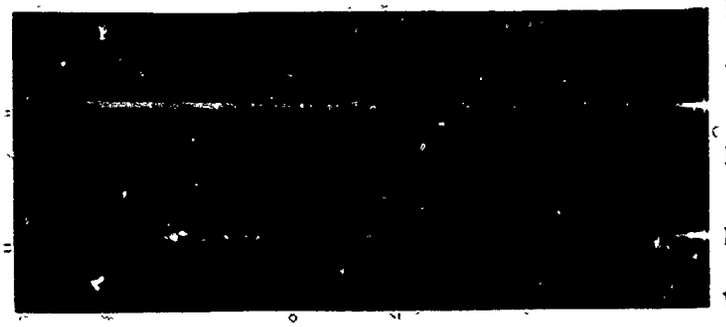

Horizontal 50 μ sec/ cm
Vertical 5 Volt/ cm

BEFORE

Horizontal 500 μsec /cm
Vertical 5 Volt /cm

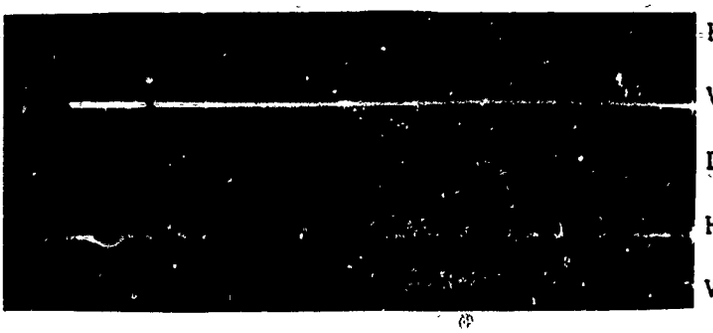

Horizontal 50 μ sec /cm
Vertical 5 Volt /cm

DURING

Horizontal 500 μ sec /cm
Vertical 5 Volt /cm

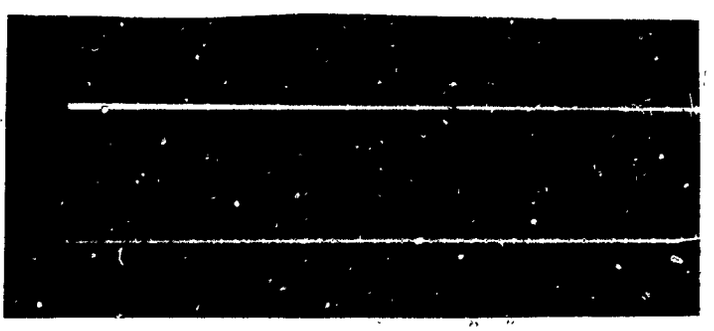

Horizontal 50 μ sec /cm
Vertical 5 Volt /cm

AFTER

Horizontal 500 μ sec/ cm
Vertical 5 Volt/ cm

BURST # 10 DATE 8/19/71

FUNCTION Slow Digital Pulses (Up)

Horizontal 50 μ sec/ cm

Vertical 5 Volt/ cm

BEFORE

Horizontal 500 μ sec /cm

Vertical 5 Volt /cm

Horizontal 50 μ sec /cm

Vertical 5 Volt /cm

DURING

Horizontal 500 μ sec /cm

Vertical 5 Volt /cm

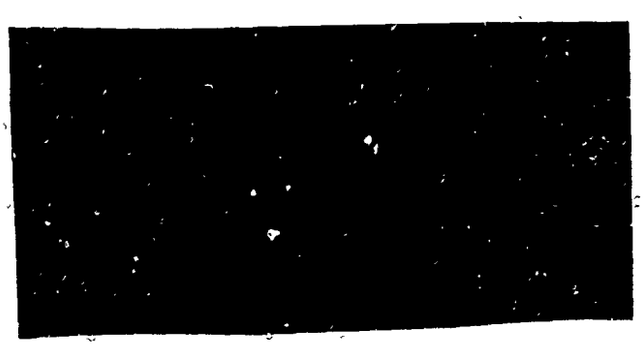

Horizontal 50 μ sec /cm

Vertical 5 Volt /cm

AFTER

Horizontal 500 μ sec/ cm

Vertical 5 Volt/ cm

BURST # 10 DATE 8/19/71

FUNCTION Slow Digital Pulses (Down)

Horizontal 20 μsec/ cm
Vertical 2 Volt/ cm

BEFORE

Horizontal 200 μ sec /cm
Vertical 2 Volt /cm

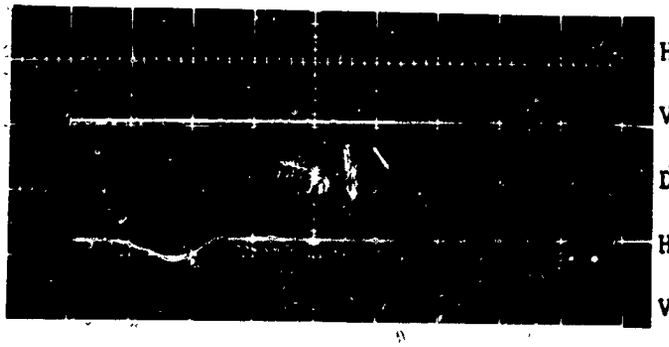

Horizontal 20 μ sec /cm
Vertical 2 Volt /cm

DURING

Horizontal 200 μ sec /cm
Vertical 2 Volt /cm

Horizontal 20 μ sec /cm
Vertical 2 Volt /cm

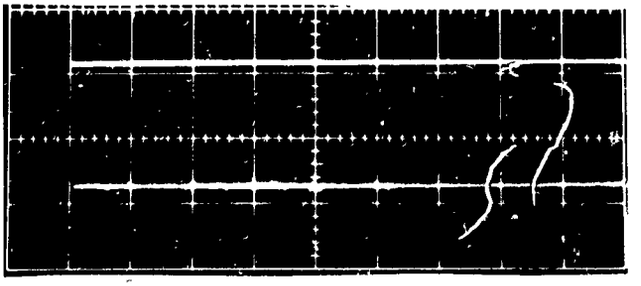

AFTER

Horizontal 200 μ sec/ cm
Vertical 2 Volt/ cm

BURST # 10 DATE 8/19/71

FUNCTION Fast Digital Pulses (Up)

Horizontal 20 μsec/ cm

Vertical 2 Volt/ cm

BEFORE

Horizontal 200 μ sec /cm

Vertical 2 Volt /cm

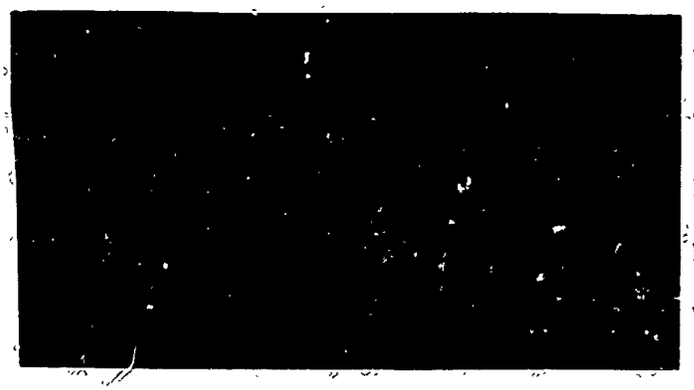

Horizontal 20 μ sec /cm

Vertical 2 Volt /cm

DURING

Horizontal 200 μ sec /cm

Vertical 2 Volt /cm

Horizontal 20 μ sec /cm

Vertical 2 Volt /cm

AFTER

Horizontal 200 μ sec/ cm

Vertical 2 Volt/ cm

BURST # 10 DATE 8/19/71

FUNCTION Fast Digital Pulses (Down)

Horizontal 50 μsec/ cm

Vertical 1 Volt/ cm

BEFORE

Horizontal 500 μsec /cm

Vertical 1 Volt /cm

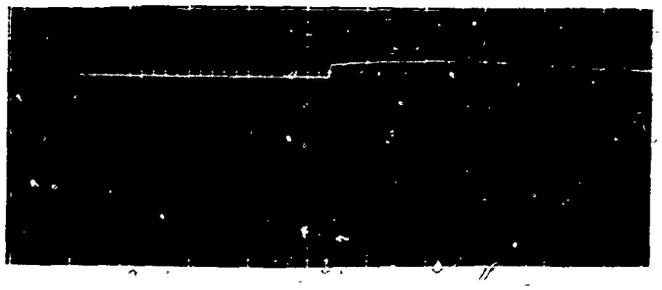

Horizontal 50 μsec /cm

Vertical 1 Volt /cm

DURING

Horizontal 500 μsec /cm

Vertical 1 Volt /cm

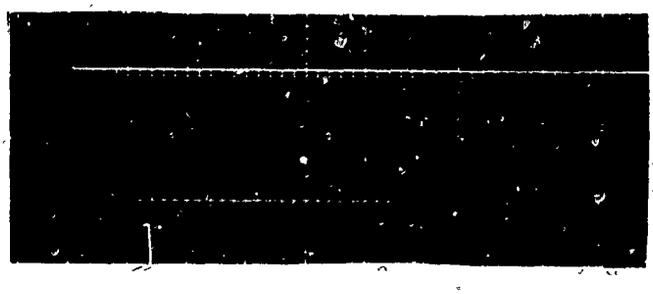

Horizontal 50 μsec /cm

Vertical 1 Volt /cm

AFTER

Horizontal 500 μsec/ cm

Vertical 1 Volt/ cm

BURST # 10 DATE 8/19/71

FUNCTION Start Monitor

Horizontal 500 μsec/ cm

Vertical 10 Volt/ cm

BEFORE

Horizontal 500 μsec /cm

Vertical 5 Volt /cm

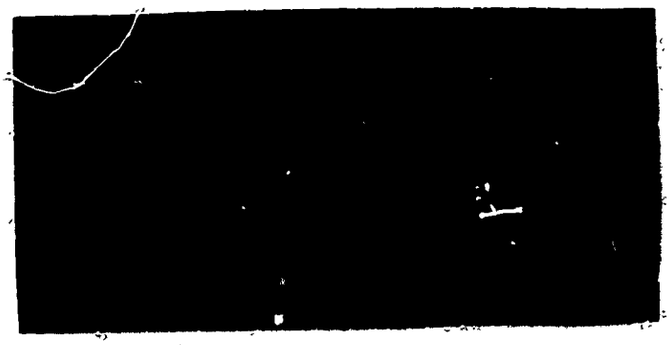

Horizontal 500 μ sec /cm

Vertical 10 Volt /cm

DURING

Horizontal 500 μ sec /cm

Vertical 5 Volt /cm

Horizontal 500 μ sec /cm

Vertical 10 Volt /cm

AFTER

Horizontal 500 μ sec/ cm

Vertical 5 Volt/ cm

BURST # 10 DATE 8/19/71

FUNCTION Upper = 10V Supply; Lower = 5V Supply

Horizontal 100 μ sec/ cm

Vertical 0.5 Volt/ cm

BEFORE

Horizontal 100 μ sec /cm

Vertical 0.5 Volt /cm

Horizontal 100 μ sec /cm

Vertical 0.5 Volt /cm

DURING

Horizontal 100 μ sec /cm

Vertical 0.5 Volt /cm

Horizontal 100 μ sec /cm

Vertical 0.5 Volt /cm

AFTER

Horizontal 100 μ sec/ cm

Vertical 0.5 Volt/ cm

BURST # 10 DATE 8/19/71

FUNCTION Germanium Photodetector

Horizontal 50 μsec/ cm
Vertical 5 Volt/ cm

BEFORE

Horizontal 500 μ sec /cm
Vertical 5 Volt /cm

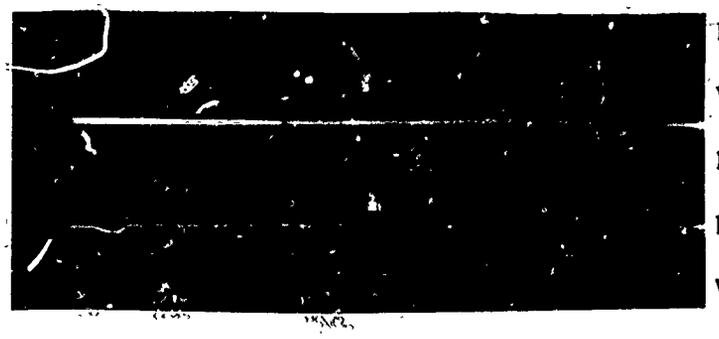

Horizontal 50 μsec /cm
Vertical 5 Volt /cm

DURING

Horizontal 500 μ sec /cm
Vertical 5 Volt /cm

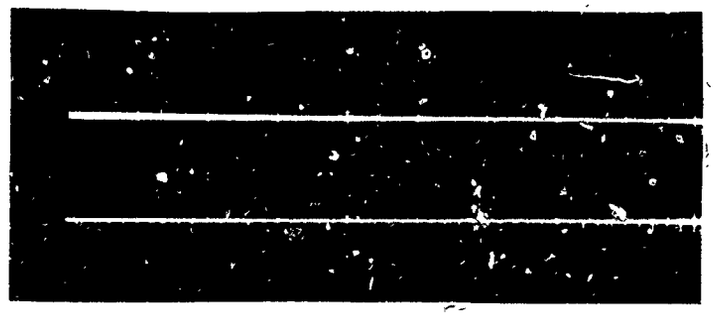

Horizontal 50 μ sec /cm
Vertical 5 Volt /cm

AFTER

Horizontal 500 μ sec/ cm
Vertical 5 Volt/ cm

BURST # 11 DATE 8/20/71

FUNCTION Slow Digital Pulses (Up)

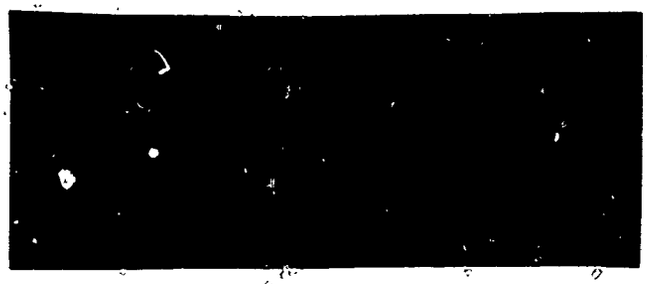

Horizontal 50 μ sec/ cm
Vertical 5 Volt/ cm

BEFORE

Horizontal 500 μ sec /cm
Vertical 5 Volt /cm

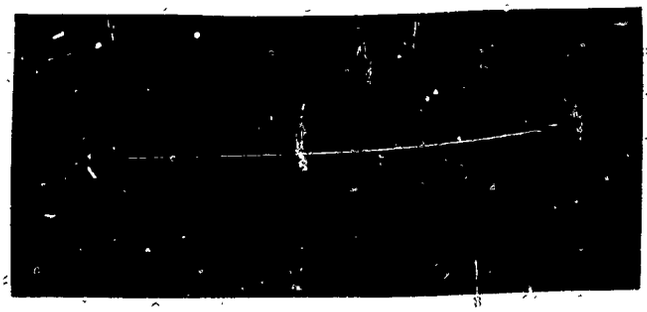

Horizontal 50 μ sec /cm
Vertical 5 Volt /cm

DURING

Horizontal 500 μ sec /cm
Vertical 5 Volt /cm

Horizontal 50 μ sec /cm
Vertical 5 Volt /cm

AFTER

Horizontal 500 μ sec/ cm
Vertical 5 Volt/ cm

BURST # 11 DATE 8/20/71

FUNCTION Slow Digital Pulses (Down)

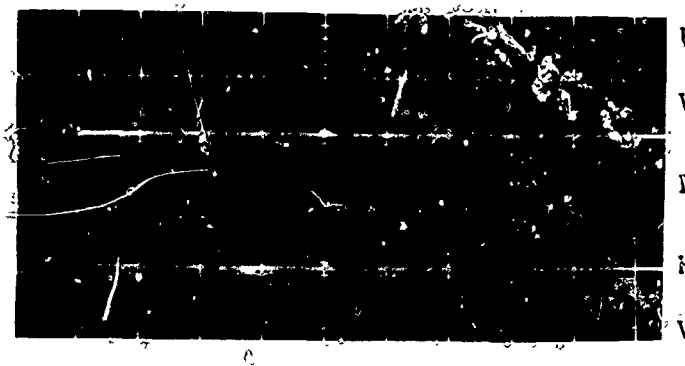

Horizontal 20 μsec/ cm
Vertical 2 Volt/ cm

BEFORE

Horizontal 200 μsec /cm
Vertical 2 Volt /cm

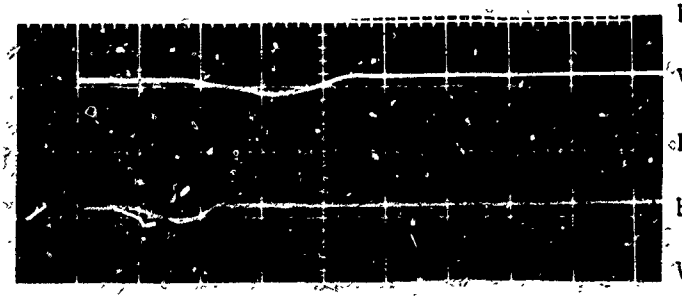

Horizontal 20 μsec /cm
Vertical 2 Volt /cm

DURING

Horizontal 200 μ sec /cm
Vertical 2 Volt /cm

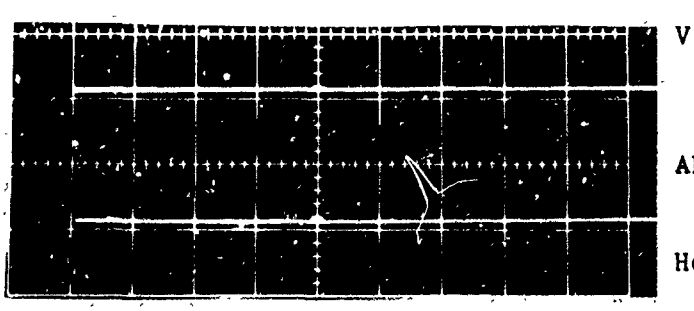

Horizontal 20 μ sec /cm
Vertical 2 Volt /cm

AFTER

Horizontal 200 μ sec/ cm
Vertical 2 Volt/ cm

BURST # 11 DATE 8/20/71

FUNCTION Fast Digital Pulses (Up)

Horizontal 20 μsec/ cm

Vertical 2 Volt/ cm

BEFORE

Horizontal 200 μ sec /cm

Vertical 2 Volt /cm

Horizontal 20 μ sec /cm

Vertical 2 Volt /cm

DURING

Horizontal 200 μ sec /cm

Vertical 2 Volt /cm

Horizontal 20 μ sec /cm

Vertical 2 Volt /cm

AFTER

Horizontal 200 μ sec/ cm

Vertical 2 Volt/ cm

BURST # 11 DATE 8/20/71

FUNCTION Fast Digital Pulses (Down)

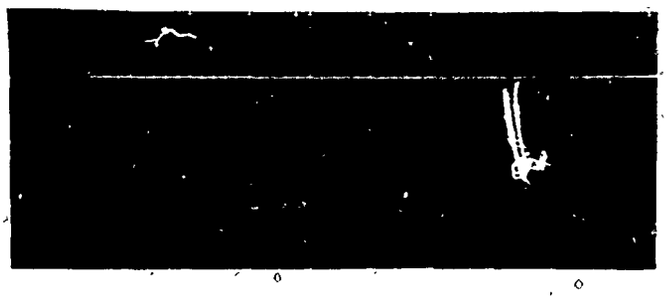

Horizontal 50 μ sec/ cm

Vertical 1 Volt/ cm

BEFORE

Horizontal 500 μ sec /cm

Vertical 1 Volt /cm

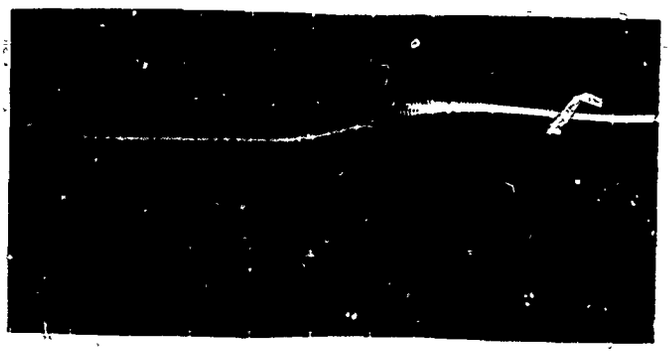

Horizontal 50 μ sec /cm

Vertical 1 Volt /cm

DURING

Horizontal 500 μ sec /cm

Vertical 1 Volt /cm

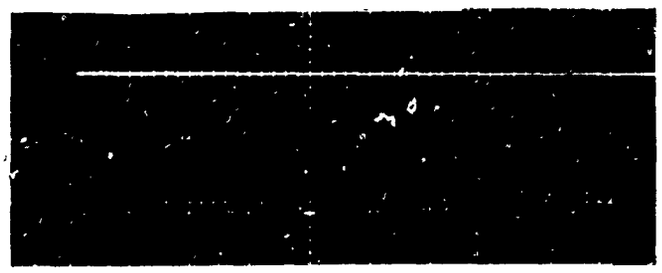

Horizontal 50 μ sec /cm

Vertical 1 Volt /cm

AFTER

Horizontal 500 μ sec/ cm

Vertical 1 Volt/ cm

BURST # 11 DATE 8/20/71

FUNCTION Start Monitor

Horizontal 500 μsec/ cm
Vertical 10 Volt/ cm

BEFORE

Horizontal 500 μsec /cm
Vertical 5 Volt /cm

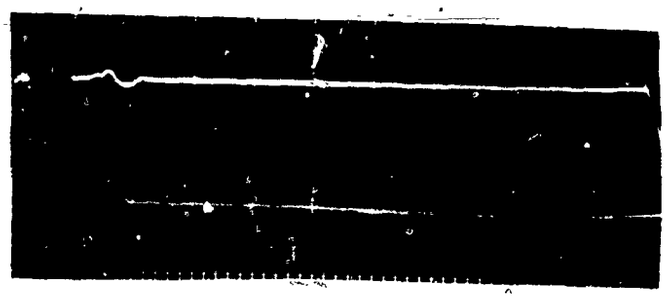

Horizontal 500 μ sec /cm
Vertical 10 Volt /cm

DURING

Horizontal 500 μ sec /cm
Vertical 5 Volt /cm

Horizontal 500 μ sec /cm
Vertical 10 Volt /cm

AFTER

Horizontal 500 μsec/ cm
Vertical 5 Volt/ cm

BURST # 11 DATE 8/20/71

FUNCTION Upper = 10 Volt Supply; Lower = 5 Volt Supply

Horizontal 100 μsec/ cm

Vertical 0.5 Volt/ cm

BEFORE

Horizontal 100 μsec /cm

Vertical 0.5 Volt /cm

Horizontal 100 μsec /cm

Vertical 0.5 Volt /cm

DURING

Horizontal 100 μ sec /cm

Vertical 0.5 Volt /cm

Horizontal 100 μ sec /cm

Vertical 0.5 Volt /cm

AFTER

Horizontal 100 μ sec/ cm

Vertical 0.5 Volt/ cm

BURST # 11 DATE 8/20/71

FUNCTION Germanium Photodetector

Horizontal 50 μsec/ cm
Vertical 5 Volt/ cm

BEFORE

Horizontal 500 μsec /cm
Vertical 5 Volt /cm

Horizontal 50 μsec /cm
Vertical 5 Volt /cm

DURING

Horizontal 500 μsec /cm
Vertical 5 Volt /cm

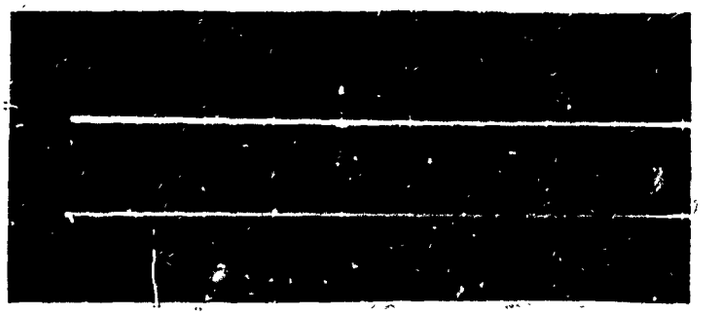

Horizontal 50 μsec /cm
Vertical 5 Volt /cm

AFTER

Horizontal 500 μsec/ cm
Vertical 5 Volt/ cm

BURST # 12 DATE. 8/20/71

FUNCTION Slow Digital Pulses (Up)

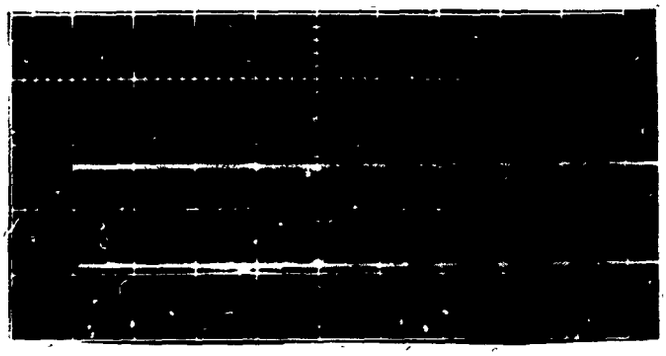

Horizontal 20 μ sec/ cm

Vertical 2 Volt/ cm

BEFORE

Horizontal 200 μ sec /cm

Vertical 2 Volt /cm

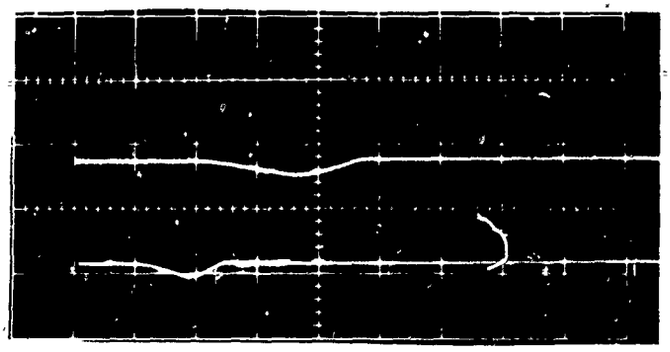

Horizontal 20 μ sec /cm

Vertical 2 Volt /cm

DURING

Horizontal 200 μ sec /cm

Vertical 2 Volt /cm

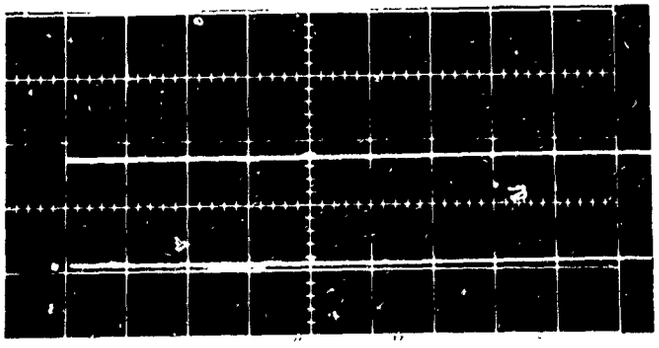

Horizontal 20 μ sec /cm

Vertical 2 Volt /cm

AFTER

Horizontal 200 μ sec/ cm

Vertical 2 Volt/ cm

BURST # 12 DATE 8/20/71

FUNCTION Fast Digital Pulses (Up)

Horizontal 20 μsec/ cm

Vertical 2 Volt/ cm

BEFORE

Horizontal 200 μsec /cm

Vertical 2 Volt /cm

Horizontal 20 μsec /cm

Vertical 2 Volt /cm

DURING

Horizontal 200 μsec /cm

Vertical 2 Volt /cm

Horizontal 20 μsec /cm

Vertical 2 Volt /cm

AFTER

Horizontal 200 μsec/ cm

Vertical 2 Volt/ cm

BURST # 12 DATE 8/20/71

FUNCTION Fast Digital Pulses (Down)

Horizontal 50 μsec/ cm

Vertical 1 Volt/ cm

BEFORE

Horizontal 500 μsec /cm

Vertical 1 Volt /cm

Horizontal 50 μ sec /cm

Vertical 1 Volt /cm

DURING

Horizontal 500 μ sec /cm

Vertical 1 Volt /cm

Horizontal 50 μ sec /cm

Vertical 1 Volt /cm

AFTER

Horizontal 500 μ sec/ cm

Vertical 1 Volt/ cm

BURST # 12 DATE 6/20/12

FUNCTION Start monitor

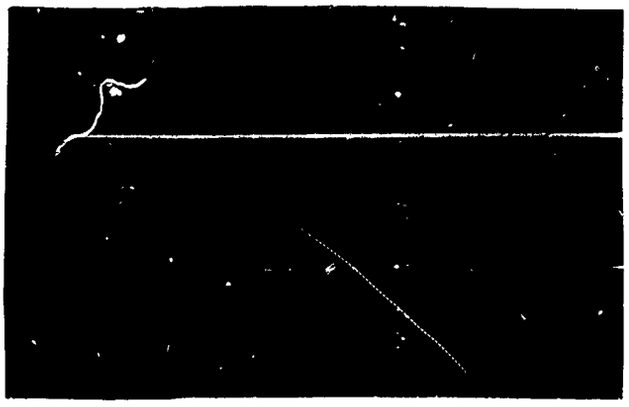

Horizontal 500 μsec/ cm

Vertical 10 Volt/ cm

BEFORE

Horizontal 500 μsec /cm

Vertical 5 Volt /cm

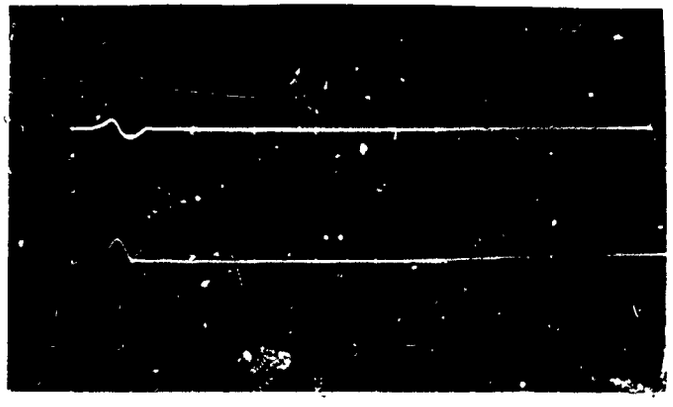

Horizontal 500 μ sec /cm

Vertical 10 Volt /cm

DURING

Horizontal 500 μ sec /cm

Vertical 5 Volt /cm

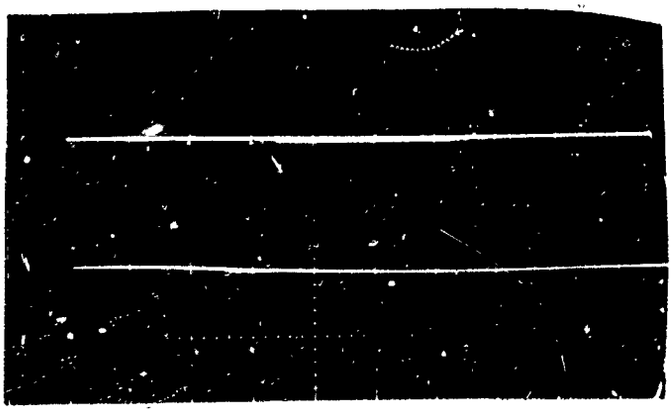

Horizontal 500 μ sec /cm

Vertical 10 Volt /cm

AFTER

Horizontal 500 μ sec / cm

Vertical 5 Volt / cm

BURST # 12 DATE 8/20/71

FUNCTION Upper = 10 Volt Supply; Lower = 5 V Supply

Horizontal 100 μ sec/ cm
Vertical 0.5 Volt/ cm

BEFORE

Horizontal 100 μ sec /cm
Vertical 0.5 Volt /cm

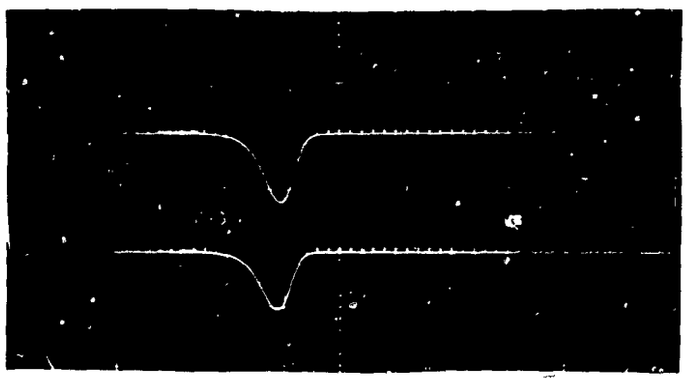

Horizontal 100 μ sec /cm
Vertical 0.5 Volt /cm

DURING

Horizontal 100 μ sec /cm
Vertical 0.5 Volt /cm

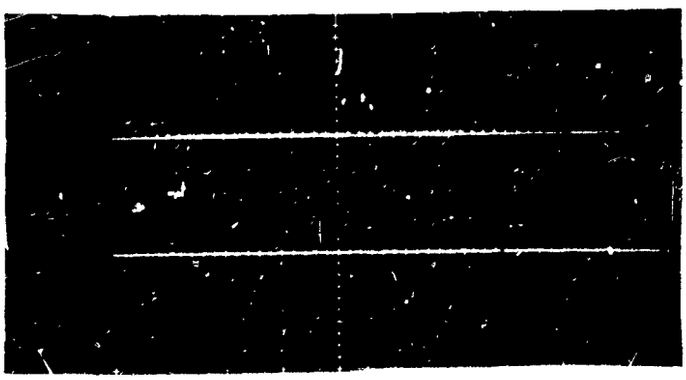

Horizontal 100 μ sec /cm
Vertical 0.5 Volt /cm

AFTER

Horizontal 100 μ sec/ cm
Vertical 0.5 Volt/ cm

BURST # 12 DATE 8/20/71

FUNCTION Germanium Photodetector

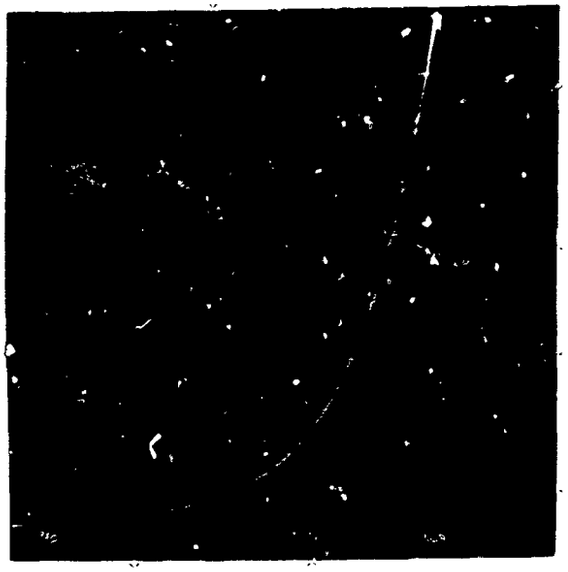

a) H = 0.1 Volt/cm

V = 0.5 ma/cm

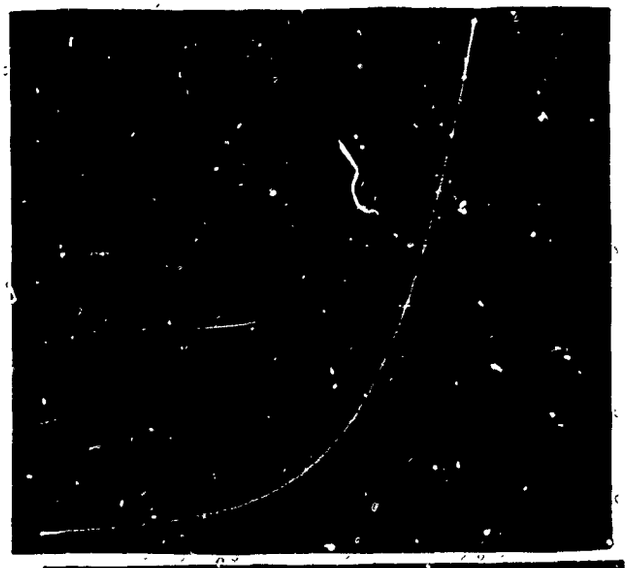

b) H = 0.1 Volt/cm

V = 0.5 ma/cm

c) H = 1.0 Volt/cm

V = 10 ma/cm

TEXAS INSTRUMENTS GERMANIUM PHOTODETECTOR

FORWARD AND REVERSE I/V CHARACTERISTICS

a) Forward I/V Non-Irradiated

b) Forward I/V Irradiated With 1.74×10^{14} N/cm^2

c) Reverse I/V Irradiated With 1.74×10^{14} N/cm^2

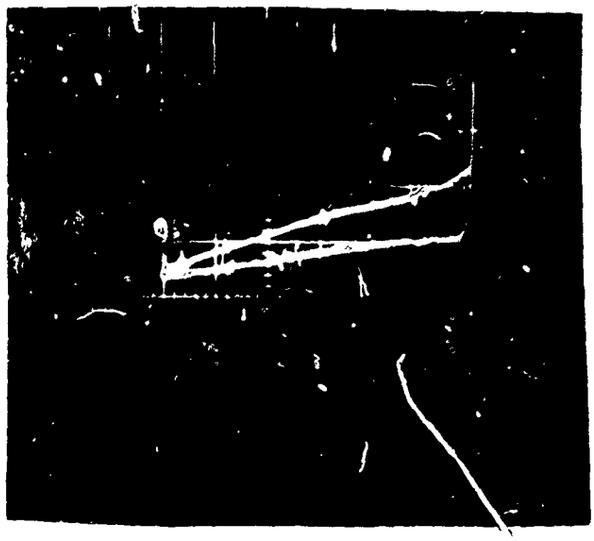

a) H = 1 Volt/cm

V = 1 ma/cm

b) H = 1 Volt/cm

V = 10 ma/cm

TEXAS INSTRUMENTS GERMANIUM PHOTODETECTOR

REVERSE BIAS I/V CHARACTERISTICS

a) Non-Irradiated

b) Irradiated With 3.5×10^{14} N/cm^2

a) H = 0.1 Volt/cm

V = 0.5 ma/cm

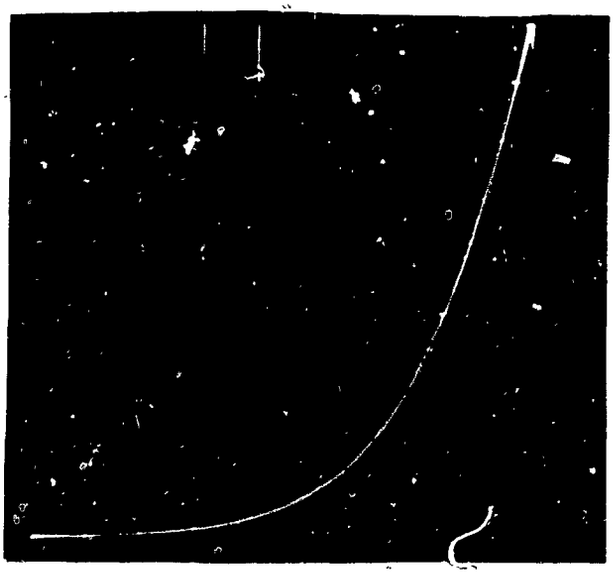

b) H = 0.1 Volt/cm

V = 0.5 ma/cm

TEXAS INSTRUMENTS GERMANIUM PHOTODETECTOR

FORWARD I/V CHARACTERISTICS

a) Nor-Irradiated

b) Irradiated With 3.5×10^{14} N/cm^2

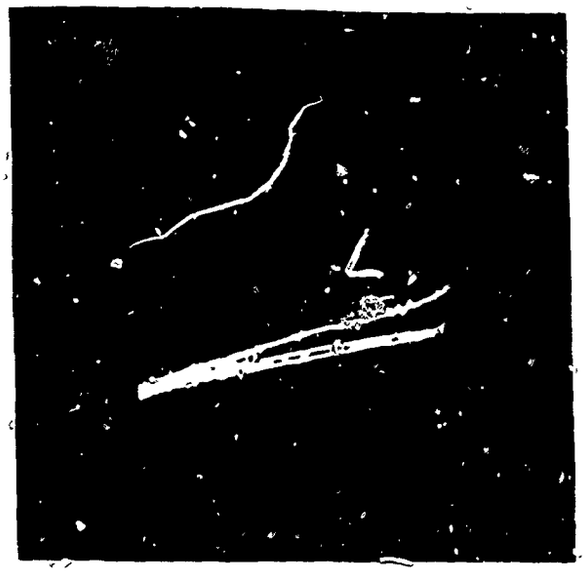

a) H = 1.0 Volt/cm

V = 1.0 ma/cm

b) H = 1 Volt/cm

V = 10 ma/cm

PHILCO-FORD CERMANIUM PHOTODETECTOR

REVERSE CURRENT I/V CHARACTERISTICS

a) Non-Irradiated

b) Irradiated With 6.1×10^{13} N/cm^2

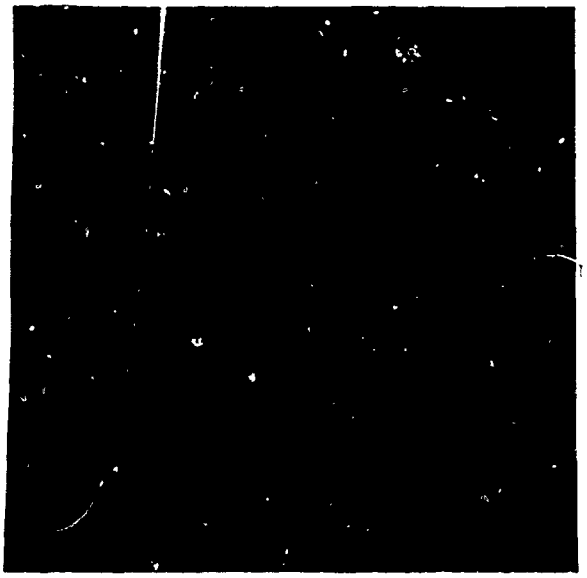

a) H = 0.1 Volt/cm

V = 0.5 ma/cm

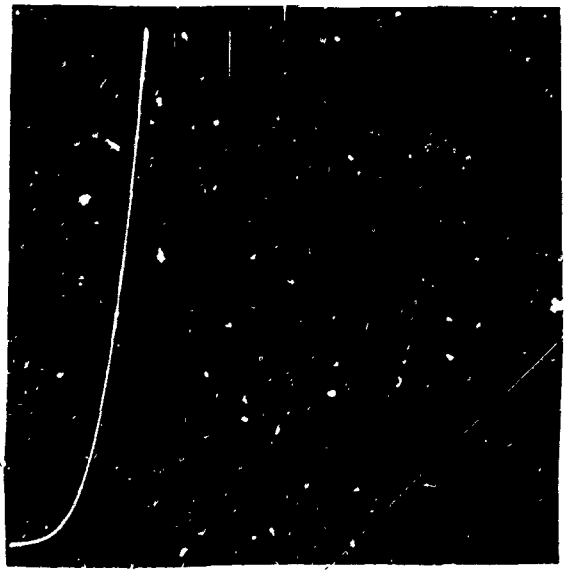

b) H = 0.1 Volt/cm

V = 0.5 ma/cm

PHILCO-FORD GERMANIUM PHOTODETECTOR

FORWARD I/V CHARACTERISTICS

a) Non-Irradiated

b) Irradiated With 6.1 x 10^{13} N/cm^2

a) H = 0.5 Volt/cm

V = 1 ma/cm

b) H = 0.5 Volt/cm

V = 1 ma/cm

1N748A ZENER DIODE

REVERSE VOLTAGE (BREAKDOWN) I/V CHARACTERISTICS

a) Non-Irradiated

b) Irradiated With 1.75×10^{14} N/cm^2

a) H = 0.5 Volt/cm

V = 1 ma/cm

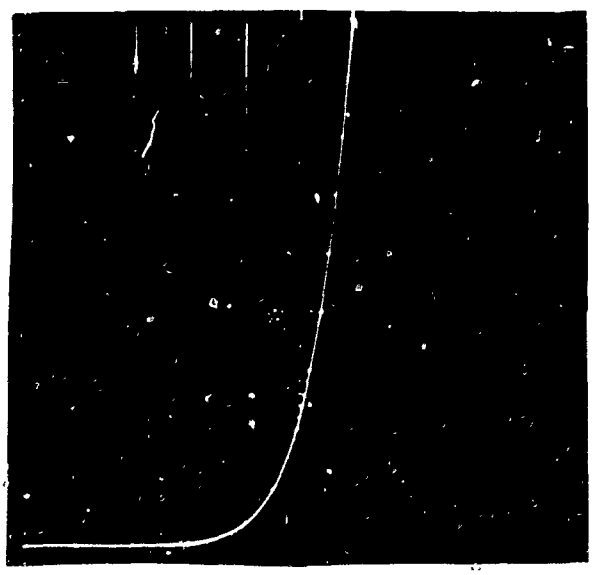

b) H = 0.5Volt/cm

V = 1 ma/cm

1N746A ZENER DIODE

REVERSE (BREAKDOWN) I/V CHARACTERISTICS

a) Non-Irradiated

b) Irradiated With 1.75×10^{14} N/cm^2

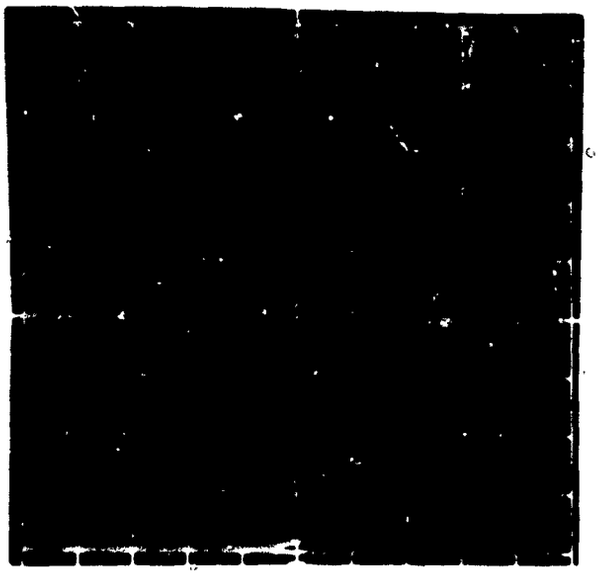

a) V = 1 ma/cm

H = 0.5 V/cm

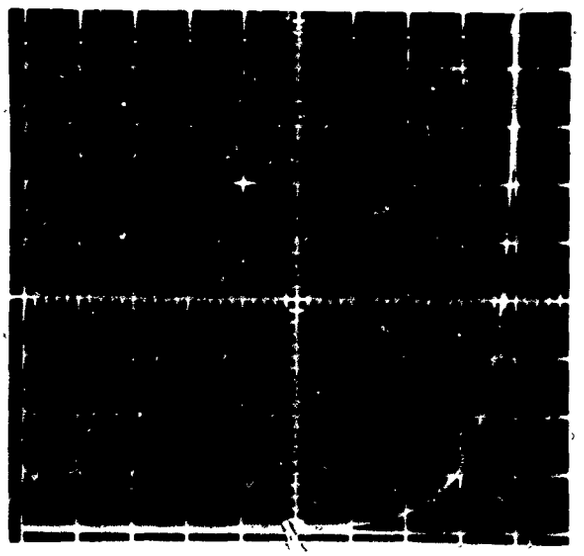

b) V = 1 ma/cm

H = 0.5 V/cm

LOW VOLTAGE AVALANCH ZENER DIODES

REVERSE BREAKDOWN I/V CHARACTERISTICS

a) 4.3 Volt Zener

b) 4.7 Volt Zener

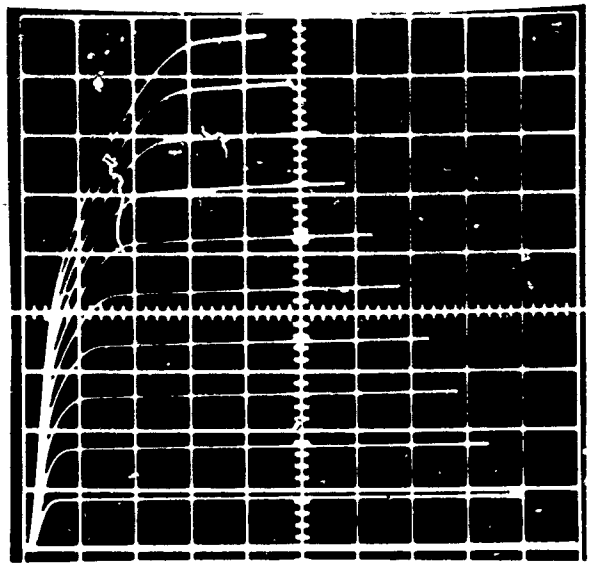

a) H = 0.5 Volt/cm

V = 100 ma/cm

Base I: 10 steps @ 0.5 ma/step

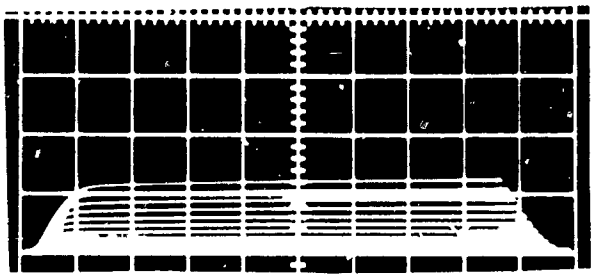

b) H = 0.5 Volt/cm

V = 100 ma/cm

Base I: 10 steps @ 0.5 ma/step

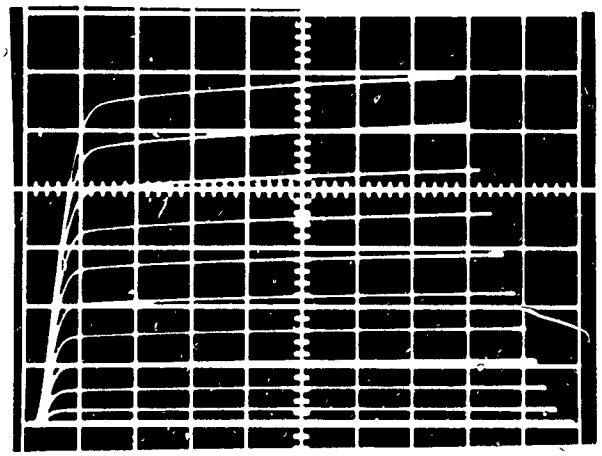

c) H = 0.5 Volt/cm

V = 20 ma/cm

Base I: 10 steps @ 0.5 ma/step

BR100F TRANSISTOR
COLLECTOR I/V CHARACTERISTICS

a) Typical Non-Irradiated

b) After 1.5 x 10^{14} N/cm^2

c) Vertical Expansion of (b)

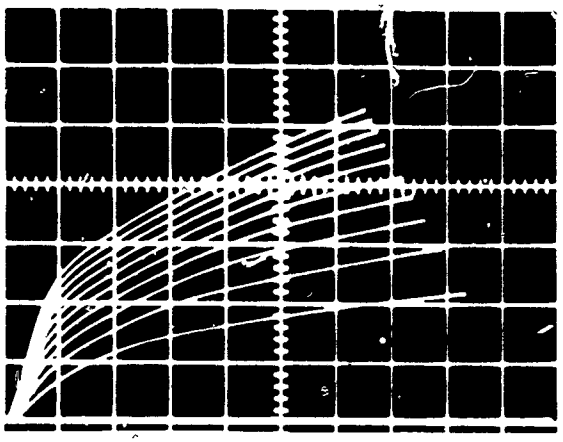

a) V = 0.5 ma/cm

H = 0.2 Volt/cm

Base I: 10 steps @ .005 ma/step

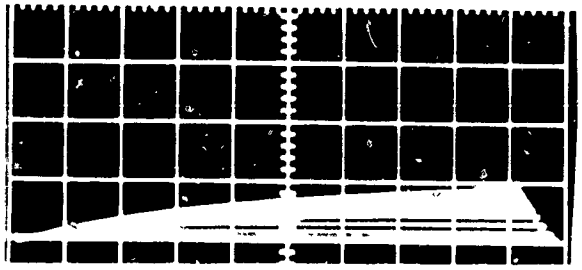

b) V = 0.5 ma/cm

H = 0.2 Volt/cm

Base I: 10 steps @ .005 ma/step

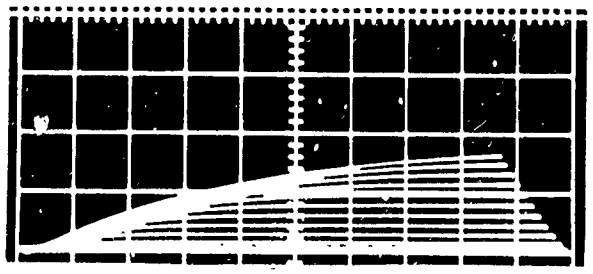

c) V = 0.5 ma/cm

H = 0.2 Volt/cm

Base I: 10 steps @ .005 ma/step

2N4878 TRANSISTOR
COLLECTOR I/V CHARACTERISTICS

a) Typical Non-Irradiated

b) Worst Case After 1.5×10^{14} N/cm^2

c) Best Case After 1.5×10^{14} N/cm^2

Table AI. Reactor Dosimetry Data

Burst No.	Dosimeter Location	Gamma Rate ($\dot{\gamma}$) 10^8 Rad (si)/Sec	Neutrons, 10^{13} N/cm^2
1	1	1.04	3.77
	2	0.86	3.25
	3	1.32	4.64
	4	1.26	3.97
	5	1.15	3.99
	6	1.21	4.24
2	1	1.10	4.07
	2	1.19	3.40
	3	1.44	5.08
	4	1.25	4.28
	5	1.58	4.53
	6	1.43	4.57
3	1	0.95	4.11
	2	0.87	3.27
	3	1.36	5.05
	4	1.10	4.21
	5	1.25	4.53
	6	1.25	4.48

Table AI. Reactor Dosimetry Data (Continued)

Burst No.	Dosimeter Location	Gamma Rate ($\dot{\gamma}$) 10^8 Rad (si)/Sec	Neutrons, 10^{13} N/cm^2
4	1	1.13	4.49
	2	1.09	3.17
	3	1.39	5.14
	4	1.21	4.06
	5	1.23	4.40
	6	1.27	4.63
5	1	1.40	4.88
	2	1.37	4.65
	3	1.39	4.43
	4	1.32	4.11
	5	error	4.26
	6	1.48	4.44
6	1	1.34	5.06
	2	1.30	4.66
	3	1.30	4.57
	4	1.18	4.50
	5	1.19	4.35
	6	1.30	4.59

Table AI. Reactor Dosimetry Data (Continued)

Burst No.	Dosimeter Location	Gamma Rate ($\dot{\gamma}$) 10^8 Rad (si)/Sec	Neutrons, 10^{13} N/cm^2
7	1	1.74	5.04
	2	1.78	4.62
	3	1.74	4.54
	4	1.50	4.71
	5	1.52	4.37
	6	1.48	4.46
8	2	1.20	4.54
	3	1.18	4.52
	4	1.27	4.61
	5	1.23	4.46
	6	1.38	4.73
	1 not used		
9	1	1.02	3.14
	2	1.16	3.93
	3	1.14	3.52
	4	1.20	3.68
	5	1.43	4.35
	6	1.53	4.23

Table AI. Reactor Dosimetry Data (Concluded)

Burst No.	Dosimeter Location	Gamma Rate ($\dot{\gamma}$) 10^8 Rad (si)/Sec	Neutrons, 10^{13} N/cm^2
10	1	1.56	3.81
	2	1.75	4.33
	3	1.25	3.47
	4	1.79	4.45
	5	2.04	4.83
	6	1.95	4.88
11	1	1.15	3.52
	2	1.35	4.24
	3	1.17	3.31
	4	1.45	4.04
	5	1.74	4.75
	6	1.47	4.35
12	1	0.66	2.96
	2	0.78	3.24
	3	0.58	2.37
	4	0.76	3.01
	5	0.89	3.56
	6	0.83	3.35

APPENDIX D
THE LASER GYRO

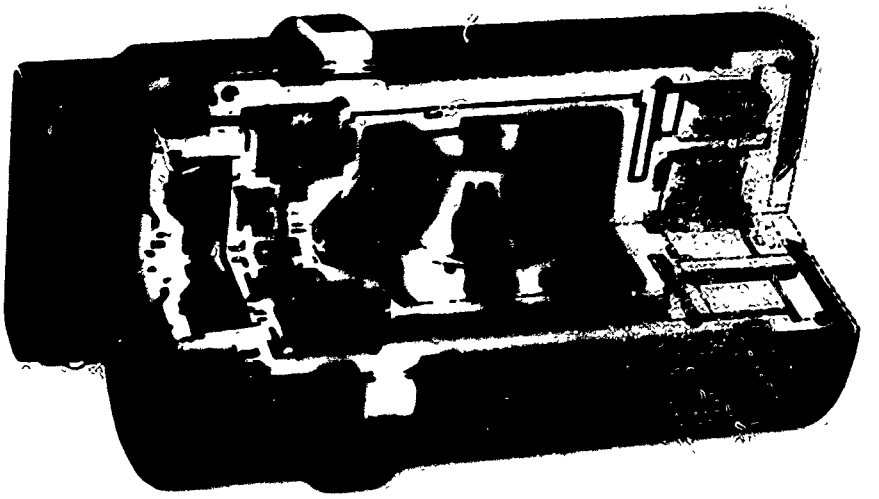

FIGURE 1. Conventional gyro.

The laser gyro

Now in the research and development stage, the laser gyro shows promise of replacing many conventional inertial gyroscopes. It is not subject to prolonged starting time or to the effects of sudden acceleration—ideal specifications for our space-age aeronautic society

Joseph Killpatrick *Honeywell Inc.*

One of the most dramatic recent developments in optical technology is the laser gyro, which combines the properties of the optical oscillator, the laser, and general relativity to produce an integrating rate gyroscope. This gyro measures rotation in inertial space, but does not use a spinning mass as conventional gyros do. Because of the absence of spinning mass, the gyro's performance is not affected by accelerations; and it can sense very high rates with great accuracy. Other important advantages of the laser gyro are lack of special cooling, low power consumption, and simplicity of construction.

The ideal sensor for inertial rotation (angular motion with respect to the "fixed" stars) would be a device whose output gives angle increments, just as an angle encoder measures rotation between two mechanical elements. The device would have a well-defined input axis about which the rotations were measured. The angle sensed also would be free of acceleration effects, both angular and linear, independent of the rate at which the angle is measured, and independent of special environmental factors such as temperatures. The output of the instrument should be if possible, high-resolution digital signals that are easily handled. Such a device is available in the form of a single-axis rate-integrating gyro, and it is currently used in many different control systems. Inertial guidance systems control airplanes, helicopters, the stabilization of guns, cameras, and radar antennas, the guidance of ships, aircraft, and other vehicles by using gyroscopes of this type to provide attitude references.

In order to sense attitude changes for motions in any direction, three such sensors must be used to independently sense the rotations about three axes, usually orthogonal, and use this information to determine the precise angles between the coordinate system defined by the gyros and the "fixed" stars.

In general, the gyro is fixed to the vehicle and, as such,

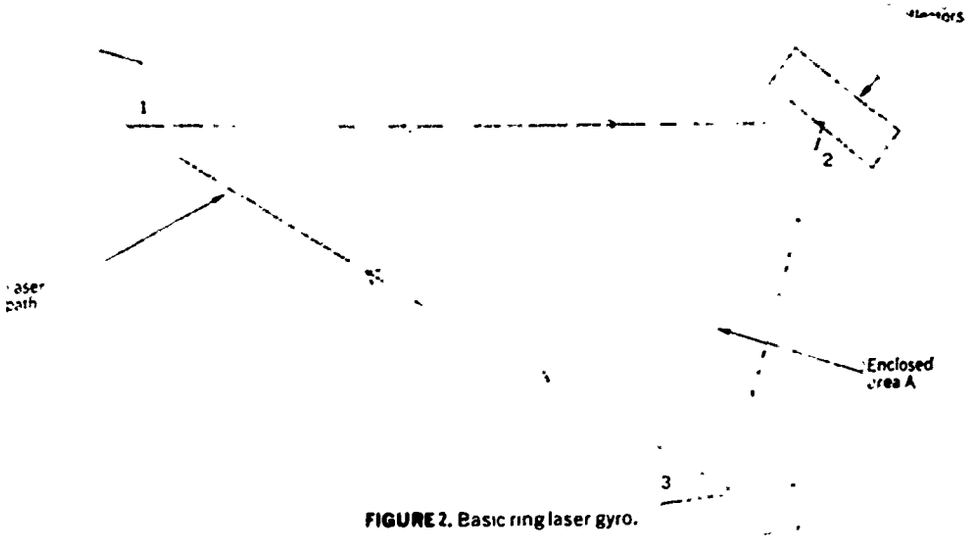

FIGURE 2. Basic ring laser gyro.

will find its input axis orientation varying with time. The output is in the form of a phase shift between two electric signals, and is the integral of the input rate about its input axis:

$$\Delta\theta = \int_{t_1}^{t_2} \Omega(t)\mathbf{n}(t)\,dt \qquad (1)$$

$$\theta_2 - \theta_1 = \int_{t_1}^{t_2} \Omega_{in} \cdot \mathbf{n}\,dt \qquad (2)$$

where Ω is the input rate, $\mathbf{n}$ is the input-axis unit vector, and $\Delta\theta$ is the phase shift between the two signals.

Why a laser gyro?

Conventional gyros using a spinning mass as a sensing element suffer inaccuracies due to many error sources. These include mass unbalance and structure instabilities that give rise to acceleration and acceleration-squared effects, and high rate effects. High costs are associated with the many elements, as well as the precision machining, assembly, and cleanliness required in their manufacture (Fig. 1). The laser gyro will avoid many of these problems, and will probably be very low in cost.

In addition, the run-up time of this gyro is the time it takes to ionize the gas discharge and start the current through the cavity. Times of the order of several milliseconds are typical. Inherently, this gyro is capable of operating within several milliseconds after pushing a start button. The "spin-up" of a mass, as used in a conventional gyro, is completely avoided.

The laser gyro is an integrating-rate gyro that senses inertial angles with high precision. Its most dramatic features are its ability to sense those angles in the presence of high accelerations, and high input rates as well as low accelerations. Its input is digital, and in its simplest form it is a device with an input axis and two electric outputs, one for positive and the other for negative angle increments. Whenever the rotation about the input axis equals the size of the output increment (typically one arc second) a pulse appears. If the input rate is constant, the output pulses will appear at a constant rate.

The rate at which the pulses occur is obviously directly proportional to the input rate to the gyro. By counting these pulses, the total angle through which the gyro has rotated can be measured.

It is paradoxical that, although simple in construction and operation, the laser gyro's description and analysis require consideration of extremely small effects. In fact, this is one of the most precise instruments resulting from the development of laser technology. It must measure path differences of less than 10^{-8} A, and frequency changes of less than 0.1 Hz (a precision of better than one part in 10^{13}) in order to read rotation rates of less than 0.1 degree per hour. The instrument is simply a laser that has three or more reflectors arranged to enclose an area.* The three mirrors, together with the light-amplifying material in the laser path, comprise an oscillator (laser), as in Fig. 2. In fact, there are two oscillators, one that has energy traveling clockwise, and one that has energy traveling counterclockwise around the same path.

The frequencies at which these oscillators operate are determined by the optical length of the path they travel. In order to sustain oscillation, two conditions must be met: The gain must be equal to unity at some power level set by the amplifying medium, and the number of wavelengths in the cavity must be an exact integer (that is, the phase shift around the cavity must be zero). If the first condition is to be achieved, the laser frequency must be such that the amplifying medium has sufficient gain to overcome the losses at the reflectors and other elements in the laser path. In addition, the wavelength must be an exact integer fraction of the path around the cavity. This last condition actually determines the oscillation frequency of the laser.

When the enclosed ring is rotated in inertial space, the clockwise and counterclockwise paths have different lengths. (This effect is *not* due to a Doppler shift.) The path difference in these two directions causes the two

* It is interesting to note that the word "gyro" is derived from the Greek "gyros," meaning ring. In this context the laser gyro is perhaps more of a true gyro than the conventional rotating wheel, for it is simply a laser arranged in a ring, by using three or more reflectors.

I. Path difference as related to area and input rate

Area, square meters	Ω, degrees per hour	ΔL, angstroms
1	10	66.7×10^{-4}
10	10	66.7×10^{-3}
10	10	66.7
10	10	667
1	10	667

oscillators to operate at different frequencies. The difference is proportional to the rate at which the ring is rotating, since path difference is proportional to inertial rotation rate. The readout of the gyro is accomplished by monitoring the frequency difference between the two lasers. The total phase shift, $\Delta\phi$, between the oscillator, cycles of output $\times 2\pi$, is the integral of the input rate, Ω:

$$\Delta f = \Omega \tag{3}$$

$$\frac{d(\phi - \phi)}{dt} = \Omega \tag{4}$$

$$\Delta\phi \propto \int_0^t \Omega \, dt \tag{5}$$

The laser gyro assembly consists of the gain media, the reflectors defining the path and enclosed area, and a readout method for monitoring the difference between the two oscillators. This is accomplished by evaluating the phase shift between the two oscillators, using two detectors to separate positive and negative phase shifts (to separate clockwise inertial rotation from counterclockwise rotations).

Basic principle: how the same path can be different

The key to the operation of the laser gyro is the description of the phenomena by which the path around the ring can be different for observers (photons) traveling *with* the direction of rotation than for observers traveling *against* the direction of rotation.

General relativity[1] predicts that two observers, traveling around a closed path that is rotating in inertial space, will find that their clocks are not in synchronization when they return to the starting point (traveling once around the path but in opposite directions). The observer traveling in the direction of rotation will experience a small increase, and the observer traveling in the opposite direction will experience a corresponding small decrease in clock time. The difference in the readings of these clocks, Δt, depends upon the inertial rotation rate Ω, the area A enclosed by the path, and the speed of light c.

$$\Delta t = \frac{\Omega}{c^2} 2A + \frac{\Omega}{c^2} 2A = \frac{4A\Omega}{c^2} \tag{6}$$

Since the laser gyro uses photons, traveling at the speed of light, for observers, the time difference appears as an apparent length change in the two paths of ΔL. This length change is equal to the observers' velocity times their time difference

$$\Delta L = c\Delta t = \frac{4A\Omega}{c} \tag{7}$$

Thus, even though both observers travel the same physical path, they see an apparent length change, which is proportional to the enclosed area of the path and its rotation rate in inertial space. The relation of ΔL to A and Ω (see Table I) shows that, in order to obtain path differences large enough to measure by conventional interferometric techniques, either the rotation rate must be quite high or the enclosed area must be very large. In 1913 Sagnac[2] conducted an experiment to investigate this effect by using a small enclosed path about 0.1 m², rotated at 2 revolutions per second, and was able to detect length changes of 100 to 200 A. In 1925 Michelson[3] conducted an experiment using the rotation rate of the earth (10 h) and an enclosed area of 2×10^{4} m². In this experiment the detected length change was about 1000 A. In both experiments good agreement was obtained with the equation relating area, rotation rate, and change in path length. In order to measure low rates with a small enclosed area, however, a different method of measurement was clearly needed.

Measuring small length differences by laser

For measuring small length changes the use of an electrical oscillator was proposed, in which the cavity dimensions and lengths determined the oscillation frequency.[4] In this manner a small length change is transformed into an easily measured frequency difference between oscillators. The laser gyro uses two oscillators at high frequencies (3×10^{14} Hz). Exact frequencies are determined by the length of the two cavities, one for clockwise and the other for counterclockwise traveling radiation.

The laser oscillator operates at light frequencies and, as in all oscillators, it must have a gain mechanism arranged in such a way that the losses are equalized. It must also operate at a frequency controlled so that the phase shift for a trip around the cavity is zero.

The gain is usually provided in a laser gyro with an electrical gas discharge in a mixture of ten parts of helium to one part of neon at a total pressure of 1 to 10 mm of mercury. This gas discharge is like that of a neon sign. Because of a combination of energy transfer from the helium to the neon, wall effects, and decay rates, a gain results. In other words, at certain wavelengths, a light ray will experience a gain of from 1 to 5 percent when it passes through the gas discharge. Principally because of Doppler effects, this gain exists over a range of frequencies about 1.5 GHz wide. In general, the losses are determined by the reflectivity of the laser reflectors, diffraction losses that occur as a function of the cavity size, and the manner in which the light radiation travels around the cavity. Typically, the losses due to the reflectors are less than 0.3 percent per mirror or 0.9 percent for three mirrors. Since the gain must be greater than the loss, there is a limited range over which oscillation may occur. This range is typically 1 GHz.

In addition to the oscillator conditions of gain and loss, the condition of zero phase shift must also exist. Another way of saying this is that the number of wavelengths in the cavity must be equal to an integer; in the laser gyro, this integer is about one million. Many frequencies will satisfy these conditions of zero phase, but they are separated by an amount equal to c/L (the speed of light divided by the total length of the cavity). For a total length of one meter the frequency separation is 300 MHz. Thus, for a cavity of this size, there may be two or three possible frequencies of oscillation—that is, frequencies at

Z9080-3010FR
Vol. II

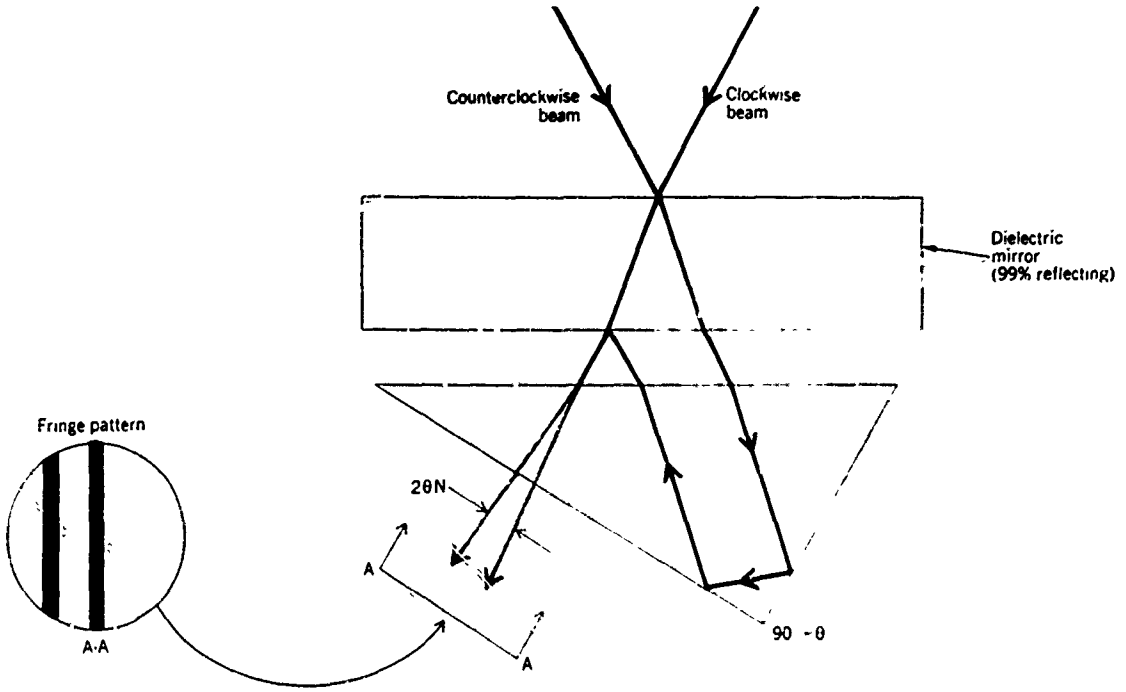

FIGURE 3. Laser gyro readout optics.

FIGURE 4. Lissajous pattern of two detector outputs.

which both the gain is greater than the losses and the phase shift around the cavity is zero. The laser frequency is determined primarily by the length of the cavity. The frequency band in which the gas medium has gain determines which of the many possible frequencies will "lase" or oscillate.

In practice, the exact phase shift must be considered, and this involves a study of phase-shift terms due to the gain, nonlinear saturation of the gain, scattering, and the role of various isotopes of neon.

The length differences in the two paths due to inertial rotation rates cause a difference in the frequency of these two oscillators, whereas physical changes in length caused by temperature, vibration, etc., do not cause major frequency differences. The fundamental boundary condition is that the laser wavelength λ must be equal to an integer fraction of the optical length around the cavity. N is an integer typically in the range of 10^3 to 10^6, and

$$\lambda = \frac{L}{N} \tag{8}$$

A length change of ΔL will cause a wavelength change of

$$\Delta\lambda = \frac{\Delta L}{N} \tag{9}$$

The corresponding frequency change is given as

$$\frac{\Delta f}{f} = \frac{\Delta L}{L} \tag{10}$$

Therefore, given small length differences Δl and reasonable cavity lengths l, the operating frequency should be as high as possible

The relation between inertial input rates Ω and apparent length change Δl has been given as

$$\Delta l = \frac{4A\Omega}{c} \tag{11}$$

The relation between Δl and Ω, in terms of the gyro size and wavelength, is determined by substituting Eq. (10) into Eq. (11), giving

$$\Delta f = \frac{4A\Omega}{\lambda l} \tag{12}$$

Readout of the laser gyro

Frequency difference is monitored quite simply, as shown in Fig. 3. A small amount of the laser energy is

transmitted through the mirror. This transmitted energy is uniquely related to the frequency and phase of the energy in the cavity. The two transmitted beams are superimposed to create a fringe pattern of alternate interference, and if the phase between the two oscillators remains fixed, the fringe pattern will also remain fixed. However, if the phase between the two oscillators changes (a frequency difference between the two oscillators), the fringe pattern will appear to move to the right or left. The direction of motion is determined by the direction of phase change (which oscillator is at the higher frequency), and the magnitude is measured by the number of fringes. Each fringe represents a phase change of one cycle, or 2π radians.

The output consists of two detectors mounted at the readout prism and spaced so that they are about a quarter of a fringe spacing apart. With this spacing, their outputs are phased so that the direction, as well as magnitude, of the fringe motion can be monitored. By forming a Lissajous pattern of the two detector outputs (Fig. 4), the phase shift of 90° is evident. When the gyro is rotated clockwise, the fringe pattern moves in one direction, causing the oscilloscope pattern to travel around a circle in a fixed direction, one revolution for each fringe shift.

When the gyro input is reversed, the fringe motion will reverse, as will the dot observed on the oscilloscope. These detector signals are simply processed to count the number of complete fringe motions, one direction as positive and the other as negative. (An oscilloscope is used only for monitoring and testing purposes, and is not needed for actual operational readout.)

The signal from each detector is amplified and used to trigger digital counters that monitor plus and minus counts. Each count represents a phase change of 2π radians, or one cycle (resolution of one quarter of this value can be easily achieved), between the two oscillations in the laser gyro cavity. The size of each count is dependent upon the gyro relation between input rate and output frequency difference. An input rate of 1°/h (1/15 of the earth's turning rate) will typically produce a frequency difference of 1 Hz. One degree per hour is exactly one arc second per second of time; therefore, each second an inertial angle of one arc second has been generated, producing an output phase change of one cycle, or 2π radians. Each count has a weight of one arc second, and turning the gyro through an angle of 360°, or one revolution, would produce an output of 1 296 000 pulses. For rotations in one direction, these pulses are identified as positive, and in the opposite direction they are identified as negative. (The logic is identical to that used in digital incremental-angle encoders.)

II. Output frequency and fringes per arc second as related to various parameters ($\lambda = 1\ \mu$m)

Area, m^2	Ω, deg/h	Δt, seconds	ΔL, angstroms	Δf, Hz	Fringes/ Arc Second
1	10	22×10^{-12}	66.7×10^{-4}	50	5.0
10^{-2}	10	22×10^{-14}	66.7×10^{-6}	5	0.5
10^{-2}	0.10	22×10^{-16}	66.7×10^{-8}	0.05	0.5

Table II clearly shows the role of the laser oscillator in converting small length differences of approximately 10^{-4} Å into measurable quantities of frequency and phase.

An integrating-rate gyro

The fact that the output frequency difference is proportional to the input rate, as shown in Fig. 5, often leads to the impression that the laser gyro is a rate gyro. However,

FIGURE 5. Output frequency vs. rotation rate for laser gyro.

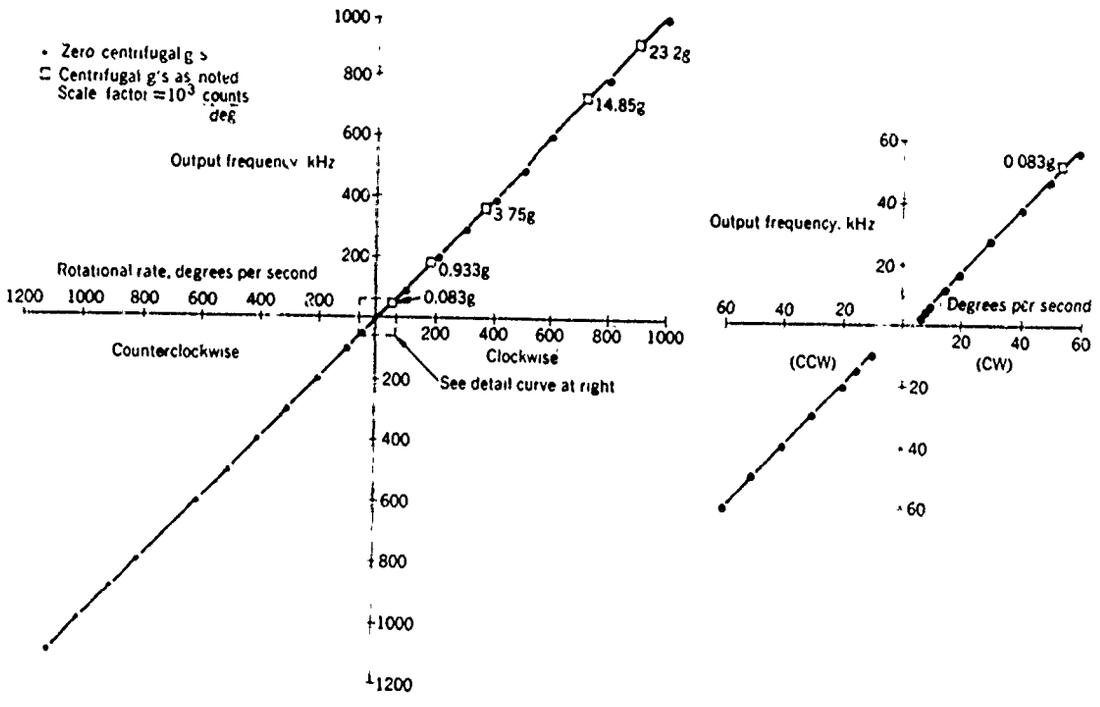

its output is the phase difference observed by the position of the interference pattern created by superimposing the energy from the two oscillators in the readout. The total phase shift change between the two oscillators over a given time interval is the integral of their frequency difference expressed as the instantaneous rate of phase change:

$$\Delta f = \frac{d(\phi_2 - \phi_1)}{dt} = \frac{4A}{\lambda L}\,\Omega \qquad (13)$$

By integrating over a time interval, the total phase change is found as

$$\Delta\phi = \frac{4A}{\lambda L}\int_{t_1}^{t_2} \Omega dt \qquad (14)$$

The inherent resolution (1 to 1 4 of a fringe) of about one arc second or less is sufficient to satisfy almost all conceivable applications. Of course, the resolution size and the smallest rate that can be sensed are not directly related, except when a minimum time to make that

FIGURE Early laser gyro model.

FIGURE 7. Single-axis laser gyro.

FIGURE 8. Construction detail of solid-block laser gyro.

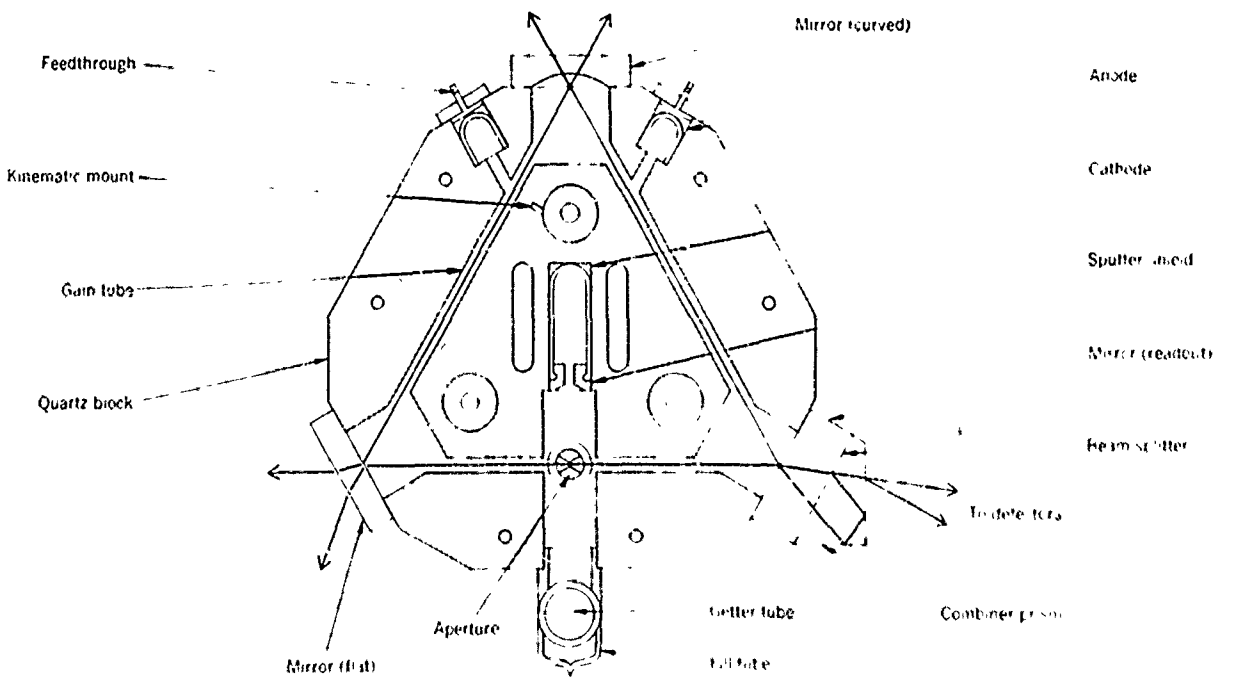

FIGURE 9. Three-axis laser gyro in solid quartz.

measurement is made. In general, the equation is written:

$$\Delta\phi = \frac{4A}{\lambda L}\int_{r_0}^{r} \Omega \cdot \mathbf{n}\, dr \qquad (15)$$

which describes the fact that the input is only that component of rate which is about the input axis of the gyro. The instrument is thus a single-axis rate-integrating gyro. Inertial rotations of the gyro about an axis orthogonal to the input axis will not create an apparent path difference, and thus will not produce any output fringe motion.

Construction of the laser gyro

The actual construction of the laser gyro varies from laboratory to laboratory, application to application, and with time as technology advances. (Figures 6 to 8 illustrate various laser gyro configurations.) However, certain elements must be observed in all cases:

Sealing. The laser cavity must be sealed, or shielded, from dust and other sources of scattering and from loss, which can affect performance in dramatic ways.

One transverse mode. The laser cavity must be designed, constructed, and aligned to support only one transverse mode of oscillation; the beam must have only one intensity maximum in its energy cross section. The reason for this is that the oscillations traveling in one direction may pick a mode distribution that is different from the mode distribution of those traveling in the other direction. The choice of mode distribution for either direction is random; it changes with vibration and small cavity perturbations if more than one transverse mode is permitted to exist. This switching, as well as the fact that these modes have different phase shifts and hence different frequencies, contributes to large noise fluctuations.

Mode position. The mode position relative to the basic laser gain distribution must be controlled to achieve maximum accuracy. The system must be simple, rugged, free of adjustments, and low in cost. The use of a solid block of quartz to define the laser cavity has proved quite successful. The anodes and cathode are attached to the housing, as are the corner mirrors defining the cavity dimensions. The entire gyro is filled with helium and neon and sealed. The gyro needs no alignment, and is both rugged and low in cost (Figs. 7 to 9).

The solutions to problems located to date do not detract from the basic simplicity or add substantially to the cost of the gyro. It is apparent that this instrument will be used in many future applications because of its many advantages over more conventional gyroscopes.

An accelerometer?

The question arises as to the use of this instrument as an accelerometer. The fundamental sensed property is a path difference arising from a rotation of a closed path in inertial space, therefore, linear acceleration and even large angular accelerations have negligible effects on the laser performance. Acceleration effects would arise only through a physical bending of the gyro housing that could break the assembly. Figure 5 shows the lack of acceleration effects as two runs are compared, one with no loading, and the other on a centrifuge with linear accelerations up to 23 g.

Error sources

The laser gyro is not perfect, and it has several factors that must be considered if it is to achieve the high performance necessary for many applications. It operates by

sensing the relative frequency differences between two laser oscillators occupying the same physical cavity and traveling in opposite directions. Therefore, any factor that can cause changes in the apparent length difference of the two cavities, other than inertial input rate, will introduce errors into the laser gyro output. The startling fact is that such terms equivalent to length changes of less than 10^{-13} A can be identified in magnitude and source. The following discussion briefly reviews some of these error terms and the methods by which they are reduced or eliminated.

The predominant effect in the laser gyro is the shift in frequency due to input rates, with the error terms being perturbations in the basic sensed parameters. Accuracies of better than one part per million, and rate sensitivities of far less than one degree per hour, are important to the description of the laser gyro. Thus, strict attention must be paid to basic laser fundamentals. It is a mark of the rapid advance and understanding of the laser that equations and descriptions of this oscillator can be made to accuracies of far better than 0.1 Hz, even though the oscillator frequency is 3×10^{14} Hz.

Ultimate limits of performance

Before we explore the practical problems, it is important to examine the fundamental limit for the gyro, in order to establish how close to this limit we are today, and to determine whether basic factors exist that may restrict its ultimate potential.

The inherent frequency limit of a laser is determined by spontaneous emission from the laser gain medium, just as thermal noise determines the inherent limit in a conventional electrical oscillator. Each spontaneous-emission photon has a magnitude of $h\nu$, where h is Planck's constant and ν the frequency of the radiation. At a wavelength of 1 μm, each photon has an energy of 1.2 electron-volts ($h\nu = 1.2$ eV). When this emission of $h\nu$ occurs (it must be in the proper direction in order to interact with the laser mode energy), it may bear any phase relation with the oscillator energy, and thus may cause both magnitude and phase fluctuations in the laser output. The output power can be represented by a vector whose power magnitude is $Nh\nu$ per second, where N is the number of photons in the laser mode, a number equal to 10^{15} or greater. The spontaneous-emission photon can add a phase to this original oscillator of a magnitude of $1/N$. This phase shift, $\Delta\phi$, is quite small, but occurs in a random manner. This variation gives rise to a frequency spread in the laser output equal to

$$\Delta f = \frac{8\pi h\nu(\Delta\nu_a)^2}{P_t} \tag{16}$$

For typical conditions, this frequency spread Δf_n is 1 to 10^{-2} Hz, and arises from phase fluctuations as small as 10^{-15} radian that occur at rates up to 10^{15} per second. The spontaneous-emission photons occur about every 10^{-1} second, each one causing a phase fluctuation of about 10^{-15} radian in the oscillator energy. The frequency spread would be about 0.1 Hz:

$$\Delta f = \frac{\Delta\phi}{\Delta t} \doteq \frac{1 \cdot 10^{-15}}{2\pi \cdot 10^{-15}} \sim 0.1 \text{ Hz} \tag{17}$$

However, since this is a random process, the actual measured frequency fluctuations will decrease with the square root of the time of measurement. Townes gives a clear illustration of this point,[7] and gives the following equation relating the apparent or observed line width $\Delta\nu_a$ to a oscillation of minimum line width $\Delta\nu_m$, in a time t and with an oscillation power of P:

$$\Delta\nu = \Delta\nu_m \left(\frac{h\nu}{P_t}\right)^{1/2} \tag{18}$$

With conservative estimates for $\Delta\nu_m$ of 1 Hz and a P of 10^{-9} watt, a measurement time of 1 second will measure frequency fluctuations of only 4×10^{-5} Hz.

In practice, the working limit of the frequency fluctuations is determined by the minimum phase that can be measured. This phase is usually sensed by the voltage on a detector or detectors that are measuring the relative phase between two oscillators (as in the laser gyro case). If a signal-to-noise ratio of 10^4 is obtained in the detected signal, the minimum detectable phase shift is 10^{-4} radian. In one second, the apparent frequency fluctuation caused by detector noise is approximately 10^{-4} Hz:

$$\Delta\nu_{\text{detector noise}} = \frac{10^{-4}}{2\pi} \text{ Hz} \tag{19}$$

This number is greater than the actual laser frequency fluctuation for this measurement time. For these particular parameters, the error caused by the phase fluctuation of the oscillator would not exceed the minimum detectable value until the time of measurement exceeded 10 minutes. The exact figures will vary from one laser configuration to another; but, for times up to several hundred seconds, the fundamental limit of rate measurement is always determined by the phase resolution. The measured fluctuation for times of only a few milliseconds would turn out to be about 10^{-2} Hz, if it could be measured. Since a rough rule of thumb is that 1 Hz is equivalent to an input rate of 1 degree per hour, the inherent capability of this gyro far exceeds 10^{-2} degree per hour. In fact, for periods of one hour, the fundamental accuracies exceed 10^{-6} to 10^{-7} degree per hour. Clearly, if such fundamental accuracies can be achieved, this gyro would be far superior to any gyro in operation today. An angle of 10^{-7} degree is the angle subtended by 10 cm at a distance equal to that from the earth to the moon, or 386 000 km.

Another, and perhaps more meaningful, expression of this fundamental limit is the total phase error between the two laser oscillators. The gyro output is the phase difference between the two oscillators, and therefore descriptions of this phase error can be directly related to measured outputs. This error will grow with the square root of time as in any random process, and will have a minimum value (as given in the previous example) of 10^{-4} radian when the time is less than about 10^{-2} second.

For times less than several days the inaccuracy in the laser gyro output phase is less than 10^{-6} radian, or about 10^{-1} arc second. (A phase error of one count, 2π radians, is equal to an inertial error angle of only one arc second.)

In summary, the gyro output, which is the phase angle between the two oscillators, is affected by the fundamental noise process of spontaneous emission by amounts so small that their detection is virtually impossible. A laser gyro system operating at this fundamental limit would be able to measure inertial angles for times up to several days, with errors not exceeding 10^{-1} to 10^{-2} arc second. In particular laser gyro applications these numbers may vary; but in all cases the laser gyro, as limited by this fundamental process, would be orders of magnitude more

accurate than any existing gyro. It is doubtful that these limits will be reached in the foreseeable future.

After examining the most basic limit to the gyro performance (spontaneous-emission noise) and establishing that this term does not in any way limit the laser performance, those factors actually encountered must be considered as practical limits. These factors include lock-in, null shifts due to direct current, null shifts due to differential loss mechanisms, and the bias techniques used to overcome lock-in phenomena.

Lock-in

The first of these factors that affect the frequency difference between the two oscillators is a phenomenon called "lock-in," which arises from coupling between the two laser oscillators. Lock-in in a laser gyro was initially observed in early 1963,[2] and has been observed for many decades in conventional electrical oscillators.

When the output of the laser gyro is observed as a function of the rotation rate it can be seen that the difference frequency is proportional to the input at high rates. However, as the input rate is reduced, the frequency difference between the two oscillators will fall to zero before the input rate goes to zero, which is apparent from the fact that the output fringe pattern does not move. The input rate at which this lock-in, zero-difference frequency, occurs is called the lock-in rate.

The lock-in rate is found to depend upon the wavelength, the coupling factor r, and the enclosed area A. Thus in order to reduce the lock-in rate these rules apply:

1. The smaller the wavelength, the better.
2. The bigger the gyro unit, the better.
3. The smaller the coupling factor r, the better.

In practice, the choice of wavelength is restricted to values at which laser oscillation can occur and by the fact that r is not completely independent of wavelength. The limiting values of r are determined by Rayleigh scattering, which increases rapidly as the wavelength decreases, thus prohibiting the application of rule 1 indefinitely.

Rule 2 also presents problems, since for practical considerations of size, weight, and power, the gyro should be as small as possible. Also, very large gyros create other laser locking effects that complicate operation.

Rule 3 has practical limits that are defined by the quality of the laser cavity. Scattering from windows, mirrors, and other elements within the cavity must be reduced to an absolute minimum. In practice, coupling factors of less than 10^{-6} have been achieved by very careful design and assembly. By examination of all the factors contributing to coupling, reduction in its value by many orders of magnitude does not look promising. Coupling arising from the scattering of the gas molecules in the laser gain medium will limit the value of r so that lock-in rates

FIGURE 10. Gas flow in a dc laser discharge

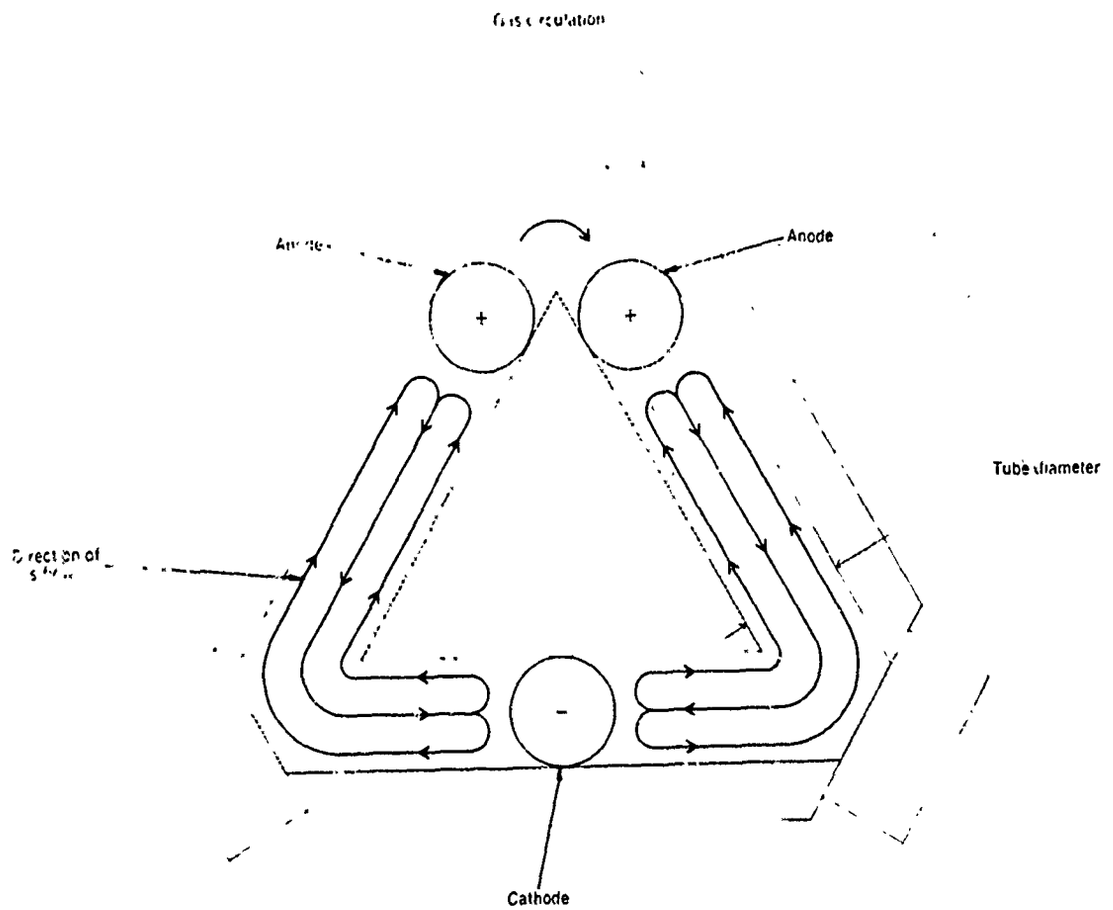

of less than a degree per hour may be very difficult to reach. (The word impossible would be used if it weren't such a dangerous technical term.)

In practice, the magnitude of the lock-in rate is typically 300 Hz, or 100 h for a ring of about 0.1 m² enclosed area and a wavelength of 6328 A (red light).

It should be emphasized that it is the scattering (coupling) that leads to lock-in, and not the loss or absorption of energy. (The fact that the gain or loss in a laser cavity is not uniform generates lock-in terms that are low in magnitude, and are usually hidden by other factors.)

Null shifts due to direct current

A second source of errors is the null shift, equivalent to a fixed bias torque in a conventional gyro, which arises from the direct current used to excite the laser gyro. Null shifts resulting from this parameter must both be considered and reduced. When a gas discharge is sustained with a direct current the gas flows in the discharge cavity. The flow is established by the combination of several effects, including wall collisions, charge distribution on the wall, and the electric field along the discharge. The result is a flow of gas toward the cathode in the center of the discharge, and a flow back toward the anode in a region close to the laser cavity walls (Fig. 10). The laser energy is concentrated in the center portion of the cavity, and therefore passes through gas that is flowing toward the cathode. The flow produces a shift in the index of refraction that depends upon the relative directions of the laser energy and the gas flow. Therefore, the cavity will appear longer in one direction than the other, and will cause an apparent null shift in the input rate sensed by the gyro. As can be seen from the diagram, Fig. 7, this effect is reduced by constructing the gyro in a balanced configuration, with a single cathode and two anodes. This tends to cancel the current effects, as energy traveling around the cavity passes through gas traveling both with and against the laser energy. By balancing the two anode currents, the null shifts due to this effect can be greatly reduced. If only one anode is used, apparent input rates of several hundred degrees per hour are introduced. This effect can be used to an advantage, since by unbalancing the currents a null shift can be introduced into the gyro either to cancel other null shift terms or to introduce known input rates purposely.

High rates

Another potential problem is high input rates; but this turns out to an advantage for the laser gyro, as it can sense high rates very accurately. The gyro's ability to sense high rates is determined by the inherent frequency capability of the laser and the detector-amplifier. The laser gain medium has a width of approximately 1 GHz. Since the frequencies in the laser change as the input rate changes, both frequencies must lie within the permitted gain region of the laser. Since an input rate of one degree per hour typically produces an output frequency difference of 1 Hz, an input rate of up to 10^9 degrees per hour could be sensed by this device. In practice, when the frequency difference becomes a large fraction of the gain distribution width, deviations in linearity are to be expected. For rates up to 10^7 degrees per hour, however, the laser gyro performance should be virtually ideal. Current test results support this statement, with performances at rates over 10^8 degrees per hour having been demonstrated. Figure 5 shows the excellent linearity for input rates up to 4 million degrees per hour.

The predicted problem is the detector-amplifier combination since, at 10^9 degrees per hour, bandwidths of 100 MHz are required in the amplifying circuits. Such bandwidths are achieved, but not without some very careful design and assembly. Here the high resolution works to our disadvantage.

Biasing of the laser gyro

Lock-in phenomena prevent the laser gyro from accurately measuring low input rates unless some means is provided to overcome this effect. Lock-in rates vary for gyros of different size, quality of the surfaces in the laser cavity, and wavelength of the laser oscillations; but for

FIGURE 11. Biasing through rotation, using Faraday cell.

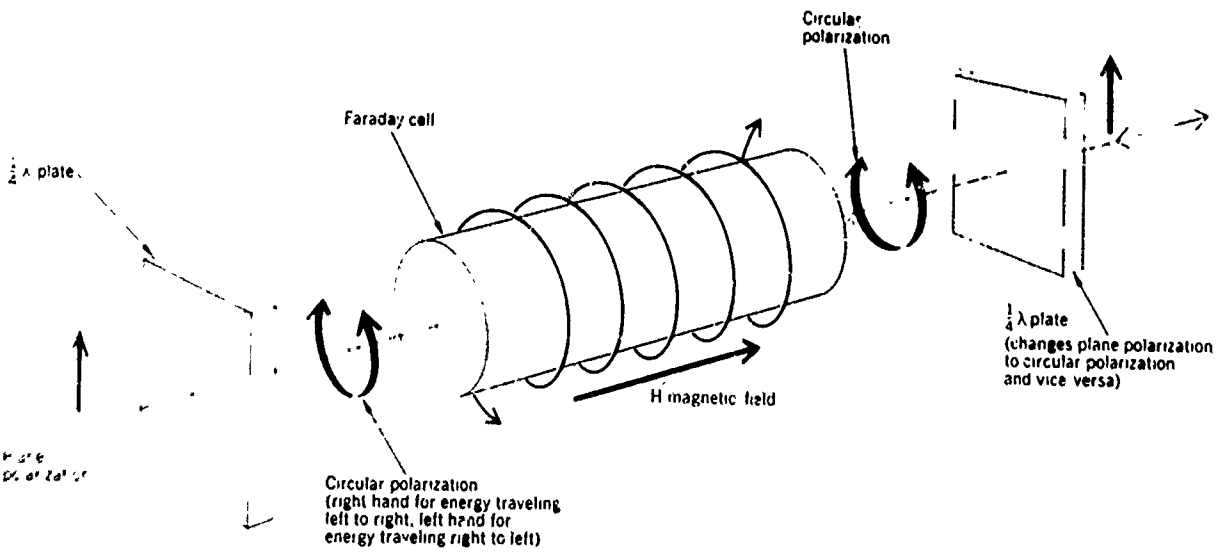

[illegible] The laser gyro

practical sizes and other factors, lock-in rates of less than a few hundred to tens of degrees per hour, at the best, are observed. These lock-in rates agree with theory, and cannot be expected to drop rapidly in the future.

Clearly, in order to measure rates of less than a degree per hour, some means of avoiding this effect must be employed. One technique is to introduce another known, or effective, input rate to the gyro. Such biasing moves the operating point of the laser gyro away from very low rates, where lock-in occurs, to much higher rates, where the operation of the laser gyro approaches the ideal. The total input rate to the gyro is the sum of the true input rate plus the bias rate. The actual input can be measured by merely subtracting the known bias from the gyro output.

In general, biasing is accomplished by either of two ways. One method involves physically rotating the gyro, thus producing an input rate, and then subtracting the angle of rotation. A second method is to introduce into the laser cavity an optical element having a index of refraction dependent upon the direction in which the radiation is passing through the element. The magnitude and direction of this index difference are usually controlled by a magnetic field in a Faraday cell; see Fig. 11. Since the path around the laser gyro cavity is larger in one direction than the other, the laser gyro is biased away from the lock-in region.

Either of these general techniques can be employed in two ways: by holding the bias fixed, measuring the input rate or angle (Fig. 12) and observing differences in the laser output due to input rate; or by introducing a negative-to-positive alternating bias (Fig. 13).

One method of producing a fixed bias is to rotate the entire gyro, producing an input rate and angle, and thus biasing the gyro away from the lock-in region. The gyro output is proportional to this bias, plus any input rates to the entire gyro. Therefore, by subtracting the bias angle vs. time from the gyro output, only the desired input angle is left. This technique also can be employed using elements in the cavity to produce a fixed bias, and subtracting that bias in the output in order to measure the actual input rate and angle.

Fixed-bias techniques require strict stability, and are subject to errors arising from drifts or changes in the bias magnitude or the inherent gyro linearity. For example, an internal bias of 10^6 degrees per hour must be stable to one part in 10^8, to measure input rates of 10^{-2} degree per hour.

In an effort to reduce this absolute requirement for stability, the bias may be oscillated from positive to negative states. Since the gyro is an integrating-rate gyro, only the net rotation angle appears in the output. Therefore, the laser is biased out of the lock-in region most of the time, and the gyro operation integrates the input rate. This oscillation reduces the requirement for absolute magnitude stability. The bias technique can be employed using either optical means, such as varying the magnetic field of the internal bias element, or by mechanical means, such as oscillating the entire gyro.

One method of accomplishing this ac bias is to oscillate (dither) the entire gyro at a frequency of 20-40 Hz, at an amplitude of several hundred arc seconds. Dithering can be accomplished by a number of electromechanical methods, causing the input rate to the gyro to vary sinusoidally from a maximum positive value to a maximum negative value. An additional input to the gyro will add to this bias rate, increasing its value during one half of the bias cycle, and decreasing its value during the other half. Since the laser gyro is an integrating-rate gyro, the bias integrates to zero. The output, due to the input rate, will appear as a net accumulation of the output cycles. The slope of this accumulation of counts, or angle, is the input rate. Experiments and techniques for biasing are being pursued in many laboratories; the bias technique is one of the most important design aspects of the laser gyro.

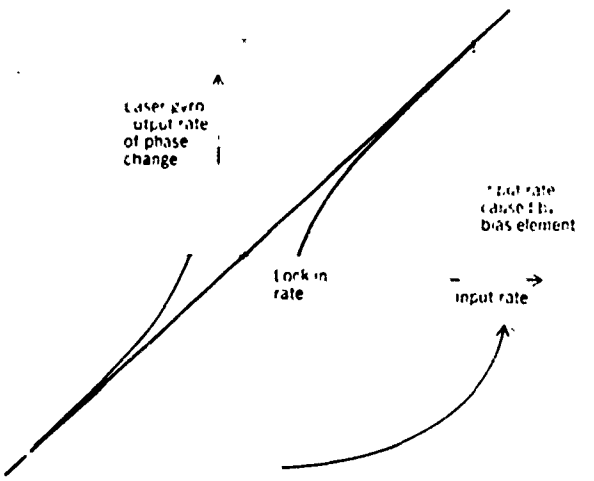

FIGURE 12. Laser gyro fixed bias.

FIGURE 13. Laser gyro alternating-bias technique.

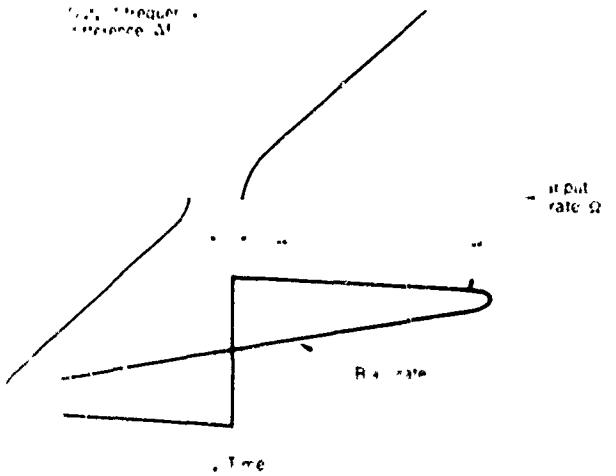

Other problems

In addition to these problems of lock-in, current balance, etc., there are several other factors that must be considered. The role of multimoding* is particularly important in the operation of the laser gyro; the role of differential loss and gain factors can be of dominant importance in some laser gyro systems.[3] There are other fac-

* Multimoding is the phenomena of more than one frequency (mode of oscillation) traveling around the cavity in each direction.

tors such as linearity, stability, and alignment each of which is an interesting discussion in itself. For our purposes it is important to note that these additional problems and factors all appear to have solutions in keeping with the general objective of a simple, low-cost device.

The future

At present, the laser gyro is in advanced research and development, making promising progress toward an accurate, low-cost instrument. The fate of the laser gyro is difficult to predict beyond three to five years in the future; but it is clearly not limited by fundamental considerations (basic line-width analysis shows that the gyro has a limit of less than 10^{-4} degree per hour), but by construction, cleanliness, bias techniques, and other factors. The progress of the laser gyro, as measured by its ability to measure low rates accurately, has been quite rapid. Since the first announced laser gyro, in early 1963,[7] of 1 m² in area and a threshold of 50 degrees per hour, the published performance has improved to about a 0.1 degree per hour,[8] with gyro areas more than an order of magnitude smaller than the first gyro. Further improvements are to be expected, as well as additional problems that have not as yet been identified or solved. The future should see laser gyros in many applications requiring low cost, lack of acceleration sensitivity, and high rate capability; such requirements will make the laser gyro the indisputable choice over other, more conventional, sensors.

REFERENCES

1. Landau, L., and Lifshitz, E., *Classical Theory of Fields*. Cambridge, Mass.: Addison-Wesley, 1951.

2. Post, E. J., "Sagnac effect," *Rev. Mod. Phys.*, vol. 39, pp. 475-493, Apr. 1967.

3. Michelson, A. H., and Gale, H. G., "The effect of the earth's rotation on the velocity of light," *Astrophys. J.*, vol. 61, p. 140, Apr. 1925.

4. Rosenthal, A., "Regenerative circulatory multiple-beam interferometry for the study of light-propagation effects," *J. Opt. Soc. Am.*, vol. 52, pp. 1143-1148, Oct. 1962.

5. Schawlow, A. L., and Townes, C. H., "Infrared and optical masers," *Phys. Rev.*, vol. 112, pp. 1940-1949, 1958.

6. Townes, C. H., "Some applications of optical and infrared masers" in *Advances in Quantum Electronics*, X. X. Singer, ed. New York: Columbia University Press, 1961, pp. 9-11.

7. Macek, W. M., and Davis, D. T. M., Jr., "Rotation rate sensing with traveling-wave ring lasers," *Appl. Phys. Letters*, vol. 2, pp. 67-68, 1966.

8. Lee, P. H., and Atwood, J. G., "Measurement of saturation induced optical nonreciprocity in a ring laser plasma," *IEEE J. Quantum Electronics*, vol. QE-2, pp. 235-242, Sept. 1966.

9. Hutchings, T. J., Winocur, J., Durrett, R. H., Jacobs, E. D., and Zingery, W. L., "Amplitude and frequency characteristics of a ring laser," *Phys. Rev.*, vol. 152, pp. 467-473, 1966.

BIBLIOGRAPHY

Adler, R., "A study of locking phenomena in oscillators," *Proc. IRE*, vol. 34, pp. 351-357, June 1946.

Aronowitz, F., "Theory of traveling-wave optical maser," *Phys. Rev.*, vol. 139, pp. A635-A646, 1965.

Aronowitz, F., and Collins, R. J., "Mode coupling due to backscattering in a He-Ne traveling-wave ring laser," *Appl. Phys. Letters*, vol. 9, pp. 55-58, 1966.

Bogaev, S. N., Kuznetsov, V. S., Troitskii, Yu. V., and Troshin, B. I., "Spectral characteristics of a gas laser with traveling wave," *JETP Letters*, vol. 1, no. 4, pp. 114-116, 1965.

Bogaev, S. N., Troitskii, Yu. V., and Troshin, B. I., "The polarization of radiation and the frequency characteristics of ring lasers with a triangular resonator," *Opt. Spectr. USSR*, pp. 768-769, 1964.

Bogaev, S. N., Belenov, E. M., and Letokhov, V. S., "Diffraction synchronization of optical masers," *Sov. Phys.-Doklady*, vol. 10, pp. 236-238, 1965.

Batifol, E., and Pecile, D., "Effect of the flow of the active medium of a ring gas laser," *Phys. Abstr.*, vol. 72, pp. 3128-3146, 1967.

Belenov, E. M., Markin, E. P., Morozov, V. N., and Oraevskii, A. N., "Interaction of traveling waves in a ring laser," *JETP Letters*, vol. 3, pp. 54-58, 1966.

Bershtein, I. L., "Frequency-pulling band of a laser oscillator," *Sov. Phys.-Doklady*, vol. 10, pp. 607-609, 1966.

Bershtein, I. L., and Zaitsev, Yu. I., "Operating features of the ring laser," *Sov. Phys. JETP*, vol. 22, pp. 663-667, 1966.

Bertem, F., and Petit, F., "Sur l'effet de perturbations apportées aux miroirs dans un laser," *Compt. Rend. Acad. Sci. (Paris)*, vol. 259, pp. 2980-2983, 1964.

Bridges, T. J., and Rigrod, W. W., "Output spectra of the argon ion laser," *IEEE J. Quantum Electronics*, vol. QE-1, pp. 303-308, Oct. 1965.

Catherin, J. M., and Dessus, B., "Traveling wave laser gyrocompass," presented at 1967 Conf. on Laser Engineering and Applications, Washington, D. C., June 6-9.

Christiansen, D., "Laser gyro comes in quartz," *Electronics*, 1966.

Collins, S. A., Jr., and Davis, D. T. M., Jr., "Modes in a triangular ring optical resonator," *Appl. Opt.*, vol. 3, pp. 1314-1317, 1964.

de Lang, H., "Derivation of the relation between two weakly coupled nonlinear optical oscillators," *Appl. Phys. Letters*, vol. 9, pp. 205-207, 1966.

Dessus, B., and Catherin, J. M., "Effets non réciproques de couplages dans un laser en anneau," *Comp. Rend. Acad. Sci. (Paris)*, vol. 262, pp. 1691-1694, 1966.

Fenster, P., and Kahn, W. K., "Single-beam-laser rotation-rate sensor," *Electron. Letters*, Sept. 1966.

Hercher, M., Young, M., and Smoyer, C. B., "Traveling-wave ruby laser with a passive optical isolator," *J. Appl. Phys.*, vol. 36, p. 3351, 1965.

Itzhak, I., "A circular ring laser," *Proc. IEEE (Correspondence)*, vol. 53, p. 164, Feb. 1965.

Khromykh, A. M., "Ring generator in a rotating reference system," *Sov. Phys. JETP*, vol. 23, pp. 185-186, 1966.

Klass, P. J., "Laser unit challenges conventional gyros," *Aviation Week*, Sept. 12, 1966.

Klimontovich, Yu. L., Kuryatov, V. N., and Landa, P. S., "Wave synchronization in a gas laser with a ring resonator," *Sov. Phys. JETP*, vol. 24, pp. 1-7, 1967.

Letokhov, V. S., and Markin, E. P., "On the statistics of laser emission," *Sov. Phys. JETP*, vol. 20, pp. 509-510, 1964.

Macek, W. S., Schneider, J. R., and Salamon, R. M., "Measurement of Fresnel drag with the ring laser," *J. Appl. Phys.*, vol. 35, pp. 2556-2557, 1964.

Podgorski, T., and Aronowitz, F., "Langmuir flow effects in the laser gyro," presented at 1967 Conf. on Laser Engineering and Applications, Washington, D. C., June 6-9.

Post, E. J., and Yildiz, A., "Cavity resonances in accelerated systems," *Phys. Rev. Letters*, vol. 15, pp. 177-178, 1965.

Proctor, E. K., "On the minimum detectable rotation rate for a laser rotation sensor," *Proc. IEEE (Correspondence)*, vol. 51, p. 1035, July 1963.

Ratemik, H. J., Stadt, H. v. d., Velzel, C. H. F., and Dijkstra, G., "Development of a ring laser for polarimetric measurements," *Appl. Opt.*, vol. 6, pp. 813-820, 1967.

Rigrod, W. W., "The optical ring resonator," *Bell System Tech. J.*, pp. 907-916, 1965.

Rigrod, W. W., and Bridges, T. J., "Bistable traveling-wave oscillations of ion ring laser," *IEEE J. Quantum Electronics*, vol. QE-1, pp. 298-303, Oct. 1965.

Smith, R. C., and Watkins, L. S., "A proposed method for reducing the locking frequency of a ring laser," *Proc. IEEE (Correspondence)*, vol. 53, p. 161, Feb. 1965.

Tang, C. L., and Statz, H., "Phase-locking of laser oscillators by injected signal," *J. Appl. Phys.*, vol. 38, pp. 323-324, 1967.

Thomson, A. F. H., and King, P. G. R., "Ring-laser accuracy," *Electron. Letters*, Oct. 1966.

Walsh, P., and Kemeny, G., "Laser operation without spikes in a ruby ring," *J. Appl. Phys.*, vol. 34, pp. 956-957, 1963.

White, J. A., "Stability of traveling waves in lasers," *Phys. Rev.*, vol. 137, pp. A1651-A1654, 1954.

Zaitsev, Yu. I., "Radiation fluctuations in a gas laser," *Sov. Phys. JETP*, vol. 23, pp. 349-354, 1966.

Zhelnov, B. L., Kazantsev, A. P., and Smirnov, V. S., "Mode interaction in a gas laser," *Sov. Phys. JETP*, vol. 23, pp. 1291-1295, 1966.

Zhelnov, B. L., Kazantsev, A. P., and Smirnov, V. S., "Stimulated traveling-wave radiation in lasers," *Sov. Phys.-Solid-State*, vol. 7, pp. 2276-2279, 1966.

APPENDIX E

PREDICTED EFFECTS OF X-RADIATION UPON THE GLOW DISCHARGE AND OUTPUT SIGNAL OF A HELIUM-NEON LASER

APPENDIX E

PREDICTED EFFECTS OF X-RADIATION UPON THE GLOW DISCHARGE AND OUTPUT SIGNAL OF A HELIUM-NEON LASER

1.0 INTRODUCTION

(U) When a glow discharge is exposed to intense X-radiation, the primary effect is an increase in the conductivity of the plasma due to increased ionization of the gas and liberation of electrons from walls and electrodes. The X-radiation will generally also affect the discharge external circuit (power supply, etc.). However, this analysis will only consider the effect of the X-radiation on the positive column of the glow discharge. For this analysis it is assumed that the power supply and ballast remain constant, no shunting of the tube takes place because of ionization of the surrounding air, and the increased electron emission from the cathode under X-ray exposure is negligible compared to the increased volume ionization in the glow discharge.

(U) If no damage occurs to laser resonator components (e.g., the multi-layer dielectric mirrors), the effect of the X-ray exposure on the laser is assumed to be related to the first order of the increased electron density in the tube. This can be treated as a fictitious increase in current. The performance of the laser as a function of discharge current is well known.

2.0 PROPERTIES OF THE GLOW DISCHARGE

(U) The positive column of a glow discharge is the region of the discharge bounded at the cathode end by the Faraday dark space and at the anode end by the anode dark space (Reference 1, 2, 3, and 4). The oppositely directed waves traveling around a ring laser pass through this region. The positive column contains ions, electrons, and neutral gas molecules. In pure noble gases only positive ions are present. The neutral gas may exist either in the ground state or in various excited states.

(U) In the dc discharge tube both positive ions and electrons contribute to the current flowing through the tube. However, the current in the positive column is almost totally carried by the electrons because of the small mobility and drift velocity of the heavy positive ions. It is assumed that the total current through the tube is equal to the electron current (Reference 5).

$$i = i_+ + i_e \cong i_e \qquad \text{(B-1)}$$

The complex conductivity due to electrons in the positive column is given by Brown[4] as

$$\sigma = \sigma_r + j\ \sigma_i \qquad \text{(B-2)}$$

$$\sigma_r = \frac{ne^2}{m}\left(\frac{\nu_e}{(\omega^2 + \nu_e^2)}\right) \qquad \text{(B-3)}$$

$$\sigma_i = -\frac{ne^2}{m}\left(\frac{\omega}{(\omega^2 + \nu_e^2)}\right) \qquad \text{(B-4)}$$

For a direct current $\omega = 0$ and

$$\sigma = \sigma_r = \frac{ne^2}{m\nu_e} \qquad \text{(B-5)}$$

where n is the electron density in number per cubic meter, e is the electronic charge in coulombs, m is the electronic mass in kgms and ν_e is the electron collision frequency in the gas discharge in sec^{-1}.

(U) Under the assumption that the electrons have a Maxwellian velocity distribution, the collision frequency can be calculated if the electron temperature and mean free path are known. Young (Reference 6) gives the electron temperature as a function of He-Ne ratio and pD (pressure X tube diameter) values. In his paper the electron temperature T_e is a function only of the product pD, the nature of the gases, and their relative concentrations, and is independent of the current through the tube or the plasma density.

(U) Brown (Reference 7) gives the electron collision frequency as:

$$\nu_e = \frac{v}{\lambda_e} \qquad \text{(B-6)}$$

where the electron speed v is

$$v = \sqrt{\frac{8kTe}{\pi m}} \qquad \text{(B-7)}$$

and the electron mean free path is

$$\lambda_e = \frac{1}{pP_c} \qquad \text{(B-8)}$$

where P_c is a collision probability. The electron speed v is in cm/s, the mean free path in cm, Boltzmann's constant in ergs/mode °K, and the pressure p in torr. In the He-Ne laser the gas fill ratio is typically He : Ne :: 10 : 1 so that the gas may be treated as pure He for collision considerations. Brown (Reference 7) gives P_c in He as a function of electron temperature in volts, so that λ_e may be found.

(U) In the glow discharge tubes shown in Figure B-1, the 0.070 inch (1.8 mm) inside diameter tube has been built and a voltage-current plot made for a gas fill of 8 torr He-Ne at a 5.7 : 1 ratio, (see Figure B-2). With 1 milliamp of current flowing through the tube the voltage drop across the tube was 900V. Since the discharge was normal the voltage drop at the cathode was about 150V. Neglecting the drops in the large cathode entrance tube and at the anode the gradient in the positive column of the discharge tube is

$$X = \frac{V_T - V_c}{I} \quad \frac{900 - 150}{4 \times 2.5} = \frac{75 \text{ v}}{\text{cm}} = 7500 \frac{\text{v}}{\text{m}} . \qquad \text{(B-9)}$$

The conductivity is

$$\sigma = \frac{i_o}{AX} \qquad \text{(B-10)}$$

where A is the cross-sectional area of the discharge tube. At $i_o = 10^{-3}$ amp and with $A = 2.5 \times 10^{-6} m^2$

$$\sigma = \frac{10^{-3}}{2.5 \times 10^{-6} \times 7500} = 5.3 \times 10^{-2} \frac{\text{mhos}}{\text{m}} . \qquad \text{(B-11)}$$

For this tube pD = 8 torr x 1.8 mm = 14 torr-mm and the electron temperature (Reference 6) $T_e = 4.5 \times 10^4$ °K or 5.8 eV. The corresponding collision probability (Reference 7). P_c = 16/torr-cm. Thus the electron mean free path from equation (B-8) is $\lambda_e = 7.8 \times 10^{-3}$ cm. This agrees well with the value calculated from kinetic theory (Reference 5). The electron speed from equation (B-7) is 1.3×10^8 cm/s, so that the collision frequency from equation (B-6) is 1.4×10^{10} sec^{-1}. From the above information the electron density can be found from equation (B-5).

$$n = \frac{\sigma m \nu_e}{e^2} \qquad \text{(B-12)}$$

$$= \frac{5.3 \times 10^{-2} \times 9.1 \times 10^{-31} \times 1.4 \times 10^{10}}{(1.6 \times 10^{-19})^2}$$

$$= 2.6 \times 10^{16} \text{ m}^{-3} = 2.6 \times 10^{10} \text{ cm}^{-3}$$

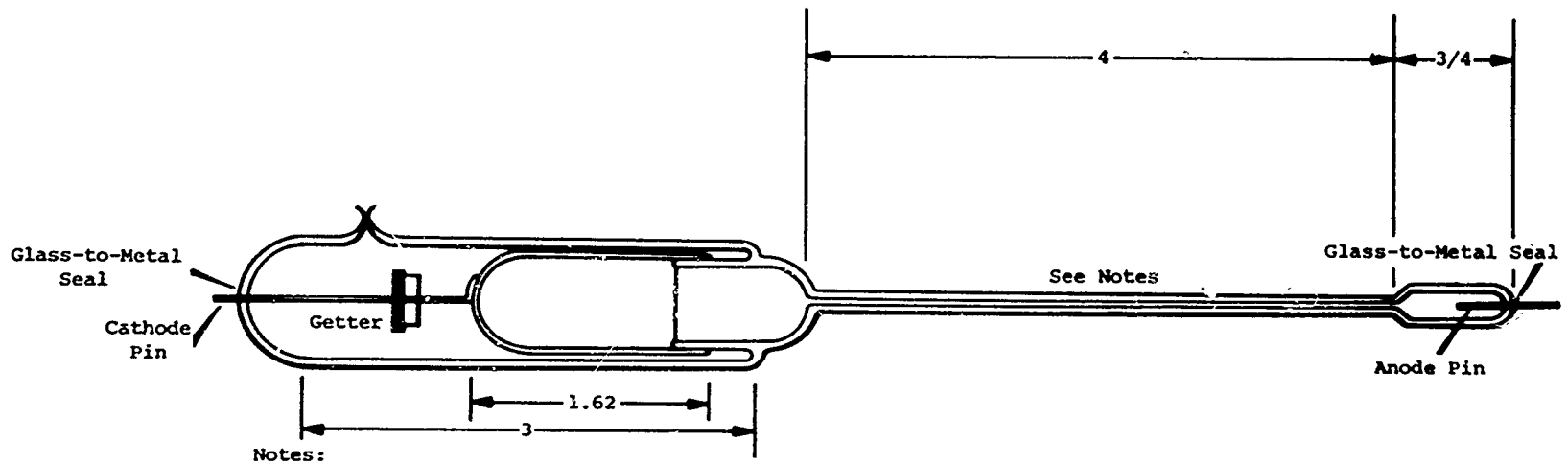

Figure B-1. (U) Glow Discharge Tube

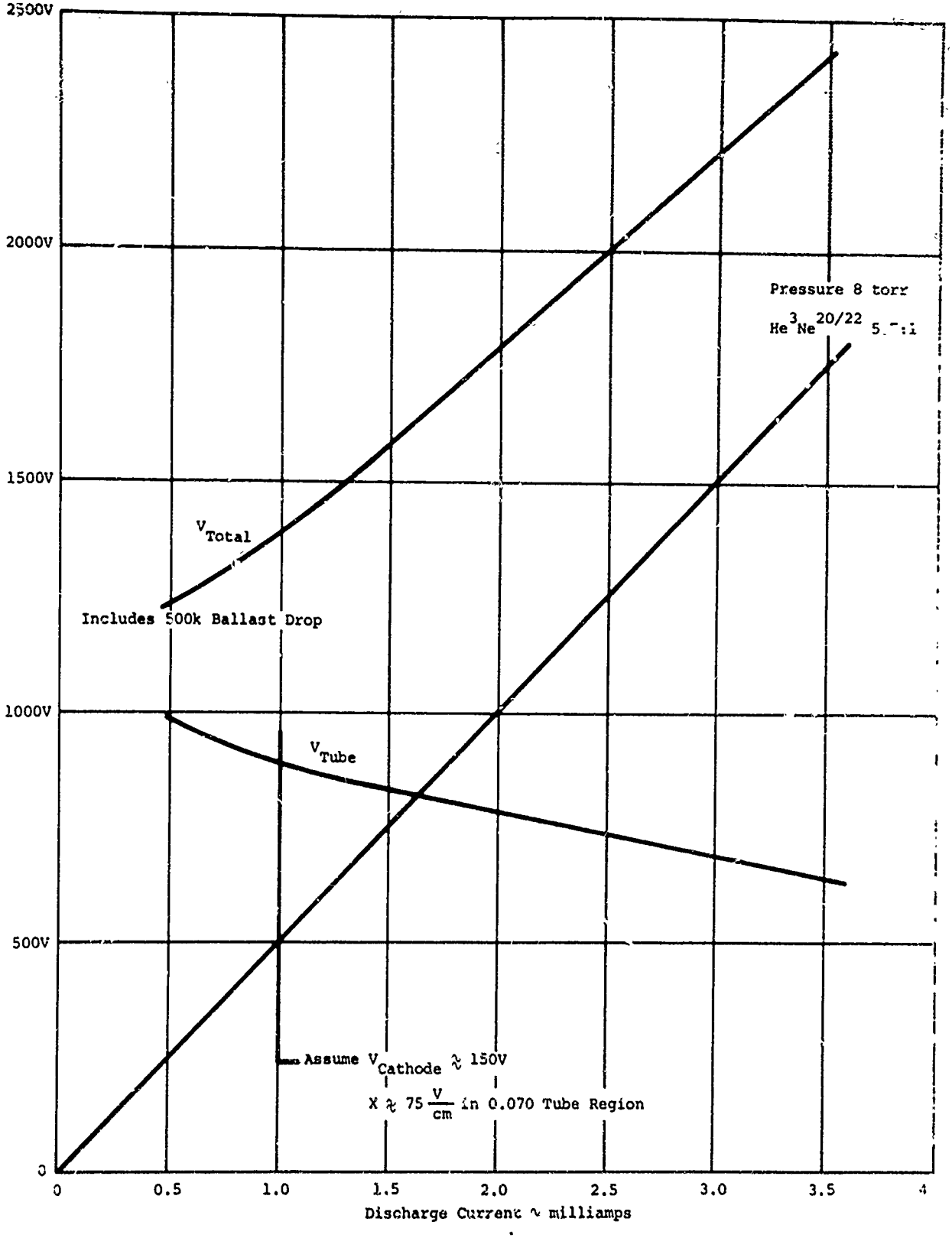

Figure B-2. (U) Voltage Current Plot for a Gas Fill of 8 Torr He-Ne at a 5.7:1 Ratio

3.0 BEHAVIOR OF THE POSITIVE COLUMN UNDER X-RADIATION

(U) When a beam of X-rays impinges on the glow discharge tube the immediate effect is the creation of electron-ion pairs. The resultant increase in electron density will effectively increase the conductivity of the tube and result in an increased current flow (equation B-5). Since the photon-atom interaction time is exceedingly small the increase in electron density will in all probability follow the increase in X-ray intensity. However, the increase in current through the tube will be limited by the external circuit parameters.

(U) The additional electrons should reach thermal equilibrium in a time two or three orders of magnitude longer than the collision time $\tau_c \approx 1/\nu_e \approx 10^{-10}$ second. (The energy lost by an elastic collision of an electron of mass m with an atom of mass M is on the average 2 m/M, although the fraction lost in an inelastic collision may be appreciably higher. The time also depends on the initial electron energy obtained from the X-ray field.) Since the population inversion necessary to generate the lasing action is created by electron-atom collisions, the laser is expected to react to the increase in electron-density in a time on the order of $10^3\ \tau_c$. The actual laser behavior can then be described in terms of a fictitious current i_c which is just

$$i_f = \frac{n_x}{n}\ i_o \qquad \text{(B-13)}$$

where n_x is the electron density function in the presence of X-radiation and n is the normal electron density present in the tube when the unperturbed current i_f flows through it. Note that i_f is not the increased current flow through the tube due to the increased conductivity. The current flow through the tube will lag the increase in electron density with a time constant associated with the complete electrical circuit, including power supply. In addition, the magnitudes will be different.

(U) When the X-radiation is removed from glow discharge tube the decay in n_x to n is governed by the electron recombination time. Electrons are removed from the gas by volume recombination with positive ions or by diffusion to the walls where recombination occurs. Under conditions prevailing in He-Ne discharges the diffusion process to the walls is called ambipolar diffusion and is the governing electron loss mechanism (Reference 2). A value for the volume recombination coefficient α_e in He and in Ne is given by Brown (Reference 7) where.

$$\frac{1}{n} = \frac{1}{n_o} + \alpha_e t \qquad \text{(B-14)}$$

If α_e is on the order of 10^{-8} cm^3/s, in a plasma with n on the order of $10^{11}/cm^3$ and defining a volume recombination time τ_v as the time it takes for n to decrease to n_o/e, then, from equation (B-14), $\tau_v \approx 10^{-3}$ second.

(U) The ambipolar diffusion speed is given by von Engel (Reference 1) as:

$$v_a = -D_a \frac{1}{n} \frac{dn}{dr} . \qquad \text{(B-15)}$$

This can be used to make an order of magnitude estimate of the ambipolar diffusion time constant for loss of electrons, τ_a. The Shottky theory of the positive column gives a radial electron distribution described by a Bessel function of zero order:

$$n_r = n_o J_o(2.4\ r/a) \qquad \text{(B-16)}$$

where $n_r = 0$ at the wall of the discharge tube, $r = a$. Thus $dn/dr \approx n/a$ where $n_o \approx n$ is assumed. Thus

$$v \approx - \frac{D_a}{a} \qquad \text{(B-17)}$$

where a is the radius of the discharge tube positive column. Now because of ambipolar diffusion

$$\frac{dn}{dt} \approx -2n \frac{V_a}{a} \qquad \text{(B-18)}$$

and

$$\tau_a \approx \frac{a}{2v_a} = \frac{a^2}{2D_a} \qquad \text{(B-19)}$$

(U) According to von Engel, in He

$$D_a p \approx 550 \ \frac{cm^2}{s} \cdot \text{torr}. \qquad \text{(B-20)}$$

Thus, at 8 torr $D_a \approx 69\ cm^2/s$ and $\tau_a \approx 10^{-5}$ second in the 0.09 cm radius tube.

(U) When the X-radiation is removed the electron density will decay with a time constant of $\tau_a \approx 10^{-5}$ second and the laser should return to normal with this time constant.

(U) The change in the actual current flow through the tube can be found from the circuit shown in Figure B-2 and equation (B-5). In the self-start (overvoltage start) configuration, a power supply with a sufficiently high voltage to assure gas breakdown is used and the ballast then chosen to limit the current to the desired value. Assume that $V_s = 2900V$ is required to start the discharge tube and at the desired current of 1 mA the voltage drop across the tube is 900V. The ballast resistance from

$$V_s - i_o R_B = V_T \qquad \text{(B-21)}$$

is $R_B = 2 \times 10^6$ ohm.

(U) When an ionizing pulse of X-radiation falls on the discharge tube the electron density increases. The ionization constant at 8 torr is about 4×10^6 ion pairs/cm^3 rad (Reference 8). Since the maximum X-ray dosage the tube is expected to see is 2×10^4 rads, the concentration of electrons in the tube immediately after exposure is $n_x = 8 \times 10^{10}$/ cm^3 (from X-radiation) + 2.6×10^{10}/cm^3 (from normal current flow) = 11×10^{10}/cm^3. Assuming no change in the electron collision frequency the conductivity of the positive column depends only on the electron density. The conductivity of the tube has two components, the cathode fall part and the positive column part; only the latter is assumed to change. Thus,

$$R_T = R_c + R_p = R_c + \frac{n}{n_x} R_{op} \qquad \text{(B-22)}$$

where R_{op} is the resistance of the positive column when the normal current i_o flows through it. Thus, when the X-radiatic pulse falls on the tube the tube resistance decreases from $R_T = 9 \times 10^5$ ohms to about 3×10^5 ohms. Thus, current flowing through the circuit of Figure B-2 will thus rise from i_o - 1 mA to about i_x = 1.3 mA.

4.0 SUMMARY

(U) Assuming a square wave X-ray pulse impinging on a laser gyro discharge tube (Figure B-3a), the electron density will build up as shown in Figure B-3. The corresponding fictitious current used to describe the laser behavior is shown in Figure 3c. Since gain is a parabolic function of current, laser output as a function of time is as shown in Figure 3d. Finally, discharge current through the tube is as shown in Figure 3e. The numbers indicated are representative of a laser with gain tubes similar to the discharge tube described above.

(U) From the above analysis, it can be concluded that the only significant change in ring laser components is an increase in the output signal strength and perhaps an increase in noise if the laser multimodes when the gain is increased. The laser recovery is fast, on the order of 10 μ's after lifting of the X-radiation.

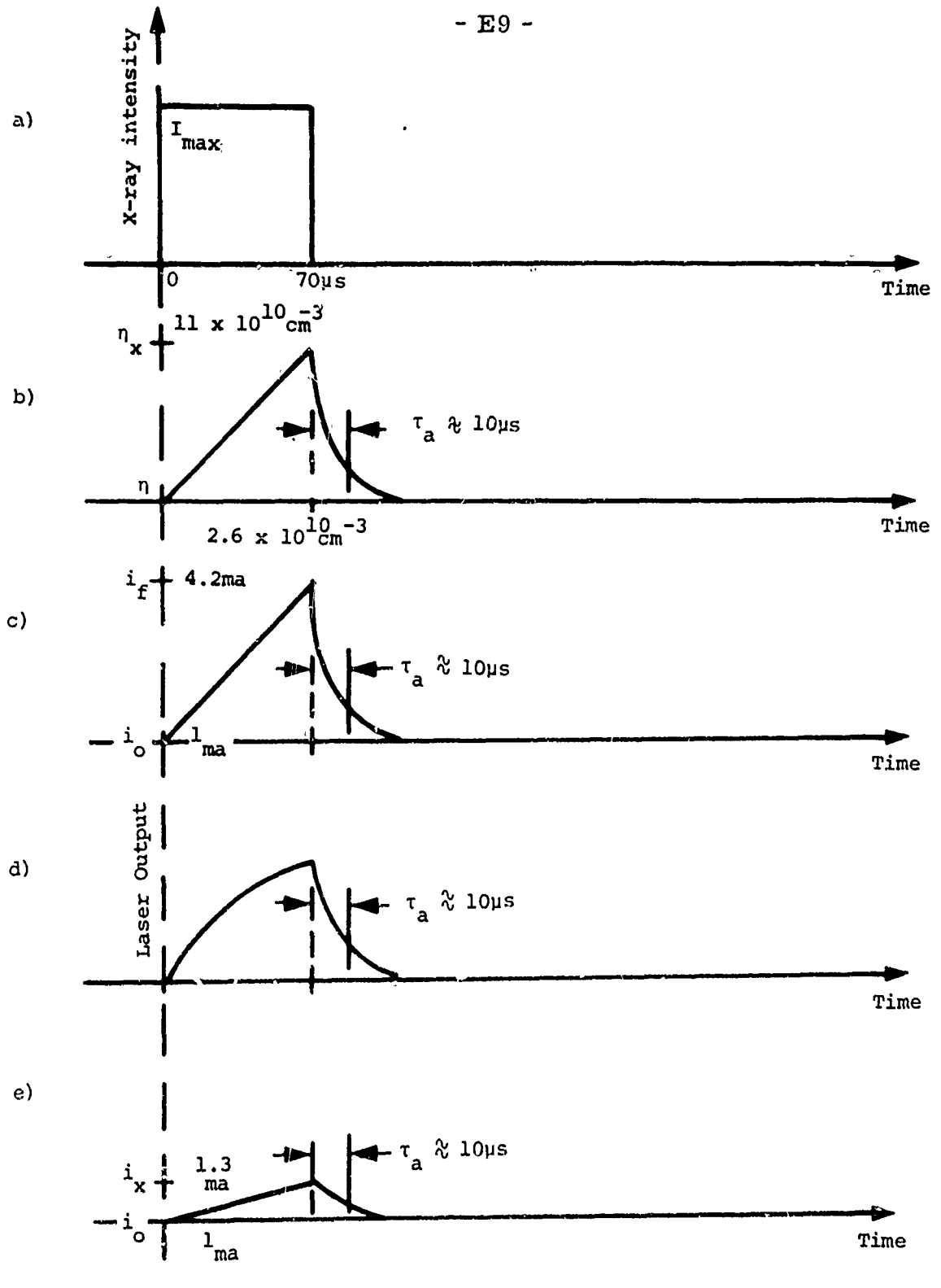

Figure B-3. (U) a) Parameter Changes Due to X-Radiation Pulse, b) Electron Density, c) Fictitious Current, d) Laser Output, e) Discharge Current

REFERENCES

1. A. von Engel, "Ionized Gases," Oxford Press, New York (1965).

2. G. Francis, "The Glow Discharge at Low Pressure," Encyclopedia of Physics, Volume XXII, Gas Discharges II, Springer, Berlin, (1956).

3. J. D. Cobine, "Gaseous Conductors," Dover, New York (1958).

4. S.C. Brown, "Introduction to Electrical Discharges in Gases," Wiley, New York (1966).

5. T.J. Podgorski, "Summary Report - Current Bias Effects in the Laser Gyro," Contract No. PA-01-021-AMC-14533 (Z), August 1967.

6. R.T. Young, "Calculation of Average Electron Energies in He-Ne Discharges," J. Appl. Phys., 36, 2324 (August 1965).

7. S.C. Brown, "Chapter 10 - Conduction of Electricity in Gases," "Handbook of Physics," McGraw-Hill (1958).

8. Private communication, J. Crook.